FROM GENESIS TO JUXTAPOSITION: THE EVOLUTION OF THE IVISARTOQ GREENSTONE BELT, SOUTHWEST GREENLAND

MARIANNE M. MADER

From Genesis to Juxtaposition: The Evolution of the Ivisârtoq Greenstone Belt, Southwest Greenland

by

©Marianne M. Mader, B.Sc. (Hons.)

A thesis submitted to the School of
Graduate Studies in partial fulfillment
of the requirements for the degree of

Master of Science

Department of Earth Sciences
Memorial University of Newfoundland
St. John's, Newfoundland

July, 2005

Abstract

The Ivisârtoq greenstone belt is situated ~40 km south of the Isua greenstone belt within the Godthåbsfjord region of southwest Greenland. This region is part of the Archean gneiss complex of Greenland, a major component of the 3800-2500 Ma North Atlantic Craton. Compared to the Isua greenstone belt, which has been the focus of intense study because it contains some of the oldest known (~ 3.8-3.7 Ga) rocks on Earth, little work has been carried out on the Ivisârtoq greenstone belt. The Ivisârtoq greenstone belt is exceptionally well-exposed in three dimensions with relief of 1200m, and primary features are better preserved here than in any other Archean greenstone belt in Greenland. Consequently, this belt provides an exceptionally good opportunity to characterise early to middle Archean magmatism, deformational processes, and tectonic environments.

The Ivisârtoq greenstone belt was multiply deformed and metamorphosed at amphibolite facies. The belt forms an upright southwest-closing, V-shaped synform. This study concentrated on the 3 km thick southern limb of the synform, where the most complete section of the supracrustal rocks is preserved, and where there are pillow lava structures with way-up indicators. The southern limb was found to comprise a tectonostratigraphy made up of two main components, termed the northern and southern parts. These composite rock units differ in composition and intensity of deformation and are separated by a major high strain zone.

The northern part of the belt is generally less deformed than the southern part and is characterized by heterogeneously deformed amphibolite, derived from variolitic and homogeneous basaltic pillow lavas, interlayered with boudins of olivine-bearing ultramafic rocks and quartz-feldspar-mica gneiss and schist. The southern part consists predominantly of strongly deformed rocks including banded amphibolite, homogeneous granitoid, gabbroic rocks, and a thick layer of predominantly quartz-feldspar-biotite-schist.

New major and trace element geochemical data, LAM ICP-MS U-Pb zircon geochronology, and field mapping have shed new light on the origin and evolution of the Ivisârtoq greenstone belt. This new work indicates that the northern and southern parts of the belt represent discrete packages of rocks that formed in different environments and were juxtaposed after ~2895 Ma, after the main volcanism associated with each part had ceased. Each package of rocks suffered separate deformational events before juxtaposition: two discrete deformational phases were recognized in the less deformed

northern part, whereas the southern part was much more intensely deformed and individual events could not be differentiated.

Crustal contamination signatures of the amphibolites in the northern part of the belt suggest formation in a back-arc basin environment, in which the basaltic magma ascended through *thin*, patchy or immature crust. A U-Pb zircon age of an intrusive tonalite sheet demonstrates that the northern basaltic pillow lavas were deposited before ~3165 Ma.

In contrast, the southern part of the belt appears to have formed on a *thick* continental crust. This interpretation is based on several lines of evidence: crustal contamination signatures of the banded amphibolite, the presence of a thick sequence of quartzofeldspathic metasedimentary rocks, an A-type granitoid, and a horizon of metamorphosed meymechite, which is indicative of deep melting of subcontinental mantle. A maximum age of ~2895 Ma was determined for the deposition of the southern metasedimentary rocks.

The interpreted juxtaposition of the northern and southern packages of the Ivisârtoq belt is consistent with lateral collisions of terranes perhaps by plate tectonic processes.

Acknowledgements

This work was supported by NSERC through a grant to John Myers and through a postgraduate scholarship (PGS-B).

Many people contributed to the production and completion of this project. Firstly, I would like to thank my supervisors John Myers and Paul Sylvester. John provided me with the opportunity to work in Greenland, which is an experience I will always treasure. John's mapping expertise, knowledge of Greenland geology and attention to detail were greatly appreciated. Paul is thanked for his clear vision and guidance, especially during the final stages of the project. His immense geochemical knowledge was of great benefit for my research and his sense of humour and patience were of great benefit to my sanity.

As with all scientific research, there are many people 'behind the scenes' without whom, the project could not have been completed. The 'fifth floor' technical staff at MUN including, Pam King (XRF), Mike Tubrett (LAM-ICP-MS), Marc Poujol (TIMS), and Lakmaili Hewa (ICP-MS), helped with many aspects of sample analysis and/or preparation, and their ever-ready smiles always seemed to lighten the workload. Rick Soper is thanked for preparation of thin sections and I am grateful to Darren Smith for his computer support.

My field season would not have been possible without the support of the Greenland Bureau of Minerals and Petroleum and the Geological Survey of Denmark and Greenland (GEUS). The Department of Geological Mapping in Copenhagen is also thanked for help with map production. I would especially like to thank Brain Chadwick for the use of his immaculate field maps.

I greatly appreciate the assistance and companionship of my field assistant Andrea Markey and colleague Julie Brown, who provided fascinating conversations, great food, and made living in remote Greenland truly enjoyable.

I am extremely grateful to my family and friends, who provided constant encouragement throughout my studies, notably, my parents Karen and Dennis Mader, my office-mate and confidant Tanya Tettelaar, Catherine Gribbin, Owen Gaskill, Cindy O'Driscoll, Joanne O'Neill, Jason Rhinelander, Don Wright, and of course, the ever-changing Franklyn Inn Crew. Carol Bartlett and Alison Gollop are especially thanked for their unwavering support and friendship. I am extremely thankful to have had the opportunity to live in Newfoundland. St. John's has become my 'second home' and the friendships I have made here will undoubtedly last a lifetime.

Table of Contents

Chapter 2: Geology and Geochronology of the Ivisârtoq Greenstone Belt

Chapter Three: Geochemistry of the Ivisârtoq greenstone belt

List of Tables

List of Figures

List of Maps

Chapter One: Introduction and Background

1.1 INTRODUCTION

Greenstone belts are a geologically and economically important component of Archean[1] (>2.5 Ga) terrains. They mainly comprise deformed and metamorphosed volcanic rocks with a smaller amount of intrusive sheets (sills and dykes) and metasedimentary rocks. They typically form long narrow belts between larger areas of granitoid gneisses. These associations are known as granite-greenstone terrains and form a major component of Archean continental crust (Goodwin, 1991).

This research project is part of a larger project titled "Archean Tectonics of the Godthåbsfjord region, Southwest Greenland" led by Dr. John Myers at the Memorial University of Newfoundland, which is supported by the Denmark and Greenland Geological Survey (GEUS), the Greenland Bureau of Minerals and Petroleum, and NSERC. The project is investigating a transect across the Godthåbsfjord region of southwest Greenland, studying the geological evolution and tectonic history. This region encompasses early, middle, and late Archean rocks and includes the most extensive, best exposed and most intensely studied early Archean rocks on Earth (Myers and Crowley, 2000). The Ivisârtoq greenstone belt lies 40 km southeast of the Isua greenstone belt (also known as the Isua supracrustal belt) within the Archean gneiss complex of southwest Greenland. The Isua region has been the focus of intense study because it contains some of the oldest known (~3.8-3.7 Ga) rocks on Earth. However, relatively little research has

[1] In this study the division of the Archean into early (4000-3400 Ma), middle (3400-3000) Ma, and late (3000-2500 Ma) follows the division in Palmer, A.R. (1983).

been conducted within the Ivisârtoq belt. This thesis focuses on the Ivisârtoq greenstone belt which is fundamental for understanding the Archean geological evolution of the wider Isua-Ivisârtoq region.

The thesis will investigate several aspects of the Ivisârtoq greenstone belt, including the protolith lithology, geochronology, and geochemistry of the various tectonostratigraphic units. The basis for this research is field mapping at 1:10 000 scale, which improves upon a map at 1:20 000 (Chadwick, unpublished) and upon the most recent published map which was at a scale of 1:100 000 (Chadwick and Coe, 1988).

1.2 STRUCTURE OF THESIS

The layout of this thesis includes four chapters. The first chapter provides an introduction to the thesis topic and area. It includes general background information such as regional geology, an overview of the thesis area, objectives of the thesis, and methodology. The second and third chapters are laid out in the style of independent research papers which are prepared as "stand alone" documents. Each of these chapters includes an introduction, methodology, general text body, and conclusions. As a result some repetition between these chapters is unavoidable. The second chapter focuses on the nature of the Ivisârtoq greenstone belt. The main components of the belt are re-evaluated in terms of protolith lithologies and the age of the belt is addressed. The third chapter concentrates on the geochemistry of the different lithological units within the belt. The fourth chapter provides a summary that unites the content of the previous chapters into a cohesive outline of the geological evolution of the Ivisârtoq greenstone belt.

1.3 REGIONAL GEOLOGY

1.3.1 North Atlantic Craton

The Ivisârtoq greenstone belt is part of the Archean gneiss complex of Greenland which forms a major part of the 3900-2500 Ma North Atlantic Craton (Fig. 1.1; Nutman, 1997). The North Atlantic Craton is a remnant of a larger Archean continent and is truncated by younger orogens: the Nagssugtoquidian belt to the north; the Torngat orogen to the west in eastern Labrador; and to the east, the Archean Lewisian complex of north-western Scotland which was reworked in the Laxfordian orogeny. The eastern margin of the North Atlantic Craton is obscured by the Caledonian fold belt. The North Atlantic Craton is composed of numerous complexes which consist of heterogeneously deformed, amphibolite to granulite facies gneisses. Tonalitic-trondhjemitic-granodioritic gneisses (TTG) are the most abundant rocks within these complexes, whereas supracrustal units, dominated by mafic metavolcanic rocks, make up at most 20% of the complexes.

1.3.2 Greenland Archean Gneiss Complex

The Greenland Archean gneiss complex is derived primarily from basaltic volcanic and sedimentary rocks that were intruded by middle to late Archean tonalite and granodiorite, and a small amount of granite and diorite (Myers and Crowley, 2000). These rocks were repeatedly deformed and metamorphosed, resulting in the formation of new tectonic layering and in various periods of recrystallization (Bridgwater et al., 1976). Much of the Greenland Archean gneiss complex is obscured by the Greenland Inland Ice cap or lies on continental shelves and is therefore unavailable for detailed study.

However, the glaciated periphery of Greenland is well exposed and provides an excellent opportunity for investigations of middle to deep levels in the Archean crust (Nutman, 1997). The Godthåbsfjord region of the southwest coast of Greenland contains some of the oldest rocks on Earth (~3.8-3.7 Ga; Nutman et al., 1996) and is thought to host the oldest evidence of life on Earth (Mojzsis et al., 1996), and therefore has attracted more attention than other parts of the Greenland Archean.

1.3.3 Godthåbsfjord Region

The Godthåbsfjord region of Greenland is located in the centre of the Greenland Archean gneiss complex on the west coast near Nuuk (formerly Godthåb and Nûk) (Fig. 1.2). Within this region, early Archean quartzofeldspathic gneisses and early and middle Archean supracrustal rocks were intruded by and were tectonically interleaved with late Archean plutonic rocks.

Detailed mapping of the area began in the 1960's and 1970's. During this time an informal lithotectonic nomenclature was introduced which aided further field mapping and description of the rocks. The terms Isua supracrustal belt, Ameralik dykes, Amîtsoq gneiss, Nûk gneisses, Akilia association, and Malene supracrustals were used to describe different rocks whose relative ages could be determined by field relationships. It was widely inferred that many of the rocks grouped under one name were the same age and were cogenetic (Nutman et al., 1996).

These names have become entrenched in geological literature which in some cases has fostered confusion as many of the terms group together rocks of different origin

and age (Nutman et al., 1996). Some of the terms have been redefined and new names have been introduced to alleviate this problem. The 'old' and 'new' terms are discussed in the following section.

Early Archean rocks

Thin, tabular bodies of amphibolite derived from basic dykes were termed ***Ameralik dykes*** by McGregor (1968). Ameralik dykes with primary textures and minerals have been observed in the Isukasia area, where they are thought to be the least deformed. Based on cross-cutting relationships several generations of compositionally diverse dykes have been described (Chadwick, 1981).

Early studies in the Godthåbsfjord region by McGregor (1968, 1973) subdivided the quartzofeldspathic gneisses into two groups, an older and a younger group, based on the presence or absence of Ameralik dykes. In small areas of relatively low strain, the older gneisses, called ***Amîtsoq gneisses*** by Black et al. (1971), were observed to be cut by the Ameralik dykes. In most of the Godthåbsfjord region, the dykes and host rocks were deformed together to form a common gneissosity, however the presence of the Ameralik dykes, even as concordant layers of amphibolite, was used to distinguish the unit as Amîtsoq gneiss. The term ***Nûk gneisses*** was used to describe younger calc-alkaline rocks that post-date the Ameralik dykes.

The relative ages of Amîtsoq and Nûk gneisses were supported during the 1970's, when a multitude of Rb-Sr, Pb-Pb, and U-Pb isotopic studies were conducted. Protolith ages of the Amîtsoq gneisses ranged between ~3.8-3.62 Ga (Black et al., 1971; Moorbath

et al., 1972; Baadsgaard, 1973; Moorbath et al., 1975; Michard-Vitrac et al., 1977) and the Nûk gneisses were determined to range from ~3.0-2.8 Ga (Pankhurst et al., 1973; Moorbath and Pankhurst, 1976). Over time the term Amîtsoq gneisses became synonymous with 'early Archean quartzofeldspathic gneisses in the Nuuk region' (Nutman et al., 1996). The danger with this assumption was that some geologists may have had the impression that all of the Amîtsoq gneisses were derived from the same protolith. In reality, the Amîtsoq gneisses include a considerable range of rock types which have undergone different metamorphic and deformational histories. Some rocks originally mapped as Amîtsoq gneisses were shown to have ages of 3180-3235 Ma (Duke and Nutman, unpublished data; cited in Nutman et al., 1996) and 2920 Ma (Kinny, 1987; Schiøtte et al., 1989). These rocks were excluded from the Amîtsoq gneisses by Nutman et al. (1989). Caution should be used when identifying Amîtsoq gneisses; the presence of Ameralik dykes should not be used as the only evidence supporting their identification and age.

The term ***Akilia association*** was introduced by McGregor and Mason (1977) to encompass all inclusions of rock within Amîtsoq gneisses, excluding the Isua supracrustal belt. Rocks termed the Akilia association included supracrustal rocks, metabasic and ultramafic intrusive rocks, and some rocks of uncertain origin. Due to its significant size, the Isua greenstone belt was given a separate name. The 3800-3700 Ma ***Isua supracrustal belt*** (also referred to as the Isua greenstone belt) is the largest-known body of early Archean supracrustal rocks. This term is still used in literature today

however, it currently refers to the geographical entity and does not necessarily imply that the packages of rocks within the belt were derived from originally related rocks.

Nutman et al. (1996) strongly suggested discontinuing the use of the terms Amîtsoq gneisses and Akilia association because each includes unrelated rocks. In replacement, Nutman et al. (1996) proposed using the term ***Itsaq Gneiss Complex*** which includes all Early Archean rocks (Amîtsoq gneisses, Isua supracrustal belt and Akilia association) of the Godthåbsfjord region. The term was introduced to emphasise the existence of many groups of unrelated early Archean rocks formed over a period of 300 million years. Currently, the term Amîtsoq gneiss is still in use by some geologists and is applied to ~3.65 Ga tonalitic gneisses from the type locality. The term 'Akilia association' is also still in use as an informal term for *all* the enclaves of older rocks in the Amîtsoq gneisses in the Godthåbsfjord region with the exception of those in the Isua greenstone belt (Myers and Crowley, 2000).

Middle - Late Archean rocks

As mentioned above, the term ***Nûk gneisses*** was used to describe calc-alkaline rocks in the Godthåbsfjord region that do not contain Ameralik dykes. The ages of the Nûk gneisses were determined to range from ~3.0-2.8 Ga (Pankhurst et al., 1973; Moorbath and Pankhurst, 1976). McGregor et al. (1991) redefined the term Nûk gneisses based on the theory that the Godthåbsfjord region is composed of different terranes. This was necessary as the 'Nûk gneisses' were reinterpreted as the products of several unrelated events which occurred in different terranes (McGregor et al., 1991). The term

Nûk gneisses has been retained for the rocks around the town of Nuuk and on Sadelø and Bjørneøen, and for other gneisses in the Akia terrane (see Terrane section) that could be correlated with them (3060-2940 Ma; Duke, 1993). The term ***Ikkattoq gneisses***, is used instead of "Nûk gneisses" to describe granodiorite that intruded ~2820-2750 Ma in the Tre Brødre terrane (Friend et al., 1988; Nutman et al., 1989). The tonalitic-granodioritic gneisses (2860-2820 Ma) of the Tasiusarsuaq terrane which had been previously interpreted as Nûk gneisses were not given a collective name.

Large bodies and belts of supracrustal material are observed throughout the Godthåbsfjord region. Early studies by McGregor (1969) collectively labelled the metavolcanic and metasedimentary schists and gneisses in the vicinity of Nuuk as ***Malene supracrustals***. This term was eventually applied to all rocks throughout southwest Greenland having lithological characteristics and structural setting like those of the type units in the Nuuk area. They were thought to have been laid down between 3600 and 3070 Ma, after the formation of the Amîtsoq gneisses and before the intrusion of the Nûk gneisses, respectively (Chadwick and Nutman, 1979; Nutman and Bridgwater, 1983). A study by Schiøtte et al. (1988) questioned the hypothesis that all Malene supracrustal rocks pre-dated the Nûk gneisses. They interpreted a depositional age between ~2900 and ~2650 Ma for two samples using $^{207}Pb/^{206}Pb$ zircon ages from a sensitive high-resolution ion microprobe (SHRIMP). The original hypothesis was therefore found to be invalid and the use of the term Malene supracrustals to represent a single lithostratigraphic unit was discouraged. McGregor et al. (1991) further discouraged the term Malene supracrustals, as different groups of the metavolcanic and

metasedimentary rocks were interpreted to have been formed in separate terranes, and therefore had diverse ages and origins. Some studies have retained the use of the term "Malene supracrustals" for descriptive and historical convenience (e.g. Smith et al., 1992), with the knowledge that these units may not be related.

The term ***Qôrqut granite*** was used by McGregor (1973) to describe a suite of granites found in an elongate zone between Ameralik and Kapisigdlit kangerdluat. Subsequent mapping revealed that the Qôrqut granite and associated pegmatite extend from the vicinity of Færingehavn (~150 km northeast) through Qôrqut to the Inland Ice at Ivisârtoq (Friend et al., 1985 and references therein; Fig. 1.2a). Within the Qôrqut area the granitic rocks were seen to be varied in terms of composition and internal structure; they are markedly polyphase and form a sheeted body. Therefore, Brown and Friend (1980) proposed that the name ***Qorqut granite complex*** should be used for the entire suite of rocks; this term is still in use.

1.3.4 Terrane Model

Early interpretations (prior to the late 1980's) regarded the Godthåbsfjord region as a single tectonic terrane. However, later studies reinterpreted the Godthåbsfjord region in terms of separate terranes, which evolved independently prior to assembly in the late Archean , similar to other granite greenstone terranes, for example Barberton (e.g. Lowe et al., 1999), and the Superior Province (e.g. Percival et al., 2001). This reinterpretation conforms to current models which interpret granite-greenstone terranes as representing higher crustal levels than the gneiss complexes (Percival et al., 2001 and references

therein). Thus, as stated by Friend and Nutman (2005), "greenstone-granite terranes and gneiss complexes probably represent nothing else but different exposure levels through Archean crust, rather than having formed by entirely different mechanisms". Many geologists view the existence of distinctive terranes in the Archean as strong evidence for some form of Archean plate-tectonic process (e.g. Nisbet, 1987).

Within the Godthåbsfjord region Friend et al. (1987) initially defined three mylonite-bounded terranes, including the Færingehavn, Tre Brødre, and Tasiusarsuaq terranes after studying the Færingehavn-Tre Brødre area . This concept was extended to the northeast to include all of the Godthåbsfjord region and a fourth terrane called Akia was recognized (Friend at al., 1988; Nutman et al., 1989). Further detailed mapping was conducted by McGregor et al. (1991) and new terminology was introduced. They grouped the Færingehavn and Tre Brødre terranes together under one name: the Akulleq terrane (McGregor et al., 1991).

The terrane model has been further modified by Friend and Nutman (2005), who have expanded upon their original four terrane model (Friend at al., 1988, Nutman et al., 1989) and have added two new terranes: the Isukasia terrane and the Kapisilik terrane (Fig.1.2b). Friend and Nutman (2005) suggested that in time, as further detailed mapping and geochronology is conducted within the Godthåbsfjord region, the boundaries of these terranes may be modified or perhaps even more terranes may be identified. The following sections provide a brief outline of the most recent model of the six proposed terranes.

Akia terrane

The Akia terrane is the most northerly of the six terranes (Fig. 1.2b) and underwent granulite metamorphism at ~ 3000 Ma. The Akia terrane consists largely of tonalitic (Nûk gneisses), dioritic, trondhjemitic, and granitic gneisses mixed with amphibolite, predominantly derived from volcanic rocks, and with a smaller portion of leucogabbroic and noritic intrusions, all of which formed between 3230 and 3000 Ma (McGregor et al., 1991; Nutman 1997; Myers and Crowley, 2000). The northern extent of the terrane is unknown.

Isukasia terrane

The Isukasia terrane extends from Ujarassuit Nunaat north to the Isukasia area, including the Isua greenstone belt (Fig. 1.2b). The Isukasia terrane has been distinguished from the Færingehavn terrane based on geochronological studies (Friend and Nutman, 2005). This terrane is dominated by ~3800 and 3700 Ma tonalites, ~3650 Ma granite intrusive sheets and ~3700 and 3800 Ma supracrustal, ultramafic and gabbroic rocks (Friend and Nutman, 2005 and references therein). The 3810-3600 Ma gneisses have undergone both ~2960 Ma and ~2700 Ma metamorphism and did not experience early Archean granulite facies metamorphism.

Færingehavn terrane

The Færingehavn terrane (Fig. 1.2b) includes early Archean rocks (3850-3600 Ma) which have undergone early Archean granulite facies metamorphism in most parts

by 3600 Ma (Griffin et al., 1980). This terrane does not appear to contain ~2940 Ma metamorphic overprints based on over a thousand SHRIMP zircon U-Pb analyses on ~50 rocks (data in Nutman et al., 2002 and references therein). The ~2960 Ma metamorphism in the Isukasia terrane distinguishes this terrane from the Færingehavn terrane and indicates that they were separate entities at that time (Friend and Nutman, 2005).

Kapisilik terrane

The Kapisilik terrane, as defined by Friend and Nutman (2005) is located east of the Ivinnguit fault (Fig. 1.2b) and has undergone amphibolite grade metamorphism. The terrane is dominated by ~3000 Ma rocks including tonalitic to granitic orthogneisses which surround supracrustal units dominated by amphibolites, most notably the Ivisârtoq greenstone belt. The Kapisilik terrane is interpreted to be in tectonic contact with early Archean rocks (Isukasia terrane) to the north (Friend and Nutman, 2005).

Tre Brødre terrane

The Tre Brødre terrane is located west of the Kapisilik terrane and is dominated by 2800-2750 Ma Ikkattoq gneisses which contain supracrustal enclaves and anorthosite complex rocks (Friend et al.,1987; Friend et al., 1988). The supracrustal bodies include amphibolites with associated ultramafic rocks as well as metasedimentary rocks, whereas the anorthosite complex rocks include large units of anorthosite, leucogabbro, and the derivatives of gabbros and melagabbros. This terrane has been subjected to upper amphibolite facies metamorphic conditions (Friend et al., 1987).

Tasiusarsuaq terrane

The Tasiusarsuaq terrane, which is the most southerly terrane, was metamorphosed to granulite facies at ~2820 Ma, and subsequently experienced extensive retrogression to amphibolite facies (McGregor et al., 1991; Nutman 1997). The Tasiusarsuaq terrane is dominated by tonalitic-granodioritic gneisses (2920-2800 Ma) that were originally intruded as sheets into metavolcanic rocks (now observed as layers of amphibolites), layered anorthosite sheets, and minor sedimentary units (McGregor et al., 1991; Nutman 1997; Myers and Crowley, 2000).

Tectonic interpretation of terranes

Friend and Nutman (2005) concluded that each terrane is geologically unique. Each one is characterized by distinct quartzofeldspathic gneisses, supracrustal units, and mafic rock inclusions. The terranes are typically separated by mylonitic belts that are interpreted as tectonic breaks. Friend and Nutman (2005) interpreted the early Archean Færingehavn and Isukasia terranes as remnants from a more extensive complex of early Archean crust, that were rifted apart starting ~3500 Myr ago. Later these terranes were juxtaposed with younger terranes of the Nuuk region in several late Archean events.

Assembly of the terranes is interpreted to have taken place in at least two episodes. The first episode involved the intercalation of the > 3600 Ma Isukasia terrane with the 3075-2960 Ma Kapisilik terrane at ~2950 Ma, and was followed by the second episode, in which the composite Isukasia-Kapisilik block was juxtaposed with the

composite Færingehavn and Tre Brødre terranes after 2825 Ma (Friend and Nutman, 2005).

Friend and Nutman (2005) consider it most likely that the Tre Brødre terrane (and associated Færingehavn terrane) are presently structurally above the Kapisilik terrane. Furthermore, on Ujarassuit Nunaat and northern Ivisârtoq, the northern limit of the Kapisilik terrane is interpreted to be structurally above the early Archean rocks to the north which comprise the Isukasia terrane (Fig. 2b; Friend and Nutman, 2005).

Overall, Friend and Nutman (2005) consider the movement and assembly of the individual terranes to be analogous to modern collisional orogeny and interpret this as key evidence for the operation of some form of early Precambrian plate tectonics.

1.4 IVISÂRTOQ GREENSTONE BELT

This section outlines the previous work conducted in the area, provides a brief summary of the local geology, examines outstanding problems, and discusses the thesis goals.

1.4.1 Previous Work

The Ivisârtoq greenstone belt is situated 40 km south of the Isua greenstone belt. The Isua region has been the focus of intense study because it contains some of the oldest known (~3.8-3.7 Ga) rocks on Earth, however, although they are comparable in size, relatively little research has been conducted within the Ivisârtoq belt.

The Ivisârtoq region was initially mapped by mainly helicopter reconnaissance by Walton (1976) and by Allaart et al. (1977). The greenstone belt itself was mapped in more detail by Friend and Hall (1977), who reported pillow structures indicating way-up. Hall (1981) used the field data collected during the summer of 1976 for his PhD, concentrating on petrography, metamorphism, structural geology, and geochemistry of the Ivisârtoq greenstone belt. However, ultimately there was insufficient data to define the stratigraphy of the belt. The sole geochronological datum from early work in the area was acquired by Baadsgaard (1976) while doing work on the entire Godthåbsfjord region. A U/Pb age of 2580 Ma from zircons in a single sample of an assumed paraschist was interpreted as a metamorphic age.

A team from University of Exeter did further mapping within the Ivisârtoq region from 1981-1983 and in 1985 in order to complete the necessary detail for the Geological Survey of Greenland 1: 100 000 map sheet 64 V.2 N (Chadwick and Coe, 1988). From this work a host of PhD theses were produced, including: Robertson (1985); Brewer (1985); Park (1986); Crewe (1986). During this time Chadwick mapped the Ivisârtoq greenstone belt in detail at a scale of 1:20 000 (unpublished map) and eventually determined a stratigraphic sequence for the belt (Chadwick, 1990). There has been little published on the Ivisârtoq greenstone belt prior to the onset of this study. However, as the research within and around the Isua region starts to broaden, it seems inevitable that the Ivisârtoq greenstone belt will be the focus of future studies.

Recent work by Friend and Nutman, (2005) indicate that this is likely. Their reinterpretation of the terrane model for the Godthåbsfjord region is based on new

geochronology of samples mostly collected from the Ivisârtoq region and inner Godthåbsfjord in 1976. Friend and Nutman, (2005) have obtained three additional ages from the belt. They obtained a weighted mean average of 3075±15 Ma from 23 zircon SHRIMP analyses in a sulphide-rich felsic schist, which they interpreted to be volcanosedimentary in origin. The dated zircons were interpreted as igneous in nature and the obtained age was used to provide a minimum time of deposition of at least part of the belt. An age of 2961±11 Ma was obtained from 7 SHRIMP analyses of two zircon grains in a weakly deformed granite (sample GGU200499) collected from the 'dome' of gneisses north of the belt and was interpreted as a minimum age constraint for the belt. Their third analysis was of a granodioritic gneiss, interpreted as an intrusion into anorthositic rocks in the southern limb of the belt. They obtained an age of 2963±8 Ma from fourteen SHRIMP analyses on thirteen zircons which they interpreted as the minimum age of the gabbro-anorthosite unit.

1.4.2 Brief Outline of Local Geology

The Ivisârtoq greenstone belt forms a southwest-closing, V-shaped structure and was subjected to amphibolite facies metamorphic conditions. The two ridges of supracrustal rock that form the V-shape range in topographic relief from sea level to 1200 m and are exceptionally well exposed. Field mapping for this study concentrated on the 3 km thick southern limb of the V-shaped structure, where the most complete stratigraphic section is preserved, and where pillow lava structures with way-up indicators are observed (Fig. 1.3). The southern limb has been divided into two components, termed the

northern and southern parts. A high strain zone, containing a predominantly quartzofeldspathic layer and an ultramafic schist layer, is used as a tectonostratigraphic marker separating the southern and northern parts. The northern part is characterized by heterogeneously deformed amphibolite derived from basaltic pillow lavas interlayered with boudins of coarse-grained olivine-bearing ultrabasic rocks, and quartz-feldspar-mica gneiss and schist which are continuous for a few hundred metres. The southern part contains more intensely deformed amphibolite derived from pillow lavas and homogeneous amphibolites. Diffusely banded, pale quartzofeldspathic gneisses and schists, are also present in the southern part. There are also mafic dykes and felsic pegmatites in the northern and southern parts of the belt.

1.4.3 Thesis Goals

The overall goal of the thesis is to determine the nature of the Ivisârtoq greenstone belt. The thesis focussed on several aspects of the belt with this goal in mind, including:

- What are the nature and protoliths of the lithologic units?
- Does the belt represent a stratigraphic sequence or a tectonostratigraphic collage - how do the units relate to each other?
- When did the belt form?
- What are the geochemical characteristics of the belt and what do these attributes reveal about the magmatic history of the different lithological units?
- What is the tectonic history of the belt?

To address these problems the thesis has been broken down into several components which include:

a) A detailed field and petrographic description of the lithological units of the greenstone belt, including a field map of the study area;

b) Geochronological data to provide insight into the age of the belt;

c) Extensive major and trace element geochemical analysis of the major units within the belt in order to define differences within and between units and geochemical constraints on the magmatic evolution of these rocks;

d) Geological synthesis: combining all of these observations to construct a general model of the tectonic evolution of the Ivisârtoq greenstone belt.

1.5 METHODOLOGY

The basic goal of this study is to understand the nature of the various lithological units within the Ivisârtoq greenstone belt and how they relate to each other. This was accomplished using various research and analytical methods, including: field mapping, geochronology, and major and trace element geochemistry. The following is a brief description of the principals and applicability of each technique.

1.5.1 Field Work/Map Production

The basis for this research was field mapping at 1:10 000 scale which is an improvement upon a previously unpublished map at 1:20 000 and upon the most recent published map which was at a scale of 1:100 000 (Chadwick and Coe, 1988). Field work

was conducted between late June - early September, 2001, with support from the Greenland Bureau of Minerals and Petroleum and the Geological Survey of Denmark and Greenland (GEUS). The research included detailed mapping and sample collection within the Ivisârtoq greenstone belt, and focused primarily on the southern limb of an asymmetric syncline, where the most complete stratigraphic section is preserved. Samples were collected for petrographical, geochemical and geochronological studies in order to better define the stratigraphy and lithological units of the belt. Samples were collected and thin sections were made which were perpendicular to the main foliation and parallel to the lineation; and, where appropriate, parallel to the foliation. Samples which appeared to have some possible economic value or significance were collected for the Bureau of Minerals and Petroleum. These samples, which are primarily from rusty alteration zones, were collected for trace element analysis.

A 1:10 000 digital map was compiled using new data collected from the 2001 field season in conjunction with a previously unpublished 1:20 000 scale map produced by Brian Chadwick (see insert map). Digital topography was provided by GEUS and additional digital stereo-mapping of airphotos was completed at the Department of Geological Mapping of GEUS in Copenhagen, Denmark. All of the data (digital topography, digitized contacts, and field data) was compiled using MapInfo Version 6.5. Using MapInfo allows the map to be 'spatially' correct and data is assigned a specific coordinate in space.

1.5.2 U-Pb Geochronology

Archean greenstone belts can be composed of many different rock types and commonly have very complicated metamorphic and deformational histories. Performing geochronological work within these regions can prove to be challenging. The primary goal varies from study to study and may include focuses such as: dating the primary age of the belt, its metamorphic history, its tectonic history, etc. Ideally, to constrain these ages well documented field relationships of the unit(s) in question are needed. Once the goal is clear the radiometric dating method must be determined as well as the specific technique(s) that will be utilized (an extensive review of radiometric dating methods can be found in Geyh and Schleicher, 1990).

U-Pb isotope analysis was chosen for the basis of this study because this study focussed on dating zircon grains. U-Pb geochronology relies on the decay of U to Pb in a closed system and is based on the following equations:

$$\frac{^{206}Pb^*}{^{238}U} = (e^{\lambda_{238}t} - 1) \text{ and } \frac{^{207}Pb^*}{^{235}U} = (e^{\lambda_{235}t} - 1)$$

where Pb^* represents radiogenic lead only. These equations will yield concordant ages, for minerals that provide a closed system for U and Pb. Concordant ages will plot on a concordia curve which is a graphical representation of the isotopic compositions in a closed system for the two U/Pb isotopic systems with relation to the decay constant and successive values of t (Faure, 1986).

U-Pb ages can plot off the concordia curve, and are termed discordant, if lead has been lost from the grain(s) being dated. In this case the data typically form a linear array

on the diagram. The discordia line intersects the concordia curve at two points, 1) at the time of original crystallization, and 2) at a younger age which may represent the time when the grain was disturbed (Wetherill, 1956). If the disturbance is related to present day lead loss, then the discordant data yield a straight line that intersects at or near the origin. If the lead loss is related to a later event, then the lower intersect may represent the age of disturbance (e.g., a metamorphic event). A lower intercept may also represent a meaningless "young age" which is the result of lead loss integrated over time. Tilton (1960) suggested that, over time, Archean minerals undergo continuous lead loss by diffusion. Without geological evidence of a specific lead loss event, no age-significance should be inferred from the lower intersection of the discordia line (Dickin, 1995).

Zircon ($ZrSiO_4$) was selected for dating as the U-Pb systematics of this mineral are highly robust. Zircon readily incorporates uranium, but not lead, into its structure during crystallization, therefore, most of the lead found in present-day samples is radiogenic (Potts, 1987). Furthermore, diffusion of Pb from zircon is extremely slow, so the grains retain age information through high-temperature episodes (Hanchar and Miller, 1993) and are considered to provide a closed system for U and Pb.

Zircon is also an ideal candidate for dating as it occurs in a wide range of granitoid rocks and their volcanic equivalents. The crystal morphology of zircons can reflect these differing igneous environments (Vavra, 1993). Zircons are also capable of surviving high grades of metamorphism (even partial melting) and are resistant to weathering and alteration.

Geologists should be acutely aware of this robust behaviour. Zircons are able to survive in the crust almost indefinitely, however, they are not unchanging. Major events that zircons undergo leave their imprints and, therefore, exceptionally complicated histories can be recorded in a single grain (Hanchar and Miller, 1993). Zircon can form initially in an igneous or high-grade metamorphic environment, and due to its resistance to chemical and physical processes, it also occurs in many sedimentary rocks (Cox, 2002). Any of these zircons can be overprinted during subsequent metamorphism episodes. These events or any combination therein, can cause growth and/or degradation (e.g. partial dissolution, metamictization, mechanical breakage) of the grain. The fact that these events can be recorded in zircon grains, by way of distinctive morphology and internal zoning (Hanchar and Miller, 1993), reveals the powerful nature of zircon geochronology. It also becomes clear that analysing these attributes is essential in order to accurately interpret the zircon's history and heritage.

Once zircons are separated from a collected sample they can be grouped superficially into populations based on morphology. Single crystals or groups of crystals can be dated using isotope dilution-thermal ionization. Single grains can also be analysed using a sensitive high-resolution ion microprobe (SHRIMP) or laser ablation microprobe (LAM) linked to an inductively coupled plasma mass spectrometer (ICPMS), both of which have the added capability of measuring *in situ* grains.

Regardless of the dating method, imaging zircons is a vital prerequisite, as transmitted light optical microscopy on its own is inadequate to reveal the internal complexity of many crystals (Whitehouse et al., 1999). Studying the zoning patterns of

zircon populations can be achieved by numerous imaging techniques, including: petrographic examination of acid etched crystals, scanning electron microscopy (back-scattered electron (BSE) images, cathodoluminescence (CL) and charge-contrast imaging, and X-ray mapping (details of these techniques are outlined in Cox, 2002).

Internal imaging is fundamental in the later interpretation of the data as it is necessary to recognize if the grains contain inherited cores and/or overgrowths. Without knowledge of the internal structure of a single grain (or multiple grain fractions) a hybrid (and effectively 'false') age could be obtained using isotope dilution thermal ionization mass spectrometry (ID-TIMS). Without imaging, even laser techniques are in danger of positioning the beam on overlapping zones and thereby producing isotopic data which can be easily misinterpreted, or important growth phases may not be analysed at all (Whitehouse et al., 1999).

These concerns were taken into account during the geochronological study of the Ivisârtoq greenstone belt. The study utilized both back-scattered electron and cathodoluminescence techniques to image grains from the Ivisârtoq greenstone belt. Laser ablation microprobe inductively coupled plasma-mass spectrometry (LAM ICP-MS) and isotope dilution thermal ionization mass spectrometry (ID-TIMS) were chosen to constrain the age of the belt.

1.5.3 Major and Trace Element Geochemistry

Major and trace element geochemical analysis are useful tools which can provide insight into the petrological and petrogenetic magmatic history of igneous rocks. Trace elements are particularly useful in helping with protolith interpretation of deformed and metamorphosed rocks, especially in regards to Archean-aged rocks, and differentiating between rocks which have similar field and petrographic characteristics. Major elements tend not to be as reliable in this capacity due to their more mobile nature.

Geochemical data must be evaluated for the effects of secondary mobility of elements prior to interpreting primary geochemical characteristics. Element mobility describes the chemical changes which take place in rocks after their formation. These chemical changes typically take place during weathering, diagenesis and metamorphism, or through interaction with hydrothermal fluids. Rollinson (1993) noted that the mobility of major elements is controlled by three main factors:

1) the stability and composition of the minerals in the unaltered rock;
2) the stability and composition of the minerals in the alteration product;
3) the composition, temperature and volume of the fluid phase.

Bivariant plots, primitive mantle-normalized trace element diagrams, and low H_2O and CO_2 contents [reflected in low loss on ignition (LOI) values] have been used in this study to assess the mobility of major and trace elements. Scattered trends on variation diagrams can indicate that the element in question has been mobile. However, it should be noted that chemical alteration may produce systematic changes which may mimic other mixing processes (i.e. crystal fractionation). These apparent trends may

result from volume changes arising from the removal or addition of a single component of the rock (Rollinson, 1993).

Primitive mantle-normalized trace element diagrams are useful for assessing the mobility or immobility of specific elements or groups of elements. Consistent and coherent patterns in a suite of rocks suggest that the original magmatic concentrations for the selected elements have been preserved. Elements are plotted with respect to their abundance in "primitive mantle": the hypothetical mantle composition before extraction of the continental crust. On primitive mantle-normalized trace element diagrams elements are arranged in order of increasing compatibility in mantle mineral assemblages. Element abundances are plotted on a logarithmic scale. The elements used in this study include light rare earth elements [LREE; (La, Ce, Pr, Nd)], middle rare earth elements [MREE; (Sm, Eu, Gd, Tb, Dy, Ho)], and heavy rare earth elements [HREE; (Er, Tm, Yb, Lu,)] as well as high field strength elements [HFSE; (Th, Zr, Hf, Ti, Nb, Ta). Large ion lithophile elements, which are low field strength elements (LFSE) are alteration sensitive and hence were not used due to their mobile nature in Archean terranes.

Primitive mantle-normalized trace element diagrams are also extremely valuable in determining relationships between different elements, or groups of elements, which can be invaluable for petrogenetic interpretations. Such diagrams make clear:

1) the relationship of HFSE to REE of similar compatibility [e.g. Nb (Ta)-La, Zr-Sm, Hf-Sm];

2) intercomparison of major elements with HFSE of similar compatibility (e.g. Ti/Zr)

3) HFSE/HFSE ratios (e.g. Nb/Ta, Zr/Hf, Zr/Nb; Kerrich and Wyman, 1997).

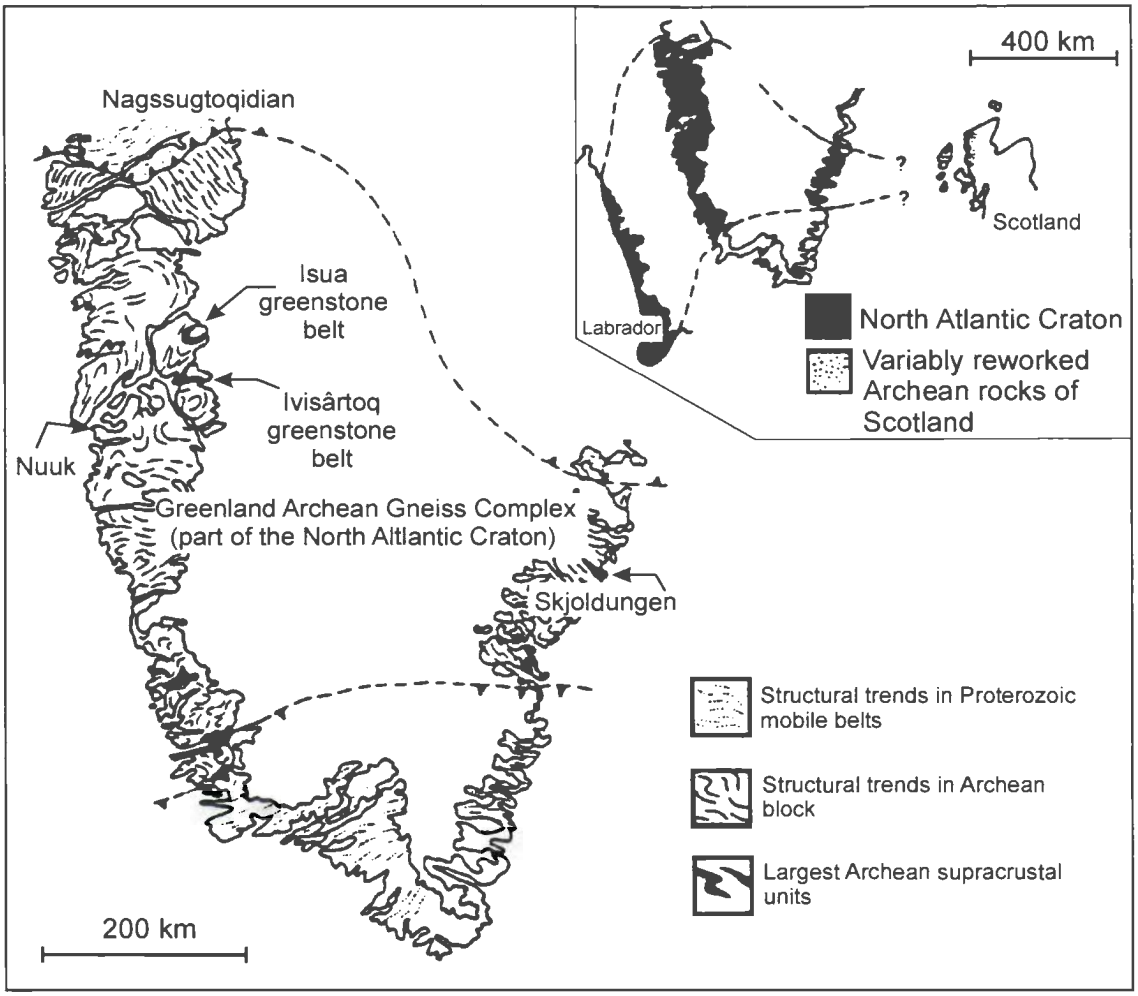

Figure 1.1. The North Atlantic Craton (from Nutman, 1997).

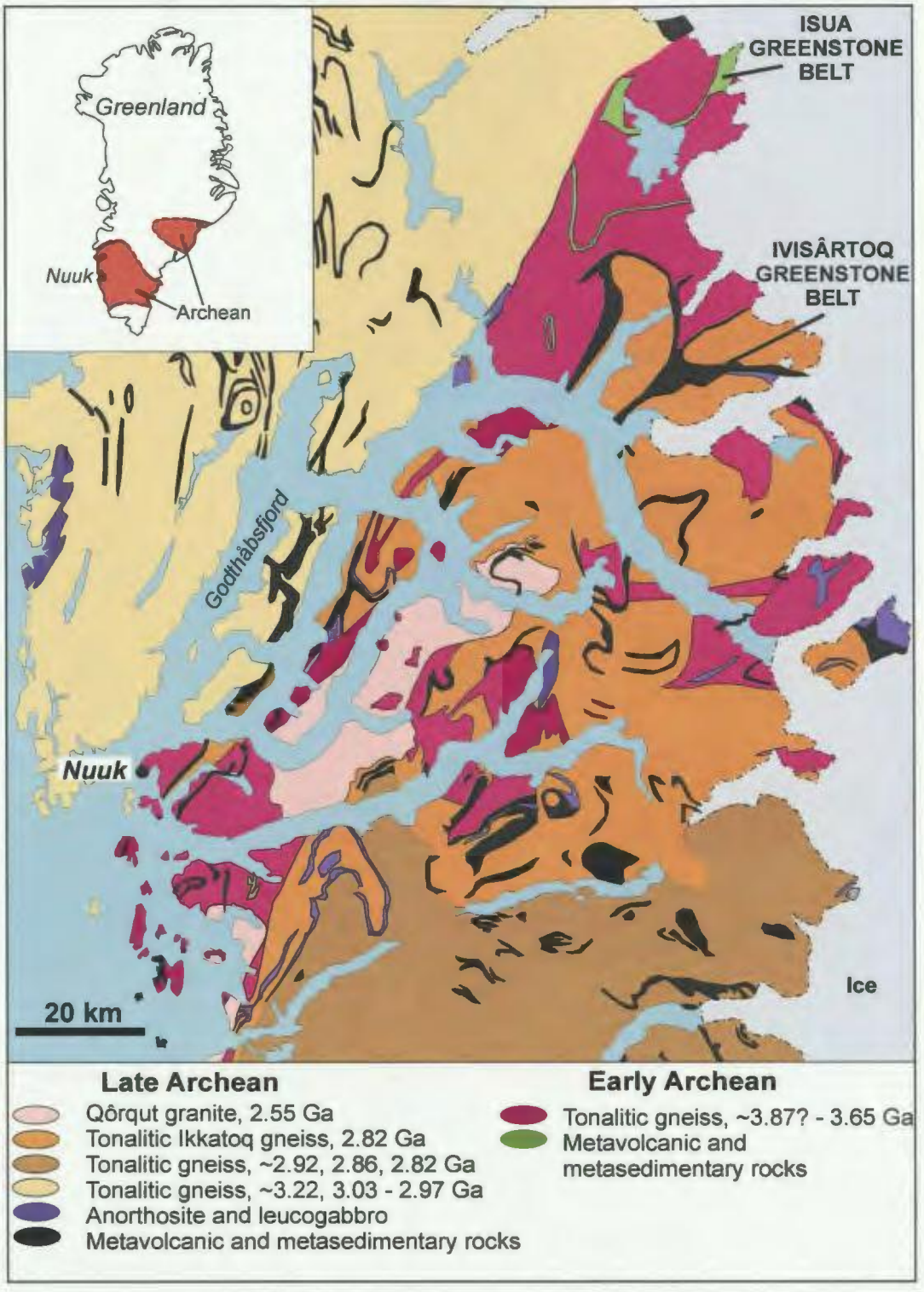

Figure 1.2a. Geologic map of the Godthåbsfjord region (from Myers and Crowley, 2000) compiled from maps by Allaart (1982), Chadwick and Coe (1983,1988), Garde (1987, 1989) and McGregor (1984) and geochronology from Nutman et al. (1996) and Nutman (1997). The inset map of Greenland locates Nuuk and the main regions of Archean gneiss.

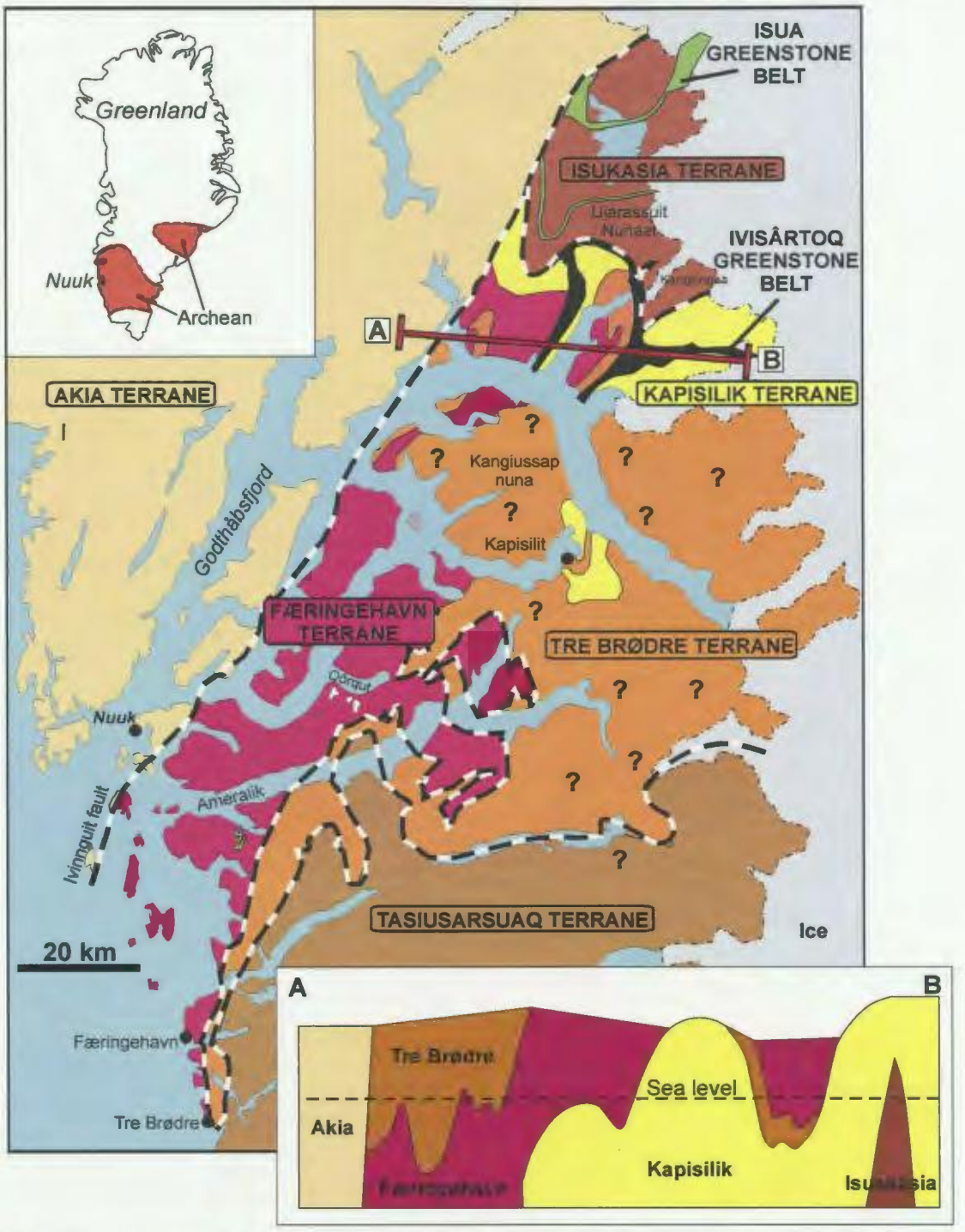

Figure 1.2b. Sketch map of the terranes of the Godthåbsfjord region as defined by Friend and Nutman (2005). The top left inset map of Greenland locates Nuuk and the main regions of Archean gneiss. The bottom right inset shows a cross-section at sea level along the line AB (from Friend and Nutman, 2005). Note: different colours represent different terranes and do not correspond exactly with geological units as defined in Fig. 1.2a. Dashed lines indicate terrane boundaries.

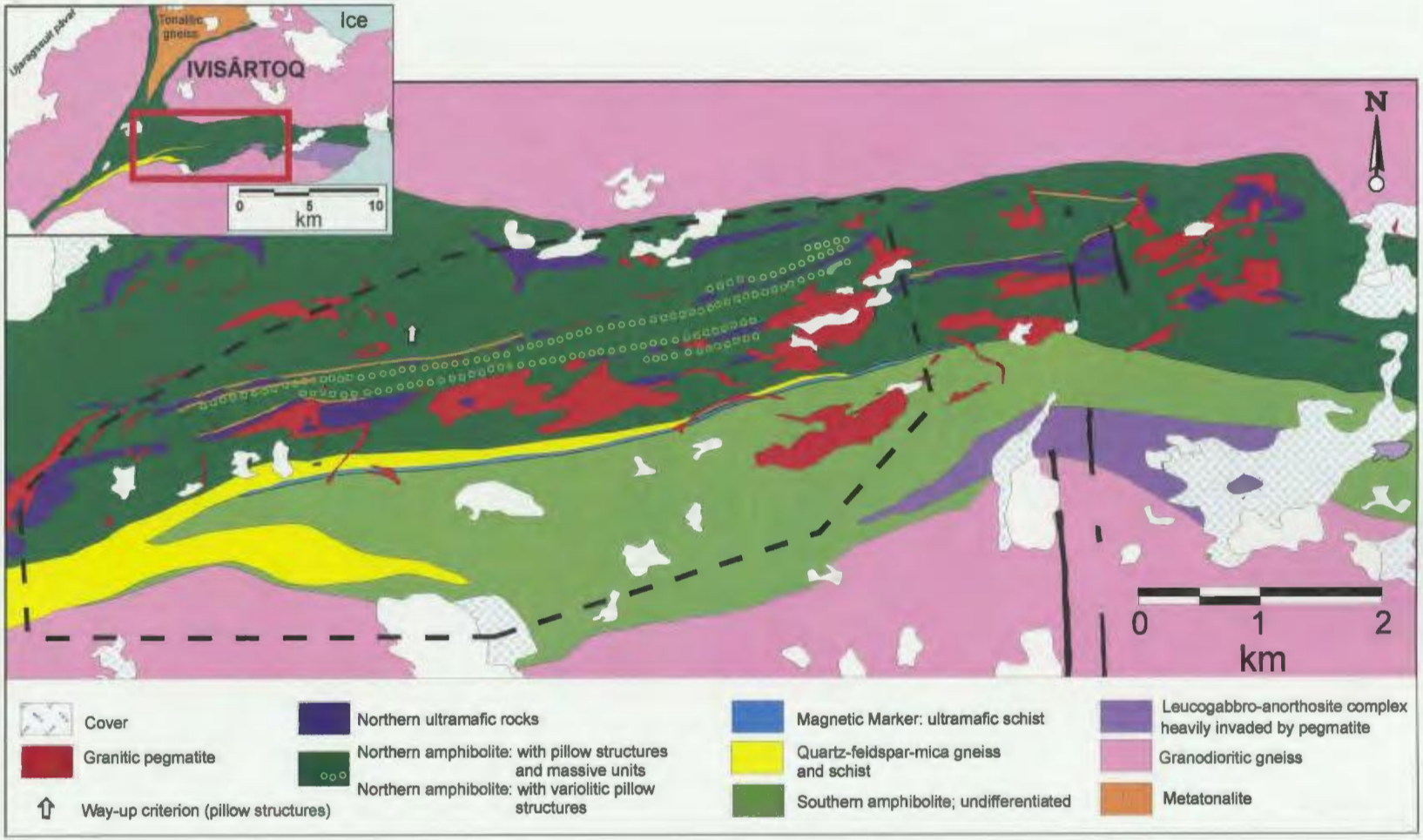

Figure 1.3. Simplified map of the Ivisârtoq greenstone belt. Dashed outline indicates field area.

Chapter Two:
Geology and Geochronology of the Ivisârtoq greenstone belt

2.1 ABSTRACT

The Ivisârtoq greenstone belt is exceptionally well-exposed in three dimensions, and primary features are better preserved here than in any other Archean greenstone belt in Greenland. The belt forms a southwest-closing, V-shaped synform, and was subjected to amphibolite facies metamorphism. This study concentrated on the 3 km thick southern limb of the synform, where the most complete section of supracrustal rocks is preserved, and where pillow lava structures indicate way-up. The southern limb has been redefined as a tectonostratigraphy and comprises two main components, termed the northern and southern parts. These two units differ in composition and intensity of deformation and are separated by a major high strain zone.

The northern part of the southern limb is generally less deformed than the southern part and is characterized by heterogeneously deformed amphibolite, derived from variolitic and homogeneous basaltic pillow lavas, interlayered with boudins of olivine-bearing ultramafic rocks and quartz-feldspar-mica gneiss and schist. The southern part consists of strongly deformed rocks including banded amphibolites, homogeneous granitic rocks, gabbroic rocks, and a thick layer of predominantly quartz-feldspar-biotite-schist.

Reconnaissance LAM ICP-MS U-Pb zircon geochronology, and field mapping have shed new light on the timing of magmatic, depositional, and deformational events. A U-Pb zircon age of an intrusive tonalite sheet demonstrates that the northern basaltic

pillow lavas were deposited before ~3165 Ma. A maximum age of ~2895 Ma was determined for the deposition of the youngest unit in the southern part, interpreted as a quartzofeldspathic metasedimentary rock. This work supports a new interpretation in which the northern and southern parts of the belt represent discrete packages of rocks that were juxtaposed after the main volcanism associated with each part had ceased (after ~2895 Ma).

2.2 INTRODUCTION

The Ivisârtoq greenstone belt is part of the Archean gneiss complex of West Greenland (Fig. 2.1; Nutman, 1997). The Greenland Archean gneiss complex is characterised by basaltic volcanic rocks and sedimentary rocks that were intruded by middle to late Archean tonalite and granodiorite, and a small amount of granite and diorite (Myers and Crowley, 2000). These rocks were repeatedly deformed and metamorphosed, resulting in the formation of new tectonic laying and in various episodes of recrystallization (Bridgwater et al., 1976). These events have generally obliterated primary structures in the supracrustal remnants and therefore recognition of original stratigraphy/tectonostratigraphy has proven to be difficult (Chadwick, 1990).

Most work within the Archean gneiss complex of West Greenland has concentrated on the Godthåbsfjord region. This region is located on the west coast near Nuuk (formerly Godthåb and Nûk) (Fig. 2.2) and contains the most extensive, best exposed and most intensely studied early to middle Archean rocks on Earth (Myers and Crowley, 2000). The Isua greenstone belt has been the focus of most studies within the

Godthåbsfjord region, as it hosts some of the oldest rocks on Earth (~3.8-3.7 Ga) and is thought to contain the oldest evidence of life on Earth (Rosing, 1999). The Ivisârtoq greenstone belt lies 40 km south of the Isua greenstone belt within the Ivisârtoq region. Therefore, work in this area is fundamental for understanding the Archean geological evolution of the wider Isua-Ivisârtoq region. The Ivisârtoq greenstone belt is distinct in that it contains an exceptionally well-exposed tectonostratigraphic section of Archean metavolcanic rocks which include well-preserved, primary pillow lava structures. The belt is also distinct because relatively little research has been done within the region. These distinctions make the Ivisârtoq greenstone belt an ideal candidate for detailed investigation.

This paper examines several aspects of the Ivisârtoq greenstone belt, including the protolith composition and age of the various stratigraphic units. Detailed field and petrographical work, as well as U-Pb zircon dating techniques, were used for the investigation. The basis for this research is field mapping at 1:10 000 scale which is an improvement upon a map at 1:20 000 (Chadwick, unpublished) and upon the most recent published map which is at a scale of 1:100 000 (Chadwick and Coe, 1988).

2.3 REGIONAL GEOLOGY

The Godthåbsfjord region of Greenland is located in the centre of the Greenland Archean gneiss complex on the west coast near Nuuk (formerly Godthåb and Nûk; Fig. 2.2). Within this region, Early Archean quartzofeldspathic gneisses and early and middle

Archean supracrustal rocks were intruded by and were tectonically interleaved with late Archean plutonic rocks.

Early interpretations regarded the Godthåbsfjord region as a single tectonic terrane (Nutman, 1997). However, later studies reinterpreted the Godthåbsfjord region in terms of separate terranes, which evolved independently prior to assembly in the late Archean; similar to other granite greenstone terranes, for example Barberton (e.g. Lowe et al., 1999), and the Superior Province (e.g. Percival et al., 2001). Currently the Godthåbsfjord region is thought to comprise six terranes: the Akia, Isukasia, Færingehavn, Kapisilik, Tre Brødre, and Tasiusarsuaq terranes (Friend and Nutman, 2005; Fig. 2.2b). The Isukasia terrane includes the Isua greenstone belt and the Kapisilik terrane contains the Ivisârtoq greenstone belt.

Assembly of the terranes is interpreted to have taken place in at least two episodes (Friend and Nutman, 2005): the >3600 Ma Isukasia terrane was first intercalated with the 3075-2960 Ma Kapisilik terrane at ~2950Ma and subsequently this composite block was juxtaposed with the composite Færingehavn and Tre Brødre terranes after ~2825 Ma. Friend and Nutman (2005) interpret the Tre Brødre terrane (and associated Færingehavn terrane) to now lie structurally above the Kapisilik terrane. Furthermore, on Ujarassuit Nunaat and northern Ivisârtoq, the northern limit of the Kapisilik terrane is interpreted to be structurally above the early Archean rocks to the north, which are included in the Isukasia terrane (Fig. 2.2b). One of the goals of ongoing mapping and geochronology in the Godthåbsfjord region is to test and if necessary, modify the terrane model.

2.4 IVISÂRTOQ GREENSTONE BELT

The Ivisârtoq greenstone belt forms a southwest-closing, V-shaped structure and was subjected to amphibolite facies metamorphic conditions. The two ridges of supracrustal rock that form the V-shape range in topographic relief from sea level to 1200 m and are exceptionally well exposed. Field mapping for this thesis concentrated on the 3 km thick southern limb of the V-shaped structure, where the most complete tectonostratigraphic section is preserved (Fig. 2.3).

2.4.1 Previous Work

The Ivisârtoq region was initially mapped by mainly helicopter reconnaissance by Walton (1976) and by Allaart et al. (1977). The greenstone belt itself was mapped in more detail by Friend and Hall (1977), who reported pillow structures indicating way-up. Hall (1981) used the field data collected during the summer of 1976 for his PhD, concentrating on petrography, metamorphism, structural geology, and geochemistry of the Ivisârtoq greenstone belt. The sole geochronological datum from early work in the area was acquired by Baadsgaard (1976) while doing work on the entire Godthåbsfjord region. A U/Pb age of 2580 Ma from zircons in a single sample from a rock interpreted as a paraschist was interpreted as a metamorphic effect.

A team from University of Exeter did further mapping within the Ivisârtoq region from1981-1983 and in 1985 in order to complete the necessary detail for the Geological Survey of Greenland 1: 100 000 map sheet 64 V.2 N (Chadwick and Coe, 1988). From this work a host of PhD theses were produced, including: Robertson (1985); Brewer

(1985); Park (1986); Crewe (1986). During this time Chadwick mapped the Ivisârtoq greenstone belt in detail at a scale of 1:20 000 (unpublished map) and eventually determined a stratigraphic sequence for the belt which is currently accepted (Chadwick, 1990). Otherwise, there has been little work published on the Ivisârtoq greenstone belt prior to the onset of this study. However as the research within and around the Isua region starts to broaden, it seems inevitable that the Ivisârtoq greenstone belt will be the focus of future studies.

Recent work by Friend and Nutman (2005) included reconnaissance geochronology from the Ivisârtoq area. They obtained three additional ages from the belt and have incorporated the area into a new terrane model which encompasses the Godthåbsfjord region.

2.4.2 Stratigraphy/Tectonostratigraphy

Chadwick (1990) described the southern limb of the Ivisârtoq V-shaped structure as a stratigraphic section comprising two groups of amphibolites: a lower group and an upper group. A distinctive seam of magnetic ultrabasic rocks, termed the 'magnetic marker' was used as a stratigraphic marker horizon to separate the two groups (Chadwick,1990).

He distinguished an upper amphibolite group based on the presence of heterogeneously deformed pillow structures interlayered with ultramafic amphibole schists, metagabbro, and boudins of coarse-grained, olivine-bearing, ultrabasic rocks. Within the amphibolites with pillow lava structures, Chadwick (1990, pg. 644) observed

structures that "show unambiguously that the section on the southern limb of the syncline is right way-up". Sheets rich in quartz and sulphides and quartz-feldspar-mica gneisses and schists were also noted in the upper group.

Chadwick described the lower group as containing more intensely deformed and homogeneous amphibolites with pillow lava structures. Within this group he observed diffusely banded, pale quartzofeldspathic gneisses and schists, and he noted that olivine-rich sheets like those in the upper group are typically absent. Chadwick (1990) also mapped a major body of leucogabbro with minor anorthosite and melanogabbro within the southeastern region of the lower group.

Chadwick (1990, pg. 642) noted that "amphibolite dykes are relatively common in parts of the amphibolites and a few have been noted in the metasedimentary and olivine-rich ultrabasic rocks". In the upper group, he observed dykes containing small aggregates of feldspar.

Newly established tectonostratigraphy

Recent mapping has re-evaluated the 'stratigraphy' as defined by Chadwick (1990). The extensive rock exposure of the belt allowed for a broad-scale structural assessment of the geological units to determine if they correspond to a simple layer-cake stratigraphic interpretation.

Chadwick (1990) separated the section into two amphibolite groups, the upper (northern part of the southern limb) and the lower group (southern part of the southern limb), based primarily on compositional differences. However, recent mapping revealed

that in addition to lithological differences, the northern and southern parts of the southern limb also appear to differ in intensity of deformation. The northern part is generally less deformed than the southern part: in the north, large km-scale isoclinal folds are recognizable, whereas, the rock units of the southern part are deformed into parallelism. If the two parts represent a continuous stratigraphic section then both parts would have been isoclinally folded by the same event and therefore, one would expect to see repeated lithological units throughout the two parts of the belt's southern limb. This is not observed. In contrast, distinct rock units are observed in the northern part and southern part of the southern limb.

In addition, the margins of most units are intensely deformed. Areas if intense deformation were studied to determine if they could represent tectonic breaks. The widest zone (30-200 m) of intense deformation runs E-W along the centre of the southern limb of the belt. This zone, termed the Marker High Strain Zone in this study, is composed of two layers: a quartzofeldspathic layer with amphibolitic horizons and the magnetic marker layer. The boundaries of the deformed zone are relatively sharp with less deformed rocks to the north and south. The zone includes mylonitized units and locally dextral and sinistral shear-sense indicators were noted in the field. These features suggest that this zone suffered high strain, and likely had a complicated deformational history. The structural features combined with the observation of different rock units to the north and south of this zone suggested that it might represent a tectonic break. This theory is further supported by geochronological (see Section 2.6) and geochemical (see Chapter 3) data.

Based on this interpretation, the layers of different rock types, in the southern limb of the belt, are not thought to represent a simple 'layer-cake' primary stratigraphy and are herein described as a tectonostratigraphic assemblage. This study divides the southern limb of the belt into two parts: the northern and southern, which are separated by the major zone of intense deformation.

The following sections systematically describe the two parts of the southern limb of the Ivisârtoq greenstone belt in terms of lithological units and protolith interpretation. These parts are herein described as simply the northern and southern parts of the belt, with the understanding that they refer to the southern limb of the belt.

2.5 MAJOR COMPONENTS OF THE IVISÂRTOQ GREENSTONE BELT

2.5.1 Northern Part of the Southern Limb

The northern part of the Ivisârtoq greenstone belt is characterized by heterogeneously deformed amphibolites derived from basaltic pillow lavas interlayered with olivine-bearing ultramafic rocks which have been disrupted into boudins, and with discontinuous layers of quartz-feldspar-mica gneisses and schists. Mafic dykes and felsic pegmatites were noted in the northern and southern parts of the belt.

2.5.1.1 Northern Amphibolites

The northern part of the Ivisârtoq greenstone belt is dominated by recrystallized amphibolites which were mostly derived from two distinct types of heterogeneously deformed pillow lavas. These two distinct protoliths are homogeneous basaltic pillow

lavas (Fig. 2.4, 2.5), and variolitic pillow lavas (Fig. 2.6). The best-preserved pillow structures are slightly flattened and range from 10 cm to 1 m in length (x-axis of strain ellipsoid), with an average length of 50 cm and average axial ratios of 2:1:1 (x:y:z). The original way-up direction of the pillow lavas can be determined where pillows have smooth, convex tops and cuspate bases (Fig. 2.4a,). The bottom of the upper pillows were moulded onto the convex upper surfaces of the lower pillows producing a cuspate geometry (Philpotts, 1990).

A transition from relatively undeformed pillows to banded amphibolite can be traced in the field (Fig. 2.5), and has been noted elsewhere in southwest Greenland (Bridgwater et al., 1976; Friend et al., 1981; Myers, 1985). Some of the amphibolites have been heterogeneously affected by alteration, which may be of hydrothermal origin. This alteration is now mainly marked by epidote veins and diffuse zones which locally overprint well-preserved pillow structures in low-strain zones and are deformed with the pillow structures to form banded amphibolites in the high strain zones (Fig. 2.7). A third, subordinate type of amphibolite was observed, which is composed of dark oblate structures within an epidote-rich matrix, and may correspond with deformed 'ultramafic' pillows described by Hall (1980, 1981; Fig. 2.8).

The amphibolites derived from homogeneous basaltic pillow lavas are the most abundant rock type in the northern part of the Ivisârtoq greenstone belt. These layers range from tens to hundreds of metres in thickness (Fig. 2.4b), and locally grade into massive flows. Spectacular, well-preserved pillow structures, which indicate way-up, were noted in several localities (Fig. 2.4a, see map). These pillows are characterised by

dark, amphibole-rich marginal zones which sharply contrast with the paler, yellow-green, epidote-pyroxene-rich cores of the pillows (Fig. 2.4, 2.9). Individual pillows are outlined by thin (0.5 cm) leucocratic selvages. Although the original structure of some of the pillows has been retained, the mineral assemblages generally have been altered and recrystallized. The marginal zones of the pillows are composed primarily of hornblende, with lesser amounts of epidote and plagioclase (Fig. 2.9, 2.10). The pillow cores range from fine to coarse grained and comprise various amounts of epidote, clinopyroxene, plagioclase, hornblende, and lesser amounts of garnet and calcite (Fig. 2.11). Titanite is a ubiquitous accessory mineral, and locally constitutes up to 7 modal % of the matrix. The observed assemblages may have resulted from secondary metasomatic replacement, which was likely modified during subsequent metamorphism (See Table 2.1).

The more deformed homogeneous pillow structures are strongly flattened (Fig. 2.5b), and in their most deformed state are banded, dark green-light green amphibolites (Fig. 2.5c). The dark layers are rich in dark-green hornblende and represent the pillow rims; light green layers are composed of clinopyroxene, epidote, plagioclase, hornblende, garnet, and titanite, and correspond to the pillow cores (Fig. 2.12).

The amphibolites derived from variolitic, basaltic pillow lavas were mapped as distinct layers within the northern part of the Ivisârtoq greenstone belt, and are up to a few kilometres in length (Fig. 2.3). The best-preserved pillow structures are defined by thin (average 0.5 cm) leucocratic inter-pillow selvages (Fig. 2.6a). The mineral assemblage of the pillow cores is dominated by recrystallized amphibole, plagioclase, and accessory titanite ($\leq$3 modal %). The proportions of these minerals differ between the

leucocratic varioles, which are composed of roughly equal proportions of elongate hornblende and polygonal plagioclase, and the dark matrix of the pillow cores, which are dominated by coarse-grained hornblende (Fig. 2.13). The hornblende and plagioclase grains define a moderate to strongly developed foliation, which probably reflects the main deformational event. Late, lath-shaped growths of clinozoisite, oriented at an angle to the main foliation, are likely related to the slightly retrograde metamorphic conditions of the latest deformational event (Fig. 2.13b)

The varioles within the best-preserved pillow structures are up to 2 cm long (x-axis), and have axial rations of 4:1:1. They are observed both as clumps within cores of well-preserved pillows, and as separate spherical bodies near pillow margins (Fig. 2.6a). Varioles were not observed within the pillow selvages. Flattened varioles are distinct in moderate to strongly deformed pillows (Fig. 2.13a). In the most intensely deformed samples, the leucocratic varioles and pillow selvages contrast strongly with the dark matrix of the pillow cores, creating banded black and white rocks (Fig. 2.6c). The dark layers, representing deformed cores, are composed predominantly of hornblende with smaller amounts of plagioclase, and the lighter layers are composed primarily of plagioclase and tremolite.

Varioles are widespread in Archean mafic volcanic rocks and are defined as macroscopic globular textures (Fowler et al., 2002). Variole is a non-genetic term used to describe generally leucocratic ovoid structures visible on the weathered surfaces of mafic rocks (Fowler et al., 2002) and is sometimes used as a field criterion to identify high-Mg basalts (Myers, pers. comm.; Cawthorn et al.. 1979). Possible interpretations of their

origins include devitrification or liquid immiscibility. Devitrification can result in the formation of spherulites, which are described as masses of acicular crystals, commonly of feldspar, which radiate from a central point (Fowler, 1986). They grow directly from the liquid as a result of supercooling. Liquid immiscibility can result in the formation of amoeboid shaped globules in which spherical feldspar arrays are not found. In contrast to spherulites, liquid immiscibility globules are composed of a variety of textures and minerals, including quartz alkali feldspar (Fowler et al., 2002). The delicate primary textures which can differentiate between these processes have not been preserved within the Ivisârtoq basaltic lavas. Therefore, their origin cannot be determined and the more general term, variolitic, is used to describe the pillow lavas which contain leucocratic, ovoid structures.

The amphibolites derived from both homogeneous and variolitic, basaltic pillow lavas have heterogeneously been affected by alteration now marked by epidote. The alteration is observed as pale-green, epidote-rich patches and veins which locally overprint well-preserved pillow structures in low-strain zones (Fig. 2.7). In zones of higher strain, the alteration patterns become deformed with the pillow structures. Locally, basaltic pillow lavas marked by this alteration are cross-cut by ultramafic and quartzofeldspathic layers. Similar alteration features are not observed in the adjacent ultramafic layers and quartzofeldspathic schists. The alteration is interpreted to be the result of hydrothermal fluids and occurred after the solidification of the pillow lavas but before the emplacement of the ultramafic layers and protolith of the quartzofeldspathic schists. The original mineral assemblage of the alteration zones is uncertain, as it has

likely been affected by the later deformational and metamorphic events. The observed epidote-rich assemblage likely reflects the amphibolite-facies metamorphism related to the most recent major deformational event.

A third, distinct type of amphibolite was observed within the northern part of the Ivisârtoq greenstone belt. It forms a discontinuous layer, separated from a layer of amphibolite derived from homogeneous pillow basalt by a massive amphibolitic dyke. This third type of amphibolite is characterised by dark, hornblende-rich ovoid structures set within a pale green, epidote-rich matrix (Fig. 2.8). The matrix resembles the epidote-rich alteration veins and patches which overprint the amphibolites derived from homogeneous and variolitic pillow basalts. This unit may correspond with structures interpreted by Hall (1980, 1981) as ultramafic pillows. Hall (1981) described hornblenditic pillows, which range in shape and size, set within a pale green matrix rich in epidote and clinopyroxene. He noted that the proportion of matrix material (30%) is greater than that which is associated with typical pillows (0-10%), and he did not observe mineralogical or textural evidence of chilled margins (Hall, 1981). This description generally fits the third type of amphibolite observed during this study. However, it should be noted that smooth, convex tops and cuspate bases, typical of well-preserved pillows, were not observed within this unit. Alternatively, these hornblende-rich oblate bodies may relate to the alteration event. The pillow-like structures may be the result of a pervasive alteration pattern which penetrated a massive flow or sill.

Discussion of northern amphibolites

The amphibolites derived from homogeneous and variolitic, basaltic pillow lavas define distinct layers of great extent in the northern part of the Ivisârtoq greenstone belt. At map-scale, these layers form sequential repetitions between ultramafic layers (Fig. 2.3). Amphibolites derived from variolitic pillow basalts were observed directly adjacent to the ultramafic layers, whereas amphibolites derived from homogeneous pillow basalts occur between the variolitic layers. The sequence is repeated a number of times from south to north (see insert map), and was initially thought to represent a thrust sequence. However, this theory was disproved using geochemical analysis (see Chapter 3). Instead, the repetition of homogeneous and variolitic basalts is interpreted to represent interstratified flows of different compositions. These layers were isoclinally folded during a later deformational event.

The isoclinal folding event has previously been used to explain the heterogeneous deformation of the pillow lava-derived amphibolites (Hall, 1981). Detailed mapping conducted during this study has revealed that the heterogeneous deformation pattern of the amphibolites is inconsistent with the isoclinal folding. Isoclinal folding should have resulted in more intense deformation along the limbs and relatively less-deformed rocks in the hinge zone. However, heterogeneous deformation was observed across lithostratigraphic units within fold limbs, and some of the least deformed rocks are located in fold limbs, rather than fold cores. Therefore, this heterogeneity cannot be explained by isoclinal folding. High- and low- strain rocks form planar zones which are parallel with compositional layering, and are folded with the compositional layering into

large-scale isoclinal folds. Therefore the development of these variations in strain pre-date the isoclinal folding and likely formed during an earlier event. The rocks were likely modified during the later deformational event(s), however, they did not obliterate the strain variations established during the earlier event.

2.5.1.2 Northern Ultramafic Layers

Yellow-brown-weathering ultramafic layers, up to 600 m long and 30 m thick, are the most prominent topographic feature within the northern part of the Ivisârtoq greenstone belt (Fig. 2.14). In the field, the layers generally appear massive, coarse grained and homogeneous (Fig. 2.15). The layers have been disrupted into boudins which crop out as low 'whale back' ridges. The boudin necks are typically filled with granitic pegmatite. The two most prominant layers of ultramafic rocks within the study area are isoclinally folded (Fig. 2.3; see insert map) and small-scale folding was seen within parts of the layers. Two different fold orientations were noted within the largest, 200 m thick, boudin and this internal folding may account for its thickened nature (Fig. 2.16). Some ultramafic layers contain green schistose layers (Fig. 2.17), and at one locality, layers of banded amphibolite were noted within a brown-weathering boudin.

Four different ultramafic layers, including the two layers which define large-scale isoclinal folds, were investigated in detail. Samples were collected for detailed petrographic analysis along and across strike within the four layers. Compositions and textures differ between samples, and can be observed at thin-section scale. Remnant igneous olivine (Fig. 2.18) and pyroxene grains are preserved in low-strain pockets,

surrounded by more strongly deformed, fine-grained material, which comprise predominately chlorite and actinolite-tremolite. Within the high strain zones, there are syn-tectonic porphyroblasts of clinopyroxene (Fig. 2.18b). These millimetre-scale, low and high strain zones are thought to mimic the larger-scale heterogeneity and are considered analogous to the less strongly deformed central regions and to the more strongly deformed margins of the ultramafic layers, respectively.

The samples with the best preserved remnants of primary mineral assemblages come from the central region of some of the massive, brown-weathering boudins. Remnants of igneous olivine, orthopyroxene, and a few clinopyroxene crystals were observed, but recrystallization has destroyed igneous textures. The preservation of these primary minerals differs throughout the layers, from large grains with irregular grain boundaries in the least altered samples, to small, rounded grains in the more altered samples (Fig. 2.19).

The olivine grains have been altered to serpentine (antigorite), magnetite, iddingsite, amphibole (actinolite- tremolite), talc, and chlorite (Fig. 2.20; Fig. 21). The alteration products of the pyroxenes generally consist of amphibole (actinolite-tremolite), talc, chlorite, and serpentine (for orthopyroxene) (Fig. 2.22; Fig. 2.23). Large metamorphic amphibole (tremolite, cummingtonite) grains are abundant, with alteration products of talc, serpentine, and tremolite (Fig. 2.22).

The more recrystallized and deformed rocks from central regions of the four layers also contain phlogopite, magnesite, and minor amounts of disseminated pyrite and chalcopyrite. These rocks have a moderately to strongly developed foliation, locally

overgrown by syntectonic clinopyroxene porphyroblasts (Fig. 2.18b). Strain shadows of chlorite, phlogopite, or carbonate locally surrounding clusters of remnant olivine and clinopyroxene porphyroblasts, indicate that fluids were present during deformation (Passchier and Trouw, 1996). Late, lath-shaped growths of cummingtonite, tremolite, and chlorite, aligned at an angle to the main foliation, are interpreted as products of late retrograde metamorphism (Fig. 2.24). Locally, these grains are randomly oriented, which likely indicates that amphibolite metamorphism outlasted the latest deformational event.

The margins of the ultramafic layers are schistose zones made up of fine-grained talc, actinolite-tremolite, serpentine, and chlorite. Magnesite is locally present (Fig. 2.25). A well-developed foliation, principally defined by chlorite and tremolite, is present in most of the samples (Fig. 2.26). The texture and mineral assemblages of the marginal zones suggest that they have undergone intense deformation and hydrothermal alteration. The contacts between the ultramafic layers and neighbouring units are generally sharp, and the schistosity within the ultramafic bodies is most intense within 1 metre of the margin. This implies that most of the strain that affected the ultramafic bodies was partitioned to the margins. There is generally no corresponding change in the amount of deformation in the adjacent amphibolites, derived from basaltic pillow lava, and gabbroic intrusions.

Previously, Crewe (1986) interpreted the protolith of the ultramafic layers as dunite or harzburgite by correlating the present metamorphic mineral assemblages to an original anhydrous assemblage. However, this was based on simplistic assumptions. For instance, Crewe (1986) assumed that all antigorite was derived from olivine; however,

serpentine minerals can also be an alteration product of either, or both, orthopyroxene and amphibole. Furthermore, Crewe (1986) did not consider the impact of multiple metamorphic/metasomatic events in his reconstruction of the original mineral assemblages.

The Ivisârtoq ultramafic layers provide an excellent example of multiple metamorphic/metasomatic episodes. A minimum of two episodes of serpentine formation can be inferred in the most pristine samples. Within one sample, the earlier serpentine formed as an alteration product of original olivine and orthopyroxene, and was later overgrown by amphibole crystals (Fig. 2.27). These amphibole grains were affected by a second serpentinization event (Fig. 2.27b). The amphiboles may have been alteration products of olivine or pyroxenes and therefore the associated serpentine cannot be exclusively related to original olivine or pyroxene grain. In addition, the original relative proportions of olivine and pyroxene is unclear because olivine and orthopyroxene have similar, and in some cases, overlapping alteration products. It is therefore difficult to classify the rocks petrographically as either lherzolite or harzburgite. The ultramafic layers are not interpreted as having a dunitic protolith as the most pristine samples contain both olivine and pyroxene. The protolith of the ultramafic layers is therefore classified as a peridotite (Le Maitre, 2002).

This example clearly indicates that even the best preserved rocks were affected by multiple metamorphic events. However, unravelling the complete deformational and metamorphic history of the ultramafic layers using petrographic means is difficult, since the most recent metamorphic event(s) have generally obscured earlier features. Magnetite

appears to be the most useful mineral for gleaning evidence of the earlier events in the ultramafic rocks because it remains relatively stable during progressive metamorphism.

Magnetite is commonly produced in ultramafic rocks during serpentinization. The serpentine varieties chrysotile and antigorite are unable to accommodate iron from the breakdown of olivine and orthopyroxene, and magnetite is produced (Bucher and Frey, 1994). The following reaction illustrates the serpentinization of an Mg-rich, Fe-bearing olivine ($Fo_{90}Fa_{10}$ olivine):

$$3\ Fe_2SiO_4 + O_2 \rightarrow 2\ Fe_3O_4 + 3SiO_{2aq}$$

Fayalite Magnetite

$$3\ Mg_2SiO_4 + SiO_{2aq} + 4\ H_2O \rightarrow 2\ Mg_3Si_2O_5(OH)_4$$

Forsterite Chrysotile

The resulting assemblage is chrysotile (serpentine) + magnetite. Progressive metamorphism results in chrysotile reacting to form antigorite. However, the magnetite will remain stable and does not dissolve during prograde metamorphism (Bucher and Frey, 1994).

The magnetite within the Ivisârtoq ultramafic layers range in modal percent from 1-15%. As previously mentioned, there have been at least two episodes of serpentinization within these layers and there were probably multiple related episodes of

magnetite growth. Porphyroblasts of clinopyroxene overgrow magnetite grains indicating that this magnetite grew earlier in the rock's history.

The texture of magnetite grains gives evidence of earlier deformational events. In the more deformed and recrystallized ultramafic samples, magnetite grains typically define a moderate to strong foliation which locally outlines pseudomorphs of fine grained material made up of tremolite-actinolite or talc (Fig. 2.28). The original mineral was probably primary olivine or pyroxene that survived after partial serpentinization, but was altered during subsequent metamorphism. The magnetite-defined foliation developed before the primary minerals had completely broken down.

Other magnetite grains are concentrated in clusters (Fig. 2.29). These clusters may represent locations where primary olivine or pyroxene grains had been completely broken down to serpentine and magnetite. Later, during progressive metamorphism, the serpentine would have recrystallized to other metamorphic minerals, such as amphibole, while the magnetite remained stable. These clusters are overgrown by later metamorphic minerals, including amphiboles. Subhedral magnetite grains were also observed. Locally, they contain silicate inclusions which define a foliation. This foliation appears to have been rotated which indicates that the magnetite grew syntectonically (Fig. 2.30).

Discussion of northern ultramafic layers

In the field, the four major ultramafic layers appear massive and homogeneous; however, in thin section they were observed to be mineralogically and texturally heterogenous. Despite the dissimilarities, all of the observed mineral assemblages are

consistent with a peridotitic protolith. The primary minerals have been heterogeneously modified by various deformation and metamorphic events and igneous textures are no longer preserved in any of the studied samples.

Hall (1981) and Chadwick, (1986, 1990) noted diffuse layering within the ultramafic boudins, and speculated that this layering could be attributed to igneous layering. Chadwick (1986) reported that the ultramafic sheets locally grade up into gabbro and noted small mushroom-shaped apophyses of gabbro at the top of some sheets. These features were not observed by Crewe (1986) within the ultramafic layers in Ujaragssuit nunât or during the detailed mapping of Ivisârtoq in the present study. In contrast, sharp boundaries were typically seen between the ultramafic bodies and adjacent gabbroic layers. In several localities, the gabbro units were identified as dykes, because they crosscut the ultramafic boudins (Fig. 2.41). Chlorite-rich, schistose layers were the only compositional differences observed within the ultramafic layers during recent field mapping. These green, schistose layers are similar to the margins of the ultramafic layers and could have been formed by fluid movement that exploited planes of weaknesses, such as fractures and intensely deformed zones, within the ultramafic layers.

Based on field and petrographic evidence, it is difficult to conclusively determine the origin and emplacement mechanism of the ultramafic layers, a problem also noted by Crewe (1986). The layers were likely thicker than their current attenuated state and they are inferred to have been more coarse grained. The most pristine ultramafic samples preserve primary olivine and pyroxene grains up to 7mm. The original grains would have been larger as alteration reactions have reduced the grains to their current size. The

margins of the ultramafic layers are strongly deformed and primary contact relationships are obscured. The ultramafic layers have been interpreted by previous workers as sheet injections (Chadwick, 1991; Brewer et al., 1984), as tectonically emplaced slices of mantle residua (Hall, 1981), or as a combination of both processes (Crewe, 1986). Another possibility is that they may have originated as flows.

Thick ultramafic flows would probably be layered with a lower component of cumulate dunite and an upper spinifex textured component. The various deformational and metamorphic events may have modified this layering, however, it is doubtful that these events would have completely destroyed it. No layering attributable to igneous processes was observed within the Ivisârtoq ultramafic rocks. Due to the intensely deformed nature of the margins, one cannot rule out the possibility that an original spinifex textured portion had been removed tectonically.

Crewe (1984, 1986) interpreted some of the ultramafic layers as tectonically emplaced slices of mantle residua, a theory also suggested for similar rocks in the Fiskenaesset region (Friend and Hughes, 1978). The massive, coarse-grained nature of the unit is consistent with the protolith forming at depth. However, geochemical data from this study (see Chapter 3) are not compatible with this theory. Also, if the original layer was tectonically juxtaposed with the surrounding rocks, a gradation within the country rocks from high strain to low strain should be present. The contacts with the host rocks are sharp and a strain gradation is not observed.

The third hypothesis: that the ultramafic layers originated as sills, is the preferred interpretation. Brewer et al. (1984) and Crewe (1986) interpreted an intrusive origin for

the layers based on the observation of sheet-like inclusions of banded amphibolites, which were interpreted to be deformed basaltic pillow lava, within the ultramafic layers. A few thin layers of banded amphibolite, within the ultramafic units were observed during the present study. However, their primary relationship with the ultramafic rocks is unclear and therefore is not considered definitive proof in of an intrusive origin for the ultramafic layers. The observed banded amphibolite layers are all located in a region of multiple phases of folding and therefore could be an infolded part of the adjacent amphibolite derived from basaltic pillow lava.

Nevertheless, the ultramafic layers are interpreted to be sills as this model can account for their homogeneous nature. As shown by fluid mechanics, heavy solid particles in fluids coursing through pipes and slots tend to migrate away from the walls and form high concentration slug-like flows in channel centres (Leal, 1980). If the magma which formed the ultramafic sills contained phenocrysts (which is likely, as indicated by their coarse grain size), then these crystals would have migrated away from the walls to the flow centre (Marsh and Philipp, 1996). Thus sills with a very coarse grained centre portion and fine grained margins may have developed. Later deformation likely exploited this grain size variation to focus strain along the fine-grained margins.

2.5.1.3 Northern Quartzofeldspathic Schists and Gneisses

Numerous, thin layers of rusty-brown quartzofeldspathic schists and gneisses, were observed in the northern part of the Ivisârtoq greenstone belt. Some layers were also noted in the quartzofeldspathic and magnetic marker layers within the Marker High

Strain Zone. These layers range in thickness from a few centimetres to tens of metres, and are typically continuous for a few hundred metres, although, locally, they also occur as sporadic lenses. Continuous layers were noted adjacent to the medium green schistose margins of the ultramafic layers and sporadically within amphibolites derived from basaltic pillow lava (see insert map). The most noticeable layers have a bright orange-yellow colour, attributed to the weathering of sulphide minerals, and strongly contrast with the adjacent green amphibolites (Fig. 2.31b). The quartzofeldspathic schists and gneisses are moderately to strongly foliated and the contacts between these layers and neighbouring units are generally sharp.

Typically the quartzofeldspathic layers are parallel to the margins of the adjacent units. However, at one locality, (MM01-69) a continuous, rusty, quartzofeldspathic layer which follows the margin of an ultramafic layer is seen to diverge where the ultramafic layer is locally folded (Fig. 2.31). The quartzofeldspathic layer is not folded with the ultramafic layer; instead the layer continues into an amphibolite unit and cuts across pillow structures (Fig. 2.31). Along strike of this locality, a later gabbroic dyke cuts across the quartzofeldspathic layer and adjacent ultramafic layer. These contact relationships suggest that this quartzofeldspathic layer developed after the ultramafic layer was isoclically folded, and before the intrusion of the gabbroic dyke (see Table 2.1). In contrast, a quartz-feldspar-mica schist adjacent to another ultramafic layer which defines a separate isoclinal fold, is isoclinally folded with the ultramafic layer. This suggests that the protolith of this quartz-feldspar-mica schist developed before the isoclinal event.

Mineralogically, the assemblages of the various quartzofeldspathic schists and gneisses are typically recrystallized and primary textures are generally not preserved. Most of the northern quartzofeldspathic layers are dominated by polygonal quartz and feldspars (mostly plagioclase and lesser amounts of microcline), with differing amounts of biotite, amphibole (hornblende), muscovite, clinozoisite-epidote, and small amounts of garnet, anthophylite, chlorite, tourmaline, zircon, rutile, and titanite. Sulphide mineralization constitutes up to 5 modal % of the mineral assemblages and consists of fine-grained, eu-anhedral pyrite and minor amounts of chalcopyrite. Locally, the sulphides are altered to hematite.

Locally (MM01-73), a relict igneous texture, marked by interlocking, irregularly-shaped, quartz and feldspar grains was noted in a thin discontinuous rusty lens within the quartzofeldspathic layer of the Marker High Strain Zone. This rusty lens has a similar geochemical signature to the northern quartzofeldspathic layers which is different from the quartzofeldspathic layer of the Marker High Strain Zone (see Chapter 3). This rusty lens is relatively enriched in pyrite (5-7 modal %) and displays coarse compositional layering defined by layers rich in amphibole in contrast to layers rich in feldspar. The feldspar-rich layer is characterized by interlocking plagioclase grains which have undergone some degree of dynamic recrystallization; however a relict igneous texture is nonetheless preserved (Fig. 2.32).

Typically the main foliation in the quartzofeldspathic schists and gneisses is moderately to strongly developed and is generally defined by tabular micas and amphiboles, which are set within a polygonal matrix of quartz and feldspars (Fig. 2.33).

A grain size variation between coarse and fine grain layers, locally defines a small-scale gneissosity (Fig. 2.33), which in some samples appears broadly folded. The main foliation is locally folded and crenulated (Fig. 2.34) and an axial planar foliation is locally preserved. A later foliation is also locally defined in samples by muscovite and anthophylite grains which are at an angle to the main foliation (Fig. 2.35). Locally, muscovite grains are randomly oriented, which likely indicates that amphibolite metamorphism outlasted the latest deformational event.

An earlier fabric, is locally preserved as an inclusion trail within inter-tectonic garnets (Fig. 2.36; Passchier and Trouw, 1996). These garnets were observed within the quartzofeldspathic layer which is isoclinally folded with an ultramafic layer. The relict foliation within the garnets supports the interpretation that the quartzofeldspathic layer was affected by at least two deformation events.

Evidence of the early deformational event is also preserved in a sample (MM01-50) from the quartzofeldspathic layer which is isoclinally folded with the ultramafic layer which defines the westerly isoclinal fold. The early foliation is defined by compositional layering between biotite-rich quartzofeldspathic layers and biotite-poor layers (Fig. 2.37). A biotite-poor layer was observed to be folded and the biotite grains observed in the other layers were seen to be axial planar to this folding. The foliation defined by biotite may be an axial planar fabric related to the isoclinal folding event.

Discussion of northern quartzofeldspathic schists and gneisses

The mineral assemblages of the quartzofeldspathic schists and gneisses, in the northern part of the Ivisârtoq greenstone belt, are indicative of amphibolite facies metamorphism. This interpretation is supported by Hall (1981), who concluded that these rocks were subjected to temperatures between 550°C and 650°C, and to pressures between 3 and 6 kilobars. The quartzofeldspathic layers were locally affected by later retrogression to lower amphibolite facies conditions.

Chadwick (1990) interpreted the quartzofeldspathic schists and gneisses in the northern part of the Ivisârtoq greenstone belt as representing acid-intermediate tuffaceous sediments. His interpretation was based on unpublished compositional data and diffuse bedding characteristics which he observed in a thicker quartzofeldspathic-biotite-garnet gneiss in the southern part of the belt (Fig. 2.3; Chadwick, 1990). Hall (1981) also interpreted the quartzofeldspathic schists and gneisses as metasedimentary in origin, and interpreted differences in sulphide concentration between layers to represent "original sedimentary distribution, indicating rapidly fluctuating oxidation conditions during the deposition of the sediments" (Hall, 1981, pp. 72).

Within the present study, layering within the northern quartzofeldspathic schists and gneisses were seen to be moderately to strongly deformed and display evidence of dynamic recrystallization and grain boundary reduction. The layering observed is attributed to deformational processes and is not thought to reflect primary bedding. Furthermore, locally a relict igneous texture was preserved (Fig. 2.32) which suggests

that these layers may be intrusive and had a tonalitic protolith; this interpretation is supported by geochemistry (see Chapter 3).

This theory is strengthened by the observation of a quartzofeldspathic layer cutting across amphibolites derived from pillow lavas (Fig. 2.31). Hall (1981) also noted two localities in which "a thin horizon of quartz-biotite schist obliquely truncates neighbouring amphibolites" (pp. 71). Hall (1981) suggested that these contacts may be tectonic or that they many represent original sedimentary cross-cutting relationships. An intrusive protolith could also account for Hall's observations. Tonalitic intrusions would likely have intruded along planes of weakness, such as the boundary between the ultramafic layers and the amphibolites. Field evidence suggests that they may have intruded during two different episodes.

2.5.1.4 Mafic Dykes and Sills

There are numerous amphibolite dykes and sills present within the northern part of the Ivisârtoq greenstone belt. They are actually observed throughout the belt and were identified within the Marker High Strain Zone and within the southern part of the belt. The dykes cut previously deformed tonalite layers, ultramafic layers, and layers of amphibolite derived from basaltic pillow lavas. The most common types observed were equigranular, gabbroic dykes and sills, and dykes containing large relict plagioclase phenocrysts set within a fine-grained matrix, which superficially resemble the B-type Ameralik dykes found in the Amîtsoq gneisses (Chadwick, 1981). The matrix of both types of dykes is dominated by hornblende and plagioclase. The equigranular dykes have

an average grain size of 0.5 mm -1 mm (Fig. 2.38). Large, relict plagioclase phenocrysts in the other variety range in size from 1 cm - 30 cm (Fig. 2.39) and range in intensity of deformation from ovoid shapes to stretched, elongate lenses (Fig. 2.40). Other fine grained, schistose, amphibolitic dykes were locally observed in the northern part of the belt and are composed primarily of pale green-yellow pleochroic actinolite.

The mafic dykes and sills range in width from centimetres to tens of metres. They also range in strike length from a few metres to hundreds of metres. In the northern section, the gabbroic sills are parallel to the contacts of other lithological layers, including , ultramafic layers, quartzofeldspathic layers, and layers of amphibolites derived from basaltic pillow lavas. Some gabbroic dykes are locally parallel with the other units, but along strike are seen to branch and cross-cut these units (Fig. 2.41).

The amphibolite dykes and sills can be hard to distinguish in the field from metavolcanic amphibolites. Initially some of the sills were interpreted as massive flows within amphibolite derived from pillow lava, however, detailed mapping revealed sharp contacts which cut the pillows instead of a gradational contact. Gabbroic sills adjacent to ultramafic sheets were also difficult to differentiate from possible layering within the ultramafic bodies. The sharp boundaries between the gabbroic rocks and ultramafic sheets suggest that they were intrusive and do not represent primary layering.

In the Ivisârtoq greenstone belt, the amphibolite dykes and sills are very weakly to moderately deformed. Gabbroic dykes which contain only partially recrystallized feldspar grains and exhibit a very weakly developed foliation are interpreted as being weakly deformed (Fig. 2.42). Whereas equigranular feldspar which have been completely

recrystallized, are used to indicate more strongly deformed dykes. Foliations are defined by elongate patches of leucocratic minerals and by euhedral hornblende. The more deformed rocks have a well-developed mineral lineation.

Discussion of the mafic dykes and sills

The amphibolite dykes and sills observed in the Ivisârtoq greenstone belt are typically completely recrystallized to hornblende-plagioclase assemblages. They may have intruded at different times during the deformation history of the belt indicated by cross-cutting field relationships and by the differences in foliation development and recrystallization (Table 2.1). Chadwick (1990) stated that some of the amphibolite dykes may have been feeders to the volcanic rocks, or that they may be part of a younger swarm of dykes seen to the north in Kangilíngua (Chadwick, 1990).

2.5.1.5 Felsic Pegmatites

Large, felsic pegmatite bodies (kilometre-scale) are visible on 1:10 000 airphotos within the northern and southern parts of the Ivisârtoq greenstone belt, as well as within the Marker High Strain Zone. Smaller, finer-grained granitic dykes (metre-size) were observed exclusively within the Marker High Strain Zone and the southern section (Fig. 2.44). The large, leucocratic pegmatites are typically homogeneous, coarse-grained, with an average grain size > 2 cm, and locally contain large muscovite or biotite books. The large pegmatite bodies intruded as sheets and have a sub-horizontal orientation (Fig. 2.45). They are observed within boudin necks of the disrupted ultramafic layers in the

northern part of the Ivisârtoq greenstone belt (see insert map), and are seen to cross-cut the other main units of the belt including amphibolites derived from pillow lavas, and quartzofeldspathic schists and gneisses. No contact metamorphic effects were observed in the adjacent rocks.

The pegmatitic sheets are relatively undeformed. They are not lineated and a very weak foliation is only locally developed. The sheets are not folded and are therefore thought to have intruded after the major deformational events (see Table 2.1). Any resemblance to fold-like patterns on an airphoto scale is simply the effect of topography.

The pegmatite bodies are composed of quartz + feldspar (plagioclase and microcline) ± magnetite ± muscovite ± biotite with minor amounts of apatite, titanite, zircon and epidote (or clinozoisite), and contain less than 5% mafic minerals (Hall, 1981; Robertson, 1985). Petrographical analysis revealed deformation structures within plagioclase grains, including microfracturing, undulose extinction, and tapering deformation twins (Fig. 2.46), which are attributed to low grade conditions (300-400°C; Passchier and Trouw, 1996). The presence of subgrain boundaries and bulging, irregular grain boundaries (Fig. 2.47) indicate that recovery and recrystallization processes were also operating (Passchier and Trouw, 1996); however, these processes are preserved at an early stage in their development and are not extensive. Muscovite and clinozoisite were locally noted along microcracks and grain boundaries and may be indicative of fluid migration along these planes (Fig. 2.48). Also, the plagioclase grains had a dusty appearance due to localized sericite formation (Fig. 2.46b).

Discussion of felsic pegmatites

The large, coarse-grained sheets of granitic pegmatite in the Ivisârtoq region have previously been correlated with the Qôrqut granite complex (Hall, 1981; Brewer, 1985; Robertson, 1985). The Qôrqut granite complex is generally accepted to be ~ 2550 Ma (McGregor, 1973; Moorbath et al., 1981; Friend et al., 1985). Within the Ivisârtoq region the following ages, obtained from granites and pegmatites, have been reported: Ivisârtoq: Rb-Sr 2430 ± 60 Ma, Pb/Pb 2615 ± 35 Ma (Taylor et al., 1980); Kangiussap nuna (southwest of Ivisârtoq): Rb-Sr 2490 ± 20, Pb/Pb 2625 ± 15 Ma (Robertson, 1985); Nunatarssuaq (south of Ivisârtoq): Rb-Sr 2553 ± 39 Ma (Brewer, 1985). The textures and field relationships of the pegmatite sheets observed during the present study support a relatively young emplacement age for these pegmatites.

Robertson (1985) suggested that the absence of contact metamorphic aureoles around the pegmatitic sheets, indicate that regional metamorphism persisted until ~2600 Ma. He further stated that "if this were not the case, retrogression would have certainly taken place given the amount of water present in the Qôrqut granite and pegmatite magmas" (Robertson, 1985; pp 84). This conclusion is supported by petrographical evidence observed within the ultramafic and quartzofeldspathic layers in the northern section of the Ivisârtoq greenstone belt. Randomly oriented amphibolite-grade minerals are locally observed and likely indicate that amphibolite facies metamorphism outlasted the latest deformation event, an interpretation also supported by Chadwick (1985) and Robertson (1985).

2.5.1.6 Sequence of events for northern part

The northern part of the greenstone belt is generally less deformed than the southern part of the belt. This distinction allowed age relationships between units to be discerned and ultimately a relative sequence of events for the northern part of the belt to be defined (Table 2.1).

Based on cross-cutting field relationships the amphibolites derived from basaltic pillow lavas appear to be the oldest units. Some of the amphibolites have been heterogeneously affected by alteration, marked by epidote veins and diffuse zones, which are cross-cut by later units, including ultramafic and tonalitic sills.

A heterogeneous strain gradient, which is evident within the amphibolite units, marks the earliest deformational event, termed DN_1 ("N" indicates northern part of the belt). This event affected the amphibolites, ultramafic layers, and some tonalitic layers. In thin section magnetite textures in ultramafic rocks (Fig. 2.29), and textures within tonalitic layers (Fig. 2.36; Fig. 2.37) record this early deformational event.

Following DN_1, the major units were intruded by mafic dykes. All of the units were then deformed by a second major deformational event, termed DN_2. This event resulted in the development of E-W isoclinal folds and formed a steeply dipping, approximately east-west oriented axial planar foliation which is observed within most units. In thin section this well developed foliation is observed in most units, including, ultramafic rocks (Fig. 2.26), tonalitic layers (Fig. 2.33, Fig. 2.34), and amphibolites (Fig. 2.12; Fig. 2.13).

Later tonalite sheets then intruded the northern part of the belt, followed by the intrusion of other mafic dykes. These units are not isoclinally folded and have only a weakly developed foliation.

A later, regional deformational event (DR), caused large-scale folding, forming the southwest-closing V-shaped structure of the belt. In thin sections of amphibolite (Fig. 2.13b), ultramafic (Fig. 2.24), and tonalitic (Fig. 2.35) rocks, a foliation oriented at an angle to the main DN_2 foliation is likely indicative of this event. Locally, randomly oriented amphibolite-grade minerals in most lithologies indicate that metamorphism outlasted the latest deformational event.

The youngest intrusive unit in the northern part of the belt is represented by large bodies of felsic pegmatite, which have only suffered low-grade deformation.

Table 2.1: Sequence of events for Northern part of the belt

11		Coarse leucogranite pegmatite (equivalent to Qôrqut?);
10	DR	Regional, large-scale folding of belt. Amphibolite-epidote amphibolite facies metamorphism; randomly oriented amphibolite-grade minerals in most lithologies also indicate that metamorphism outlasted deformation
9		Intrusion of mafic dykes and sills
8		Intrusion of tonalite sheets (e.g. outer edge of the westerly isoclinal fold); unit not folded with the ultramafic layer; cut pillow structures and is cut itself by later gabbroic dyke
7	DN_2	Major deformational event and associated amphibolite facies metamorphism - formed isoclinal folding.
6		Mafic dykes intrude; cut previously intensely deformed basaltic pillow lavas, tonalite sheets, and ultramafic sheets; cut early alteration of pillow lavas
5	DN_1	Intense heterogeneous deformation; strain variation established within units (SN_1 foliation preserved locally in garnet porphyroblasts of tonalite sheets)
4		Intrusion of tonalite sheets (e.g. inner side of the easterly isoclinal fold);
3		Intrusion of ultramafic sills: form massive ultramafic sheets with sharp boundaries
2		Extensive hydrothermal alteration; (epidote-diopside-garnet) vein networks and in pillow cores
1		Deposition of homogeneous and variolitic pillow lavas

2.5.2 Southern Part of the Southern Limb

The southern part of the Ivisârtoq greenstone belt is distinct from the northern part in terms of composition and intensity of deformation. The southern part consists of strongly deformed schists and gneisses of diverse composition, which contrast the well-preserved primary structures, such as pillows, in the northern part of the belt. Furthermore, the southern part does not contain ultramafic layers like those found in the northern part.

The Marker High Strain Zone is described as a separate unit within the southern part of the belt due to its intensity of deformation. The strain gradient across the northern margin of the Marker High Strain Zone into the northern part of the belt is locally gradational but regionally is sharp. Directly south of the Marker High Strain Zone, amphibolites with moderately to strongly deformed pillow structures were observed. These amphibolites become progressively more deformed forming banded amphibolites to the south. Further southwards, a heterogeneous area of different compositional layers was studied. This region consists of banded amphibolites, homogeneous metagranodiorite, gabbroic rocks, and a wide layer of predominately quartz-feldspar-biotite-schist (see insert map). The nature and protolith interpretation of each unit in the southern region are addressed in the following sections.

The primary relationships and relative ages of the different units in the southern part of the belt could not be determined from field observations due to the intensity of deformation and highly strained boundaries of most rock types. Therefore a relative

sequence of events, as determined for the northern part of the belt, could not be interpreted for the southern part.

2.5.2.1 Marker High Strain Zone

The boundary between the northern and southern parts of the Ivisârtoq greenstone belt is marked by a distinct, E-W trending zone of intense deformation, termed the Marker High Strain Zone. This zone comprises two main layers: a layer of highly strained quartzofeldspathic rocks intercalated with thin amphibolite horizons, and a layer of ultramafic schists termed the magnetic marker (Fig. 2.3). Locally, mylonitic textures were observed. The zone is bordered to the north and south by deformed amphibolites derived from basaltic pillow lava.

2.5.2.1.1 Quartzofeldspathic and Amphibolitic Marker Layer

The quartzofeldspathic and amphibolitic layer is characterized by thin to coarse (centimetre to metre scale) horizons of amphibolite intercalated with more abundant quartzofeldspathic rocks (Fig. 2.49). The layer ranges in width from 20 m to 150 m with an average width of 100 m, and has a strike length of at least 8 km. Primary textures are typically not preserved. The boundaries between this layer and adjacent units to the north and south are sharp. To the west this layer is continuous with a thick layer of quartz-feldspar-biotite-garnet schist and gneiss (see section 2.4.2.2). Poorly preserved pillow structures were recognized adjacent to the northern margin, whereas the southern margin is bordered by the magnetic marker. Several minor components were also

observed within the quartzofeldspathic and amphibolitic layer of the Marker High Strain Zone, including a thin, rusty quartzofeldspathic layer, a folded fine-grained granitic layer (Fig. 2.44), and a folded gabbroic dyke (Fig. 2.50). The thin, rusty quartzofeldspathic layer is grouped with the northern quartzofeldspathic (tonalitic) layers based on its mineralogical (see Section 2.5.1.3) and geochemical (see Chapter 3) characteristics. The folded fine-grained granitic layer is interpreted as the recrystallized equivalent of coarse-grained pegmatites which are observed throughout the belt.

The thin amphibolite horizons are composed almost exclusively of hornblende. The typically recrystallized quartzofeldspathic layer contains biotite and/or muscovite ± garnet ± amphibole (hornblende and/or cummingtonite) ± garnet, ± ilmenite ± sillimanite, lesser amounts of dark green tourmaline (schorl), sulphides and rutile, and trace amounts of zircon. The felsic layer superficially resembles the thin quartzofeldspathic (tonalitic) layers observed in the northern part of the greenstone belt. However, detailed petrographical and geochemical work (see Chapter 3) revealed that the felsic layer within the Marker High Strain Zone is distinct from the northern quartzofeldspathic layers. Aluminous minerals such as garnet and sillimanite (observed as needles and as fibrous masses termed fibrolite, Fig. 2.51a) are more abundant in samples from the Marker High Strain Zone compared to the layers studied in the northern part of the belt. The quartzofeldspathic layer in the Marker High Strain Zone more closely resembles the thick quartz-feldspar-biotite-garnet unit in the southern part of the belt (see Section 2.5.2.2).

Felsic rocks from the Marker High Strain Zone typically exhibit compositional layering of mica-rich and poor layers (Fig. 2.52) which may be attributable to metamorphic segregation of these minerals during deformation. Variations between coarse-grained and fine-grained layers were also noted (Fig. 2.53). The quartz and feldspar grains are typically fine-grained and polygonal, whereas the mica grains define a moderate to strong foliation. Lenses of coarser grained quartz were also noted (Fig. 2.51b). These lenses may have formed by the transposition of mica-poor, quartz-rich layers and thus may be the result of two phases of deformation: the first event would have formed the compositional layering, and the second event would have transposed the layers, forming lenses (Fig. 2.54). The quartz lenses may also solely be an effect of metamorphic segregation or a combination of both transposition and metamorphic segregation. The large grain size of the quartz comprising the lenses may be attributed to static recrystallization. In the quartzofeldspathic rocks, the quartz lenses are not thought to be augen, typical of intensely deformed zones, as generally augen are composed of feldspar. This is because quartz behaves as the weaker mineral at low-medium grades and deforms ductilely, whereas feldspars deform by the development of core-and-mantle structures (Passchier and Trouw, 1996).

Garnet porphyroblasts also preserve evidence of multiple phases of deformation. Some of these grains preserve an earlier foliation, typically at an angle to the main foliation which wraps around the porphyroblasts (Fig. 2.55). This indicates that the porphyroblasts were inter-tectonic; they grew after an early deformation event and before the onset of a later event which rotated the grains. Locally, staurolite inclusions were

noted in large garnet porphyroblasts (Fig. 2.56). An earlier foliation was also noted in some feldspar grains (Fig. 2.57). Microprobe analysis was used to verify that these grains were feldspars and not inclusion-rich corderite grains. An S-C fabric indicative of dextral shearing may have been locally preserved within these grains (Fig. 2.57b). This suggests that the rock may have a complicated history comprising several deformational events, an interpretation which is also supported by field evidence. Unfortunately, due to the structural complexity of the southern region of the belt, microstructure features could not be correlated with relative deformational events.

Discussion of quartzofeldspathic and amphibolitic layer in Marker High Strain Zone

The intensely deformed nature of the quartzofeldspathic layer above the magnetic marker makes a protolith interpretation difficult. Previously, this unit was interpreted as metasedimentary in origin; Chadwick (1990) had grouped this unit with a thick unit of quartz-feldspar-biotite-garnet schist/gneiss in the southern part of the belt (see section 2.5.2.2). Based on mineral assemblages, notably Al-rich minerals such as garnet and Al-silicates (sillimanite), and on field relationships (the fact that the layer is continuous with the thick quartz-feldspar-biotite-garnet layer) this interpretation is plausible. Geochronological (see Section 2.6.2.2) and geochemical (see Chapter 3) data also support this interpretation. The thin amphibolite horizons observed within the quartzofeldspathic layer resemble highly deformed pillows (which has been confirmed geochemically, see Chapter 3). Their interleaved nature may be the result of tectonic processes. The complex deformational history of the Marker High Strain Zone is evident from inclusion

patterns within garnet and feldspar grains. Folded granitic pegmatites and mafic dykes suggest that a relatively late deformational event occurred (post ~2.5 Ga: the interpreted age of the pegmatites).

2.5.2.1.2 Magnetic Marker

A magnetite-rich layer called the 'magnetic marker' by Chadwick (1990) has received a lot of attention in previous studies of the Ivisârtoq greenstone belt (Appel, 1988; Chadwick, 1990). The layer was interpreted as an ultrabasic pyroclastic deposit by Chadwick (1990) and was used by Chadwick to subdivide the belt into an upper and lower amphibolite groups. It is within the Marker High Strain Zone which is used in this study as the dividing feature separating the northern and southern parts of the belt.

This layer of ultramafic rocks is unique. The grey-green layer is distinguished by a high magnetic susceptibility, and was suitably termed the 'magnetic marker' by Chadwick (1990). This study retains the use of this term. In the field, the layer is more difficult to spot than the other ultramafic layers, because it does not share their typical brownish-yellow colour or their relatively high relief. The layer ranges in width from 10 to 50 m and has a strike length of at least 7 km. It is generally schistose and locally mylonitic with tight folds (Fig. 2.58), which may explain the variation in thickness along strike. The southern margin is typically bordered by banded amphibolite, however, this margin is locally obscured by dolerite dykes or by strongly foliated quartzofeldspathic layers.

The magnetic marker was studied in detail at approximately twenty localities during this study. Samples were collected along two detailed transects across the width of the magnetic marker (17 samples total; Fig. 2.59), as well as from four other localities (Fig. 2.59). The composition of the unit differed along the transects.

The rock is typically composed of chlorite, tremolite, phlogopite, talc, and serpentine, which are overgrown by pyroxene and less abundant olivine porphyroblasts (Fig. 2.60). Strain shadows of chlorite, surrounding these porphyroblasts indicate that fluids were present during deformation (Fig. 2.62; Passchier and Trouw, 1996). Remnant igneous olivine grains are preserved locally (Fig. 2.61). Pseudomorphs after clinopyroxene or olivine contain randomly oriented chlorite laths (Fig. 2.63), which likely indicate that lower amphibolite grade metamorphism outlasted the latest deformation event.

Up to 15-35 modal % of magnetite was noted, a significantly higher proportion than was observed in other ultramafic layers. The magnetite grains typically define a strong foliation and locally define textures similar to those observed in the other ultramafic sheets. These textures include outlines surrounding zones of altered minerals which likely represent the location of an original mineral (Fig. 2.64), and magnetite clusters which represent an area where an original olivine or pyroxene grain had been completely broken down (Fig. 2.65). Hematite is locally associated with magnetite, and with minor (<5%) amounts of chalcopyrite and pyrite grains.

Other rock types observed in the transects include carbonate-rich rocks (up to 50% carbonate) seen in transect 2 and a coarse-grained, garnet-pyroxene-epidote-

amphibolite schist which forms a metre wide zone on the northern edge of transect 1. The coarse-grained schist also contains magnesite and 5-10 modal % titanite (Fig. 2.66). This zone may correspond to a layer described as a garnet skarn by Appel (1988) who also reported scheelite. This unit may represent a highly metasomatised version of the intensely deformed amphibolites derived from basaltic pillow lava and is not considered part of the magnetic marker. Several thin (<4 m), highly deformed quartzofeldspathic layers are also present within both transects (Fig. 2.59), but are likewise not considered to represent a component of the magnetic marker unit.

Discussion of magnetic marker

The magnetic marker is distinct from the ultramafic sheets within the northern part of the Ivisârtoq greenstone belt. It is more schistose, has a higher magnetic susceptibility, and has a higher proportion of carbonate-rich zones. However, in thin section, some magnetic marker samples resemble the strongly deformed samples of the northern ultramafic layers. Initially, this similarity was thought to indicate that the magnetic marker represents a more deformed and metasomatised version of the ultramafic layers. However, the uniqueness of this layer was confirmed by geochemistry which demonstrated that the magnetic marker and the ultramafic layers have different origins (see Chapter 3).

Chadwick (1990) speculated that the magnetic marker formed as an "ultrabasic pyroclastic deposit with intersheeted ultrabasic sills or flows". This theory was based on the compositions and internal structures including 'small-scale lenticular structures'

which Chadwick (1990) compared to lapillistones found in a komatiitic complex in Finland (Saverikko, 1985). During this study, a location of interest outside of the detailed, measured transects contained centimetre-scale, weathering-resistant, rounded structures (0.5cm - 3cm; Fig. 2.67). These ovoids may correspond to the lenticular structures observed by Chadwick (1990). Detailed petrography revealed that the ovoids are composed of large olivine grains (Fig. 2.67b). It is difficult to determine if these grains are primary or secondary in nature, and therefore it is uncertain if they represent a primary volcanic feature. Overall geochemical data (see Chapter 3) and observations by Chadwick (1990) suggest that the magnetic marker is an intensely deformed ultramafic pyroclastic deposit, which contains later quartzofeldspathic intrusions. Variations in composition and texture may be attributed to the difference in deformation, metamorphism, and/or in the original composition of the unit along and across strike.

2.5.2.2 Units South of Marker High Strain Zone

The area directly south of the Marker High Strain Zone is characterized by intensely deformed and carbonatized amphibolites. Recognizable pillow structures are locally preserved directly adjacent to the magnetic marker. They are seen to be transformed to banded amphibolites along strike, and across strike to the south. Overall the intensity of deformation in the region south of the Marker High Strain Zone increases southwards. The banded amphibolites are characterized by medium-green layers alternating with dark green layers, similar to banded amphibolites observed in the northern part of the belt (Fig. 2.68).

The central portion of the southern part of the belt is similarly characterized by banded amphibolites, however, homogeneous amphibolites were also noted. The relationship between these rock types is unclear; the massive zones may represent amphibolites derived from basaltic flows or sills. The amphibolites in this area are generally at a lower altitude than those of the northern part of the belt, and were typically hard to differentiate due to lichen obscuring exposed areas. Carbonate alteration effects were observed in this area, and were characterised by the pock-marked (pitted) appearance of many outcrops (Fig. 2.69).

The most southerly part of the belt is distinguished by the presence of a thick layer of quartz-feldspar-biotite-garnet schist/gneiss and of homogeneous grey metagranodiorite and metagabbroic rocks, which are not observed in the northern part of the Ivisârtoq greenstone belt. The most southerly units in this area are typically strongly foliated and folded together, locally forming complex folds patterns (Fig. 2.70). Other rock types in this area include banded amphibolites, homogeneous amphibolites, mafic dykes, and felsic pegmatitic dykes, all of which have been described in previous sections. This section will therefore focus on the thick quartz-feldspar-biotite-garnet layer and the homogeneous grey metagranodiorite and metagabbroic rocks.

Thick quartz-feldspar-biotite-garnet schist/gneiss layer

The thick (500 metre wide) quartz-feldspar-biotite-garnet unit has a brown-coloured weathered surface and varies in deformational intensity from schist to gneiss. This unit also includes thin layers of amphibolite which are locally folded with

the schists/gneisses (Fig. 2.71). Locally within a schistose part of the layer (Station MM01-91), there are small (2-5 centimetre), siliceous lenses (Fig. 2.72). Large, oval felsic fragments were also observed at this locality (Fig. 2.73). One fragment, which texturally and compositionally resembles rhyolite, is 10 cm long and 5 cm in height. It has a white weathering matrix with 1 mm quartz phenocrysts. Another fragment is 60 cm long, 15 cm in height, and texturally and compositionally resembles a tonalitic gneiss. The surrounding schist consists of millimetre-size quartz, feldspar, biotite, and deep red garnet grains. Both of the larger fragments have a foliation which is not aligned with the main foliation of the matrix.

In thin section the schistose/gneissic region of the layer is composed primarily of quartz (30-50%), plagioclase (and associated sericite alteration; 30-40%), biotite (10-20%), amphibole (cummingtonite and Ca-rich hornblende; 0-7%), and garnet (≤5%). There are variable minor amounts of pyrite, tourmaline, rutile, and zircon. The unit is characterized by a matrix dominated by quartz and feldspar (Fig. 2.74), with a general seriate-polygonal grain texture (as defined in Fig. 3.30 Passchier and Trouw, 1996). The quartz grains exhibit evidence of dynamic recrystallization (fine grained ~μm and bulging boundaries) and grain area boundary reduction (coarser grained, ~0.5 mm, polygonal shape with no undulose extinction). The larger grains are common in monomineralic or polymineralic quartz ribbons. Seams of tourmaline were also noted within this unit (Fig. 2.74).

A strong foliation is defined primarily by biotite grains which are concentrated in layers or dispersed throughout the matrix. Locally these grains define an S-C fabric (Fig.

2.75). The main foliation is axial planar to folds defined by quartz ribbons. The unit also exhibits compositional layering and layering marked by variations in grain size.

Garnet porphyroblasts are fractured and range in size from 1.25 mm to 5 mm. They contain numerous inclusions such as biotite (in healed cracks and individual grains), plagioclase, amphibole, quartz, and opaque minerals. Locally the garnet inclusions are oriented and indicate that the garnets grew throughout the deformation history of the unit (Fig. 2.76).

Homogeneous metagranodiorite

Light grey, medium, even grained, homogeneous, granitoid rocks (Fig. 2.77) are observed in discontinuous layers which are interlayered and folded with banded amphibolites, mafic dykes, and the thick quartz-feldspar-biotite-garnet schistose/gneissic layer.

The light grey rocks are characterized by 15-30% amphibole, 15-25% untwinned feldspars (mostly plagioclase and associated sericite alteration), 20-30% quartz, 10-15% biotite, ± garnet (≤5%), ± sillimanite, ± chlorite, ± epidote, and minor amounts of rutile, ilmenite, and zircon. The amount of alkali feldspars is uncertain. Based on its major element composition (Chapter 3), this unit is classified as a granodiorite. The matrix is dominated by polygonal quartz and feldspars. Tabular amphibole and biotite typically define a weak to moderate foliation and locally, these minerals also define an S-C fabric. The foliation wraps pre-tectonic garnets which have an eroded appearance. Locally, untwinned feldspar grains with many small inclusions of sillimanite and/or ilmenite

resemble pinitized corderite, however, microprobe analysis verified that these grains are plagioclase. No cordierite was detected within these rocks.

Locally a homogeneous granitoid was seen to cross-cut a foliated gabbroic rock (Fig. 2.78). The two units were subsequently deformed together resulting in a folded contact. The cross-cutting relationship suggests that the granitoid rock (which has a granodioritic composition) is intrusive in nature but was later modified. It is presently referred to as a metagranodiorite.

Homogeneous metagabbro

Locally homogeneous, dark grey gabbroic rocks (Fig. 2.79) were observed within the southern part of the belt, but are less abundant than other units. Most gabbroic outcrops are too small to be showen on the 1:10 000 map (insert at back of thesis). These rocks can be difficult to differentiate from the light grey metagranodiorites in the field due to their similar textures and typically lichen-covered surfaces, however they are easily distinguished by petrographical means. Mineralogically the metagabbros are characterized by recrystallized amphibole (40-60%), plagioclase (20-30%, anorthite content >50), quartz (<5%), ± biotite, ± epidote ± garnet. A weak to moderate foliation is typically defined by amphibole grains whereas quartz and feldspar grains are equigranular. Locally, an interlocking relict igneous texture is preserved (Sample MM01-92). Using the IUGS QAP classification (Le Maitre, 2002), the gabbroic unit is classified as hornblende gabbro.

Discussion of units south of the Marker High Strain Zone

Previously, the homogeneous metagranodiorites were not recognized as a separate mappable unit (Chadwick, 1990; Chadwick, unpublished 1:20 000 map). It is difficult to differentiate the quartz-feldspar-biotite-garnet schistose/gneissic rocks and homogeneous metagranodiorites, even at a scale of 1:10 000, as they are relatively finely interlayered; however, they have been schematically represented on the map (see insert at back of thesis).

The metagranodiorite unit is interpreted to be younger and intrusive into the dark grey gabbroic unit (hornblende gabbro) based on an observed cross-cutting relationship. Also, the homogeneous nature of the granodioritic rocks may be a reflection of an intrusive parentage. The gabbroic unit may be related to a major body of layered leucogabbro located east of the mapped area (Fig. 2.3), however detailed petrography, geochronology, and geochemistry of these units would be needed to confirm this theory.

The thick quartz-feldspar-biotite-garnet schistose/gneissic layer has previously been interpreted as deformed acid-intermediate tuffaceous sedimentary rock based on its composition and diffuse bedding characteristics (Chadwick,1990). Chadwick (1990) described compositional banding, rare trough structures, and small-scale lenticular aggregates of quartz as primary depositional features (Chadwick, 1990). Based on recent detailed field mapping, some of these lines of evidence have been questioned. Compositional layering in the unit is thought to have resulted from deformation and metamorphic segregation of minerals. The unit is strongly recrystallized and transposed; isoclinal folds are preserved locally. The layering may therefore not be a reflection of

primary bedding. Similarly, trough structures were not observed, however, interleaving and folding of layers were recognized. In agreement with Chadwick's (1990) observations, small-scale lenticular aggregates of quartz and several large, rounded felsic fragments were observed during recent mapping. Their presence may indeed be a reflection of a sedimentary or volcanic origin for the thick schistose/gneiss layer. These round fragments may be sedimentary clasts which were preserved in a lower strain zone within the schistose host layer. Conversely, the fragments may have formed by deformational processes and could therefore be better preserved pieces of the protolith.

Overall, based on field, geochronological (see Section 2.6.2.2), and geochemical observations (Chapter 3) the interpretation that the schistose/gneissic layer was derived from a volcanoclastic or sedimentary protolith is preferred. The rounded fragments are interpreted as possible primary sedimentary clasts.

2.6 GEOCHRONOLOGY

2.6.1 Analytical Methods

Numerous geochronological studies have been performed on the Archean rocks in southwest Greenland, most within the vicinity of the Isua greenstone belt and Nuuk (Crowley et al., 2002, and references therein). Recently, the method most commonly used to date these rocks has been the ion microprobe, more specifically the sensitive high-resolution ion microprobe (SHRIMP) and the CAMECA 1270 IMS instruments area (e.g. Friend and Nutman, 2005; Whitehouse et al., 1999).

The SHRIMP and CAMECA 1270 IMS techniques have been favoured over ID-TIMS because they are able to analyse small (20-25 μm), precise spots on a single grain, thereby avoiding inherited cores, overgrowths, and metamict zones (Crowley et al., 2002; Cox, 2002). In contrast, when using ID-TIMS, the entire zircon grain, except sometimes abraded rims, is typically analysed. An ion microprobe is also cheaper to use and less time consuming than analysing grains by ID-TIMS. The major advantage of ID-TIMS is its high precision of measurement; ID-TIMS can produce a $^{206}Pb/^{238}U$ measurement with 0.02-0.4% precision for a single grain older than ca. 1000 Ma, whereas, the same measurement would have a precision around 0.5-4% using SHRIMP or CAMECA 1270 IMS (Cox, 2002). The LAM-ICPMS has similar advantages to ion microprobe techniques: it is economical, time efficient, and is able to analyse small spots.

Although an immense amount of geochronological work has been conducted within and around the Isua greenstone belt, very limited work has been performed on its neighbouring greenstone belts to the south. Before 2005, only one U/Pb age had been obtained within the Ivisârtoq greenstone belt. A U-Pb TIMS age of 2580 Ma was determined on zircons from an assumed paraschist and was interpreted as a metamorphic age (Baadsgaard, 1976). Recently, Friend and Nutman (2005) reported three more zircon ages within the southern arm of the belt using a SHRIMP. They reported a $^{207}Pb/^{206}Pb$ date of 3075 ± 15 Ma (1σ error) for a felsic schist which was interpreted as volcano-sedimentary in origin, a $^{207}Pb/^{206}Pb$ date of 2961 ± 11 Ma (1σ error) for a granitic rock north of the northern boundary of the belt, and a $^{207}Pb/^{206}Pb$ date of 2963 ± 8 Ma (1σ

error) for a granodioritic gneiss interpreted as an intrusion into the anorthosite unit (east of mapped area, see Fig. 2.3).

Considering the lack of geochronological information published for the Ivisârtoq greenstone belt, a major focus of this study was to determine primary ages of units within the belt. The geochronological methods available at the Memorial University of Newfoundland include ID-TIMS and LAM-ICPMS. Initially, ID-TIMS was chosen as the primary method of dating rocks based on the precise age constraints that could be obtained using this method, but LAM-ICPMS proved to be more appropriate for this study.

Collection of samples in the field initially focussed on locations where definitive age relationships were observed (i.e. cross-cutting units) and where protoliths could be confidently determined. Following detailed mapping, it became clear that most primary contact relationships were obscured by high strain, which made protolith interpretation difficult. Therefore, in addition to well constrained units, samples with more ambiguous histories, were also considered for dating. From all of the rocks collected, five samples were initially chosen for detailed analysis. Two of the samples were cross-cutting pegmatites (samples MM01-20, MM01-52), two were cross-cutting mafic dykes (samples MM01-106, MM01-107), and one sample was a quartzofeldspathic schist (sample MM01-81) which had previously been interpreted as a metasedimentary rock (Chadwick, 1990). ID-TIMS was chosen to date the cross-cutting rock types, whereas LAM-ICPMS was chosen to study the quartzofeldspathic schist which was thought to be of sedimentary origin. The LAM-ICPMS is ideal for detrital studies as it is more time efficient and

therefore less expensive and time consuming than ID-TIMS. The LAM-ICPMS is capable of age determinations that are precise to ca. 0.5% (Košler and Sylvester, 2003); however, typically this technique achieves errors of 1.0% (or ~30 Ma for a 3 Ga zircon; Horn et al., 2000).

Of the five initial samples, an accurate age was obtained only for the quartzofeldspathic schist. The difficulties associated with the other samples are outlined in the detailed descriptions of the units in the following 'Results' section. With the ultimate goal of dating the primary age of the greenstone belt still in mind, more samples were selected for analysis. These samples were considered 'second choice' as most of them did not have clearly defined primary relationships (i.e. intrusive contacts). It became evident that dating the greenstone belt was truly a reconnaissance mission and precision was no longer the principal concern of the study. Therefore, the less expensive and more time efficient, but less precise method of LAM-ICPMS was chosen for the continued work.

The second group of samples for dating included two recrystallized quartzofeldspathic rocks interpreted as tonalites (samples MM01-47 and MM01-50), an intensely deformed quartzofeldspathic layer from the Marker High Strain Zone (sample MM01-63), a plagioclase phyric mafic dyke (sample MM01-109), a recrystallized granodiorite rock (sample MM01-78), and a granitoid which intrudes the northern margin of the belt (sample IV03-66).

2.6.1.1 Zircon Preparation

Zircons were extracted from the collected samples using conventional mineral separation techniques, including: crushing, standard hydrodynamic techniques (Wilfley table), heavy liquids, and finally by using a Frantz isodynamic magnetic separator (zircons commonly have a magnetic susceptibility less than 1.7 amps). Zircons were hand-picked under a binocular microscope and were further separated into populations based on morphology, colour, size, and crystal quality. Ideal grains would be clear, whole, and have no cracks or inclusions.

Representative zircons from each population were mounted with epoxy in 2.5 cm diameter grain mounts and these mounts were polished to expose even surfaces at mid-depth in the grains. Before analysing the zircons using U-Pb dating techniques (TIMS or LAM-ICP-MS), the grains were imaged using back-scattered-electron (BSE) microscopy and/or cathodoluminescence (CL).

2.6.1.2 ID-TIMS

Only one sample was dated using the ID-TIMS technique (sample MM01-20). The imaged zircon populations from this sample were initially reviewed. Grains that were most likely to have grown entirely during igneous crystallization of the sample (i.e. zircons that lacked inherited cores and/or metamorphic rims) and that were not highly metamict were noted. Grains similar in appearance to the noted imaged grains were then selected for ID-TIMS analysis. The methodology for analysis is that described by Dubé et

al. (1996). The analytical work was carried out by Marc Poujol at the Department of Earth Sciences, Memorial University of Newfoundland.

The handpicked zircons were extensively air abraded to minimize any effects of Pb loss (Krogh, 1982). Following this, they were washed in dilute nitric acid and ultra-pure acetone. Single grains were placed into 0.35 ml Teflon vials together with 30 µl HF and a mixed ^{205}Pb-^{235}U tracer solution. Eight of these Teflon vials were then placed in a Parr Container for 2 days at 210°C (Parrish, 1987). The samples were measured on a Finnigan MAT 262 mass spectrometer equipped with an ion-counting secondary electron multiplier.

The calculation of common Pb was made by subtracting blanks and then assuming that the remaining common Pb has an Archean composition as determined from the model of Stacey and Kramers (1975). Data were reduced using PbDat (Ludwig, 1993). Analytical uncertainties in Table A.1 are listed at 2σ and a concordia diagram was produced using Isoplot/Ex (Ludwig, 2000).

2.6.1.3 LAM-ICP-MS

The zircon grains that had been imaged using BSE and CL techniques were analysed using LAM-ICP-MS. To determine the igneous age of the rock in question, only the clearest grains that were most likely to have grown entirely during igneous crystallization of the sample were analysed. Xenocrystic components, metamorphic rims, and metamict zones were avoided in order to obtain reliable and accurate results for an igneous age. However, where applicable, xenocrystic components were analysed to

determine the age of inherited material. For the 'detrital' study, all of the selected grains were analysed. This was done to ensure that the results were not biased towards a particular component of the rock.

The LAM-ICP-MS technique utilized corresponds to the methodology presented by Košler et al. (2002). All of the analytical work was completed at the Department of Earth Sciences, Memorial University of Newfoundland under the guidance of Mike Tubrett.

Laser Ablation Microprobe-Inductively Couple Plasma-Mass Spectrometry (LAM-ICP-MS) analyses were conducted using a VG PlasmaQuad 2 S+ mass spectrometer coupled to NUWAVE 213 nm NdYAG laser. A laser beam with a repetition rate of 10 Hz and with an energy of 0.5 - 0.7 mJ/pulse was used to ablate the zircons. The laser beam was focused 100 μm above the sample surface and was reduced to a diametre of 20 μm by masking with a white Teflon® aperture. The sample was mounted on a computer-driven motorised microscope stage which was moved during ablation to produce a square raster pit of different lengths, usually in the range of 20 to 40 μm, in order to match zircon crystal size (see Table 2.2 and A.2). Site selection and ablation progress were observed using a TV camera and monitor. A He carrier gas was used to transport the ablated material from the sample cell to the ICP-MS. As the sample was ablated, a tracer solution containing ~10 ppb of natural Tl ($^{205}Tl/^{203}Tl$=2.3871), ^{209}Bi, ^{233}U,and ^{237}Np was simultaneously introduced to the torch via nebulisation (Košler and Sylvester, 2003). This was performed to allow real-time correction for instrument mass bias.

The data acquired for each sample typically consisted of an initial 60 second measurement of He gas blank and tracer solution before the start of ablation, followed by a 180-200 second measurement of the tracer solution and the ablated sample. The data were acquired in time-resolved-peak-jumping-pulse-counting mode with 1 point measured per peak. The masses measured included 201 (flyback), ^{203}Tl, ^{204}Pb, ^{205}Tl, ^{206}Pb, ^{207}Pb, ^{209}Bi, ^{237}Np, ^{238}U, as well as oxides of Np and U. After every five unknown analyses an external zircon standard of known U-Pb age was analysed to ensure accuracy and reproducibility of the measurements. The zircon standards 91500 (Wiedenbeck et al., 1995, 2004), Košler (Aftalion et al., 1989), 02123 (used only for sample MM01-81; Ketchum et al., 2001), and MOS-2 (used only for sample MM01-81; Poujol et al., 2002)] were used for this purpose. All of these standards have been previously dated by IDTIMS. The LAM produced acceptable $^{207}Pb/^{206}Pb$ dates for the standard materials with errors of 0.5-1.0% (2σ).

The raw data were downloaded to a computer for offline processing using an in-house Excel-based spreadsheet and reduced using an in-house spreadsheet program (LAMDATE by J. Košler). Final ages and diagrams were produced using LAMDATE in conjunction with the Isoplot/Ex macro (Ludwig, 1999). U concentrations were calculated using the accepted value of the 91500 standard (76.77 ppm; Wiedenbeck et al., 1995) and the U^{238} count rates of the standard and the unknown analysis. There is at least a 20% error using this method, because there was no internal standardization possible. The results were used in a qualitative manner, strictly for comparative purposes.

2.6.2 Results

Eleven samples were collected from the northern and southern parts of the belt as defined in Section 2.4.2 Stratigraphy/Tectonostratigraphy. Photographs (where available) of the field relationships are shown and a simplified map of the field area showing the sample localities is presented in Figure 2.80. U-Pb data are presented in the next section according to location and age. Table 2.3 provides a summary of zircon crystallization ages.

The sample dated by the ID-TIMS technique (sample MM01-20) did not yield a reliable age (see following section; Table A.1).

Reliable ages were only obtained by the LAM-ICP-MS method. For samples dated using this technique, $^{207}Pb/^{206}Pb$ ages were calculated from analyses which had 94-104% concordance and had 2σ errors less than 2.2% of the calculated $^{207}Pb/^{206}Pb$ age. Concordance % is expressed as ($^{206}Pb/^{238}U/^{207}Pb/^{206}Pb$ date) x 100. Errors are given at the 2σ confidence level. Results are illustrated on concordia diagrams (Appendix A; Fig. A.1 – A.7); on weighted mean diagrams, and where appropriate, on combined histogram and cumulative probability plots. $^{207}Pb/^{206}Pb$ ages were calculated using weighted mean diagrams, in which the mean is weighted by data point errors only, and the error is given as 2σ (95% confidence). The "95% confidence" error was calculated as 1.96 times the 1σ internal error if the probability-of-fit is more than 15%, or Student's-*t* times the square root of the MSWD if the probability was less than 15%. For concordia diagrams, the decay-constant errors in the concordia curve are not shown.

Analytical results of data used for age determination are shown in Table 2.2; analyses which were not used (e.g. discordant points) are shown in Table A.2.

2.6.2.1 Results from Northern Part of Belt

Rusty, quartzofeldspathic schists and gneisses (Samples MM01-47 and MM01-50)

Thin, rusty quartzofeldspathic layers were noted in the northern part of the belt (Fig. 2.31). The protolith is interpreted to have been a tonalite which intruded into the northern amphibolites. This interpretation is supported by cross-cutting field relationships and by locally preserved relict igneous textures observed in thin section (see Section 2.5.1.3: Quartzofeldspathic schists and gneisses). Field evidence suggests that different layers may have intruded at different time intervals (see Section 2.5.1: Table 1: Sequence of events for northern part of the belt): some intruded before DN_1 and others intruded after DN_2.

Zircons from two different layers were analysed by LAM-ICP-MS: Samples MM01-47 and MM01-50. In thin section, these samples exhibit evidence of DN_1 deformation and are thus interpreted to have predated all deformation events which affected this part of the belt. Small to large (150-400 μm long) zircon grains from samples MM01-47 and MM01-50 are stubby (aspect ratio of 2:1:1) to elongate (6:1:1), and are deep red to pale pink (Fig. 2.81).

Sample MM01-47

A total of fifteen analyses were collected from eleven stubby, red to pink zircons and two elongate pale pink grains from Sample MM01-47 (Table 2.2, see Fig. A.1 for Concordia plot of all data). Ten analyses from nine separate grains are between 94-104% concordant and have an acceptable error range (2σ error < ~2% of $^{207}Pb/^{206}Pb$ age). CL imaging revealed pronounced fine, concentric, oscillatory zoning in all of the ten grains and three of the grains also contain possible xenocrystic cores (Fig. 2.82a). The seven grains which have concentric zoning without cores are interpreted as having crystallized entirely from the tonalite magma. The weighted mean $^{207}Pb/^{206}Pb$ age (3163±7 Ma; MSWD=1.12) of the analyses from the core-free grains is interpreted as the igneous crystallization age of the unit. As evident on a weighted mean plot (Fig.2.83a), the three core analyses appear to be slightly older ($^{207}Pb/^{206}Pb$ age=3178±24; 3180±28; 3200±50), however, their error ranges fall well within the range of the other analyses which do not contain cores. These analyses also have overlapping U concentrations with the zoned grains (see Table 2.2); therefore, it is therefore unclear if they represent older xenocrystic material.

Sample MM01-50

Fifteen analyses were collected from thirteen stubby, red to pink zircons from Sample MM01-50 (Table 2.2, see Fig. A.2 for Concordia plot of all data). Eleven analyses are between 94-104% concordant and have an acceptable error range (2 σ error < ~2% of $^{207}Pb/^{206}Pb$ age). Eight of these analyses were from grains which exhibit fine,

concentric, oscillatory zoning throughout the grain in CL images (Fig.2.82b). Two of the analyses were from a possible xenocrystic core (Fig. 2.82b) and one analysis was from concentrically zoned rim around a disturbed core. The eight analyses of core-free grains with concentric zoning are interpreted as having crystallized entirely from the tonalite magma. The weighted $^{207}Pb/^{206}Pb$ mean age of the concentric zoning analyses is 3169±18 Ma (MSWD=2.5) and is interpreted as the igneous crystallization age of the unit (Fig. 2.83b). Similar to sample MM01-47, the error and U concentration of one of the two core analyses ($^{207}Pb/^{206}Pb$=3183±28 Ma) overlaps with the errors of the analyses of concentric zoning. The other core analysis is older (3255±35 Ma) and has a lower U concentration than most of the zoned grains; therefore, it likely represents inherited material from an older and different rock. The concentrically zoned rim around a disturbed core yielded an older date than the interpreted igneous age for the unit: 3231±26 Ma. The disturbed core analysis was discordant (93.5%) and appears to be younger than all other analysis (see Concordia plot Fig. A.2)

Homogeneous TTG (Sample IV03-66)

Thin sheets of homogeneous, medium-grained, meta-granitoid (tonalite-trondhjemite-granodioritic; TTG) and granitic pegmatite intrude the northern margin of the Ivisârtoq greenstone belt. Within the greenstone belt, these sheets are sub-parallel to the schistosity and mylonitic fabrics of the greenstones but are much less deformed than the amphibolites. To the north, the same TTG gneiss forms the main component of the

regional granitiod gneiss. Locally, rafts of previously deformed amphibolite were observed within the tonalitic gneiss close to the contact with the greenstone belt.

Sample IV03-66, consisting of TTG and pegmatite, was collected ~1 metre from the northern edge of the greenstone belt (Fig. 2.84). The pegmatite portions of the sample were removed and zircons from the TTG portion were analysed by LAM-ICP-MS. Small to large zircon grains (150 to 400 μm long) from sample IV03-66 are stubby (aspect ratio of 2:1:1) to elongate (5:1:1), sharply faceted, translucent and pink to colourless (Fig. 2.85).

Fifteen analyses were collected from thirteen zircon grains (Table 2.2, see Fig. A.3 for Concordia plot of all data). Ten analyses are between 94-104% concordant and have an acceptable error range (2σ error < ~2% of $^{207}Pb/^{206}Pb$ age). Possible xenocrystic cores were observed in six zircons using CL imaging (Fig. 2.86). Five core analyses yielded a weighted $^{207}Pb/^{206}Pb$ mean age of 3018±14 Ma (MSWD=1.09; Fig. 2.87) and a single core analysis yielded a $^{207}Pb/^{206}Pb$ age of 3760±29 (Table 2.2). Three other analyses were collected from grains which exhibit concentric, oscillatory zoning, and from a thick rim around one of the possible xenocrystic cores. These three analyses yielded a weighted $^{207}Pb/^{206}Pb$ mean age of 2960±58 Ma. (MSWD=2.2) which is interpreted as the igneous age for the unit.

As evident on a weighted mean plot (Fig.2.87), the group of five core analyses appears to be slightly older than the interpreted igneous age, however, their error ranges and U concentrations fall within the range of the other analyses which do not contain cores. It is therefore unclear if they represent older xenocrystic material.

The single core analysis which yielded a much older age and higher U concentration likely represents xenocrystic material. The core material may have been inherited during the ascent of the tonalitic magma through continental crust composed of felsic material (e.g. ~3.7 Ga 'Amîtsoq' gneiss).

The interpreted igneous age for the tonalitic sheet intruding the northern boundary of the greenstone belt is similar to a date obtained by Friend and Nutman (2005) for a weakly deformed granite (sample GGU200499) collected from the 'dome' of gneisses north of the belt. They obtained a weighted $^{207}Pb/^{206}Pb$ mean age of 2961±11 Ma (1σ error) using a SHRIMP.

Mafic dykes (Samples MM01-106 and MM01-107)

Mafic dykes were noted throughout the Ivisârtoq greenstone belt. Two types of dyke were recognized: 1) equigranular, gabbroic dykes; 2) dykes containing large relict plagioclase phenocrysts set within a fine-grained matrix. The dykes cut previously deformed amphibolite derived from basaltic pillow lava, tonalite layers, and ultramafic layers. They may have intruded at different times during the deformation history of the belt on the basis of field relationships, and differences in foliation development and recrystallization.

Samples of each type of dyke were collected from the northern part of the belt. Sample MM01-106 is from an equigranular gabbroic dyke which cuts across an ultramafic layer (Fig. 2.88). This sample was selected to determine the minimum age of the ultramafic unit. Unfortunately, after mineral separation of the rock, neither zircons

nor any other minerals suitable for geochronology (monazite, titanite, allanite, xenotime, baddeleyite, and perovskite) were found.

The other dyke selected (sample MM01-107; Fig. 2.40) contained large plagioclase phenocrysts and cuts obliquely across a northern amphibolite derived from pillow lava which had undergone deformation and metamorphism. The sample was selected to determine the minimum age of deposition of the pillow lava. Metamorphic rutile grains rimmed by titanite were present, however, due to the composite nature of the grains and their unclear metamorphic history they were deemed unsuitable for dating.

Felsic pegmatites (Samples MM01-20 and MM01-52)

Granitic pegmatites intrude the other main units of the northern part, the Marker High Strain Zone, and the southern part of the greenstone belt. The pegmatites have previously been assumed to be equivalents of the ~2550 Ma Qôrqut granite complex (McGregor, 1973; Baadsgaard, 1976; Brown et al., 1981; Moorbath et al., 1981; Taylor et al., 1980; Robertson, 1985; Brewer, 1985). For these reasons they were considered to be an ideal target for geochronological studies; 1) to date the minimum age of the greenstone belt, and 2) to determine conclusively if they are equivalents of the Qôrqut granite complex.

Two samples were collected for this purpose. One sample (MM01- 20; Fig. 2.44) was a folded, finer grained pegmatite that cuts a quartzofeldspathic gneiss layer which contains thin amphibolite layers within the Marker High Strain Zone. This sample was chosen to give the maximum age of the latest deformational event which affected the

Marker High Strain Zone. The zircons separated from this sample are typically sub-euhedral, elongate, pale yellow or pink, and glassy. Some displayed internal magmatic zoning, while others are more homogeneous but contain uraninite inclusions, which are likely indicative of a U-rich initial magma (Fig. 2.89). Grains similar in appearance to the imaged, concentrically zoned zircons were then selected for ID-TIMS analysis. The sample was analysed using thermal-ionization mass-spectrometry (TIMS) on single grains. The results were poor: an isochron plot produced a scattering of points none of which fit concordia (Fig. 2.90; Table A.1). The discordant ages were likely the result of relatively recent Pb loss from metamict zones or along cracks. Zircon grains from granitic pegmatities are typically of poor quality due to their metamict nature and can be unreliable (Crowley, pers. comm.)

The other pegmatite sample collected was a larger, coarse-grained sheet (sample MM01-52) which was targeted to give the minimum age of an ultramafic layer, which the pegmatite cuts across (Fig. 2.91). The zircons separated from this sample are generally euhedral but contain many inclusions and cracks. They range from pink, glassy grains which displayed zoning to milky, sugary, metamict grains which contained many inclusions. Overall, the quality of the zircons was determined to be too poor for geochronology work (Fig. 2.92).

2.6.2.2 Results from Southern Part of Belt

Plagioclase phyric mafic dyke (Sample MM01-109)

Mafic dykes containing large relict plagioclase phenocrysts set within a fine-grained matrix are present in the northern and southern parts of the belt. Chadwick (1990) stated that some of the amphibolitic dykes may be part of a younger (<2800 Ma) swarm of dykes seen to the north in Kangilíngua (Chadwick, 1990). New geochronology demonstrates that this is not a valid interpretation.

The dykes in the northern part of the belt are less deformed than the dykes in the southern part. In the south, the plagioclase phyric dykes are typically folded with other rock types. Sample MM01-109 was collected from a region in the southern part of the belt which is complexly folded with banded amphibolites and light grey, granodioritic homogeneous rocks. Elsewhere in the southern part of the belt, clear cross-cutting relationships between plagioclase phyric dykes and banded amphibolites were observed (Fig. 2.39).

Small to medium (75 to 250 μm long), dark pink, stubby (aspect ratio of 2:1:1) to elongate (aspect ratio of 5:1:1) zircon grains from sample MM01-109 were analysed by LAM-ICP-MS (Fig. 2.93a). Eleven analyses were collected from ten separate grains. Six of the analyses were between 94-104% concordant and have an acceptable error range (2σ error < ~2% of $^{207}Pb/^{206}Pb$ age; Table 2.2). In CL images, four of the grains display dark, mottled centres surrounded by thin, bright overgrowths (Fig. 2.93b). Analyses from the centre of these grains yield a weighted $^{207}Pb/^{206}Pb$ age of 3066±17 Ma (MSWD=0.25), which is interpreted as the igneous age of the dyke (Fig. 2.94). The

overgrowths are attributed to a later metamorphic event because they appear to be recrystallized patches (Fig. 2.93b). CL images from two other grains show faint cores which are interpreted as being inherited in nature (Fig. 2.93b). Analyses of the cores yield $^{207}Pb/^{206}Pb$ ages of 3134±32 Ma and 3137±42 Ma. The error between the two core analyses and the five non-core analyses only marginally overlap (Fig. 3.94) and therefore likely represent discrete ages. A discordant analysis of a faintly luminescent core yielded a much older $^{207}Pb/^{206}Pb$ age of 3410±238 Ma and an age of 3872±110 Ma (1σ error) on a concordia diagram (see Fig. A.4). Although this analysis has a large error (Table A.2) the $^{207}Pb/^{206}Pb$ and concordia ages are much older than the interpreted igneous age of the rock and likely represent old inherited material.

A single, concordant grain yielded a $^{207}Pb/^{206}Pb$ age of 2578±23 Ma. This grain has a higher U content than the other grains (see Table A.2) and consequently is only slightly luminescent using CL imaging. The grain is not thought to represent the igneous age of the dyke, due to its high U content. Zircons from mafic dykes typically have low U contents (Sylvester, pers. comm.); therefore, this grain is interpreted as being metamorphic in origin.

Homogeneous metagranodiorite (Sample MM01-78)

Light grey, medium, even grained, homogeneous rocks are observed in discontinuous layers throughout the southern part of the belt (Fig. 2.95). These layers are interlayered and folded with banded amphibolites, mafic dykes, and the thick quartz-feldspar-biotite-garnet schistose/gneissic layer. The protolith of this rock type is

interpreted to have been a granodioritic intrusive body with trace element geochemical signatures similar to those of an A-type granite (see Chapter 3). This sample contained considerably fewer zircons grains (<50) than either sample MM01-63 or MM01-81 (>>200), for comparable processed sample sizes.

Small (75 to 200 μm long), light to dark pink, milky to glassy, stubby (aspect ratio of 2:1:1 to 3:1:1) zircon grains from sample MM01-78 were analysed by LAM-ICP-MS (Fig. 2.96). Ten analyses were collected from ten separate grains. Eight of the analyses are between 94-104% concordant and have an acceptable error range (2σ error < ~2% of $^{207}Pb/^{206}Pb$ age; Table 2.2). Using CL imaging, six of the more elongate grains exhibit dark centres, surrounded by patchy bright zones and rims (Fig. 2.97a). Analyses from the centre of the six grains yields a weighted $^{207}Pb/^{206}Pb$ age of 2895±25 Ma (MSWD=2.4), which is interpreted as the igneous age of the unit (Fig. 2.97b). The bright patches are thought to represent recrystallized zones and the rims are attributed to a later metamorphic event. Two other grains with different CL images yield different ages. One grain is distinct in that it appears completely homogeneous without any zoning, rims, or cores using CL imaging. This grain yields a $^{207}Pb/^{206}Pb$ age of 2994±23 Ma. A CL image of another grain, which has a slightly lower U concentration than the igneous grains, shows a faint core which is interpreted as being inherited in nature (Fig. 2.97a). Analysis of the core yielded a $^{207}Pb/^{206}Pb$ age of 3040±26 Ma.

Intensely deformed quartzofeldspathic layer (Sample MM01-63)

The Marker High Strain Zone contains a layer of intensely deformed quartzofeldspathic rocks intercalated with thin amphibolite horizons and a layer of ultramafic schists (magnetic marker). This zone is intensely deformed and has undergone several deformational events. Sample MM01-63 was collected from a quartzofeldspathic layer (Fig. 2.98). This layer is continuous with a thick unit of quartz-feldspar-biotite-garnet schist/gneiss in the southern part of the belt and is similarly interpreted as sedimentary in origin.

Zircons from Sample MM01-63 are small (100 to 200 μm long), stubby (aspect ratio of 1.5:1:1) to elongate (4:1:1), translucent, pale pink and resemble grains from the thick, southern metasedimentary unit (Sample MM01-81). The shape of the grains range from euhedral to subeuhedral (rounded ends; Fig. 2.99a). Fragments of euhedral grains were also observed. CL imaging reveals that most grains contain fine, concentric, oscillatory zoning, whereas some appear unzoned and homogeneous. A few grains have bright cores using CL imaging, which likely represent inherited material (Fig. 2.99b).

In total, fifteen zircons were analysed using LAM-ICP-MS. Thirteen analyses from separate grains were between 94-104% concordant and have an acceptable error range (2σ error < ~2% of $^{207}Pb/^{206}Pb$ age; Table 2.2). Ten grains with various characteristics including grain shape (stubby, elongate grains, euhedral, anhedral, fragments) and internal structure reflected by CL imaging (including concentrically zoned grains, bright cores, and completely homogeneous grains) yielded a weighted $^{207}Pb/^{206}Pb$ mean age of 3086±11 Ma (MSWD=2.0; Fig. 2.100a). This age is interpreted

to represent the igneous age of a single component which was the main source material from which the sedimentary unit was derived. Four other grains yielded distinctly younger ages: 3026±31 Ma, 2975±17 Ma, 2895±35 Ma, and 2789±15 Ma. These grains have distinct morphologies and thus have different explanations regarding their formation.

Two grains which exhibit fine, concentric, oscillatory zoning yielded $^{207}Pb/^{206}Pb$ ages of 3026±31 Ma and 2975±17 Ma. These analyses may represent minor igneous components within the sedimentary unit which were also recognized in Sample MM01-81. The different age populations of the interpreted igneous components of the sedimentary unit are plotted on a combined histogram and cumulative probability plot in Figure 2.100b.

A bright core from a more elongate zircon grain with rounded ends yielded a $^{207}Pb/^{206}Pb$ age of 2895±35. The origin of this grain is debatable. It may have been derived from an igneous rock which itself had contained inherited material now represented by the bright core; or, the core may represent the igneous age of the unit which is surrounded by later metamorphic material. Because this age and the U concentration (352 ppm) of the core is essentially identical to the igneous age (2895±25 Ma) and U concentrations (range: 272-643 ppm; average=385 ppm) of the homogeneous granitoid (Sample MM01-78), the core is thought to represent igneous material from the granitoid which is surrounded by a later metamorphic rim. This would suggest that the granitoid is a minor component of the sedimentary rock, and that the depositional age of the sediments is <2895±25 Ma.

A rounded, stubby grain yielded a $^{207}Pb/^{206}Pb$ age of 2789±15 Ma. This grain has a high U content (1111 ppm, see Table 2.2) which may indicate that the grain was disturbed by ancient loss of radiogenic Pb, thus this age is not thought to represent a parent igneous component from which the sedimentary unit was derived.

Thick quartz-feldspar-biotite-garnet schist/gneiss layer (Sample MM01-81)

A sample of the quartz-feldspar-biotite-garnet schist the southern part of the belt was obtained for geochronology work (Fig. 2.101). This unit is strongly deformed and most primary features have been obliterated. However, locally, there are rounded felsic fragments which could have originated as primary clasts in a sedimentary or volcanoclastic rock (Fig. 2.73). The mineral assemblages (see Section 2.5.2.2), geochemical composition (see Chapter 3), and studies by Chadwick (1990) and Friend and Nutman (2005) support an interpretation of this unit as a metasedimentary rock.

Other ages have previously been obtained from assumed paraschists in the belt. Baadsgaard (1976) obtained a U/Pb age of 2580 Ma for zircons from a rock interpreted as a paraschist and he considered this to be a metamorphic age. Recently, Friend and Nutman, (2005) reported a weighted $^{207}Pb/^{206}Pb$ mean of 3075 ±15 Ma (1σ error) for 23 zircons using a SHRIMP. This sample is from the thick, southern metasedimentary layer as described in this study.

Sample MM01-81 was the first sample dated by LAM-ICP-MS during this study. A large number of analyses (~100) were collected from this unit because of its interpreted sedimentary origin. The majority of grains are large (100 to 200 μm long), stubby (aspect

ratio of 1.5:1:1) to elongate (4:1:1), anhedral (rounded ends) to euhedral, glassy, and dark to pale pink (Fig. 2.102a). BS and CL imaging reveals that most grains contain fine, concentric, oscillatory zoning, whereas some appear unzoned and homogeneous (Fig. 2.102b). These grains strongly resemble the grains from sample MM01-63. A smaller proportion of grains were perfectly round (Fig. 2.103), and dark to light pink. These grains also display fine, concentric, oscillatory zoning using CL imaging (Fig. 2.103b). The differences in grain shape, ranging from euhedral to round grains, could be attributed to erosional processes, where some grains may have travelled farther than others (distal versus proximal).

Forty-three analyses were between 94-104% concordant and have an acceptable error range (2σ error < ~2% of $^{207}Pb/^{206}Pb$ age; Table 2.2). A weighted $^{207}Pb/^{206}Pb$ mean of all these analysis yields an age of 3072±13 Ma with an MSWD of 12. This is similar to the age (3075 ±15 Ma) obtained by Friend and Nutman (2005). Upon detailed inspection of the data forty-three analyses, four separate age groups can be defined (Fig. 104a). These different groups may represent separate igneous components which make up the metasedimentary unit. Five grains yield a weighted $^{207}Pb/^{206}Pb$ mean age of 3009±19 Ma (MSWD=1.9); thirty-two grains yield a weighted $^{207}Pb/^{206}Pb$ mean age of 3078±6 Ma (MSWD=2.1); and five grains yield a weighted $^{207}Pb/^{206}Pb$ mean age of 3130±19 Ma (MSWD=1.7). The youngest group is represented by a single, homogeneous, elongate grain with an age of 2941±21 Ma. This age overlaps with analyses from igneous grains obtained for the homogeneous granitoid (Sample MM01-78; age range 2862±26 Ma - 2925± 35 Ma). As in the quartzofeldspathic layer from the Marker High Strain Zone

(Sample MM01-63), the homogeneous granitoid may be a component of the sedimentary unit.

The mean age of the main population (3078±6 Ma) of sample MM01-81 is similar to the date obtained from the main population of sample MM01-63 (3086±11 Ma). The combined histogram and cumulative probability plots for the two samples are also similar, which supports the interpretation that they are part of the same metasedimentary unit and are derived from similar sources.

One grain yielded an age younger than all of the others. This stubby grain has a homogeneous CL image and yielded a $^{207}Pb/^{206}Pb$ age of 2774±30 Ma (Table A.2; Fig. A.7). This grain is thought to have been disturbed by ancient loss of radiogenic Pb, similar to a 2789±15 Ma aged grain from Sample MM01-63.

Table 2.3: Summary of LAM-ICP-MS zircon ages

Unit and sample number	$^{207}Pb/^{206}Pb$ age in Ma (2σ error)	Interpretation
NORTHERN SAMPLES		
TTG intruding northern boundary of belt: IV03-66	***2960±58*** 3018±14, 3760±29	***Crystallization of unit*** Xenocrysts
Thin tonalite sheets: MM01-47	***3163±7*** 3178±24; 3180±28; 3200±50	***Crystallization of unit*** Xenocrysts
MM01-50	***3169±18*** 3183±28 Ma; 3255±35	***Crystallization of unit*** Xenocrysts
SOUTHERN SAMPLES		
Metasedimentary samples:	***<2895***	***Maximum age of deposition***
Marker High Strain Zone (MM01-63)	3086±11 (dominant); 2895±35, 2975±17, 3026±31 (minor)	Ages of separate components which comprise the metasedimentary samples
Thick layer in southern part of belt (MM01-81)	3078±6 Ma (dominant); 3009±19, 3130±19, 2941±21 (minor)	
Homogeneous metagranodiorite (MM01-78)	***2895±25*** 2994±23; 3040±26	***Crystallization of unit*** Xenocrysts
Plagioclase phyric mafic dyke: Sample MM01-109	***3066±17*** 3134±32; 3137±42 3872±110 (Concordia age)	***Crystallization of unit*** Xenocrysts

2.7 DISCUSSION

The northern and southern parts of the Ivisârtoq greenstone belt are both dominated by amphibolites derived from basaltic pillow lavas, but are characterised by distinct felsic and ultramafic magmatism. The northern part contains ultramafic and tonalitic sills, whereas the southern part is characterized by a thick package of metasedimentary rocks, a distinct layer of ultramafic schist which may be pyroclastic in origin, and a granodioritic intrusion.

The two parts also differ in intensity of deformation. The northern part is generally less deformed than the southern part: in the north, large km-scale isoclinal folds are recognizable, whereas, the rock units of the southern part are deformed into parallelism. As discussed in Section 2.4.2, if the two parts represent a continuous stratigraphic section then both parts would have been isoclinally folded by the same event and therefore, one would expect to see repeated lithological units throughout the two parts of the belt's southern limb. This is not observed.

The two parts are separated by a zone of high strain which is interpreted as a tectonic break. The boundaries of the intensely deformed zone are relatively sharp with less deformed rocks to the north and south. The deformation associated with juxtaposition (DJ) seems to be localised in the Major High Strain Zone; the northern part of the belt is not greatly affected, therefore it is assumed that the intense deformation observed in the southern part was not caused by the juxtaposition event. The difference in strain intensity between the northern and southern parts is not thought to be related to the latest regional deformation event (DR) either, as this event produced a weakly to

moderately developed foliation which is at angle to the main E-W foliation seen in the northern and southern parts. It seems most likely that the northern and southern parts of the belt suffered separate deformational events prior to juxtaposition which resulted in the dominate E-W foliation seen in both parts, and afterwards were effected by the same regional deformation event (DR).

The only commonality between the two parts of the belt is the presence of mafic dykes. These dykes seem to have intruded over an extended period of time as indicated by field relationships (for example in the northern part they intruded before and after the DN_2 isoclinal folding event). Mafic dykes are relatively common in Archean supracrustal rocks (Sylvester, pers. comm.), and therefore can not necessarily be used as a criteria to link the northern and southern parts. In this study, they are thought to have formed throughout the development of the belt: some likely formed in the northern and southern parts of the belt prior to juxtaposition and others may have intruded afterwards. Due to their typically zircon-poor nature it is difficult to determine their absolute ages.

A sequence of events for the area studied within the Ivisârtoq greenstone belt is summarized in Table 2.4.

Table. 2.4: Sequence of events for the Ivisârtoq greenstone belt

	Northern part of the belt		***Southern part of the belt***
1.	Deposition of homogeneous and variolitic basaltic pillow lavas	1.	Deposition of basaltic pillow lavas and pyroclastic (?) ultramafic unit (magnetic marker)
2.	Extensive hydrothermal alteration; (epidote-diopside-garnet) vein networks and in pillow cores	2.	3066±17 Ma Intrusive age of plagioclase phyric mafic dykes
3.	Intrusion of ultramafic sills	3.	2895±25 Ma Intrusion of homogeneous (A-type) granodiorite
4	~3165 Ma Intrusion of tonalite sheets (e.g. inner side of the easterly isoclinal fold);	4.	< 2895 Ma Deposition of sediments; main zircon age group ~3080 Ma, which may represent an intrusive age of granitoid (TTG) which is not seen in the mapped area.
5.	DN_1 Heterogeneous deformation: strain variation established SN_1 foliation preserved locally in garnet porphyroblasts in tonalite sheets	5.	?Age? Intense deformation - Basaltic pillow lava forms banded amphibolite; probably at least two separate phases
6.	Mafic dykes intrude		
7.	DN_2 Isoclinal folding event		
8.	Intrusion of tonalite sheets; cut folded ultramafic layers and mafic dykes		
9.	Intrusion of mafic dykes and sills; cut isoclinally folded ultramafic layers		
10.	2960±58 Ma TTG intruded as sheets into the northern part of the greenstones, and extensively to the north		
DJ	Major deformational event Juxtaposition of northern and southern parts of the belt		
DR	~2600 Ma (?) Large-scale folding of belt. Amphibolite - epidote amphibolite facies metamorphism		
	~2550 Ma (?) Intrusion of coarse leucogranite pegmatite (equivalent to Qorqut?); absence of contact metamorphic aureoles around the pegmatitic sheets indicate that metamorphism associated with DR persisted until intrusion of pegmatites; randomly oriented amphibolite-grade minerals in most lithologies also indicate that metamorphism outlasted DR		
	Late Proterozoic (?) Faulting: demonstrated by folded (~2550 Ma ?) pegmatites within the Marker Shear Zone		

Sequence of events for the Ivisârtoq greenstone belt

Magmatism in the northern part

The earliest magmatism in the northern part of the belt includes the deposition of basaltic pillow lavas and the intrusion of large ultramafic sills. These units were intruded by tonalitic sheets which have igneous $^{207}Pb/^{206}Pb$ zircon ages of ~3163±7 and 3169±18 Ma (2σ error; samples MM01-47, MM01-50). Slightly older cores noted within some zircon grains may represent xenocrysts.

Later, thin sheets of homogeneous, medium-grained, TTG and granitic pegmatite intruded the northern part of the Ivisârtoq greenstone belt and cut out the former northern extent of the belt. An igneous $^{207}Pb/^{206}Pb$ zircon age of 2960±58 Ma (2σ error) was determined for the TTG portion (sample IV01-66). Xenocrystic cores noted within zircon grains from the tonalitic rock have distinctly different $^{207}Pb/^{206}Pb$ ages (3018±14 Ma and 3760±29 Ma; 2σ error). The older zircons may have been incorporated during magma ascent. The oldest xenocrystic core suggests that the magma may have ascended through early Archean rocks, such as a component of the ~3750 Ma Itsaq gneiss complex (e.g. 'Amîtsoq' gneiss).

The igneous age obtained in this study for the TTG portion, agrees well with an igneous SHRIMP $^{207}Pb/^{206}Pb$ zircon age (2961±11 Ma; 1σ error) obtained by Friend and Nutman (2005) for a weakly deformed granite collected from the 'dome' of gneisses north of the belt. Friend and Nutman (2005) also reported a SHRIMP $^{207}Pb/^{206}Pb$ zircon age of 2963±8 Ma from a granodioritic gneiss interpreted as an intrusion into anorthositic rocks (east of study area; see Fig. 2.3). It is unclear if this granodioritic rock is situated in

the northern or southern part of the belt, as defined in the present study. Further mapping to the east will need to be conducted to determine the relationship between the anorthositic rocks and the northern and southern amphibolites. The existing 1:100 000 geological map (Chadwick and Coe, 1988) suggests that the anorthositic rocks may lie within the southern part. However, they could also lie between these parts and/or be a fault-bounded unit.

Deformation in the northern part

The northern part of the belt was affected by at least two deformation events, referred to as DN_1 and DN_2, before juxtaposition with the southern part.

The first deformational event (DN_1) resulted in heterogeneous deformation within the northern Ivisârtoq amphibolites and predates isoclinal folding. Isoclinal folding should have resulted in more intense deformation along the limbs and relatively less-deformed rocks in the hinge zone. However, heterogeneous deformation was observed across layers within fold limbs, and some of the least deformed rocks are located in fold limbs, rather than fold cores. High and low strained rocks form planar zones which are parallel with compositional layering, and are folded with the compositional layering into large-scale isoclinal folds. Therefore the development of these variations in strain pre-date the isoclinal folding event, which is attributed to DN_2. The second deformational event formed a steeply dipping, approximately east-west oriented axial planar foliation which is observed throughout this part of the belt. The rocks were likely modified during

the later regional deformational event (DR) which affected both parts of the belt, however, these events did not obliterate the strain variations established during DN_1.

Southern part of the belt

Magmatism and sedimentation in the southern part

The earliest magmatism in the southern part of the belt includes the deposition of basaltic pillow lava, the deposition of an ultramafic pyroclastic unit (magnetic marker layer), and perhaps the emplacement of a leucogabbro-anorthosite complex (outside of mapped area; see Fig. 2.3). These units are interpreted to be older than 3066±17 Ma (2σ error) which is the zircon $^{207}Pb/^{206}Pb$ intrusive age of a plagioclase phyric mafic dyke in this part of the belt (sample MM01-109). Cores noted within zircon grains may be xenocrysts. A concordia age of 3872±110 Ma (1σ error) for a discordant core analysis (see Fig. A.4) suggests the possibility that the mafic magma ascended through early Archean rocks such as a ~3750 component of the Itsaq gneiss complex (e.g. 'Amîtsoq' gneiss).

A younger, recrystallized, homogeneous granodioritic unit (with trace element geochemical signatures similar to an A-type granite; see Chapter 3) was observed in the southern part of the belt. This unit is deformed and folded with surrounding rocks and therefore its relative age is unknown. An igneous $^{207}Pb/^{206}Pb$ zircon age of 2895±25 Ma (2σ error) is interpreted for this unit. Two older $^{207}Pb/^{206}Pb$ zircon ages (2994±23 Ma and 3040±26 Ma) may represent xenocrysts.

Quartzofeldspathic rocks in the Marker High Strain Zone (sample MM01-63) and from the thick quartz-feldspar-biotite-garnet layer in the southern part of the belt (samples MM01-81) are interpreted as being sedimentary in origin. These samples contain a spread of ages, but overall have similar combined histogram and cumulative probability plots (Fig. 2.100b and Fig. 2.104b). These plots demonstrate that the majority of zircons have an age of ~3080 Ma. These zircons are typically elongate to round and are concentrically zoned. The differences in grain shape are attributed to sedimentary transport. The elongate grains resemble typical tonalite zircons (Crowley, pers. comm.) suggesting that they were derived from a granitoid, however, a ~3080 Ma granitoid was not observed within the mapped area. This unit may have been removed by tectonic processes and therefore could have been cut out of this part of the belt or the zircons could have been transported into the belt from distal sources. Within the Ujarassuit Nunaat region (north of the mapped area), Friend and Nutman (2005) reported intrusive $^{207}Pb/^{206}Pb$ ages of ~3070 Ma for two samples which are in contact with the Ivisârtoq greenstone belt, a homogeneous granodiorite (sample G91/92) and a migmatite (sample G93/88). These intrusions may correspond with the ~3080 Ma component of the metasedimentary rocks.

Young ages observed in both metasedimentary layers (sample MM01-63: 2895±25 Ma; sample MM01-81: 2941±21 Ma) are similar to the dates obtained from igneous grains in the homogeneous metagranodiorite (Sample MM01-78; age range 2862±26 Ma to 2925± 35 Ma). This observation suggests that the metagranodiorite may be a detrital component of the sedimentary rocks, and that the depositional age of the

metasedimentary rocks is <2895±25 Ma. This theory is supported by geochemistry (see Chapter 3) which indicates that the metasedimentary rocks were derived from three main sources:

1) granodioritic unit (with A-type granite trace element geochemical signatures);
2) TTG and,
3) amphibolite (likely the southern banded amphibolites).

Geochemical models indicate that samples MM01-81 from the thick southern layer are derived from roughly equal proportions of the three components, whereas sample MM01-92 from the Marker High Strain Zone is derived almost entirely from the TTG component. U-Pb zircon geochronology indicates that the homogeneous metagranodiorite has an igneous age of ~2895 Ma, the TTG likely has an igneous age of ~3080 Ma, and the amphibolite component is older than ~3060 Ma. The small number of ~2895 Ma ages in the MM01-81 samples may be a reflection of the zircon-poor nature of the 2895 Ma homogeneous metagranodiorite (e.g. sample MM01-78).

The difference in felsic and mafic component concentrations between metasedimentary samples may reflect the original proximity to the various sources. For example, the samples from the Marker High Strain Zone may have been distal to the granodioritic and amphibolitic source; their present spatial relationship and intimate association with the amphibolites may have been the result of later deformational events (e.g. DJ juxtaposition).

Deformation in the southern part

The southern part of the belt is more strongly deformed than the northern part. Due to the intensity of deformation in the southern part and highly strained boundaries of most rock types, the primary relationships and relative ages of the different units could not be determined from field observations.

The southern part consists of strongly foliated schists of diverse rock types, which contrast the well-preserved primary structures, such as pillow lavas, in the northern part of the belt. Evidence of the structural complexity within the southern part was observed in the field (several different fold orientations were recorded) and in thin sections. Inter-tectonic, syn-tectonic, and post-tectonic garnet porphryoblasts suggest that these rocks underwent several phases of deformation, unfortunately, due to the lack of field constraints these grains could not be correlated with specific (pre-juxtaposition) deformational events.

Juxtaposition of the northern and southern parts

The noticeable compositional and deformational contrasts between the northern and southern parts of the belt support the interpretation that they formed independently and were then juxtaposed. The tectonic break separating the two parts of the belt is thought to be located along or within the the Marker High Strain Zone, a belt of intense deformation including mylonitization.

The exceptionally tectonized nature of the Marker High Strain Zone is attributed to the juxtaposition event (DJ) superimposed on rocks that were already moderately to

intensely deformed. Most of the strain associated with this event was likely accommodated along the relatively weak metasedimentary unit. This deformational event likely caused the interleaving of northern pillow lavas, identified by geochemistry (see Chapter 3), with the metasedimentary layer within the Marker High Strain Zone. The strain gradient across the northern margin of the Marker High Strain Zone into the northern part of the belt is locally gradational but regionally is sharp. The exact location of the break within the Marker High Strain Zone is unclear and may be obscured by later reactivation. This zone would benefit from future detailed studies.

The timing of juxtaposition is uncertain, but is assumed to have occurred after sedimentary deposition in the south (~2895 Ma).

Post-juxtaposition magmatism

Thin tonalitic sheets within the Marker High Strain Zone likely intruded after the juxtaposition event, as suggested by preserved relict igneous textures. Other tonalitic sheets and mafic dykes cut previously intensely deformed amphibolites derived from basaltic pillow lavas and isoclinally folded ultramafic layers. It is unclear if these units intruded before or after the juxtaposition event (DJ).

The youngest intrusive unit within the Ivisârtoq greenstone belt is represented by large bodies of felsic pegmatite assumed to be Qôrqut age (~2550 Ma).

Post-juxtaposition deformation

After juxtaposition of the northern and southern parts, the Ivisârtoq greenstone belt was affected by a regional deformational event (DR) which caused large scale folding resulting in the present day geometry of the belt. This event is defined as (D_3) by Hall and Friend (1979). Locally in the northern part, a regional foliation (S_R) was observed in thin section and is at an angle to the main foliation (SN_2). S_R is oriented in a roughly northeast-southwest direction, and appears to be axial planar to large scale folds associated with DR. The intrusion of the protolith of the Ivisârtoq granite gneiss (Robertson, 1985) may be contemporaneous with this regional event. The protolith of these gneisses intrude 'Amîtsoq' gneisses north of the belt within the Kangilíngua area (Chadwick, 1990; Robertson, 1985). A Rb-Sr isotopic age of 2750±40 Ma was reported by Robertson (1985).

The mylonitic boundaries of the belt and mylonitic layers within the belt were likely modified during Proterozoic faulting as demonstrated by folded pegmatites of assumed Qôrqut age (~2550 Ma) within the Marker High Strain Zone.

Metamorphism of the Ivisârtoq greenstone belt

The main components of the Ivisârtoq greenstone belt have been extensively recrystallized, however, no evidence of granulite facies metamorphism was noted. The mineral assemblages of the different rock types correspond to amphibolite-facies metamorphism and likely reflect the most recent deformational events.

An early alteration event, which predates the main metamorphic events, is preserved in the northern amphibolites derived from basaltic pillow lavas. These rocks were heterogeneously affected by a network of veins and diffuse zones now marked by epidote. The alteration is interpreted to be the result of hydrothermal processes, which occurred after the solidification of the pillow lavas but before the emplacement of the thick ultramafic and thin quartzofeldspathic layers. The observed epidote-rich assemblage is thought to reflect the amphibolite-facies metamorphism related to the later deformational events.

Metamorphism associated with DN_1 likely reached amphibolite facies, however, little evidence is preserved due to recrystallization in later deformation events. Staurolite and sillimanite inclusions within porphyroblasts provide the main supporting evidence of amphibolite facies metamorphism during DN_1.

Locally, epidote-amphibolite facies minerals at an angle to the main foliation (DN_2) in the main rock types suggest that retrograde conditions were associated with the latest deformation event (DR). Locally, the same types of minerals are randomly oriented suggesting that metamorphism outlasted this deformation event, an interpretation also supported by Chadwick (1985) and Robertson (1985).

2.7 CONCLUSIONS

The Ivisârtoq greenstone belt contains an exceptionally well-exposed section of Archean volcanic rocks. The present study re-evaluated the Ivisârtoq greenstone belt in terms of protoliths and the timing of magmatic and deformational events. The belt is

redefined as a tectonostratigraphic assemblage composed of two distinct packages of rocks likely affected by separate deformational events and subsequently brought together by later tectonism after ~2895 Ma.

Protolith interpretations

Northern part of the belt

New field mapping and petrography have identified two distinct types of amphibolite derived from basaltic pillow lavas: homogeneous and variolitic lavas. These distinct units are interbedded and are interpreted as being contemporaneous. Extensive coarse-grained and homogeneous ultramafic layers are interpreted as sills. Thin layers of quartzofeldspathic schists were previously interpreted as metasedimentary/volcanoclastic in origin; the present study re-interpreted these units as being derived from tonalite intrusions.

Southern part of the belt

The southern part of the belt is dominated by banded amphibolites which have been recognized as deformed basaltic pillow lavas. Quartzofeldspathic schists and gneisses are interpreted as sedimentary in origin. A previously unrecognized, discontinuous unit of light grey homogeneous rock is interpreted to be a granodioritic intrusion. A distinct layer of ultramafic schists may represent a pyroclastic deposit.

Tectonostratigraphy

A previously unrecognized major tectonic break divides the Ivisartoq greenstone belt into two distinct packages. Each part is characterised by distinct ultramafic, mafic and felsic magmatism, and separate deformational histories prior to juxtaposition. The contact between the two parts of the belt is located along or within the Marker High Strain Zone, a belt of intense deformation which includes mylonitic units.

A sequence of events based on field mapping and reconnaissance U-Pb geochronology was determined and is presented in Table 2.4. Overall, the Ivisartoq greenstone belt is older than was previously recognized: pillow lavas in the northern part were deposited before ~3165 Ma and in the southern part, pillow lavas were deposited before ~3066 Ma. The two parts were likely juxtaposed after ~2895 Ma which is the maximum age of deposition of the protoliths of the metasedimentary rocks in the southern part.

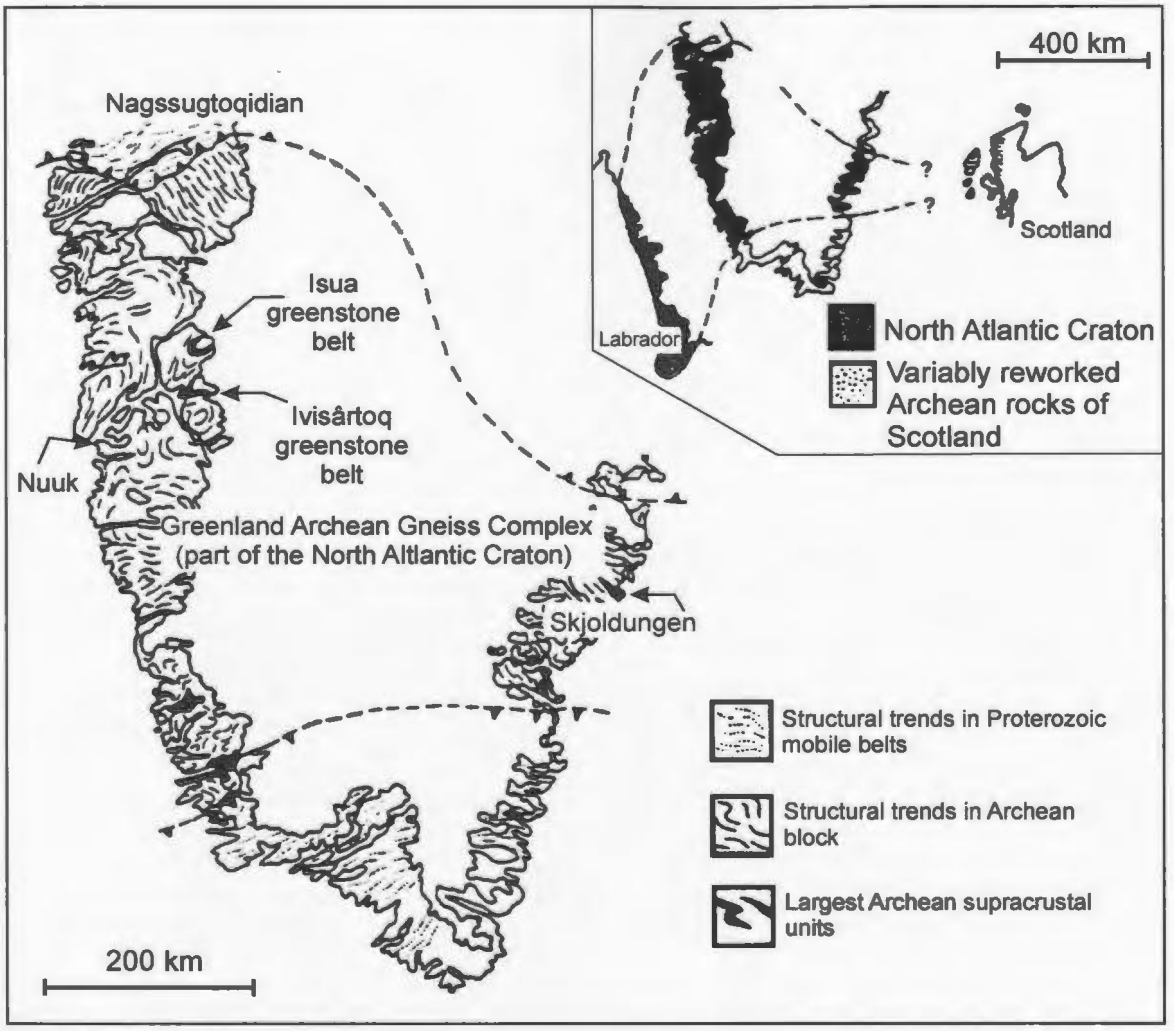

Figure 2.1. The North Atlantic Craton (from Nutman, 1997).

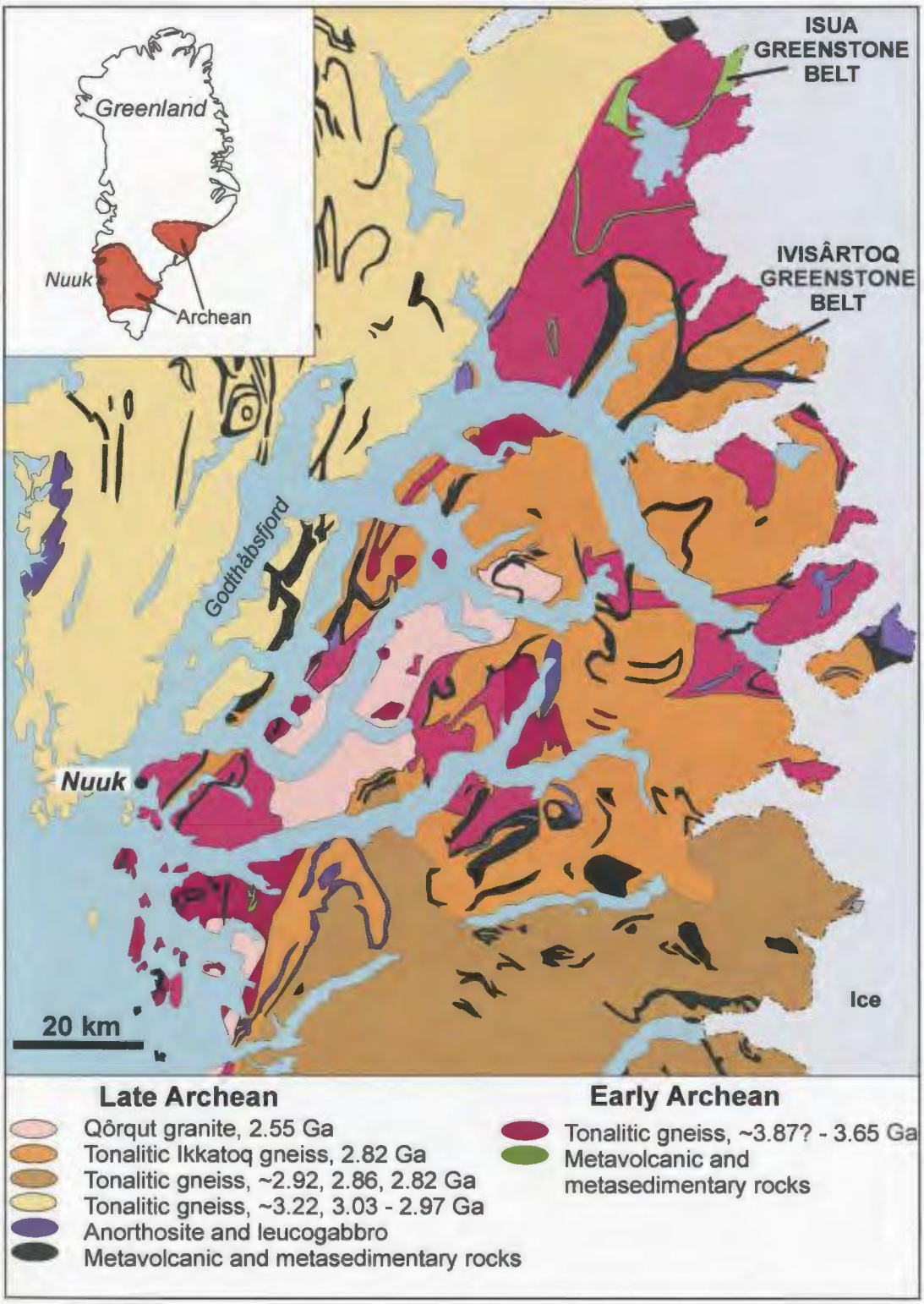

Figure 2.2a. Geologic map of the Godthåbsfjord region (from Myers and Crowley, 2000) compiled from maps by Allaart (1982), Chadwick and Coe (1983,1988), Garde (1987, 1989) and McGregor (1984) and geochronology from Nutman et al. (1996) and Nutman (1997). The inset map of Greenland locates Nuuk and the main regions of Archean gneiss.

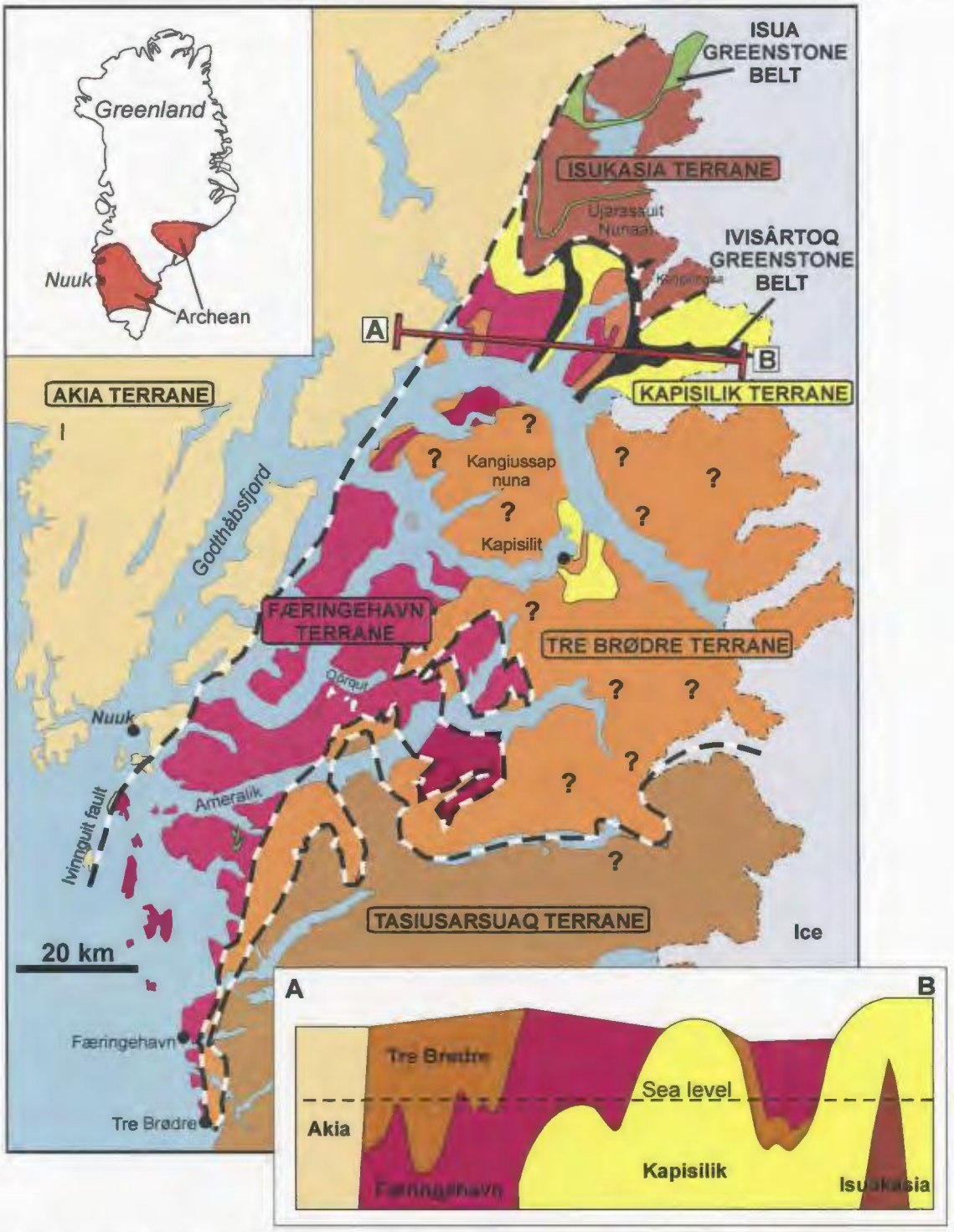

Figure 2.2b. Sketch map of the terranes of the Godthåbsfjord region as defined by Friend and Nutman (2005). The top left inset map of Greenland locates Nuuk and the main regions of Archean gneiss. The bottom right inset shows a cross-section at sea level along the line AB (from Friend and Nutman, 2005). Note: different colours represent different terranes and do not correspond exactly with geological units as defined in Fig. 2.2a. Dashed lines indicate terrane boundaries.

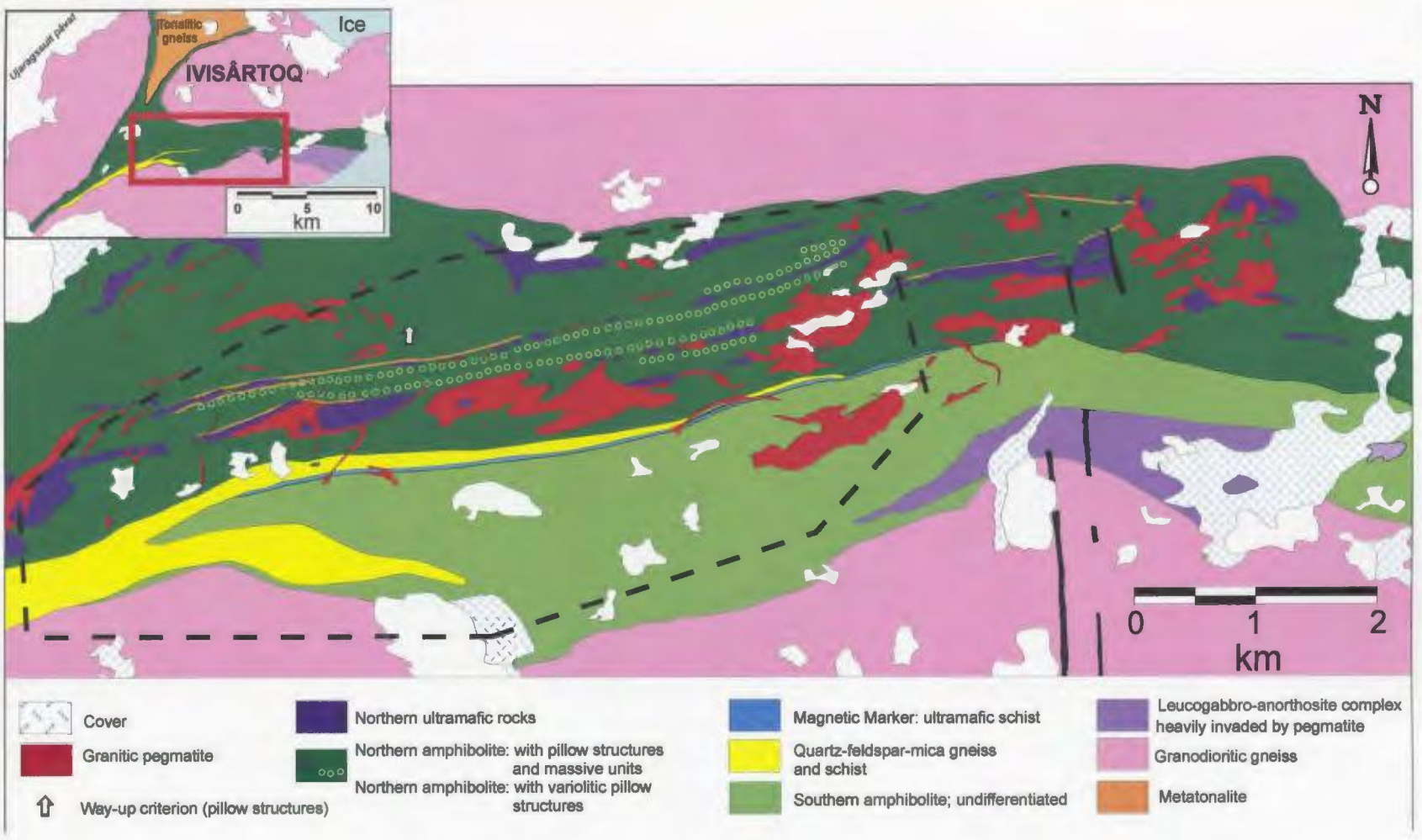

Figure 2.3. Simplified map of the Ivisârtoq greenstone belt. Dashed outline indicates field area.

a)

b)

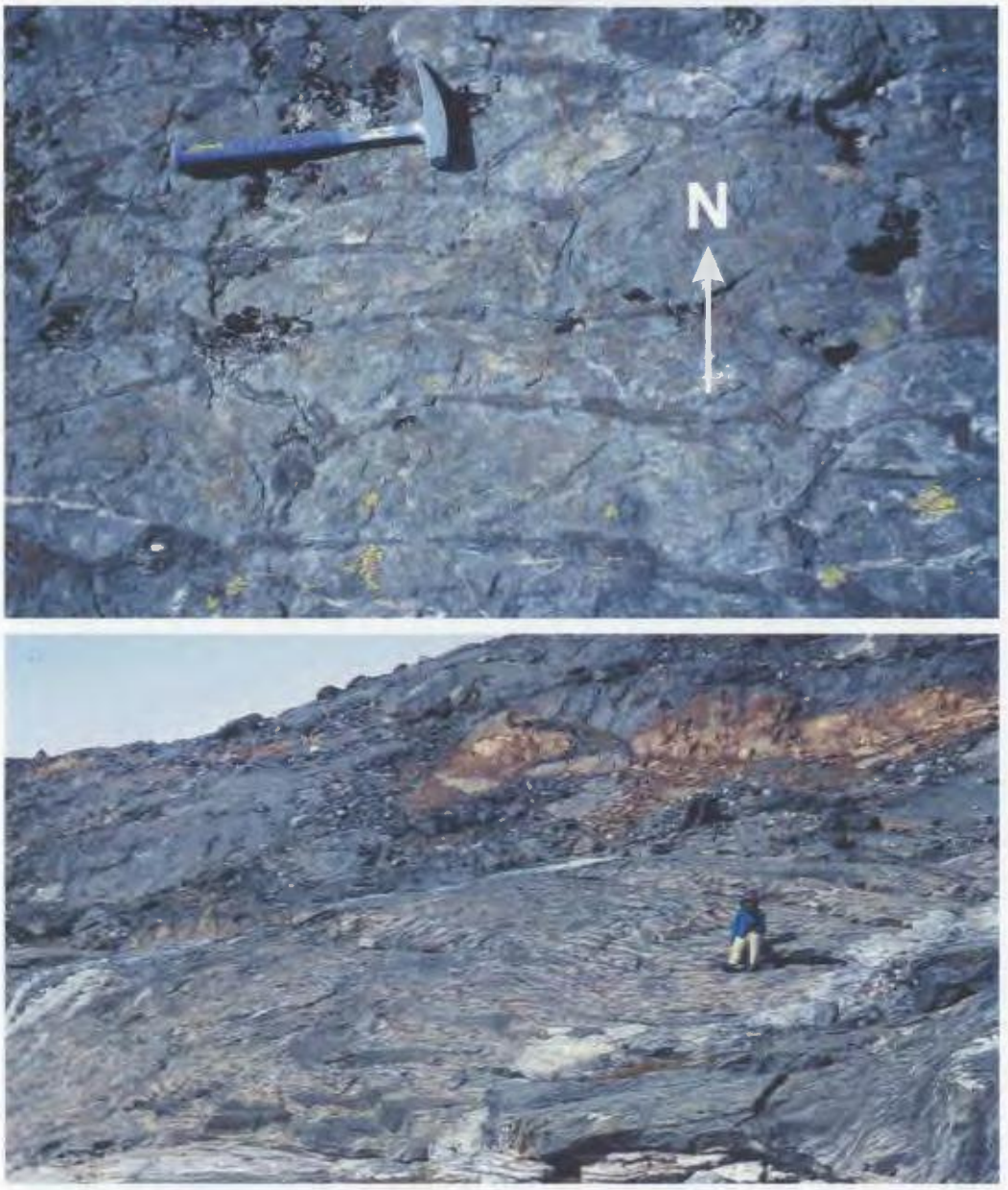

Figure 2.4. Homogeneous pillow basalts are characterised by dark, amphibole-rich marginal zones which sharply contrast with the paler, yellow-green, epidote-pyroxene-rich cores of the pillows.
a) The original way-up direction of the pillow lavas is indicated by the smooth, convex tops and cuspate bases of the pillow structures (Locality MM01-121). The younging direction of the pillow structure is to the north (N). Top of photo to north. Geological hammer is 30 cm long.
b) Photo facing WNW (Outcrop between locality MM01-71 and MM01-69).

a)

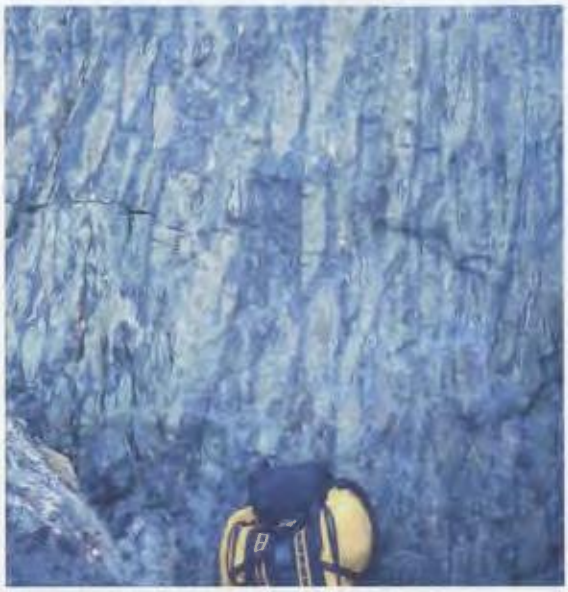

b)

c)

Figure 2.5. Deformed homogeneous pillow basalts. Pencil is 15 cm long.
a) Strongly lineated pillow structures (photo facing west).
b) Moderate-strongly deformed pillow structures (top of photo to south).
c) Banded amphibolite derived from strongly deformed pillow basalts.

a)

b)

c)

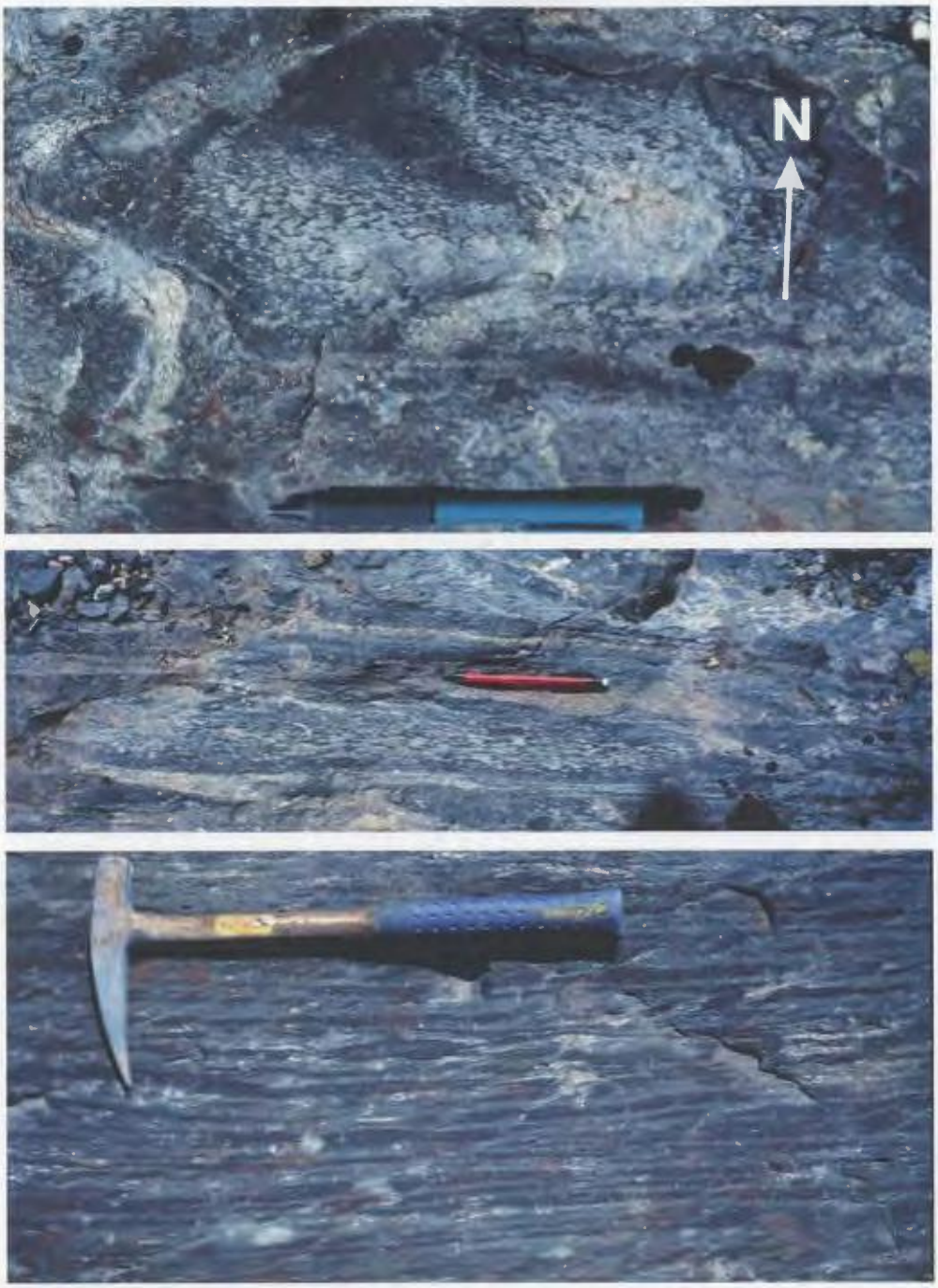

Figure 2.6. Variolitic pillow basalts.
a) Well formed pillow structure indicates younging direction to the north. Top of photo to north (Locality MM01-44).
b) Moderately deformed variolitic pillow basalt. Flattened varioles are recognizable (Locality north of MM01-48, top of photo to south).
c) Strongly deformed variolitic pillow basalt. The leucocratic varioles and pillow rims contrast strongly with the dark matrix of the pillow cores, creating banded black and white rocks.

a)

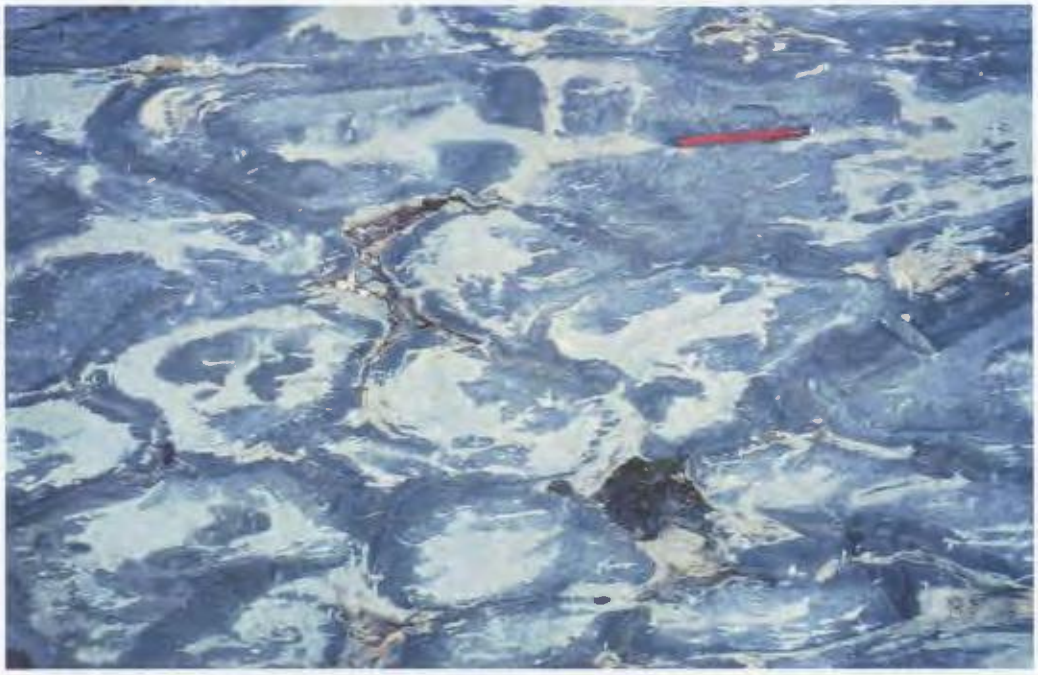

b)

Figure 2.7. Some amphibolites have been heterogeneously affected by alteration, which may be of hydrothermal origin This alteration is marked by veins and diffuse zones of epidote.
a) Alteration zones overprinting well-preserved variolitic pillow basalts (Locality MM01-110, top of photo to north).
b) Alteration veins and zones deformed with the pillow structures (top of photo to north).

a)

b)

Figure 2.8. Amphibolite characterized by dark, hornblende-rich oblate structures set within a pale green, epidote-rich matrix. This unit may correspond to deformed 'ultramafic' pillows described by Hall (1981).
a) Locality MM01-48. Top of photo to north.
b) Photo facing west.

a)

b)

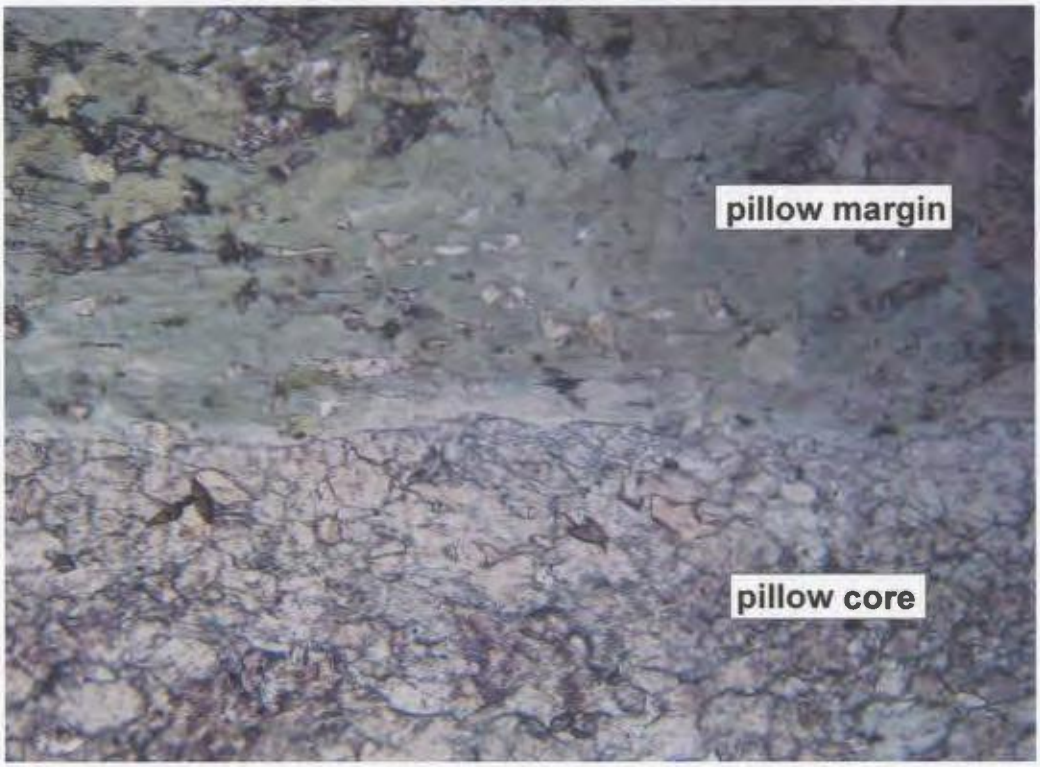

Figure 2.9.
a) Detail of homogeneous pillow margin and core, width of photo ~30 cm.
b) Photomicrograph of a dark, amphibole-rich marginal zone of homogeneous pillow, sample MM01-49a, which sharply contrasts with the paler, epidote and pyroxene-rich cores (Sample plane polarized light, width of photo 4.2 mm).

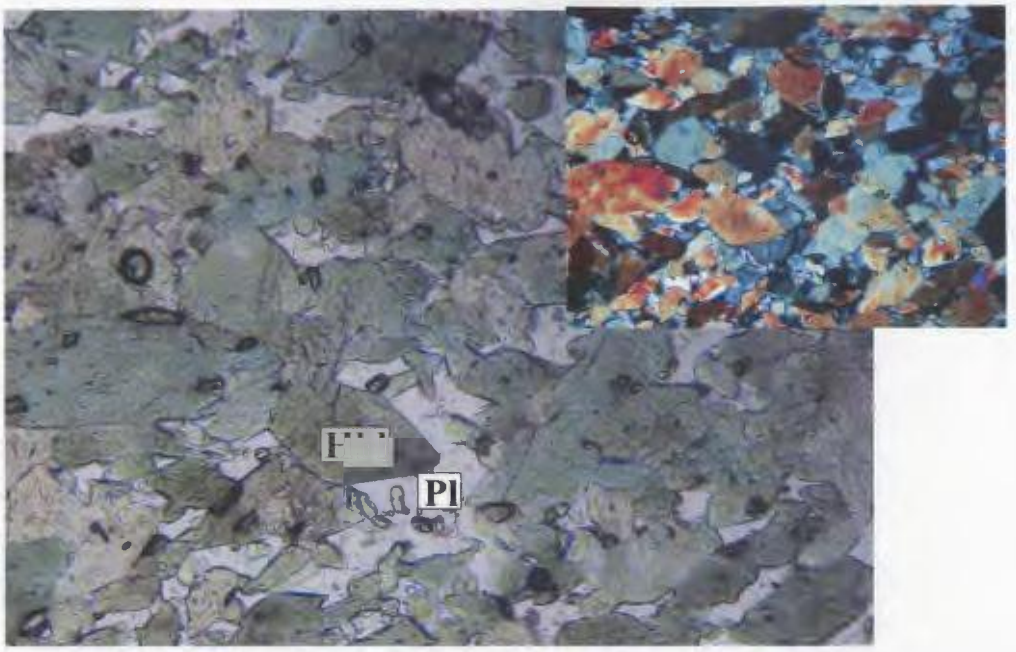

Figure 2.10. Photomicrograph of marginal zone of homogeneous pillow basalt, sample MM01-49c, which is composed primarily of yellow-green pleochroic hornblende (Hbl), with lesser amounts of plagioclase (Pl) (plane polarized light, width of photo 1.1 mm; Inset: crossed polars, width of photo 1.1 mm).

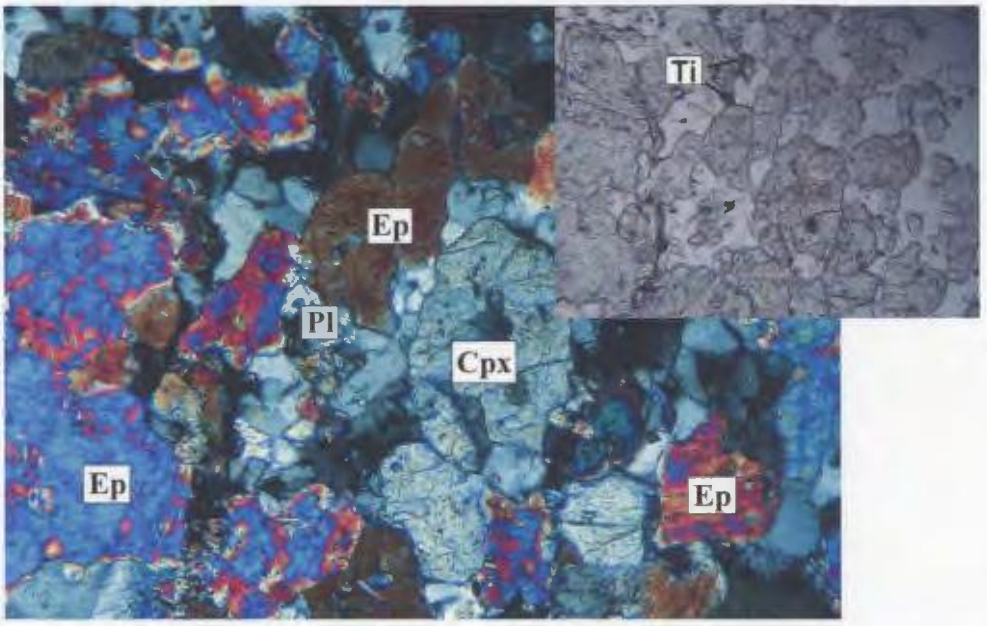

Figure 2.11. Photomicrograph of homogeneous pillow core, sample MM01-49c, composed predominately of epidote (Ep), clinopyroxene (Cpx), plagioclase (Pl) and minor titanite (Ti) (crossed polars, width of photo 1.1 mm; Inset: plane polarized light, width of photo 1.1 mm).

a)

b)

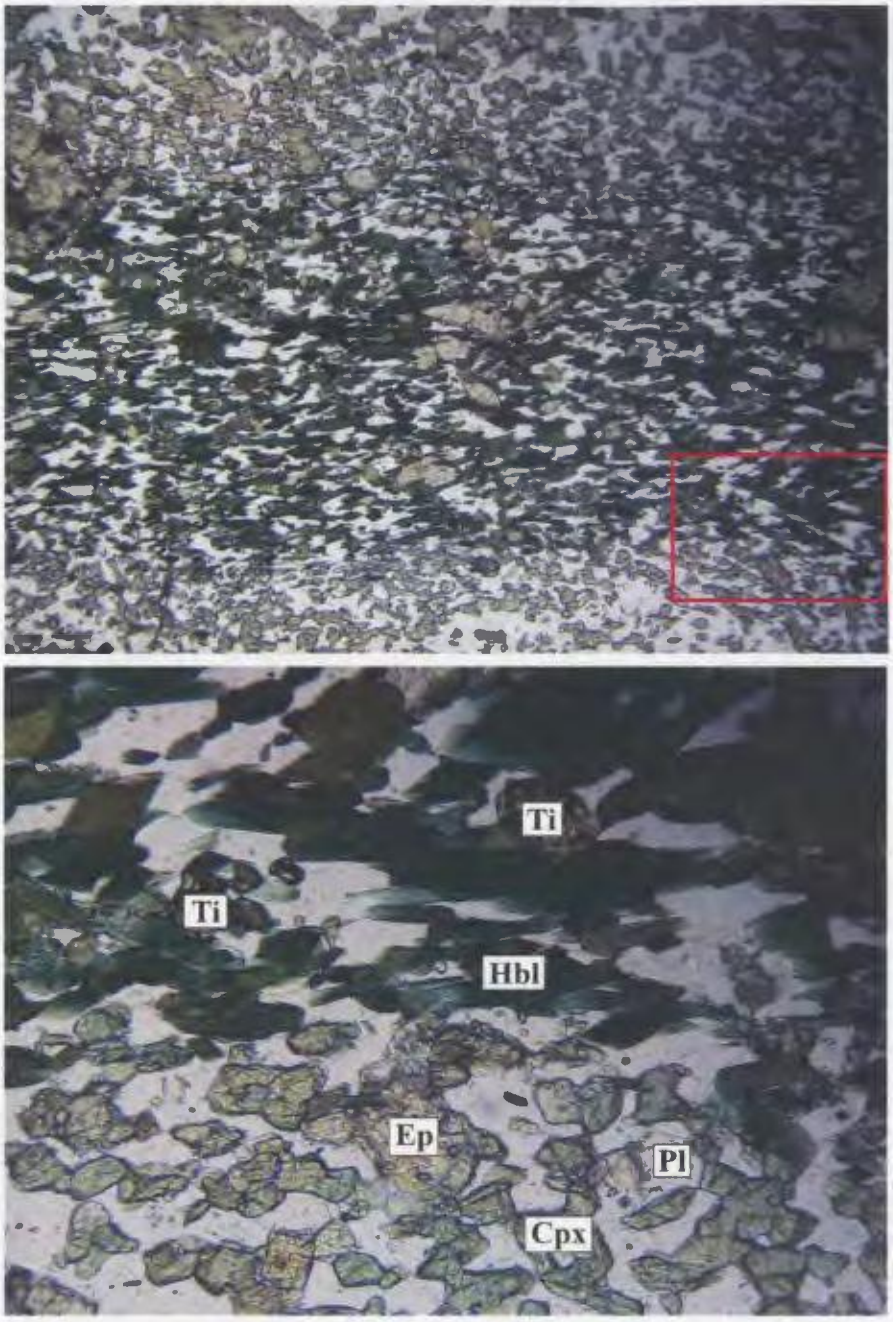

Figure 2.12. Photomicrographs of dark green-light green banded amphibolite derived from strongly deformed homogeneous pillow basalts (sample IV03-31). The dark layers are rich in dark-green hornblende and represent the pillow rims; light green layers are composed of clinopyroxene (Cpx), epidote (Ep), plagioclase (Pl), hornblende (Hbl), and titanite (Ti), and correspond to the pillow core.
a) Plane polarized light, width of photo 5.25 mm.
b) Detail of area outlined in (a); plane polarized light, width of photo 1.4 mm.

a)

b)

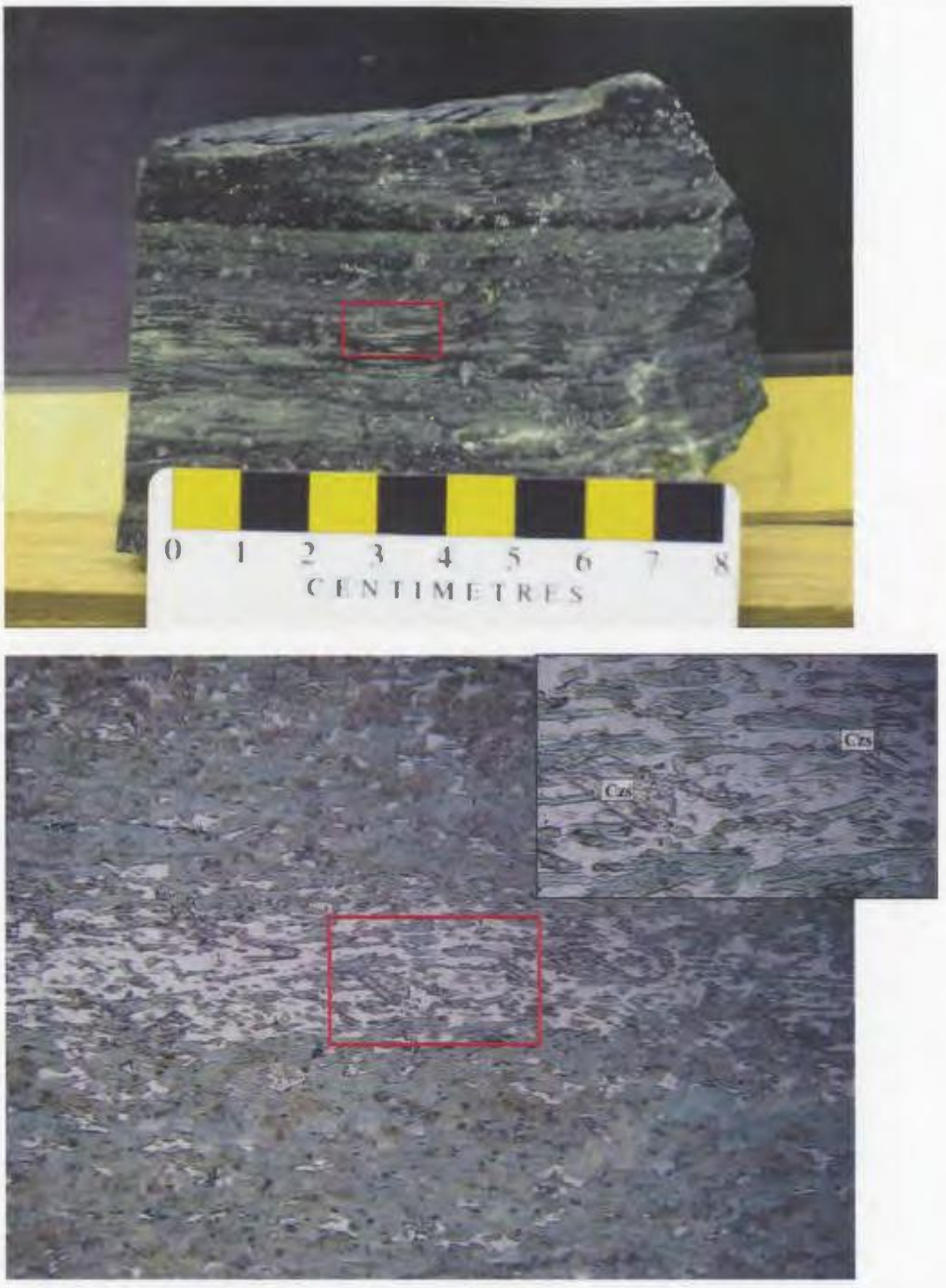

Figure 2.13.
a) Hand sample MM01-49b. Varioles within pillow core.
b) Photomicrograph of leucocratic variole within area outlined in (a). Core matrix is dominated by hornblende. Variole composed of roughly equal proportions of hornblende and plagioclase (plane polarized light, width of photo 4.2 mm. Inset: Detail of variole: area outlined in (b). Late, lath-shaped growths of clinozoisite (Czs) at angle to main foliation (plane polarized light, width of photo 1.1 mm).

Figure 2.14. Ultramafic layers in the northern part of the belt have been disrupted into boudins which crop out as low 'whale back' ridges (photo facing east).

Figure 2.15. Homogeneous nature of the ultramafic layers (near Locality 106).

Figure 2.16. Vertical folding noted in a thick ultramafic boudin (Locality MM01-11). This internal folding may account for the boudin's thickened nature (photo facing west).

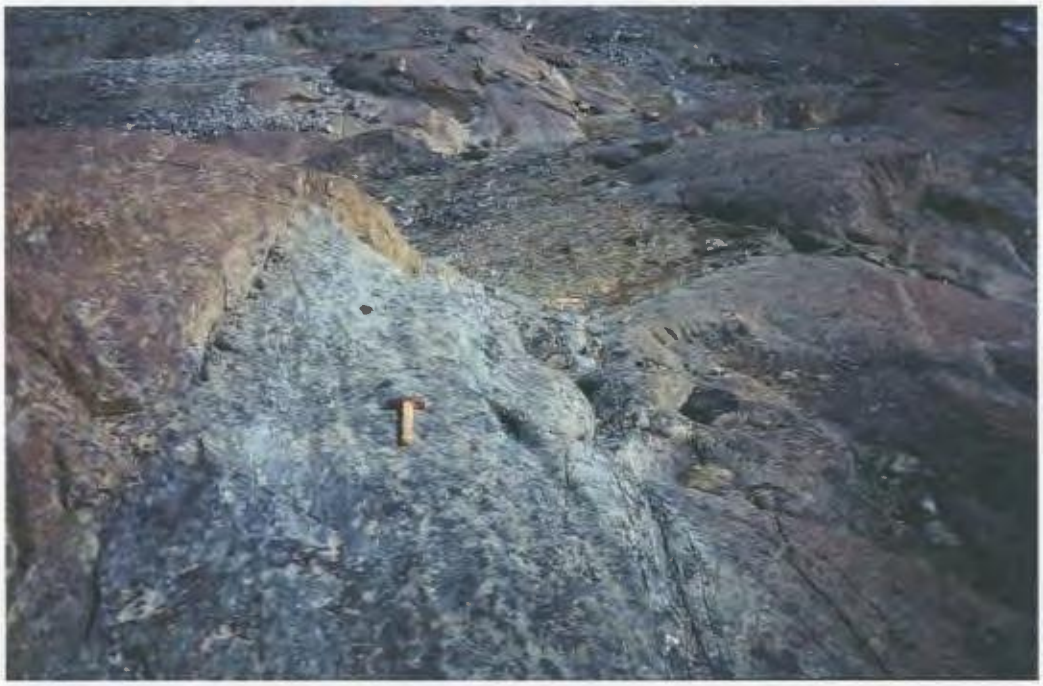

Figure 2.17. Green schistose layer 1 metre wide observed within ultramafic layer (Locality MM01-21, photo facing east).

a)

b)

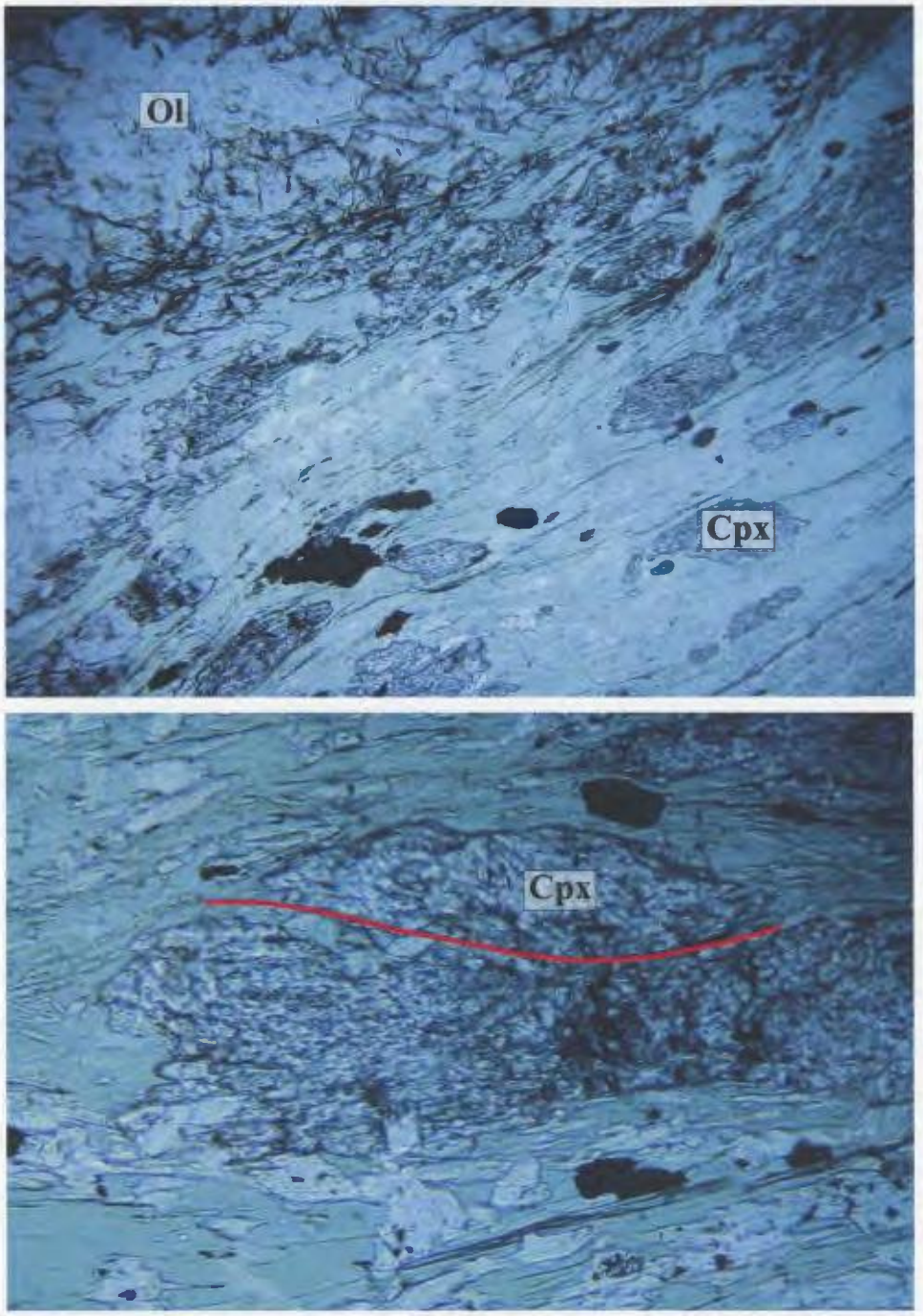

Figure 2.18. Photomicrographs of low and high strain zones within an ultramafic layer (Sample IV03-44).
a) Remnant igneous olivine (Ol) in low strain pocket (top left corner). High strain zone is characterized by a strong foliation defined by chlorite and actinolite-tremolite with clinopyroxene (Cpx) porphyroblasts (plane polarized light, width of photo 5.5 mm).
b) Detail of a syn-tectonic clinopyroxene porphyroblast (red lines indicates inclusion trail) within a high strain zone surrounded by a matrix of chlorite and actinolite-tremolite (plane polarized light, width of photo 1.4 mm).

a)

b)

c)

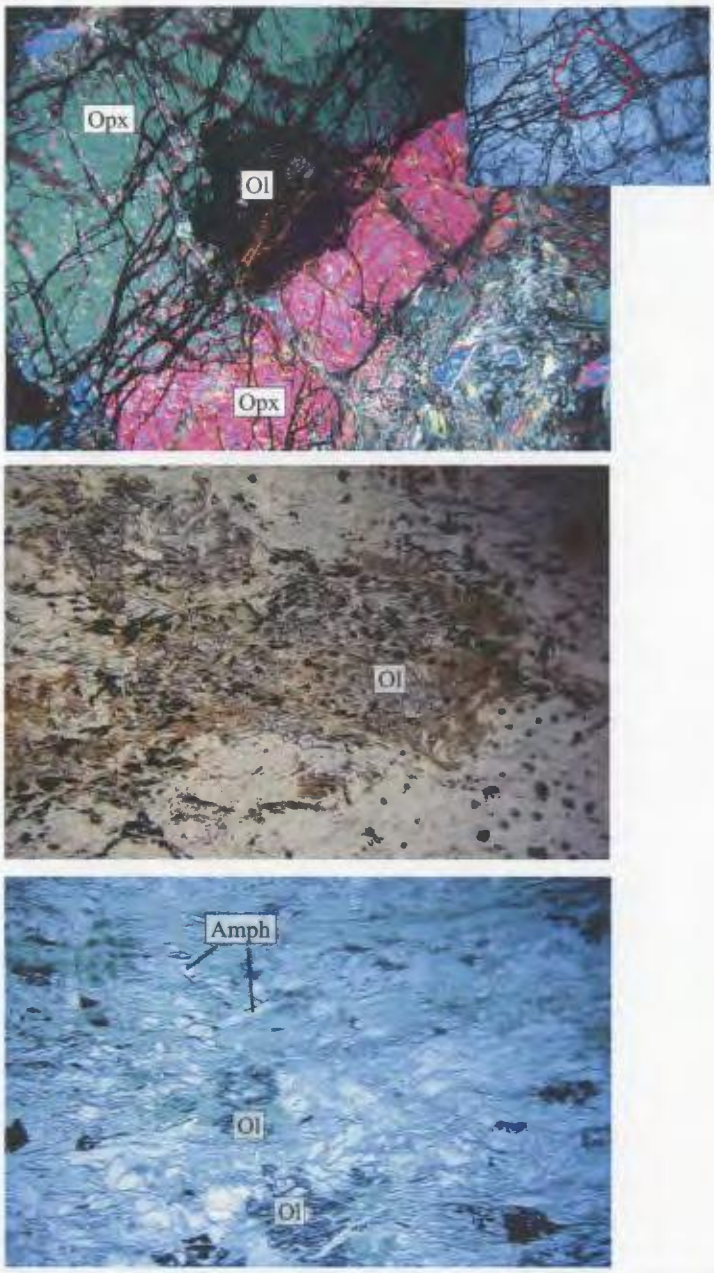

Figure 2.19. Photomicrographs of progressive stages (a-c) in the alteration of primary minerals in samples from central regions of ultramafic layers.
a) Least altered (Sample MM01-45a): remnant olivine (Ol) enclosed within orthopyroxene (Opx) grains. Note irregular boundaries (crossed polars, width of photo 4.2 mm, Inset: plane polarized light, Ol grain outlined).
b) More progressive alteration of olivine (Sample IV03-49). Note brown iddingsite alteration product (plane polarized light, width of photo 5 mm).
c) Strongly altered (Sample IV03-43). Fragments of primary igneous olivine (Ol) within a matrix of predominant chlorite. Chlorophaeite alteration (dark green) is associated with olivine grains. Late amphibole (Amph) grains cut the main foliation (plane polarized light, width of photo 5 mm).

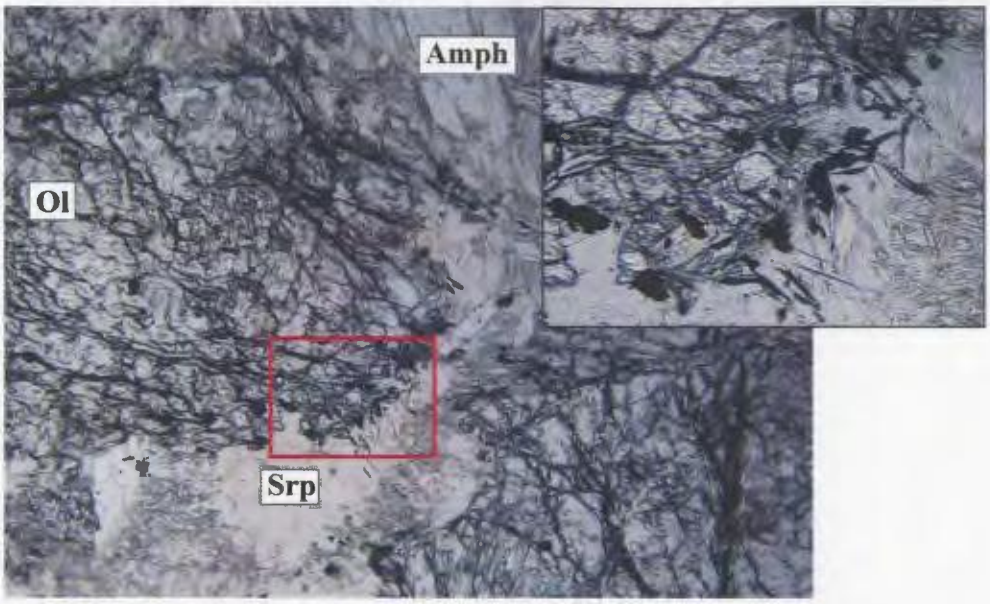

Figure 2.20. Photomicrograph of primary igneous olivine (Ol), sample IV03-44, from central region of an ultramafic layer, altering to serpentine (Srp) and opaque magnetite (Mag) along the edges of the grain. Later amphibole (amph) grains also present (plane polarized light, width of photo 4 mm; Inset: Detail of outlined olivine grain boundary, width of photo 0.8 mm).

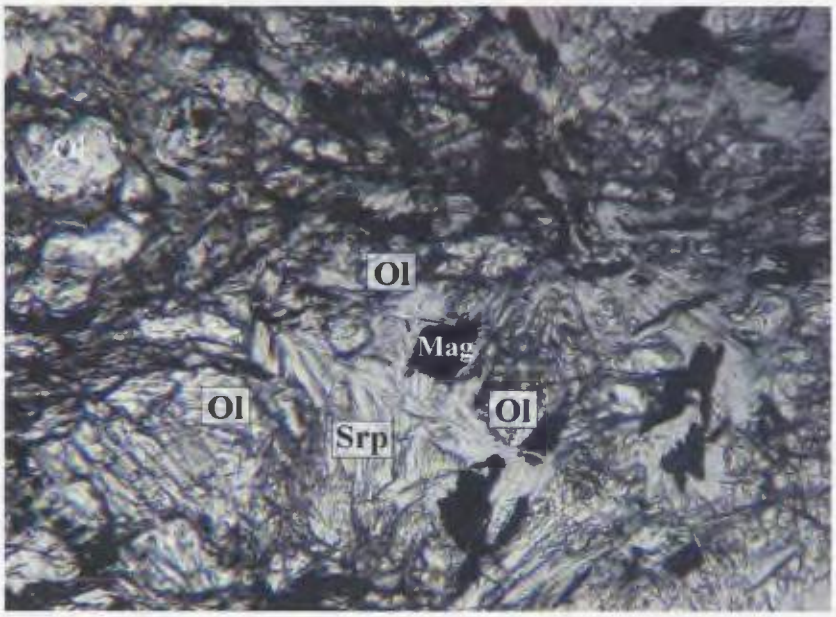

Figure 2.21. Photomicrograph of olivine (Ol) in sample from central region of an ultramafic layer (Sample MM01-45a), in more advanced stage of alteration. Small, anhedral olivine grains surrounded by serpentine (Srp) and magnetite (Mag) (plane polarized light, width of photo 1.1 mm).

a)

b)

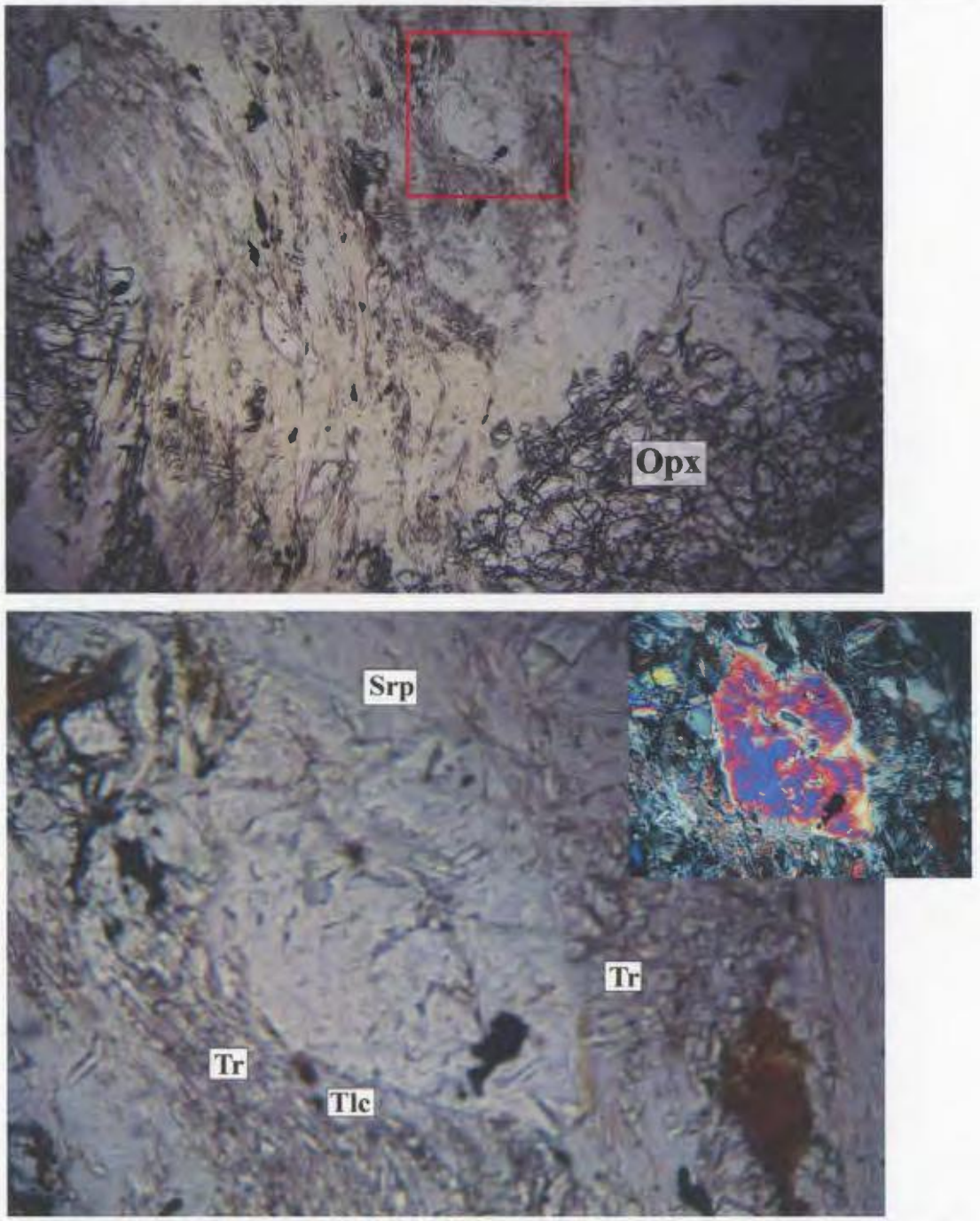

Figure 2.22. Photomicrographs of Sample MM01-45a, a sample from the central region of an ultramafic layer.
a) Orthopyroxene (Opx), altering to serpentine (colourless) and chlorite (pale green). Also, later amphibole grains overgrow fabric and are themselves being altered (see b; plane polarized light, width of photo 4.2 mm).
b) Detail of amphibole outlined in (a). Alteration products include tremolite (Tr), talc (Tlc), and serpentine (Srp), (plane polarized light, width of photo 1.4mm; Inset: crossed polars, width of photo 1.4 mm).

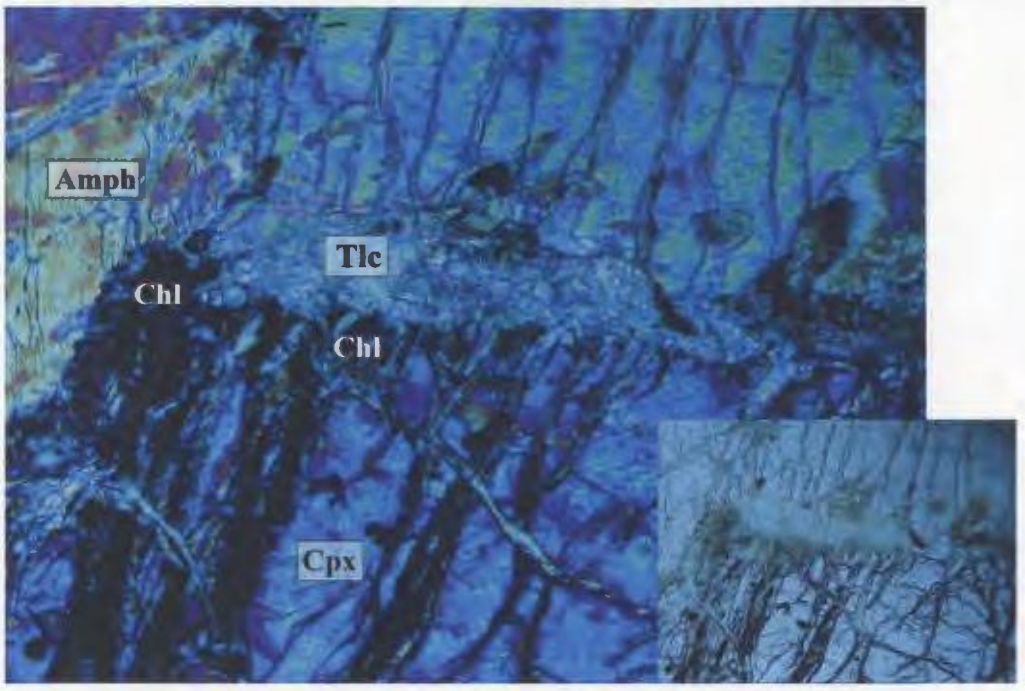

Figure 2.23. Photomicrograph of clinopyroxene (Cpx), in sample MM01-45a from the central region of an ultramafic layer, altering to talc (Tlc) and chlorite (Chl). Serpentine viens cut across the cpx grain (crossed polars, width of photo 1.25 mm; Inset: plane polarized light, width of photo 1.25 mm).

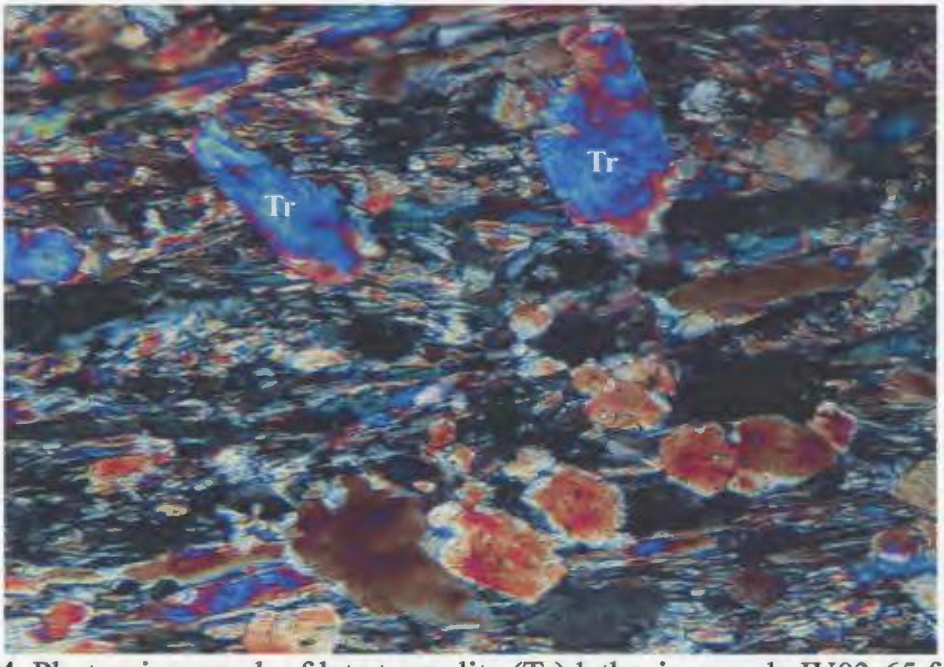

Figure 2.24. Photomicrograph of late tremolite (Tr) laths, in sample IV03-65 from the central region of an ultramafic layer, interpreted as S_R oriented at an angle to the main foliation (SN_2) (crossed polars, width of photo 1 mm).

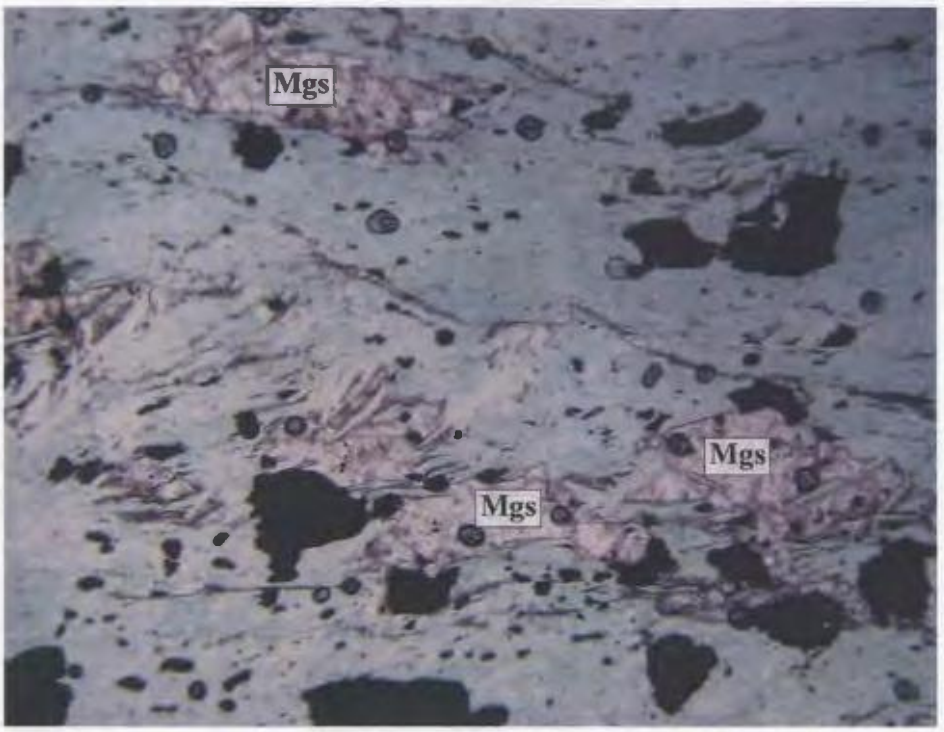

Figure 2.25. Photomicrograph of magnesite (Mgs), in sample IV03-42, from the margin of an ultramafic layer, within a matrix of chlorite and tremolite-actinolite and magnetite (plane polarized light, width of photo 4 mm).

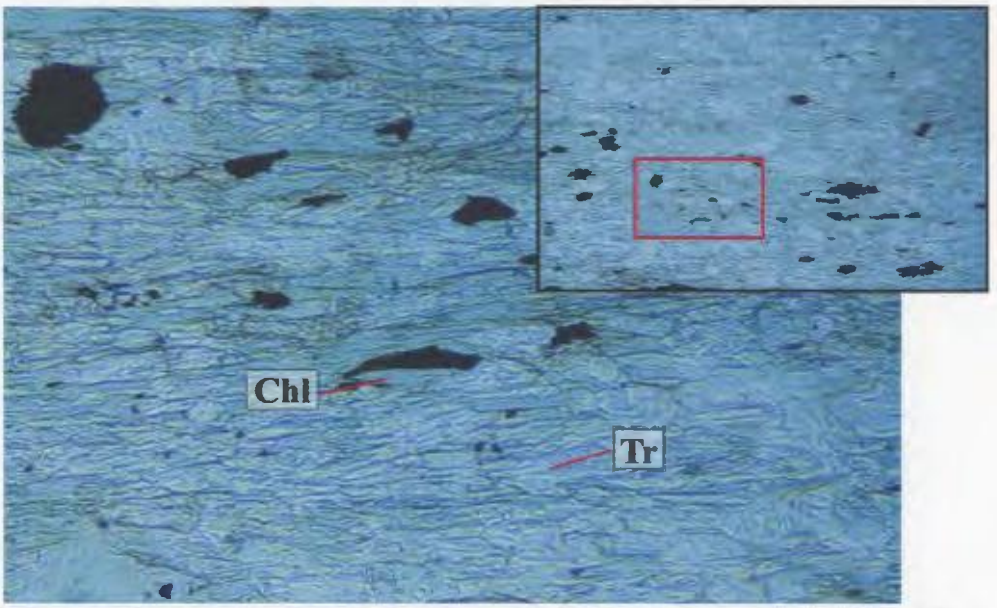

Figure 2.26. Photomicrograph of well-developed foliation in Sample MM01-69a, principally defined by chlorite (Chl) and tremolite (Tr), typical of the marginal zones of ultramafic layers (detail of outline in inset photo, plane polarized light, width of photo 1.25 mm; Inset: width of photo 4.2 mm).

a)

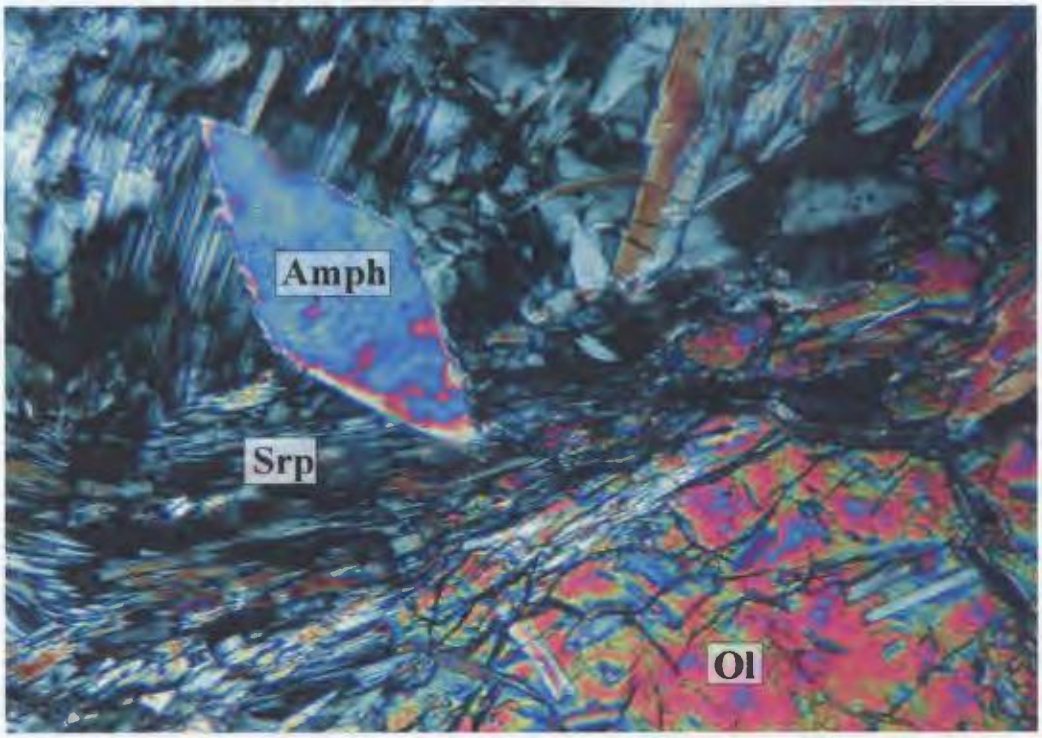

b)

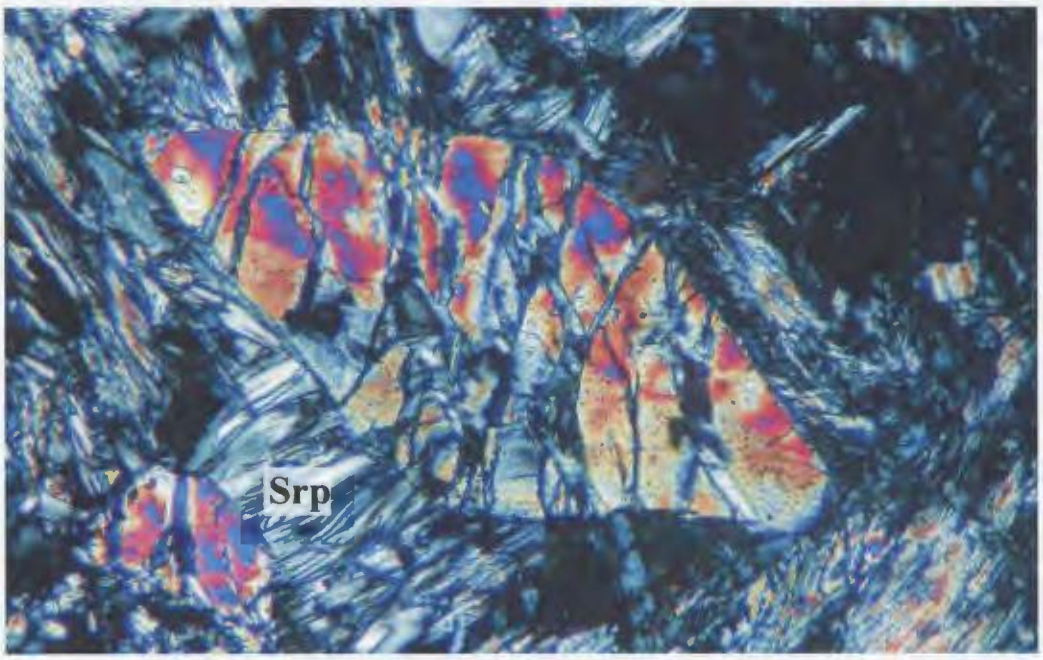

Figure 2.27. Photomicrographs of samples from the central region of an ultramafic layer.
a) Amphibole (Amph) overgrowing serpentine (Srp) which is an alteration product of olivine in Sample MM01-96 (Ol; crossed polars, width of photo 1.2 mm).
b) Amphibole grain in Sample MM01-45a which is overgrowing serpentine, has undergone a second serpentinization (Srp) event (crossed polars, width of photo 1.1 mm).

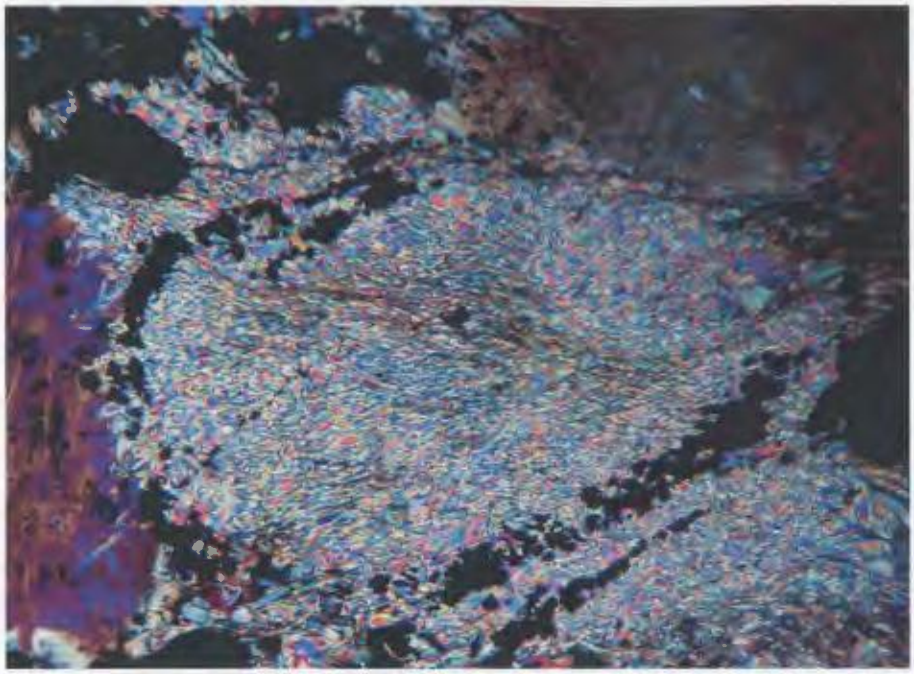

Figure 2.28. Photomicrograph of magnetite grains which outline pseudomorphs of fine grained talc, likely after olivine. Observed in sample IV03-33 from the central region of an ultramafic layer (crossed polars, width of photo 1.2 mm).

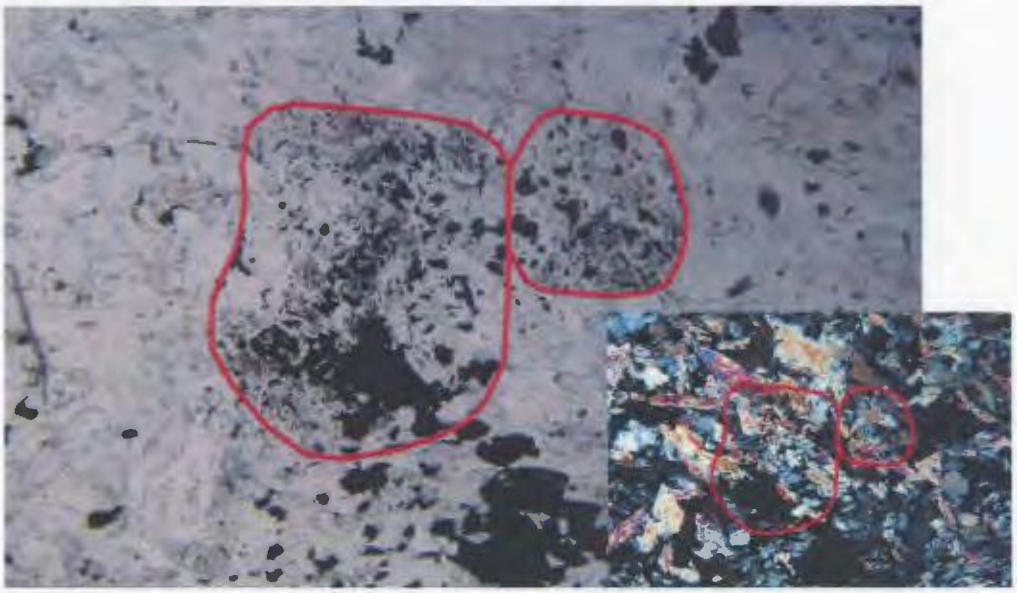

Figure 2.29. Photomicrograph of small magnetite grains concentrated in clusters which may represent locations where primary olivine or pyroxene grains had been completely broken down to serpentine and magnetite and have been overgrown by later amphibole grains. Observed in sample MM01-21b from the central region of an ultramafic layer (plane polarized light, width of photo 3.5 mm; Inset: crossed polars, width of photo 3.5 mm).

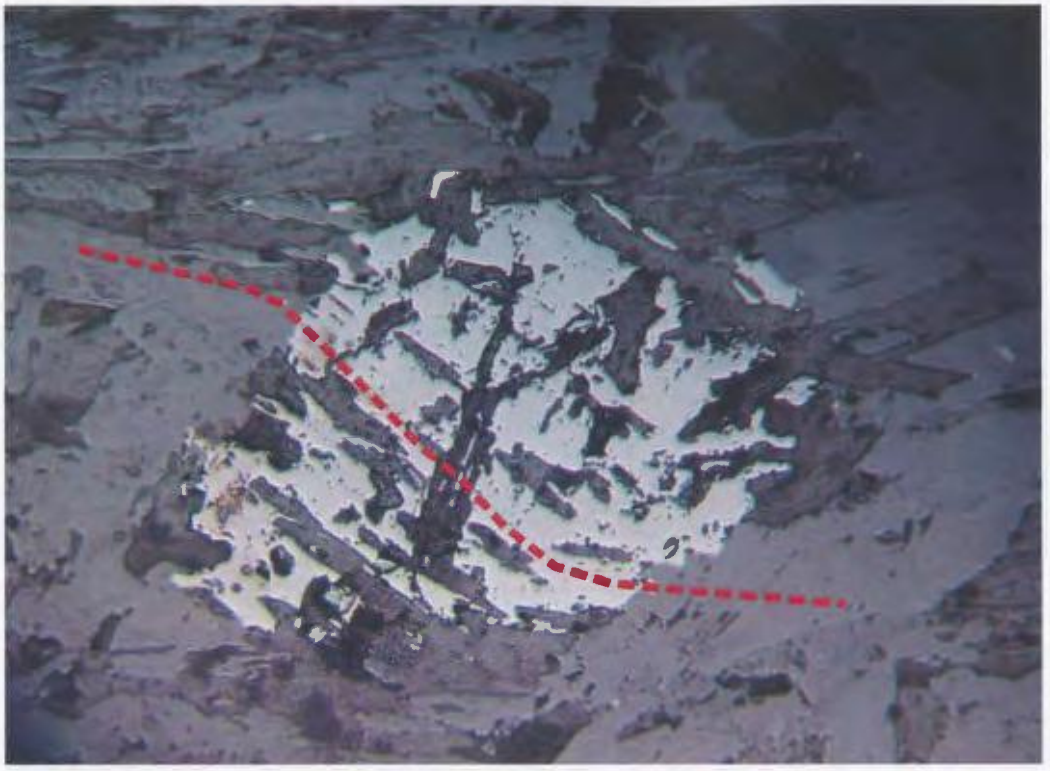

Figure 2.30. Curved pattern of silicate inclusions indicate that the magnetite grain grew syn-tectonically, likely during DN_2. Observed in sample from the central region of an ultramafic layer (reflected light, width of photo 0.7 mm).

a)

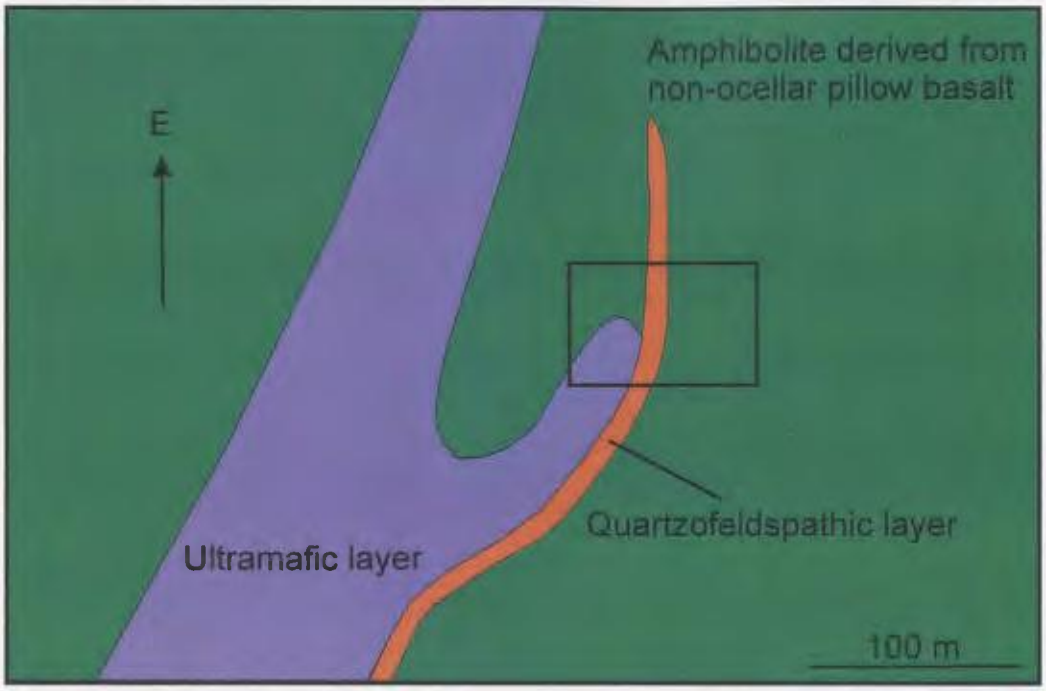

b)

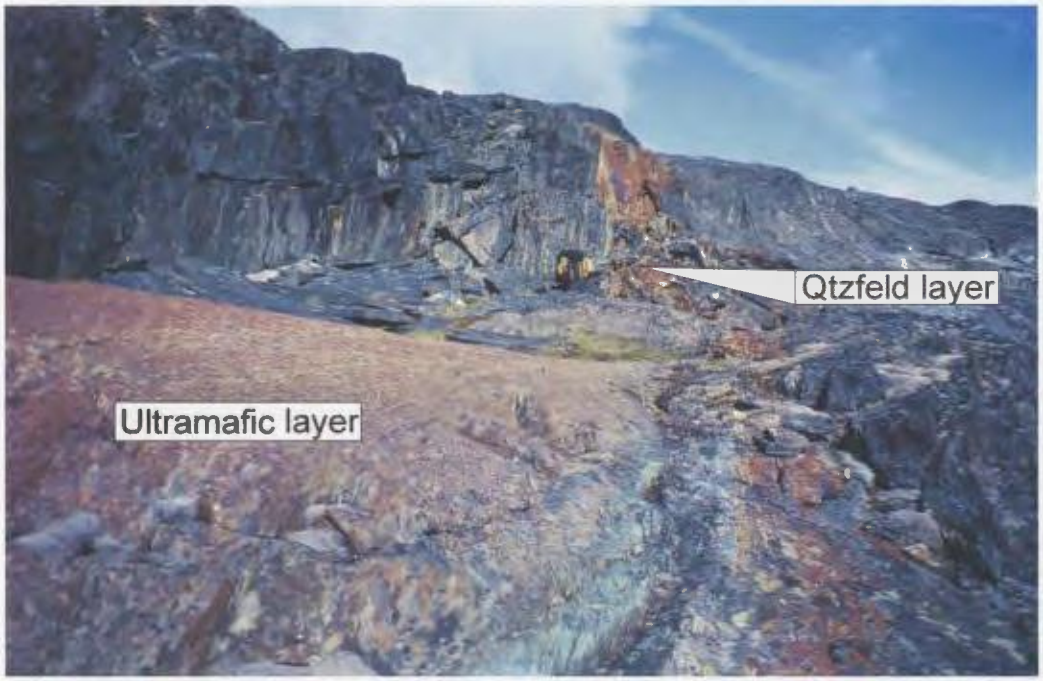

Figure 2.31.
a) Plan-view sketch of Locality MM01-69. A quartzofeldspathic layer beside an ultramafic layer is not folded with the ultramafic layer; instead the layer continues into an amphibolite unit and cuts across pillow structures.
b) Photo of area outlined in (a). The bright orange-yellow colour of the quartzofeldspathic layer is due to the weathering of sulphide minerals (photo facing east).

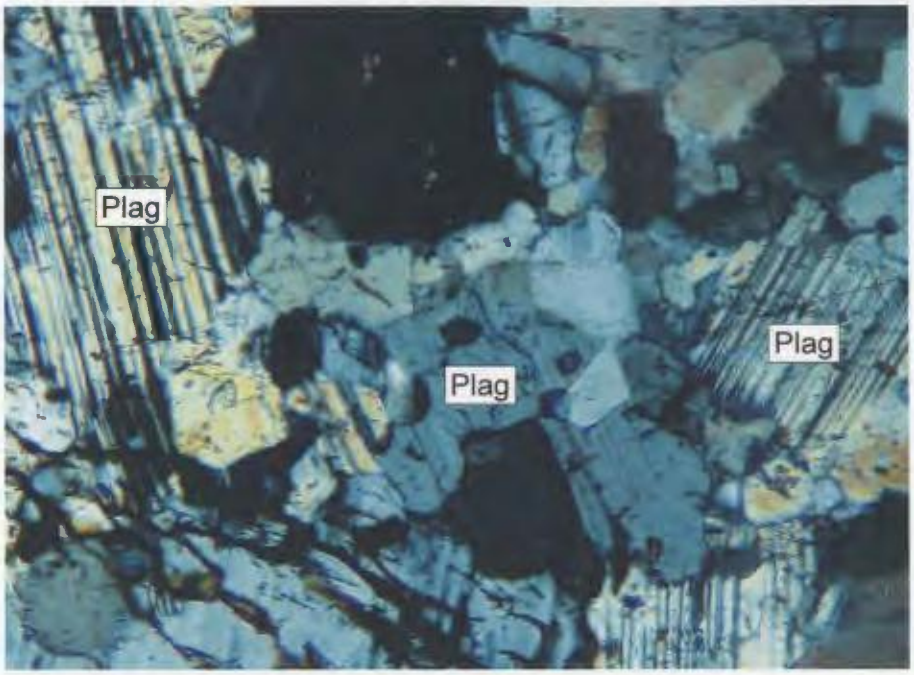

Figure 2.32. Photomicrograph of plagioclase (Plag) grains within a rusty quartzofeldspathic layer in the Marker High Strain Zone (sample MM01-73). A relict igneous texture is preserved (crossed polars, width of photo 0.8 mm).

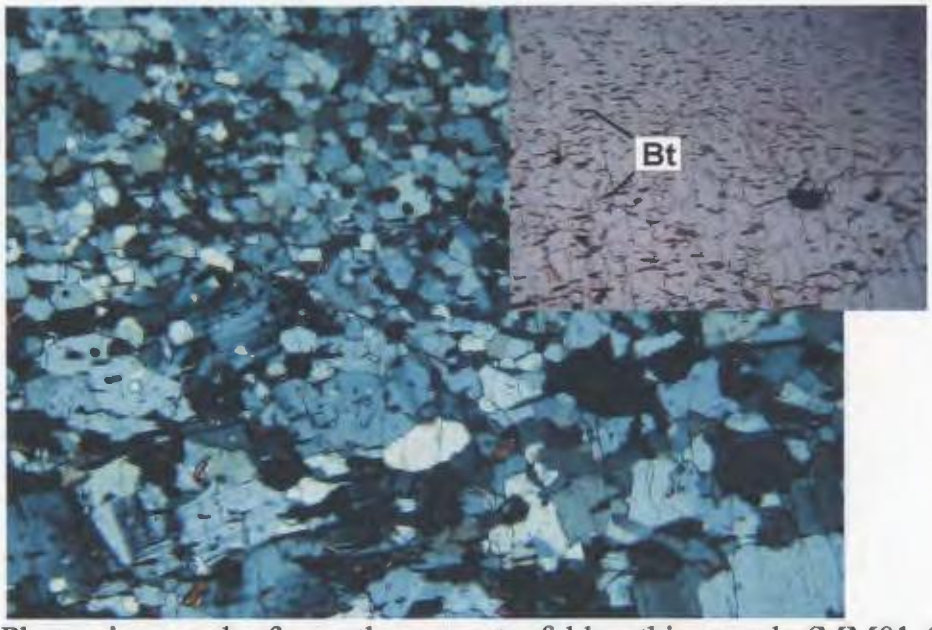

Figure 2.33. Photomicrograph of a northern quartzofeldspathic sample (MM01-64a). The main foliation (SN_2) is defined by biotite (Bt; see inset), set within a polygonal matrix of quartz and feldspars. A gneissosity is defined by fine (top half of photo) and coarse (bottom half of photo) grained layers (crossed polars, width of photo 4.2 mm. Inset: plane polarized light, width of photo 4.2 mm).

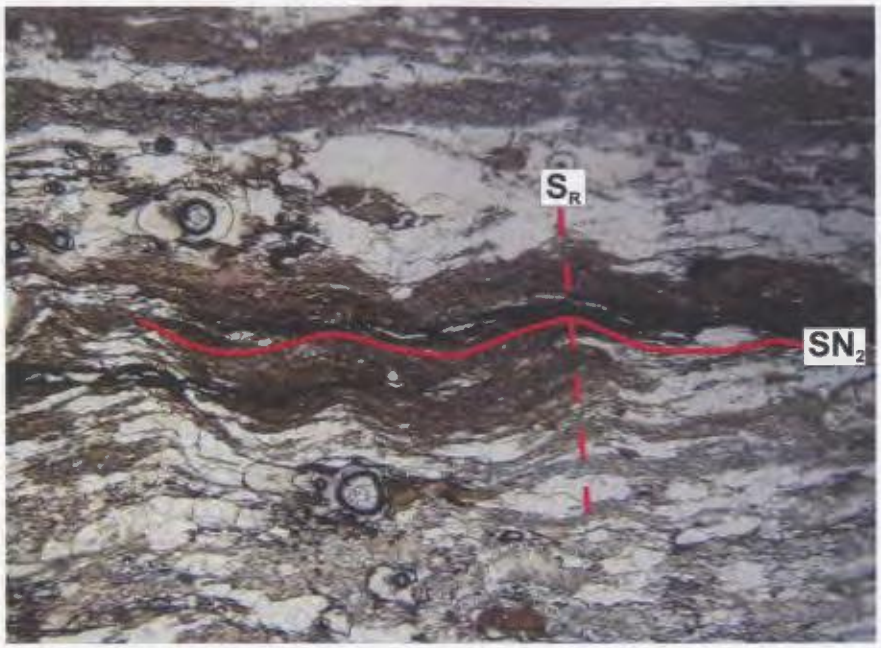

Figure 2.34. Photomicrograph of a northern quartzofeldspathic sample (IV03-67). The main foliation is locally folded producing an S_R axial planar foliation (plane polarized light, width of photo 4.2 mm).

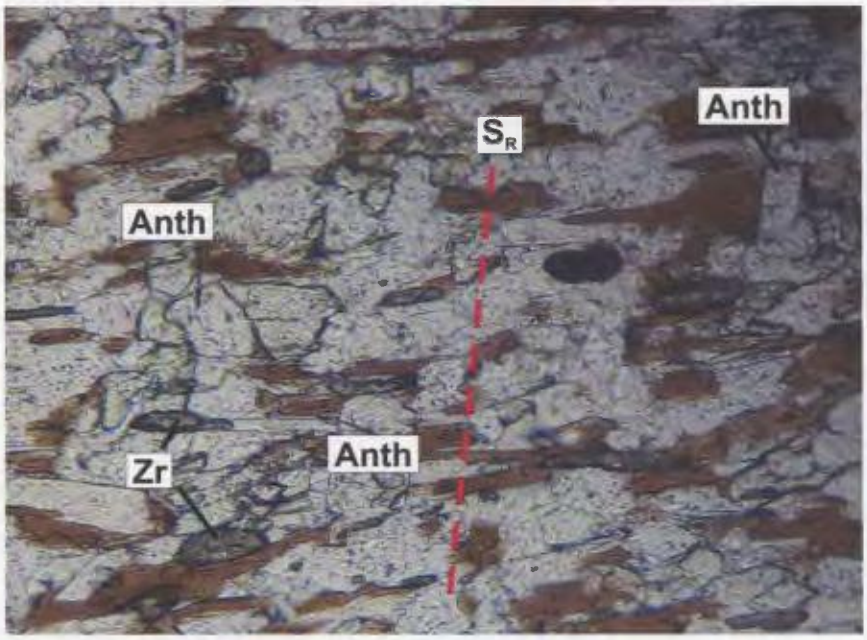

Figure 2.35. Photomicrograph of northern quartzofeldspathic sample (MM01-50). An S_R fabric is defined by anthophylite (An) grains which are at an angle to the main foliation (SN_2) defined by biotite. Zircon (Zr) grains were also noted (plane polarized light, width of photo 1.1 mm).

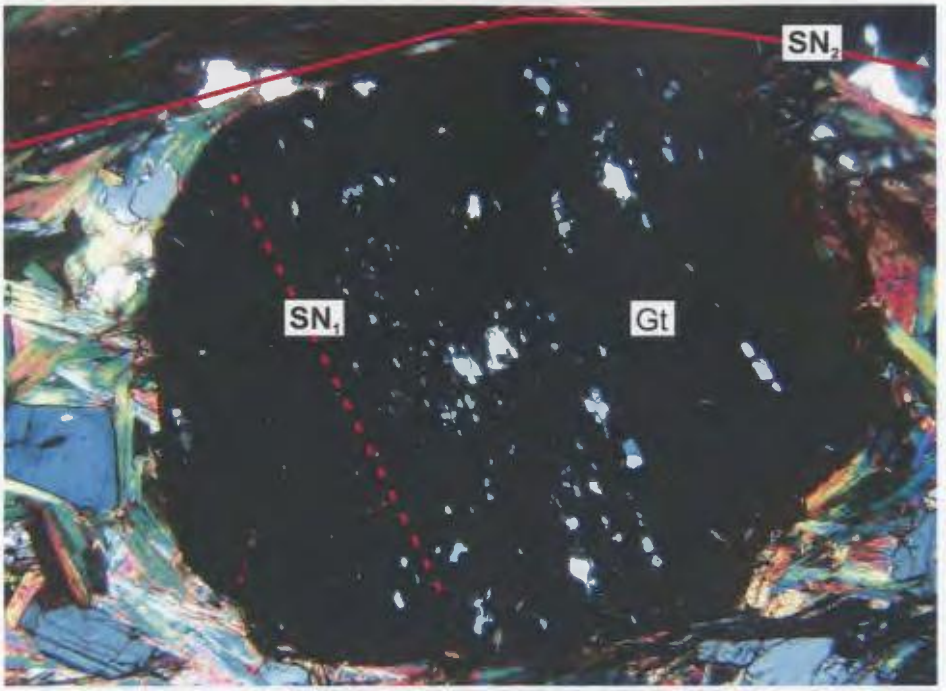

Figure 2.36. Photomicrograph of a northern quartzofeldspathic sample (MM01-47). A fabric, interpreted as SN_1 , is preserved as an inclusion trail within a garnet (Gt), and is at an angle to SN_2 (crossed polars, width of photo 4.75 mm).

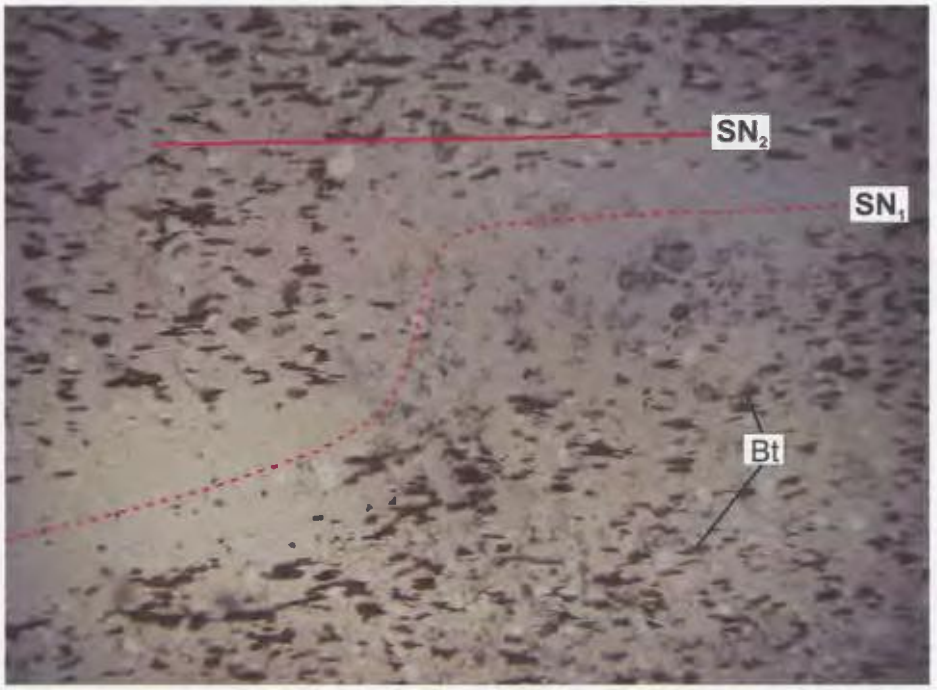

Figure 2.37. Photomicrograph of a northern quartzofeldspathic sample (MM01-50). SN_1 is defined by compositional layering between biotite-rich and biotite-poor layers; this layering is folded. Biotite grains define an axial planar (SN_2) foliation (plane polarized light, width of photo 5.5 mm).

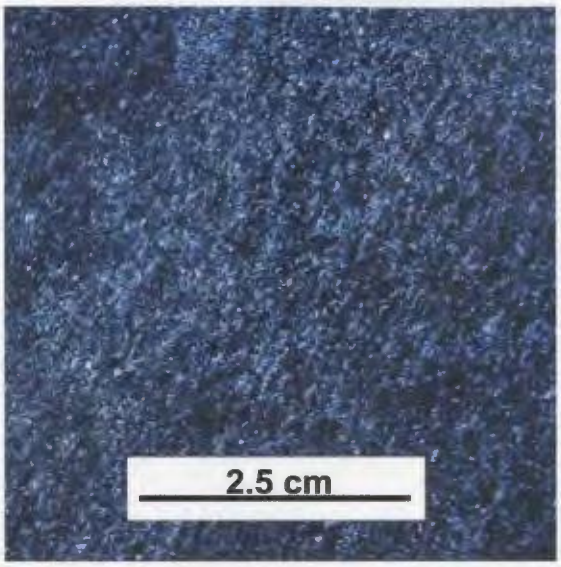

Figure 2.38. Gabbroic dykes, dominated by hornblende and feldspar, have an average grain size of 0.5 mm-1 mm.

Figure 2.39. Dyke containing large relict plagioclase phenocrysts set within a fine-grained matrix (Locality MM01-36). Phenocrysts range in size from 1 cm-30 cm (Inset: Photo of outcrop. Dotted line outlines dyke boundaries).

Figure 2.40. Dyke containing large relict plagioclase phenocrysts which range in intensity of deformation from ovoid shapes to stretched, elongate lenses (Locality MM01-107).

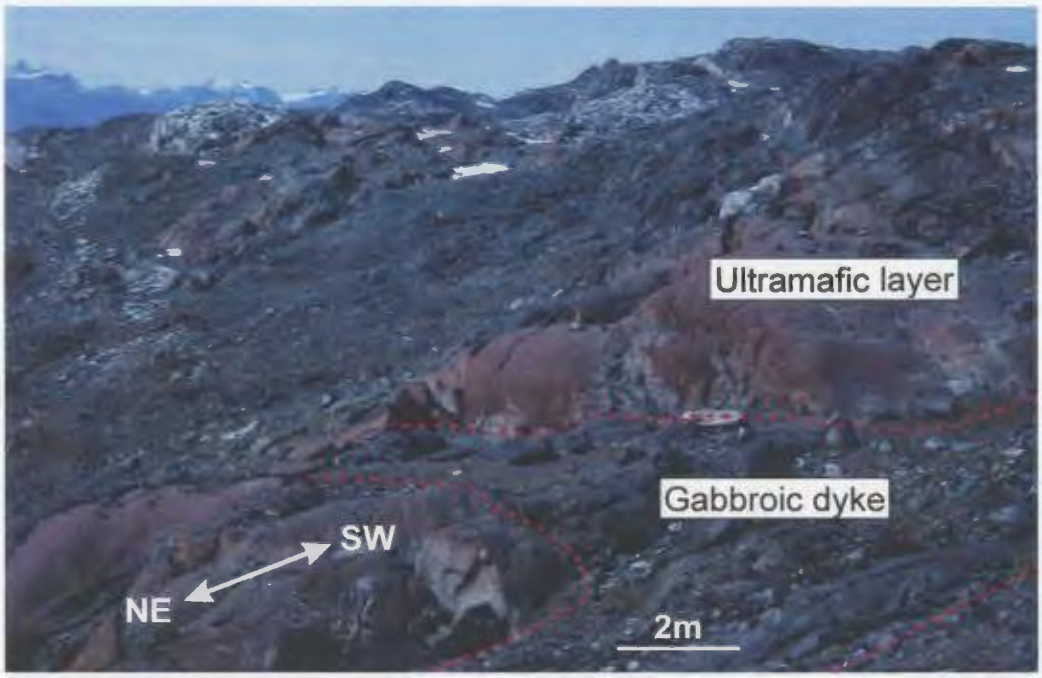

Figure 2.41. A gabbroic dyke parallel to the boundary of an ultramafic layer running northeast (NE) – southwest (SW), is seen to branch and cross-cut the ultramafic unit (Locality MM01-21, photo facing south).

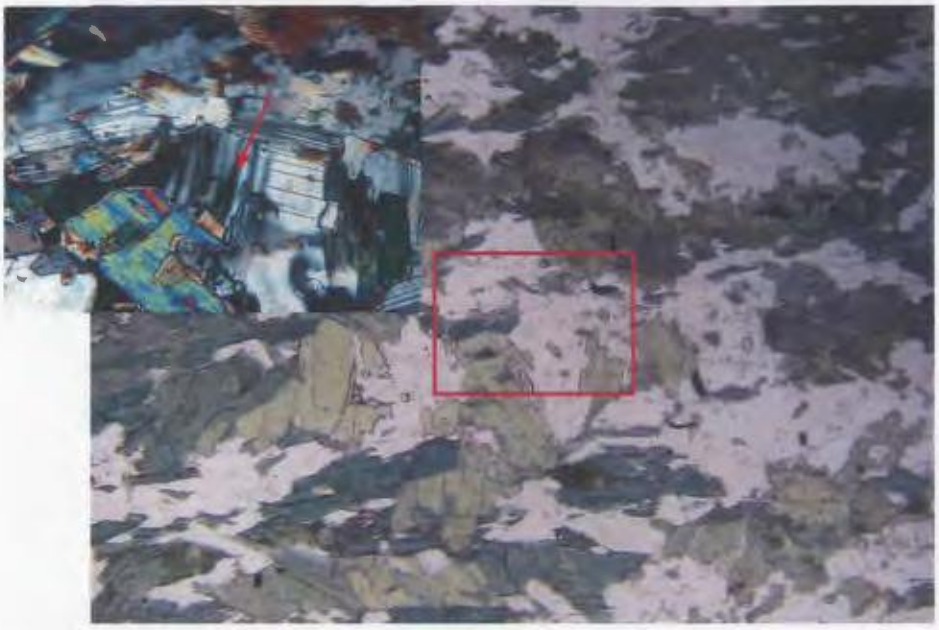

Figure 2.42. Photomicrographs of a weakly deformed gabbroic dyke (Sample MM01-96a): contains feldspar grains which are partially recrystallized and exhibit low-grade deformation features (e.g. deformation lamellae indicated by arrow in Inset). Plane polarized light, width of photo 4.2 mm. (Inset: detailed of outlined area, crossed polars, width of photo 1.1 mm).

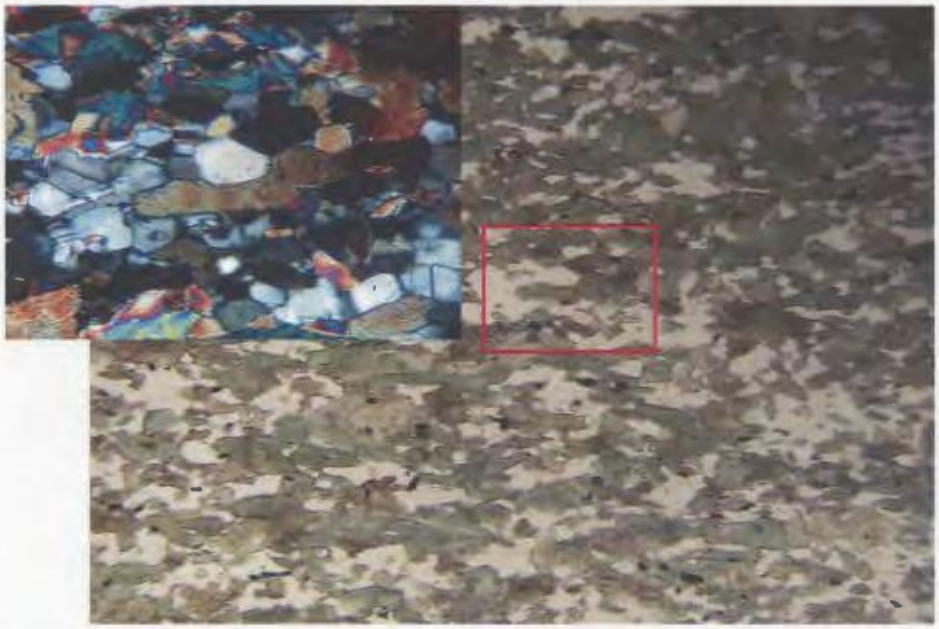

Figure 2.43. Photomicrographs of a strongly deformed gabbroic dyke (Sample MM01-71a). Composed of recrystallized feldspar grains (plane polarized light, width of photo 4.2 mm. Inset: Detail of outlined area, crossed polars, width of photo 1.1 mm).

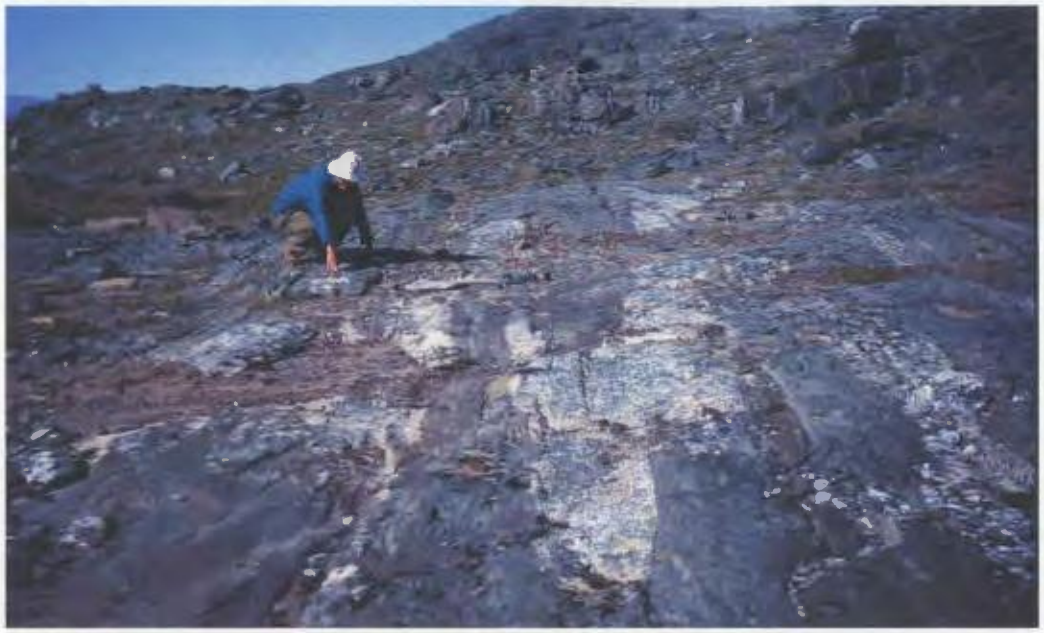

Figure 2.44. Folded fine-grained pegmatite/granite dyke within the Marker High Strain Zone (Locality MM01-20, photo facing west).

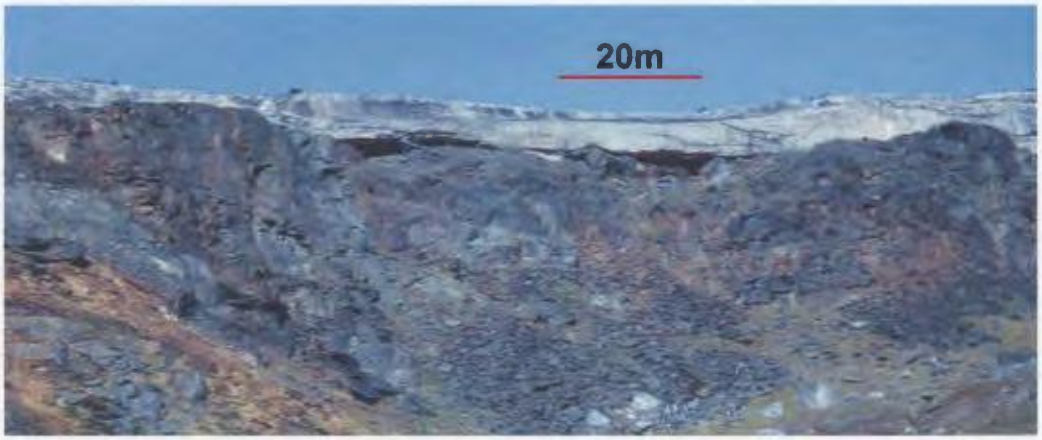

Figure 2.45. A large, sub-horizontal pegmatite sheet. Photo facing north.

a)

b)

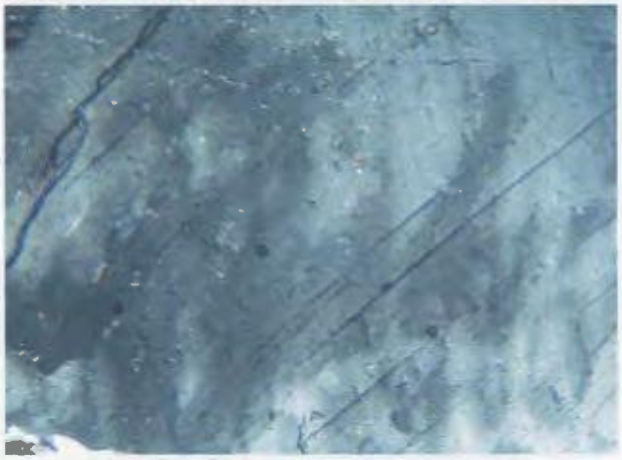

c)

Figure 2.46. Photomicrographs of a granitic pegmatite (Locality MM01-52): deformation structures in plagioclase.
a) Microfracturing: ~ vertical lines (crossed polars, width of photo 5 mm).
b) Undoluse extinction. Also note development of fine-grained sericite (crossed polars, width of photo 1.2 mm).
c) Deformation twins indicated by arrow. Note: In plagioclase, deformation twins commonly taper from the crystal rim towards the crystal centre (Passchier and Trouw, 1996). Crossed polars, width of photo 2.1 mm.

a)

b)

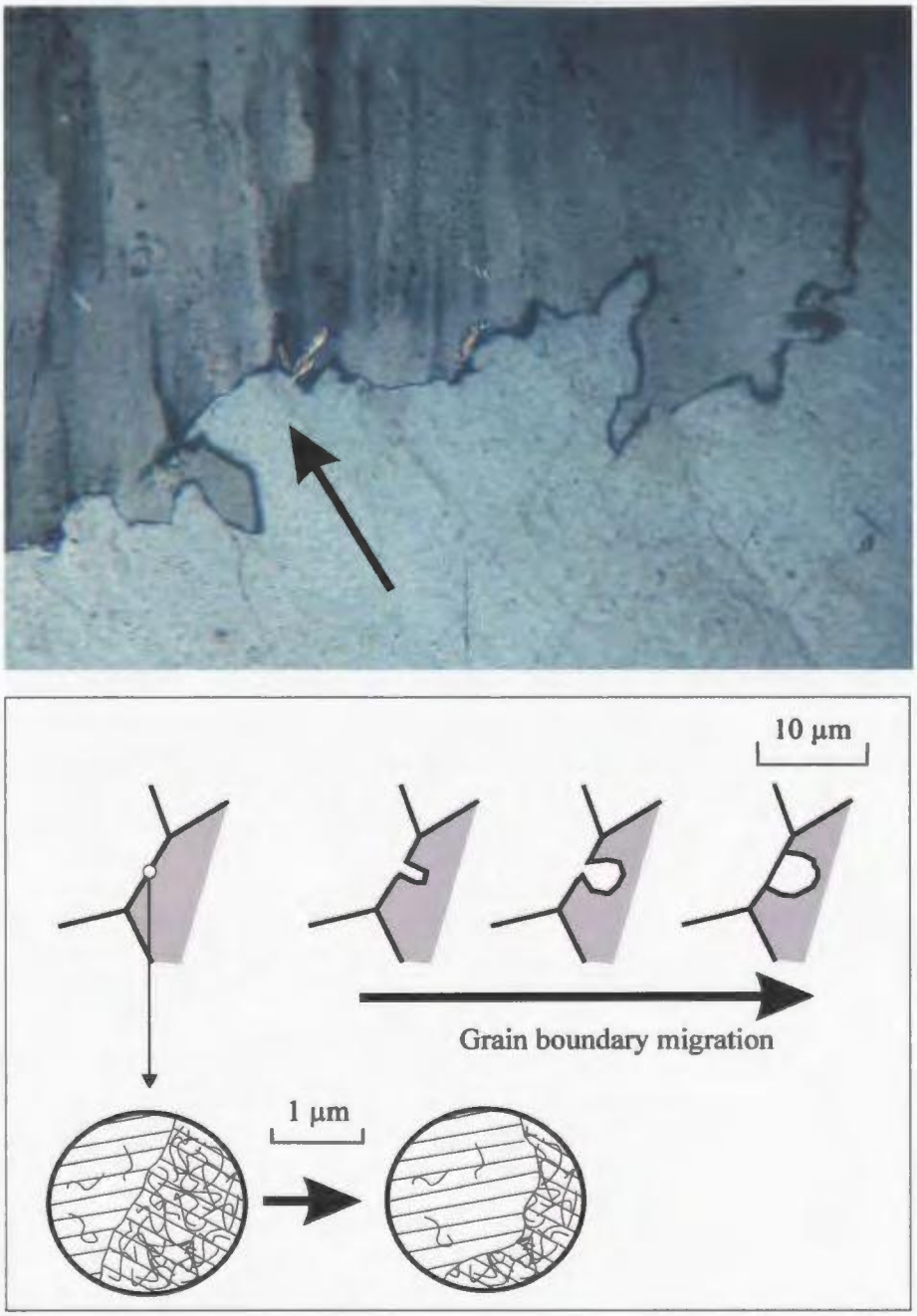

Figure 2.47.
a) Photomicrograph of a granitic pegmatite (Locality MM01-52): bulging grain boundary between two plagioclase crystals is indicative of grain boundary migration recrystallization. The less deformed grain (no undulose extinction) is bulging into the more deformed grain, as indicated by arrow (crossed polars, width of photo 1.2 mm). b) Schematic diagram of grain boundary migration recrystallization. The grain which is least deformed (lower dislocation density) bulges into the grain with higher dislocation density, and eventually the bulge develops into an independent grain (after Passchier and Trouw, 1996, pp. 36).

a)

b)

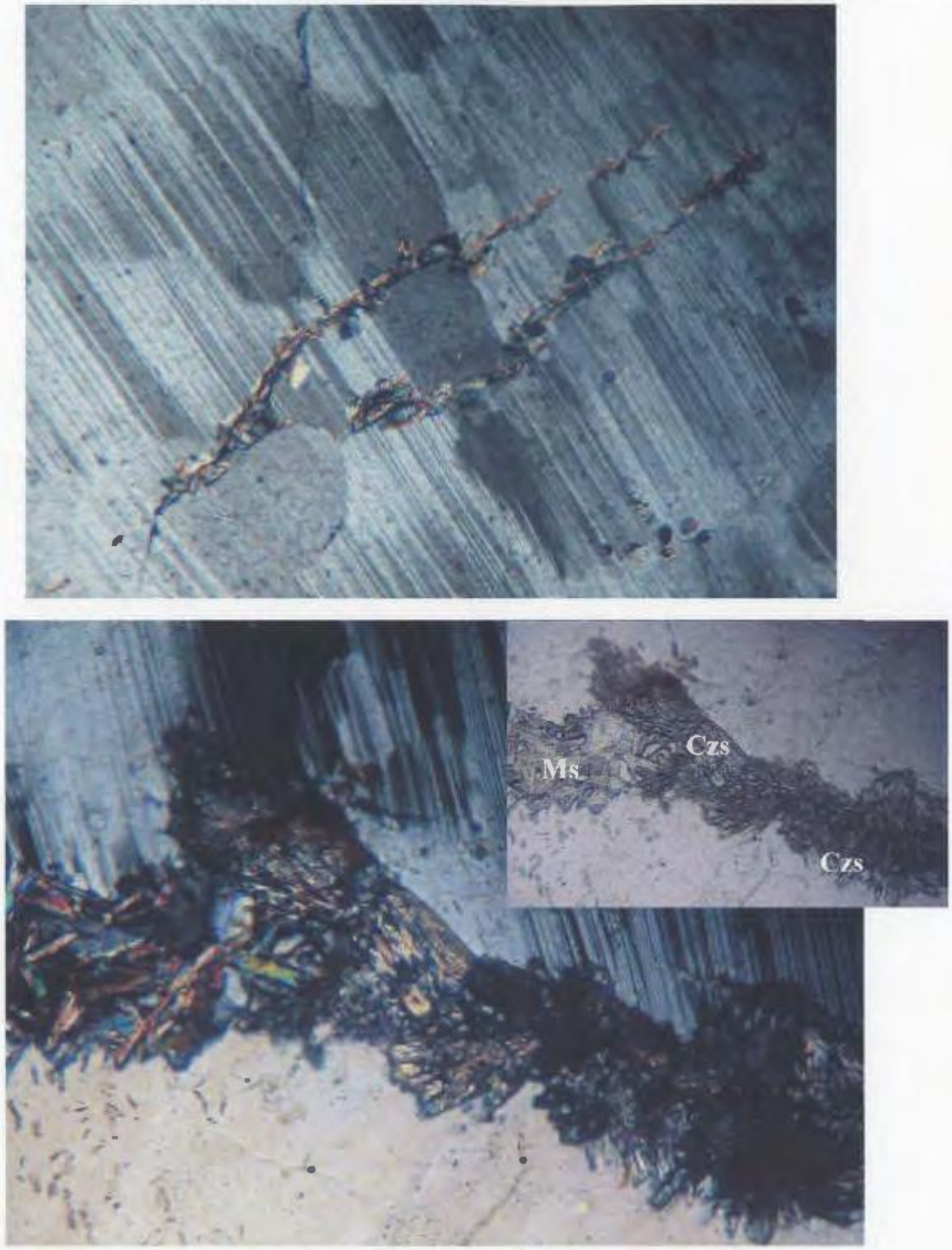

Figure 2.48. Photomicrographs of a granitic pegmatite (Locality MM01-52).
a) Muscovite along microcracks within a plagioclase grain (crossed polars, width of photo 5 mm).
b) Muscovite (Ms) and clinozoisite (Czs, bladed, high relief) along a grain boundary (crossed polars, width of photo 1.2 mm; Inset: plane polarized light, width of photo 1.2 mm).

Figure 2.49. The quartzofeldspathic and amphibolitic layer of the Marker High Strain Zone. This layer is characterized by thin to coarse (centimetre to metre scale) horizons of amphibolite intercalated with more abundant quartzofeldspathic layers (Locality MM01-35; Top of photo to southeast).

Figure 2.50. A folded amphibolitic dyke observed within the Marker High Strain Zone (Top of photo to west).

a)

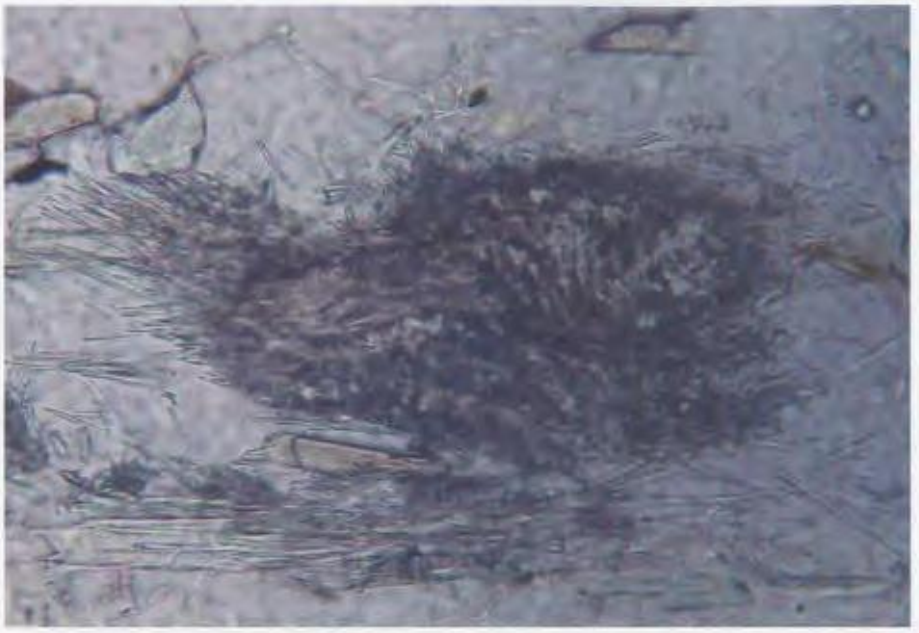

b)

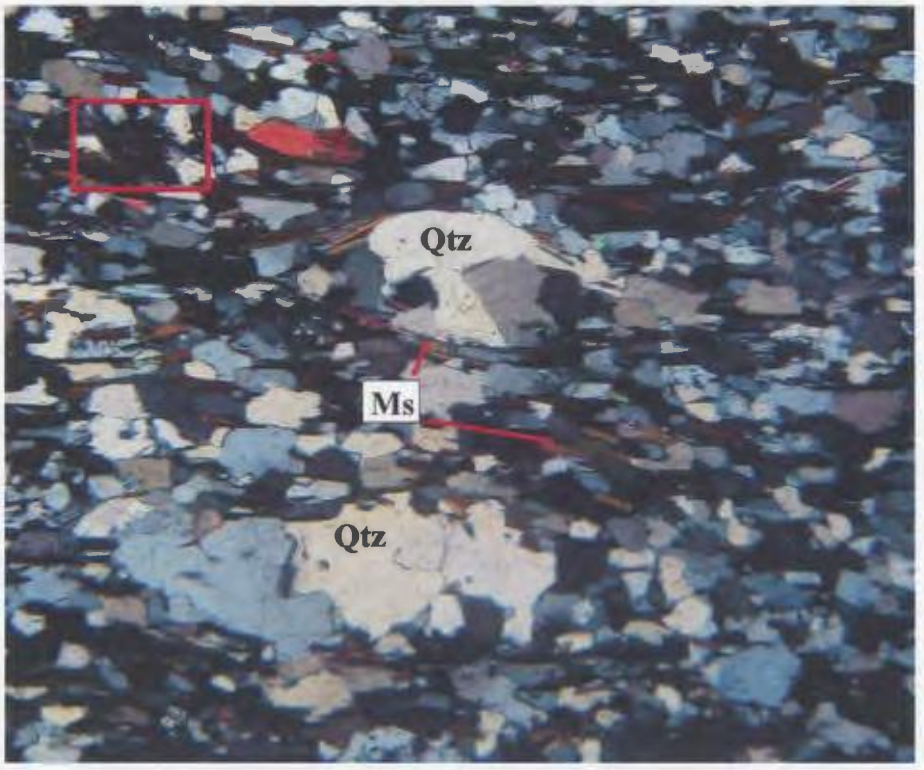

Figure 2.51. Photomicrographs from a quartzofeldspathic layer in the Marker High Strain Zone (Sample MM01-63).
a) Detail of fibrolite mass from area outlined in (b), (crossed polars; width of photo 0.6 mm).
b) Lenses of coarse grained quartz (Qtz) within equigranular quartzofeldspathic matrix; foliation defined by muscovite (Ms; crossed polars; width of photo 4 mm).

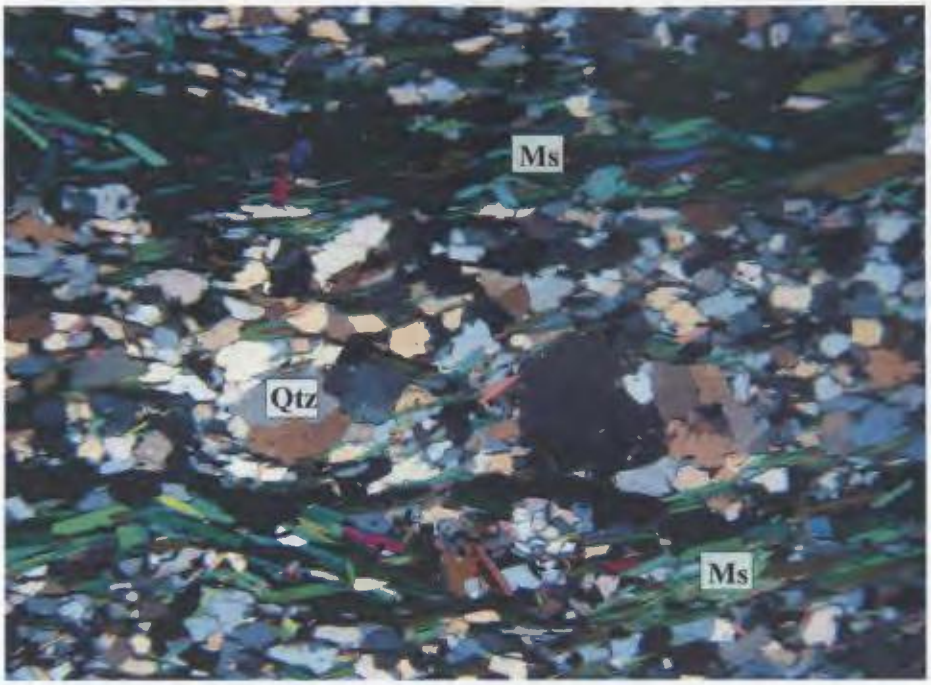

Figure 2.52. Photomicrographs from a quartzofeldspathic layer in the Marker High Strain Zone (Sample MM01-35) showing typical compositional layering of muscovite-rich (Ms) layers vs mica-poor layers (crossed polars, width of photo 5.4 mm).

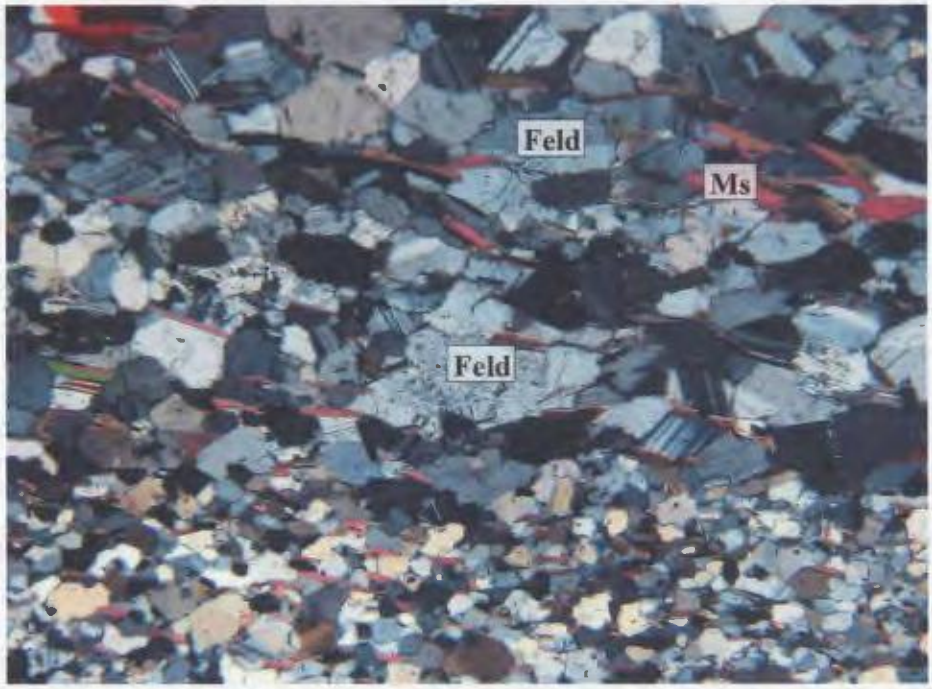

Figure 2.53. Photomicrograph from a quartzofeldspathic layer in the Marker High Strain Zone (Sample MM01-74) showing variations between coarse-grained and fine-grained layers (feldspar =Feld, crossed polars, width of photo 4 mm).

Figure 2.54. Diagram which demonstrates the effects of progressive transposition which can eliminate earlier fabrics (e.g bedding, foliation; Passchier and Trouw, 1996).

a)

b)

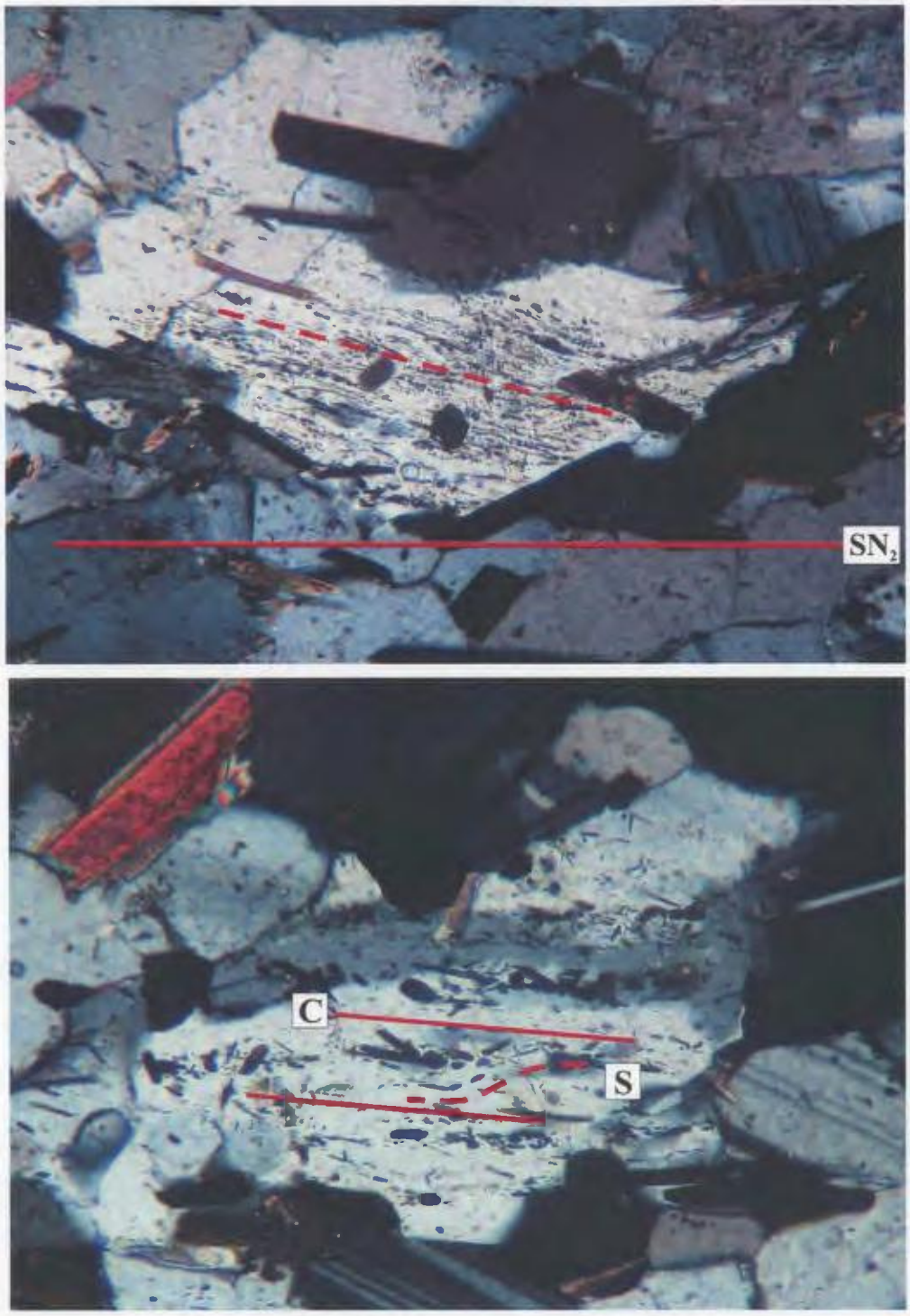

Figure 2.57. Photomicrographs from a quartzofeldspathic layer in the Marker High Strain Zone (Sample MM01-74).
a) A feldspar grain preserves an earlier foliation (dotted line) at an angle to the main foliation (SN_2, solid line; crossed polars, width of photo 1 mm).
b) A possible S-C fabric indicative of dextral shear preserved within a feldspar grain (crossed polars, width of photo 0.8 mm).

a)

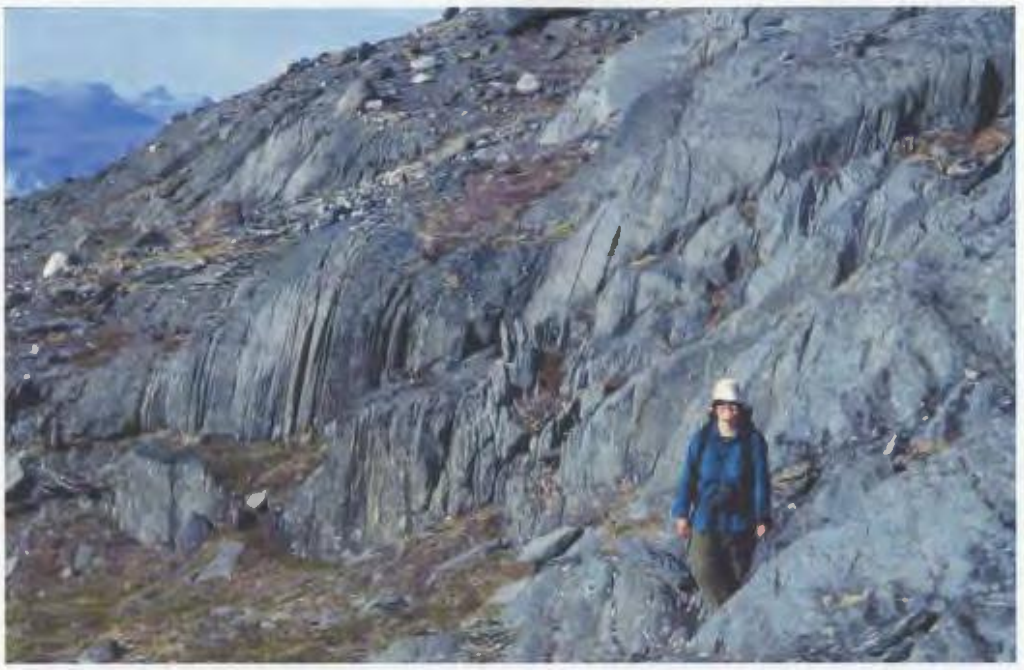

b)

Figure 2.58. The grey-green 'magnetic marker horizon' of the Marker High Strain Zone.
a) Schistose nature of the magnetic marker (photo facing west)
b) Tight folds (traced in red) within the magnetic marker horizon (top of photo to north).

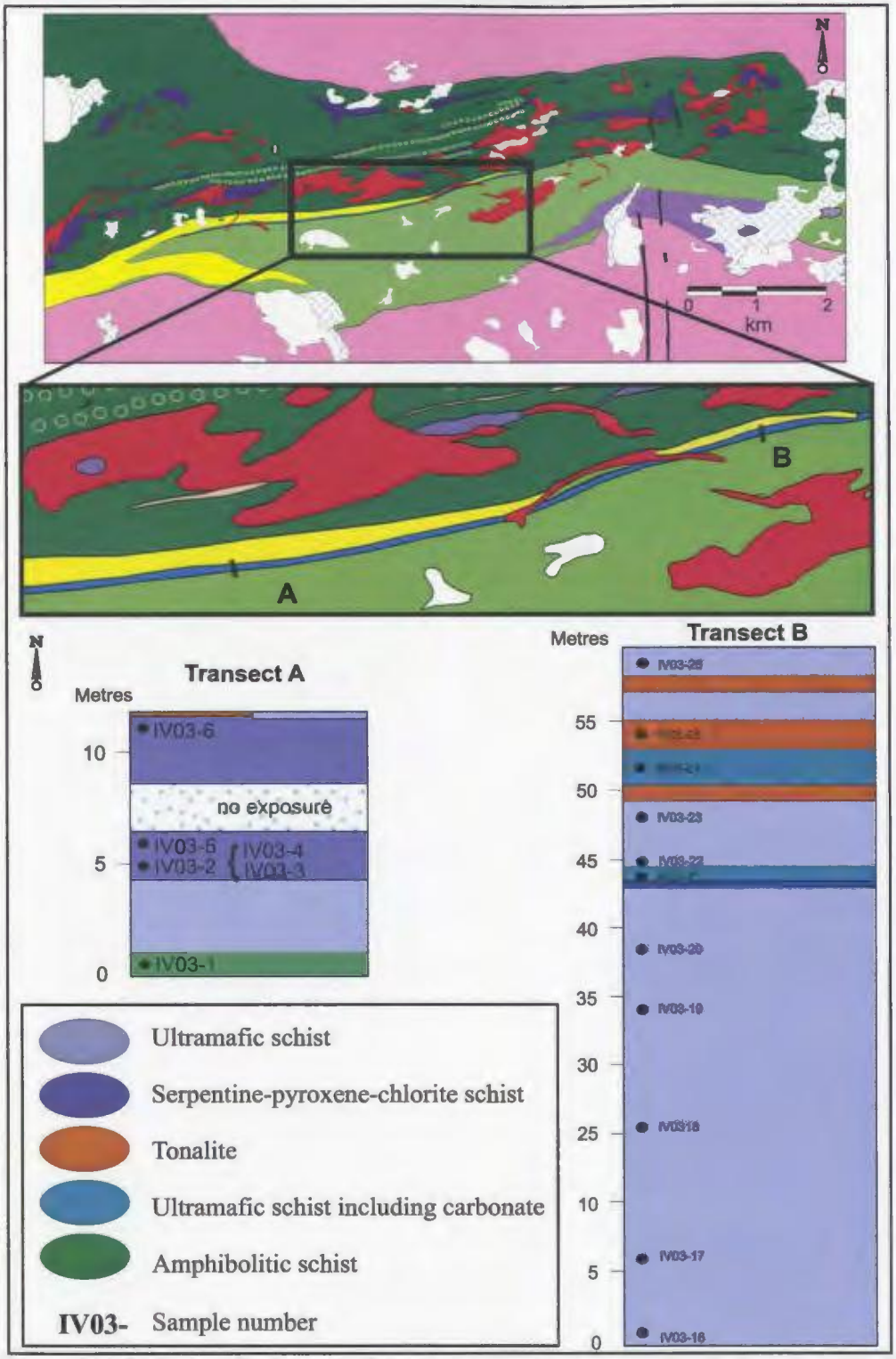

Figure 2.59. Simplified map of the Ivisârtoq greenstone belt showing detail of magnetic marker and details of transects A and B including sample locations.

a)

b)

Figure 2.58. The grey-green 'magnetic marker horizon' of the Marker High Strain Zone.
a) Schistose nature of the magnetic marker (photo facing west)
b) Tight folds (traced in red) within the magnetic marker horizon (top of photo to north).

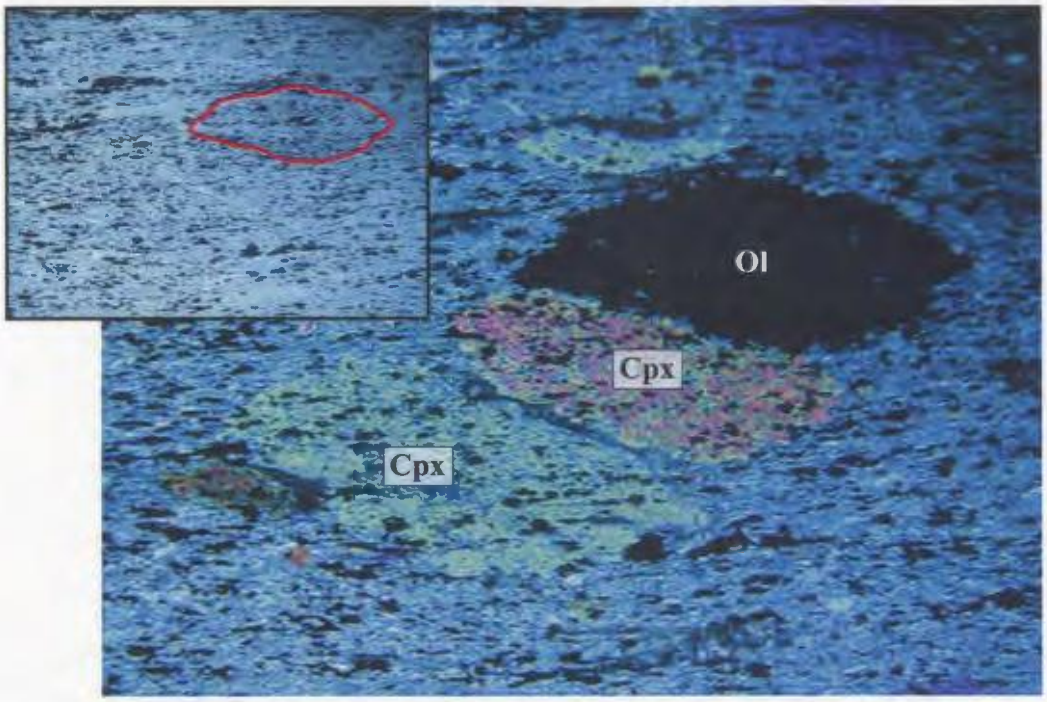

Figure 2.60. Photomicrograph of Sample IV03-16 from the magnetic marker. The matrix is composed of fine grained chlorite, tremolite,and serpentine, and is overprinted by olivine (Ol) and clinopyroxene (Cpx) porphyroblasts (crossed polars, width of photo 5 mm; Inset: plane polarized light, outline of olivine grain).

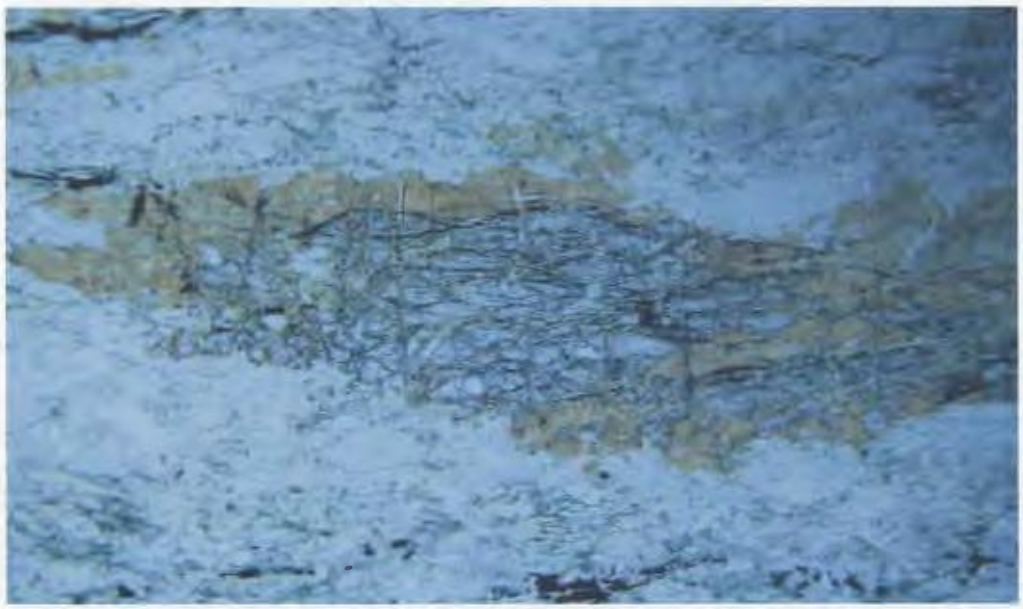

Figure 2.61. Photomicrograph of Sample IV03-23. Remnants of igneous olivine grains are preserved within the strongly deformed magnetic marker, surrounded by brown iddingsite alteration (plane polarized light, width of photo 4.2 mm).

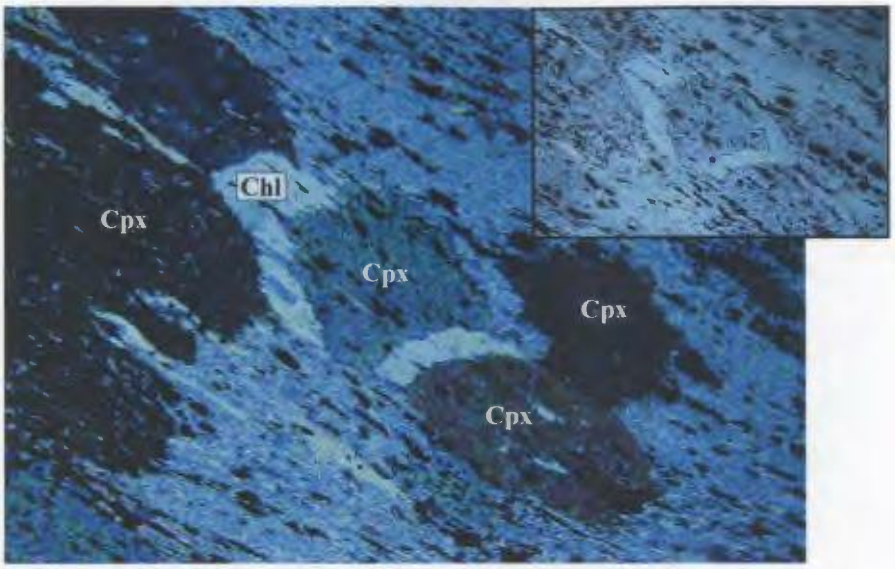

Figure 2.62. Photomicrograph of Sample IV03-16 from the magnetic marker. Strain shadows of chlorite (Chl) surround clinopyroxene (Cpx) porphyroblasts and likely indicate that fluids were present during deformation (crossed polars, width of photo 4.2 mm; Inset: plane polarized light).

a)

b)

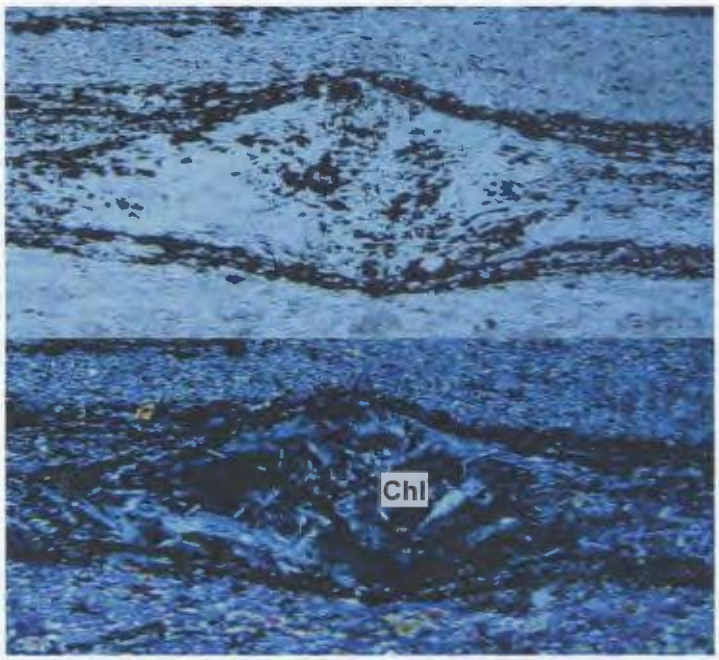

Figure 2.63. Photomicrograph of Sample IV03-17 from the magnetic marker. Pseudomorphs after clinopyroxene or olivine contain randomly oriented chlorite laths, which likely indicate that lower amphibolite metamorphism outlasted D_R deformation, width of photo 4.1 mm.
a) plane polarized light, b) crossed polars.

Figure 2.64. Photomicrograph of Sample IV03-17 from the magnetic marker. Flattened magnetite outline zones of altered minerals (mostly tremolite) and may represent the location of an original igneous mineral, such as olivine (crossed polars, width of photo 5 mm).

a)

b)

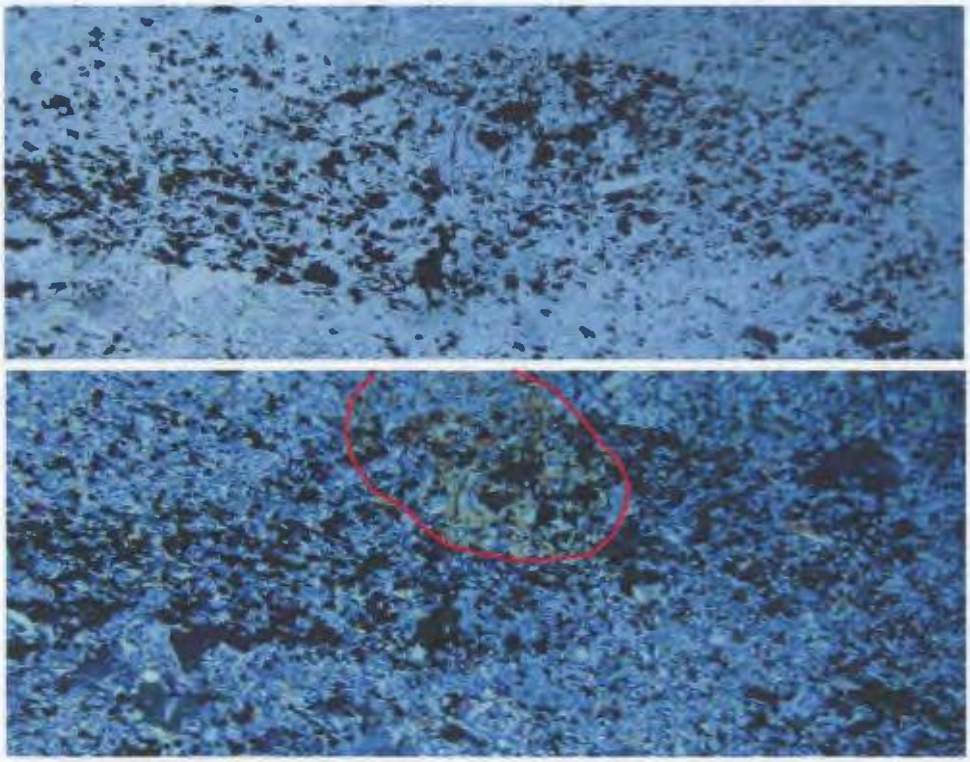

Figure 2.65. Photomicrograph of Sample MM01-105 from the magnetic marker. Magnetite cluster after an original olivine or pyroxene grain (width of photo 4.25 mm).
a) plane polarized light.
b) crossed polars, outline of olivine porphyroblast overgrowing magnetite cluster.

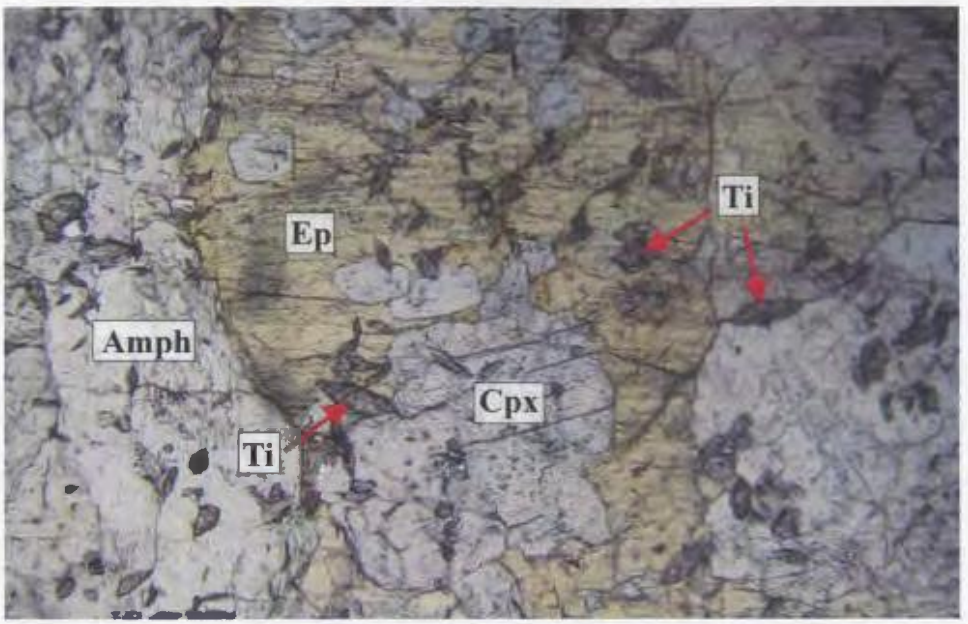

Figure 2.66. Photomicrograph of Sample IV03-9 from a metre wide zone on the northern edge of Transect 1 through the magnetic marker. Coarse-grained, garnet-pyroxene-epidote-amphibolite schist with up to 10 modal % titanite (Ti); (Ep =epidote, Cpx=clinopyroxene, Amph=amphibole). May be derived from highly metasomatised basaltic pillow lava (plane polarized light, width of photo 4.2 mm).

a)

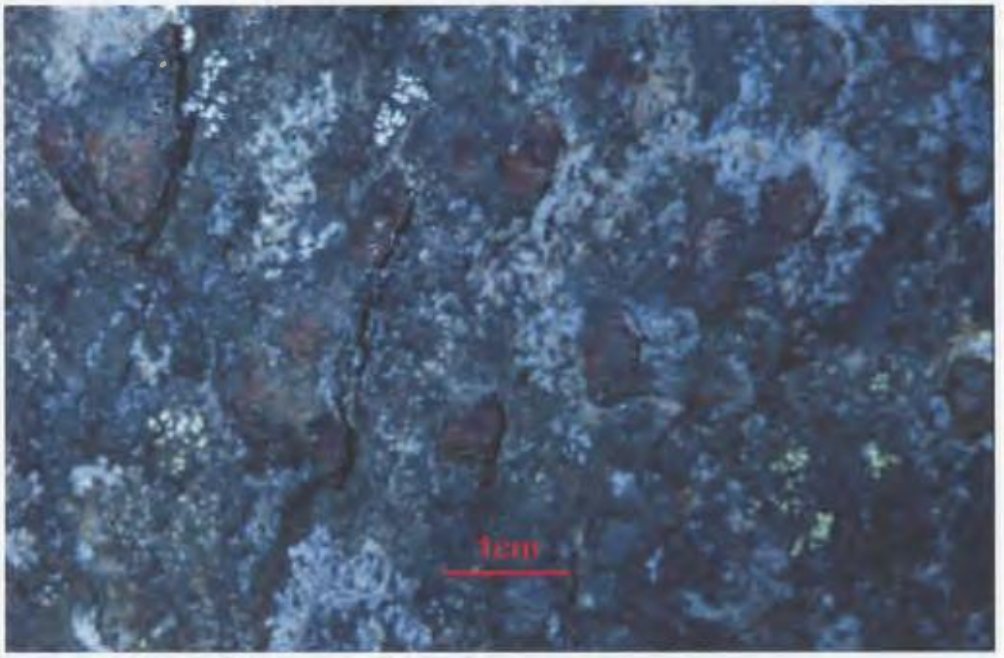

Figure 2.67. Locality MM01-105 within the magnetic marker.
a) Centimetre-scale, weathering-resistant, rounded structures may correspond to lenticular structures ('lapillistones') observed by Chadwick (1990).

b)

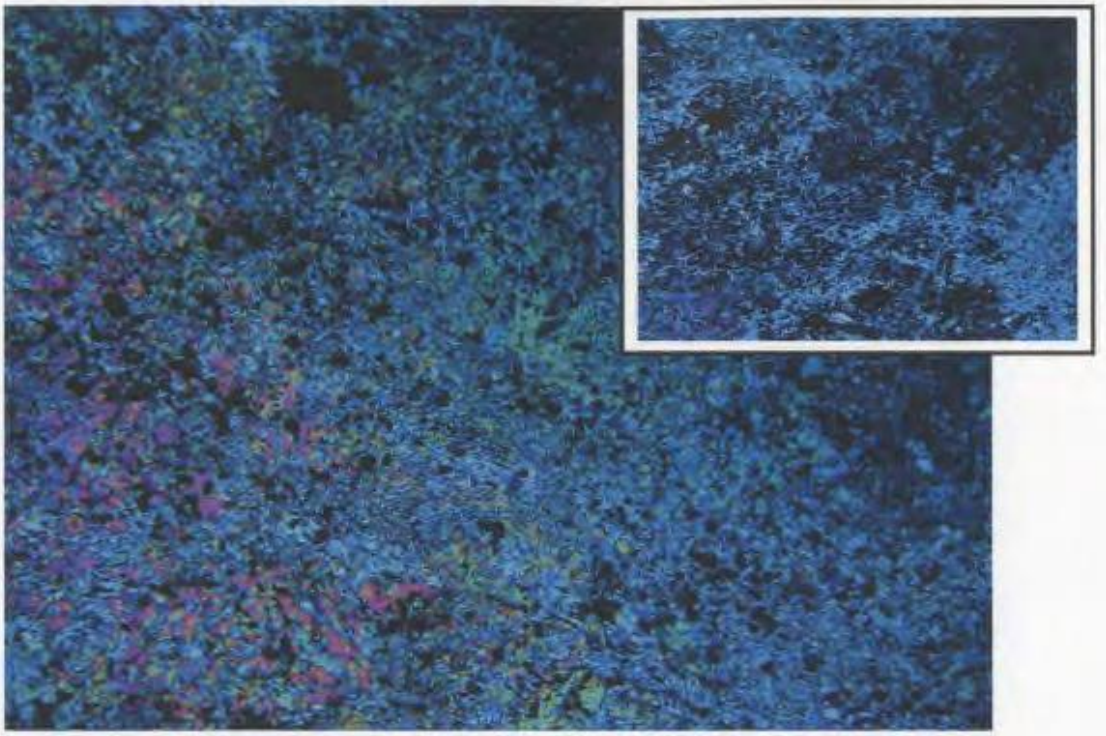

Figure 2.67.
b) Photomicrograph of part of a single, rounded structure from (a). The ovoid is a large olivine grain (width of photo=4.25 mm; Inset: thin section rotated counter-clockwise to demonstrate that olivine grain is optically continuous).

Figure 2.68. Deformed banded amphibolites in the southern part of the belt (Locality MM01-88).

a)

b)

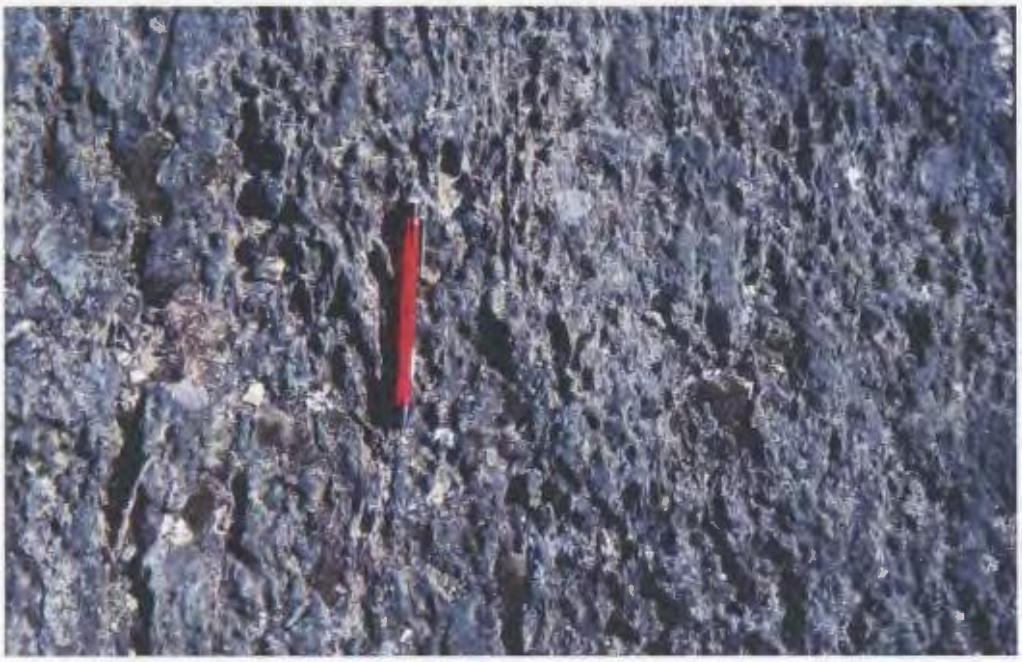

Figure 2.69. Locality MM01-55 located in the southern part of the belt.
a) Carbonate alteration marked by the pitted appearance of the amphibolites.
b) Detail of pitted nature of the rocks.

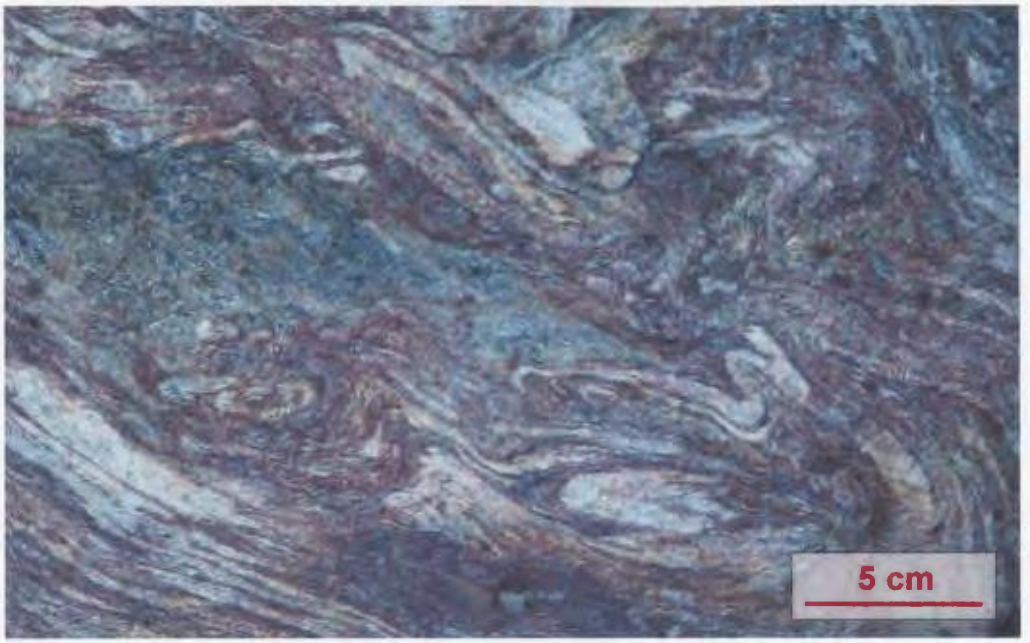

Figure 2.70. Complex folding within the thick layer of quartz-feldspar-biotite-garnet schist/gneiss of the southern part of the belt.

Figure 2.71. Locality MM01-76. Thin layers of amphibolite folded within the thick felsic unit of the southern part of the belt (top of photo to east).

Figure 2.72. Small (2-5 cm), siliceous lenses within a schistose part of the quartz-feldspar-biotite-garnet layer (Station MM01-91, top of photo to north).

a)

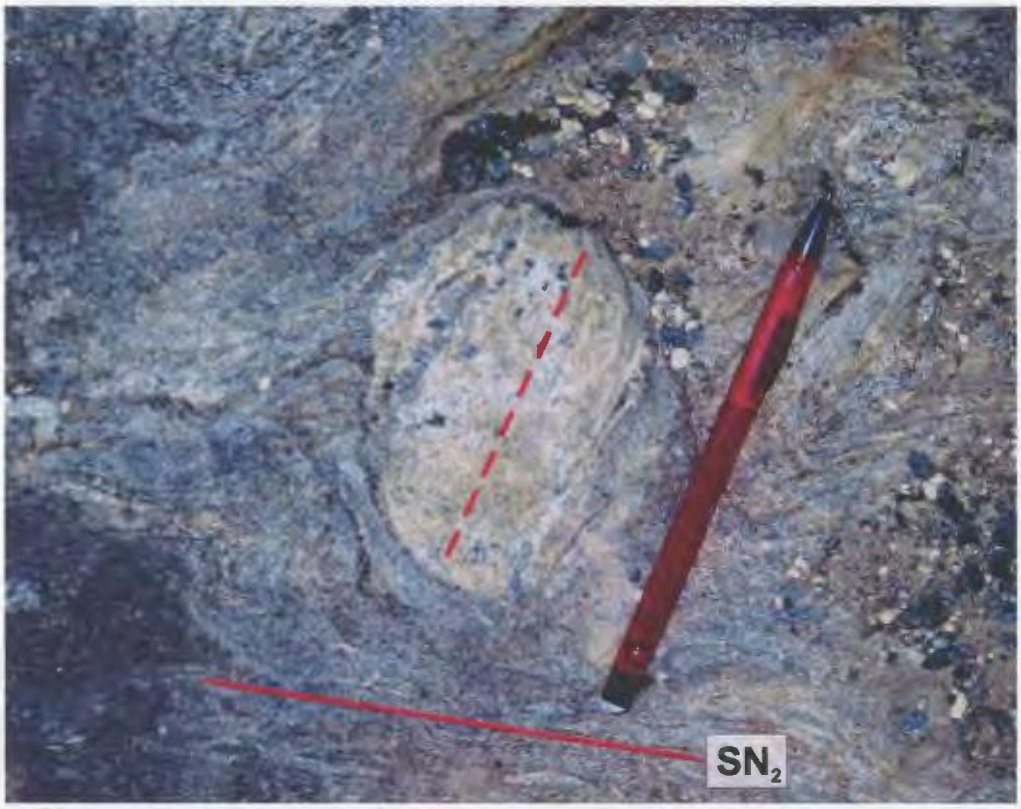

Figure 2.73. Locality MM01-91 within the quartz-feldspar-biotite-garnet layer in the southern part of the belt.
a) Large, felsic fragment with an internal foliation (parallel to dashed line) which is not aligned with the main foliation (SN_2) of the surrounding schist.

b)

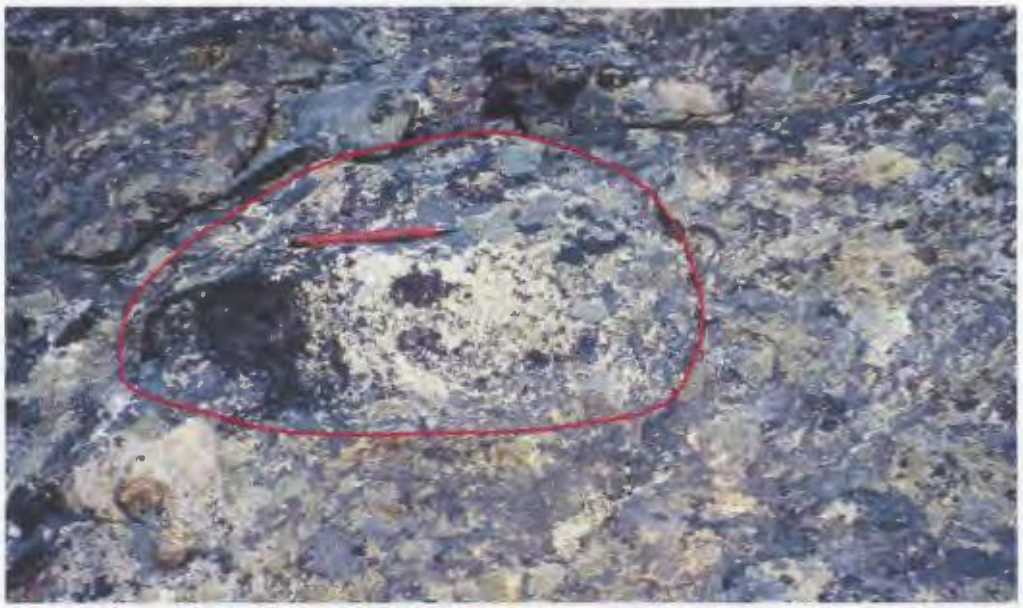

c)

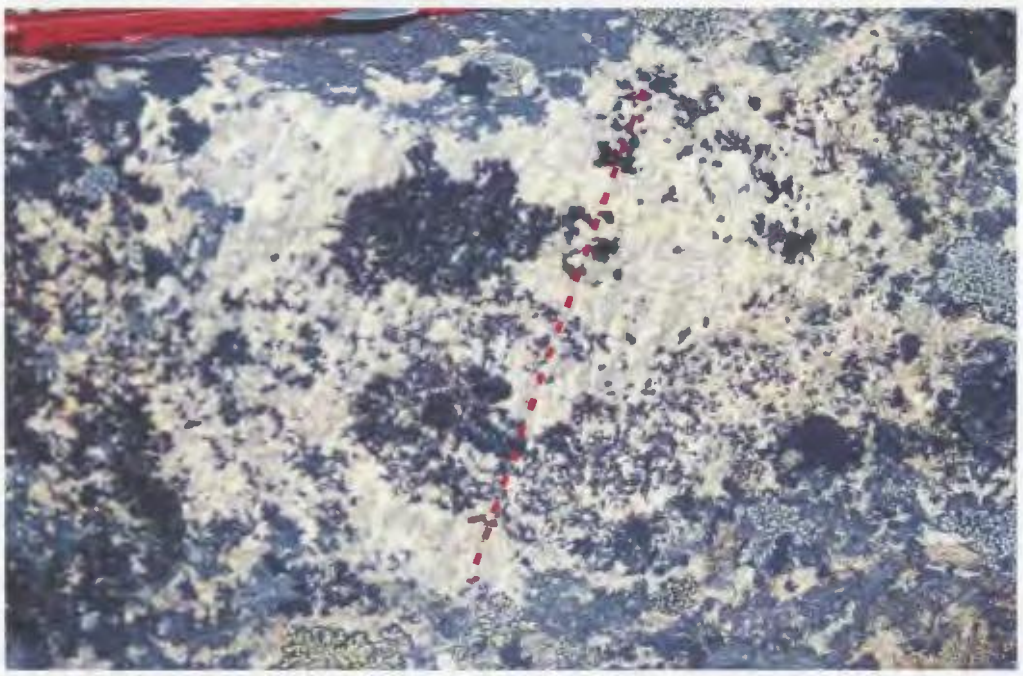

Figure 2.73.
b) Large, felsic fragment (outlined in red) within the quartz-feldspar-biotite-garnet schist layer.
c) Detail of (a). Foliation within the fragment is parallel to dashed line.

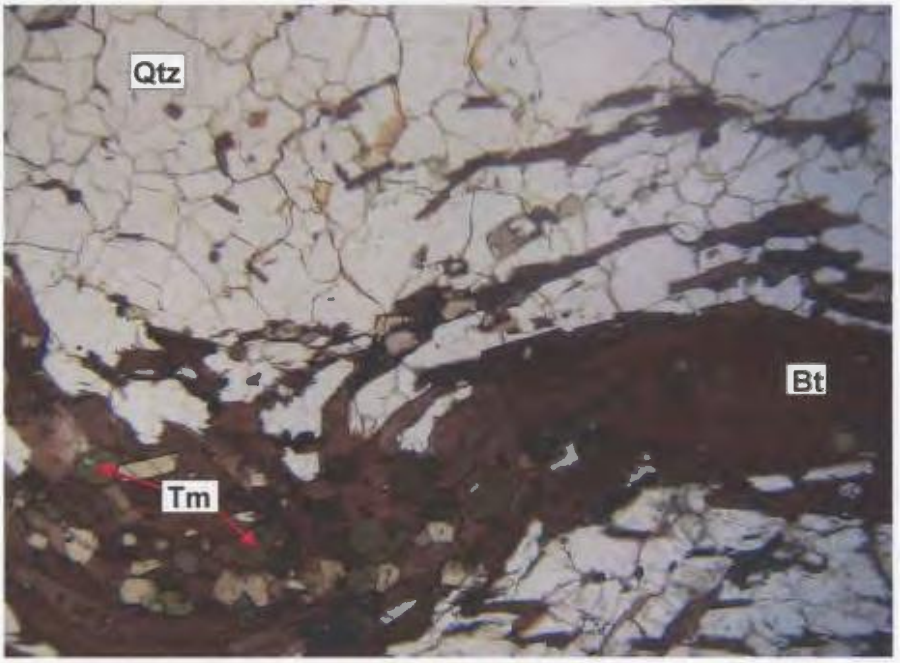

Figure 2.74. Photomicrograph of Sample MM01-81b from the thick quartz-feldspar-biotite-garnet layer in the southern part of the belt. Note the seriate - polygonal grain texture of the quartz (Qtz)–feldspar dominated matrix and the tourmaline (Tm) grains within biotite (Bt)-rich layer (width of photo 4 mm).

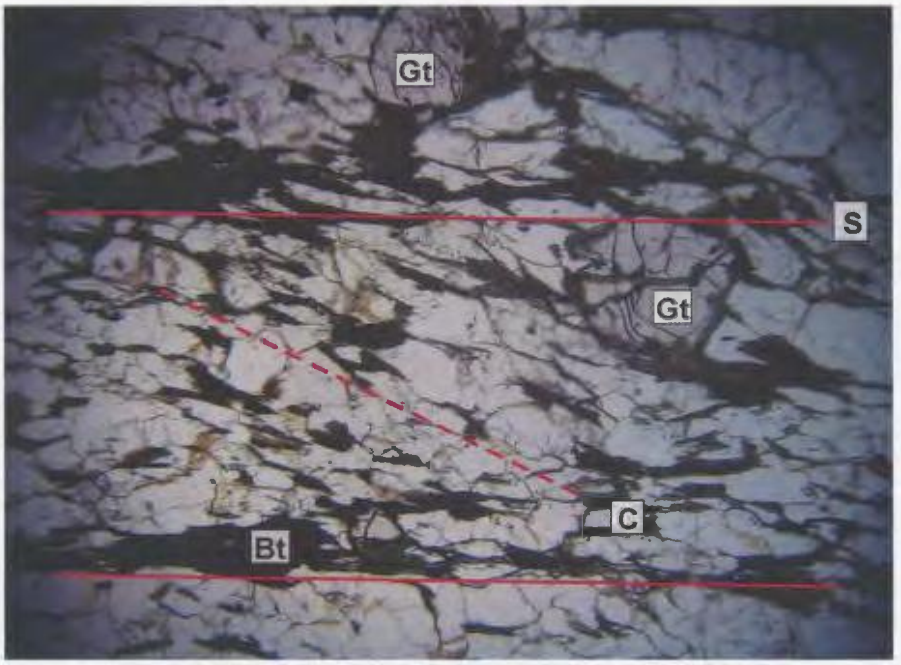

Figure 2.75. Photomicrograph of Sample MM01-87b from the thick quartz-feldspar-biotite (Bt)-garnet (Gt) layer in the southern part of the belt. An S-C fabric is defined by biotite (width of photo 5.75 mm).

a)

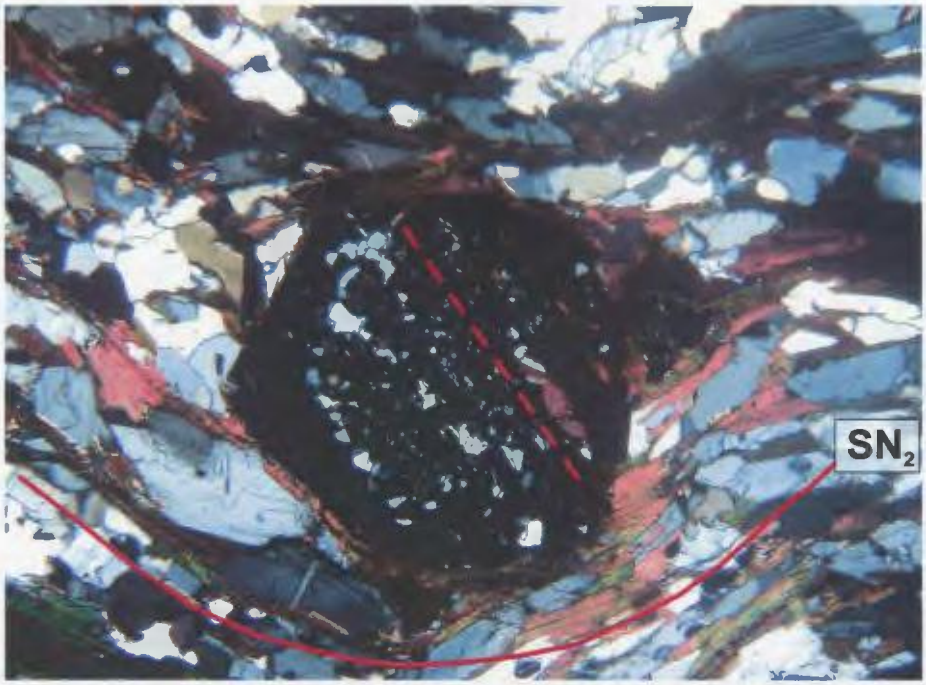

b)

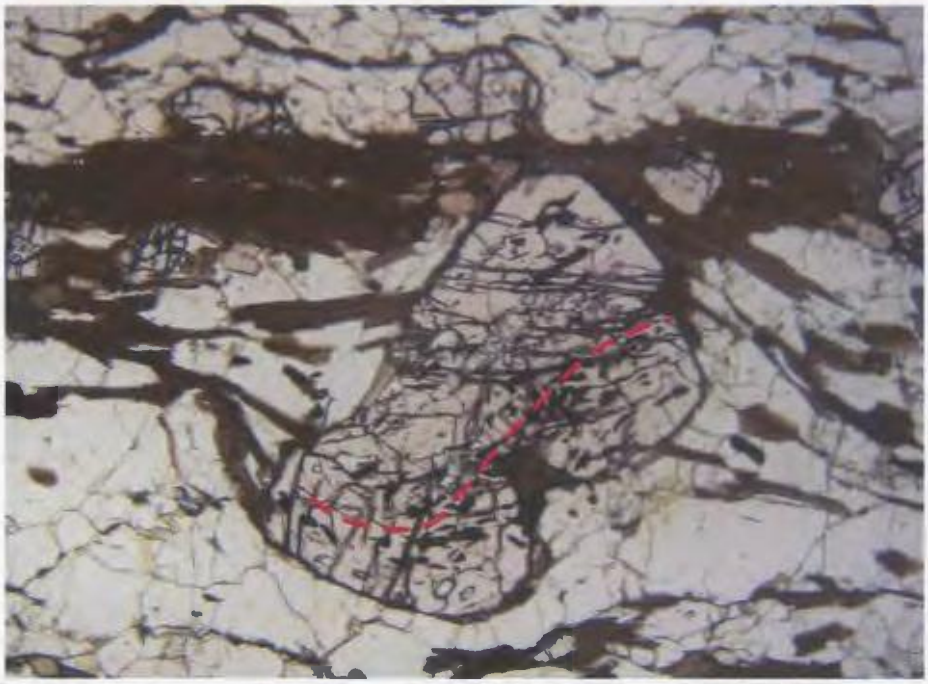

Figure 2.76. Photomicrographs of Sample MM01-81b from the thick quartz-feldspar-biotite-garnet layer in the southern part of the belt (width of photos 4 mm).
a) Intertectonic garnet which may have grown between DN_1 and DN_2. Note straight inclusion trail (dashed line) and later fabric (SN_2) which wraps around the garnet.
b) Garnet which grew syntectonically indicated by the sigmoidal inclusion trail (dashed line) within the garnet.

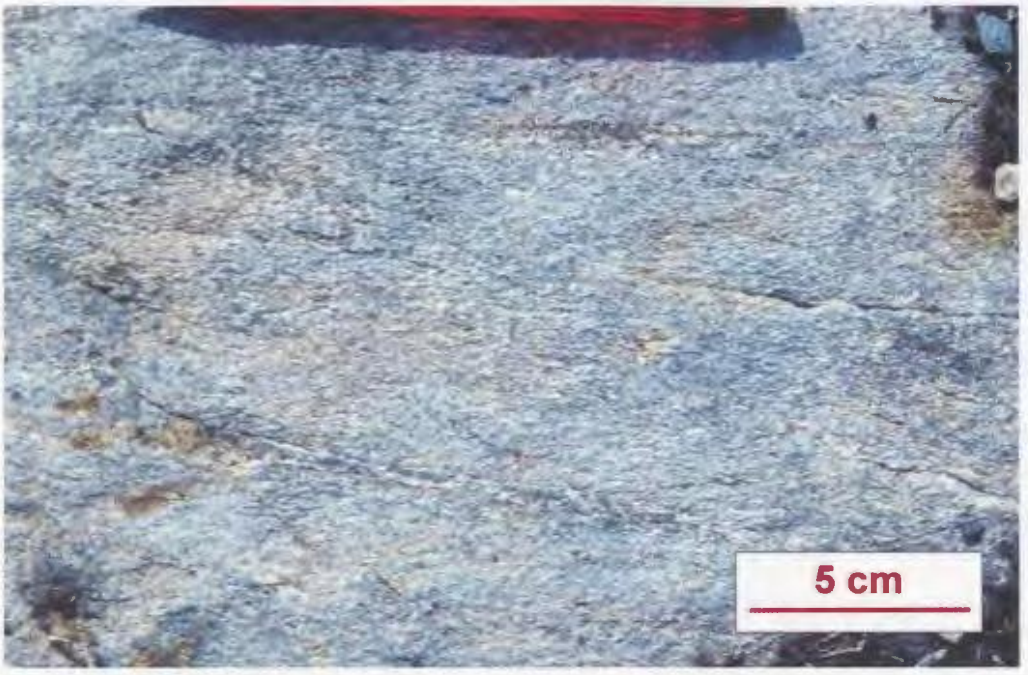

Figure 2.77. Locality MM01-114 from the southern part of the belt. Light grey, granitiod which compositionally is classified as a granodiorite.

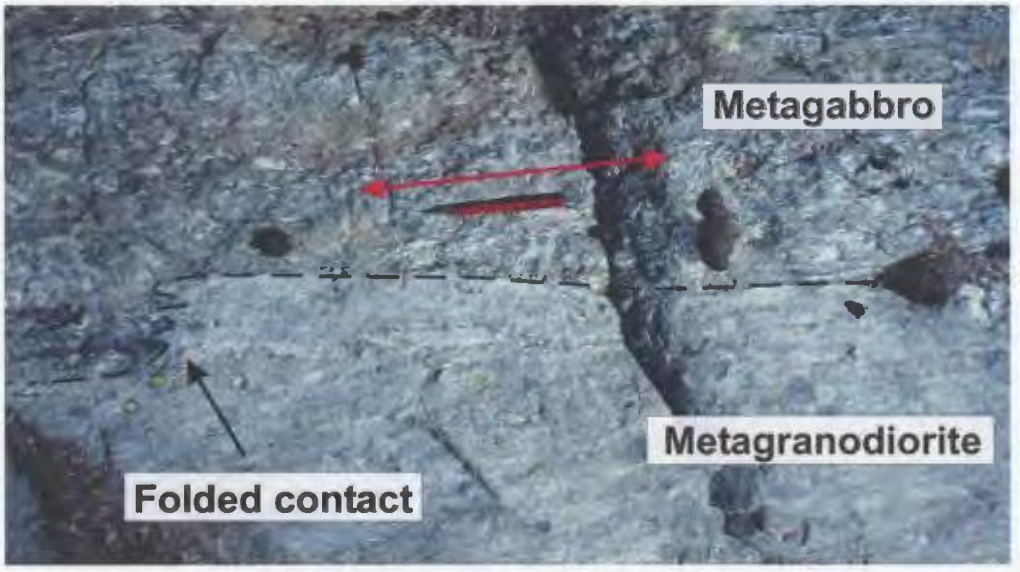

Figure 2.78. Locality MM01-60 from the southern part of the belt. The contact (dashed line) between the light grey metagranodiorite and dark grey metagabbro is folded, however a cross-cutting relationship is still preserved. The metagabbro was likely deformed by an earlier event producing a foliation (red arrow) and then intruded by the granodioritic unit. The two units were then deformed resulting in a folded contact.

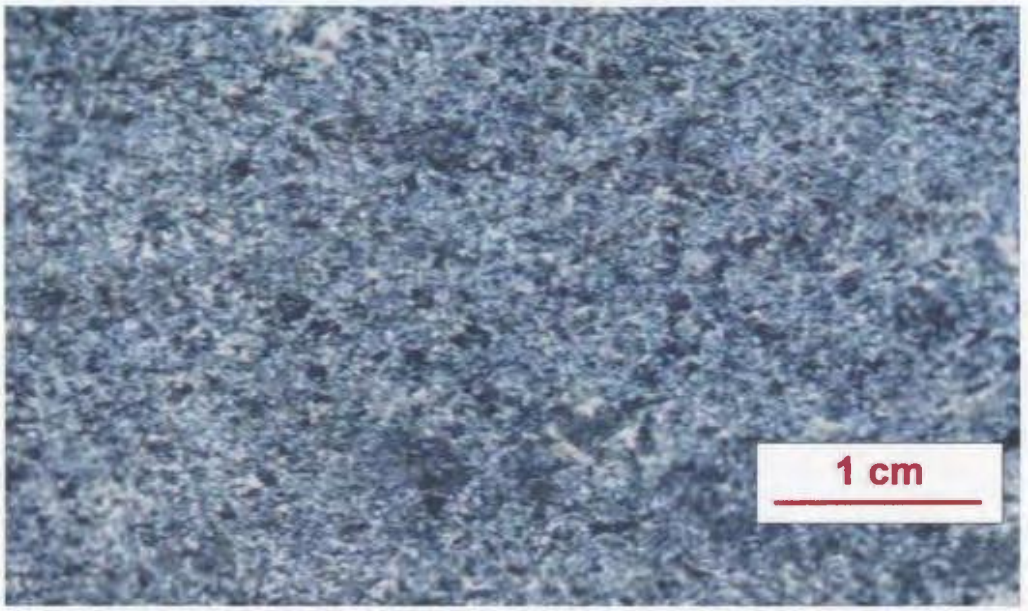

Figure 2.79. Locality MM01-30 from the southern part of the belt. Dark grey gabbroic rock composed of recrystallized amphibole, plagioclase, quartz, ± biotite and garnet.

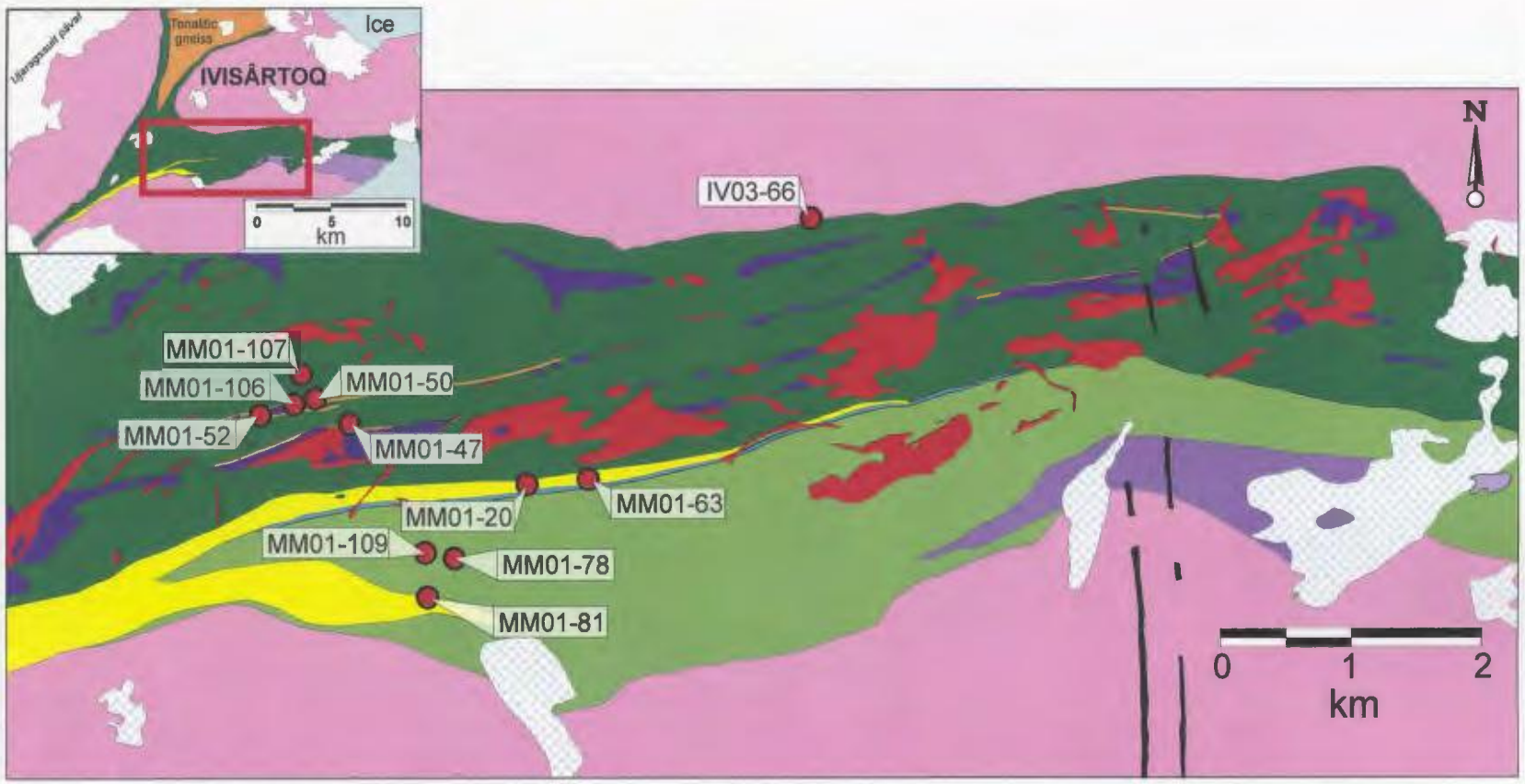

Figure 2.80. Simplified map of the Ivisârtoq greenstone belt showing locations of samples collected for geochronology. Colours of units as in Figure 2.3.

Figure 2.81. Photographs of representative zircon grains illustrating the two main types of morphology (stubby and elongate) from samples MM01-47 and MM01-50 (plane light).

a) **MM01-47**

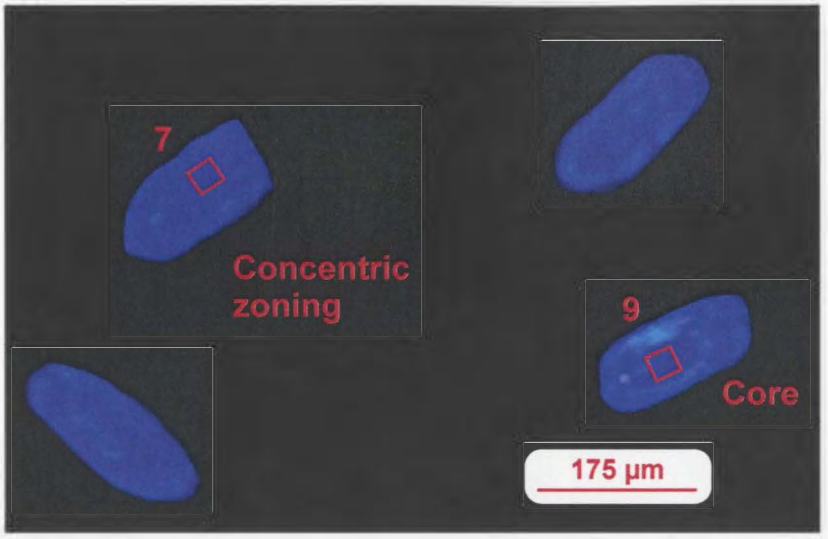

b) **MM01-50**

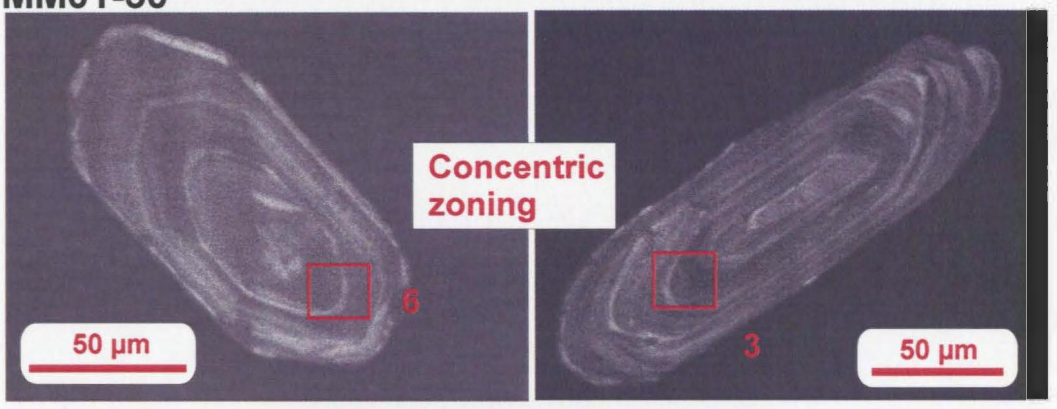

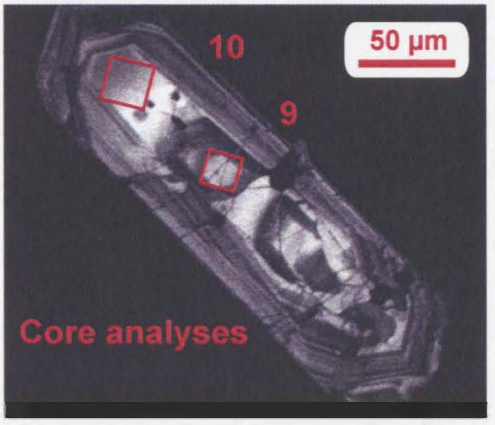

Figure 2.82. CL images of representative zircon grains from sample MM01-47 and MM01-50. Square outlines indicate locality of raster analyses.
a) sample MM01-47. Numbers represent analysis # from Table x. Images taken using colour microscope system at Memorial University of Newfoundland (MUN).
b) sample MM01-50. Numbers represent analysis # from Table 2.2. (Images taken using electron microprobe system at Dalhousie University, Nova Scotia).

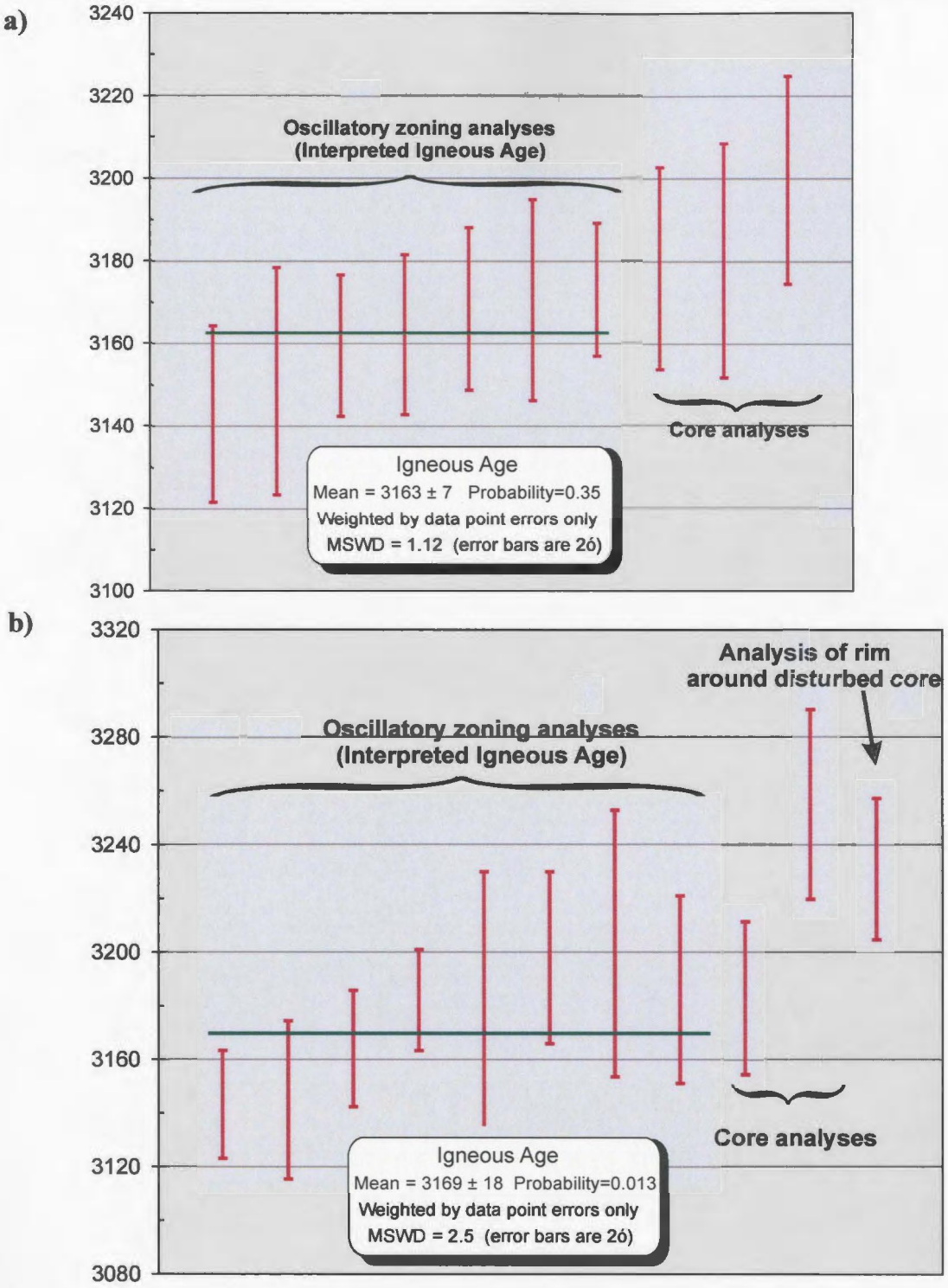

Figure 2.83. Weighted mean plots for analyses from
a) sample MM01-47 and
b) sample MM01-50.
Green, horizontal line indicates analyses used to calculate weighted mean.

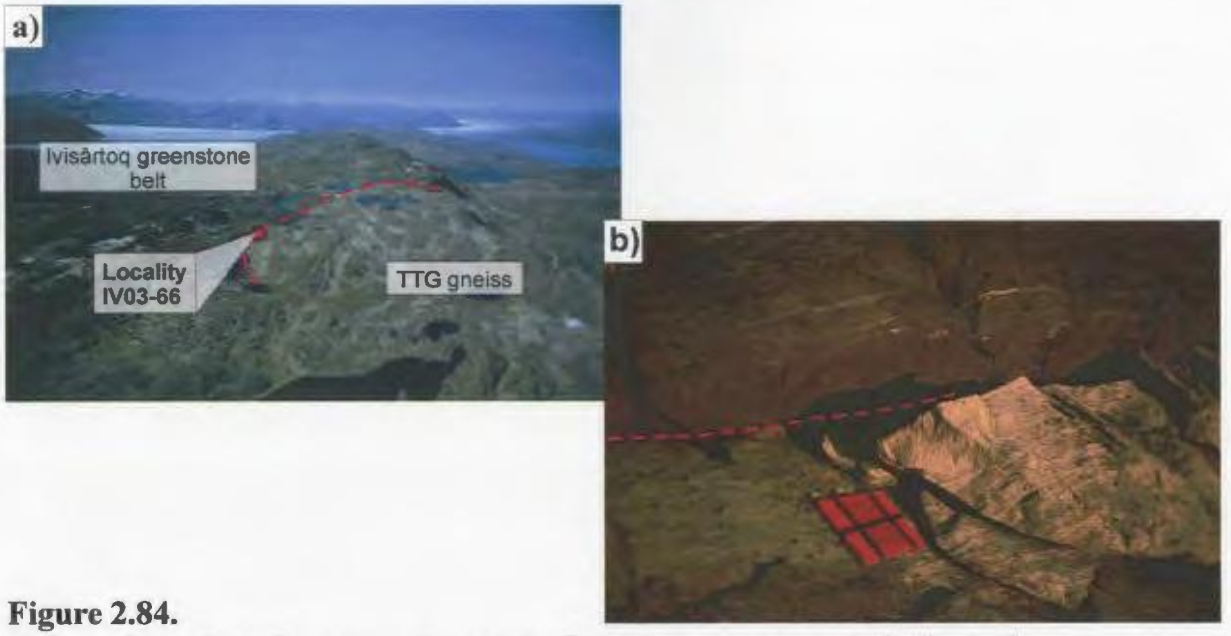

Figure 2.84.
a) Overview of northern boundary of the Ivisârtoq greenstone belt. Dashed line indicates boundary between TTG gneisses to the north and the greenstones. Photo facing west.
b) Outcrop from which tonalitic gneiss sample IV03-66 and pegmatite (removed from sample) was taken. The tonalite intrudes the northern margin of the Ivisârtoq greenstone belt. Photo facing south.

Figure 2.85. Photographs of representative zircon grains illustrating the two main types of morphology (stubby and elongate) from samples IV03-66 (plane light).

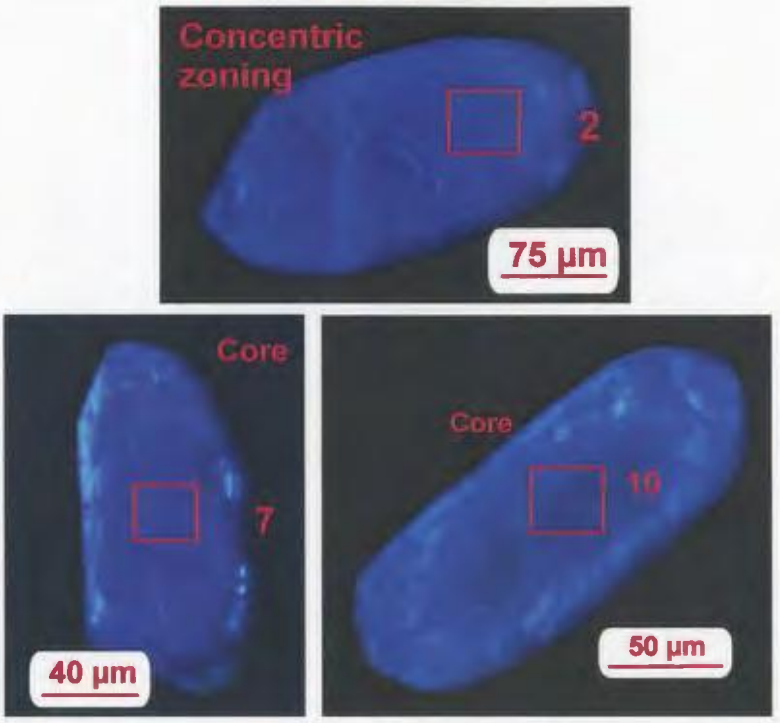

Figure 2.86. CL images of representative zircon grains from sample IV03-66. Square outlines indicate locality of raster analyses. Numbers represent analysis # from Table 2.2 and A2. (Images taken using colour microscope system at MUN).

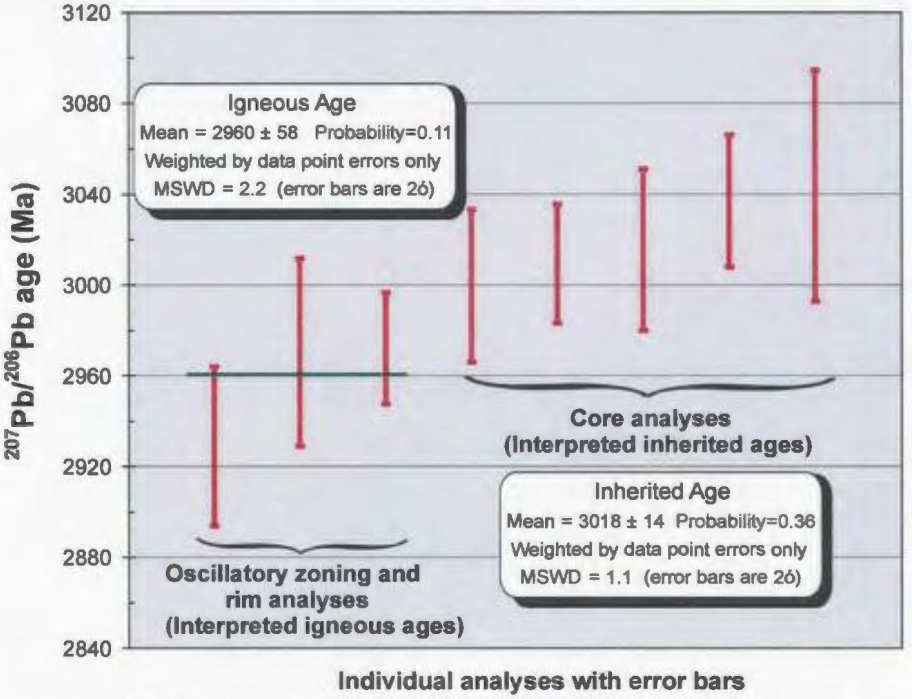

Figure 2.87. Weighted mean plot for analyses sample IV03-66. Green, horizontal line indicates analyses used to calculate weighted mean. A single core analysis (not shown) gave a $^{207}Pb/^{206}Pb$ age of 3760±29 Ma.

Figure 2.88. Locality MM01-106: an equigranular gabbroic dyke cutting across a brown-weathering ultramafic layer. Photos facing west.

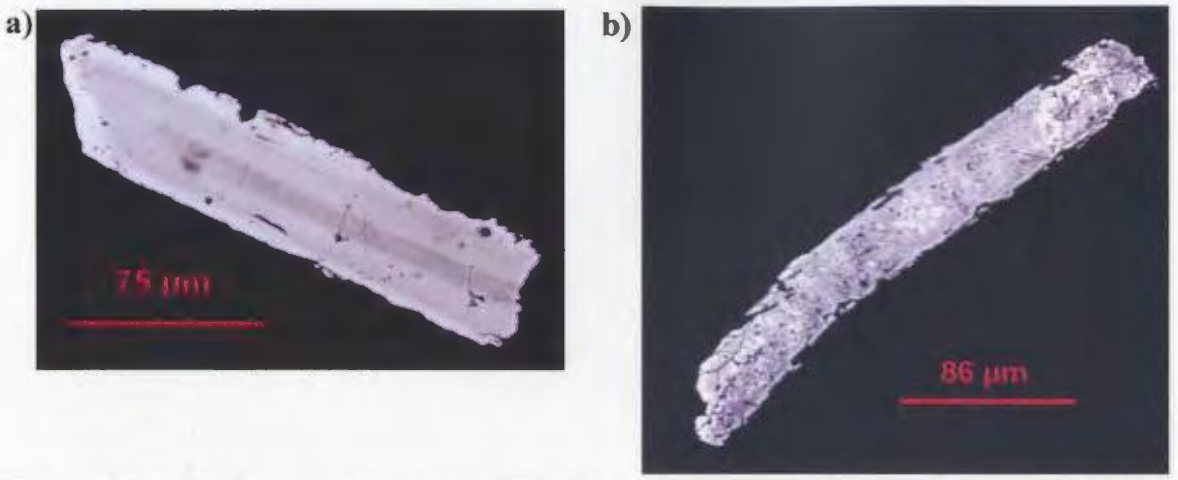

Figure 2.89. Backscattered electron (BSE) images of representative zircon grains from sample MM01-20.
a) grain with internal magmatic zoning
b) grain without zoning, but contains many uraninite inclusions.

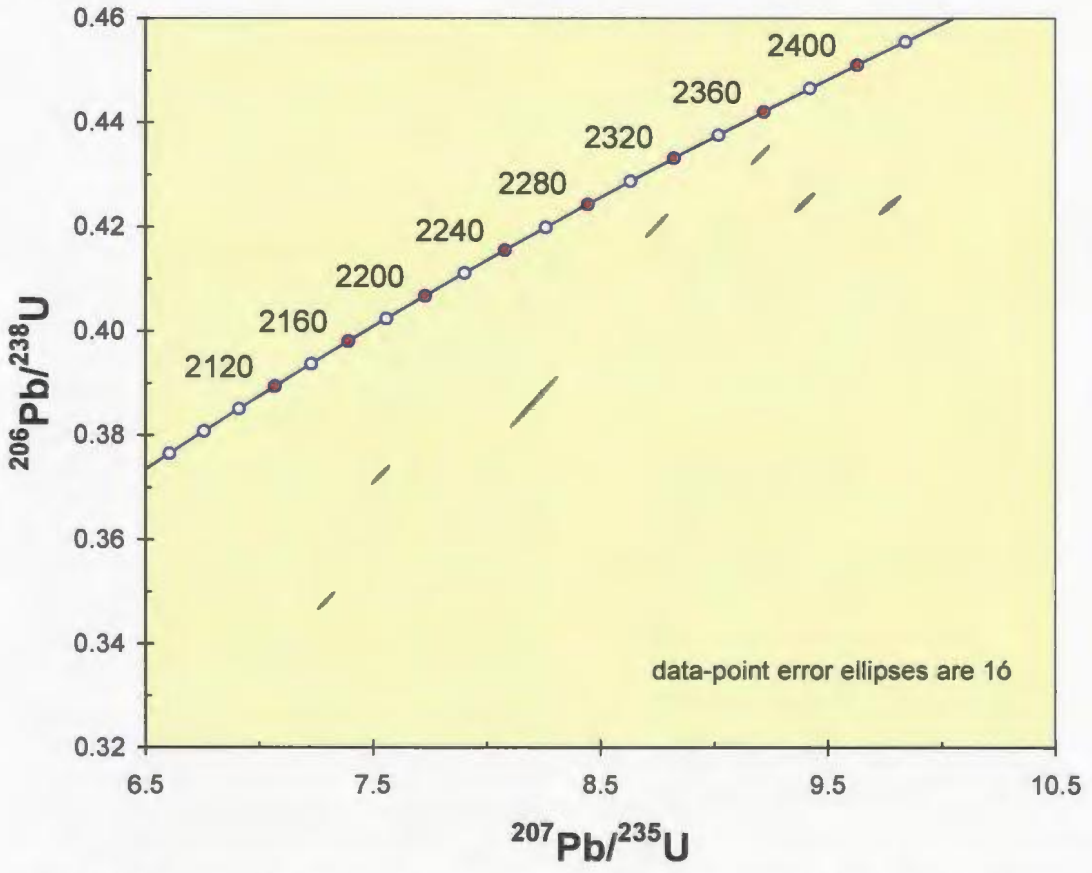

Figure 2.90. Concordia diagram for granitic pegmatite sample MM01-20 analysed by ID-TIMS. The discordant ages were likely the result of relatively recent Pb loss from metamict zones or along cracks.

Figure 2.91. Locality MM01-52: coarse grained pegmatite sheet observed within a boudin neck of a disrupted ultramafic layer. Photo facing north.

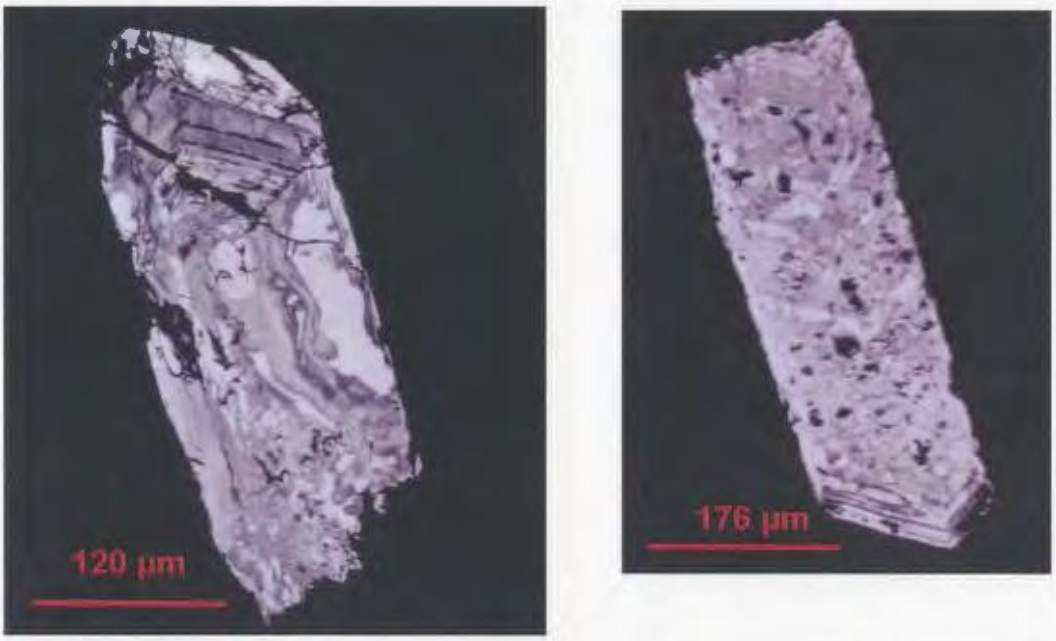

Figure 2.92. Backscattered electron (BSE) images of representative zircon grains from sample MM01-52. The quality of the zircons, including disturbed grains (a) and grains with many uraninite inclusions (b), were considered too poor for dating.

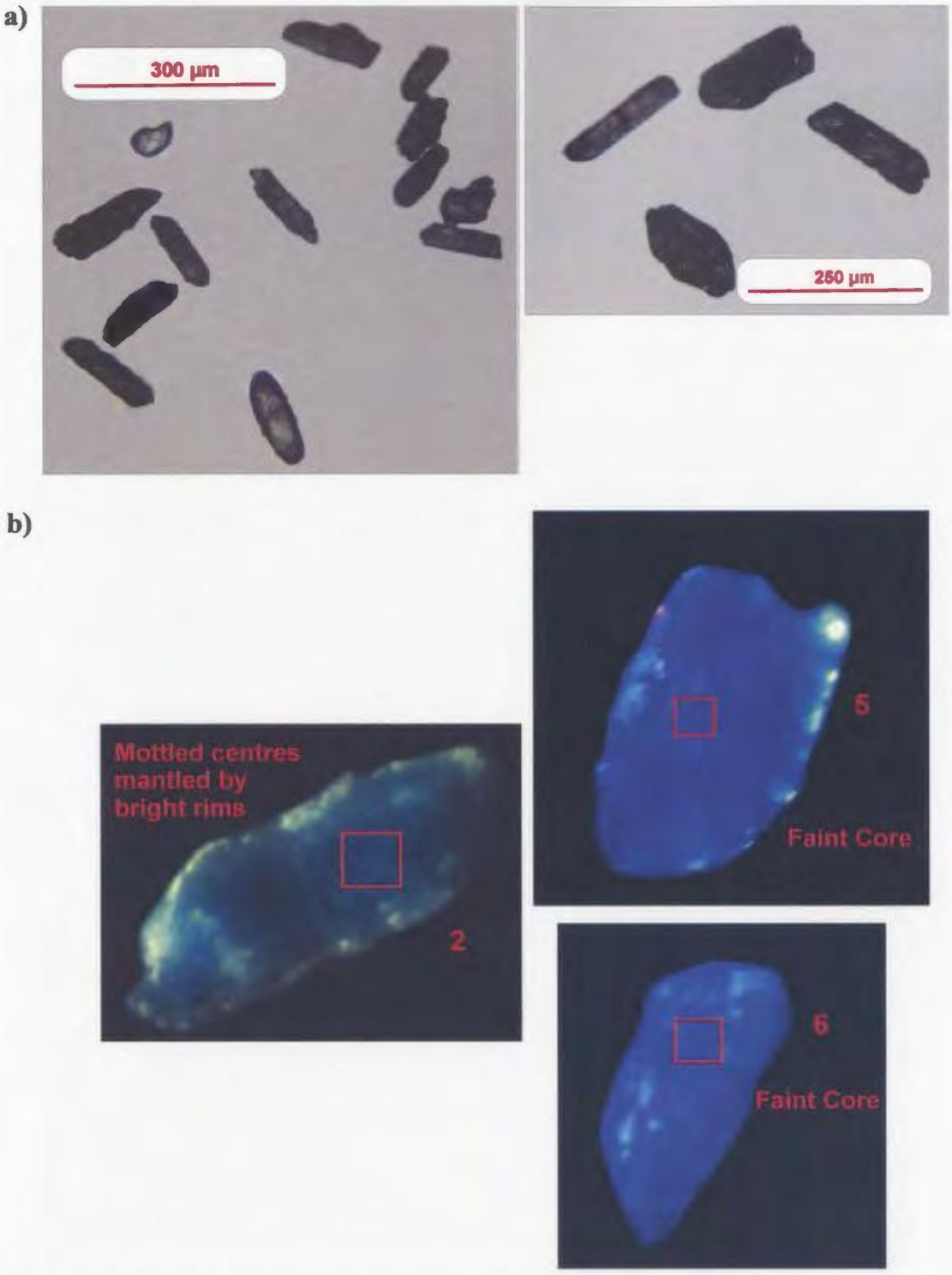

Figure 2.93. Representative zircon grains from samples MM01-109
a) Photographs illustrating different morphologies (plane light);
b) CL images, each square is 20 X 20 µm. Square outlines indicate locality of raster analyses. Numbers represent analysis # from Table 2.2. (Images taken using colour microscope system at MUN).

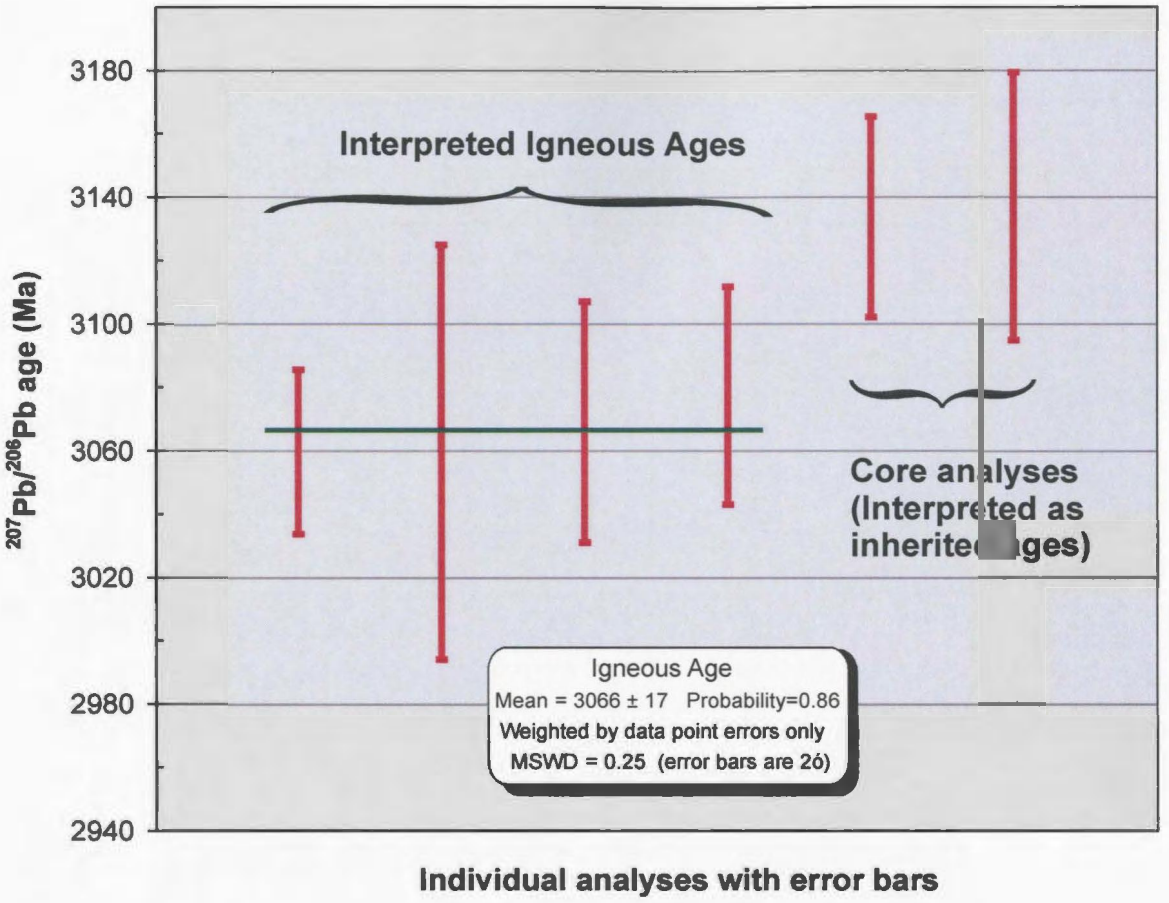

Figure 2.94. Weighted mean plot for analyses from sample MM01-109. Green, horizontal line indicates analyses used to calculate weighted mean.

Figure 2.95. Locality MM01-78: southern, homogeneous, light grey (granodioritic) unit. Photo facing east.

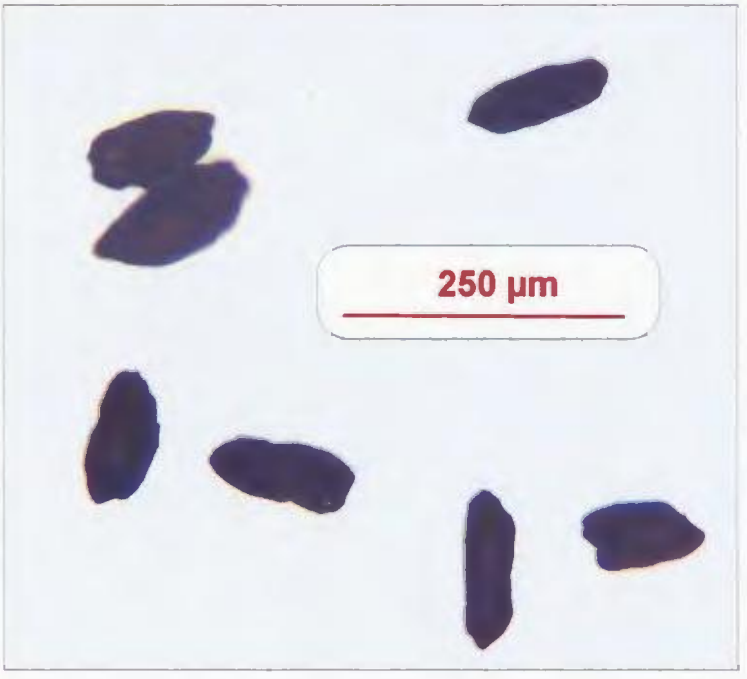

Figure 2.96. Photograph of representative zircon grains illustrating different grain morphologies (stubby and elongate) from samples MM01-78 (plane light).

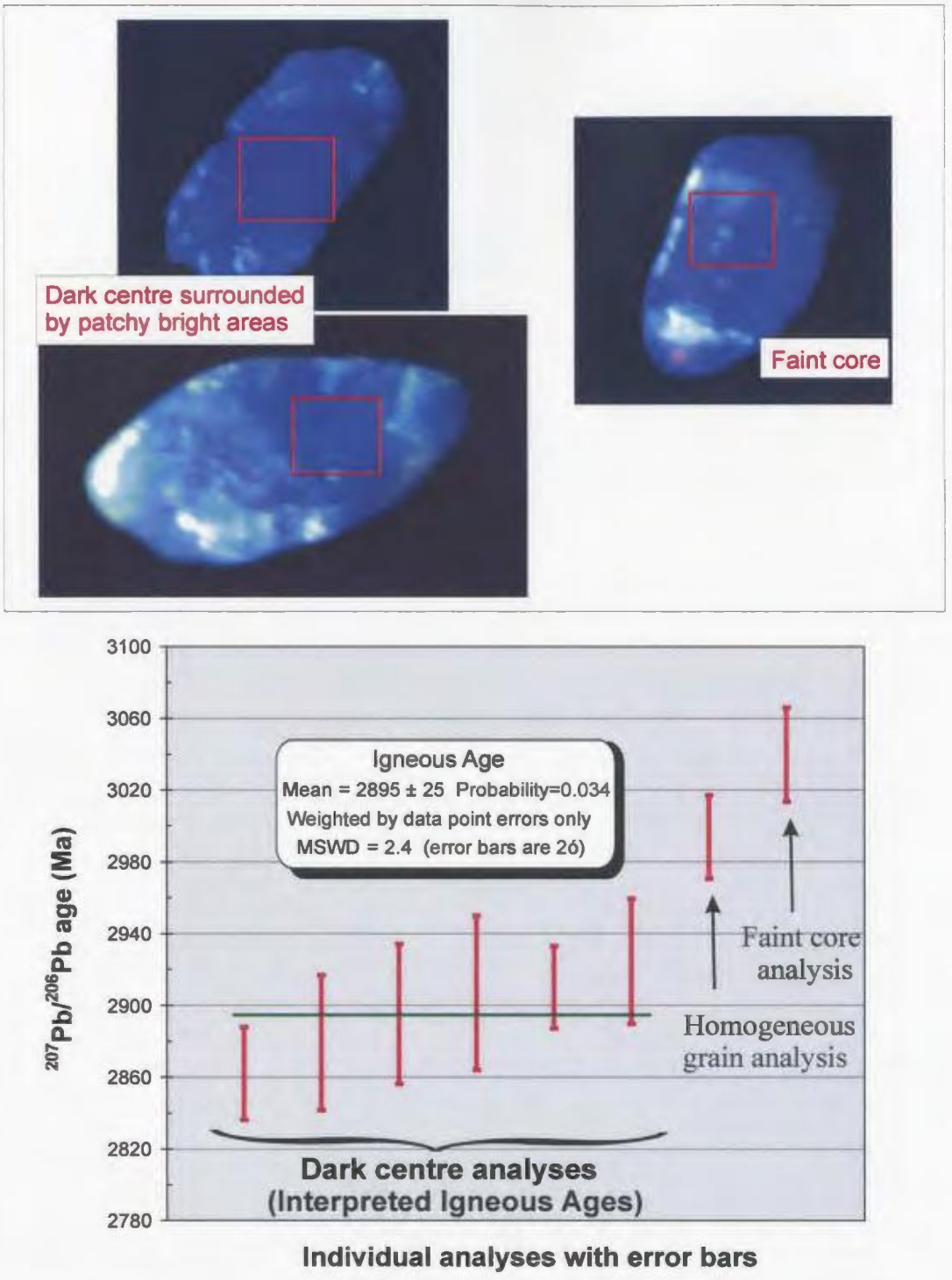

Figure 2.97. Data from sample MM01-78
a) CL images of representative zircon grains. Square outlines indicate locality of raster; analyses; each square is 20 X 20 μm.
b) Weighted mean plot. Green, horizontal line indicates analyses used to calculate weighted mean.

Figure 2.98. Locality MM01-63: sheared quartzofeldspathic layer within the Marker High Strain Zone. Photo facing west.

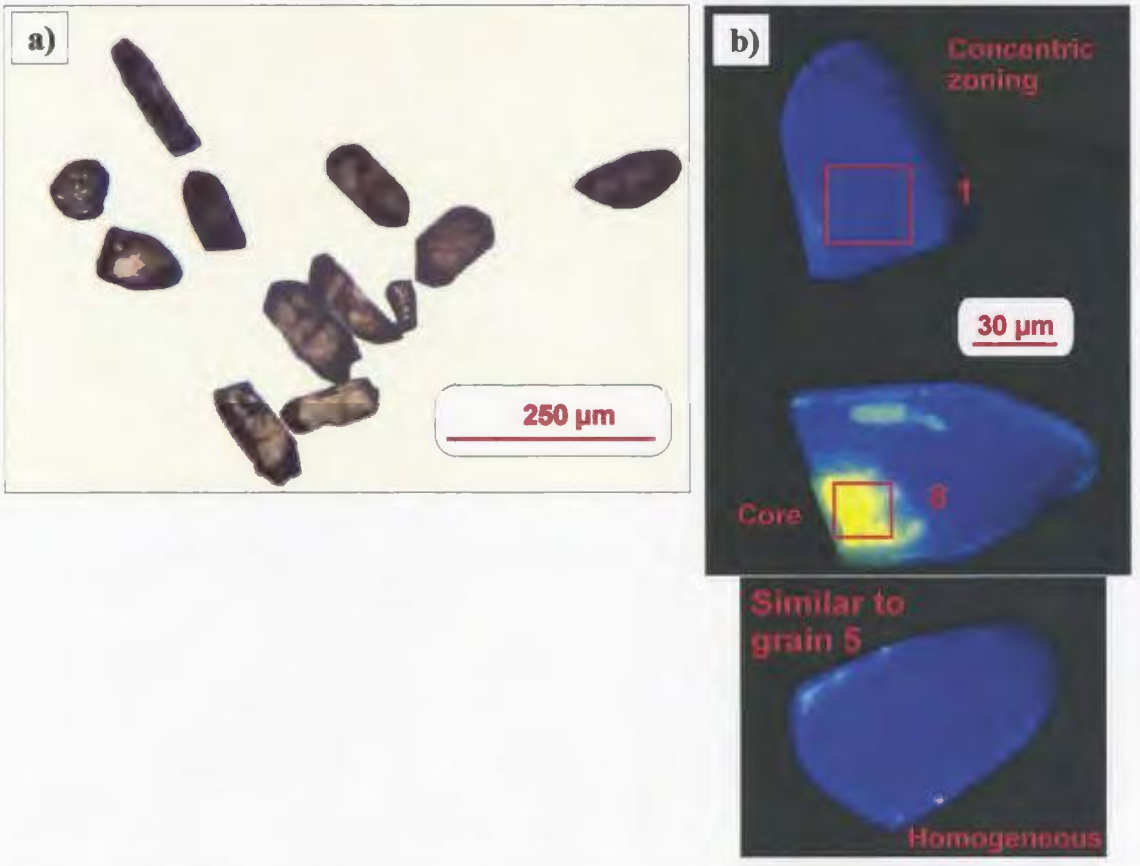

Figure 2.99. Representative zircon grains from sample MM01-63
a) Photograph illustrating different morphologies (plane light);
b) CL images taken using colour microscope system at MUN.

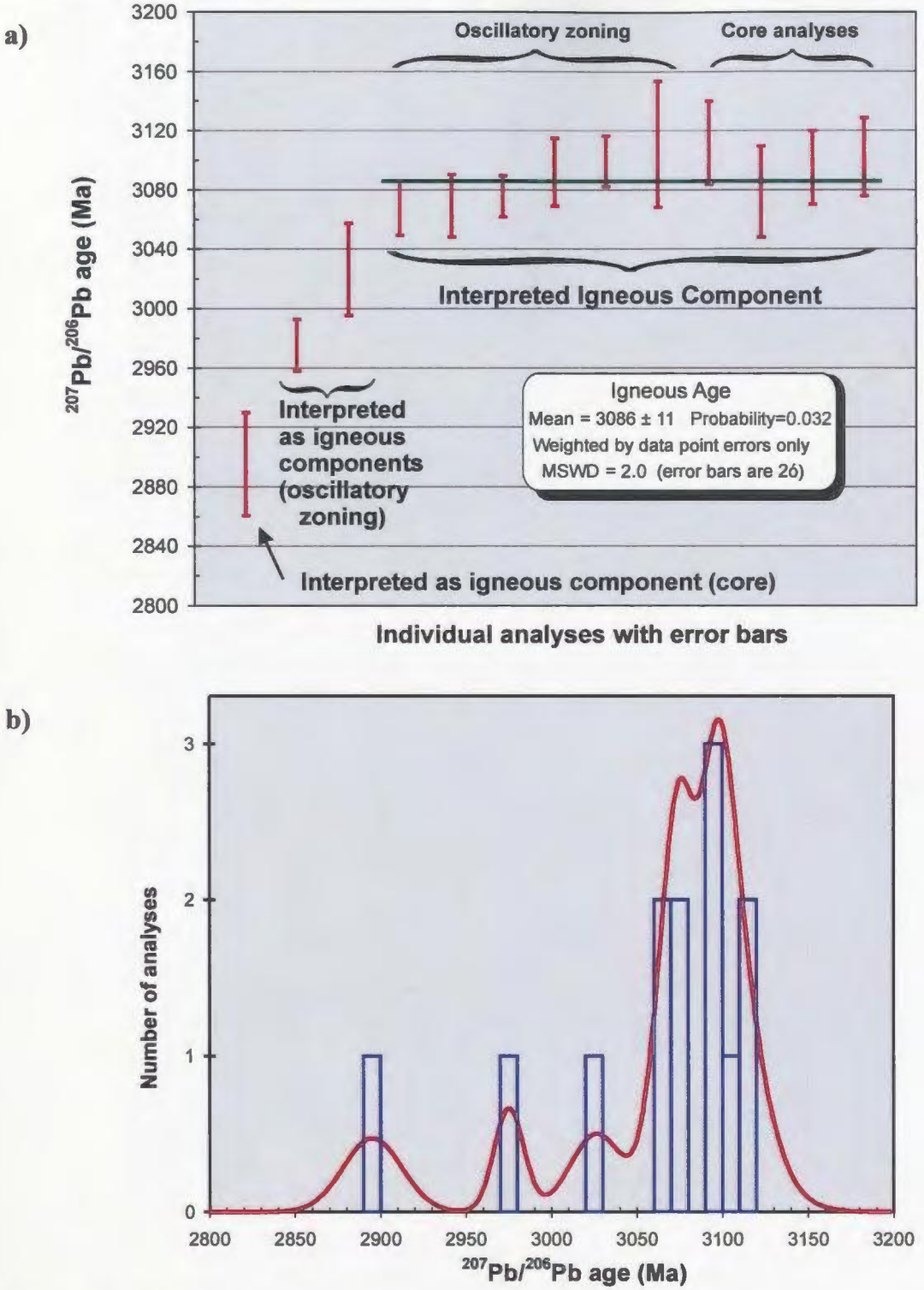

Figure 2.100. Zircon analyses from sample MM01-63
a) weighted mean plot. Green, horizontal line indicates analyses used to calculate weighted mean.
b) combined histogram and cumulative probability plot.

a)

b)

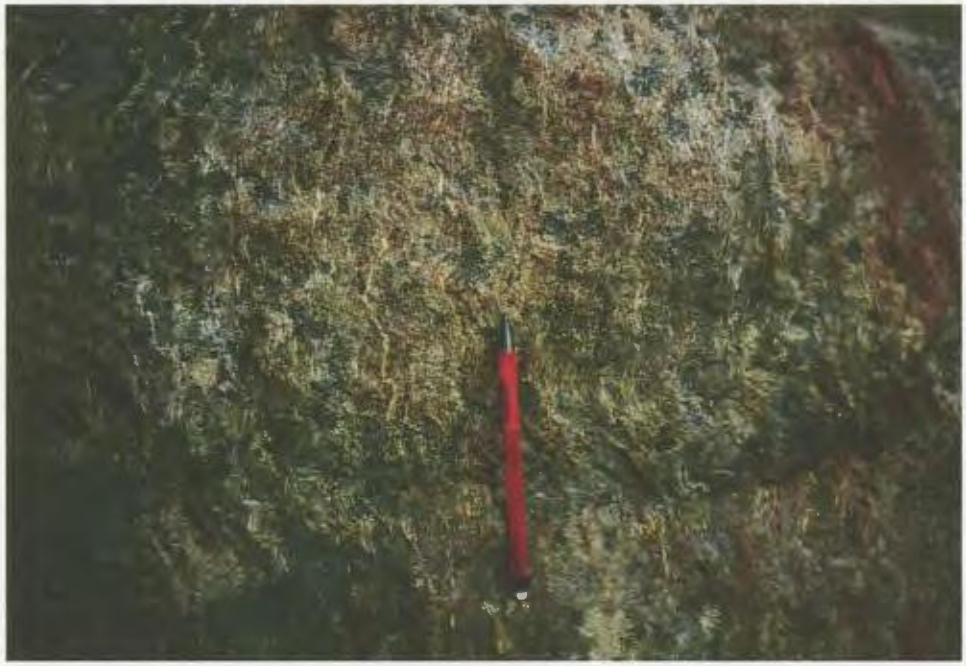

Figure 2.101. Locality MM01-81: southern, quartz-feldspar-biotite- schist.
a) Sample location. Photo facing east.
b) Detail of schist. Pencil parallel to main foliation.

a)

b)

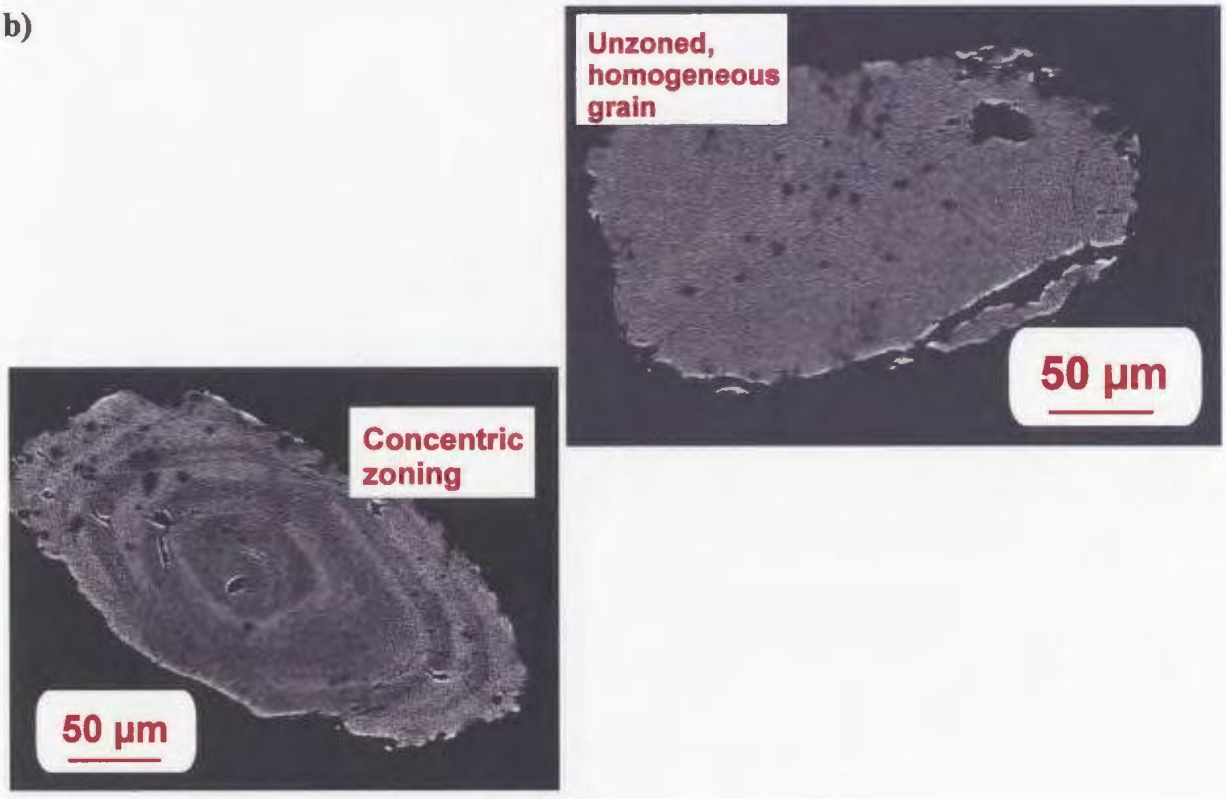

Figure 2.102. Representative zircon grains from samples MM01-81.
a) Photograph of different morphologies (plane light);
b) CL images taken using electron microprobe system at Dalhousie University, NS).

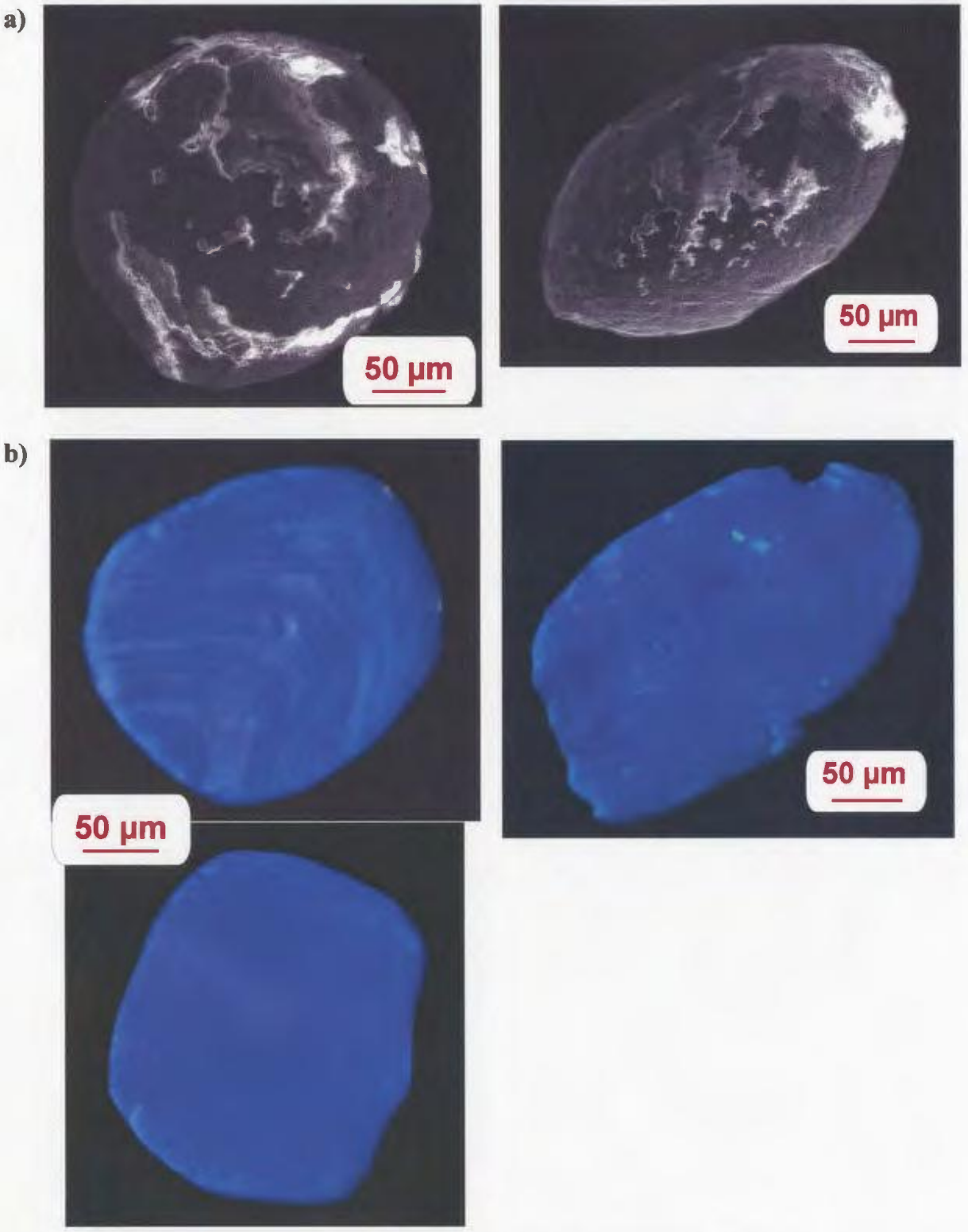

Figure 2.103. Representative round zircon grains from samples MM01-81
a) Secondary electron images
b) CL images taken using colour microscope system at MUN.

a)

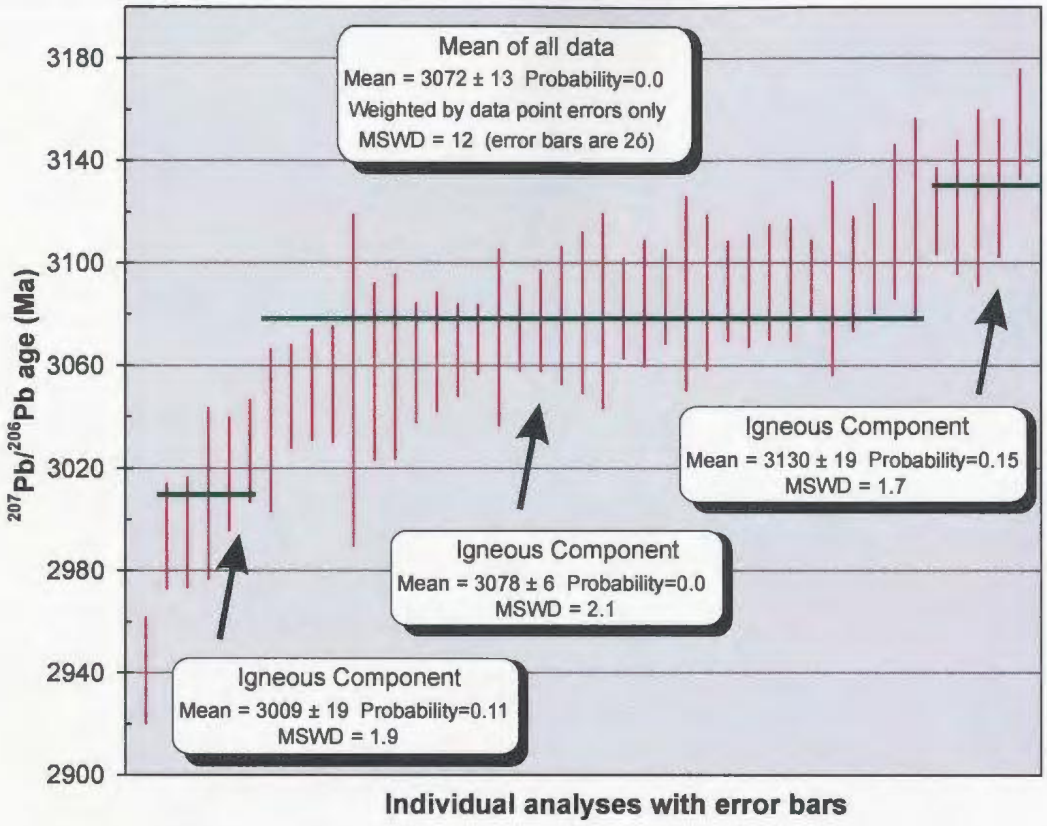

b)

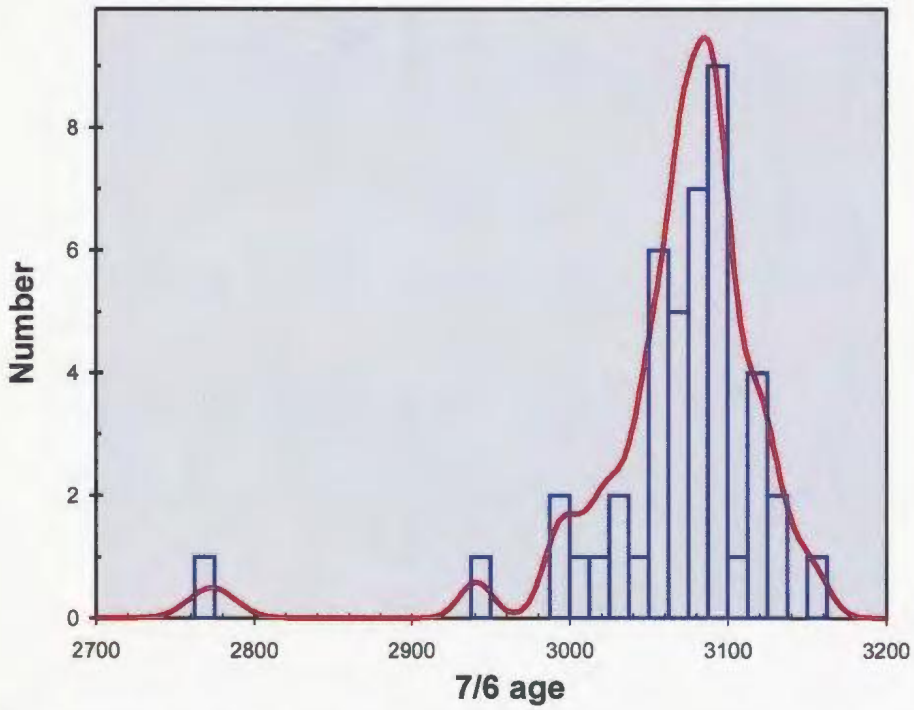

Figure 2.104. Zircon analyses from sample MM01-81
a) weighted mean plot. Green, horizontal line indicates analyses used to calculate weighted mean.
b) combined histogram and cumulative probability plot.

Table 2.2: U-Pb zircon LAM-ICP-MS analytical data

Sample MM01-47

Analysis #	pit size (µm)	Atomic ratios $^{207}Pb/^{235}U$	(±)	$^{206}Pb/^{238}U$	(±)	$^{207}Pb/^{206}Pb$	(±)	Ages (Ma) $^{207}Pb/^{235}U$	1 ó	$^{206}Pb/^{238}U$	1 ó	$^{207}Pb/^{206}Pb$	2 ó	Conc. %	% error	U (ppm)
Igneous concentrically zoned zircons																
1	20x20	21.818	1.321	0.6466	0.0317	0.2435	0.0033	3176	59	3215	124	3143	21	102.3	0.68	1025
2	30x30	21.158	0.645	0.6156	0.0129	0.2447	0.0042	3146	30	3092	51	3151	28	98.1	0.87	253
3	30x30	20.891	0.922	0.6062	0.0248	0.2461	0.0027	3134	43	3055	100	3160	17	96.7	0.54	302
4	30x30	21.652	0.570	0.6287	0.0181	0.2465	0.0030	3168	26	3144	72	3162	19	99.4	0.61	193
5	30x30	22.178	0.550	0.6444	0.0164	0.2474	0.0031	3192	24	3206	64	3169	20	101.2	0.62	246
6	30x30	22.337	0.789	0.6529	0.0203	0.2478	0.0038	3199	34	3240	79	3171	24	102.2	0.77	339
7	30x30	22.256	0.605	0.6510	0.0164	0.2482	0.0025	3195	26	3232	64	3173	16	101.9	0.51	371
Inherited zircons (cores)																
8	20x20	22.898	1.384	0.6700	0.0367	0.2490	0.0038	3223	59	3306	142	3178	24	104.0	0.77	266
9	20x20	22.848	1.484	0.6530	0.0440	0.2493	0.0045	3221	63	3240	172	3180	28	101.9	0.89	330
10	30x30	22.192	0.984	0.6277	0.0277	0.2524	0.0040	3192	43	3140	110	3200	25	98.1	0.78	235

Sample MM01-50

Analysis #	pit size (µm)	Atomic ratios $^{207}Pb/^{235}U$	(±)	$^{206}Pb/^{238}U$	(±)	$^{207}Pb/^{206}Pb$	(±)	Ages (Ma) $^{207}Pb/^{235}U$	1 ó	$^{206}Pb/^{238}U$	1 ó	$^{207}Pb/^{206}Pb$	2 ó	Conc. %	% error	U (ppm)
Igneous concentrically zoned zircons													zoning			
1	30x30	20.873	0.692	0.6270	0.0211	0.2435	0.0031	3133	32	3138	83	3143	20	99.8	0.64	439
2	30x30	20.844	0.957	0.6265	0.0244	0.2438	0.0045	3131	44	3136	97	3145	29	99.7	0.94	816
3	24x24	22.180	0.805	0.6634	0.0190	0.2467	0.0034	3192	35	3280	74	3164	22	103.7	0.69	280
4	30x30	21.668	0.704	0.6226	0.0274	0.2496	0.0030	3169	32	3120	109	3182	19	98.1	0.59	294
5	20x20	21.310	1.445	0.6219	0.0431	0.2496	0.0075	3153	66	3117	171	3182	47	98.0	1.49	205
6	24x24	23.095	1.109	0.6639	0.0351	0.2521	0.0051	3231	47	3282	136	3198	32	102.6	1.00	274
7	24x24	21.988	0.930	0.6594	0.0266	0.2529	0.0080	3183	41	3265	103	3203	50	101.9	1.55	65
8	30x30	21.162	1.747	0.6258	0.0422	0.2502	0.0055	3146	80	3133	167	3186	35	98.3	1.10	321
Inherited zircons (cores)																
9	20x20	22.158	0.700	0.6112	0.0293	0.2497	0.0045	3191	31	3075	117	3183	28	96.6	0.89	330
10	24x24	22.460	1.002	0.6328	0.0297	0.2614	0.0058	3204	43	3161	117	3255	35	97.1	1.08	54
Rim around disturbed core (analysis #15)																
11	24x24	21.921	1.065	0.6372	0.0259	0.2574	0.0043	3180	47	3178	102	3231	26	98.4	0.81	225

Table 2.2: U-Pb zircon LAM-ICP-MS analytical data (continued)

Sample MM01-66

		Atomic ratios						Ages (Ma)								
Analysis #	pit size (μm)	$^{207}Pb/^{235}U$	(±)	$^{206}Pb/^{238}U$	(±)	$^{207}Pb/^{206}Pb$	(±)	$^{207}Pb/^{235}U$	1 ó	$^{206}Pb/^{238}U$	1 ó	$^{207}Pb/^{206}Pb$	2 ó	Conc. %	% error	U (ppm)
Igneous concentrically zoned zircons																
1	30x30	17.349	0.562	0.5987	0.0175	0.2131	0.0046	2954	31	3025	71	2929	35	103.3	1.20	76
2	30x30	17.404	0.834	0.5914	0.0190	0.2186	0.0056	2957	46	2995	77	2970	41	100.8	1.39	67
3	30x30	16.989	0.602	0.5771	0.0137	0.2188	0.0033	2934	34	2937	56	2972	25	98.8	0.83	704
Inherited zircons (dark cores)																
4	30x30	18.264	1.493	0.5850	0.0626	0.2226	0.0047	3004	79	2969	255	3000	34	99.0	1.12	277
5	30x30	17.772	0.457	0.5877	0.0156	0.2240	0.0037	2977	25	2980	63	3009	26	99.0	0.87	102
6	30x30	18.906	0.544	0.6094	0.0192	0.2248	0.0050	3037	28	3068	77	3016	35	101.7	1.18	54
7	30x30	18.356	0.695	0.5878	0.0215	0.2279	0.0041	3009	36	2980	87	3037	29	98.1	0.96	133
8	30x30	17.858	1.246	0.5894	0.0234	0.2288	0.0073	2982	67	2987	95	3044	51	98.1	1.67	92
Inherited zircon (core: old age)																
9	30x30	38.074	2.678	0.7497	0.0480	0.3624	0.0068	3722	70	3606	177	3760	29	95.9	0.76	673

MM01-109

		Atomic ratios						Ages (Ma)								
Analysis #	pit size (μm)	$^{207}Pb/^{235}U$	(±)	$^{206}Pb/^{238}U$	(±)	$^{207}Pb/^{206}Pb$	(±)	$^{207}Pb/^{235}U$	1 ó	$^{206}Pb/^{238}U$	1 ó	$^{207}Pb/^{206}Pb$	2 ó	Conc. %	% error	U (ppm)
Igneous zircons																
1	20x20	18.409	0.636	0.5764	0.0187	0.2311	0.0037	3011	33	2934	77	3060	26	95.9	0.85	267
2	20x20	18.012	0.805	0.5661	0.0310	0.2311	0.0094	2990	43	2892	128	3060	65	94.5	2.14	205
3	20x20	18.817	1.208	0.5801	0.0336	0.2325	0.0055	3032	62	2949	137	3069	38	96.1	1.24	237
4	20x20	19.709	1.026	0.6099	0.0343	0.2337	0.0050	3077	50	3070	137	3077	34	99.7	1.11	180
Inherited zircons (cores)																
5	20x20	20.208	0.890	0.5939	0.0316	0.2421	0.0048	3101	43	3005	128	3134	32	95.9	1.01	307
6	20x20	20.019	1.531	0.5811	0.0526	0.2426	0.0064	3092	74	2953	214	3137	42	94.1	1.34	222

Table 2.2: U-Pb zircon LAM-ICP-MS analytical data (continued)

MM01-78

Analysis #	pit size (µm)	Atomic ratios $^{207}Pb/^{235}U$	(±)	$^{206}Pb/^{238}U$	(±)	$^{207}Pb/^{206}Pb$	(±)	Ages (Ma) $^{207}Pb/^{235}U$	1 ó	$^{206}Pb/^{238}U$	1 ó	$^{207}Pb/^{206}Pb$	2 ó	Conc. %	% error	U (ppm)
Igneous zircons (dark centres)																
1	20x20	14.999	0.570	0.5365	0.0197	0.2045	0.0032	2815	36	2769	83	2862	26	96.7	0.90	377
2	20x20	16.298	1.033	0.5581	0.0316	0.2066	0.0048	2894	61	2859	131	2879	37	99.3	1.30	272
3	20x20	15.747	0.562	0.5495	0.0181	0.2087	0.0050	2862	34	2823	75	2895	39	97.5	1.34	644
4	20x20	16.742	0.862	0.5674	0.0351	0.2102	0.0056	2920	49	2897	144	2907	43	99.7	1.47	313
5	20x20	16.655	0.633	0.5717	0.0195	0.2106	0.0030	2915	36	2915	80	2910	23	100.2	0.78	390
6	20x20	16.503	1.223	0.5649	0.0364	0.2125	0.0046	2906	71	2887	150	2925	35	98.7	1.19	311
Homogeneous zircon																
7	20x20	18.851	0.621	0.6061	0.0184	0.2218	0.0032	3034	32	3055	74	2994	23	102.0	0.78	310
Inherited zircon (faint core)																
8	20x20	18.745	0.503	0.5996	0.0168	0.2282	0.0037	3029	26	3028	68	3040	26	99.6	0.86	239

MM01-63

Analysis #	pit size (µm)	Atomic ratios $^{207}Pb/^{235}U$	(±)	$^{206}Pb/^{238}U$	(±)	$^{207}Pb/^{206}Pb$	(±)	Ages (Ma) $^{207}Pb/^{235}U$	1 ó	$^{206}Pb/^{238}U$	1 ó	$^{207}Pb/^{206}Pb$	2 ó	Conc. %	% error	U (ppm)
IGNEOUS COMPONENT																
Concentrically zoned zircon																
1	30x30	17.863	0.640	0.5904	0.0213	0.2323	0.0027	2982	34	2991	86	3068	18	97.5	0.60	395
Homogeneous zircons																
2	24x24	18.741	0.756	0.6021	0.0257	0.2325	0.0031	3029	39	3038	103	3069	21	99.0	0.69	522
3	24x24	19.375	0.479	0.6296	0.0171	0.2334	0.0020	3061	24	3148	68	3076	14	102.3	0.46	889
4	24x24	18.940	0.741	0.6286	0.0190	0.2358	0.0034	3039	38	3144	75	3092	23	101.7	0.74	919
5	24x24	19.265	0.703	0.6084	0.0228	0.2369	0.0026	3055	35	3064	91	3100	17	98.8	0.55	639
6	30x30	17.411	1.815	0.5735	0.0567	0.2387	0.0064	2958	100	2922	232	3111	43	93.9	1.37	419
7	24x24	18.345	0.610	0.5862	0.0235	0.2388	0.0042	3008	32	2974	95	3112	28	95.6	0.90	540
Analyses of bright cores of zircons																
8	20x20	17.932	1.108	0.5815	0.0420	0.2339	0.0045	2986	59	2955	171	3079	31	96.0	1.00	342
9	20x20	19.665	0.514	0.6300	0.0172	0.2363	0.0037	3075	25	3150	68	3095	25	101.8	0.81	111
10	18.4x18.4	19.213	0.987	0.6154	0.0312	0.2374	0.0039	3053	50	3091	125	3102	26	99.6	0.85	210
IGNEOUS COMPONENT																
Concentrically zoned zircon																
11	30x30	16.299	0.726	0.5726	0.0215	0.2193	0.0024	2895	43	2919	88	2975	17	98.1	0.59	585
12	30x30	17.561	0.900	0.6001	0.0251	0.2264	0.0044	2966	49	3030	101	3026	31	100.1	1.02	357
IGNEOUS COMPONENT																
Analyses of bright cores of zircons																
13	20x20	15.140	1.166	0.5528	0.0466	0.2087	0.0044	2824	73	2837	193	2895	35	98.0	1.19	352

Table 2.2: U-Pb zircon LAM-ICP-MS analytical data (continued)

MM01-81

Analysis #	pit size (µm)	Atomic ratios $^{207}Pb/^{235}U$	(±)	$^{206}Pb/^{238}U$	(±)	$^{207}Pb/^{206}Pb$	(±)	Ages (Ma) $^{207}Pb/^{235}U$	1 ó	$^{206}Pb/^{238}U$	1 ó	$^{207}Pb/^{206}Pb$	2 ó	Conc. %	% error	U (ppm)
IGNEOUS COMPONENT																
1	30x30	16.962	0.700	0.5582	0.0205	0.2147	0.0028	2933	40	2859	85	2941	21	97.2	0.72	187
IGNEOUS COMPONENT																
2	20x20	16.788	0.601	0.5817	0.0163	0.2218	0.0029	2923	34	2956	66	2993	21	98.7	0.70	N/A*
3	20x20	17.252	0.442	0.5879	0.0114	0.2220	0.0030	2949	25	2981	46	2995	22	99.5	0.73	N/A
4	30x30	16.868	0.501	0.5670	0.0190	0.2241	0.0047	2927	28	2895	78	3010	34	96.2	1.12	N/A
5	40x40	19.228	0.420	0.6172	0.0115	0.2251	0.0031	3053	21	3099	46	3018	22	102.7	0.74	150
6	30x30	17.798	0.734	0.5628	0.0207	0.2264	0.0029	2979	40	2878	85	3027	20	95.1	0.67	N/A
IGNEOUS COMPONENT																
7	40x40	19.268	0.585	0.6138	0.0190	0.2275	0.0045	3055	29	3085	76	3035	32	101.7	1.05	57
8	30x30	18.223	0.865	0.5656	0.0275	0.2294	0.0029	3002	46	2890	113	3048	20	94.8	0.67	189
9	30x30	20.038	0.614	0.6190	0.0199	0.2301	0.0032	3093	30	3106	79	3052	22	101.8	0.72	77
10	20x20	18.376	0.570	0.5897	0.0183	0.2301	0.0033	3010	30	2988	74	3053	23	97.9	0.75	N/A
11	30x30	17.713	1.079	0.5820	0.0213	0.2303	0.0093	2974	59	2957	87	3054	65	96.8	2.13	N/A
12	30x30	18.628	0.688	0.6198	0.0236	0.2308	0.0050	3023	36	3109	94	3058	35	101.7	1.14	N/A
13	30x30	20.681	1.048	0.6339	0.0321	0.2311	0.0052	3124	49	3165	127	3060	36	103.4	1.19	65
14	25x25	18.623	0.754	0.5974	0.0224	0.2313	0.0034	3023	39	3019	91	3061	24	98.6	0.77	272
15	20x20	18.314	0.938	0.6053	0.0290	0.2319	0.0034	3006	49	3051	117	3065	23	99.5	0.77	N/A
16	20x20	18.621	0.365	0.6030	0.0119	0.2320	0.0027	3022	19	3042	48	3066	18	99.2	0.60	N/A
17	20x20	18.323	0.592	0.5850	0.0194	0.2326	0.0020	3007	31	2969	79	3070	14	96.7	0.45	N/A
18	30x30	19.709	0.817	0.6014	0.0279	0.2327	0.0050	3077	40	3036	112	3071	35	98.8	1.13	42
19	20x20	18.143	0.509	0.5656	0.0189	0.2333	0.0025	2997	27	2890	78	3075	17	94.0	0.55	N/A
20	40x40	19.657	0.496	0.6066	0.0151	0.2337	0.0029	3075	24	3056	61	3078	20	99.3	0.65	149
21	20x20	18.146	1.838	0.5880	0.0670	0.2340	0.0040	2998	97	2981	272	3079	27	96.8	0.88	N/A
22	20x20	17.913	1.500	0.5878	0.0466	0.2341	0.0046	2985	81	2980	189	3081	32	96.7	1.03	N/A
23	20x20	18.672	1.511	0.5995	0.0581	0.2343	0.0056	3025	78	3028	234	3081	38	98.3	1.24	N/A
24	20x20	18.201	0.594	0.5753	0.0193	0.2344	0.0029	3000	31	2930	79	3082	20	95.0	0.65	N/A
25	25x25	19.921	0.494	0.6228	0.0164	0.2347	0.0036	3088	24	3121	65	3084	25	101.2	0.80	204
26	20x20	18.749	0.879	0.6122	0.0274	0.2351	0.0027	3029	45	3079	109	3087	19	99.7	0.60	N/A
27	30x30	17.889	0.497	0.5776	0.0125	0.2352	0.0056	2984	27	2939	51	3088	38	95.2	1.23	N/A
28	20x20	19.041	0.649	0.6204	0.0191	0.2353	0.0045	3044	33	3111	76	3088	31	100.7	0.99	N/A
29	30x30	20.030	0.622	0.6112	0.0213	0.2354	0.0029	3093	30	3075	85	3089	20	99.5	0.64	179
30	20x20	18.889	0.686	0.5949	0.0244	0.2354	0.0032	3036	35	3009	99	3089	22	97.4	0.71	N/A
31	20x20	19.960	0.805	0.6342	0.0232	0.2359	0.0034	3089	39	3166	92	3093	23	102.4	0.74	36
32	20x20	19.222	0.617	0.6172	0.0205	0.2360	0.0035	3053	31	3099	82	3093	24	100.2	0.77	N/A
33	20x20	17.587	1.130	0.5762	0.0356	0.2361	0.0022	2967	62	2933	145	3094	15	94.8	0.49	N/A
34	30x30	18.536	0.450	0.5847	0.0138	0.2361	0.0056	3018	23	2968	56	3094	38	95.9	1.23	N/A
35	30x30	17.994	0.466	0.5817	0.0126	0.2364	0.0034	2989	25	2956	51	3096	23	95.5	0.73	N/A
36	20x20	19.577	0.813	0.6201	0.0252	0.2373	0.0032	3071	40	3111	100	3102	21	100.3	0.69	N/A
37	20x20	19.004	1.113	0.6039	0.0399	0.2394	0.0046	3042	56	3045	160	3116	30	97.7	0.97	N/A
38	30x30	18.927	0.468	0.6019	0.0160	0.2397	0.0058	3038	24	3038	64	3118	39	97.4	1.24	N/A
IGNEOUS COMPONENT																
39	30x30	18.508	0.439	0.5875	0.0150	0.2400	0.0026	3017	23	2979	61	3120	17	95.5	0.55	N/A
40	30x30	22.174	0.599	0.6476	0.0206	0.2403	0.0040	3191	26	3219	81	3122	26	103.1	0.84	70
41	20x20	18.602	0.815	0.5805	0.0288	0.2408	0.0052	3021	42	2951	118	3125	35	94.4	1.11	N/A
42	20x20	18.593	0.681	0.5853	0.0237	0.2414	0.0041	3021	35	2970	96	3129	27	94.9	0.87	N/A
43	30x30	18.693	0.464	0.6016	0.0156	0.2452	0.0034	3026	24	3036	63	3154	22	96.3	0.69	N/A

*N/A = not available

Chapter Three:
Geochemical Investigation of the Ivisârtoq greenstone belt

3.1 ABSTRACT

The Ivisârtoq greenstone belt forms a southwest-closing, V-shaped synform that is exceptionally well-exposed in three dimensions. Although the belt has undergone heterogeneous deformation and amphibolite facies metamorphism, study of immobile major and trace elements reveals coherent geochemical signatures for the major lithologic units. This investigation concentrated on the 3 km thick southern limb of the synform, where the most complete tectonostratigraphic section of is preserved, and where there are pillow lava structures with way-up indicators. The studied section is made up of two major lithotectonic components, termed the northern and southern parts. In the northern part, remnant olivine grains in ultramafic sills are preserved and in the southern part a layer of meymechitic rocks was discovered. Both these features are rare occurrences in Archean rocks.

New major and trace element geochemical data have shed new light on the origin of the Ivisârtoq greenstone belt. This work supports a new model in which the northern and southern parts of the belt represent discrete packages of rocks that formed in different environments and were subsequently juxtaposed after the main volcanism associated with each part had ceased.

Based on crustal contamination signatures of the amphibolites from the northern part of the belt, an environment similar to a back-arc basin is envisioned for this region, wherein the amphibolites derived from basaltic pillow lavas ascended through thin,

patchy or immature crust. In contrast, the southern belt appears to have formed on a thick continental crust. This interpretation is based on several lines of evidence: crustal contamination signatures of the banded amphibolite, the presence of a thick sequence of quartzofeldspathic metasedimentary rocks, an A-type granitoid, and a horizon of metamorphosed meymechite, which is indicative of deep melting of subcontinental mantle.

3.2 INTRODUCTION

The Ivisârtoq greenstone belt is an exceptionally well preserved Archean greenstone belt situated ~40 km south of the Isua greenstone belt within the Godthåbsfjord region, southwest Greenland (Fig. 3.1). Although, the Isua greenstone belt has been the focus of most studies within the Godthåbsfjord region, due primarily to the antiquity of its rocks, the Ivisârtoq greenstone belt has proven to be an area of potentially great importance to Archean studies. This study shows that the Ivisârtoq greenstone belt is one of the few belts within Greenland which contains well-preserved mafic volcanic rocks that have coherent geochemical signatures. Furthermore, the belt contains relatively well preserved ultramafic units which locally preserve remnant olivine. One of these ultramafic units is especially unique as, texturally (as noted by Chadwick, 1990) and geochemically, it resembles a pyroclastic meymechite: an unusual rock which is thought to form from small degrees of partial melting at great depth (>200km). This discovery marks the first reported meymechite of Archean age. All of these features make the Ivisârtoq greenstone belt an ideal location to study magmatic processes of the early Earth.

This study greatly expands upon previous geochemical studies within the Ivisârtoq greenstone belt, most notably Hall's (1981) work which focused solely on the amphibolite units. In contrast, this study examines the geochemistry of all major units within the belt, including amphibolites derived from basaltic pillow lavas, ultramafic layers, and several quartzofeldspathic units. This comprehensive approach has facilitated the development of a new tectonic model for the belt.

3.3 REGIONAL GEOLOGY

The Ivisârtoq greenstone belt is located within the Godthåbsfjord region of Greenland which is situated in the centre of the Greenland Archean gneiss complex on the west coast near Nuuk (formerly Godthåb and Nûk; Fig. 3.1). Within this region, Early Archean quartzofeldspathic gneisses and early and middle Archean supracrustal rocks were intruded by and were tectonically interleaved with late Archean plutonic rocks.

Large bodies and belts of supracrustal material are observed throughout the Godthåbsfjord region (Fig. 3.1a). Early studies by McGregor (1969) collectively labelled the metavolcanic and metasedimentary schists and gneisses in the vicinity of Nuuk as ***Malene supracrustals***. This term was eventually applied to all rocks throughout southwest Greenland that have lithological characteristics and structural settings like those of the type units in the Nuuk area. They were thought to have been laid down after the formation of the Amîtsoq gneisses at 3600 Ma, but before the intrusion of the Nûk gneisses at 3070 Ma (Chadwick and Nutman, 1979; Nutman and Bridgwater, 1983). A study by Schiøtte et al. (1988) questioned the hypothesis that all Malene supracrustal

rocks pre-dated the Nûk gneisses. They interpreted a depositional age between ~ 2900 and ~ 2650 Ma for two samples using U-Pb techniques. The original hypothesis was therefore found to be invalid and the use of the term Malene supracrustals to describe a single lithostratigraphic unit was discouraged. McGregor et al. (1991) further discouraged the term Malene supracrustals, as different groups of the metavolcanic and metasedimentary rocks were interpreted to have been formed in separate terranes, and therefore had diverse ages and origins. Some studies have retained the use of the term Malene supracrustals for descriptive and historical convenience (e.g. Smith et al., 1992), with the knowledge that these units may not be related.

Early interpretations regarded the Godthåbsfjord region as a single tectonic terrane (Nutman, 1997). Similar to other granite greenstone terranes, for example Barberton (e.g. Lowe et al., 1999), and the Superior Province (e.g. Percival et al., 2001), later studies reinterpreted the Godthåbsfjord region in terms of separate terranes, which evolved independently prior to assembly in the late Archean.

Most recently the Godthåbsfjord region is thought to comprise six terranes: the Akia, Isukasia terrane, Færingehavn, Kapisilik, Tre Brødre, and Tasiusarsuaq terranes (Fig. 3.1b). The Isukasia terrane includes the Isua greenstone belt and the Kapisilik contains the Ivisârtoq greenstone belt. Assembly of the terranes is interpreted to have taken place in at least two episodes, the > 3600 Ma Isukasia terrane was first intercalated with the 3075-2960 Ma Kapisilik terrane at ~2950 Ma and subsequently this composite block was juxtaposed with the composite Færingehavn and Tre Brødre terranes (post-2825 Ma). Friend and Nutman (2005) interpret the Tre Brødre terrane (and associated

Færingehavn terrane) to now lie structurally above the Kapisilik terrane. Furthermore, on Ujarassuit Nunaat and northern Ivisârtoq, the northern limit of the Kapisilik terrane is interpreted to be structurally above the early Archean rocks to the north, now termed the Isukasia terrane (Fig. 3.1b). One of the goals of ongoing mapping and geochronology in the Godthåbsfjord region is to test and if necessary modify the terrane model.

3.4 IVISÂRTOQ GREENSTONE BELT

3.4.1 Previous Work

The Ivisârtoq region was initially mapped by mainly helicopter reconnaissance by Walton (1976) and by Allaart et al. (1977). The greenstone belt itself was mapped in more detail by Friend and Hall (1977), who discovered pillow lava structures indicating way-up. Hall (1981) used the field data collected during the summer of 1976 for his PhD, concentrating on petrography, metamorphism, structural geology, and geochemistry of the Ivisârtoq greenstone belt. In particular, Hall (1981) concentrated on the geochemistry of the amphibolites.

A team from University of Exeter did further mapping within the Ivisârtoq region from 1981-1983 and in 1985 in order to complete the necessary detail for the Geological Survey of Greenland 1: 100 000 map sheet 64 V.2 N (Chadwick and Coe, 1988). From this work a host of PhD theses were produced, including: Robertson (1985); Brewer (1985); Park (1986); Crewe (1986). During this time Chadwick mapped the Ivisârtoq greenstone belt in detail at a scale of 1:20 000 (unpublished map) and eventually determined a stratigraphic sequence for the belt (Chadwick, 1990). There has been little

work published on the Ivisârtoq greenstone belt prior to the onset of this study, however as the research within and around the Isua region starts to broaden, it seems inevitable that Ivisârtoq greenstone belt will be the focus of future studies.

Recent work by Friend and Nutman (2005) included reconnaissance geochronology from the Ivisârtoq area. They obtained three additional ages from the belt and have incorporated the area into a new terrane model which encompasses the Godthåbsfjord region.

3.4.2 Tectonostratigraphy

The Ivisârtoq greenstone belt forms a southwest-closing, V-shaped structure (Fig. 3.2) and was subjected to amphibolite facies metamorphic conditions. Recent mapping has re-evaluated the 'stratigraphy' of the Ivisârtoq greenstone belt defined by Chadwick (1990), which is described here as a tectonostratigraphic assemblage. This interpretation is based on field mapping (see Chapter 2), which concentrated on the 3 km thick southern limb of the V-shaped structure, and is supported by geochemical analysis of the major rock units in this area.

The southern limb of the belt is divided into two main parts, a northern and southern part, based on differences in rock types and intensity of deformation (Fig. 3.2). These parts are herein described as simply the northern and southern parts of the belt, with the understanding that they refer to the southern limb of the belt. The northern part of the belt is characterized by heterogeneously deformed amphibolites derived from basaltic pillow lavas that are interlayered with boudins of coarse-grained olivine-bearing

ultrabasic rocks, and quartz-feldspar-mica gneisses and schists which are continuous for a few hundred metres. The southern part of the belt contains more intensely deformed pillowed amphibolites and homogeneous amphibolites. A layer of ultramafic schists, a metagranodiorite unit, and diffusely banded, pale quartzofeldspathic gneisses and schists, are also included in the southern group. The northern part of the Ivisârtoq greenstone belt is generally less deformed than the southern part of the belt. The contact between the two parts of the belt is marked by a distinct high strain zone, termed the Marker High Strain Zone, which is composed of two layers: a quartzofeldspathic layer with amphibolitic horizons and a layer of ultramafic schists termed the magnetic marker. The northern part of this high strain zone is used as the dividing feature, separating the northern part of the Ivisârtoq greenstone belt from the southern part, and is thought to represent a major tectonic break. The northern and southern parts of the Ivisârtoq greenstone belt are characterised by distinct ultramafic, mafic, and felsic magmatic histories prior to juxtaposition.

Geochemical analysis of rocks from the northern and southern parts of the belt support the tectonostratigraphic model of the belt (i.e. the two parts of the belt have distinct origins) and has been invaluable in resolving several questions which remained after field work, including:

1) How do the different amphibolites derived from basaltic pillow lavas relate to each other? What are their sources?

2) Does the northern part of the belt represent a thrust repeated sequence?

3) Do the mafic and ultramafic units have a common magmatic origin?

4) What is the nature of the magnetic marker?

5) Do the quartzofeldspathic layers interpreted as tonalites have the same origin?

Geochemical work also supported protolith interpretations which were interpreted from field work and highlighted differences between units of the same mineral assemblages (e.g. quartzofeldspathic rocks).

3.5 METHODOLOGY

Samples for geochemical analysis were collected from the Ivisârtoq greenstone belt by the author during the 2001 summer field season and by Dr. John Myers during July, 2003. During sampling, highly altered or veined rocks and areas of obvious hydrothermal alteration were avoided, but due to the nature of the greenstone belt it was impossible in places to avoid sampling intensely deformed and metamorphosed rocks.

Approximately 60 whole-rock samples were cut using a rock-saw to remove weathered surfaces, crushed using a jaw crusher or a hammer and iron plate, and powdered using an agate mill. An agate puck was used instead of a tungsten-carbide puck in order to reduce contamination of Ta, Hf, and Nb. All samples were analysed for whole-rock geochemistry at the Memorial University of Newfoundland. X-Ray Fluorescence (XRF) pressed powder pellet, XRF fused glass beads, and Inductively Coupled Plasma-Mass Spectrometer (ICP-MS) acid and sinter techniques were used to obtain the data.

All X-ray fluorescence (XRF) analyses were completed using an ARL 8420+ X-Ray Fluorescence spectrometer following procedures outlined by Longerich (1995). A

preliminary analysis using pressed powder pellets was performed on all the samples. Major elements, and some trace elements with concentrations greater than 10 ppm in whole rock samples, were determined using this method. Samples were selected for XRF fused glass bead analysis for precise major element compositions based on the XRF pressed pellet data. Samples with >20% Fe_2O_3 (total iron) or >1% S could not be fused and therefore major element data from XRF pressed powder analyses were used for these samples (see Table 3.1 and Table B.1 for analytical method used for each element).

All samples were also analysed for trace elements using a HP 4500 plus ICP-MS following the protocols of Jenner at al. (1990). Some of the samples were initially analysed following HF and HNO_3 acid digestion in a Teflon beaker on a hot plate. Ideally this technique is preferred over the sinter ICP-MS method (which sinters a mixture of Na_2O_2 and the sample powder in a muffle furnace) as it is capable of determining more elements. The sinter method provides data for Y, Zr, Nb, all the lanthanides (La, Ce, Pr, Nd, Sm, Eu, Gd, Tb, Dy, Ho, Er, Tm, Yb, and Lu), Hf, Ta, and Th , whereas the acid method determines all of these elements as well as Li, Rb, Sr, Mo, Sc, Ba, Tl, Pb, Bi, and U. Unfortunately, after comparison of ICP-MS acid digestion results with the XRF pressed pellet data, it was apparent that trace element bearing accessory phases, particularly zircon, were not completely dissolved using the acid method. Therefore the sinter preparation was used for all samples. Where available, Rb and Sr values obtained by the acid ICP-MS method were preferred to XRF data, because of lower detection limits. The XRF pressed pellet data and the sinter ICP-MS data were compared to identify analytical or sample handling errors. The Nb values determined using the sinter

ICP-MS technique were systematically higher than expected for reference materials; therefore the XRF pressed pellet values for Nb were used instead.

The long-term precision and accuracy of the elements analysed for each technique have been carefully monitored by technicians at Memorial University. Using the *XRF fused bead technique*, the major elements are precise and accurate to usually much better than 5%, where concentrations of oxide exceed 0.1%. Using *XRF pressed pellet techniques*, the precision and accuracy of V, Cu, Zn, Ga, and Nb in most silicate rocks is generally better than 10%. The precision and accuracy of Sc, Ni, and Cr are not as good (10 to 25% for Sc, Ni; up to 35% for Cr) because the low levels in many rocks approach the detection limits of the method. The *sinter ICP-MS technique* produces Y and REE data accurate to 1-6% and precise to 6-11%. Using this technique Zr, Ba, Hf, Ta, and Th are reproducible to 10-18%, and accurate to 9-25% depending on their concentration. Sr and Rb values obtained using the acid dissolution ICP-MS technique are reproducible to 6-19% and are accurate to 1-5%.

Selected elements were normalized to primitive mantle (pm) based on C1 chondrite concentrations from Anders and Grevesse (1989; see Table B.2). Chondrite and primitive mantle normalized trace element anomalies (e.g. Eu/Eu*) were calculated using the geometric mean with respect to neighbouring immobile elements, as recommended by Taylor and McLennan (1985). Mg-numbers are calculated as the molecular ratio of $100[Mg^{2+}/(Mg^{2+}+Fe^{2+})]$. FeO is calculated as Fe_2O_3 (total iron) x 0.8998.

3.6 RESULTS: Major and Trace Element Geochemistry

3.6.1 Element Mobility and Alteration

The rocks within the Ivisârtoq greenstone belt have undergone amphibolite facies metamorphism, metasomatism, and polyphase deformation, destroying most primary textures and primary mineral assemblages. These processes can effectively mobilize elements and change the major and trace element abundances of the original rocks. Samples with petrographic evidence of the least intense deformation and pervasive alteration (including chloritization, serpentinization, and carbonatization) were selected for geochemical analysis. Chemical criteria for alteration were used in order to obtain a reliable dataset consisting of relatively unaltered rocks with near-primary chemical compositions for certain elements.

In order to identify elemental mobility in the samples and thus preservation of original magmatic concentrations, elements were plotted against Zr, a typically immobile high field strength element (HFSE), on variation diagrams (Appendix B: Fig. B.1-B.8). The degree of scatter on bi-element plots can indicate element mobility in a suite of rocks which are considered to be coherent on the basis of HFSE (Tomlinson et al., 1999). This approach has been used for modern (Murton et al., 1992) and Archean volcanic rocks, including rocks from the Isua greenstone belt (Polat et al., 2002) to assess the effects of alteration on element mobility. The least altered samples exhibit coherent arrays and predictable trends for Zr versus TiO_2, P_2O_3, rare earth elements (REE), Y, Zr, Nb, Ta, Th, and Hf, which are consistent with limited mobility of these elements. Some dispersion for the elements Mg, FeO, Na, Ca, K, Cr and Ni was noted, however, generally a linear array

was still recognizable. The scatter is likely a reflection of element mobility caused by post-magmatic alteration. These elements are used cautiously and interpretations of these data, where possible, are backed up with that of immobile trace elements. Other elements [e.g. large ion lithophiles (LIL)] do not define consistent trends and are considered mobile. All samples except the ultramafic samples have loss on ignition (LOI) values less than 3%, and are typically less than 1% (Table 3.1). Ultramafic samples have higher LOI, up to 12%, however, consistent geochemical trends are apparent in samples used for interpretation.

The selected samples, which exhibit the least alteration effects, have consistent and coherent primitive mantle-normalized trace element patterns (Appendix B: Fig. B.9-B.10), suggesting that the original magmatic concentrations for the selected elements have been preserved. Samples which were removed from the data set (see Appendix B; Table B.1: Fig. B.9-B.10) have more erratic mantle-normalized trace element patterns.

3.6.2 Amphibolites

3.6.2.1 Amphibolites derived from Basaltic Pillow Lavas

Three main types of amphibolites were recognised in the field based on rock type and location within the greenstone belt. In the northern part of the belt, amphibolites derived from homogeneous basaltic pillow lava and amphibolites derived from variolitic basaltic pillow lava are interbedded and are considered contemporaneous. In the southern part of the belt, banded amphibolite is predominant. For simplicity, the metamorphic

terms are replaced by their protolith interpretations and are herein termed homogeneous pillow basalts and variolitic pillow basalts.

The homogeneous pillow basalts are characterised by pillow lava structures with dark, marginal zones surrounding paler, yellow-green cores. The pillow cores range from fine to coarse-grained and comprise various but significant amounts of epidote, clinopyroxene, plagioclase, hornblende, and lesser amounts of garnet and calcite. Titanite is a ubiquitous accessory mineral, and locally constitutes up to 7 modal % of the matrix. The observed assemblages may have resulted from secondary metasomatic replacement during early hydrothermal alteration, which was likely modified during subsequent metamorphism (see Chapter 2).

The variolitic pillow basalts are characterised by the presence of varioles within the cores of well-preserved pillows, and as separate spherical bodies near pillow margins. The pillow cores are dominated by recrystallized amphibole, plagioclase, and accessory titanite (≤3 modal %); the proportions of which differ between the leucocratic varioles, which are composed of roughly equal proportions of elongate hornblende and polygonal plagioclase, and the dark matrix of the pillow cores, which are dominated by coarse-grained hornblende

The third type of amphibolite is predominant in the southern part of the belt and is observed as banded amphibolites. Locally, the transition from well-preserved homogeneous pillow lava to banded amphibolites, was observed; therefore this unit is interpreted as being derived from basaltic pillow lava. The banded amphibolites are

characterized by medium-green, epidote-rich layers which contrast dark green hornblende-rich layers.

Samples from the northern part of the belt were collected from the cores and rims of well-preserved homogeneous and variolitic pillow basalts. Samples from the southern part of the belt consisted of banded amphibolites. The three recognisable rock types have distinctive geochemical signatures. Major and trace element analysis of representative samples from each rock group are reported in Table 3.1.

The three types of amphibolites have some geochemical similarities. They have overlapping concentrations of MgO [range 3.6-10.9 weight (wt) %], Al_2O_3 (range 9.95-17.9 wt %), and TiO_2 (range of 0.36 - 0.92 wt %). They also have overlapping Mg-number (atomic fraction) values (30-76) and Zr/Y ratios (2.7-5.3) that exceed the primitive mantle value (Zr/Y = 2.52). The homogeneous pillow basalts have Al_2O_3/TiO_2 values (16-20) below the primitive mantle value (~27.8), whereas the variolitic pillow basalts and the banded amphibolites have sub- to super-primitive mantle values (16-31). The homogeneous pillow basalts tend to have lower overall concentrations of Ni (84-152 ppm) and Cr (216-269 ppm) than the other two types of amphibolite (Ni=54-517 ppm, Cr=133-1546 ppm).

Typically varioles in Archean mafic volcanic rocks have been found in rocks with high-Mg basaltic compositions (Cawthorn et al., 1979, and references therein) and have been used as a field criterion to identify high-Mg basalts (Myers, pers. comm.). However, it should be noted that the variolitic pillow basalts in the Ivisârtoq greenstone belt range

in MgO from 3.9-11 wt % (similar to the homogeneous pillow basalts) and therefore cannot strictly be classified as high-Mg basalts.

A Jensen classification diagram is useful for classifying metavolcanic rocks which have undergone mild metasomatic loss of alkalis (pg. 63, Rollinson, 1993). This diagram demonstrates that the variolitic and homogeneous pillow basalts range from high-Fe tholeiitic basalts to tholeiitic andesites (Fig. 3.3a), a progression consistent with fractional crystallization and/or crustal contamination. The banded amphibolites in the southern part of the belt plot as high-Fe tholeiitic basalts.

The major element geochemistry of Ivisârtoq amphibolites has been studied previously by Hall (1981). He analysed fifty metavolcanic amphibolites collected along two different transects within the Ivisârtoq greenstone belt: one transect was across well-preserved pillowed and homogeneous amphibolite in the northern part of the same region as this study and another was across finely banded and homogeneous amphibolite within the core of the V-shaped structure defining the belt (outside region of this study). Within both transects Hall (1981) found a range of MgO compositions (MgO=5-22 %), and he classified 20 of the samples as komatiitic and 30 as tholeiitic basalts. However, eight of the samples that Hall labelled as komatiitic plot close to the field of high-Fe tholeiitic basalts on a Jensen classification diagram and overlap with the Ivisârtoq homogeneous and variolitic pillow basalt data (Fig. 3.3b). This can also be demonstrated on a plot of Al_2O_3/TiO_2 versus Mg-number (Fig. 3.4b). This diagram demonstrates that Hall likely sampled some variolitic pillow basalts which he did not differentiate from the homogeneous pillow basalts. Three groups, which likely correspond with variolitic (7

samples), homogeneous (30), and komatiitic basalts (13 samples) can be distinguished from Hall's data (Fig. 3.4).

Hall (1981) described the ultramafic pillow lavas in the field as "hornblenditic pillows set within a pale green matrix rich in epidote and clinopyroxene" (pg. 62, Hall, 1981). The core and rim of a pillowed amphibolite fitting this description (Fig. 2.8) were analysed during this study. These samples plot as high-Fe tholeiite basalts on a Jensen diagram (Fig. 3.3a), which demonstrates that the field criteria used by Hall is not absolute in identifying komatiitic basalts. Only one sample of pillow lava structures, collected during this study, is classified as a komatiitic basalt on a Jensen diagram (Fig. 3.3). It plotted within the field defined by Hall's komatiitic samples on a Al_2O_3/TiO_2 versus Mg-number plot (Fig. 3.4). This sample did not exhibit the epidote-rich matrix as described by Hall (1981). The lack of komatiitic basalt found in the present study may have been an effect of selective sampling; whereby only amphibolites with well-preserved pillow lava structures which typically had epidote-pyroxene rich cores and amphibole-rich margins were sampled from the northern part of the belt, samples of homogeneous amphibolites were not collected, and overall fewer amphibolite samples were collected compared to Hall's study.

Hall (1981) obtained REE data for 4 samples: three ultramafic samples and one amphibolite with well-preserved pillow lava structures. These analyses do not exhibit consistent trends (Hall, 1981), which could reflect alteration processes or data quality. Trace element analysis is more accessible, economical, and more accurate than it was 20 years ago. This study expands on Hall's REE data by utilising a fuller range of trace

element results to characterize the different types of amphibolites recognized in the field: including the homogeneous pillow basalts, the variolitic pillow basalts, and the banded amphibolites.

The three types of amphibolites recognized in this study have distinct signatures on primitive mantle normalized multi-element diagrams (Fig. 3.5). The homogeneous pillow basalts exhibit slightly depleted to slightly enriched primitive mantle normalized light REE (LREE) patterns (La/Sm_{pm}=0.85-1.25); the variolitic pillow basalts are moderately LREE enriched (La/Sm_{pm}=1.16-1.54); and the banded amphibolites are strongly LREE-enriched (La/Sm_{pm}=1.58-2.25). There is also a progressive increase in the size of negative Nb and Ta anomalies from the homogeneous pillow basalts (Nb/Nb*= 0.89-1.06, Ta/Ta*=0.82-1.09), through the variolitic pillow basalts (Nb/Nb*= 0.38-0.67, Ta/Ta*=0.35-0.49), to the banded amphibolites (Nb/Nb*=0.23-0.61, Ta/Ta*=0.20-0.36). All three types of amphibolites have negative Ti anomalies. The homogeneous and variolitic pillow basalts have similar negative anomalies (Ti/Ti*=0.72-0.89), whereas comparatively, the banded amphibolites have larger negative Ti anomalies (Ti/Ti*=0.47-0.73). The one komatiitic sample of this study has a similar extended REE pattern as the variolitic basalt (exhibits Nb and Ta anomalies) with the notable difference being that the trace elements are more depleted overall (Fig 3.5).

The three types of amphibolites can also be distinguished based on their patterns on a P_2O_5 versus Zr plot (Fig. 3.6). The homogeneous pillow basalts and variolitic pillow basalts show a continuous trend of low P_2O_5/Zr ratios, whereas the banded amphibolites define a separate trend of higher P_2O_5/Zr ratios.

3.6.2.2 Mafic Dykes

Two main types of mafic dykes were noted in the field, including fine- to medium-grained dykes which contain large plagioclase phenocrysts and medium-grained, gabbroic dykes which are not plagioclase phyric. The mineral assemblages of the two types of dykes is dominated by partially to completely recrystallized hornblende and feldspar. The non-plagioclase phyric, equigranular gabbroic dykes have an average grain size of 0.5 mm-1 mm. Large, relict plagioclase phenocrysts found in the other variety, range in size from 1 cm-30 cm and range in intensity of deformation from ovoid shapes to stretched, elongate lenses.

Both rock types occur in the northern and southern parts of the belt and range in width from centimetres to tens of metres. They also range in strike length from a few metres to hundreds of metres. In the northern section, the gabbroic sills are parallel to the contacts of other lithological layers, including amphibolites derived from pillow lavas, ultramafic layers, and quartzofeldspathic layers. Some gabbroic dykes are locally parallel with the other units, but along strike are seen to branch and cross-cut these units (Fig. 2.41). Although some of the northern gabbroic dykes are geochemically similar to the homogeneous pillows (see following discussion) they are not thought to represent feeder dykes as they cross-cut the ultramafic and tonalitic layers which suggests that the dykes are younger than the basaltic pillow lavas. In the southern part of the belt, which is more strongly deformed, the mafic dykes are folded with other rock units. Both types of mafic dykes likely intruded at different times during the deformation and magmatic history of the belt. An igneous age of ~3066 Ma was obtained by U-Pb zircon geochronology for a

plagioclase phyric dyke that is thought to have intruded into the amphibolites in the southern part of the belt (see Chapter 2).

Major and trace element analysis of representative samples from each rock group are reported in Table 3.1. The two types of dykes have similar and overlapping contents of MgO (4.0-8.4 wt%), Ni (60-154 ppm), Cr (236-471 ppm), Mg-number (62-72), and Zr/Y (2.8-3.6), all of which fall within the observed ranges of the three types of amphibolites derived from pillow basalts. The two kinds of dykes can be distinguished from each other on the basis of Al_2O_3 and TiO_2 contents. The gabbroic dykes have lower overall Al_2O_3 (14.6-15.4 wt%) and TiO_2 concentrations (0.92-0.98 wt %), which are similar to the amphibolites derived from basaltic pillow lava, whereas the plagioclase phyric dykes have higher contents (Al_2O_3=15.5-21.4 wt%; TiO_2=0.89-1.12 wt%). The gabbroic dykes have Al_2O_3/TiO_2 ratios which range from 15.8-15.9, whereas the plagioclase phyric dykes have overall higher values which range from 14.1-23.7.

These two types of dykes are defined geochemically as gabbros using a total alkali-silica diagram for plutonic rocks (Wilson, 1989; Fig. 3.7). Most of the mafic dyke samples define similar trends on primitive mantle normalized multi-element patterns (Fig. 3.8). The patterns of most gabbroic and all of the plagioclase phyric dykes do not resemble any of the amphibolites derived from basaltic pillow lava. These dykes have positive Eu and Ti anomalies (see Table x), lower MREE values, and the most incompatible elements (Th-La) define a concave upward pattern.

Two exceptions are gabbroic dykes from the northern part of the belt. These two dykes have multi-element patterns similar to the homogeneous basalts; the only major

variance is among the most incompatible elements (Th-Ce). The two northern gabbroic dykes have lower Th, La, and Ce concentrations than the homogeneous pillow basalts. As a result the gabbroic dykes have lower $(La/Sm)_{pm}$ ratios (0.69-0.73) and higher $(Nb/Th)_{pm}$ ratios (1.5-1.7) than the homogeneous basalts (La/Sm_{pm}=0.85-1.25; Nb/Th_{pm}=0.84-1.17.

3.6.3 Ultramafic Bodies

3.6.3.1 Ultramafic Layers

Distinctive yellow-brown-weathering ultramafic layers up to 600 m long and 30 m thick are the most prominent topographic feature in the northern part of the Ivisârtoq greenstone belt. The central regions of the layers generally appear massive, coarse-grained and homogeneous, whereas the margins are fine-grained and schistose. Internal layering was not observed within the ultramafic layers. Remnants of igneous olivine, orthopyroxene, and a few clinopyroxene crystals were observed within the centre of the layers but alteration has destroyed igneous textures (see Chapter 2: Fig. 2.18-2.29). Alteration products include serpentine (antigorite), magnetite, iddingsite, amphibole (actinolite- tremolite), talc, and chlorite. The margins of the ultramafic layers have undergone shearing and hydrothermal alteration, and contain fine-grained talc, actinolite-tremolite, serpentine, and chlorite. Magnesite is locally present.

Samples for geochemistry were collected from the two most extensive layers, which define isoclinal folds, referred to as the inner (most westerly) and outer (most easterly) isoclinal folds (Fig. 3.2; see insert map). The least altered samples were collected from the centres of these layers, which are massive, coarse-grained and contain

remnants of primary minerals. Intensely deformed margin samples were removed from the dataset used for major and trace element diagrams based on mobility of LREE indicated by erratic patterns on bi-element plots and on primitive mantle normalized trace element diagrams (see Appendix B; Fig. B.5, B.6, B.9). Major and trace element analysis of the representative samples are reported in Table 3.1.

The ultramafic layers are characterized by MgO=34.8-41.0 wt %, Mg-number = 93-94, Ni=1749-2125 ppm, Cr=1947-7138 ppm, and Al_2O_3/TiO_2=16.5-24.2. The layers plot within the komatiite field on a Jensen cation diagram (Jensen, 1976), which demonstrates their ultramafic character (Fig. 3.9). However, these layers are composed of cumulate rocks which are komatiitic only in *composition*; i.e., they do not have spinifex textures, and are not komatiites. Komatiites, typically have less than ~29 wt% MgO (Nisbet et al., 1993).

The two largest ultramafic layers have similar flat primitive mantle normalized trace element patterns, with enrichment factors of about one times primitive mantle values (Fig. 3.10). They have negative Eu anomalies (Eu/Eu*=0.16-0.46) and differing Th and Nb values. Based on major and trace element geochemistry, the composition of the layers is consistent with the interpretation that their protolith was an olivine cumulate rock which may have formed as sills, parts of differentiated komatiitic flows, or tectonic slices of Earth's Archean mantle. Olivine data are useful to help determine the nature of these layers, as examined in the *Discussion* section of this paper.

Electron microprobe data were collected from remnant olivine grains in samples from the two large isoclinal layers (Table 3.2). The Fo contents of the grains range from

Fo_{78} to Fo_{88}. Olivine grains from the outer isoclinal fold (IV03-43, MM01-45a) contain MgO=39-46 wt % and Ni.2300-3000 ppm, whereas olivine grains from the inner isoclinal fold (MM01-96) are characterized by MgO=47-50 wt % and Ni=1740-2140 ppm.

3.6.3.2 Magnetic Marker

The magnetic marker is a schistose, grey-green layer of ultramafic rocks, which ranges in width from 10 to 50 m and has a strike length of at least 7 km. This layer is distinguished by a high magnetic susceptibility (up to 15-35 modal % of magnetite was noted), and was suitably termed the 'magnetic marker' by Chadwick (1990).

Samples were collected along two detailed transects across the width of the magnetic marker (Fig. 2.59). Based on these transects it is apparent that the unit represents a heterogeneous tectonostratigraphy. The magnetic marker is dominated by grey-green schistose rocks composed of chlorite, tremolite, phlogopite, talc, and serpentine, overprinted by pyroxene and less abundant olivine porphyroblasts. Other rock types observed in the transects include carbonate-rich rocks (up to 50% carbonate), coarse-grained, garnet-pyroxene-epidote-amphibolite schists, and highly deformed quartzofeldspathic layers. Due to recrystallization, it is unclear if the carbonate minerals are primary or secondary in nature. The garnet-pyroxene-epidote-amphibolite schists are probably highly metasomatised versions of intensely deformed amphibolites derived from basaltic pillow lava, and are not considered to be a primary component of the magnetic marker. The deformed quartzofeldspathic layers are also not considered to be

an original constituent of the magnetic marker protolith and likely represent later tonalitic intrusions.

Six samples were chosen for geochemistry (Table 3.1). Despite the schistose nature of the rocks, these samples yield remarkably consistent geochemical signatures. Initially, based on field criteria alone, it was uncertain if the magnetic maker was simply an intensely deformed version of one of the ultramafic layers found in the northern part of the belt. However, geochemical data conclusively rule out this idea, indicating that the magnetic marker is geochemically distinct from the northern ultramafic layers. This unique layer is characterized by MgO=18.0-24.4 wt %, Mg-number = 78-86, Ni=453-1484 ppm, Cr=617-1563 ppm, Al_2O_3=3.7-6.5 wt%, TiO_2=1.13-3.44 wt%, and Al_2O_3/TiO_2=1.9-4.3. The high MgO (>18 wt %) and TiO_2 (>1 wt %) values are significant, as these values in combination with SiO_2 (32-45 wt %) and $Na_2O + K_2O$ (0.15-3.15 wt %) chemically define the magnetic marker as a meymechite (also spelled meimechite). Meymechites are defined by the International Union of Geological Sciences (IUGS) as an ultramafic volcanic rock containing MgO >18%, SiO_2 between 30 and 52%, ($Na_2O + K_2O$) <2%, and TiO_2 >1% (Le Bas M.J., 2000, Le Maitre, 2002).

The magnetic marker samples fall within the IUGS meymechite field except for one sample (Fig. 3.11a). The variation in $Na_2O + K_2O$ values of the Ivisârtoq samples is likely a reflection of alteration processes. Other meymechitic rocks are plotted for comparison; including samples from the Paleoproterozoic Cape Smith Belt, Quebec and Castignon Lake, Labrador Trough, and from the type-locality, Triassic meymechites found in the Maymecha-Kotuy region of northern Siberia.

Some studies have used geochemical classification schemes other than that of the IUGS to describe meymechitic rocks: Fedorenko and Czamanske (1997) classified meymechites as volcanic or subvolcanic rocks of peridotitic composition (23-38 wt% MgO), rich in olivine phenocrysts, with a high TiO_2 content (~3 wt %) and steep REE profiles. Using this definition only two of the magnetic marker samples classify as meymechites (see Table 3.1; samples IV03-23, IV03-24). Using a different classification system designed by Hanski et al. (2001), the magnetic marker samples plot as Al-depleted picrites, picrites, and only one sample plots as a meymechite (Fig. 3.11b). In general, it is necessary to recognize that the boundaries of geochemical fields in different classification schemes are arbitrary in the sense that various alkaline-rock suites likely include a spectrum of compositions which may be genetically related. The IUGS classification scheme is used for this study.

The magnetic marker samples also define a distinct pattern on a primitive mantle normalized multi-element diagram (Fig. 3.12). Trace element concentrations are enriched and strongly fractionated [$(La/Sm)_{pm}$=1.8-4.5; $(Gd/Yb)_{pm}$=2.6-7.9], ranging from primitive mantle values for the HREE up to enrichment factors of 100 times greater for incompatible elements such as Nb and La. The magnetic marker is also characterized by slightly negative Ti (Ti/Ti*=0.65-0.72) anomalies, and flat to positive Eu anomalies (0.97-1.59). These observations are consistent with the data of Arndt et al. (1995), which show meymechites as having generally high and strongly fractionated trace element concentrations. Arndt et al. (1995) studied meymechites from the type locality in the

Maymecha-Kotuy region of northern Siberia. The magnetic marker trace element data match remarkably well with Arndt et al. (1995)'s trace element data (Fig. 3.12).

The meymechite type locality, from which the IUGS geochemical and field descriptions of meymechites are based, has been the primary source of information regarding this unique rock type. The type locality contains meymechite flows and dykes (Arndt et al., 1995); one of the flows has been dated at 245±1 Ma (Dalrymple et al., 1995). The IUGS field description defines meymechites as ultramafic volcanic rocks composed of olivine phenocrysts in a groundmass of olivine, clinopyroxene, magnetite, and glass (Le Maitre et al., 2002). This definition does not specify that the rocks form volcanic flows, pyroclastic deposits, and/or their subvolcanic equivalents (sills and dykes), or that they can have an association with carbonate-rich rocks, as seen in the Cape Smith Belt (Baragar et al, 2001) and the Castignon Lake region (Dimroth, 1970), both part of the Circum-Superior belt, Canada.

Due to the intensely deformed nature of the Ivisârtoq magnetic marker, primary textures were not found during the course of this study, however, Chadwick (1990) reported small-scale lenticular structures within the magnetic marker which he interpreted as lapillistones. These structures may have been observed within a low-strain zone within the unit, and thus the magnetic marker may represent a meymechitic pyroclastic deposit.

3.6.4 Quartzofeldspathic Schists and Gneisses

3.6.4.1 Thin, Rusty Quartzofeldspathic Layers

Numerous, thin layers of rusty-brown quartzofeldspathic schists and gneisses, were observed in the northern part of the Ivisârtoq greenstone belt, within the Marker High Strain Zone, and within the magnetic marker. These layers range in thickness from a few centimetres to tens of metres, and are typically continuous for a few hundred metres, although locally, they also occur as sporadic lenses. Continuous layers were noted adjacent to the medium green schistose margins of the ultramafic layers and sporadically within amphibolites derived from basaltic pillow lava (see insert map). The most noticeable layers have a bright orange-yellow colour, attributed to the weathering of sulphide minerals, and strongly contrast with the adjacent green amphibolites (Fig. 2.31). Based on preserved igneous textures and cross-cutting field relationships with pillow basalts, the protolith of these layers is thought to be intrusive (see Chapter 2). Field evidence (see Chapter 2) suggests that they may have intruded at different time intervals, where some intruded before juxtaposition of the northern and southern parts and some after this event. A $^{207}Pb/^{206}Pb$ igneous age of ~3165 Ma was obtained by zircon geochronology for two sheets which intruded before the juxtaposition event (see Chapter 2).

The schists and gneisses are classified largely as tonalites based on mineral proportions. Major and trace element analysis of representative samples are reported in Table 3.1. The rocks have SiO_2 contents of 54-74% and Mg-numbers of 30-69. The tonalitic layers have Chemical Index of Alteration (CIA; Nesbitt and Young, 1989)

values of 45-58 (excluding one outlier with CIA=72). Unweathered granitiods are characterized by CIA values of 45-55 (Bolhar et al., 2005), consistent with the interpreted igneous origin for these layers. CIA is based on the molecular proportions of major element oxides and is calculated using the following equation:

$CIA= Al_2O_3/(Al_2O_3+ CaO^* + Na_2O + K_2O)$ x100, where $CaO^*= CaO-CO_2-10/3\ P_2O_5$. The outlier sample was likely affected by secondary alteration processes.

Samples from the rusty layers define a pattern on a primitive mantle normalized multi-element diagram that is distinct from the other quartzofeldspathic units in the belt (Fig. 3.13). The LREE are moderately enriched (La/Sm_{pm}=1.65-4.37) whereas the HREE define a flat pattern. The rusty layers are also characterized by negative Nb (Nb/Nb*= 0.20-0.87), Ti (Ti/Ti*=0.36-1.09), Eu (Eu/Eu*=0.21-0.85) anomalies, and positive Zr (Zr/Zr*=1.21-2.12) anomalies

3.6.4.2 Granitoid Intruding Northern Boundary of Belt

Thin sheets of homogeneous, medium-grained, meta-granitoid (tonalite-trondhjemite-granodioritic; TTG) intrude the northern margin of the Ivisârtoq greenstone belt. They are considered part of the regional granodioritic gneiss which is north of the mapped area (see Fig. 3.2). Within the greenstone belt, these sheets are sub-parallel to the schistosity and mylonitic fabrics of the greenstones but are much less deformed than the amphibolites. Locally, rafts of previously deformed amphibolite were observed within the gneiss close to the contact with the greenstone belt. These sheets are thought to have intruded after the juxtaposition event (DJ; see Chapter 2). A $^{207}Pb/^{206}Pb$ igneous age of

~2960 Ma was obtained by zircon geochronology for a homogeneous TTG sheet intruding the northern boundary of the greenstone belt (see Chapter 2).

Major and trace element data for the dated TTG sheet are reported in Table 3.1. The sample has a SiO_2 content of 72%, an Mg-number of 37, and a CIA= 53, which falls within the range observed in unweathered granitoids (CIA=45-55; Bolhar et al., 2005).

The one sample collected from this unit defines a distinct pattern on a primitive mantle normalized multi-element diagram (Fig. 3.14). The light rare earth elements (LREE) are strongly enriched (La/Sm_{pm}=6.2) whereas the heavy rare earth elements (HREE) are moderately enriched (Gd/Yb_{pm}=2.56). Trace element concentrations are generally enriched, ranging from approximately primitive mantle values for the HREE up to enrichment factors 100 times greater for the incompatible element Th. The felsic layers of the high strain zone are also characterized by a large, negative Ti (Ti/Ti*=0.09) anomaly, and by moderately negative Nb (Nb/Nb*= 0.45) and Eu (Eu/Eu*=0.44) anomalies.

3.6.4.3 Southern Homogeneous Metagranodiorite

Light grey, medium, even grained, homogeneous rocks observed in the southern part of the belt define discontinuous layers which are interlayered and folded with banded amphibolites, mafic dykes, and a thick quartz-feldspar-biotite-garnet schistose/gneissic layer. The homogeneous rocks are interpreted to be intrusive in origin and a $^{207}Pb/^{206}Pb$ igneous age of ~2895 Ma was determined by zircon geochronology (see Chapter 2).

Classifying this unit based on mineral assemblages is difficult as plagioclase and alkali feldspars are both untwinned and are not easily distinguished. Geochemically, samples from this unit have dacitic to rhyolitic, or granodioritic to granitic, compositions (Fig. 3.15). Major and trace element analysis of representative samples are reported in Table 3.1. The rocks have SiO_2 contents of 66-74% and Mg-numbers of 11-38. The unit has CIA values which range from 46-55 and fall within the range observed in unweathered granitiods (45-55; Bolhar et al., 2005).

The homogeneous granodioritic rocks define a distinct and unusual pattern on a primitive mantle normalized multi-element diagram (Fig. 3.16). Trace element concentrations are generally enriched at greater than 10 times primitive mantle values for both incompatible and more compatible elements. The pattern is remarkably flat (La/Sm_{pm}=0.58-1.25; Gd/Yb_{pm}=0.66-0.92), except for large negative Nb (Nb/Nb*=0.51-0.93) and Ti (Ti/Ti*=0.03-0.32) anomalies, large to moderate negative Eu anomalies (Eu/Eu*=0.28-0.70), and a moderate positive Zr (Zr/Zr*=1.13-1.65) anomaly.

The trace element patterns of the homogeneous granodioritic rocks are similar to typical signatures of A-type granites, which exhibit strong depletions for Ti, negative Nb anomalies, and similar enrichment factors for LREE and HREE (Fig. 3.16). A-type granites can be peraluminous ($Al_2O_3 > Na_2O + K_2O + CaO$) and are characterized by high Fe/Fe+Mg ratios (Blatt and Tracy, 1996); the Ivisârtoq samples exhibit both of these traits.

3.6.4.4 Quartzofeldspathic Layer in Marker High Strain Zone

A high strain zone composed of an intensely deformed layer of quartzofeldspathic rocks intercalated with a thin amphibolite horizon, and a layer of ultramafic schists, termed the magnetic marker, is used as the dividing feature separating the northern and southern parts of the Ivisârtoq greenstone belt. The quartzofeldspathic layer, ranges in width from 20 m to 150 m with an average width of 100 m, and has a strike length of at least 8 km. Towards the west, this unit is continuous with the thick, southern quartzofeldspathic unit. The units which are found in the Marker High Strain Zone are strongly deformed; thus primary textures are typically not preserved.

Based on mineral assemblages, geochronology, and field association, the intensely deformed quartzofeldspathic layer is interpreted to have a sedimentary origin (see Chapter 2). A $^{207}Pb/^{206}Pb$ depositional age of <2895 Ma was obtained by zircon geochronology (see Chapter 2). Locally the quartzofeldspathic layer is homogeneous and exhibits an equigranular texture, attributed to recrystallization.

Major and trace element analysis of representative samples are reported in Table 3.1. In the dominant felsic layers, SiO_2 contents range from 69-73% and Mg-numbers from 33-56. In the mafic layers SiO_2 is 50-53% and the Mg-number is 42-48.

Quartzofeldspathic samples from the Marker High Strain Zone have CIA values of 58 to 61, somewhat greater than felsic igneous rocks which have values of 45-55 (Bolhar et al., 2005). Figure 3.18 shows their Al enrichment trend on an A-CN-K diagram. This is consistent with a sedimentary parentage for the unit.

Samples from the felsic layer within the Marker High Strain Zone define a distinct pattern on a primitive mantle normalized multi-element diagram (Fig. 3.17). Trace element concentrations are generally enriched and strongly fractionated (La/Sm_{pm}=4.63-8.29; Gd/Yb_{pm}=2.25-4.22), ranging from approximately primitive mantle values for the HREE up to enrichment factors of 100 times greater for the incompatible element Th. The most incompatible elements (Th-La) define a concave upward trend due to large negative Nb (Nb/Nb*=0.14-0.22) and Ta (Ta/Ta*=0.11-0.34) anomalies. The felsic layer of the Marker High Strain Zone is also characterized by large, negative Ti (Ti/Ti*=0.04-0.31) anomalies, and moderate negative Eu (Eu/Eu*=0.68-0.82) anomalies.

The quartzofeldspathic layer is geochemically similar to Archean tonalite-trondhjemite-granodiorites (TTG). Archean TTG's are typically rich in SiO_2 and Al_2O_3 and have low Fe_2O_3* + MgO + MnO + TiO_2 contents (<5%) (Martin, 1994). They are also characterized by low transition-element contents (Ni = 14 ppm; Cr = 29 ppm; V = 35 ppm) and negative Nb, Ta, and Ti, anomalies (Martin, 1994). Archean TTG's also display low Yb contents and strongly fractionated LREE and HREE trends (Martin, 1994; Fig. 3.17). The similarities between the felsic layer in the Marker High Strain Zone and Archean tonalite-trondhjemite-granodiorites (TTG) suggest that TTG's may have been a major component of the sedimentary material comprising the unit. Differences in composition between the felsic layer of the Marker High Strain Zone and the thick southern quartzofeldspathic unit likely reflect differences in concentrations of different sedimentary constituents.

Two samples from the mafic bodies within the quartzofeldspathic layer within the Marker High Strain Zone have patterns similar to each of the northern homogeneous pillow basalts and the southern banded amphibolites primitive mantle normalized multi-element diagrams (Fig.3.17).

3.6.4.5 Southern Thick Quartzofeldspathic Unit

A thick (~500 m) quartz-feldspar-biotite-garnet schist/gneissic layer is a dominant unit within the southern part of the belt (Fig. 3.2). Thin mafic horizons are intercalated with the quartzofeldspathic rocks. The felsic unit has a brown-coloured weathered surface and reflects various intensities of deformation with fabrics ranging from strong schistosity to gneissic banding. Based on geochronological evidence of more than one age population, mineral assemblages, and field textures, including felsic clasts interpreted to be primary in origin, this unit is interpreted to have been derived from a sedimentary protolith. A $^{207}Pb/^{206}Pb$ depositional age of <2895 Ma was obtained by zircon geochronology (see Chapter 2).

Major and trace element analysis of representative samples are reported in Table 3.1. SiO_2 contents range from 63-66%; Mg-numbers from 38-43; and CIA values range from 58-65 (Fig. 3.18: A-CN-K diagram), which is consistent with a sedimentary parentage for the unit. A thin mafic layer intercalated with the quartzofeldspathic rocks has SiO_2=50% and Mg-number= 32.

Samples from two localities within the thick quartzofeldspathic unit define different patterns on a primitive mantle normalized multi-element diagram (Fig. 3.19a).

Trace element concentrations from locality MM01-81 (samples a and c) are generally enriched (typically 10 times greater than primitive mantle values). The most incompatible elements (Th-La) define concave upward trends, whereas the elements Sm through to Eu define concave downward trends. The more compatible elements (Gd-Lu) are unusually enriched (~15 times primitive mantle values) and define flat patterns ($Gd/Yb_{pm} \approx 0.84$). The thick quartzofeldspathic layer is also characterized by a significant negative Ti ($Ti/Ti^* \approx 0.29$) anomaly, and a moderate negative Eu anomaly ($Eu/Eu^* \approx 0.50$). The trace element patterns of the MM01-81 samples are similar to southern homogeneous light grey rocks which classify as granodiorites (Fig. 3.19a) and have trace element patterns resembling A-type granites.

The trace element concentrations from sample MM01-91 are similar to MM01-81 except that the HREE are more depleted (~4 times primitive mantle). The LREE are moderately fractionated ($La/Sm_{pm}=3.28$) and the HREE little fractionated ($Gd/Yb_{pm}=1.14$). The most incompatible elements (Th-La) define concave upward patterns, whereas the elements Sm through to Eu define concave downward patterns. The thick quartzofeldspathic layer is also characterized by moderate negative Ti ($Ti/Ti^*=0.52$) anomalies, and moderate negative Eu anomalies ($Eu/Eu^*=0.65$). The trace element pattern of the MM01-91 sample is intermediate between the enriched samples of the quartzofeldspathic horizon in the Marker High Strain Zone and samples of MM01-81. The difference between the MM01-81 samples and sample MM01-91 may reflect differences in concentrations of different sedimentary constituents; the homogeneous

metagranodiorite (with A-type granite trace element concentrations) may be a major component of the MM01-81 samples, whereas granitiods with low HREE contents may be a major component in sample MM01-91.

Thin mafic units intercalated with the quartzofeldspathic rocks have patterns similar to the banded amphibolites on a primitive mantle normalized multi-element diagram (Fig.3.19b).

3.7 DISCUSSION

2.7.1 Northern Part of Belt

3.7.1.1 Northern Mafic Volcanism

The northern part of the Ivisârtoq greenstone belt is dominated by two types of amphibolites derived from homogeneous and variolitic pillow basalts. The units are interbedded and are therefore interpreted as being contemporaneous. However, they differ in several key geochemical characteristics: the homogeneous pillow basalts have a more restricted range of low Ni (67-152 ppm) and Cr (216-406 ppm) concentrations and they do not have negative Nb and Ta anomalies; the variolitic basalts have a larger range of high Ni (90-420 ppm) and Cr (394-1862 ppm) concentrations and have negative Nb and Ta anomalies ($Nb/Nb^* = 0.38\text{-}0.67$; $Ta/Ta^* = 0.35\text{-}0.49$). The two units have overlapping MgO values (3.2-10.9 wt%; Fig. 3.20). A third type of northern amphibolite was recognized geochemically, but is only represented by one sample. The sample is komatiitic in composition, similar to some samples analysed by Hall (1981; Fig. 3.3). The sample has a higher MgO (18.2 wt%), Ni (725 ppm) and Cr (2907 ppm) values than the

homogeneous and variolitic basalts (Fig. 3.20). However, the sample does exhibit a similar extended REE pattern as the variolitic basalts (including negative Nb and Ta anomalies) except that the trace elements are more depleted overall (Fig.3.5). Due to the identification of only one komatiitic basalt in this study, and the limited number of trace elements analysed in komatiites by Hall (1981) it is difficult to interpret their petrogenesis.

Variolitic pillow basalts

The negative Nb and Ta anomalies of the variolitic basalts, coupled with the incompatible element (LREE) enrichment and negative Ti anomalies, produce an overall chemical signature similar to rocks formed by the addition of a crustal component to a mantle-derived magma. The crustal addition can result from the modification of the mantle source region by crustal-derived fluids or melts, for example during subduction-related, metasomatic processes (Pearce et al., 1995), or through the assimilation of crustal material during passage of mafic/ultramafic magma through the continental crust (Arndt and Jenner, 1986). Other processes which could affect these elements and possibly mimic crustal addition trends, are alteration and metamorphism (highly unlikely in this case, as discussed in the Methodology section), and derivation from a heterogeneous mantle source that contained recycled crustal material, for example in a rising mantle plume.

Heterogeneous mantle plume model

This model involves the incorporation of recycled ocean crust, plus or minus sedimentary rocks and/or lithospheric mantle, into a heterogeneous plume that rises from the lower mantle and melts when it reaches shallow depths. The model has been used to explain a spectrum of negative to positive Nb and Th anomalies obtained from tholeiites within the Archean Wawa greenstone belt, in the Superior Province, Canada (Polat et al., 1999). A heterogeneous mantle plume model is not thought to be appropriate for the formation of the variolitic pillow basalts in the Ivisârtoq greenstone belt based on the following geochemical evidence.

Assimilation of crustal material by mantle-derived magma during ascent commonly generates trends of increasing SiO_2, Al_2O_3/TiO_2, La, Th, Th/Ce, and La/Sm_{pm}, and decreasing Nb/La, Mg-number, Ni, Cr, Nb/Th, and Nb/Ta with progressive contamination (McCuaig et al., 1994; Kerrich et al., 2000). Oxides, elements, and ratios that increase with contamination are enriched in the crust relative to the mantle, whereas those that decrease are comparatively depleted in the crust. As a result, crustal assimilation models predict a negative correlation between Nb/Th and La/Sm_{pm}, and positive correlations between Th/Ce and La/Sm_{pm}, and between Al_2O_3/TiO_2 and La/Sm_{pm}; all of which are exhibited by the variolitic pillow basalts (Fig. 3.21). These trends are typically not seen in rocks formed from a heterogeneous mantle plume (Polat et al., 1999; Kerrich et al., 1999; Kerrich et al., 2000). In contrast, this mechanisml commonly produces little or no correlation at all between Nb/Th, Th/Ce and La/Sm_{pm} (Kerrich et al., 1999; Kerrich et al., 2000). This is because compositions of magmas derived from

heterogeneous mantle sources depend not only on the amount of recycled crustal components but also on the extent and depth of melting.

Crustal addition: Assimilation of crust versus subduction-related processes

Determining the process by which crustal material was added to mantle-derived magma, in particular by crustal assimilation or through subduction-related processes, is difficult due to the similar chemical signatures produced by these two models. Geological constraints (such as the presence of crustal xenoliths in basalts) have typically been used to favour one model over the other (e.g. Green et al., 2000). However, Bolhar et al. (2003) demonstrated that incompatible trace element ratios that are insensitive to alteration, metamorphism, melting conditions, and fractional crystallization can be used to distinguish between the two processes. Using a La/Sm_{pm} versus Zr/Y diagram of Bolhar et al. (2003) it can be demonstrated that the variolitic basalts deviate from the field of oceanic arcs and have closer affinities with the field designated for basalts contaminated by crustal assimilation (Fig. 3.22).

Crustal contamination modelling

It is possible to make quantitative estimates of the extent of contamination in the variolitic pillow basalts using appropriate end-member components and mixing models. The most likely crustal contaminant would have been an Archean tonalite-trondhjemite-granodiorite (TTG) which was older than ~3165 Ma (which is the minimum age of the northern basaltic pillow lavas; see Chapter 2). A component of the Itsaq Gneiss complex

fits this criteria; therefore, a sample from the ~3650 Ma type-locality Amîtsoq gneiss was chosen as the crustal contaminant (Sample 155807; Kamber et al., 2002). A typical, uncontaminated, ~3 Ga high-Mg basalt (MgO=13.4 wt %; Sample KYT374 from the Red Lake greenstone belt, Superior Province; Tomlinson et al., 1998) was chosen as the mafic end-member for the variolitic pillow. This basalt end-member is somewhat depleted relative to primitive mantle with $(Nb/Th)_{pm} = 1.0$ and $(La/Sm)_{pm} = 0.48$. A komatiitic parent is considered unlikely, due to the generally low MgO concentration of the variolitic pillow basalts.

A mixing curve for crustal contamination can be generated using pairs of high field strength elements (HFSE) or REEs that have similar partition coefficients during typical basaltic petrogenesis and which have concentration ratios which differ in the contaminant and the mantle source (Green et al., 2000). The ratios Nb/Th and $(La/Sm)_{pm}$ are ideal as Nb/Th is much greater in the mantle and $(La/Sm)_{pm}$ is much greater in the crust; thus mixing produces a wide range of values. Basalts with higher Nb/Th are interpreted to be the least contaminated by crustal material. Using the high-Mg basalt and TTG end-members, it can be shown that the maximum level of contamination for the variolitic pillow basalts was 3-5% (Fig. 3.23). The results are dependent on the end-members chosen. In particular, if a more enriched basaltic end-member was involved, levels of contamination would be even less.

Ratios of other element pairs were considered to test the crustal contamination model for internal consistency. With increasing contamination Al_2O_3/TiO_2 and $(La/Sm)_{pm}$ should increase whereas Nb/Th, Ni and Cr should decrease. The expected negative trends

occur for Al_2O_3/TiO_2 versus Nb/Th, and positive trends for Al_2O_3/TiO_2 versus $(La/Sm)_{pm}$ (Fig. 3.23). A mixing curve generated using the same mafic and felsic end-members for the variolitic pillow basalts corresponds with the maximum level of contamination (3-5%).

On plots of Ni and Cr versus Nb/Th and $(La/Sm)_{pm}$, there is considerable scatter of data for variolitic pillow basalts (Fig. 3.24). The scattering is likely the effect of dilution and mobility of Ni and Cr during hydration and secondary alteration, which is consistent with the erratic distribution of these elements and with samples having a very low Ni and Cr where LOI>1.5% (Fig. 3.24). In order to assess the Ni and Cr more critically, the mixing curves were plotted using the Cr/Ni ratio. Variolitic basalts plot consistently on the low Cr/Ni side of the mixing curves (Fig. 3.25). It is unlikely that this is the result of alteration because scatter both above and below the mixing curve would be expected. Instead the data indicate that the variolitic basalts underwent fractional crystallization of chromite during or before crustal contamination. Removal of chromite from the magmatic liquid will result in decreased Cr/Ni ratios.

Komatiitic basalts

The major element chemistry of the 14 komatiitic basalt samples studied by Hall (1981) did not, unfortunately, also include detailed trace element data. One sample with komatiitic basalt composition was identified in this study. This sample has a primitive mantle normalized trace element pattern similar to the variolitic basalts although it is generally more depleted (Fig. 3.5). It plots with the variolitic pillow basalts on a Nb/Th

versus $(La/Sm)_{pm}$ diagram (Fig. 3.21). However, the sample has higher MgO (18 wt %), Ni (~720 ppm), and Cr (~2900 ppm) values than the variolitic basalts. These differences indicate that the sample with komatiitic composition did not assimilate the same amount of crustal material as the variolitic basalts.

Homogeneous pillow basalts

The homogeneous pillow basalts do not exhibit LREE enrichment or Nb and Ta anomalies (Fig. 3.5). They are therefore not considered to have assimilated crustal material, to have formed above a subduction zone, or to have been derived from a compositionally heterogeneous mantle plume. The Ni and Mg-number values (Fig. 3.26) of the homogeneous pillow basalts reflect a "submarine plateau trend" as defined by Condie (1994). In contrast with the variolitic pillow basalts, Ni does not seem to have been mobilized extensively during secondary alteration. Ni exhibits a coherent linear trend on a bivariant element plot with Zr (Fig. B.2) and does not decrease with an increase in LOI (Fig. 3.24). Condie (1994) noted that a trend in which Ni decreases very little with Mg-number (i.e. Mg-number = 45 corresponds with Ni = 80-100 ppm) is characteristic of modern submarine plateau basalts; it has also been recognized in continental flood basalts of various ages. Condie (1994) suggested that the high-Ni trend of these basalts may be characteristic of mantle plumes, where temperature is higher than ambient mantle, and thus the Ni content of derivative basaltic magma is greater (Arndt, 1991). A modern subduction trend, which includes most arc-related basalts would be characterized by Ni decreasing rapidly with falling Mg-number (Fig. 3.26).

Two gabbroic dykes in the northern part of the belt have the same major and trace element compositions as the homogeneous pillow basalts (Table 3.1, Fig. 3.8). These similarities suggest that these dykes may represent feeder dykes for the homogeneous pillow basalts; however, cross-cutting field relationships indicate otherwise. These dykes post-date isoclinally folded ultramafic sills and ~3165 Ma tonalitic sheets. The similarity in chemical compositions between the two gabbroic dykes and the homogeneous pillow basalts may indicate that they are related to the same magmatic event. The magmatism may have lasted over a protracted period of time, both before intrusion of the northern ultramafic sills and tonalitic units, and continuing afterwards. Detailed geochronological studies would be needed to confirm this hypothesis.

Are the homogeneous and variolitic pillow basalts related?

An important question is whether the two main types of interbedded northern pillow basalts, which are interpreted as being contemporaneous, are related to a common magma source, such that the homogeneous pillow basalts are the uncontaminated parent magmas of the variolitic basalts. The homogeneous basalts are interpreted as being uncontaminated based on their flat LREE patterns and lack of negative Nb and Ta anomalies.

According to the mixing diagram in Figure 3.23, which plots both homogeneous and variolitic pillow basalts, this proposed relationship is unlikely. The homogeneous pillow basalts do not plot on the mixing curve generated using a high-Mg basalt and a sample of the ~3650 Ma type-locality Amîtsoq gneiss (Sample 155807; Kamber et al.,

2002) as end-members. If a depleted (high Nb/Th, low La/Sm_{pm} ratios) homogeneous Ivisârtoq sample is used as the mafic end-member, a distinct mixing curve is generated and the variolitic pillow basalts do not plot on this curve (Fig. 3.27). Except for one sample the data are consistent with trivial (<2%) crustal contamination.

Furthermore, if the homogeneous pillow basalts represent the uncontaminated parent of the variolitic pillow basalts, then the homogeneous pillow basalts should have *higher* MgO, Ni, and Cr contents; as these elements become diluted during crustal contamination. This is not observed (Fig. 3.20). The homogeneous pillow basalts tend to have *lower* Ni and Cr concentrations and overlapping MgO values compared to the contaminated variolitic pillow basalts (Table 3.1). The lower Ni and Cr values of the homogeneous pillow basalts cannot be attributed to dilution by hydration processes, as demonstrated on a Ni, Cr, versus LOI plot (Fig. 3.24).

It appears more likely that the homogeneous basalts were derived from a different mantle source than the variolitic basalts. Their lower MgO, Ni, and Cr contents suggest that they formed at shallow depths or by smaller degrees of melting in the mantle than the variolitic basalts. The contrasting amounts of felsic crustal contamination in the variolitic and homogeneous basalts may be a reflection of different magmatic plumbing systems and the nature of the crust through which the magmas intruded. The crust may have been immature (i.e. tonalite arc as described by Condie, 1980), and rifted and dispersed, in which case it would be thinner and more heterogeneous, containing a higher proportion of mafic material than typical mature sialic continental crust. The parent magma of the homogeneous pillow basalts may have intruded through a more mafic-rich

portion of crust or have been insufficiently hot to melt and assimilate the country rock. In contrast, the minor crustal contamination signature (3-5%) of the variolitic pillow basalts may reflect hotter parent magmas or intrusion through more fusible felsic components of the thin, immature crust.

3.7.1.2 Northern Ultramafic Magmatism

Distinctive yellow-brown-weathering ultramafic layers are the most prominent feature in the northern part of the Ivisârtoq greenstone belt. The two most extensive layers define isoclinal folds with east-west trending axial planes, referred to as the inner (most westerly) and the outer (most easterly) isoclinal layers. Based on their petrographic similarity to each other, intensely deformed boundaries, and apparent sequential repetition with different kinds of basaltic pillow lavas (Fig. 3.2) it was thought that the ultramafic layers could have been a thrust-repeated sequence (see Chapter 2). This would imply that all of the layers could be derived from a single layer and should therefore have overlapping compositions. This assessment is not easy, however, because the whole rock compositions of the ultramafic layers tend to be much more disturbed by secondary alteration and metamorphism than the basaltic pillow lavas. Most of the minerals are metamorphic in origin; fortunately however, remnant igneous olivine grains are present.

Remnant igneous olivine grains from the inner and outer layers were analysed using an electron microprobe. These grains have reacted to form serpentine along grain boundaries and within cracks which is attributed to the infiltration of fluids. Parts of grains separated by serpentine-filled cracks are optically continuous, thus demonstrating

that they were part of a single original igneous grain (Fig. 3.28). These grains are unzoned (see backscattered images, Fig. 3.28), do not exhibit coronas, and their Ni and Cr concentrations are relatively homogeneous across the grains, from core to rim (see Table 3.2). These observations suggest that Ni and Cr were not redistributed during hydrothermal events and can reflect primary magmatic compositions.

Remnant olivine grains from the two large inner and outer layers (Fig. 3.28) have different chemical compositions (Table 3.2); they define separate groups on a Ni versus MgO plot (Fig. 3.29). The olivine groups do not define a trend consistent with fractionation of a common source, i.e. decreasing Ni content with decreasing MgO, instead they range from high Ni, low Mg olivine to low Ni, high-Mg olivine. Furthermore, if the MgO and Ni whole rock data from the ultramafic layers are compared with their respective olivine compositions, inner and outer layer samples define crossing trend lines (Fig. 3.29). These trends reflect a mixing array between olivine (high Ni, high MgO) and a magmatic component with lower Ni and MgO values, possibly trapped melt and pyroxene in the original cumulates. Samples which are olivine-rich plot closer to the olivine end-member. The fact that whole rock and olivine data of the two ultramafic layers define crossing MgO-Ni trends suggests that they formed from different parent magmas implying that these layers were not derived from a single layer by thrust-stack repetition.

The olivine data may also be used to determine the origin of these layers; i.e. do they represent mafic or ultramafic sills, parts of differentiated komatiitic flows, or tectonic slices of Archean mantle? The Fo contents of the olivine grains (Fo_{82-88}) are

significantly lower than what is expected for mantle olivine grains (Fo_{90-94}; McGetchen et al., 1981); therefore, they are not thought to represent slices of the mantle.

Based on their cumulate textures and inclusion of banded amphibolite horizons (see Chapter 2), the ultramafic layers are not thought to represent the more melt-rich portions of komatiitic flows. They more likely represent mafic/ultramafic sills or the cumulate portions of differentiated komatiites. This can be assessed geochemically by using olivine compositions to estimate the MgO content of the parent magma of the ultramafic layers. If the layers represent cumulate portions of komatiitic flows, a parent magma with high (>18%) MgO (i.e. komatiitic composition) would be expected.

In order to determine the MgO content of the parent liquid from olivine forsterite (Fo) contents, the olivine-liquid Mg-Fe distribution coefficient (K_D) and the FeO content of the liquid from which the olivine crystallized are needed (Nisbet et al., 1993). The FeO content of the liquid can be difficult to determine; however, it is commonly assumed to correspond to the whole-rock FeO content; an assumption which is correct if the rock is not a cumulate (Nisbet et al., 1993). In this study the ultramafic rocks in question are assuredly cumulates; therefore, the average FeO content of the most likely parent magmas of these rocks, the northern amphibolites derived from tholeiitic and komatiitic basalts, was used. Although there are several types of northern amphibolites (homogeneous, variolitic, and komatiitic), they all have remarkably similar FeO values at MgO of 9-22%. Based on data from this study and Hall (1981), an average value of FeO = 11% was determined (Fig. 3.30). A curve representing the forsterite content of olivine

in equilibrium with a parent liquid with FeO = 11% was generated (Fig. 3.31) using an olivine-liquid Mg-Fe distribution coefficient (K_D) of 0.33 (Bickle, 1982).

A rock that formed directly through crystallization of a magnesian liquid would contain olivine grains with a range of compositions reflecting various stages of differentiation. If the most magnesian olivine grain from a sample plots on an olivine-liquid equilibrium curve, this indicates that the MgO content of the whole rock is that of the liquid from which the olivine crystallized; if the olivine plots below the curve, this indicates that the rocks have accumulated olivine (Révillon et al., 2000). The MgO content of a liquid in equilibrium with an individual olivine grain, or group of olivine grains, can be read directly from the diagram (Fig. 3.31). Using the least differentiated (highest MgO) olivine from each sample in the ultramafic layers, it can be seen that the MgO of their parent magmas ranged between 9-16%. Based on this test, the ultramafic layers were not derived from a komatiitic (Mg>18 wt%) magma and are therefore not thought to represent cumulate portions of komatiite flows. The derived MgO content of the parent magma composition of the layers corresponds well with the assumed parent of the variolitic pillow basalts (MgO =13.4%; sample KYT374; Tomlinson et al., 1998).

In order to assess whether the ultramafic layers and the variolitic pillow basalts are derived from similar parent magmas, the Ni content of olivine in the ultramafic layers may be modelled. This model involves calculating Ni expected in the olivine grains of the ultramafic rocks assuming that they crystallized from magmas with the Ni content of the variolitic basaltic parent magma. The Ni content of the variolitic pillow basalts is lower than in its parent magma because of crustal contamination. Therefore, a value from

a similar, but uncontaminated rock (i.e. KYT374 from Tomlinson et al., 1998), must be assumed as the parent magma concentration.

An equation is needed to describe how Ni partitions between olivine and silicate melt $D_{Ni}^{Ol/Liq}$. Kinzler et al. (1990) developed the following equation which is accurate to ± 13%:

$$\ln((D_{Ni}^{Ol/Liq} / X_{Fo}^{Ol}) = 3.355 - 1.263 \ln X_{MgO}^{Liq}$$

where, X_{Fo}^{Ol} represents the Fo content of the olivine grain and X_{MgO}^{Liq} represents the MgO concentration of the liquid. Using the minimum and maximum MgO concentration of the parent liquid of the ultramafic layers (16 and 9%), obtained above, and the corresponding measured Fo content of the olivine grains in the layers (Fo=0.88 and Fo=0.808, respectively), $D_{Ni}^{Ol/Liq}$ was calculated to be 12.7-24.1. Using these values and the Ni values of the assumed parent magma of the variolitic pillow basalt (209 ppm; sample KYT374 from Tomlinson et al., 1998), the expected Ni concentration in the olivine grains in the layers is between 2655-5041 ppm. The range overlaps with the most primitive (i.e. highest) Ni values (1742-2984 ppm) measured for these olivine grains. Low Ni olivine grains probably formed from more differentiated magmas. Based on these calculations, the ultramafic layers likely formed from discrete pulses of high-Mg basalt (9-16%) which formed sills. They could have formed from the same parent magma as the variolitic pillow basalts.

3.7.1.3 Northern Felsic Magmatism

Thin, rusty, northern layers of the quartzofeldspathic schists and gneisses have previously been interpreted as deformed acid-intermediate tuffaceous metasedimentary rocks (Chadwick, 1990). The protoliths of these units have been re-evaluated using new field and geochemical evidence.

Northern, rusty quartzofeldspathic layers

Rusty quartzofeldspathic sheets were observed adjacent to northern ultramafic layers and locally within the northern amphibolites, the tonalitic marker horizon, and the magnetic marker. Based on their geochemical compositions (e.g. average CIA= 50, excluding one outlier; Fig. 3.18), cross-cutting field relationship with basaltic pillow lavas, and remnant igneous textures, these layers are thought to represent tonalitic intrusions.

Field relationships suggest that these layers did not intrude at the same time; some may have intruded before the first deformational event which affected the northern part of the belt (DN_1), and some may have formed after the isoclinal folding event (DN_2) (see Chapter 2). Two pre-DN_1 layers yielded an igneous $^{207}Pb/^{206}Pb$ age of ~3165 Ma (see Chapter 2). Despite their differences in relative age, all of the layers have similar geochemical compositions and these patterns are notably different from the other quartzofeldspathic units within the belt.

3.7.2 Southern Part of Belt

3.7.2.1 Southern Mafic Magmatism

The southern part of the Ivisârtoq greenstone belt is dominated by banded amphibolites that are derived from basaltic pillow lavas. They share several characteristics with the variolitic basalts of the northern part, but there are also some key differences between these units. Similar to the variolitic basalts, the banded amphibolites are enriched in LREE and have significant Nb, Ta, and Ti anomalies; however, these features are more pronounced in the banded amphibolites (Fig. 3.5). The banded amphibolites also plot within the crustally contaminated greenstone field on the La/Sm_{pm} versus Zr/Y diagram (Fig. 3.22). These similarities suggest that the banded amphibolites are more extensively contaminated by assimilation of crustal material than the northern amphibolites. Like the northern amphibolites, the protolith of the banded amphibolites are not thought to have formed from a heterogeneous mantle containing recycled crust, as they exhibit a negative correlation between Nb/Th and La/Sm_{pm}, Th/Ce and Nb/Ta, and between MgO and La/Sm_{pm} (Fig. 3.21). These correlations are consistent with crustal contamination.

Based on these similarities one might consider that the southern banded amphibolites and the northern variolitic basalts could be related to the same parent magmas, the only difference between the two units being the degree of crustal contamination, with the banded more crustally contaminated than the variolitic basalts. However, the fact that the two units have overlapping MgO, Ni and Cr values, for the least hydrothermally altered samples (lowest LOI) suggests that they are not related in

this way (Fig. 3.20; 3.24). If they were, one would expect the banded amphibolites to have more diluted Mg, Ni, and Cr contents, as these elements are comparatively depleted in the crust. The two units also define separate trends on immobile variation plots such as P_2O_5 versus Zr (Fig. 3.6). This supports the idea that the northern and southern basalts are derived from separate magma sources.

The source of the southern banded amphibolites was likely more Mg-rich and contained higher amounts of Ni and Cr than the parental magma of the northern variolitic basalts. The banded amphibolites were therefore likely derived from partial melting at greater depths or from larger degrees of melting than the variolitic basalts. Their parent magmas may have been komatiitic in composition. Mixing lines of Nb/Th, $(La/Sm)_{pm}$, and Al_2O_3/TiO_2 generated using an uncontaminated komatiitic composition (AUK average from Sproule et al., 2002) as the mafic end-member and an example of a TTG from southwest Greenland (sample of ~3650 Ma type-locality Amîtsoq gneiss from the Itsaq Gneiss Complex) as the felsic end member, indicate that a hypothetical komatiitic parent of the banded amphibolites would have assimilated between 15-23% crust (Fig. 3.32). A sample of ~3650 Ma type-locality Amîtsoq gneiss was chosen as the felsic contaminant based on geochronological evidence which suggests that mafic dykes in the southern part of the belt may have inherited zircon material from a component of the Itsaq Gneiss complex (see Chapter 2, section 2.5.2.3). Similar to the northern variolitic pillow basalts, mixing models using Cr/Ni versus Nb/Th or $(La/Sm)_{pm}$ are not consistent with crustal contamination (i.e. the data does not fit on a mixing curve, mainly falling toward the low Cr/Ni side; Fig. 3.33). As in the northern variolitic basalts, the observed

trends likely relate to the fractional crystallization of chromite, whereby the removal of chromite causes a decrease in the Cr/Ni ratio with increased crustal contamination.

3.7.2.2 Southern Ultramafic 'Volcanism'

Ultramafic magmatism in the southern part of the Ivisârtoq greenstone belt is restricted to the magnetic marker layer which is notably different from the ultramafic, cumulate sheets in the northern part of the belt. The schistose magnetic marker layer is located in the Marker High Strain Zone and has been disturbed by alteration and serpentinization. As discussed in Section 3.6.1, the trace elements in these samples are considered immobile based on bi-element plots against Zr (e.g. Fig. B6), and are not thought to have not been affected by these processes. TiO_2 and P_2O_5 are also considered immobile (Fig. B5). Other elements, such as NaO and CaO, have obviously been modified and show great disturbance on bi-element plots (Fig. B5). Although MgO does show a small degree of scatter on a bi-element plot against Zr, its pattern more closely resembles the coherent patterns of the immobile elements. In this study MgO is interpreted as being primary in nature.

The magnetic marker may be volcanic in origin and is geochemically classified as meymechite, an alkaline-ultramafic rock. The alkaline nature of the magnetic marker is well demonstrated by the contents of some of the less mobile trace elements (Table 3.1). According to Shervais (1982), alkali magmas have Ti/V ratios typically in excess of 50. The Ti/V ratio, which is unaffected by most conditions of metamorphism and alteration, is a particularly effective discriminant of source environment, at least partly because of

the inverse dependence of vanadium compatibility on oxygen fugacity. The magnetic marker samples, with an average Ti/V of 77, are highly alkaline.

The Ivisârtoq meymechites are significant as worldwide alkaline ultramafic extrusive rocks are volumetrically insignificant and previously unreported in the Archean. The timing of emplacement of alkaline-ultramafic rocks relative to subalkaline mafic/ultramafic rocks differs in different occurrences worldwide. The meymechite-carbonatite rocks reported from the Paleoproterozoic Cape Smith Belt, Quebec and from Castignon Lake, Labrador Trough (both within the Circum-Superior Belt, Canada) lie at the base of their respective volcanic assemblages, and are among the earliest magmatic activity in each area (Baragar et al, 2001; Dimroth, 1970). In contrast, the type-locality Triassic meymechites capping the Siberian basalt plateau (Arndt et al., 1995; Arndt et al., 1998), and the Tertiary nephelinites and basanites capping the East Greenland basalt plateau and nunataks (Brooks et al., 1979; Brown et al., 1996; Bernstein et al., 2000) were emplaced late in the formation of their respective igneous provinces.

It is difficult to determine the stratigraphic position, and thus timing of emplacement of the magnetic marker within the southern part Ivisârtoq greenstone belt. The unit does not contain minerals (such as zircon) suitable for dating using U-Pb geochronological techniques. Due to the strongly deformed nature of the southern part of the belt, primary features (pillow lava structures or sedimentary bedding) which would indicate way-up were not observed. However, if the southern part of the belt is interpreted as a simple layer-cake stratigraphy, as concluded by Chadwick (1990), with

north as the way-up, then the magnetic marker would be the upper-most (youngest) volcanic unit.

Cryptic primary layering

Alkaline-ultramafic rocks of diverse composition (e.g. ankaramites, trachybasalts, mela-nephelinites, and meymechites) in Siberia are thought to be associated with the same magma source (Fedorenko and Czamanske, 1997; Arndt et al., 1998; Fedorenko et al., 2000). The Siberian alkaline-ultramafic rock types have similar REE trends and define a trend towards depleted mantle compositions on a La/Sm versus Sm/Yb plot (Fig. 3.34). Fedorenko et al. (2000) suggested that this trend represents magmas formed by increasing degrees of melting in the same source region, whereby the rocks with lower Sm/Yb and La/Sm ratios were generated by the greatest amount of melting.

On a La/Sm versus Sm/Yb plot (Fig. 3.34) the magnetic marker samples plot off the trend line defined by Fedorenko et al. (2000) and two groups are defined. The two groups also differ in major element composition; the two samples with higher Sm/Yb ratios (samples IV03-23, IV03-24) have higher MgO and TiO_2 contents. They are situated in the northern part of the magnetic marker (Fig. 2.59). The two geochemical groups may thus define cryptic primary layering. If north is assumed as the way-up, then the lower (southern) part of the magnetic marker is characterised by a picritic-meymechitic composition (lower MgO, and TiO_2 contents) and the upper (northern) part is true meymechite (higher Ti and MgO contents). A detailed geochemical transect across the unit would need to be done to support this idea.

Meymechite genesis

Geochemically, the magnetic marker samples clearly resemble meymechites from the type locality in Siberia. Therefore, a direct comparison is deemed appropriate and is used to determine the conditions of melting and the compositions of the mantle source of the magnetic marker.

Arndt et al. (1998) considered several aspects to constrain the genesis of the Siberian meymechites:

1. The high MgO, Ni, and Cr contents in the meymechitic liquids

2.Very high concentrations of incompatible trace elements.

3. Extremely low concentrations of moderately compatible major and trace elements (e.g. Al_2O_3/TiO_2 .1.1 in Siberian meymechites compared to ~20 in primitive mantle) and strongly sloping REE patterns.

In combination, these characteristics provide evidence for the melting conditions and composition of the source of the Siberian meymechites and a comparison can be used to constrain the nature of the source of the magnetic marker.

The high-MgO (~20 wt %), -Ni (~ 1053 ppm), and -Cr (~ 1292 ppm) contents of the magnetic marker suggest that the source contained olivine and had a dominantly peridotitic, rather than pyroxenitic or eclogitic composition (Arndt et al., 1998). These high compatible element concentrations coupled with the high concentrations of incompatible trace elements suggest that partial melting occurred at great depth in the stability field of majorite garnet (Arndt et al., 1998). This is substantiated by the very low Al_2O_3 content (Al_2O_3/TiO_2 ~2.8 for the magnetic marker), which in combination with

high MgO content, indicate that melting occurred at 8-10 GPa (a depth of 250-300 km, assuming a dry mantle; Arndt et al., 1998). If significant volatiles were present, the depths would be less. As pointed out by Arndt et al. (1998), the depleted signature for alumina also suggests that garnet is retained in the source during partial melting and that this also accounts for the high degree of fractionation of the heavy REE (HREE; $(Sm/Yb)_{pm}$ which averages 8.4 for magnetic marker samples and 3.6-11.9 for Siberia meymechites. Melting at great depth could be indicative of a thick overlying continental crust and mantle lithosphere; this is consistent with the geochemistry of the mafic components of the southern part of the belt.

Arndt et al. (1998) used differences in trace element ratios to provide further information about melting conditions and demonstrated that the depth of melting progressively changed during the course of the Siberian meymechitic-picritic magmatic event. This technique can also be applied to the magnetic marker wherein two groups (northern-higher MgO and southern-lower MgO) have been geochemically defined. Overall, $(Tb/Yb)_{pm}$ values of the northern magnetic marker samples are higher than southern samples, but at about the same Yb concentration (Fig. 3.35). In contrast the Siberian meymechitic suite trends from high $(Tb/Yb)_{pm}$ ratios at low Yb concentrations for true meymechites to lower $(Tb/Yb)_{pm}$ ratios at higher Yb for picrites. The trend is consistent with increasing degree of partial melting in the presence of garnet. For comparison, tholeiites commonly define a trend of decreasing Yb concentration at constant $(Tb/Yb)_{pm}$ with increasing degree of partial melting in a garnet-free source. Following the reasoning of Arndt et al. (1998), this suggests that the source of the

Ivisârtoq magnetic marker samples left a large proportion of garnet in its residue of melting which can be attributed to small degrees of melting at great depth. The similar low Yb for both the northern and southern magnetic marker samples suggests that they formed from similar small degree melts, but the higher $(Tb/Yb)_{pm}$ for the northern samples suggests melting at greater depths. The implication is that the deeper sources of the northern samples were more volatile-rich than the southern samples, reducing the solidus of the former and resulting in similar degrees of melting with increasing pressure. If the magnetic marker is stratigraphically positioned with north as the way-up, and if the two groups define cryptic primary layering, then the depth of melting may have progressively increased during the course of meymechitic magmatism at Ivisârtoq.

Comparison/relationship of banded amphibolites and magnetic marker

The principal magmatism of the southern part of the Ivisârtoq greenstone belt exhibits remarkable parallels with the Maymecha River basin, Siberia; however on a notably smaller scale. Similar to the Siberian magma series, the southern part of the belt contains two distinctly different magma series, tholeiitic and meymechitic, which appear to have formed in different parts of the mantle and seem to have behaved differently during passage from source to surface. The banded amphibolites likely developed from partial melting at moderate mantle depths and assimilated continental crust during ascent and/or within an open-system magma chamber. In contrast, the parental magmas of the magnetic marker originated from deeper sources and were not contaminated during ascent. Arndt et al. (1998) proposed that this difference in behaviour, as seen in Siberia,

may be due to the presence of volatiles associated with the more alkaline magmas. This may also be the case for the southern part of the Ivisârtoq greenstone belt.

Although the Ivisârtoq basaltic pillow lavas and meymechites are thought to have formed from different parts of the mantle, they may be genetically related, as proposed in Siberia. Arndt et al. (1995) compared Nd and Sr isotopic data of Siberian flood basalts (Wooden et al., 1993), which have crustally contaminated signatures, with Siberian meymechite data. The meymechite compositions lies on the extension of a linear trend defined by the isotopic compositions of Siberian flood basalts (Fig. 8 *in* Arndt et al., 1995). Based on this evidence, Arndt et al. (1995) suggested that meymechite melting was linked with the arrival of the mantle plume that was the source of Siberian basaltic flood volcanism. This relationship may also be true for the banded amphibolites and meymechites in the southern part of the Ivisârtoq greenstone belt, however, further work, including isotopic and possibly geochronological studies, would be needed to support this theory.

3.7.2.3 Southern Felsic Magmatism and Sedimentation

In the southern part of the Ivisârtoq greenstone belt, the thick quartzofeldspathic unit and continuous layer in the Marker High Strain Zone were previously interpreted as deformed acid-intermediate tuffaceous metasedimentary rocks (Chadwick, 1990). The homogeneous metagranodiorite unit had previously been unrecognized. The protoliths of these units have been re-evaluated using new field and geochemical evidence. The thick southern quartzofeldspathic unit and associated layer in the Marker High Strain Zone are

likely sedimentary in origin, however, the southern, homogeneous granodioritic rocks are thought to be intrusive in nature.

Southern homogeneous metagranodiorite

The trace element patterns of the light grey, homogeneous metagranodiorite unit are geochemically similar to typical A-type granite signatures: they exhibit strong depletions in P, Ti, and Nb, and comparable enrichment of LREE and HREE (Fig. 3.16). A-type granites can be peraluminous ($Al_2O_3 > Na_2O + K_2O + CaO$) and are characterized by high Fe/Fe+Mg ratios, high Ga contents (Fig. 3.36), and Ga/Al ratios (Blatt and Tracy, 1996); the Ivisârtoq samples exhibit all of these traits. A variance between the Ivisârtoq samples and typical A-type granites is that the most incompatible trace elements (Th to Pr) of the Ivisârtoq samples are generally less enriched than typical A-type granite concentrations.

A-type granites are not thought to originate through subduction-related or convergent plate processes, but result from remelting of materials that are residua of earlier melting episodes. A common geologic interpretation of their genesis is that they form in the interiors of stable continental plates (Blatt and Tracy, 1996); wherein highly differentiated felsic magmas can be generated by slow cooling in large magma chambers.

Southern metasedimentary rocks

Geochronology and field evidence (Chapter 2) suggest that the quartzofeldspathic layer in the Marker High Strain Zone and the thick quartz-feldspar-biotite-garnet

schist/gneissic unit in the southern part of the belt are part of a single deformed, metasedimentary package. Samples from these two layers differ in major and trace element geochemistry, which may reflect differences in concentrations of different constituents. Potential components from which detrital materials were likely derived include a ~3085 Ma TTG, the southern ~2895 Ma homogeneous metagranodiorite, which has trace element signature similar to an A-type granite, and southern amphibolites derived from pillow basalts. Initial comparisons of the trace element patterns revealed that an Archean TTG was likely a major component of the felsic horizon in the Marker High Strain Zone and in sample MM01-91 from the southern, thick quartz-feldspar-biotite-garnet schist/gneissic layer, whereas the homogeneous metagranodirorite (with A-type granitoid trace element concentrations) was likely a major component of the MM01-81 samples from the thick layer.

Mixing models, which combine different amounts of each source component, can be established using major (Fig. 3.37) and trace element concentrations (Fig. 3.38). The following combinations of components gives the best mass balances:

- *felsic horizon in the Marker High Strain Zone*:

  4% amphibolite, 1% metagranodiorite, 95% TTG;

- *sample MM01-91*: 40% amphibolite, 10% metagranodiorite, 50% TTG;

- *samples MM01-81*: 30% amphibolite, 35 % metagranodiorite, 35% TTG.

The interpretation that the samples from the thick, southern unit contain a higher percentage of mafic material can be confirmed using a mixing band (McLennan and Taylor, 1984; Taylor and McLennan, 1985) plotted on a La-Th-Sc ternary diagram (Fig.

3.39; Smith et al., 1992). The band was defined using geochemical compositions of Archean sedimentary rocks from greenstone belts in Australia and South Africa (McLennan and Taylor, 1984; Taylor and McLennan, 1985). The band represents different mixtures of material from a bimodal source of mafic volcanic rocks and sodic tonalite-trondhjemite gneiss (McLennan and Taylor, 1984). The felsic Marker High Strain Zone samples plot towards the La-apex, suggesting that the protolith was derived primarily from felsic material, whereas the samples from the thick, southern unit (samples MM01-81, -91) plot closer to the Sc corner, indicating that the protolith was likely derived from a mixture of felsic and mafic components.

The present spatial relationship of mafic horizons intercalated with the metasedimentary rocks is interpreted to be a purely tectonic relationship. These units are not thought to be contemporaneous based on geochronological data; the basaltic protolith of the banded amphibolites is older than ~3060 Ma whereas the depositional age of the sedimentary horizons is <2895 Ma (see Chapter 2). The difference in felsic and mafic component concentrations between metasedimentary samples may reflect the original proximity to the various sources. For example, the samples from the Marker High Strain Zone may have been distal to the A-type granitoid and amphibolitic source; their present geography and intimate association with the amphibolites may have been the result of later deformational events.

3.7.3 Tectonic Implications

The Ivisârtoq greenstone belt is surrounded by Archean gneisses and was formerly thought to be bounded by tectonic contacts; a relationship which is interpreted to be the result of early phase thrusting and subsequent large scale folding (Hall and Friend, 1979; Hall, 1981; Hall et al., 1987). However, whether these tectonic contacts represented deformation of an original cover-basement relationship or represent sutures bringing together originally unrelated rock units, has been the subject of considerable discussion.

Hall investigated this dilemma by studying Ameralik dykes within Amîtsoq gneisses (part of Itsaq gneiss terrain; Hall, 1981; Hall et al., 1987). Hall argued that if the Amîtsoq gneisses formed an early Archean continental crust through which the Ivisârtoq basic lavas were originally injected to form a cover to that crust, then basic feeder dykes of equivalent composition to the lavas should be preserved within the Amîtsoq gneisses. He noted that the Ameralik dykes were (at the time) the "only recognized basic intrusive rocks within the Amîtsoq gneisses" (Hall, 1981, pg. 398). Based on geochemical differences, Hall concluded that the Ameralik dykes could not have fed the Ivisârtoq metavolcanics, and ultimately concluded that the metavolcanics of the Ivisârtoq greenstone belt could not have been extruded originally through the Amîtsoq sialic 'continent' (Hall, 1981; Hall et al., 1987). He envisioned an oceanic setting for the formation of the belt.

New field work and major and trace element geochemical data presented here have greatly expanded on previous studies of the Ivisârtoq greenstone belt. This work

supports a new model in which amphibolites in the northern and southern parts of the Ivisârtoq greenstone belt were crustally contaminated, suggesting that an original cover-basement relationship between the older gneisses and greenstones existed.

3.7.4 New Model for the Ivisârtoq Greenstone Belt

The Ivisârtoq greenstone belt preserves a tectonostratigraphic sequence which consists of two main packages of rock, defined in this study as the northern and southern parts. The two parts are separated by a zone of intense deformation which represents a tectonic break. A quartzofeldspathic unit within this high strain zone and a layer of ultramafic schist, termed the magnetic marker, are considered to be part of the southern package of rocks. The contrasting rock types, intensity of deformation (see Chapter 2), and geochemical compositions of the northern and southern parts suggest that the two parts formed independently of each other and were juxtaposed after the main volcanism associated with each part had ceased.

The northern part of the belt is characterised by amphibolite derived from two types of interlayered basaltic pillow lavas, interpreted as being contemporaneous, but derived from different magma sources. The homogeneous pillow basalts are low to moderate-Mg tholeiites which have not been crustally contaminated. They may have been derived from a moderate degree of partial melting of the upper mantle. The variolitic basalts are low to high-Mg basalts which incorporated minor amounts (<5%) of continental crust. They may have been derived, on average, from somewhat deeper sources and/or from larger degrees of partial melting of the mantle. The northern volcanic

package was intruded by later ultramafic and quartzofeldspathic (tonalitic) dykes and sills. The northern ultramafic layers are cumulates derived from parental magmas similar to those that formed the variolitic pillow basalts.

The southern part of the belt is characterised by amphibolite derived from more strongly deformed basaltic pillow lavas which are now observed as banded amphibolite. Although they are more tectonized, they exhibit consistent and distinct geochemical characteristics which are different than the northern basaltic pillow lavas. The parent magmas of amphibolites in the southern part assimilated large amounts of crust (15-20%). The parent magmas were likely more Mg-rich than the parent magmas of the northern basaltic pillow lavas, and may have been komatiitic in composition. The southern part also contains felsic-intermediate metasedimentary rocks, a metagranodiorite unit which has A-type granitoid trace element concentrations, and a meymechitic layer.

Geochemical indices of crustal contamination and geochronological studies (see Chapter 2) suggest that the parent magmas of the northern and southern amphibolites erupted through continental crust which was likely composed of Amîtsoq gneiss or similar felsic rocks. The contrasting degrees of contamination may in part reflect the thickness and character of the continental crust through which the mafic magmas ascended. The parent magmas of the northern amphibolies may have ascended through a thin layer of continental crust, whereas the parent magma of the southern amphibolites erupted through a thick continental crust. One might also explain the contrast in degrees of crustal contamination by differences in igneous processes, whereby the more Mg-rich (hotter) southern parent magmas simply assimilated more crust than the cooler northern

parent magma. This interpretation is not preferred as it does not take other evidence, such as the presence of an A-type granodioritic unit, felsic-intermediate metasedimentary rocks, and a meymechitic horizon into consideration. Highly differentiated granites and meymechites are typically associated with thick continental crust in younger terranes. The meymechitic unit is thought to represent small degrees of partial melting at great depth (>200 km; i.e. normally below a thick continental crust and at or below mantle lithosphere), explaining its unusual Mg-rich, incompatible-element-rich chemistry.

The new model proposes that a relatively thin, immature, and possibly rifted continental crust may have been associated with the northern package of rocks. The variolitic pillow basalts may have encountered the most fusible components of this crust, whereas the homogeneous basalts, which are not crustally contaminated, did not. In terms of tectonic setting, these scenarios could be compatible with either very immature, mafic-rich island-arc crust or highly extended sialic crust such as in a back-arc basin environment.

The mafic and ultramafic magmatism in the southern part of the belt is thought to have erupted through a thick continentral crust and may be analogous to hot-spot or plume-related modern continental flood basalts. The meymechite melting event may have been initiated by the arrival of a mantle plume that was the source of the basaltic pillow lavas which are now preserved as banded amphibolites. Similar to the type locality of meymechites in the Siberian traps of Russia (Arndt, 1998), there may have been two very different plumbing systems which formed the mafic and ultramafic units in the southern

part of the Ivisârtoq belt. All of these interpretations would fit with a continental flood basalt environment which is envisioned for the southern package of rocks.

2.8 CONCLUSIONS

The Ivisartoq greenstone belt is one of the best exposed, well-preserved Archean greenstone belts in Greenland. However, despite the presence of exceptionally preserved pillow lava structures, the mineral assemblages are predominantly metamorphic and most primary textures have been destroyed. Trace element geochemistry has been invaluable in correlating variably deformed and metamorphosed rocks and in confirming protolith interpretations. Furthermore, geochemistry was key in determining the magmatic origins of the protoliths and describing their petrogenesis. Field work and geochronology have demonstrated that the belt represents a tectonostratigraphic assemblage consisting of two parts (see Chapter 2); geochemical studies support this model and were able to expand on it by providing insight into the tectonic environment for each part.

The following summary outlines geochemical conclusions for the northern and southern parts of the belt.

Northern part of belt

The northern part of the Ivisârtoq greenstone belt is dominated by two types of amphibolites derived from contemporaneous homogeneous and variolitic pillow basalts. The homogeneous basalts were likely formed at shallow depths or by smaller degrees of melting in the mantle compared to the variolitic basalts. Furthermore, the homogeneous

pillow basalts were not crustally contaminated whereas, the parent magmas of the variolitic pillow basalts incorporated minor amounts (<5%) of continental crust. The contrasting amounts of felsic crustal contamination in the variolitic and homogeneous basalts may be a reflection of different magmatic plumbing systems and the nature of the crust through which the magmas intruded. A third type of northern amphibolite was recognized geochemically, but is only represented by one sample. The sample is komatiitic in composition, similar to some samples analysed by Hall (1981), and presumably formed by large degrees of mantle melting.

Compositions of rarely preserved remnant olivine grains from the extensive coarse-grained ultramafic layers demonstrate that these layers likely formed as cumulates from discrete pulses of high-Mg basalt (MgO =9-16%) that intruded as sills. These layers could have formed from the same parent magma as the variolitic pillow basalts.

Major and trace element geochemistry of thin, rusty, layers of quartzofeldspathic schists and gneisses support field evidence which suggests that these layers were derived from tonalitic intrusions, not deformed acid-intermediate tuffaceous metasedimentary rocks as previously thought (Chadwick, 1990).

Overall, geochemistry of the northern part of the belt supports a model in which these rocks formed in a very immature island-arc environment or in a back-arc basin environment.

Southern part of the belt

The southern part of the belt is dominated by amphibolites derived from pillow basalt which likely originated from partial melting at greater depths or from larger degrees of melting than the northern variolitic pillow basalts. Their parent magmas may have been komatiitic in composition and assimilated between 15-23% continental crust.

A unique layer of ultramafic schists, termed the magnetic marker, does not resemble the northern ultramafic layers and is also geochemically distinct. This layer resembles a pyroclastic meymechite: an unusual rock which is thought to form from small degrees of partial melting at great depth (>200 km). This discovery marks the first reported meymechite of Archean age. This unit is strongly deformed, however variations in composition across the unit suggest that cryptic primary layering may be preserved. If north is the way-up, then the lower (southern) part of the magnetic marker is characterised by a picritic-meymechitic composition (lower MgO, and TiO_2 contents) and the upper (northern) part is true meymechite (higher Ti and MgO contents). The differences in composition between these two groups suggest that the depth of melting may have progressively increased during the course of magmatism.

A previously unrecognized unit of homogeneous metagranodiorite was identified. Major and trace element geochemical studies demonstrated that this unit is likely intrusive, and has trace element concentrations similar to A-type granitic rocks. A thick quartzofeldspathic unit which is continuous with an intensely deformed layer in the Marker High Strain Zone, were previously interpreted as deformed acid-intermediate tuffaceous metasedimentary rocks (Chadwick, 1990). This study supports the

interpretation that these layers are sedimentary in origin. The metasedimentary rocks were likely derived from three main sources:

1) granodioritic unit (with A-type granite trace element concentrations);
2) TTG and,
3) amphibolite (likely the southern banded amphibolites).

Overall, the geochemistry of the southern part of the belt is consistent with a continental flood basalt environment for this package of rocks.

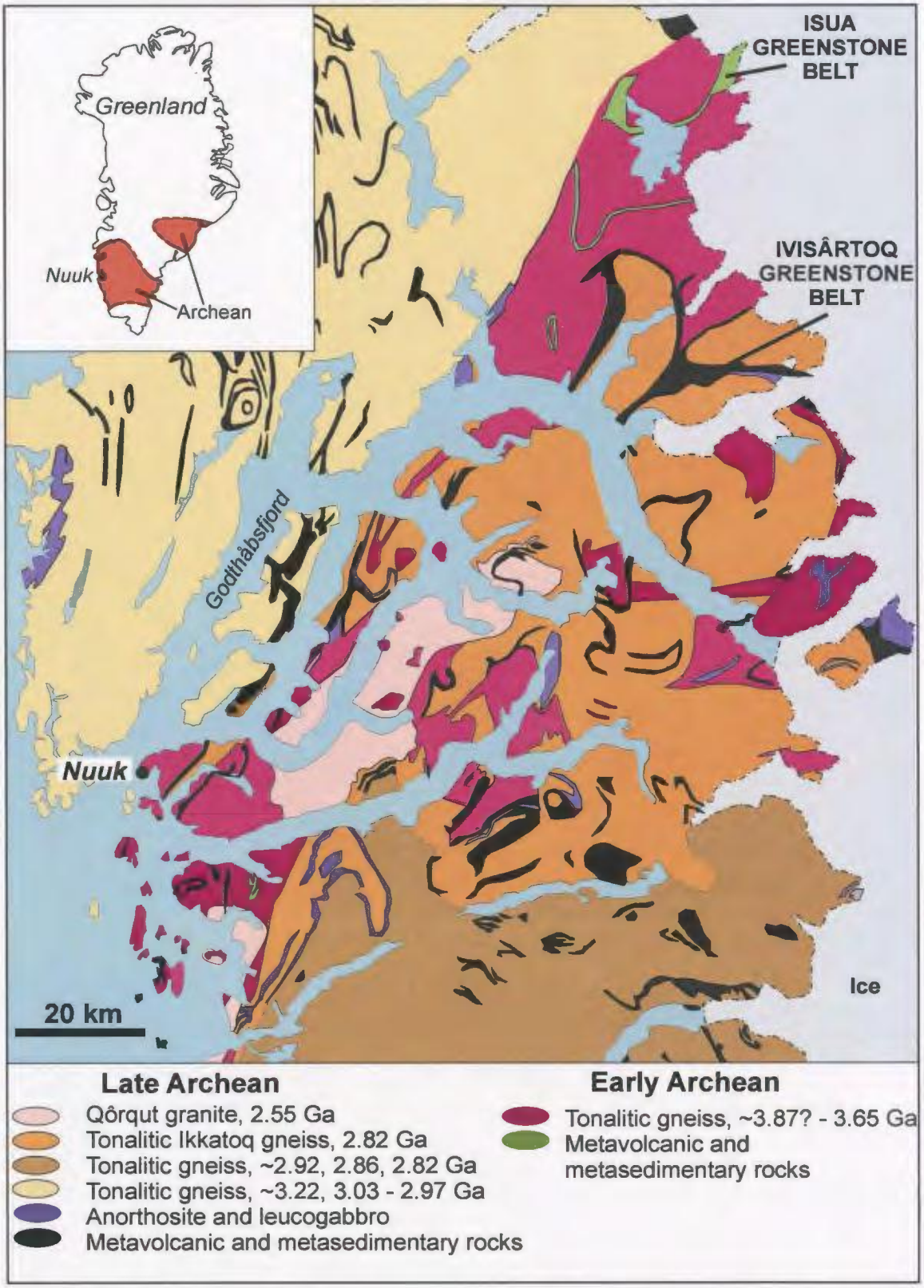

Figure 3.1a. Geologic map of the Godthåbsfjord region (from Myers and Crowley, 2000) compiled from maps by Allaart (1982), Chadwick and Coe (1983,1988), Garde (1987, 1989) and McGregor (1984) and geochronology from Nutman et al. (1996) and Nutman (1997). The inset map of Greenland locates Nuuk and the main regions of Archean gneiss.

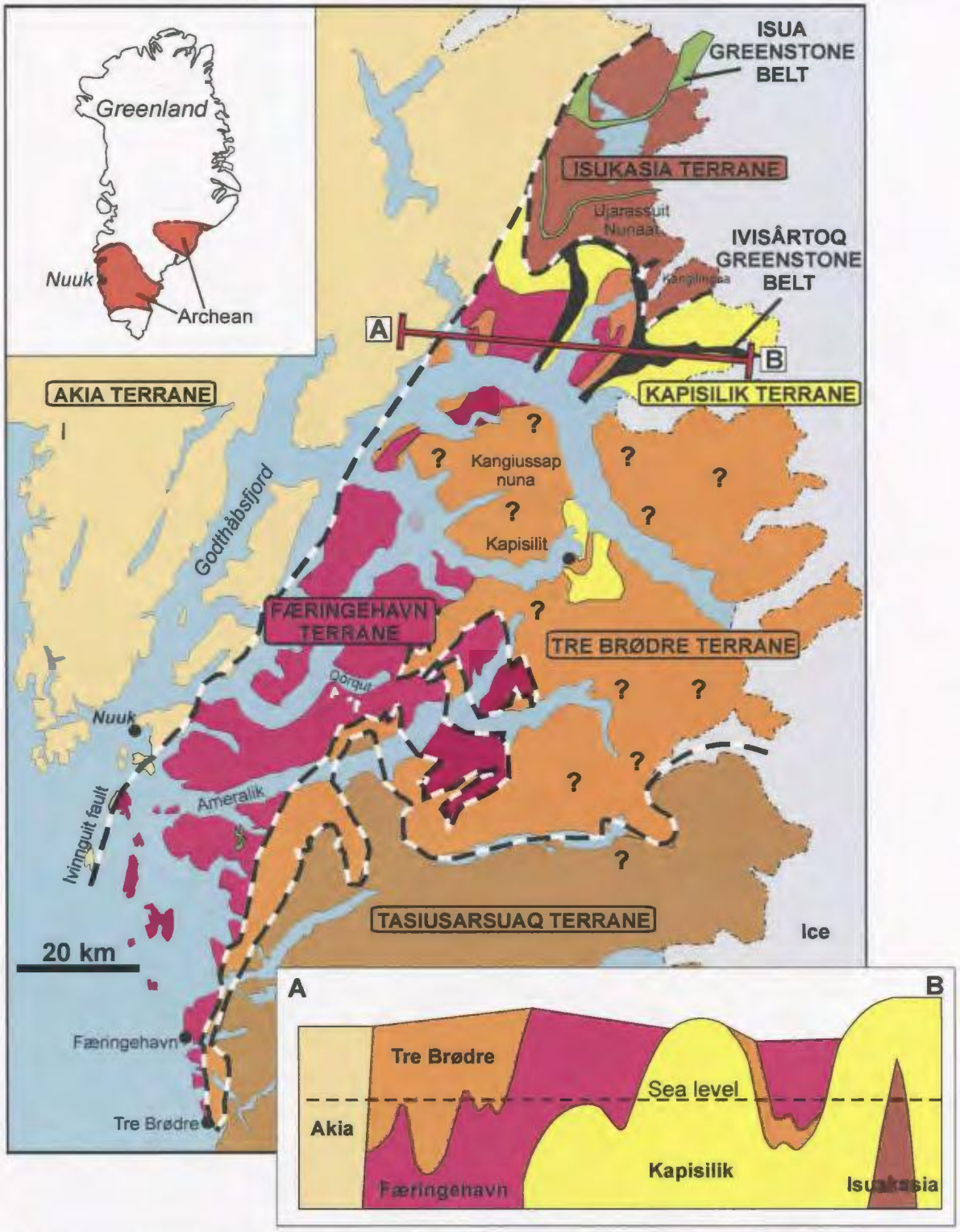

Figure 3.1b. Sketch map of the terranes of the Godthåbsfjord region as defined by Friend and Nutman (2005). The top left inset map of Greenland locates Nuuk and the main regions of Archean gneiss. The bottom right inset shows a cross-section at sea level along the line AB (from Friend and Nutman, 2005). Note: different colours represent different terranes and do not correspond exactly with geological units as defined in Fig. 3.1a. Dashed lines indicate terrane boundaries.

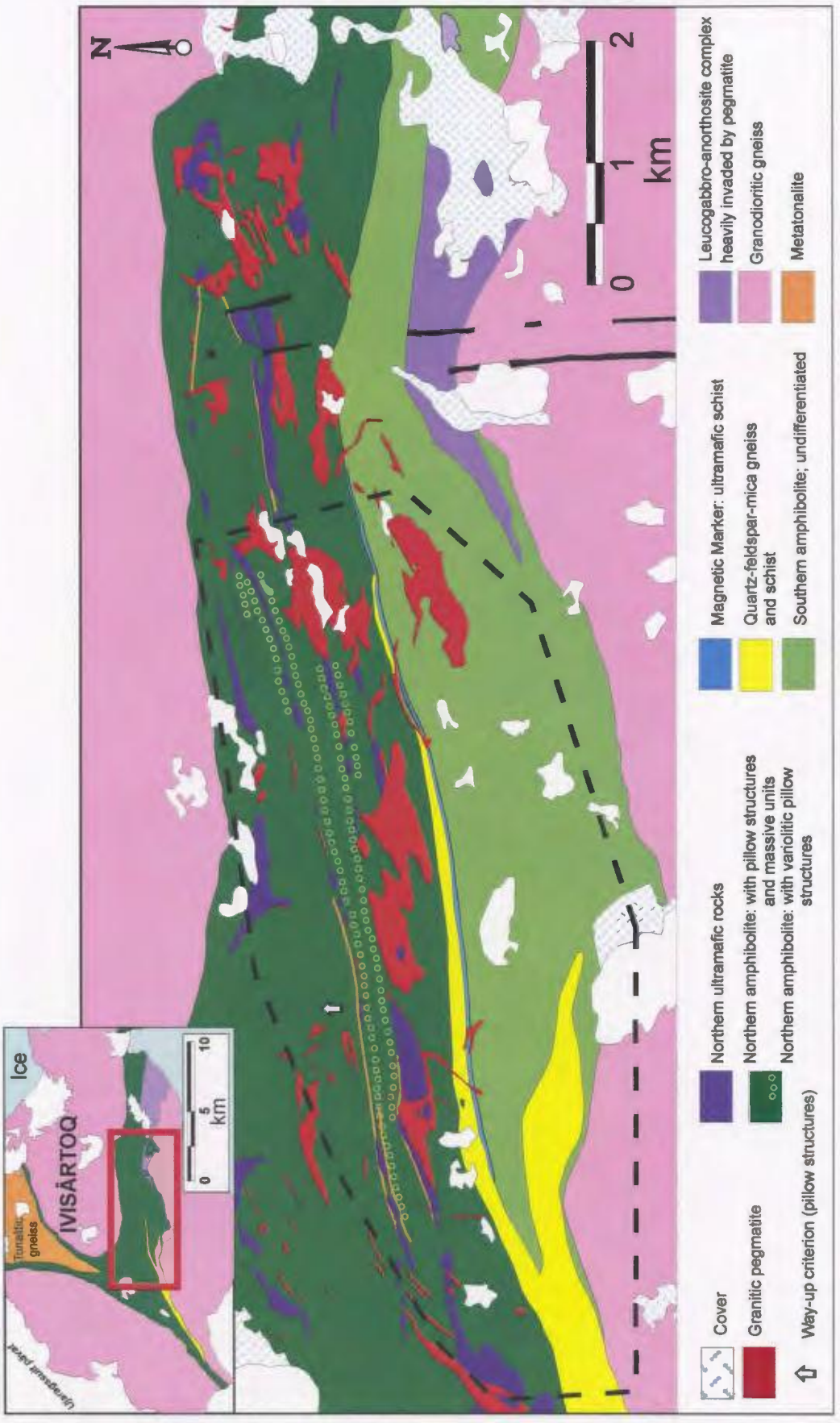

Figure 3.2. Simplified map of the Ivisârtoq greenstone belt. Dashed outline indicates field area.

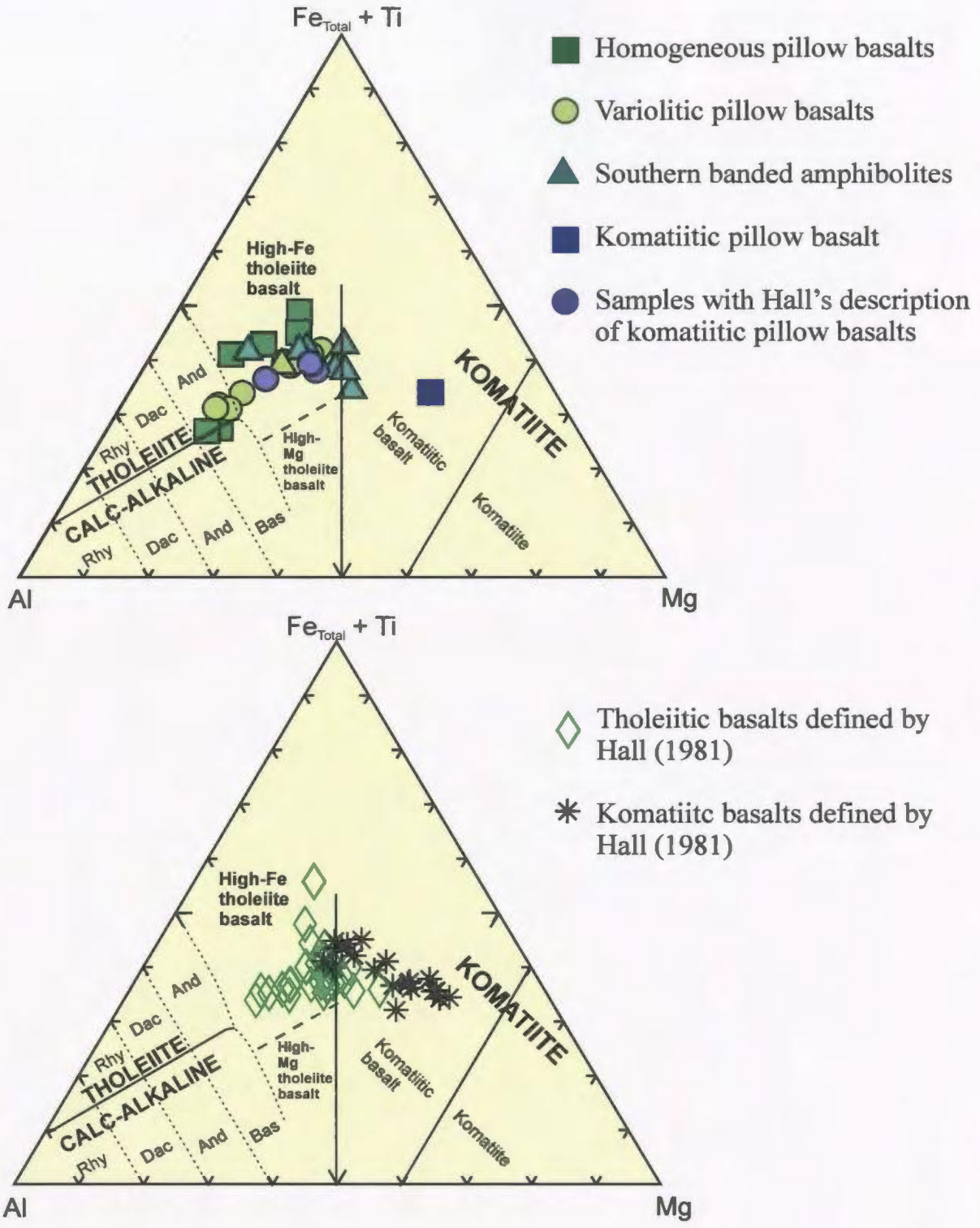

Figure 3.3. Jensen plots
a) Ivisârtoq amphibolites derived from basaltic pillow lavas.
b) Hall's data (1981) using Hall classification terms.

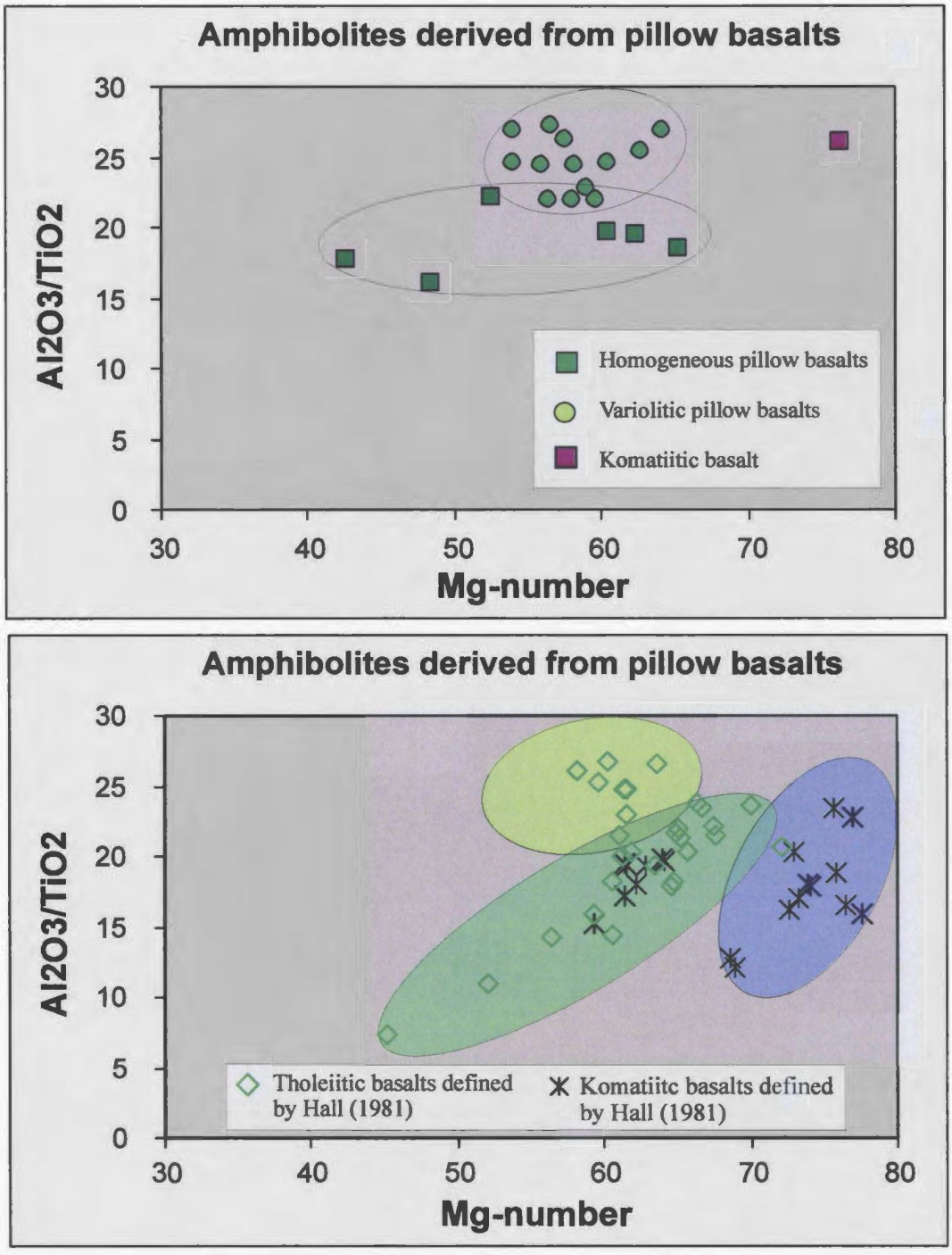

Figure 3.4. Al_2O_3/TiO_2 versus Mg-number.
a) Ivisârtoq amphibolites derived from basaltic pillow lavas.
b) Hall's data (1981). Pale green ellipse defines variolitic pillow compositions; dark green ellipse defines homogeneous pillow compositions; purple ellipse defines komatiitic basalt compositions.

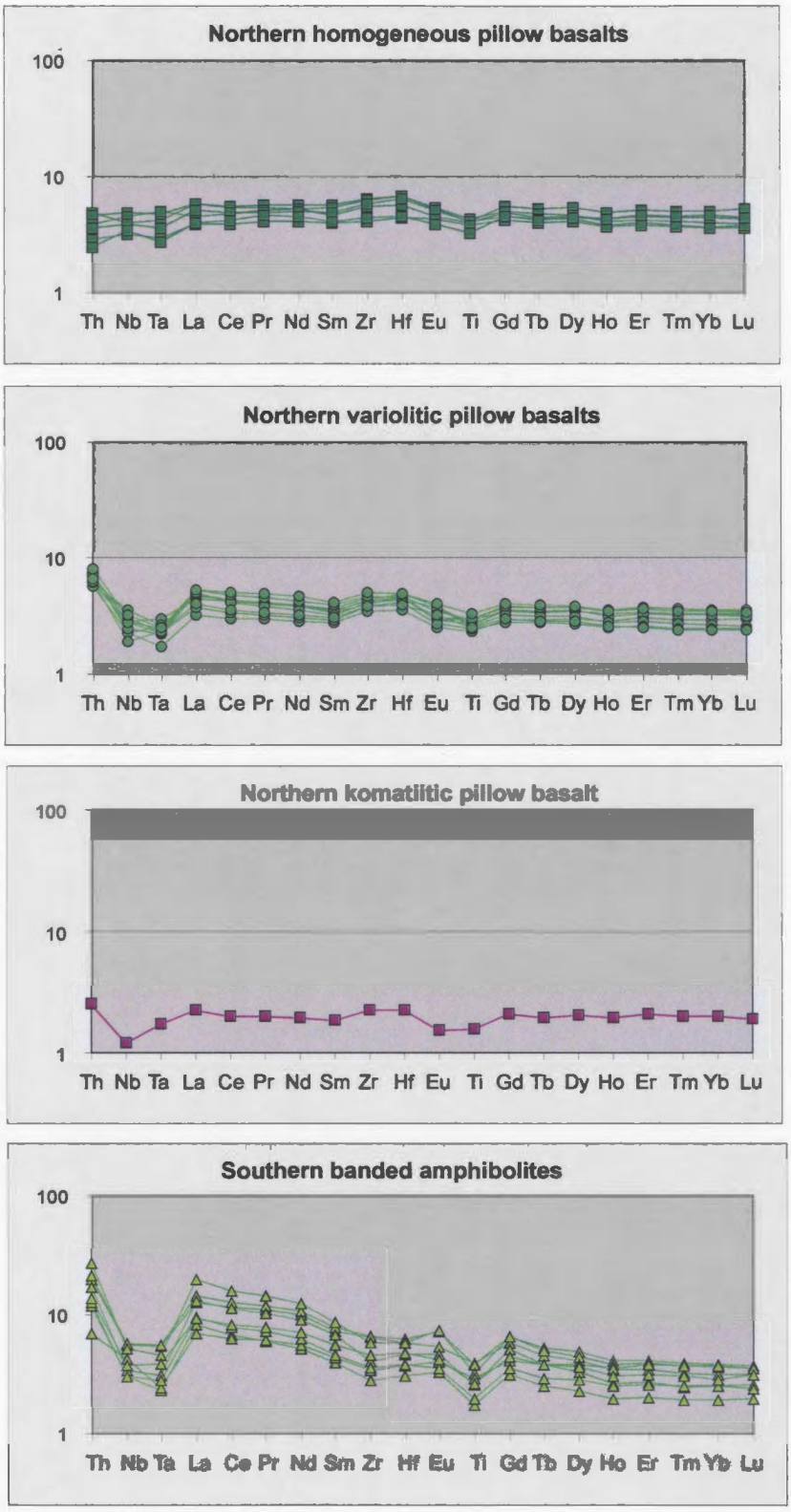

Figure 3.5. Primitive mantle normalized multi-element diagrams for amphibolites derived from basaltic pillow lavas.

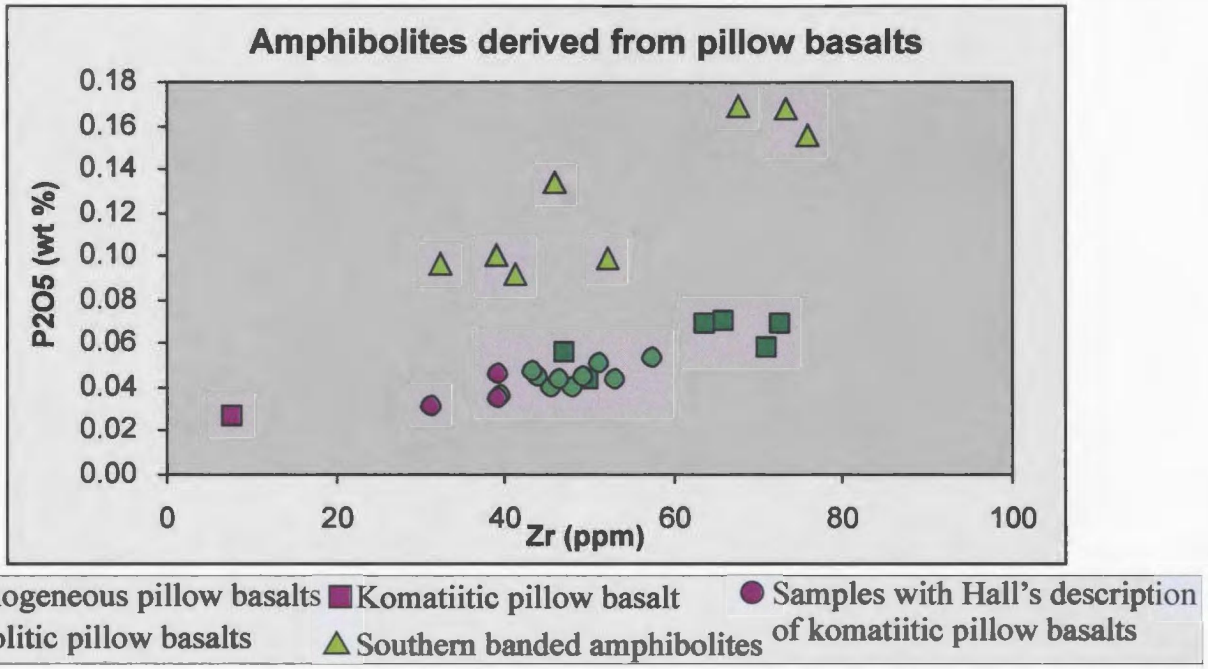

Figure 3.6. P_2O_5 vs Zr plot for the three main types of amphibolites derived from basaltic pillow lavas. Note: the homogeneous pillow basalts and variolitic pillow basalts show a continuous trend of high P_2O_5/Zr ratios, whereas the banded amphibolites define a separate trend of lower P_2O_5/Zr ratios.

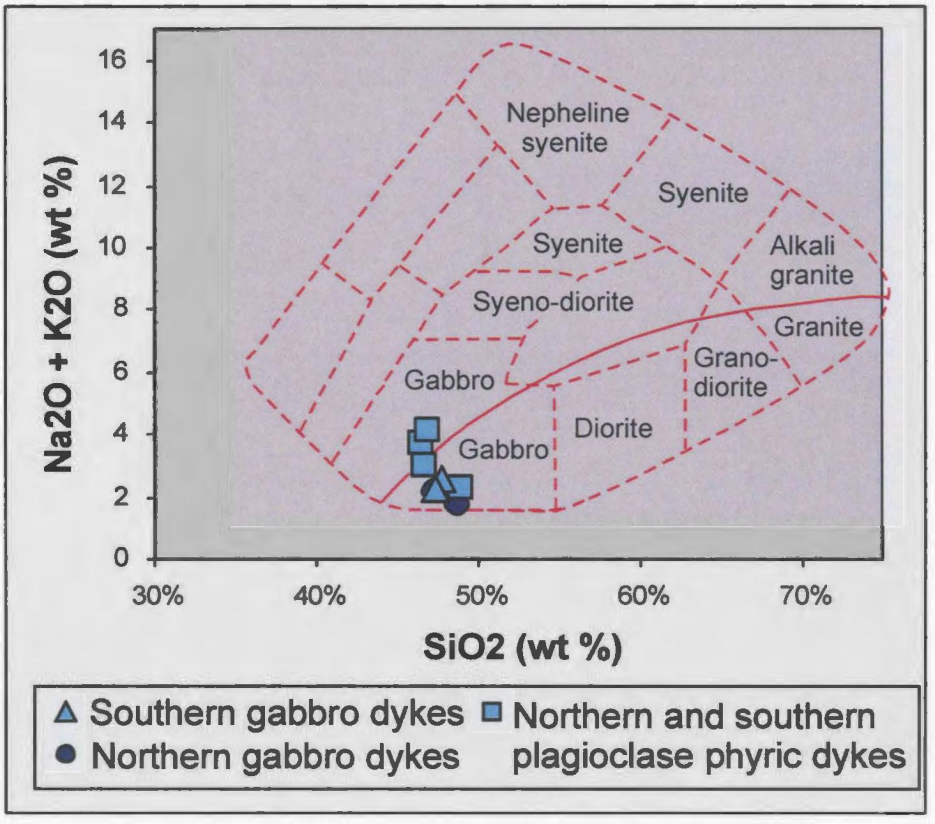

Figure. 3.7. Gabbroic rocks plotted on a total alkalis-silica diagram for plutonic rocks (Wilson, 1989). The curved solid line subdivides the alkalic from subalkalic rocks.

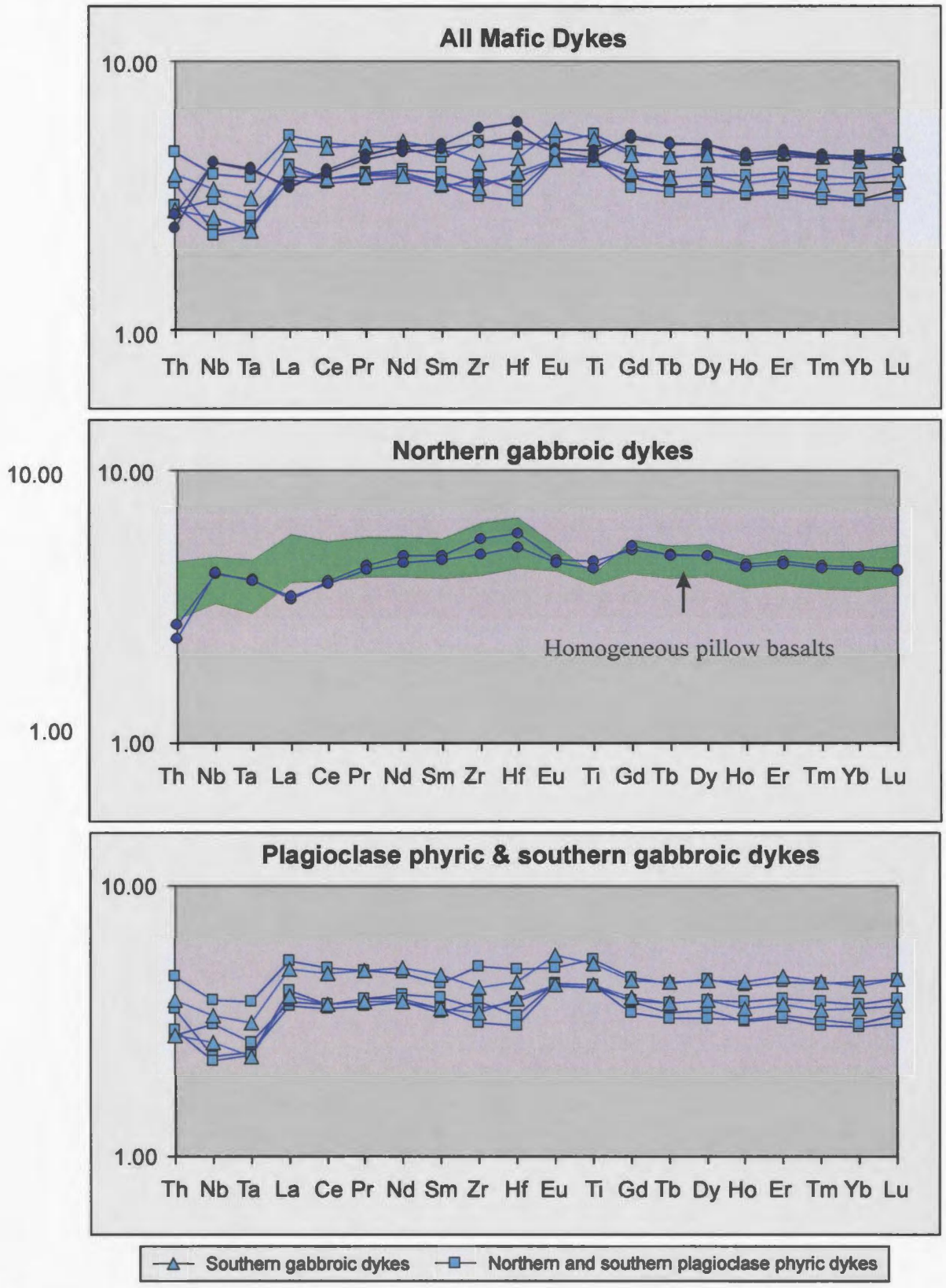

Figure 3.8. Primitive mantle normalized multi-element diagrams for mafic dykes.

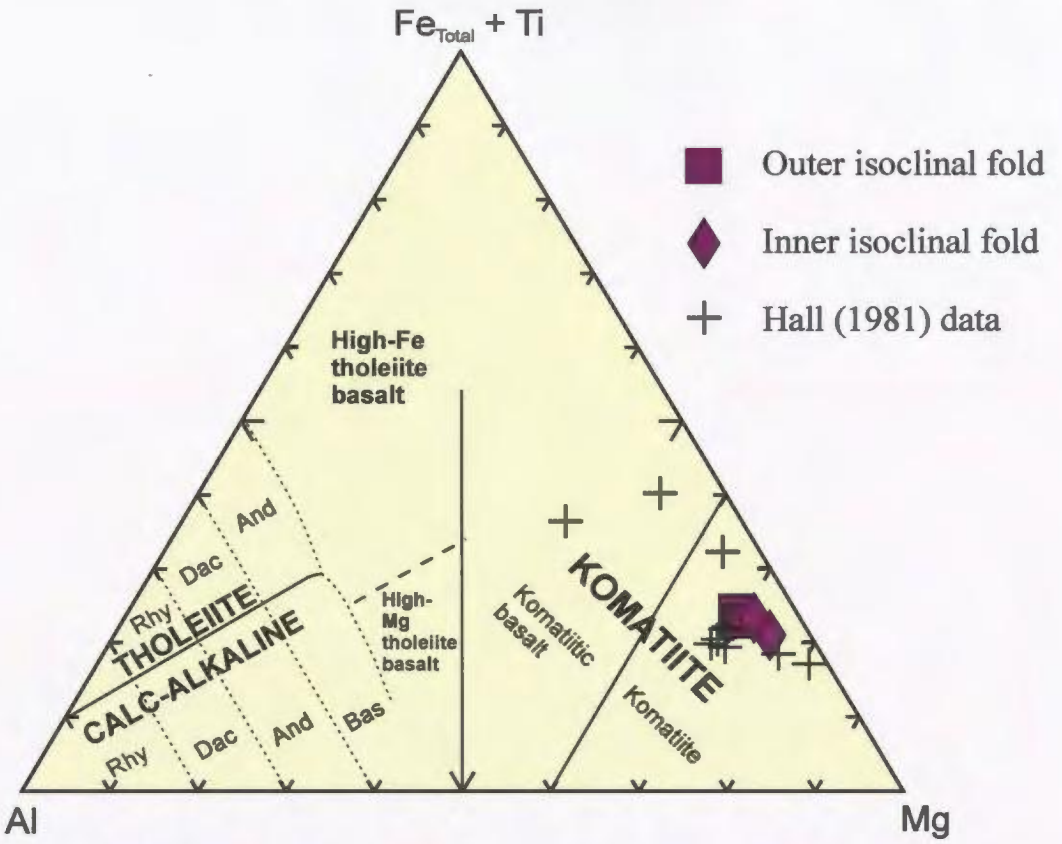

Figure 3.9. Samples from northern ultramafic layers, which define large scale isoclinal folds (distinguished as Inner and Outer folds), on a Jensen cation plot (Jensen, 1976). Data from Hall (1981) are also plotted.

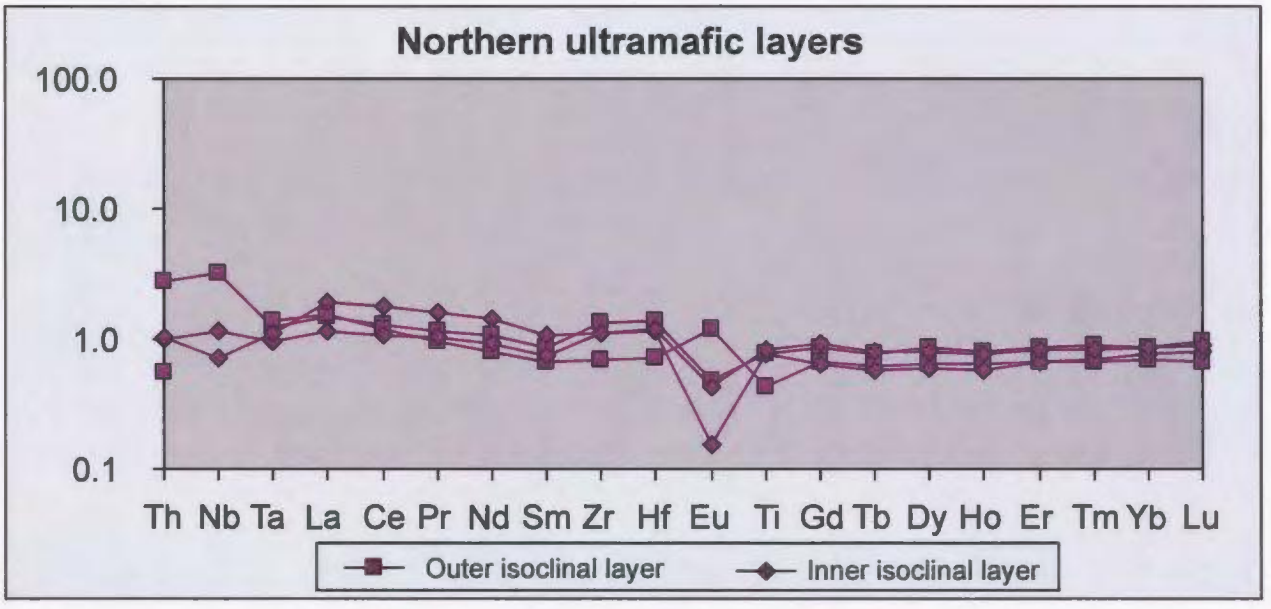

Figure 3.10. Primitive mantle normalized multi-element diagrams for northern ultramafic layers which define large isoclinal folds.

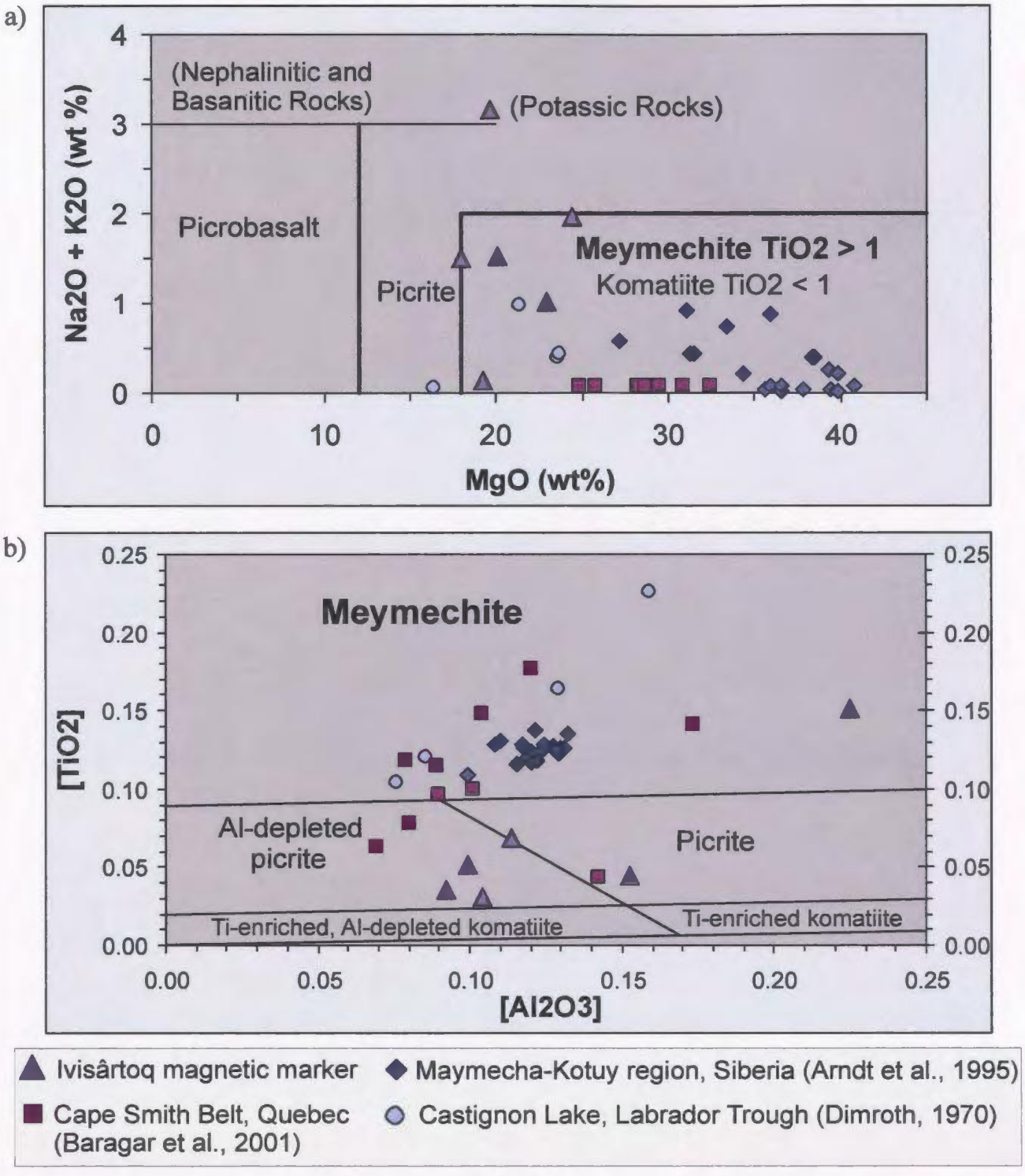

Figure 3.11.
a) IUGS chemical classification scheme for high-Mg volcanic rocks
b) Classification scheme for high-MgO volcanic rocks proposed by Hanksi et al., (2001). $[Al_2O_3]$ and $[TiO_2]$ are Al_2O_3 and TiO_2 projected from olivine composition and are calculated in mole proportions (normalized to unity) using the following equations: $[Al_2O_3] = Al_2O_3/(2/3 - MgO - FeO)$ and $[TiO_2] = TiO_2/(2/3 - MgO - FeO)$.

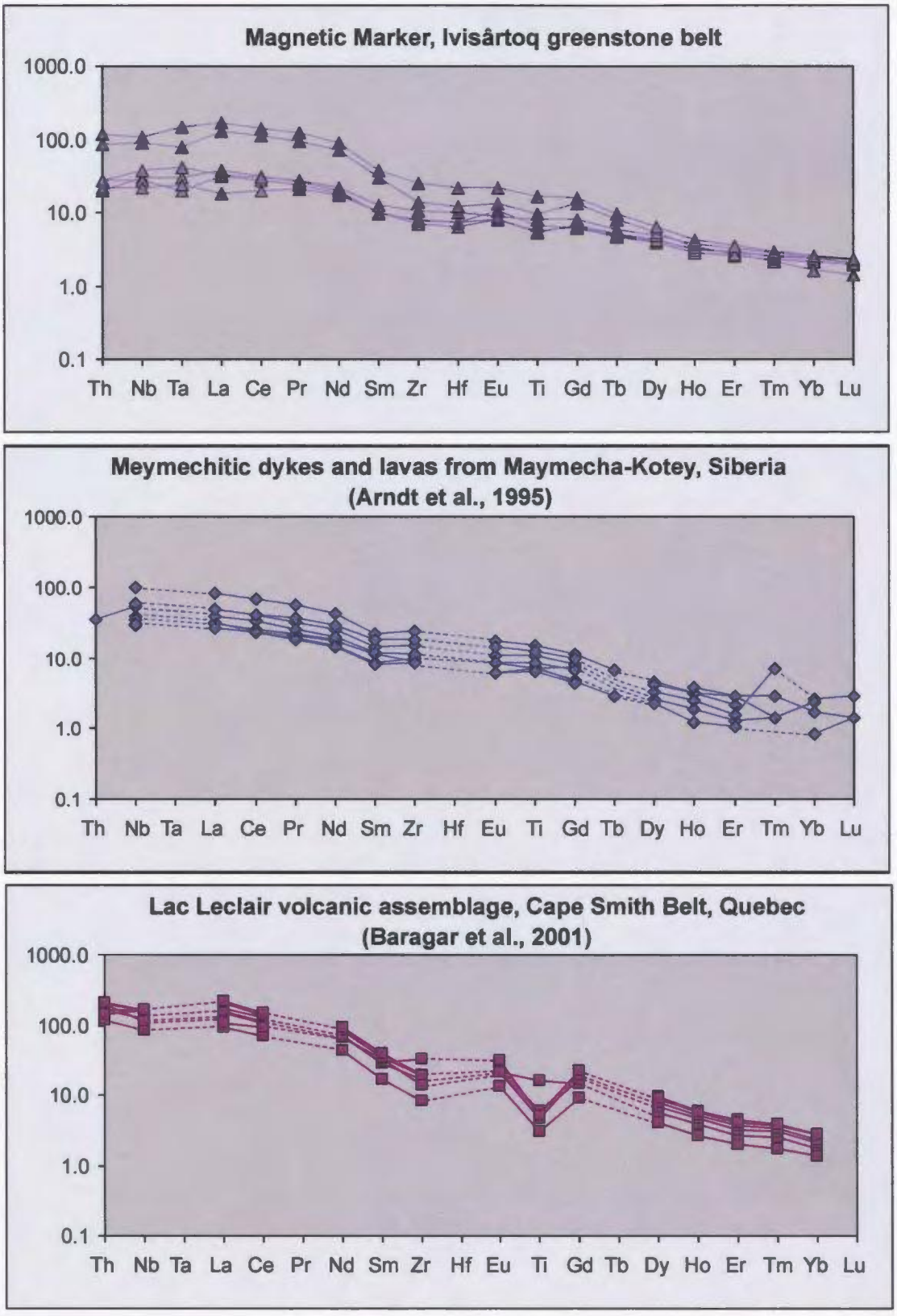

Figure 3.12. Primitive mantle normalized multi-element diagrams for meymechetic rocks.

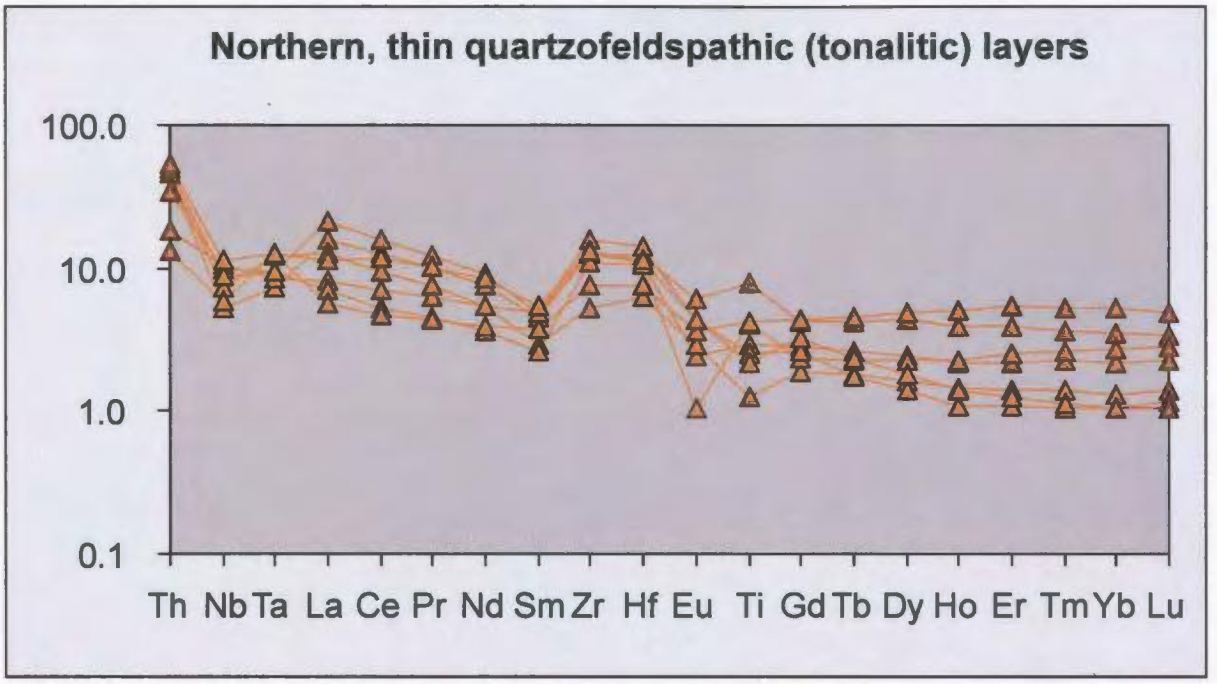

Figure 3.13. Primitive mantle normalized multi-element diagram for samples from the northern, thin quartzofeldspathic (tonalitic) layers.

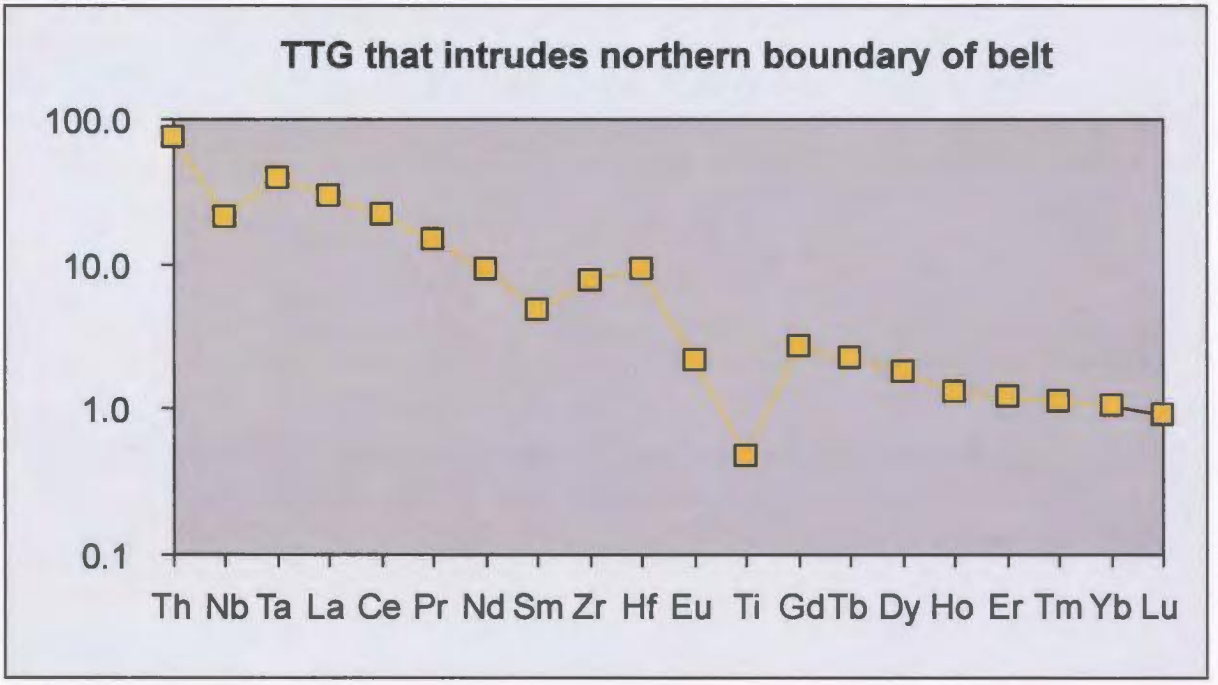

Figure 3.14. Primitive mantle normalized multi-element diagram for the TTG unit which intrudes the northern boundary of the greenstone belt.

a)

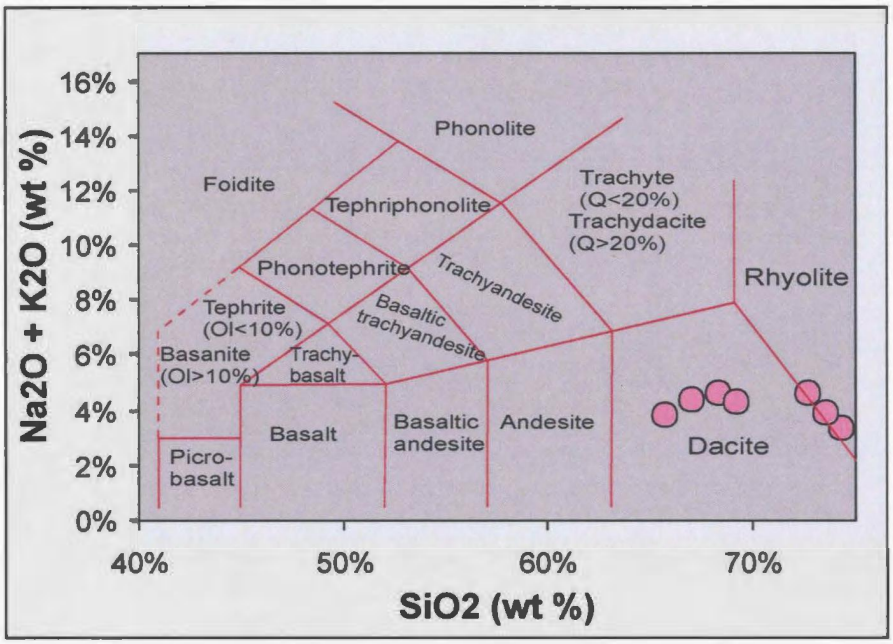

b)

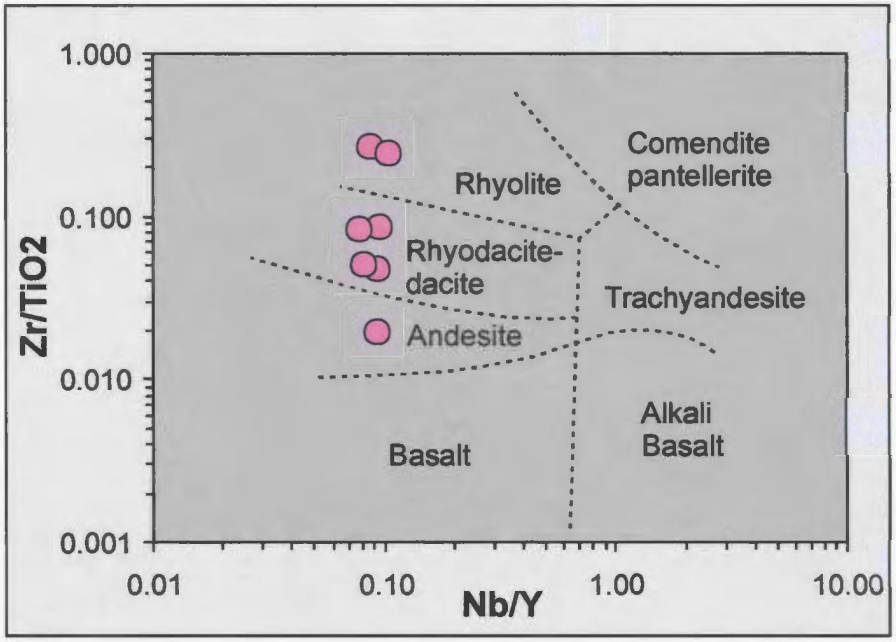

Fig. 3.15. Homogenous, light grey rocks from the southern part of the belt plotted on discriminant diagrams for volcanic rocks. These diagrams demonstrate that the light grey rocks have mostly dacitic to rhyolite (granodiorite to granite) compositions.
a) Total alkali-silica diagram for volcanic rocks (Le Maitre, 2002).
b) Discriminant diagram for volcanic rock types (Winchester and Floyd, 1977). This diagram uses trace elements which are less mobile than major elements (see Appendix B).

a)

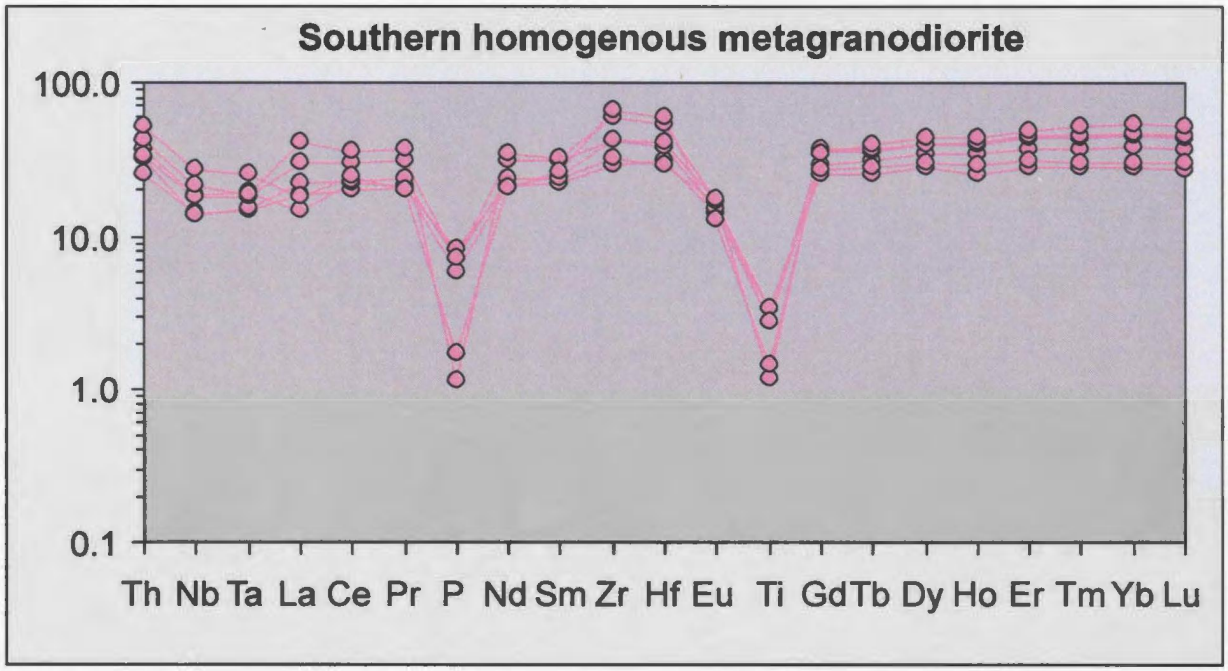

b)

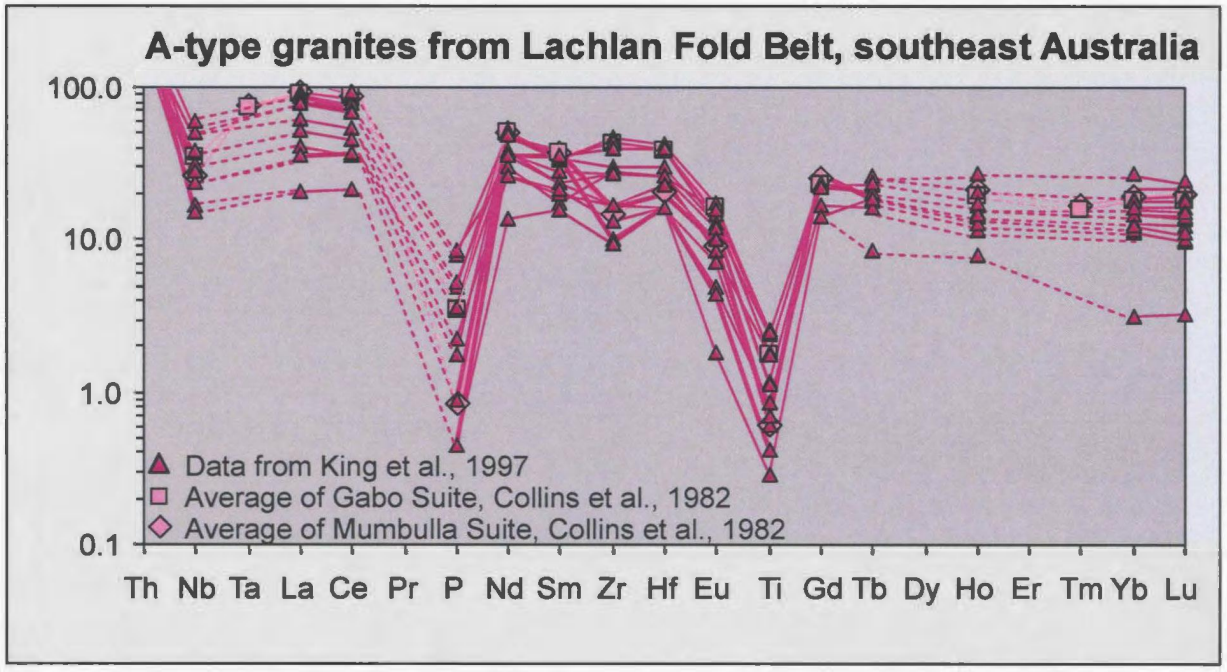

Figure 3.16. Primitive mantle normalized multi-element diagrams for
a) the southern Ivisârtoq, homogeneous metagranodirorite
b) A-type granites from the Lachlan Fold Belt, southeast Australia.

a)

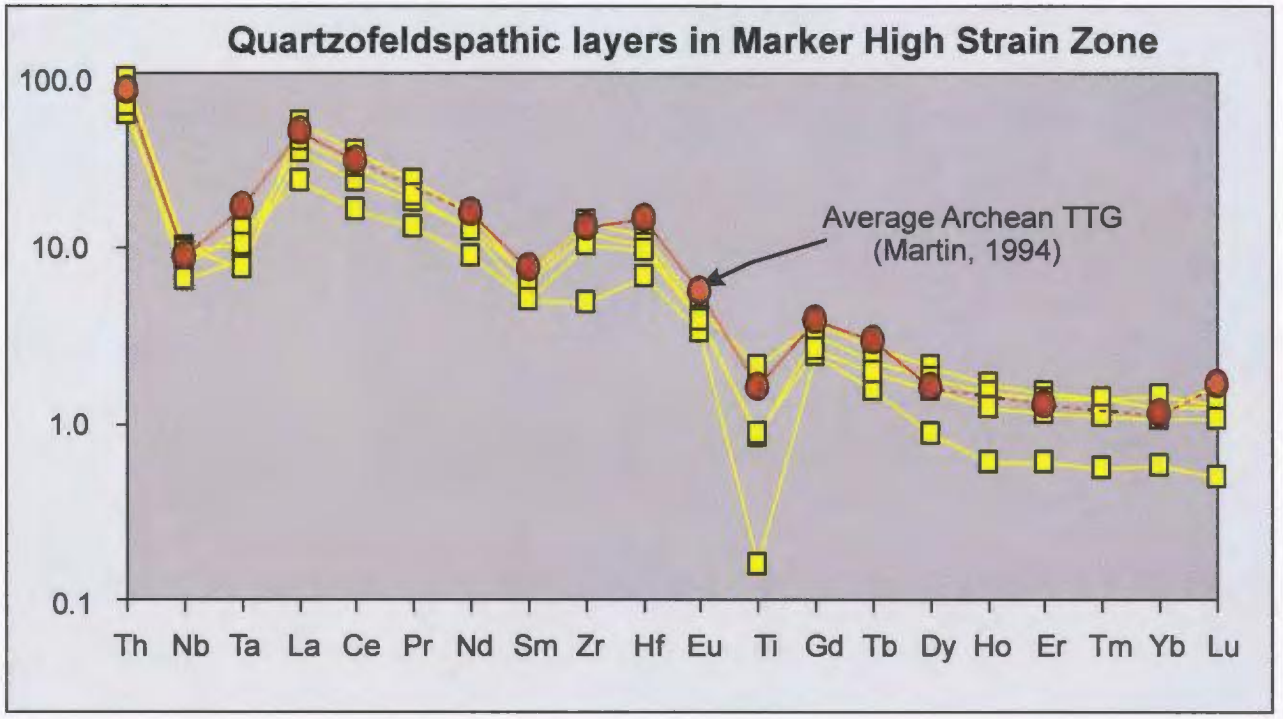

b)

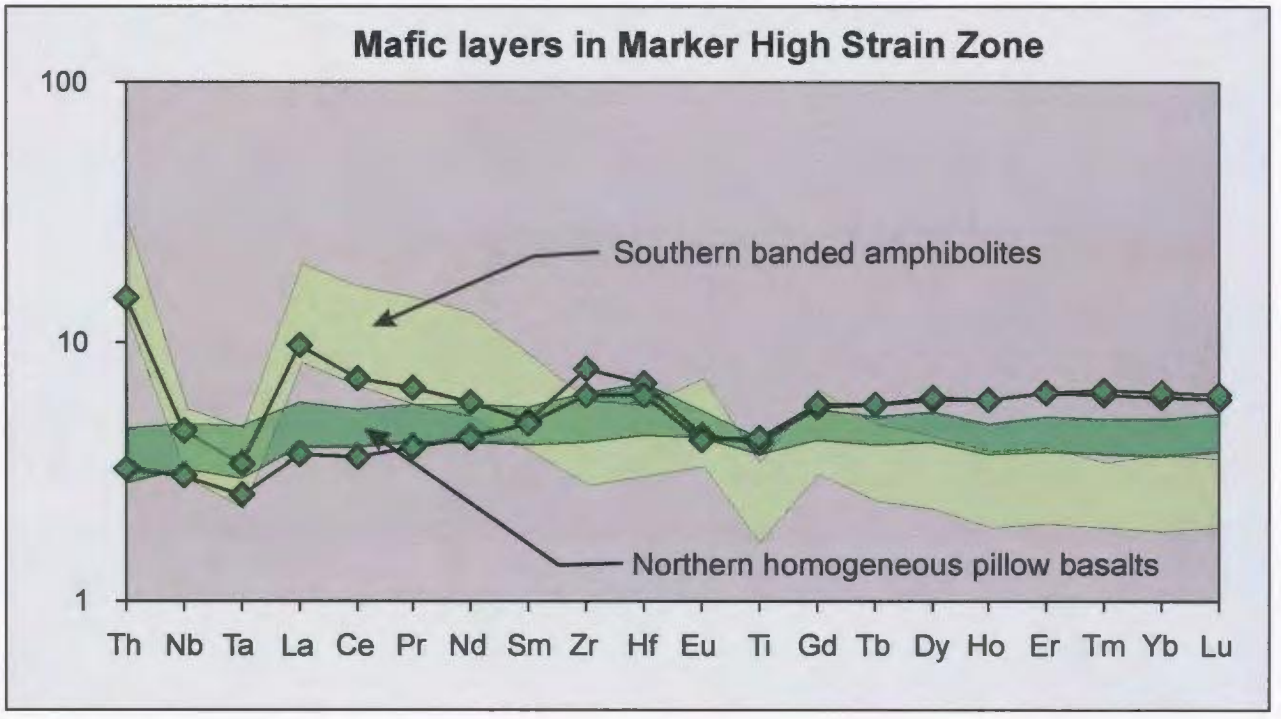

Figure 3.17. Primitive mantle normalized multi-element diagrams for layers in the Marker High Strain Zone.
a) Samples from the quartzofeldspathic layer
b) Samples from thin mafic layers.

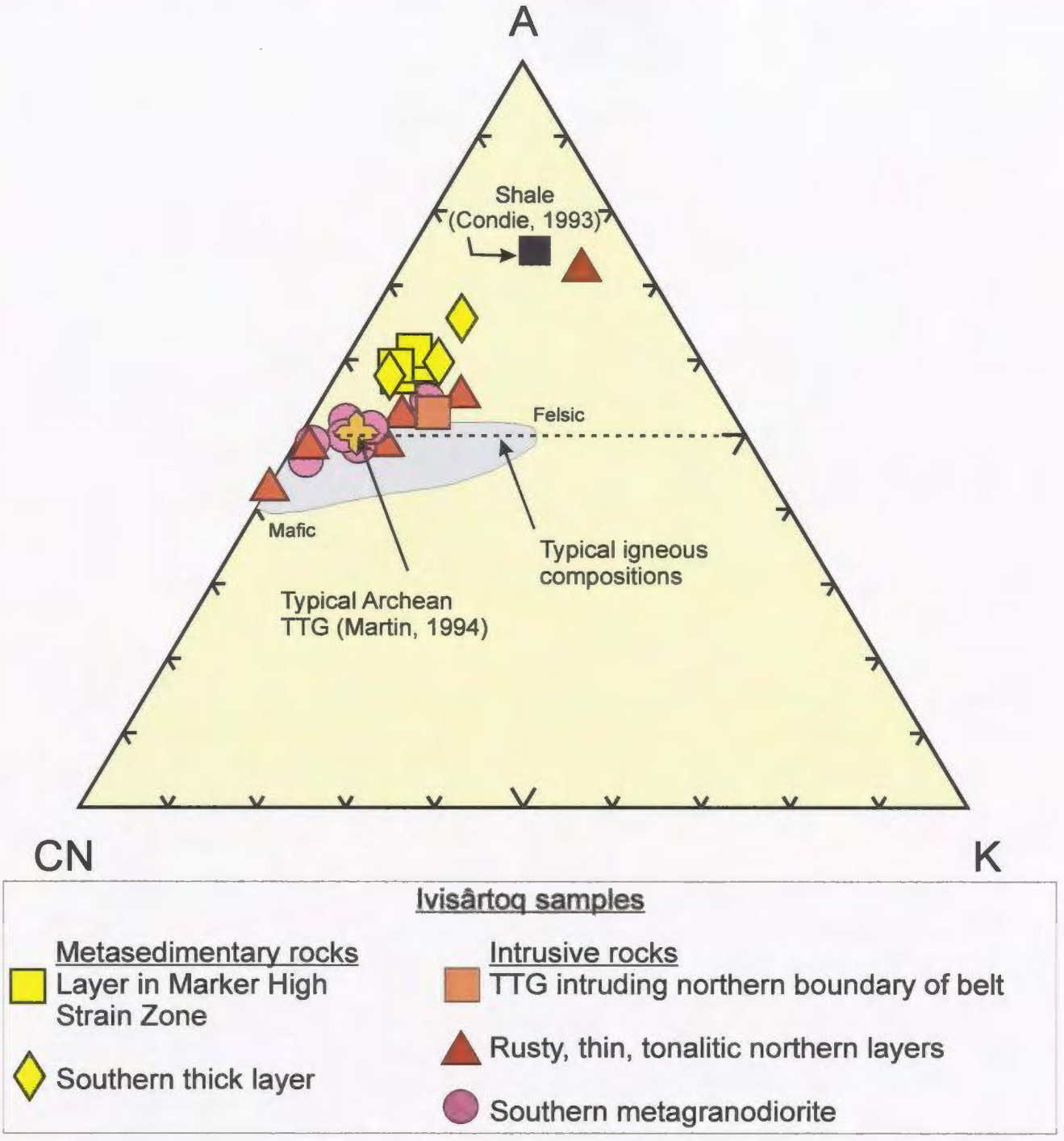

Figure 3.18. A-CN-K plot for felsic rocks within the Ivisârtoq greenstone belt. The apices are ratios based on the equation for chemical index of alteration (CIA) from Nesbitt and Young (1989) and uses molecular proportions of major element oxides.
$A= Al_2O_3/(Al_2O_3+ CaO^* + Na_2O + K_2O)$ x100;
$CN=(CaO^*+Na_2O)/(Al_2O_3+ CaO^* + Na_2O + K_2O)$ x 100
$K= K_2O/(Al_2O_3+ CaO^* + Na_2O + K_2O)$ x 100; where $CaO^*= CaO-CO_2-10/3\ P_2O_5$.

a)

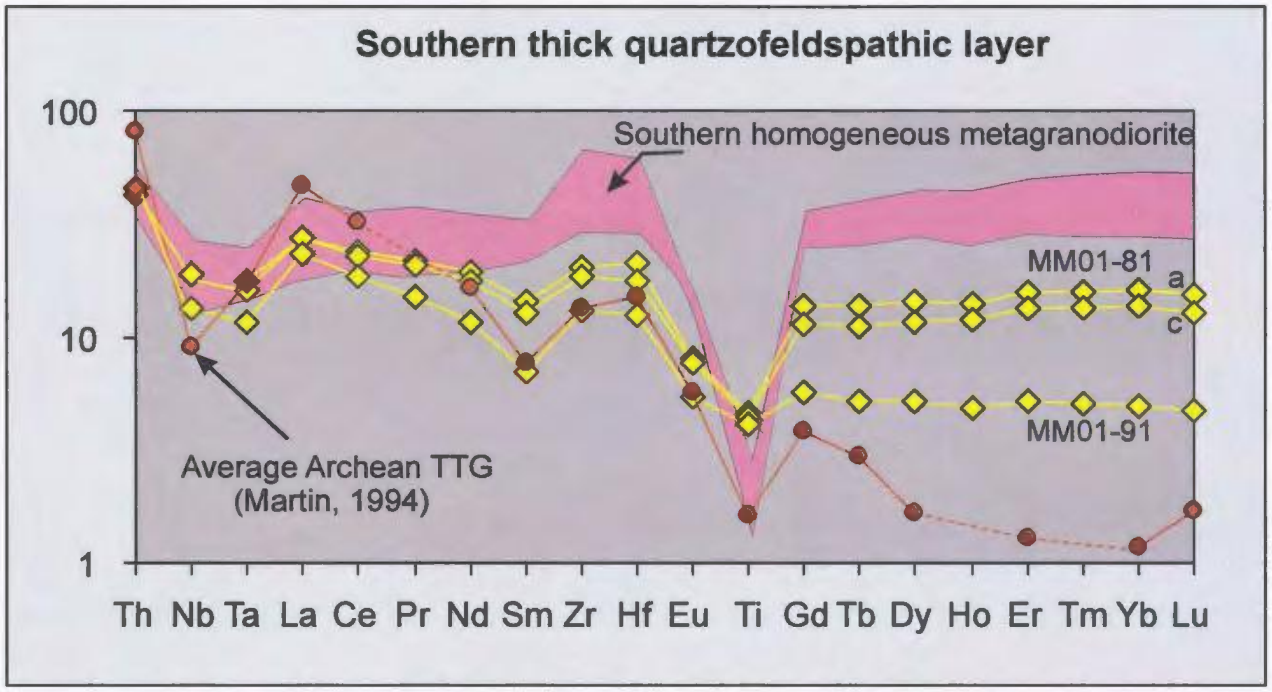

b)

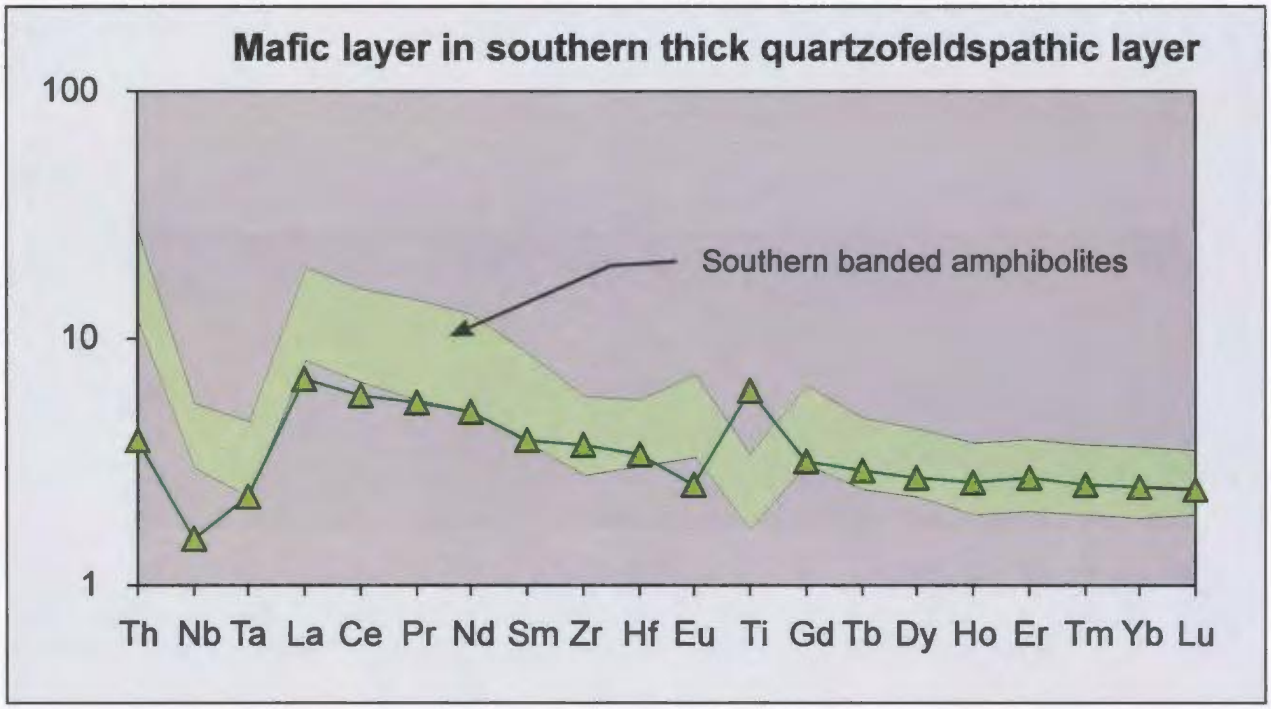

Figure 3.19. Primitive mantle normalized multi-element diagrams for samples from
a) southern thick quartzofeldspathic unit
b) mafic layer within the southern thick quartzofeldspathic unit.

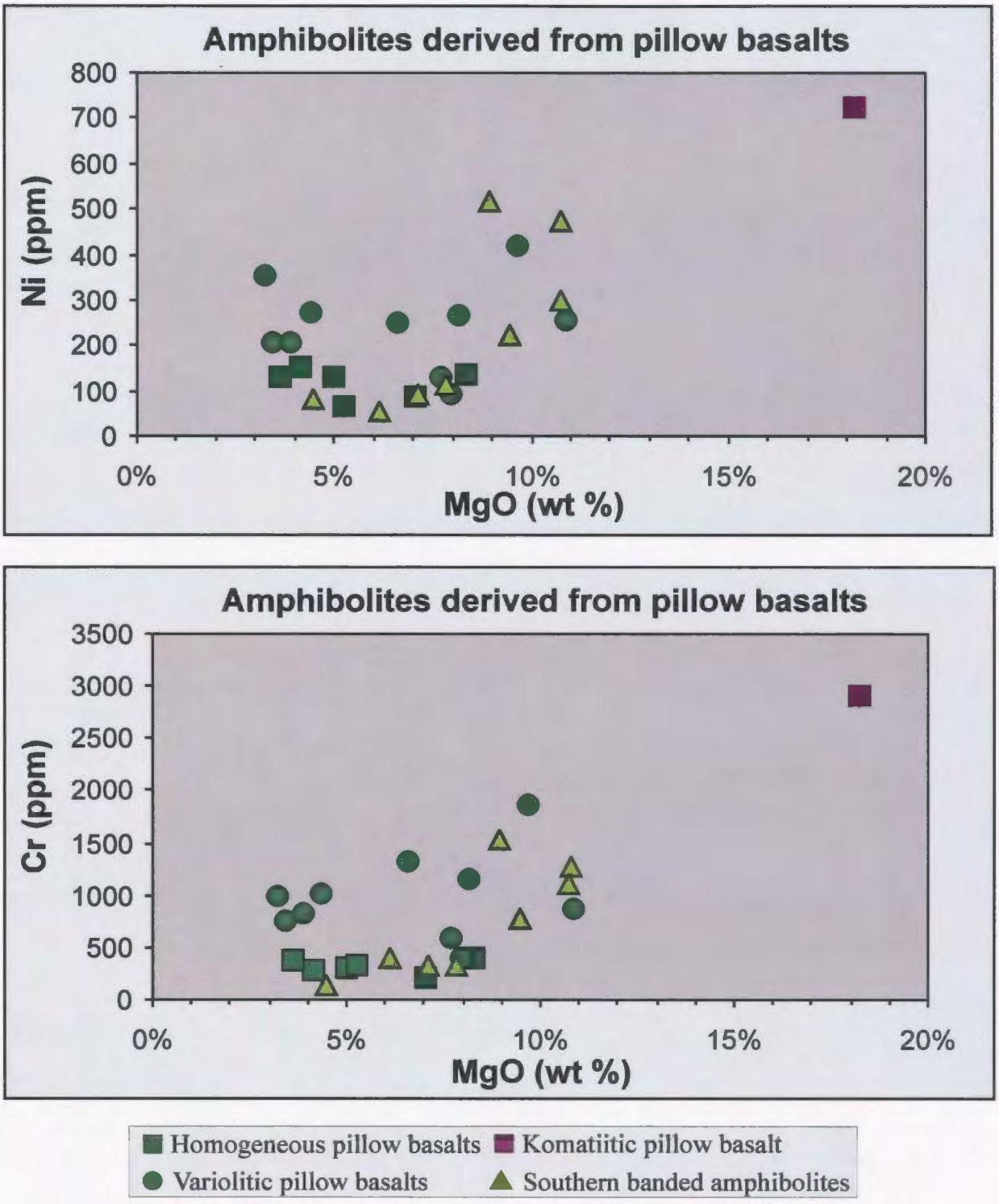

Figure 3.20. Ni and Cr versus MgO weight % for amphibolites derived from basaltic pillow lavas.

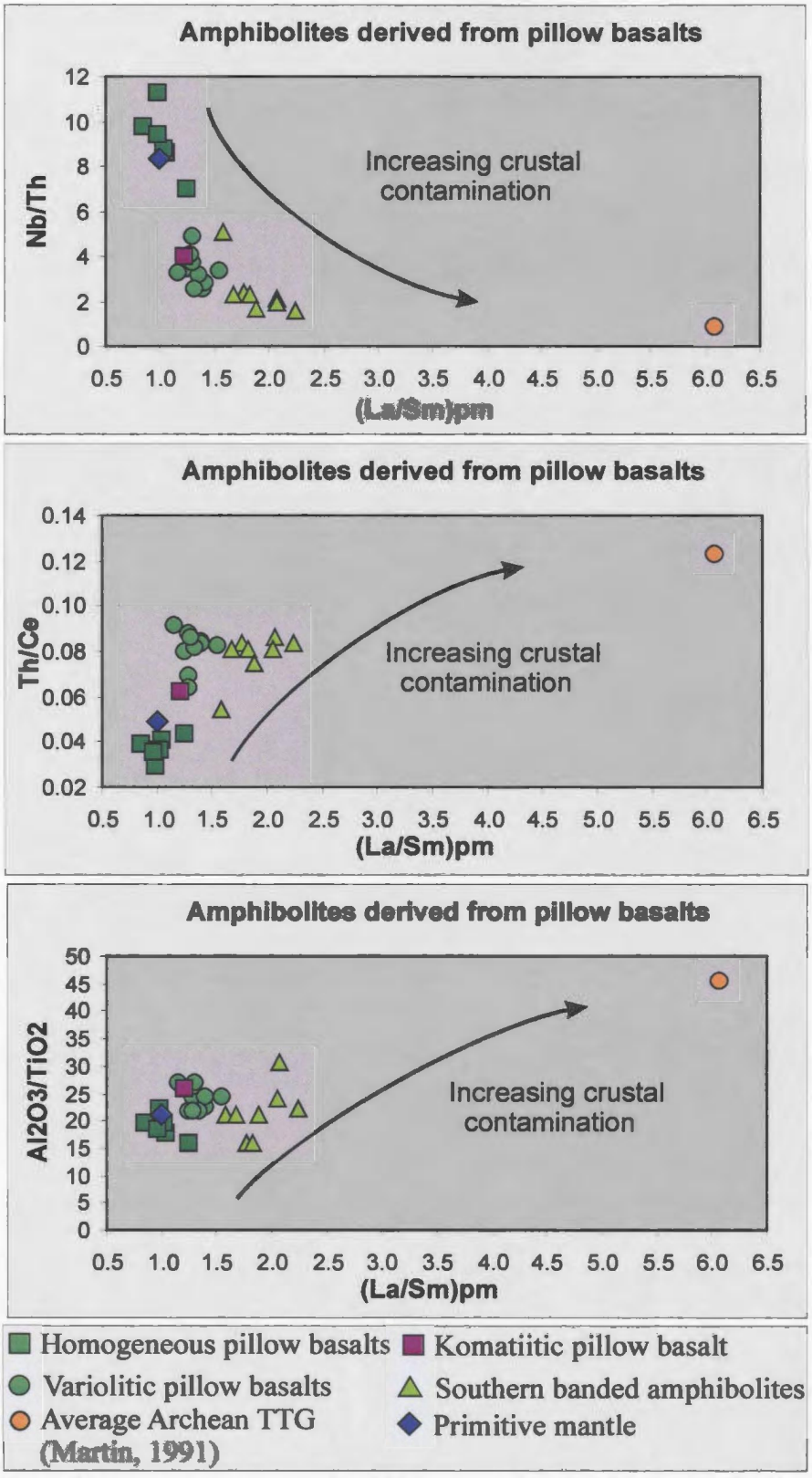

Figure 3.21. Plots that support a crustal addition model for the amphibolites derived from homogeneous and variolitic pillow basalts. A crustal addition model predicts a negative correlation between Nb/Th and La/Sm_{pm}, and a positive correlation between Th/Ce and La/Sm_{pm}, and A_2O_3/TiO_2 and La/Sm_{pm}.

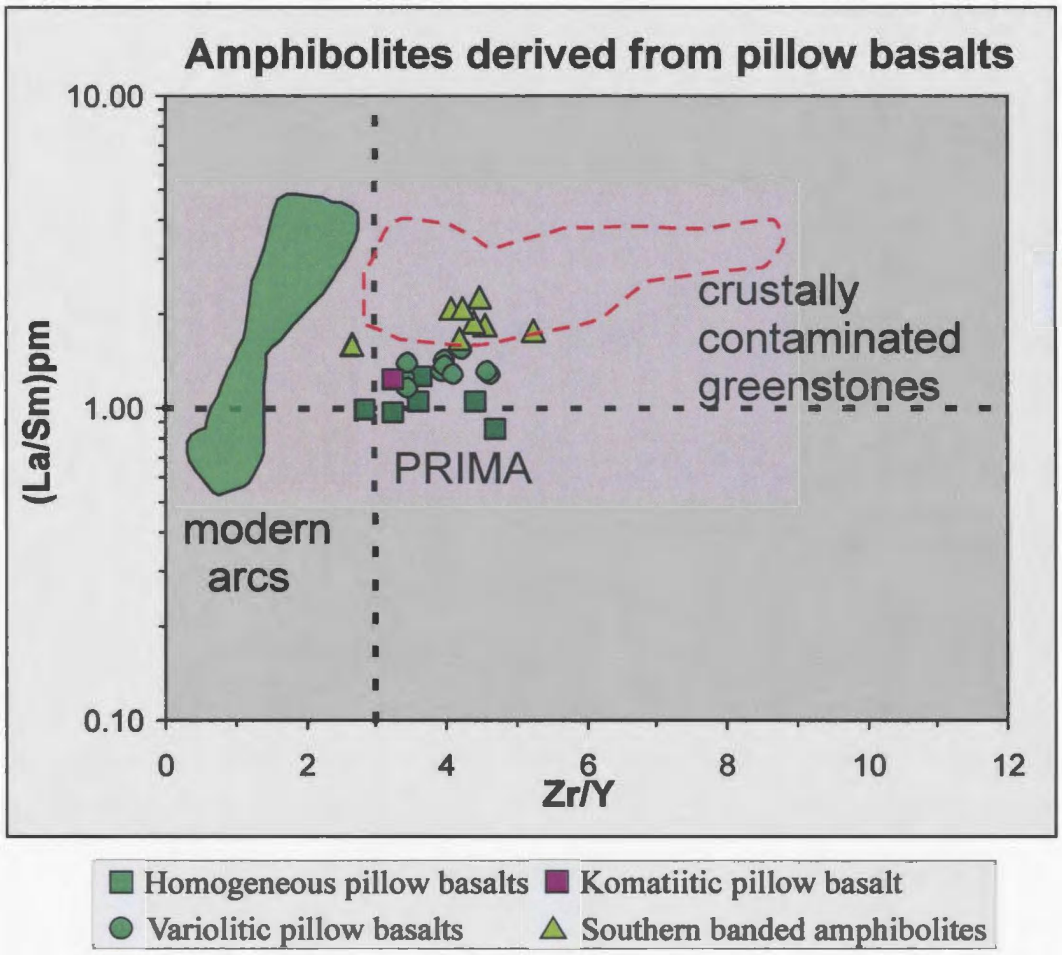

Figure 3.22. La/Sm_{pm} versus Zr/Y plot (after Bolhar et al., 2003) illustrating that trace element features of Ivisârtoq amphibolite samples have closer affinities with crustally contaminated magmas than rocks from subduction zone settings.
PRIMA = primitive mantle; In accordance with Bolhar et al. (2003), normalizing values used are from Sun and McDonough (1989).

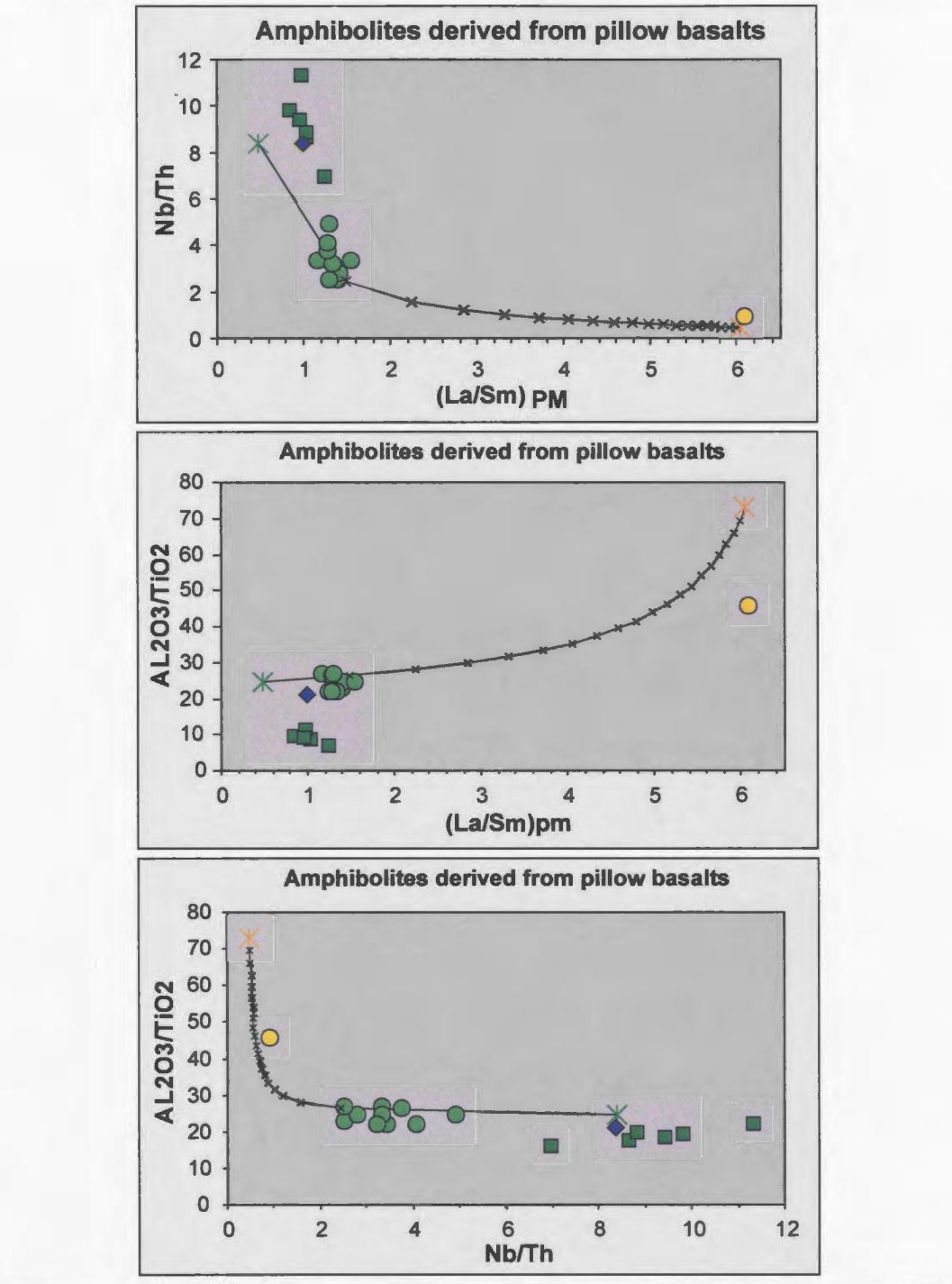

Figure 3.23. Using a high-Mg basalt end-member (Sample KYT374 from the 3.0 Ga Red Lake greenstone belt, Superior Province; Tomlinson et al., 1998) and a felsic end-member (Sample 155807 from the Itsaq Gneiss complex, Kamber et al., 2002), mixing curves (black lines) were generated for different element plots and are used to estimate the amount of crustal contamination (indicated in %) for the variolitic pillow basalts.

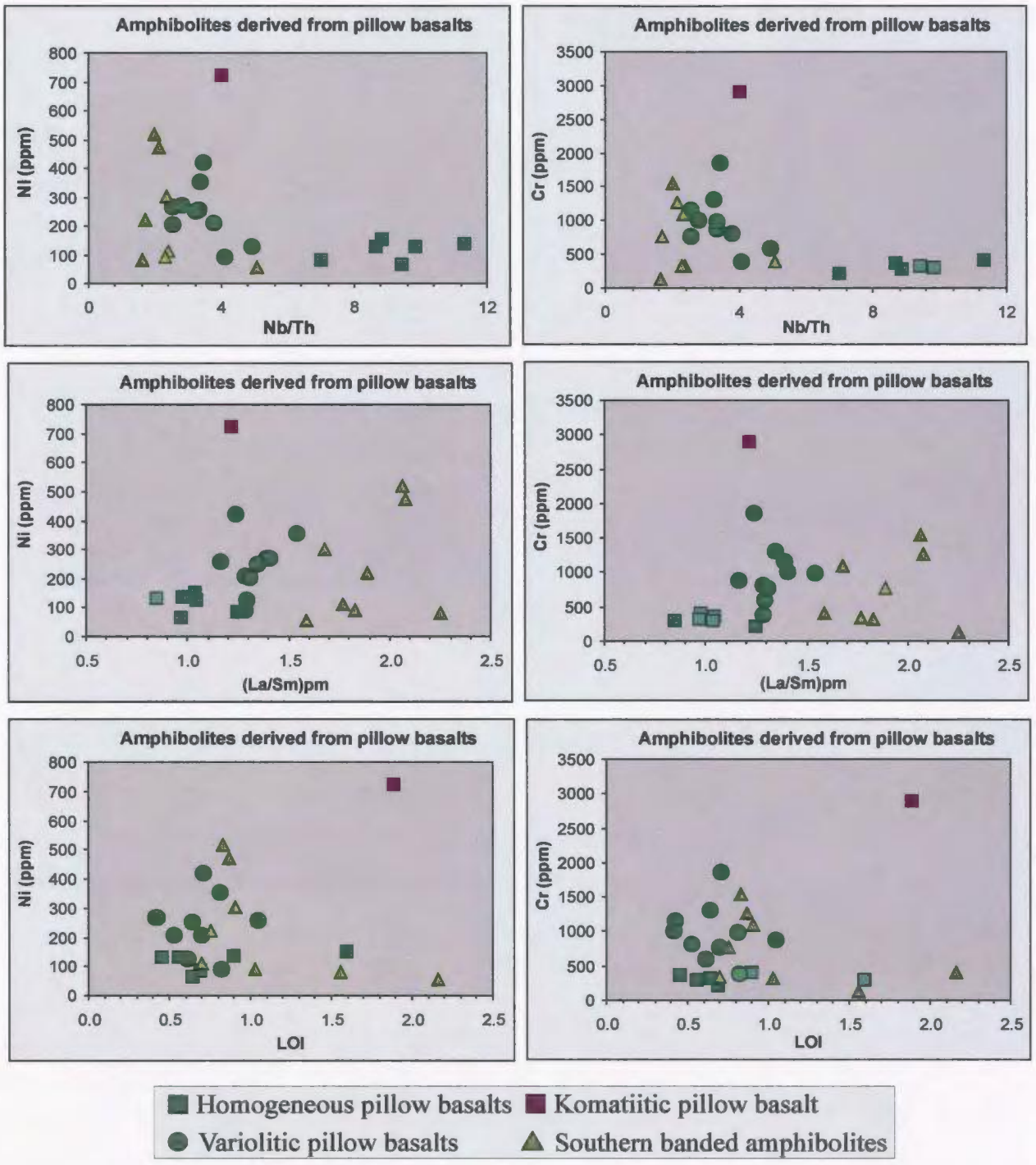

Figure 3.24. On plots of Ni and Cr vs Nb/Th and $(La/Sm)_{pm}$ considerable scatter of data points is observed. The scattering is likely the effect of Ni and Cr dilution during hydration, which is consistent with the decrease of these elements with increasing LOI observed in the homogeneous pillow basalt and the banded amphibolite samples. The variolitic pillow basalts do not exhibit the same degree of scatter and the Ni and Cr values do not decrease with increase in LOI.

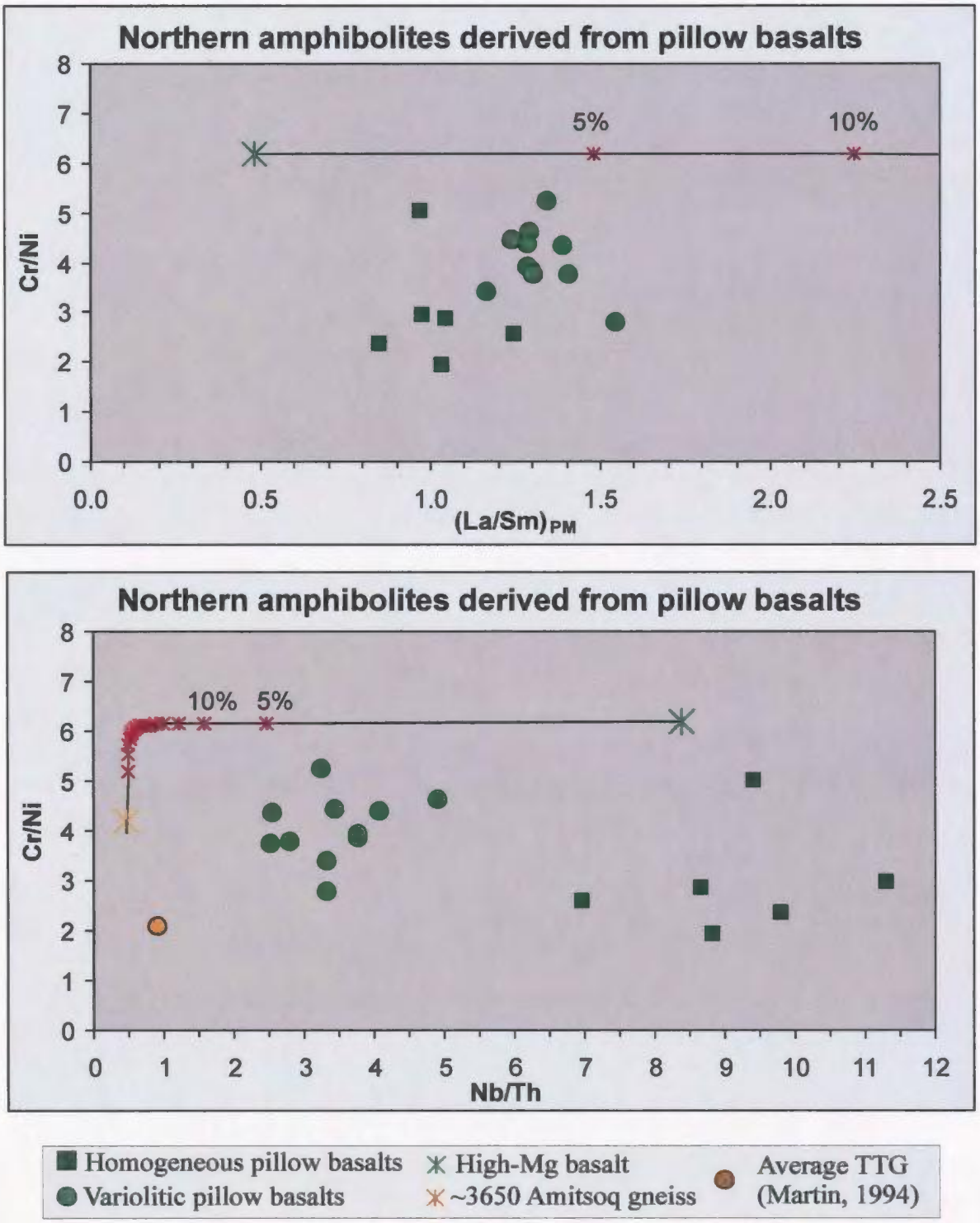

Figure 3.25. A coherent trend is produced for variolitic pillow basalt samples on Cr/Ni vs Nb/Th and $(La/Sm)_{pm}$ plots. These trends are not reflective of crustal contamination as they do not agree with mixing curves generated using a high-Mg basalt and a TTG felsic end members (see black mixing curves).

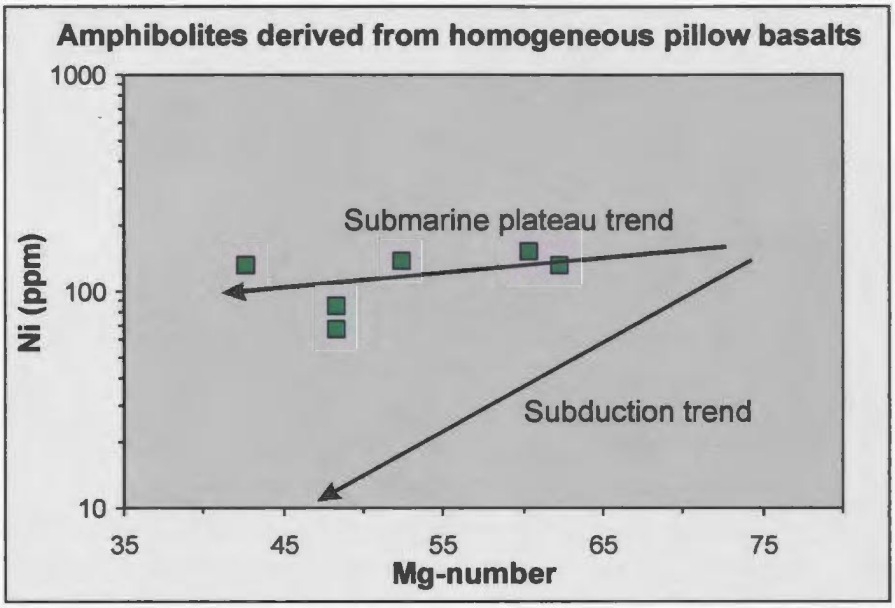

Figure 3.26. The homogeneous pillow basalt samples reflect a "submarine plateau trend" as described by Condie (1994). Condie noted that at an Mg-number of 45 submarine plateau basalts typically have Ni contents of 80-100 ppm. A modern subduction trend, which includes most arc-related basalts would be characterized by Ni decreasing rapidly with falling Mg-number

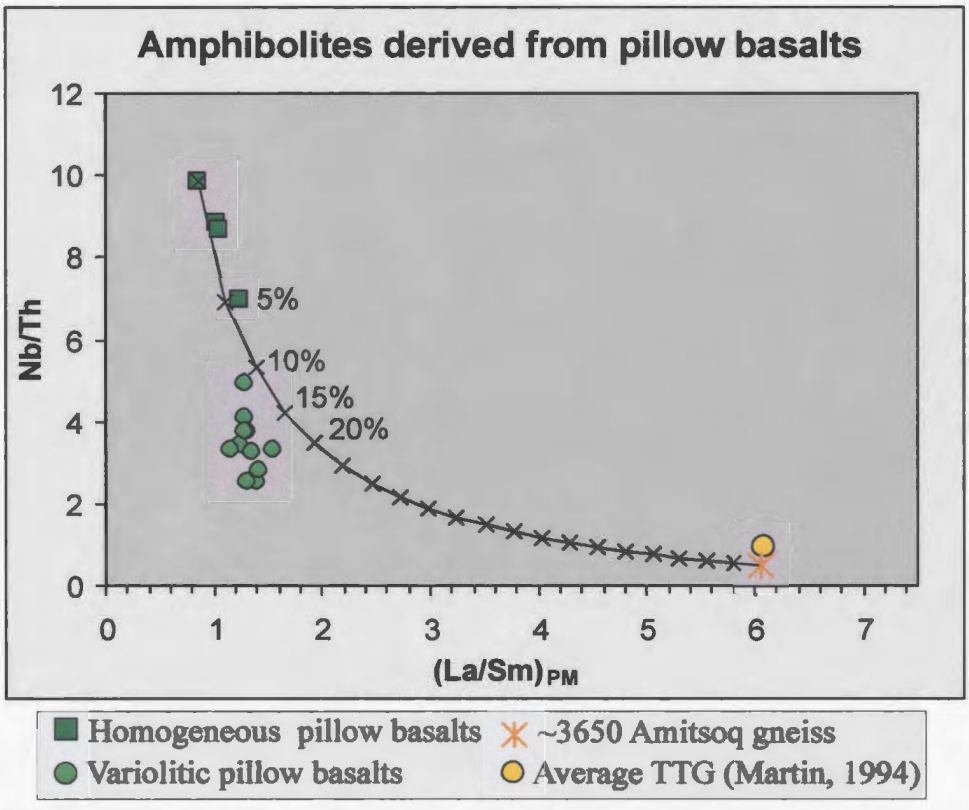

Figure 3.27. The variolitic pillow basalts do plot on a mixing curve (black curve) generated using a depleted homogeneous sample as the mafic end-member and sample 155807 from the Itsaq Gneiss complex (Kamber et al., 2002) as the felsic end-member.

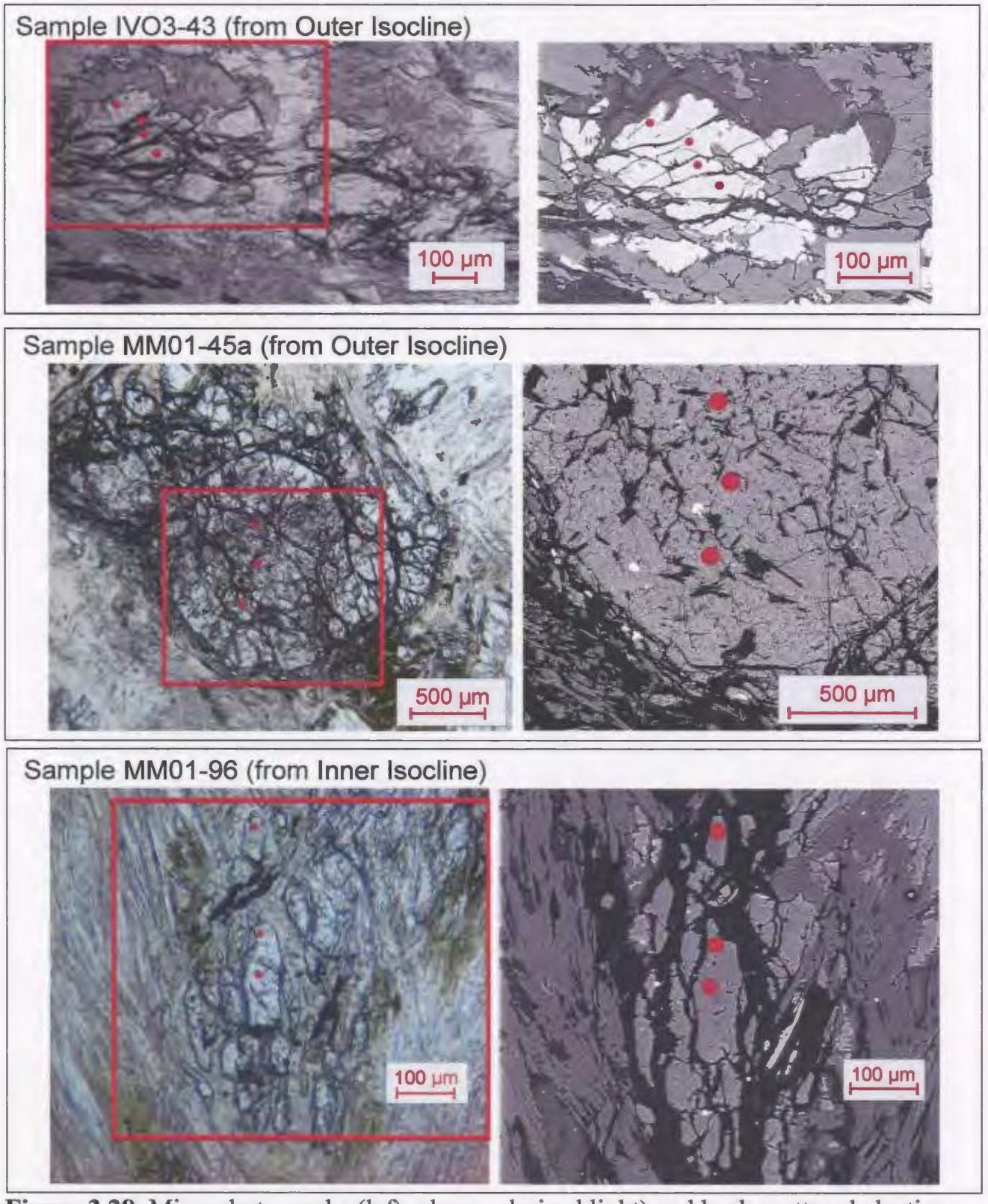

Figure 3.28. Microphotographs (left; plane polarized light) and back scattered election (BSE) images (right) of representative analyzed olivine grains from the folded ultramafic layers. Red outlines indicate BSE imaged area. Red dots indicate locations of individual analysis. For each grain at least one analysis from a rim area and core area were collected.

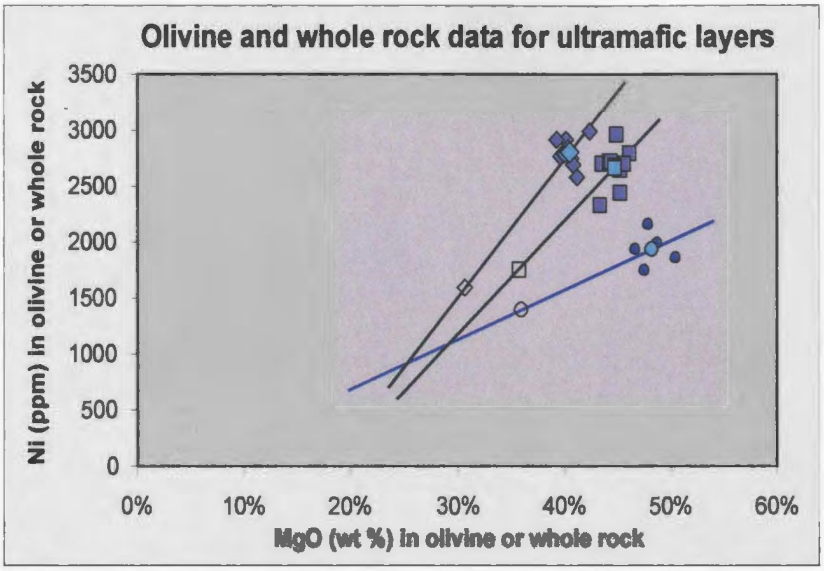

Figure 3.29. MgO and Ni whole rock data from the two ultramafic layers is compared with their respective olivine data; crossing trends are defined (Fig. 3.28). These trends reflect a mixing array between olivine (high Ni, high MgO) and a magmatic component with lower Ni and MgO values.

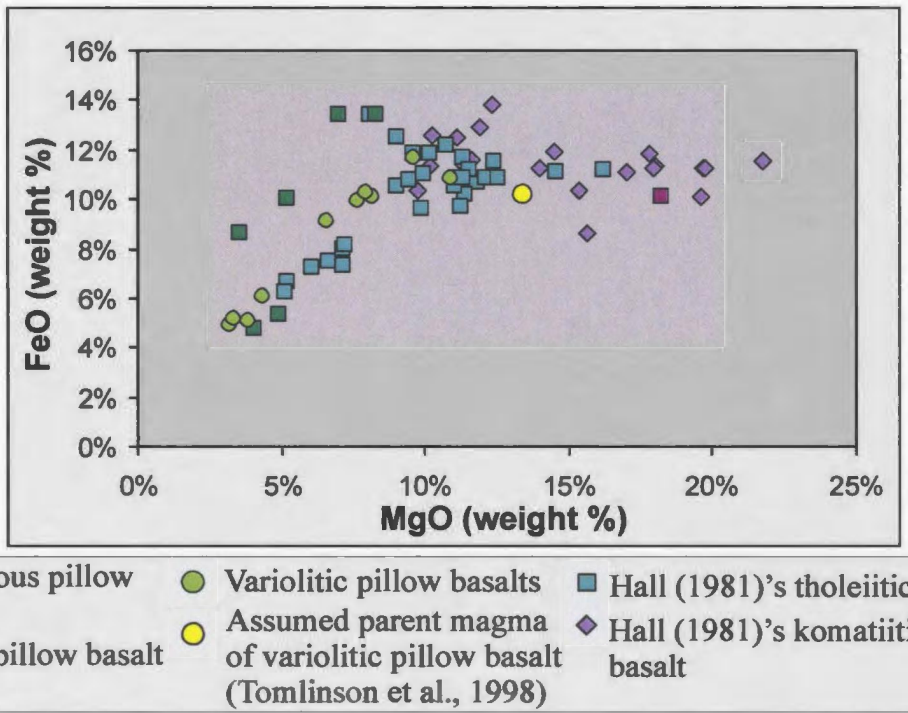

Figure 3.30. MgO and FeO whole rock data from the northern amphibolite units derived from basaltic pillow lavas. FeO varies little with MgO content at MgO>9%. Samples with MgO = 10-23% have an average FeO weight % value of ~11%.

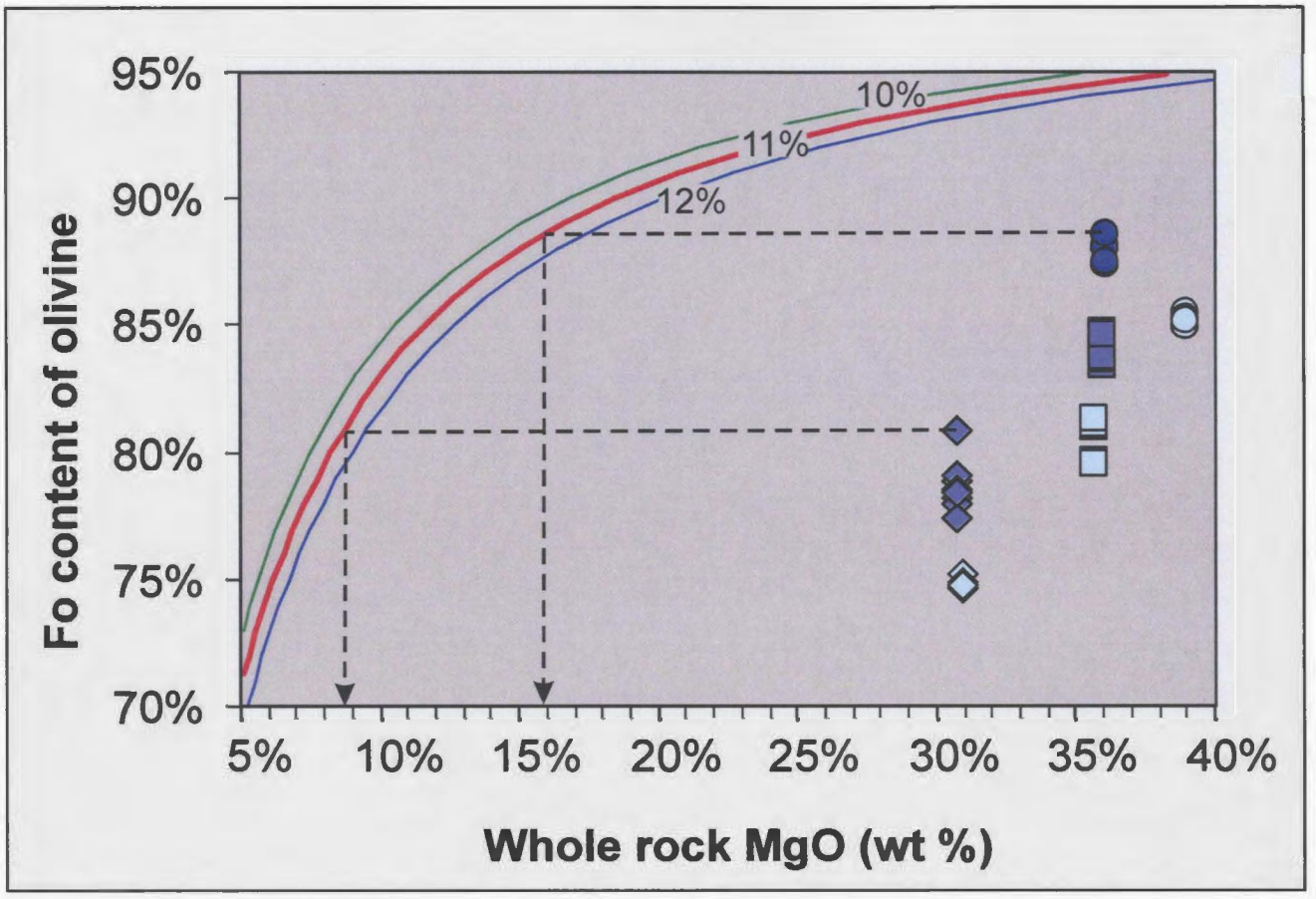

Figure 3.31. Fo contents of olivine versus MgO of whole rocks from ultramafic layers within Ivisârtoq greenstone belt (samples IV03-43, MM01-45a, and MM01-96) and from ultrabasic layers within the nearby Ujaragssuit nunât area (Crewe, 1986). The curves represent the liquid MgO content calculated from the Fo content of olivine in equilibrium with liquids containing 10, 11, and 12% FeO. The calculations were made using an olivine-liquid Mg-Fe distribution coefficient (K_D) of 0.33 (Bickle, 1982). The MgO content of a liquid in equilibrium with an individual olivine grain, or group of olivine grains, can be read directly from the diagram (see dotted lines). The MgO content of the Ivisârtoq ultramafic rocks' parent magma ranged between ~9-16%.

.

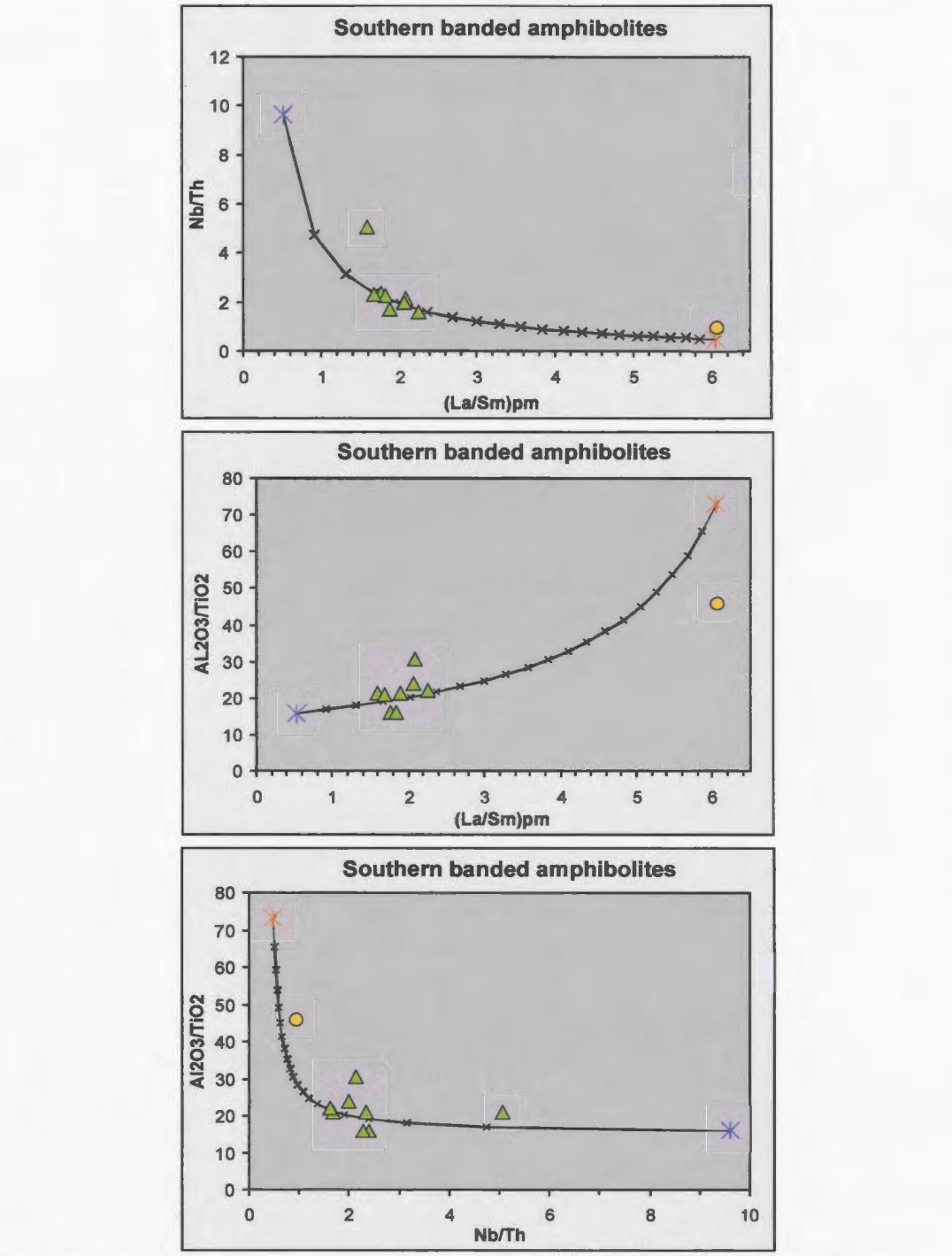

Figure 3.32. Using an uncontaminated komatiitic end-member (AUK average from Sproule et al., 2002) and a felsic end-member (Sample 155807 from the Itsaq Gneiss complex; Kamber et al., 2002), mixing curves (black lines) were generated for different element plots and are used to estimate the amount of crustal contamination (indicated in %) for the southern banded amphibolites.

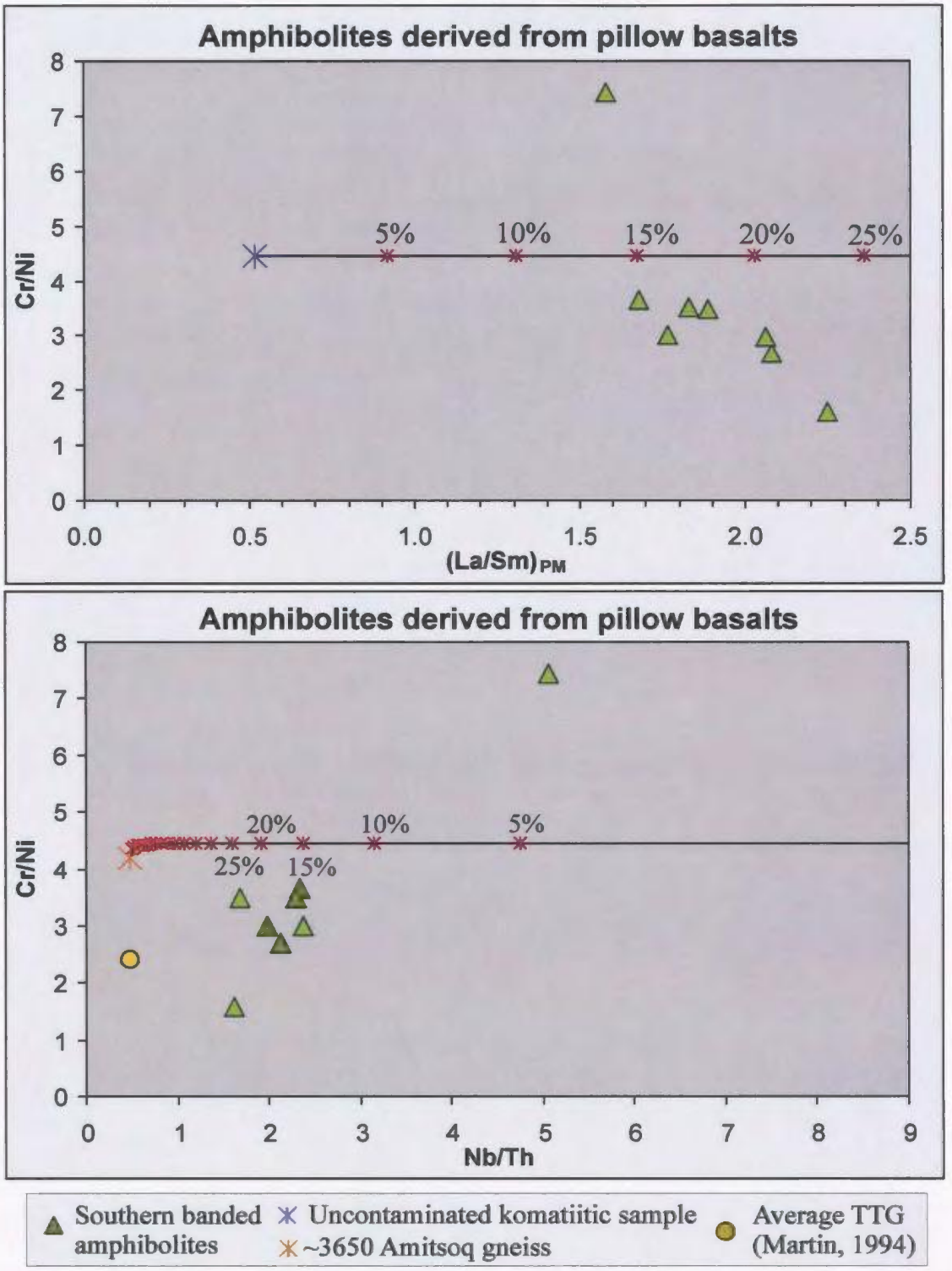

Figure 3.33. A coherent trend is produced for banded amphibolite samples on Cr/Ni vs Nb/Th and $(La/Sm)_{pm}$ plots. These trends are not reflective of crustal contamination as they do not agree with mixing curves generated using an uncontaminated komatiitic and a TTG felsic end members (see black mixing curves).

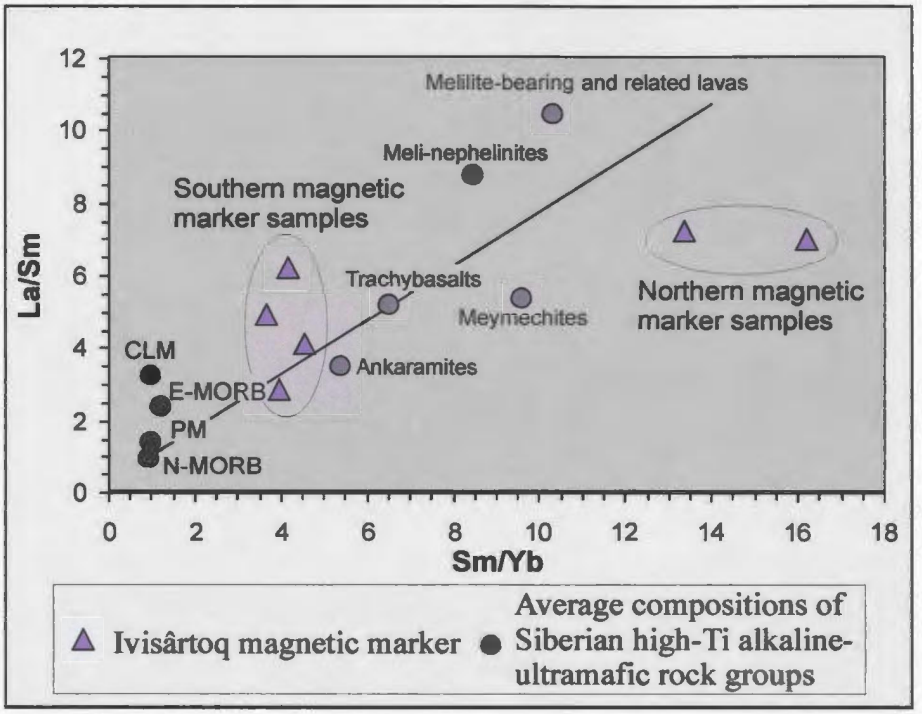

Figure 3.34. The Siberian high-Ti alkaline-ultramafic rock types define a trend (black solid line) towards depleted mantle compositions (after Fedorenko et al., 2000). Magnetic marker samples plot off the trend line and define two groups. Samples from the southern part of the magnetic marker have lower values whereas two more northern samples have higher values. CLM = continental lithospheric mantle (McDonough, 1990); E-MORB = enriched mid-oceanic ridge basalts, N-MORB = normal mid-oceanic ridge basalts, PM = primitive mantle (Sun and McDonough, 1989).

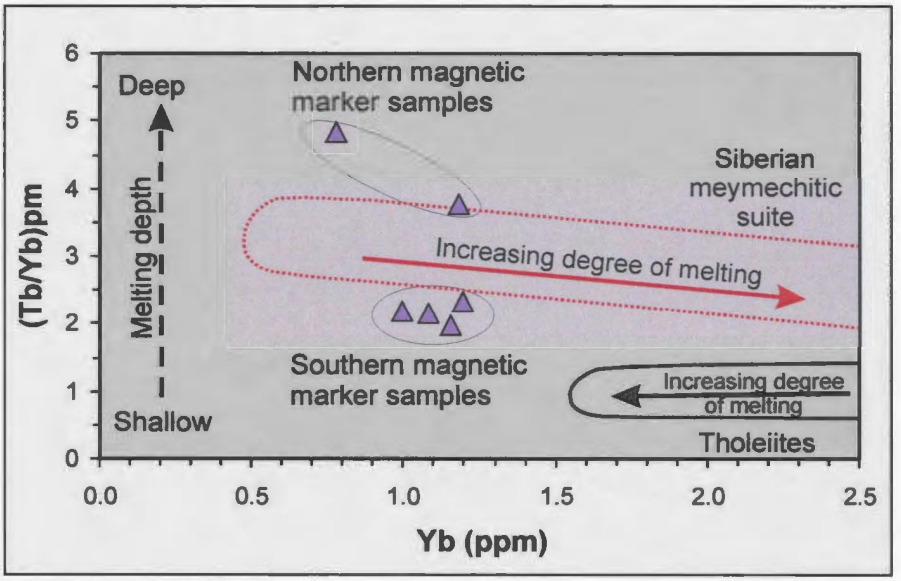

Figure 3.35. $(Tb/Yb)_{pm}$ and Yb values of the magnetic marker samples are similar to true meymechites from the Siberian type-locality (red, dotted outline; Arndt et al., 1998). Arndt et al. (1998) noted that this indicates that meymechites formed from small degree melts at great depths in contrast to larger degree melting at shallow depths, which form tholeiites.

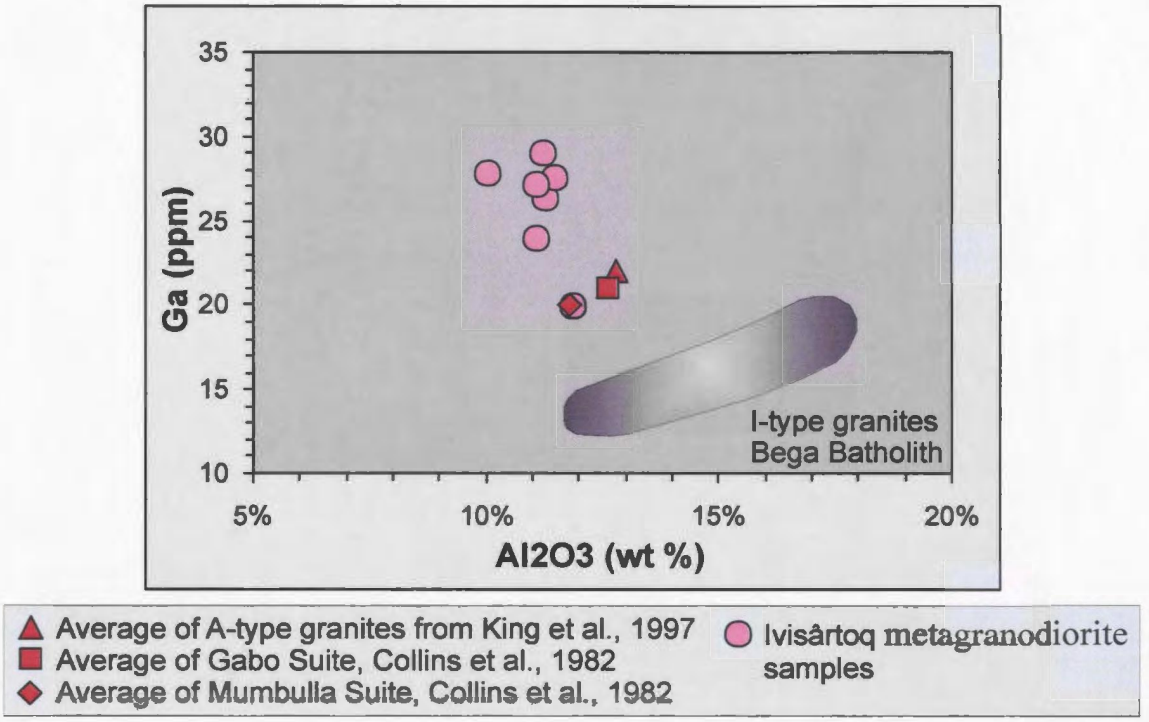

Figure 3.36. Ga versus Al_2O_3 plot demonstrates the similarity of the Ivisârtoq metagranodiorite samples with Australian A-type granites. An I-type granite field based on data from Collins et al. (1982) is plotted for comparison.

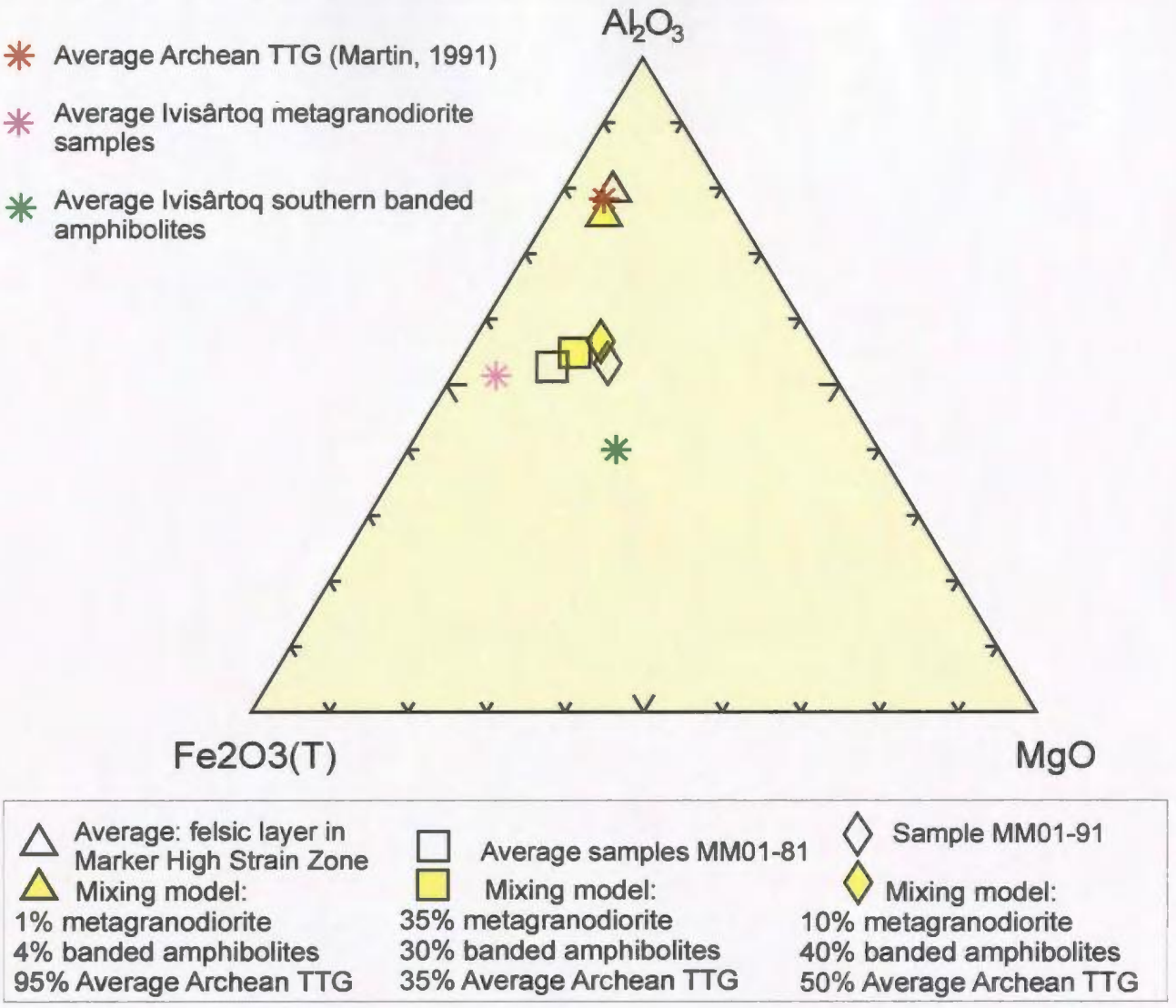

Figure 3.37. Ternary diagram of Al_2O_3,Fe_2O_3, and MgO which illustrates proposed mixing models agree with major element compositions observed in different southern Ivisârtoq metasedimentary rocks.

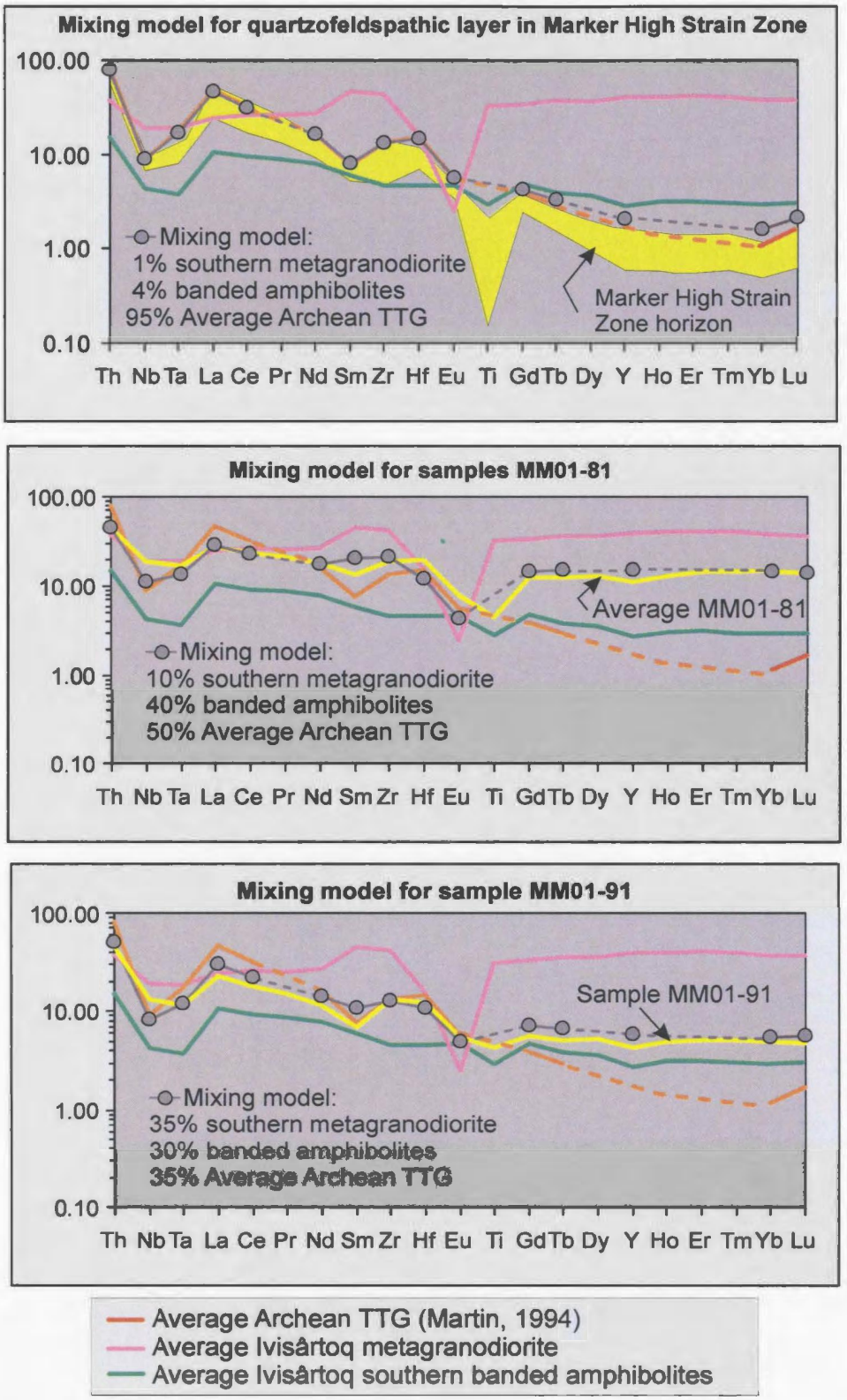

Figure 3.38. Primitive mantle normalized multi-element diagrams which illustrate mixing models proposed for different southern metasedimentary rocks.

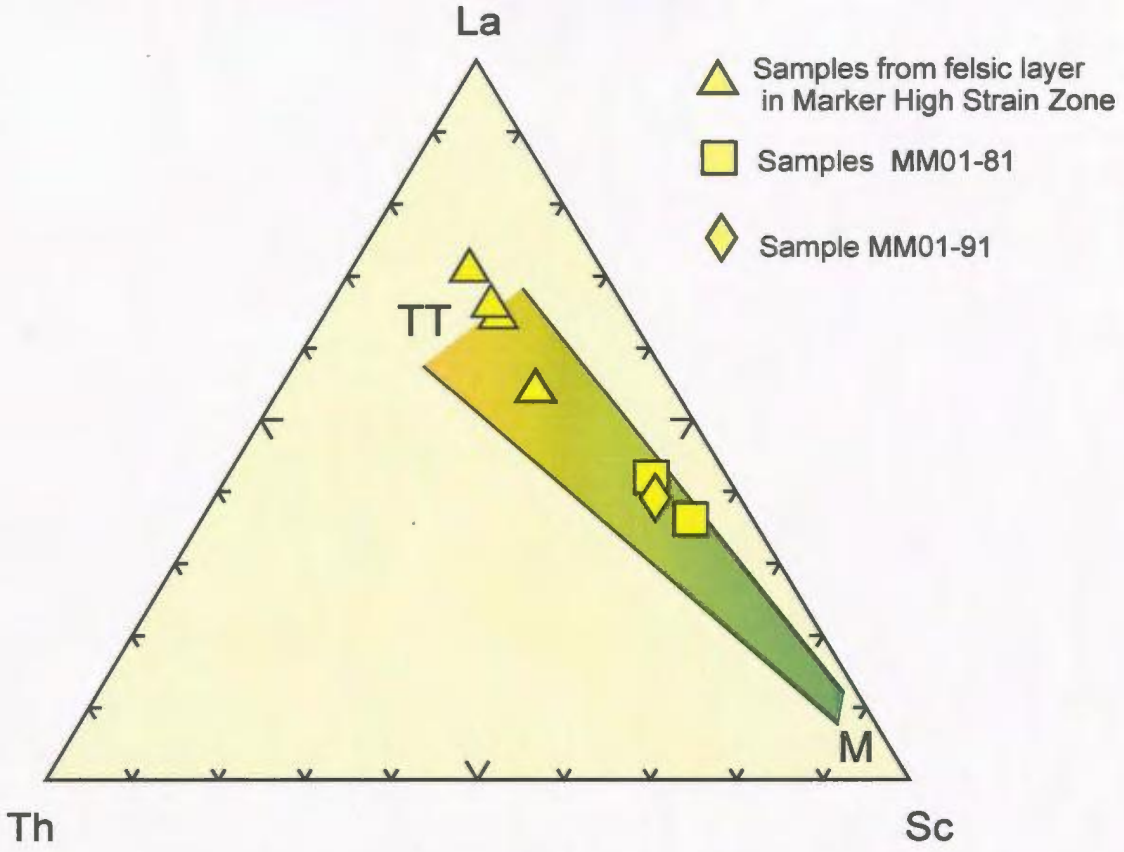

Figure 3.39. Different southern Ivisârtoq metasedimentary rocks plotted on a La-Th-Sc ternary diagram. The felsic Marker High Strain Zone samples plot towards the La-apex, suggesting that the protolith was derived primarily from felsic material, whereas the samples from the thick, southern layer (samples MM01-81, -91) plot closer to the Sc corner, indicating that the protolith was likely derived from a mixture of felsic and mafic components. Mixing band from McLennan and Taylor (1984)
M = mafic component; TT=felsic, tonalite-trondhjemite component

Table 3.1. Major and trace element analyses of the major lithological units of the Ivisârtoq greenstone belt, Greenland.

Northern Homogeneous Pillow Basalts						
	IV03-28	**IV03-31**	**IV03-34a**	**IV03-34b**	**IV03-38**	**MM01-45b**
(weight %)	pillow core	pillow core	pillow rim	pillow core	pillow core	BA within umfc layer
SiO2	49.98	51.36	54.91	53.18	45.06	52.97
TiO2	0.84	0.88	0.92	0.87	0.70	0.80
Al2O3	13.55	15.52	17.90	17.16	15.51	14.77
Fe2O3(T)	14.89	9.58	5.94	5.33	14.90	11.12
MnO	0.21	0.22	0.10	0.13	0.20	0.17
MgO	7.06	3.60	4.98	4.11	8.32	5.26
CaO	11.03	14.19	9.33	15.34	11.63	9.17
K2O	0.15	0.17	0.19	0.05	0.72	0.27
Na2O	1.63	2.42	4.34	1.53	2.22	4.14
P2O5	0.07	0.07	0.06	0.07	0.04	0.06
Sum	99.41	98.01	98.66	97.78	99.32	98.72
LOI	0.69	0.45	0.56	1.60	0.90	0.64
Mg #	48.44	42.71	62.41	60.46	52.53	48.36
(ppm)						
S	22	19	35	51	25	306
Cl	1741	726	1036	1465	929	3737
Sc	45	37	49	39	52	58
V	309	271	324	281	328	351
Cr	216	369	308	293	406	330
Ni	84.5	130	131	152	138	66.0
Cu	46.7	152	65.4	155	65.9	54.5
Zn	49.7	42.7	35.1	23.3	76.0	45.6
Ga	14.8	16.1	19.3	19.5	14.9	18.4
Rb	0.571	1.02	1.78	0.494	11.8	1.37
Sr	115.39	225.43	249.32	262.50	265.45	132.84
Nb	2.87	3.44	3.26	2.75	2.44	2.31
Y	17.40	20.06	15.02	14.82	17.38	14.30
Zr	63.8	72.7	71.1	66.0	49.9	47.0
Ba	23.2	23.9	35.2	18.6	54.3	127
La	3.92	3.97	3.07	3.46	2.75	2.66
Ce	9.48	9.63	8.36	8.44	7.30	6.89
Pr	1.39	1.46	1.32	1.27	1.19	1.05
Nd	6.84	7.45	6.81	6.50	5.99	5.32
Sm	1.97	2.39	2.27	2.10	1.76	1.72
Eu	0.72	0.86	0.88	0.83	0.63	0.70
Gd	2.75	3.16	2.84	2.59	2.56	2.37
Tb	0.47	0.56	0.50	0.45	0.44	0.43
Dy	3.18	3.76	3.30	3.03	3.09	2.88
Ho	0.69	0.79	0.67	0.62	0.69	0.60
Er	2.08	2.36	1.95	1.84	2.12	1.75
Tm	0.31	0.35	0.29	0.27	0.32	0.26
Yb	2.08	2.37	1.88	1.71	2.17	1.72
Lu	0.30	0.37	0.28	0.26	0.31	0.27
Hf	1.69	2.02	2.04	1.95	1.36	1.32
Ta	0.17	0.19	0.20	0.15	0.11	0.12
Th	0.41	0.40	0.33	0.31	0.22	0.25

Analytical method:

Major elements (including S and Cl): X-ray fluorescence fused glass beads method

Trace elements analytic method: ICP-MS Sinter technique

ICP-MS Acid technique

LOI – loss on ignition; BA = banded amphibolite; Umfc = ultramafic

Table 3.1. Major and trace element analyses of the major lithological units of the Ivisârtoq greenstone belt, Greenland (continued).

Northern Variolitic Pillow Basalts										
	MM01-49a	**MM01-70**	**IV03-47**	**IV03-52**	**IV03-55a**	**IV03-55b**	**IV03-57**	**IV03-58**	**IV03-58b**	**IV03-61**
(weight %)	pillow rim	rim + core	pillow core	pillow core	pillow rim	pillow core	pillow core	pillow rim	pillow core	pillow core
SiO2	47.77	47.84	50.20	49.05	62.02	62.10	53.85	63.33	62.47	49.45
TiO2	0.62	0.57	0.62	0.49	0.56	0.54	0.63	0.52	0.52	0.68
Al2O3	13.68	12.92	15.04	13.21	13.73	13.13	13.83	13.54	14.09	15.01
Fe2O3(T)	12.92	11.20	11.00	12.03	6.79	5.48	10.10	5.69	5.72	11.39
MnO	0.24	0.30	0.18	0.22	0.11	0.14	0.16	0.11	0.10	0.19
MgO	9.64	8.15	7.71	10.89	4.37	3.25	6.61	3.90	3.40	7.97
CaO	12.68	15.90	13.11	10.40	11.40	13.39	11.49	11.19	12.11	12.98
K2O	0.19	0.19	0.14	0.58	0.09	0.05	0.20	0.10	0.10	0.23
Na2O	1.40	0.91	1.31	2.28	0.39	0.22	0.92	0.35	0.29	0.87
P2O5	0.04	0.04	0.05	0.04	0.05	0.04	0.04	0.04	0.05	0.05
Sum	99.19	98.03	99.35	99.18	99.51	98.34	97.84	98.78	98.85	98.83
LOI	0.71	0.42	0.62	1.05	0.42	0.81	0.64	0.53	0.70	0.82
Mg #	59.64	59.06	58.13	64.20	56.04	54.04	56.45	57.63	54.05	58.10
(ppm)										
S	21	61	26	20	28	55	34	16	22	24
Cl	1620	1121	1299	601	355	440	695	937	641	846
Sc	51	47	43	40	43	40	46	44	41	34
V	268	254	256	247	252	221	290	240	238	250
Cr	1862	1160	593	873	1016	986	1316	818	768	394
Ni	421	268	129	258	271	355	252	209	206	90.1
Cu	30.8	45.9	34.5	39.5	85.9	140	35.2	48.1	49.9	44.3
Zn	61.1	57.4	30.6	44.6	22.6	18.6	67.6	11.5	7.5	50.9
Ga	13.5	9.39	14.4	7.62	14.0	13.0	12.7	12.6	17.0	17.8
Rb	5.00	3.72	1.38	113	0.75	0.95	2.00	1.96	1.96	1.16
Sr	52.64	88.51	132.41	93.37	56.05	37.96	132.75	54.87	60.33	105.29
Nb	2.01	1.63	2.54	1.60	1.75	2.00	2.20	1.98	1.36	2.29
Y	14.09	13.08	12.96	11.46	12.33	10.95	13.36	9.46	9.37	13.94
Zr	48.2	45.5	51.2	39.7	49.5	46.6	53.3	44.0	43.3	57.5
Ba	27.4	49.4	29.3	80.9	18.3	14.0	57.7	20.3	21.5	17.8
La	2.97	3.21	3.18	2.18	3.34	3.37	3.53	2.53	2.71	3.62
Ce	7.30	7.58	7.46	5.25	7.49	7.20	8.30	5.94	6.24	8.77
Pr	1.04	1.04	1.06	0.77	1.04	0.99	1.16	0.83	0.87	1.26
Nd	5.08	4.97	5.10	3.75	4.98	4.65	5.55	3.97	4.24	6.03
Sm	1.50	1.45	1.54	1.17	1.49	1.37	1.65	1.24	1.30	1.76
Eu	0.47	0.47	0.56	0.41	0.61	0.60	0.50	0.44	0.52	0.65
Gd	2.10	1.95	1.98	1.67	2.04	1.83	2.16	1.59	1.69	2.31
Tb	0.39	0.36	0.36	0.30	0.36	0.33	0.39	0.29	0.30	0.41
Dy	2.60	2.43	2.44	2.09	2.46	2.20	2.61	1.88	1.98	2.69
Ho	0.57	0.52	0.53	0.45	0.51	0.45	0.55	0.40	0.41	0.56
Er	1.69	1.56	1.56	1.40	1.51	1.29	1.65	1.18	1.17	1.68
Tm	0.26	0.22	0.23	0.20	0.22	0.19	0.24	0.17	0.17	0.24
Yb	1.68	1.55	1.54	1.38	1.51	1.23	1.66	1.15	1.13	1.63
Lu	0.24	0.22	0.23	0.21	0.22	0.18	0.25	0.17	0.17	0.24
Hf	1.38	1.36	1.41	1.07	1.48	1.30	1.36	1.25	1.16	1.47
Ta	0.12	0.11	0.11	0.07	0.09	0.10	0.09	0.09	0.10	0.10
Th	0.58	0.64	0.52	0.48	0.63	0.60	0.68	0.53	0.54	0.56

Analytical method:
Major elements (including S and Cl):X-ray fluorescence fused glass beads method
Trace elements analytic method: ICP-MS Sinter technique
ICP-MS Acid technique

LOI= loss on ignition

Table 3.1. Major and trace element analyses of the major lithological units of the Ivisârtoq greenstone belt, Greenland (continued).

	Northern Pillow Basalts resembling Hall (1981) field description of ultramafic pillows			Northern Komatiitic Basalt
	MM01-48a	MM01-48b	MM01-48c	IV03-51
(weight %)	pillow core	pillow rim	pillow core	pillow core
SiO2	53.36	55.97	52.93	49.13
TiO2	0.50	0.45	0.52	0.33
Al2O3	12.61	12.17	12.87	8.56
Fe2O3(T)	9.92	7.30	10.42	11.17
MnO	0.19	0.19	0.18	0.24
MgO	8.40	4.80	8.03	18.22
CaO	12.05	17.57	12.73	9.33
K2O	0.09	0.09	0.07	0.42
Na2O	1.37	0.22	0.70	0.98
P2O5	0.05	0.03	0.03	0.03
Sum	98.53	98.79	98.49	98.40
LOI	0.63	0.64	0.62	1.89
Mg #	62.67	56.56	60.42	76.36
S	36	319	18	35
Cl	731	2676	1247	660
Sc	36	39	42	23
V	229	198	256	172
Cr	1067	1941	2385	2907
Ni	278	231	259	722
Cu	71.3	59.7	28.6	4.67
Zn	34.4	30.0	48.4	47.4
Ga	12.5	11.8	14.1	9.01
Rb	1.34	28.8	1.25	28.4
Sr	121.47	165.39	136.86	19.35
Nb	1.96	2.78	1.91	0.87
Y	10.93	11.18	13.42	7.76
Zr	39.2	31.4	39.2	25.5
Ba	20.2	30.2	58.3	123
La	2.64	2.40	1.51	1.52
Ce	6.06	5.13	4.27	3.47
Pr	0.85	0.73	0.70	0.51
Nd	4.20	3.55	3.74	2.55
Sm	1.27	1.07	1.21	0.78
Eu	0.52	0.41	0.37	0.25
Gd	1.80	1.59	1.87	1.20
Tb	0.31	0.29	0.34	0.20
Dy	2.14	1.98	2.41	1.42
Ho	0.44	0.43	0.52	0.32
Er	1.31	1.29	1.57	0.95
Tm	0.19	0.19	0.24	0.14
Yb	1.28	1.29	1.57	0.93
Lu	0.20	0.19	0.23	0.13
Hf	1.10	0.87	1.06	0.68
Ta	0.11	0.18	0.13	0.07
Th	0.52	0.30	0.36	0.22

Analytical method:
Major elements (including S and Cl): X-ray fluorescence fused glass beads method
Trace elements analytic method: ICP-MS Sinter technique
ICP-MS Acid technique

LOI= loss on ignition

Table 3.1. Major and trace element analyses of the major lithological units of the Ivisârtoq greenstone belt, Greenland (continued).

Southern Banded Amphibolites								
	MM01-31a	**MM01-31b**	**MM01-32a**	**MM01-39a**	**MM01-42b**	**MM01-55**	**MM01-98**	**MM01-102**
(weight %)								
SiO2	49.79	49.33	48.43	47.34	48.24	47.61	48.19	48.98
TiO2	0.81	0.79	0.54	0.36	0.68	0.62	0.41	0.56
Al2O3	13.06	12.80	11.52	11.17	15.08	13.17	9.95	11.85
Fe2O3(T)	11.39	10.61	10.06	9.03	10.26	9.25	10.99	10.65
MnO	0.22	0.21	0.20	0.20	0.20	0.24	0.20	0.19
MgO	7.82	7.10	9.46	10.78	4.46	6.15	8.94	10.73
CaO	11.45	12.57	15.09	18.56	18.16	19.62	17.95	13.74
K2O	0.93	2.17	0.41	0.44	0.25	0.32	0.26	0.72
Na2O	2.43	1.95	1.66	0.52	1.34	1.72	1.45	1.46
P2O5	0.17	0.16	0.13	0.10	0.17	0.10	0.09	0.10
Sum	98.07	97.70	97.51	98.50	98.86	98.80	98.44	98.99
LOI	0.70	1.03	0.76	0.86	1.56	2.16	0.83	0.91
Mg #	57.64	57.02	65.08	70.27	46.27	56.84	61.71	66.60
(ppm)								
S	18	36	27	25	36	29	56	106
Cl	923	199	1288	2163	27	1713	1021	1120
Sc	37	34	41	36	44	41	44	35
V	272	247	224	199	259	263	209	221
Cr	339	320	772	1267	133	402	1546	1102
Ni	113	91.4	221	472	83.4	54.1	518	301
Cu	19.7	314	81.8	127	60.1	29.0	19.4	30.5
Zn	56.7	49.5	43.6	38.1	53.9	51.5	50.9	63.9
Ga	15.2	13.0	13.4	13.0	16.6	14.9	7.69	12.1
Rb	21.3	65.9	13.3	18.3	9.77	12.0	3.63	47.9
Sr	212.43	271.86	306.42	320.65	303.44	238.71	114.01	187.76
Nb	4.01	4.11	2.47	2.17	3.73	3.03	2.18	2.71
Y	13.93	16.62	10.49	7.91	15.14	14.62	9.71	12.44
Zr	73.4	75.8	46.1	32.4	67.6	39.0	41.1	52.3
Ba	394	1153	275	214	238	228	30.5	1110
La	8.74	9.81	8.80	5.64	13.37	4.70	6.47	6.31
Ce	20.09	22.18	19.54	11.86	27.58	10.91	13.65	14.40
Pr	2.82	3.08	2.65	1.54	3.69	1.58	1.87	2.03
Nd	13.07	14.12	11.79	6.80	16.34	7.28	8.29	9.25
Sm	3.10	3.36	2.92	1.70	3.73	1.86	1.97	2.36
Eu	0.86	1.14	0.75	0.53	1.18	0.64	0.58	0.68
Gd	3.26	3.67	2.87	1.76	3.65	2.34	2.01	2.51
Tb	0.48	0.55	0.40	0.26	0.52	0.40	0.31	0.40
Dy	2.89	3.39	2.33	1.62	3.06	2.67	1.98	2.53
Ho	0.56	0.66	0.43	0.32	0.61	0.57	0.41	0.50
Er	1.60	1.87	1.24	0.92	1.79	1.75	1.18	1.43
Tm	0.23	0.27	0.17	0.14	0.26	0.26	0.18	0.21
Yb	1.49	1.78	1.17	0.90	1.72	1.75	1.17	1.35
Lu	0.22	0.26	0.18	0.14	0.25	0.25	0.17	0.22
Hf	1.74	1.88	1.38	0.91	1.71	1.12	1.16	1.41
Ta	0.22	0.23	0.13	0.10	0.19	0.10	0.12	0.16
Th	1.68	1.80	1.46	1.02	2.30	0.60	1.10	1.16

Analytical method:

Major elements (including S and Cl): X-ray fluorescence fused glass beads method

Trace elements analytic method: ICP-MS Sinter technique

ICP-MS Acid technique

LOI – loss on ignition

Table 3.1. Major and trace element analyses of the major lithological units of the Ivisârtoq greenstone belt, Greenland (continued).

Mafic Dykes								
	Northern	***Northern***	***Southern***	***Southern***	***Northern***	***Southern***	***Southern***	***Southern***
	MM01-71a	**MM01-106**	**MM01-26**	**MM01-29**	**MM01-107**	**MM01-109**	**MM01-40b**	**MM01-79**
(weight %)	Gabbroic	Gabbroic	Plag phyric	Plag phyric	Plag phyric	Plag phyric	Gabbroic	Gabbroic
SiO2	47.43	48.91	46.48	46.98	49.11	46.75	47.88	47.46
TiO2	0.98	0.92	1.12	0.91	0.89	0.91	1.08	0.91
Al2O3	15.43	14.64	15.89	21.44	16.00	19.33	16.25	15.55
Fe2O3(T)	12.47	13.04	12.13	9.69	12.05	11.99	12.40	13.00
MnO	0.19	0.21	0.18	0.13	0.18	0.19	0.17	0.18
MgO	8.20	8.45	7.76	3.97	7.64	6.97	6.57	7.70
CaO	11.40	10.98	10.03	9.99	11.23	10.65	10.79	10.66
K2O	0.17	0.26	1.38	0.64	0.22	0.60	0.26	0.16
Na2O	1.98	1.54	2.29	3.49	2.01	2.43	2.27	2.15
P2O5	0.07	0.07	0.12	0.14	0.11	0.12	0.13	0.09
Sum	98.31	99.01	97.38	97.39	99.44	99.93	97.81	97.86
LOI	0.78	0.83	0.82	0.69	0.78	1.46	0.66	0.91
Mg #	56.56	56.22	55.90	44.82	55.66	53.55	51.22	53.99
(ppm)								
S	59	35	34	52	27	30	35	29
Cl	810	1558	1072	1362	1060	987	1142	1544
Sc	50	47	41	29	43	24	50	44
V	291	291	242	160	260	197	249	227
Cr	383	328	298	241	437	323	471	236
Ni	154	136	138	60.0	148	129	98.7	93.8
Cu	77.5	142	23.3	51.3	42.2	23.3	17.5	80.7
Zn	49.4	71.0	46.5	36.7	46.8	52.8	53.5	45.7
Ga	18.9	15.3	19.6	19.4	17.5	16.8	19.7	17.6
Rb	4.92	10.2	89.4	22.2	4.54	43.0	5.71	1.81
Sr	103.66	95.16	164.23	464.32	109.77	167.05	140.18	159.61
Nb	2.98	3.01	2.69	1.68	2.19	1.62	2.38	1.89
Y	17.56	17.54	16.71	12.75	14.13	12.56	16.70	13.63
Zr	64.1	56.4	57.1	42.5	40.1	35.8	48.1	38.7
Ba	70.7	55.1	161	41.1	43.4	113	51.9	29.3
La	2.30	2.35	3.59	2.45	2.56	2.78	3.34	2.68
Ce	6.87	6.71	8.67	6.13	6.39	6.38	8.29	6.39
Pr	1.16	1.12	1.25	0.93	0.99	0.98	1.25	0.97
Nd	6.36	6.01	6.24	4.87	5.18	5.04	6.55	4.91
Sm	2.08	2.01	1.85	1.45	1.64	1.50	2.00	1.51
Eu	0.76	0.74	0.80	0.70	0.69	0.70	0.90	0.69
Gd	2.91	3.01	2.61	2.12	2.14	1.93	2.55	2.21
Tb	0.52	0.51	0.46	0.36	0.39	0.34	0.46	0.39
Dy	3.44	3.44	3.18	2.45	2.66	2.29	3.16	2.67
Ho	0.73	0.71	0.69	0.51	0.60	0.52	0.71	0.57
Er	2.15	2.09	2.03	1.48	1.77	1.52	2.12	1.69
Tm	0.31	0.31	0.31	0.21	0.26	0.22	0.31	0.24
Yb	2.09	2.04	2.09	1.42	1.71	1.45	2.02	1.66
Lu	0.30	0.30	0.32	0.22	0.27	0.24	0.32	0.25
Hf	1.78	1.57	1.48	1.00	1.12	0.92	1.32	1.16
Ta	0.16	0.16	0.15	0.10	0.11	0.10	0.13	0.10
Th	0.23	0.21	0.39	0.30	0.24	0.25	0.32	0.24

Analytical method:
Major elements (including S and Cl):X-ray fluorescence fused glass beads method
Trace elements analytic method: *ICP-MS Sinter technique*
ICP-MS Acid technique
LOI– loss on ignition; Plag=plagioclase

Table 3.1. Major and trace element analyses of the major lithological units of the Ivisârtoq greenstone belt, Greenland (continued).

Northern Ultramafic Layers				
	MM01-45a	**IV03-43**	**IV03-54**	**IV03-59**
(weight %)	Outer Fold	Outer Fold	Inner Fold	Inner Fold
SiO2	45.88	48.55	44.34	46.87
TiO2	0.17	0.09	0.16	0.18
Al2O3	4.01	3.55	2.90	2.90
Fe2O3(T)	10.72	8.63	9.86	9.67
MnO	0.17	0.15	0.11	0.11
MgO	35.99	30.75	41.03	34.81
CaO	2.59	6.55	0.68	4.68
K2O	0.01	0.02	0.01	0.01
Na2O	0.01	0.02	0.02	0.09
P2O5	0.01	0.01	0.01	0.01
Sum	99.57	98.32	99.13	99.32
LOI	4.41	6.33	11.80	8.74
Mg #	86.93	87.60	89.19	87.70
(ppm)				
S	300	41	76	102
Cl	3204	408	1390	1323
Sc	12	13	9	15
V	83	57	53	71
Cr	7138	5210	2115	1947
Ni	1749	1589	2125	2017
Cu	6.29	8.56	17.1	42.0
Zn	43.4	46.5	37.0	37.8
Ga	2.78	3.32	3.48	3.26
Rb	0.270	2.07	0.560	0.320
Sr	19.66	135.34	4.10	19.88
Nb	2.31	< LD	0.82	0.52
Y	3.07	2.67	2.53	3.12
Zr	15.4	8.07	12.8	12.9
Ba	8.431	6.19	7.14	5.69
La	1.01	1.05	0.78	1.31
Ce	2.28	2.12	1.89	3.16
Pr	0.30	0.25	0.26	0.42
Nd	1.40	1.06	1.20	1.88
Sm	0.37	0.28	0.32	0.45
Eu	0.08	0.19	0.03	0.07
Gd	0.50	0.38	0.37	0.52
Tb	0.08	0.07	0.06	0.09
Dy	0.61	0.46	0.42	0.57
Ho	0.13	0.11	0.09	0.13
Er	0.39	0.31	0.30	0.38
Tm	0.06	0.05	0.05	0.06
Yb	0.41	0.33	0.37	0.40
Lu	0.07	0.05	0.06	0.06
Hf	0.43	0.22	0.35	0.36
Ta	0.05	0.06	0.04	0.05
Th	0.24	0.05	0.09	0.09

Analytical method:

Major elements (including S and Cl):X-ray fluorescence fused glass beads method

Trace elements analytic method: *ICP-MS Sinter technique*

ICP-MS Acid technique

LOI= loss on ignition

Table 3.1. Major and trace element analyses of the major lithological units of the Ivisârtoq greenstone belt, Greenland (continued).

Magentic Marker						
	MM01-104	**IV03-1**	**IV03-3**	**IV03-16**	**IV03-23**	**IV03-24**
(weight %)						
SiO2	41.41	45.24	44.03	42.67	44.32	31.98
TiO2	1.41	1.17	1.13	1.65	2.02	3.44
Al2O3	6.08	4.98	3.74	4.03	4.23	6.51
Fe2O3(T)	19.18	16.82	19.23	20.91	15.54	21.77
MnO	0.25	0.26	0.23	0.30	0.23	0.37
MgO	19.60	17.98	20.03	19.24	24.39	22.89
CaO	7.41	10.66	9.04	10.61	6.45	10.39
K2O	2.44	0.63	1.01	0.03	1.58	0.63
Na2O	0.71	0.88	0.52	0.11	0.38	0.39
P2O5	0.10	0.07	0.09	0.10	0.42	0.49
Sum	98.58	98.69	99.04	99.66	99.55	98.85
LOI	1.92	1.49	1.68	2.41	4.00	10.30
Mg #	66.94	67.92	67.36	64.57	75.67	67.57
(ppm)						
S	31	21	29	24	28	28
Cl	1019	812	780	734	395	1507
Sc	27	25	30	35	26	24
V	179	191	185	174	121	174
Cr	1563	1371	1510	1405	617	1285
Ni	1157	1016	1484	1385	453	824
Cu	27.3	450	440	180	8.86	11.9
Zn	72.4	60.4	54.1	67.4	57.5	85.3
Ga	10.2	5.09	3.44	5.03	7.75	12.2
Rb	246	42.7	53.6	<LD	70.8	25.1
Sr	216.71	394.51	199.52	100.44	220.91	602.70
Nb	21.31	19.28	15.78	26.35	64.28	77.76
Y	10.56	11.70	11.45	13.28	12.46	15.81
Zr	92.8	78.5	85.8	120	159	290
Ba	704	450	346	12.3	262	137
La	25.88	20.93	12.49	22.59	88.37	114.07
Ce	55.08	48.07	35.25	52.14	191.72	248.53
Pr	6.60	6.00	5.25	6.90	24.12	31.15
Nd	25.60	23.98	22.61	28.46	92.37	118.10
Sm	4.14	4.24	4.32	5.44	12.58	15.78
Eu	1.69	1.29	1.31	1.39	2.13	3.58
Gd	3.43	3.67	3.77	4.53	7.43	8.82
Tb	0.49	0.51	0.52	0.62	0.84	0.99
Dy	2.67	2.89	2.96	3.37	3.73	4.51
Ho	0.46	0.51	0.50	0.59	0.55	0.69
Er	1.19	1.31	1.33	1.50	1.23	1.58
Tm	0.16	0.18	0.17	0.20	0.15	0.20
Yb	0.99	1.16	1.08	1.20	0.78	1.18
Lu	0.14	0.16	0.14	0.16	0.10	0.16
Hf	2.16	1.94	2.16	2.97	3.62	6.53
Ta	1.21	0.82	0.97	1.68	3.21	6.18
Th	1.67	2.30	1.88	2.34	7.31	9.94

Analytical method:

Major elements (including S and Cl):X-ray fluorescence fused glass beads method

Trace elements analytic method: ICP-MS Sinter technique

LOI= loss on ignition

Table 3.1. Major and trace element analyses of the major lithological units of the Ivisârtoq greenstone belt, Greenland (continued).

	Northern thin rusty quartzofeldspathic (tonalitic) sheets							TTG intruding
	MM01-47c	MM01-50	MM01-64b	MM01-69b	MM01-73b	IV03-11	IV03-25	N boundary of belt
(weight %)								IV03-66
SiO2	73.90	59.39	70.11	63.61	54.36	67.75	67.99	72.26
TiO2	0.61	1.65	0.26	0.85	0.89	0.53	0.46	0.10
Al2O3	13.82	18.21	15.45	18.21	16.63	15.83	15.26	16.20
Fe2O3T	2.43	6.66	1.40	1.51	6.48	4.37	2.96	1.08
MnO	0.02	0.12	0.02	0.02	0.12	0.06	0.04	0.04
MgO	2.31	2.06	0.85	1.61	7.44	1.47	1.26	0.32
CaO	0.40	5.41	1.17	5.91	11.78	2.07	2.33	1.12
K2O	3.66	4.75	2.79	3.53	0.07	2.34	0.54	3.80
Na2O	0.46	0.03	5.47	2.93	0.65	3.28	7.27	5.08
P2O5	0.03	0.06	0.03	0.04	0.05	0.15	0.16	0.03
Sum	97.65	98.35	97.56	98.23	98.47	97.86	98.27	100.03
LOI	2.48	2.58	0.51	0.47	N/A	0.97	0.24	N/A
Mg#	65.33	38.01	54.62	67.94	69.46	40.01	45.75	36.96
(ppm)								
S	58	42	25	32	22204	17	20	61
Cl	949	609	964	807	89	730	312	73
Sc	30	42	47	34	68	8	11	3
V	145	373	70	274	181	75	52	4
Cr	200	773	114	550	835	75	76	9
Ni	103	213	69.5	51.8	93.0	22.2	27.0	0.068
Cu	250	88.2	141	16.6	243	12.7	6.60	1.22
Zn	28.6	115.82	47.1	81.8	44.3	30.7	21.0	22.2
Ga	16.7	25.0	19.5	17.6	14.0	18.8	20.0	27.5
Rb	182	140	150	135	3.99	56.7	15.7	194
Sr	9.57	83.19	47.53	84.38	84.40	163.91	86.95	170.65
Nb	3.79	7.54	5.30	7.11	4.16	6.38	8.06	15.22
Y	8.28	14.49	5.82	9.47	20.19	4.70	5.83	6.19
Zr	145	146	60.4	126	88.0	181	152	88.1
Ba	574	1385	477	3533	24.6	480	201	853
La	10.80	5.54	8.54	4.84	3.93	14.48	7.76	20.18
Ce	22.43	12.51	16.95	9.27	8.37	27.48	20.96	38.67
Pr	2.63	1.66	1.94	1.17	1.13	3.20	2.67	3.78
Nd	9.87	7.29	7.17	4.73	5.25	12.04	11.33	12.07
Sm	1.96	2.10	1.27	1.14	1.60	2.08	2.37	2.04
Eu	0.40	0.99	0.48	0.17	0.59	0.70	0.71	0.35
Gd	1.61	2.38	1.06	1.34	2.48	1.51	1.88	1.53
Tb	0.28	0.45	0.19	0.24	0.49	0.19	0.25	0.24
Dy	1.74	3.04	1.16	1.59	3.50	0.98	1.28	1.28
Ho	0.35	0.62	0.23	0.36	0.82	0.18	0.23	0.21
Er	1.01	1.81	0.66	1.18	2.49	0.51	0.58	0.55
Tm	0.16	0.26	0.10	0.18	0.37	0.07	0.08	0.08
Yb	1.04	1.69	0.61	1.28	2.50	0.49	0.49	0.49
Lu	0.16	0.24	0.10	0.20	0.35	0.08	0.07	0.06
Hf	3.31	3.75	1.95	3.18	2.28	4.33	3.44	2.78
Ta	0.31	0.36	0.51	0.40	0.53	0.39	0.53	1.61
Th	4.00	1.56	3.96	2.94	1.15	4.27	4.58	6.36

Analytical method:

Major elements (including S and Cl):X-ray fluorescence fused glass beads method

Trace elements analytic method: *X-ray fluorescence pressed pellets method*; *ICP-MS Sinter technique*; *ICP-MS Acid technique*

LOI= loss on ignition; N/A= not applicable

Table 3.1. Major and trace element analyses of the major lithological units of the Ivisârtoq greenstone belt, Greenland (continued).

Southern homogenous metagranodiorite (A-type granitoid)							
	MM01-27	MM01-38b	MM01-54a	MM01-78	MM01-83	MM01-114	MM01-116
(weight %)							
SiO2	68.30	67.05	72.76	65.77	69.26	74.30	73.54
TiO2	1.03	0.72	0.58	0.72	0.59	0.26	0.31
Al2O3	11.87	11.30	11.50	11.26	11.08	10.08	11.12
Fe2O3T	13.94	10.81	8.85	11.96	8.74	6.53	4.32
MnO	0.16	0.10	0.13	0.12	0.11	0.08	0.08
MgO	0.95	1.30	2.73	0.72	0.56	1.11	1.34
CaO	3.23	2.16	3.22	4.07	2.66	2.35	3.01
K2O	0.41	2.27	1.59	0.51	1.49	0.74	1.02
Na2O	4.19	2.08	3.04	3.27	2.80	2.63	2.86
P2O5	0.35	0.19	0.13	0.16	0.16	0.03	0.04
Sum	104.43	97.97	104.53	98.56	97.45	98.09	97.64
LOI	N/A	0.29	N/A	0.19	0.78	0.95	0.67
Mg#	11.86	19.21	37.95	10.61	11.32	25.27	38.04
(ppm)							
S	486	42	115	24	58	17	23
Cl	117	48	155	1904	1051	1666	1064
Sc	37	18	15	26	14	7	10
V	< LD	< LD	3	5	6	5	4
Cr	9	< LD	48	6	11	8	2
Ni	5.18	5.28	7.69	6.72	8.61	8.82	30.8
Cu	31.1	3.11	2.79	14.4	30.7	8.60	36.2
Zn	81.0	42.7	60.6	65.9	29.1	31.1	40.3
Ga	19.9	26.3	27.4	28.9	27.1	27.7	23.9
Rb	15.0	133	95.7	19.2	90.3	28.6	67.7
Sr	90.88	91.90	91.30	89.42	102.10	70.68	80.02
Nb	6.30	10.39	13.61	9.82	12.97	15.17	19.65
Y	66.33	110.56	142.75	119.62	162.85	171.48	187.56
Zr	197	340	492	368	488	683	752
Ba	145	340	237	153	277	149	100
La	4.34	13.04	10.10	15.29	20.96	28.03	12.59
Ce	11.34	35.51	39.60	40.34	53.60	62.97	42.83
Pr	2.00	5.38	5.63	6.11	8.16	9.60	5.16
Nd	11.64	27.98	28.24	31.85	41.74	46.42	27.03
Sm	4.69	9.41	10.53	10.32	13.35	14.10	11.28
Eu	1.72	2.32	2.48	2.73	2.85	2.89	2.08
Gd	8.34	14.51	16.56	15.84	20.26	21.47	20.10
Tb	1.65	2.70	3.30	2.99	3.85	3.96	4.23
Dy	11.74	19.79	24.40	21.12	28.46	27.89	31.46
Ho	2.65	4.13	5.54	4.66	6.33	6.55	7.23
Er	8.18	13.25	17.32	14.41	20.34	20.86	22.91
Tm	1.24	2.00	2.63	2.14	3.09	3.24	3.62
Yb	8.23	13.35	18.02	14.29	21.46	22.22	25.29
Lu	1.22	1.96	2.60	2.14	3.14	3.26	3.74
Hf	4.77	9.41	11.78	8.93	12.67	16.33	18.12
Ta	0.30	0.62	0.80	0.64	0.75	0.77	1.04
Th	1.20	2.22	3.14	2.77	2.83	3.70	4.52

Analytical method:

Major elements (including S and Cl):X-ray fluorescence fused glass beads method
X-ray fluorescence pressed pellets method

Trace elements analytic method: ICP-MS Sinter technique
ICP-MS Acid technique

LOI= loss on ignition; N/A= not applicable

Table 3.1. Major and trace element analyses of the major lithological units of the Ivisârtoq greenstone belt, Greenland (continued).

	Quartzofeldspathic layer in Marker High Strain Zone				Southern, thick quartzofeldspathic unit		
	MM01-2 g	MM01-35	MM01-63	MM01-63c	MM01-81a	MM01-81c	MM01-91c
(weight %)							
SiO2	73.35	69.10	72.74	72.08	66.15	63.19	65.17
TiO2	0.03	0.44	0.18	0.19	0.98	0.92	0.86
Al2O3	13.66	15.88	15.26	14.60	14.23	13.08	15.51
Fe2O3T	2.65	3.71	1.91	2.26	7.74	10.48	7.59
MnO	0.11	0.09	0.03	0.04	0.11	0.18	0.13
MgO	1.24	0.93	1.24	1.44	3.00	3.24	2.68
CaO	2.68	1.61	2.70	2.98	1.04	2.05	3.13
K2O	1.56	2.18	1.65	1.40	2.07	2.16	1.50
Na2O	2.15	3.62	1.90	2.01	2.16	1.81	2.59
P2O5	0.04	0.14	0.07	0.07	0.10	0.10	0.12
Sum	97.46	97.70	97.68	97.07	97.57	97.20	99.29
LOI	1.00	1.00	0.95	1.13	1.74	0.98	0.975
Mg#	48.06	33.28	56.22	55.77	43.40	37.98	41.16
(ppm)							
S	19	14	30	21	23	25	18
Cl	1015	846	1207	1732	674	972	804
Sc	9	7	7	9	22	29	20
V	6	42	9	15	162	202	192
Cr	14	58	8	11	206	389	235
Ni	2.20	24.9	3.08	9.19	75.7	62.7	81.4
Cu	11.6	8.44	3.47	3.84	43.4	60.3	19.0
Zn	38.9	31.2	7.69	10.4	54.0	70.4	55.6
Ga	19.5	18.5	18.4	18.3	20.5	18.5	21.2
Rb	58.1	51.1	52.0	46.8	59.5	82.9	42.8
Sr	128.22	94.91	103.21	114.38	88.91	108.37	217.77
Nb	5.72	4.77	7.29	6.90	13.59	13.46	9.56
Y	2.76	7.21	6.65	5.18	55.34	47.29	19.52
Zr	55.3	164	139	121	230	212	151
Ba	369	363	535	366	430	417	488
La	16.29	24.52	35.75	28.39	18.77	18.50	15.66
Ce	29.12	43.08	61.43	51.07	41.89	40.18	32.10
Pr	3.41	4.75	6.40	5.18	5.67	5.29	3.87
Nd	11.87	17.28	21.09	16.66	25.24	23.29	15.33
Sm	2.20	2.95	2.70	2.20	6.13	5.44	2.99
Eu	0.55	0.74	0.65	0.64	1.30	1.24	0.89
Gd	1.41	2.17	1.83	1.54	7.78	6.48	3.23
Tb	0.16	0.29	0.24	0.21	1.43	1.18	0.55
Dy	0.63	1.47	1.27	1.10	10.00	8.22	3.67
Ho	0.10	0.27	0.24	0.20	2.27	1.93	0.79
Er	0.28	0.70	0.65	0.53	7.21	6.15	2.37
Tm	0.04	0.10	0.10	0.08	1.11	0.95	0.35
Yb	0.28	0.59	0.67	0.50	7.59	6.49	2.35
Lu	0.03	0.09	0.09	0.08	1.09	0.90	0.33
Hf	2.07	3.57	3.23	2.98	6.36	5.36	3.80
Ta	0.52	0.36	0.33	0.43	0.66	0.72	0.48
Th	4.91	5.71	7.78	6.75	3.93	3.66	3.91

Analytical method:

Major elements (including S and Cl):X-ray fluorescence fused glass beads method

Trace elements analytic method: ICP-MS Sinter technique

ICP-MS Acid technique

LOI= loss on ignition

Table 3.2. Olivine analyses from two ultramafic layers which define large isoclinal folds.

Outer Ultramafic Layer

Sample IV03-43

Analysis number	MgO (wt%)	FeO (wt%)	Fa	Fo	Ni (ppm)
Grain 1 core	40.27	19.80	21.60	78.40	2900
Grain 1 ↓	40.37	20.09	21.80	78.20	2827
Grain 1 ↓	40.73	19.56	21.20	78.80	2747
Grain 1 rim	39.36	19.81	22.00	78.00	2912
Grain 2 core	41.00	19.36	20.90	79.10	2687
Grain 2 rim	39.63	20.66	22.60	77.40	2751
Grain 3 core	41.28	20.17	21.50	78.50	2566
Grain 3 ↓	40.03	19.65	21.60	78.40	2778
Grain 3 rim	42.43	18.02	19.20	80.80	2984
	40.57	**19.68**	**21.38**	**78.62**	**2795**

Sample MM01-45a

Analysis number	MgO (wt%)	FeO (wt%)	Fa	Fo	Ni (ppm)
Grain 1 core	43.63	15.44	16.60	83.40	2694
Grain 1	43.49	15.19	16.40	83.60	2319
Grain 1	46.31	15.24	15.60	84.40	2769
Grain 2 rim	45.10	14.53	15.30	84.70	2940
Grain 2 ↓	45.32	14.83	15.50	84.50	2635
Grain 2 ↓	44.43	14.83	15.80	84.20	2710
Grain 2 rim	44.60	15.44	16.30	83.70	2710
Grain 3 core	44.84	14.64	15.50	84.50	2669
Grain 3 ↓	45.71	14.96	15.50	84.50	2676
Grain 3 rim	45.34	14.67	15.40	84.60	2432
	44.88	**14.98**	**15.79**	**84.21**	**2655**

Inner Ultramafic Layer

Sample MM01-96

	MgO (wt%)	FeO (wt%)	Fa	Fo	Ni (ppm)
Grain 1	48.77	11.69	11.90	88.10	1987
Grain 1	46.78	11.97	12.60	87.40	1934
Grain 1 rim	50.48	11.61	11.40	88.60	1858
Grain 2 core	48.29	11.76	12.00	88.00	1919
Grain 2 ↓	48.00	10.96	11.40	88.60	2143
Grain 2 rim	47.67	12.19	12.50	87.50	1742
	48.33	**11.70**	**11.97**	**88.03**	**1931**

Chapter 4: Summary and Implications

4.1 SUMMARY OF THESIS GOALS AND MAJOR CONCLUSIONS

New field, petrographic, geochronologic, and major and trace element investigations of the major units which comprise the Ivisârtoq greenstone belt have provided important insights into its nature and origin. Several key aspects, outlined in Chapter 1 have been addressed, including:

- What are the nature and protoliths of the lithologic units?
- Does the belt represent a stratigraphy or a tectonostratigraphy - how do the units relate to each other?
- When did the belt form?
- What are the geochemical characteristics of the belt and what does the geochemical data reveal about the magmatic history of the different lithological units?
- What is the tectonic history of the belt?

This study has shown that the mapped region represents a tectonostratigraphic assemblage composed of two distinct packages of rocks. These packages, termed the northern and southern parts of the belt, contain different rock types, differ in degrees of deformation (see Chapter 2), and are geochemically distinct from each other.

The northern part is characterised by amphibolite derived from basaltic pillow lavas. The parent magmas incorporated minor amounts (<5%) of continental crust. The basaltic pillow lavas were intruded by ultramafic sills, now cumulate residues, and then

by sheets of tonalite. This package of rocks suffered two distinct deformational events before juxtaposition.

The southern part of the belt is dominated by banded amphibolite derived from basaltic pillow lavas. The parent magmas assimilated large amounts of crust (15-20%). The southern part also contains quartzofeldspathic metasedimentary rocks, a homogeneous granodiorite with A-type granitoid trace element concentrations, and a unique ultramafic layer derived from (?) pyroclastic meymechite. The southern part was strongly deformed before juxtaposition with the northern part.

4.2 BROADER IMPLICATIONS

Comparing and contrasting Ivisârtoq with Isua

The Ivisârtoq greenstone belt lies 40 km southeast of the Isua greenstone belt which is one of the most intensely studied greenstone belts in the world. The Isua region is of great interest because it contains some of the oldest known (~3.8-3.7 Ga), moderately well-preserved metavolcanic rocks on Earth and is thought to contain the oldest evidence of life on Earth (Rosing, 1999). The Ivisârtoq greenstone belt contains exceptionally well-preserved pillow lava structures and part of it has been shown in this study to be older than ~3165 Ma. Comparing and contrasting the geology of the two belts is useful for understanding the Archean geological evolution of the wider Isua-Ivisârtoq region, and early to middle Archean processes in general.

A notable similarity between the two belts is that they both comprise a tectonostratigraphy composed of fault-bounded lithotectonic sequences in which

amphibolites derived from basaltic pillow lavas are the most abundant rock type (Myers, 2001; Nutman et al., 2002; Polat and Hofmann, 2003). They also both contain ultramafic units and perhaps clastic metasedimentary rocks. Two important lithological differences are the absence of chert-BIF and the presence of komatiitic pillow lavas (Hall, 1981) in the Ivisârtoq belt. Most units in both belts are strongly deformed, and have been recrystallized under amphibolite facies metamorphic conditions.

Geochemical studies of the amphibolites in the Isua and Ivisârtoq greenstone belts indicate that their volcanic protoliths were geochemically heterogeneous (Isua studies: Polat and Hofmann, 2003; Komiya et al., 2004). In the Isua greenstone belt, Polat and Hofmann (2003) and Komiya et al. (2004) defined two geochemically distinct volcanic associations which are found in different lithotectonic sequences, although their classification of these groups differs. Polat and Hofmann (2003) defined low-HFSE ('boninitic') and high-HFSE ('basaltic-picritic') associations which have distinct trace element patterns on primitive mantle-normalised diagrams (Fig. 4.1). They concluded that the low-HFSE association was derived from a shallower and more depleted mantle source than the high-HFSE association, and that the low-HFSE ('boninitic') association originated in an intra-oceanic subduction zone tectonic setting.

The two types of tholeiitic basalt defined by Komiya et al. (2004) include a mid-oceanic ridge basalt (MORB: LREE depleted) and an oceanic island basalt (OIB: flat REE pattern). They interpreted the greenstone belt as an intra-oceanic accretionary complex which preserved a plate tectonic history "from mid-oceanic ridge through plume magmatism to (incorporation in a) subduction zone" (pg. 47, Komiya et al., 2004).

Regardless of specific differences in geochemical classifications in the two studies, geological and geochemical evidence from the Isua greenstone belt, in these and other studies, is consistent with an intraoceanic setting for the deposition of the Isua volcanic rocks (Rosing et al., 1996; Myers, 2001: Nutman et al., 2002; Polat and Hofmann, 2003; Komiya et al., 2004). There is no evidence from published Sr, Nd, Hf, and Pb isotope data from Isua for crustal contamination by significantly older rocks (see Kamber et al., 2001).

These observations for Isua contrast with those found for the Ivisârtoq greenstone belt in this study. Geochemical evidence presented here suggests that the protoliths of Ivisârtoq amphibolites were crustally contaminated and that the belt is composed of two distinct packages of rocks. These rock packages formed in different geologic environments, and were brought together after the main volcanism associated within each part had ceased. In plate tectonic terms, a very immature island-arc or back-arc basin environment is compatible with data from the northern part of the belt, whereas a continental flood basalt environment built on older thick, continental crust is interpreted for the southern package of rocks

Nutman et al. (2002) suggested that different lithotectonic units comprising the Isua greenstone belt were juxtaposed by accretionary Phanerozoic-like plate tectonic processes operating in the early Archean. The interpreted juxtaposition of the northern and southern packages of the Ivisârtoq belt is consistent with lateral collisions of terranes perhaps by plate tectonic processes.

Re-evaluation of Regional Terrane model in relation to the Ivisârtoq greenstone belt

Presently the Godthåbsfjord region is thought to comprise six terranes: the Akia, Isukasia terrane, Færingehavn, Kapisilik, Tre Brødre, and Tasiusarsuaq terranes (Friend and Nutman, 2005; Fig. 1b from Friend and Nutman). The Ivisârtoq greenstone belt is considered part of the 3075-2960 Ma Kapisilik terrane, as defined by Friend and Nutman (2005) whereas the >3600 Ma Isukasia terrane includes the Isua greenstone belt. Friend and Nutman (2005) suggested that these two terranes collided at ~2950 Ma and that the boundary is now marked by a mylonite zone. This Isukasia-Kapislik block is thought to have been further modified during a later collision with the Tre Brødre terrane after ~2825 Ma (Friend and Nutman, 2005).

New field and geochronological data obtained during this study suggest that the Kapisilik terrane is older than interpreted by Friend and Nutman (2005) and is itself composed of previously unrecognized, discrete tectonic packages of rocks. In the northern part of the Ivisârtoq belt, basaltic pillow lavas were deposited and ultramafic sills intruded before ~3165 Ma. In the southern part, basaltic pillow lavas and a meymechitic, (?) pyroclastic horizon were deposited before ~3066 Ma.

A ~3760 Ma $^{207}Pb/^{206}Pb$ age was obtained from a xenocrystic zircon core in the extensive ~2960 Ma granitoid (TTG) unit which intrudes and cuts off the Ivisartoq greenstone belt in the north. These data suggest that the tonalite likely intruded through early Archean continental crust that could correlate with the oldest component of the Isukasia terrane. A similar but less constrained interpretation could be made for a single,

very poorly-constrained age (concordia age=3873 ±220 Ma, $^{207}Pb/^{206}Pb$ age=3410 ±477 Ma) obtained from a mafic dyke from the southern part of the belt. These results, along with geochemical evidence from the amphibolites, suggest that the volcanic rocks associated with each part of the belt were deposited at least in part on older gneissic material, similar to components of the Isukasia terrane. Therefore, the bases for the subdivision proposed by Friend and Nutman (2005) of this part of the Godthåbsfjord region into the Isukasia and Kapisilik terranes is in doubt. The mylonite zone they describe as separating these terranes may have developed during later deformational events. Further detailed geological mapping and geochronology needs to be conducted to determine whether or not the Kapisilik and Isukasia terranes existed as different crustal entities.

4.3 DIRECTIONS FOR FUTURE STUDIES

Although this thesis has presented a large amount of new geological, geochronological, and geochemical data, study of the Ivisartoq greenstone belt is still in its infancy. There is much scope for future studies and research; the possibilities are extensive. As such, only a limited list of suggestions is included, with the understanding that further work will inevitably present more questions.

Proposed future work:

- Expand field mapping to constrain the boundary between the northern and southern parts of the belt and to determine how the anorthositic unit to the east

relates to the tectonostratigraphy. Conduct a detailed structural study of the Marker High Strain Zone;

- Isotopic work (particularly Sm-Nd) is needed to constrain the petrogenesis of major units, in particular the mafic and ultramafic rocks, and to determine potential crustal contaminants and mantle sources;
- Detailed geochronology (both *in situ* LA-ICPMS or SHRIMP and high-precision TIMS) is needed to constrain the magmatic, deformational, and metamorphic histories of the northern and southern parts of the belt. This study could focus on tonalite sheets and mafic dykes for which the relative timing is known from field relationships;
- A detailed metamorphic study would shed light on the pressure-temperature-time path evolution of these rocks, which could be incorporated into the tectonic evolution of the area.

a)

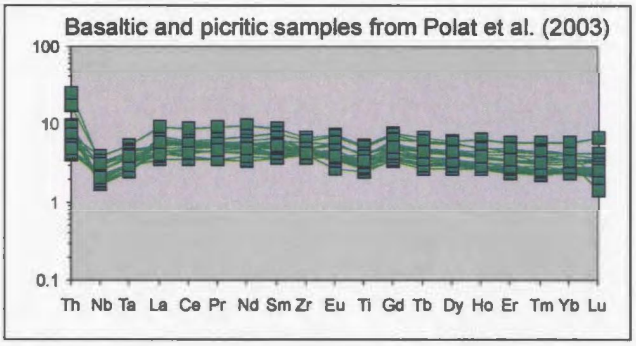

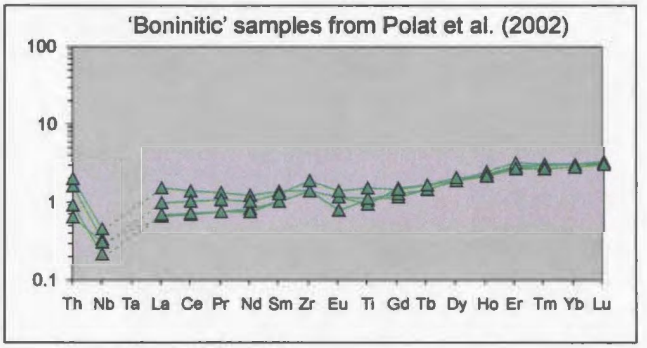

b)

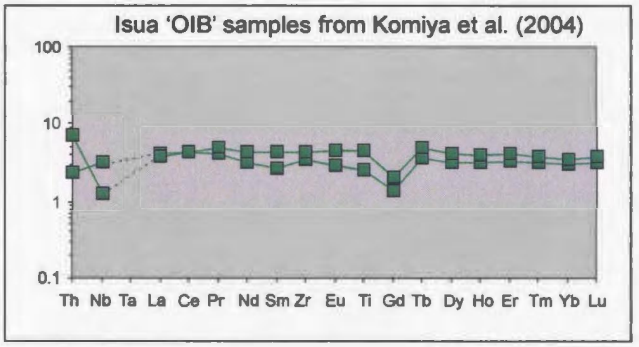

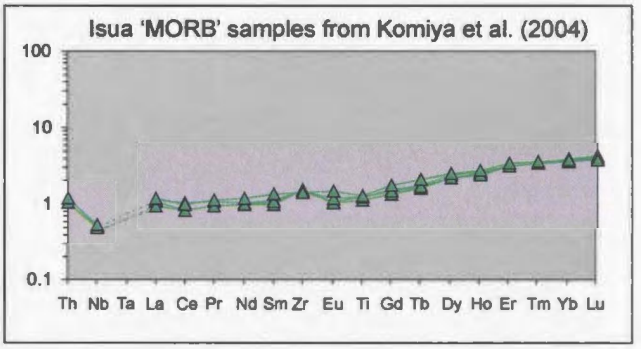

Figure 4.1. Primitive mantle normalized multi-element diagrams for amphibolites from the Isua greenstone belt. (a) Polat and Hofmann (2003) and (b) Komiya et al. (2004) define two geochemically distinct volcanic associations which are found in different lithotectonic sequences, although their classification of these groups differs.

Appendix A

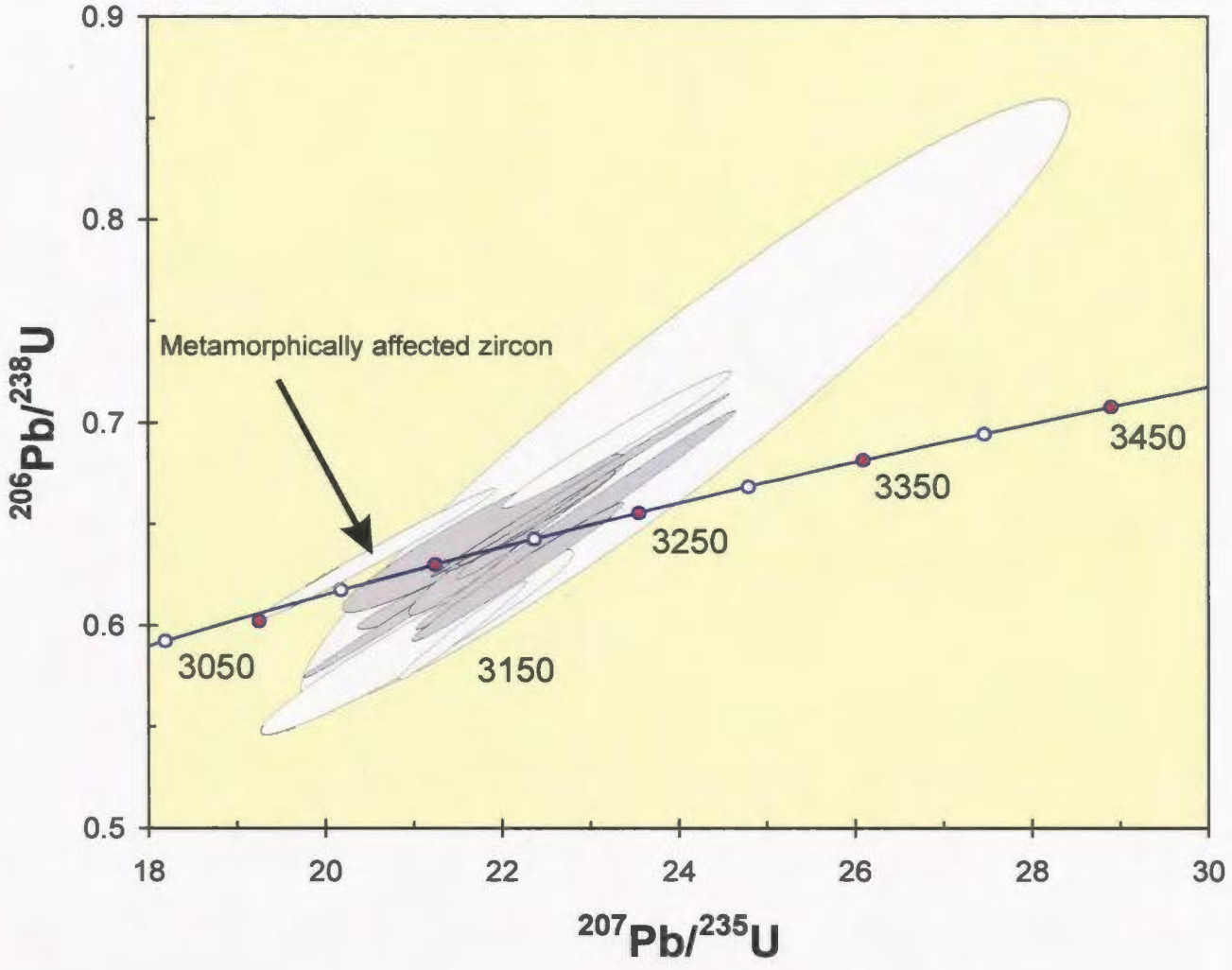

Figure A1. Concordia diagram for northern, rusty quartzofeldspathic sample MM01-47. Error ellipses are 1σ. Grey ellipses indicate analyses use for age interpretations; they are between 94-104% concordant and have a % error <2.2. White ellipses indicate data which was not used for age interpretations (<94% or >104% concordant, and/or % error >2.2, and an analysis from metamorphic grain). Plot was constructed with Isoplot (Ludwig, 2000).

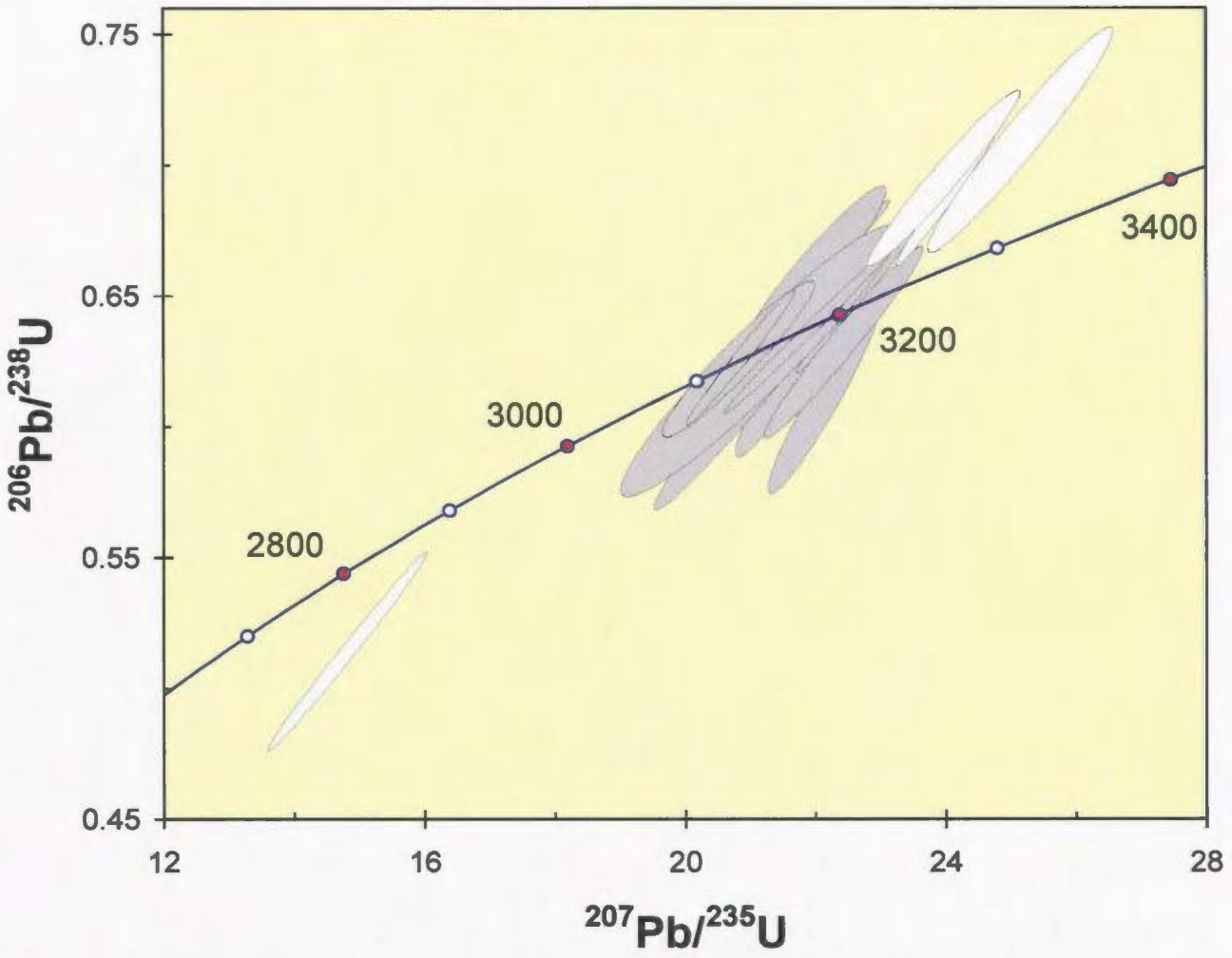

Figure A2. Concordia diagram for northern, rusty quartzofeldspathic sample MM01-50. Error ellipses are 1σ. Grey ellipses indicate analyses use for age interpretations; they are between 94-104% concordant and have a % error <2.2. White ellipses indicate data which was not used for age interpretations (<94% or >104% concordant, and/or % error >2.2). Plot was constructed with Isoplot (Ludwig, 2000).

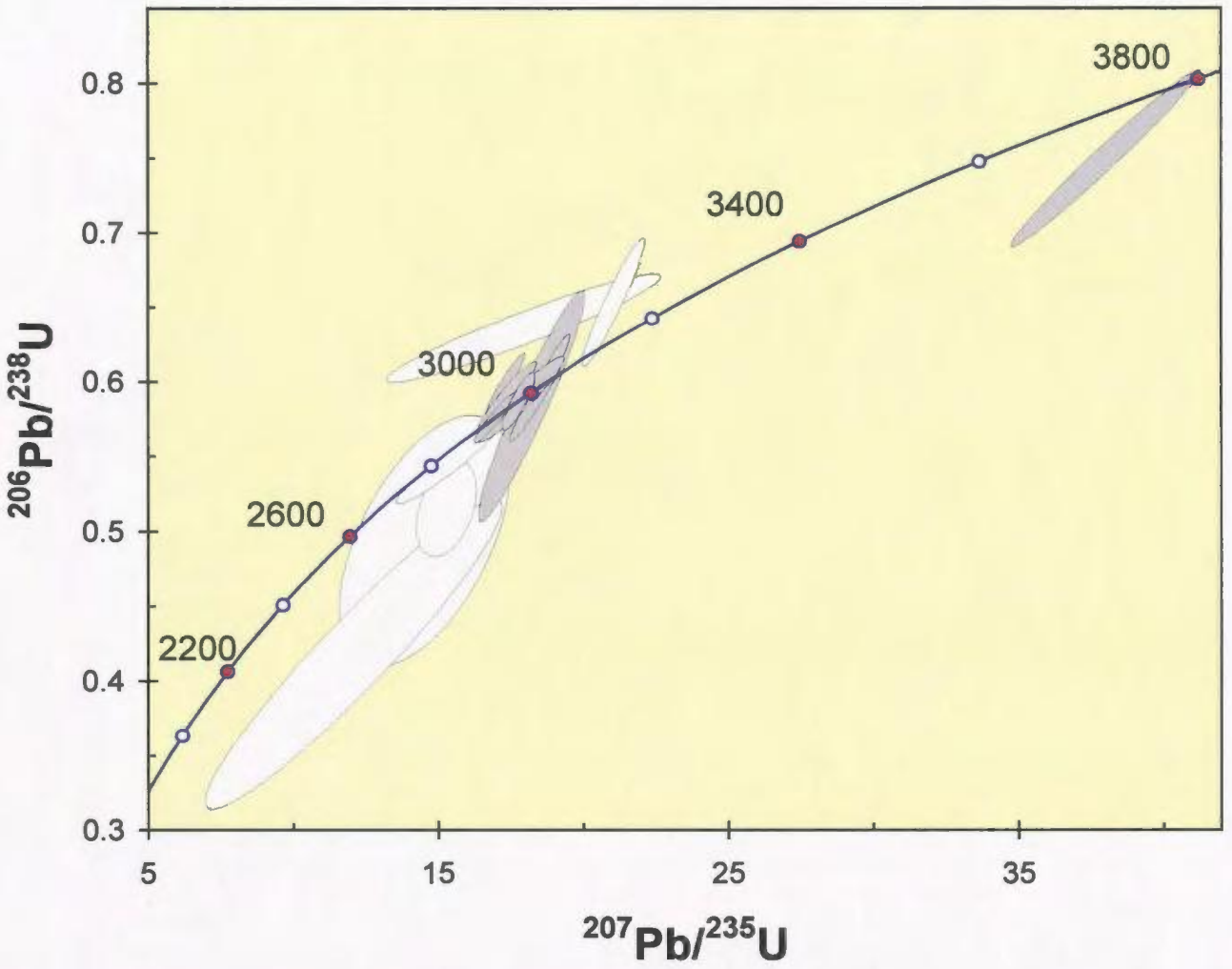

Figure A3. Concordia diagram for homogeneous TTG, sample IV03-66, which intrudes the northern margin of the greenstone belt. Error ellipses are 1σ. Grey ellipses indicate analyses use for age interpretations; they are between 94-104% concordant and have a % error <2.2. White ellipses indicate data which was not used for age interpretations (<94% or >104% concordant, and/or % error >2.2). Plot was constructed with Isoplot (Ludwig, 2000).

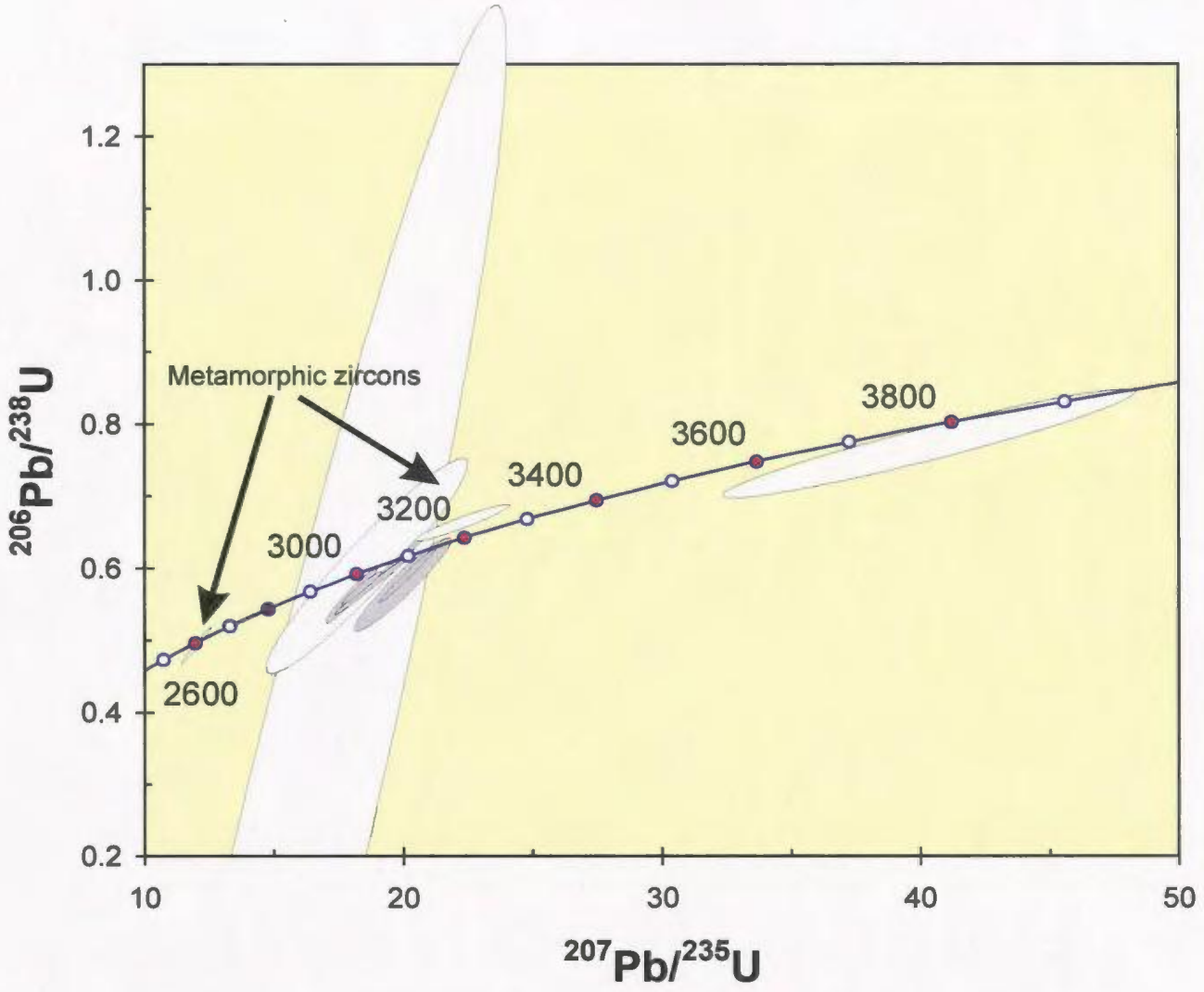

Figure A4. Concordia diagram for southern, plagioclase phyric mafic dyke sample MM01-109. Error ellipses are 1σ. Grey ellipses indicate analyses use for age interpretations; they are between 94-104% concordant and have a % error <2.2. White ellipses indicate data which was not used for age interpretations (<94% or >104% concordant, and/or % error >2.2, and an analysis from metamorphic grain). Plot was constructed with Isoplot (Ludwig, 2000).

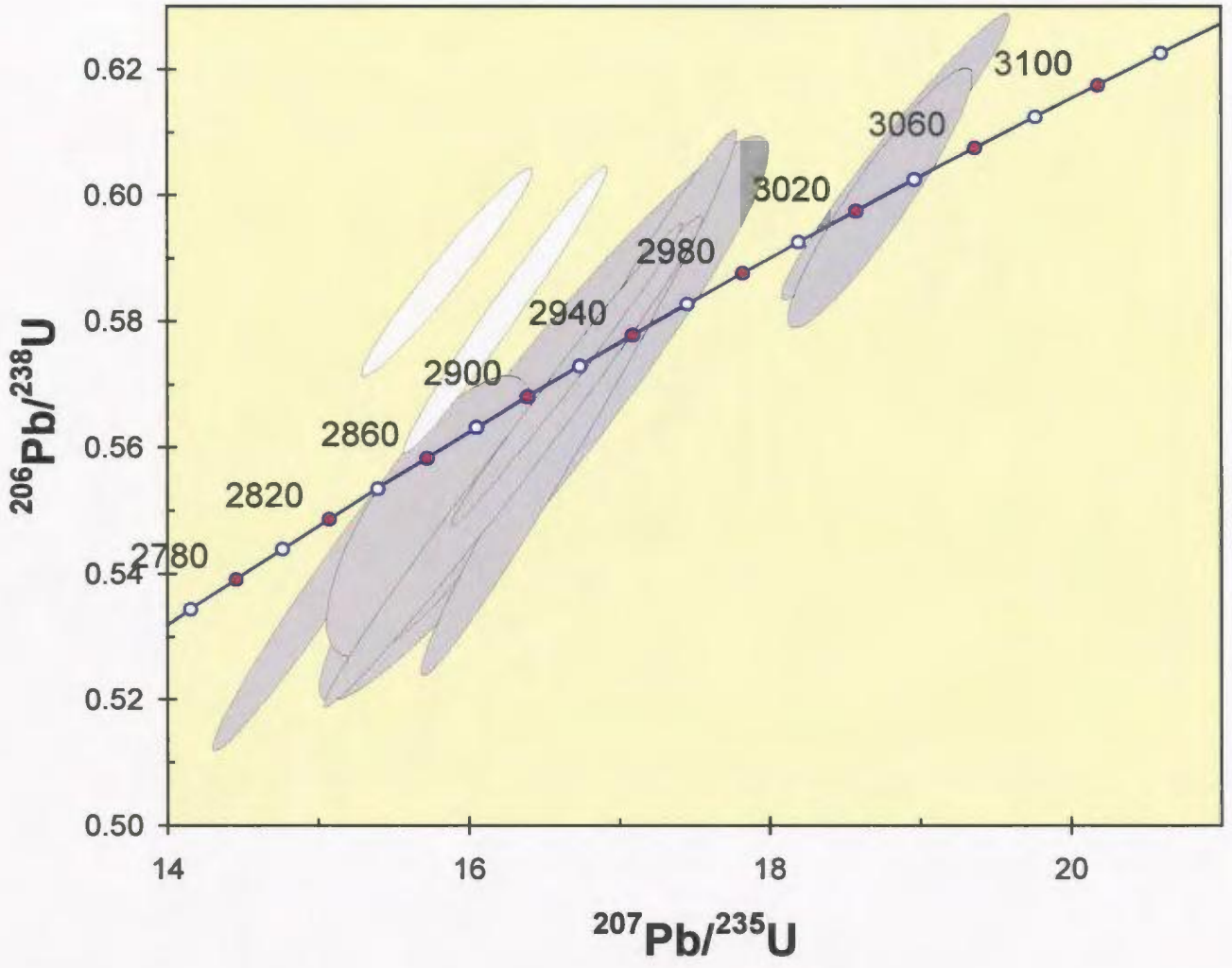

Figure A5. Concordia diagram for southern, homogeneous, light grey (granodioritic) sample MM01-78. Error ellipses are 1σ. Grey ellipses indicate analyses use for age interpretations; they are between 94-104% concordant and have a % error <2.2. White ellipses indicate data which was not used for age interpretations (<94% or >104% concordant, and/or % error >2.2). Plot was constructed with Isoplot (Ludwig, 2000).

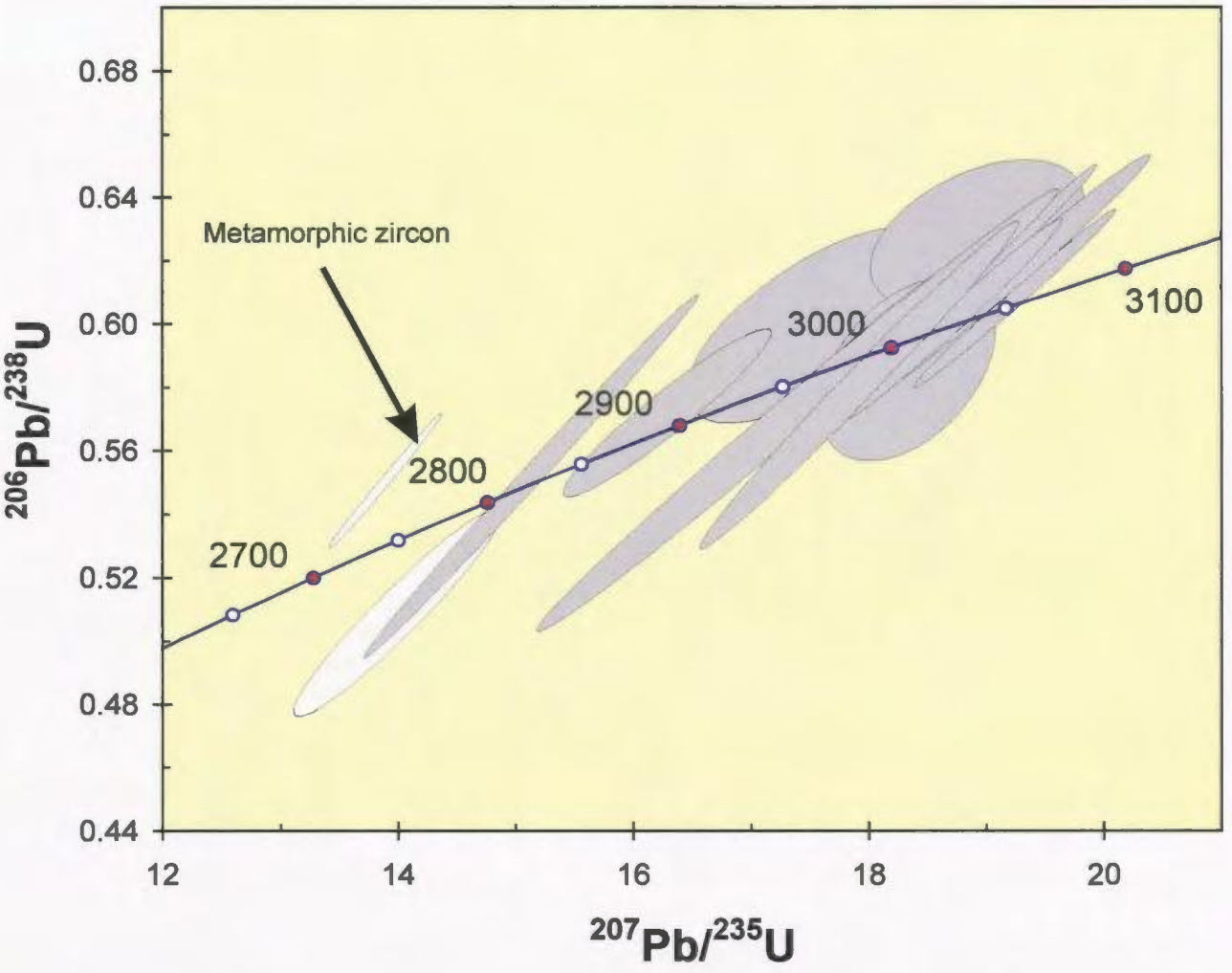

Figure A6. Concordia diagram for quartzofeldspathic sample MM01-63 from the Marker High Strain Zone. Error ellipses are 1σ. Grey ellipses indicate analyses use for age interpretations; they are between 94-104% concordant and have a % error <2.2. White ellipses indicate data which was not used for age interpretations (<94% or >104% concordant, and/or % error >2.2, and an analysis from metamorphic grain). Plot was constructed with Isoplot (Ludwig, 2000).

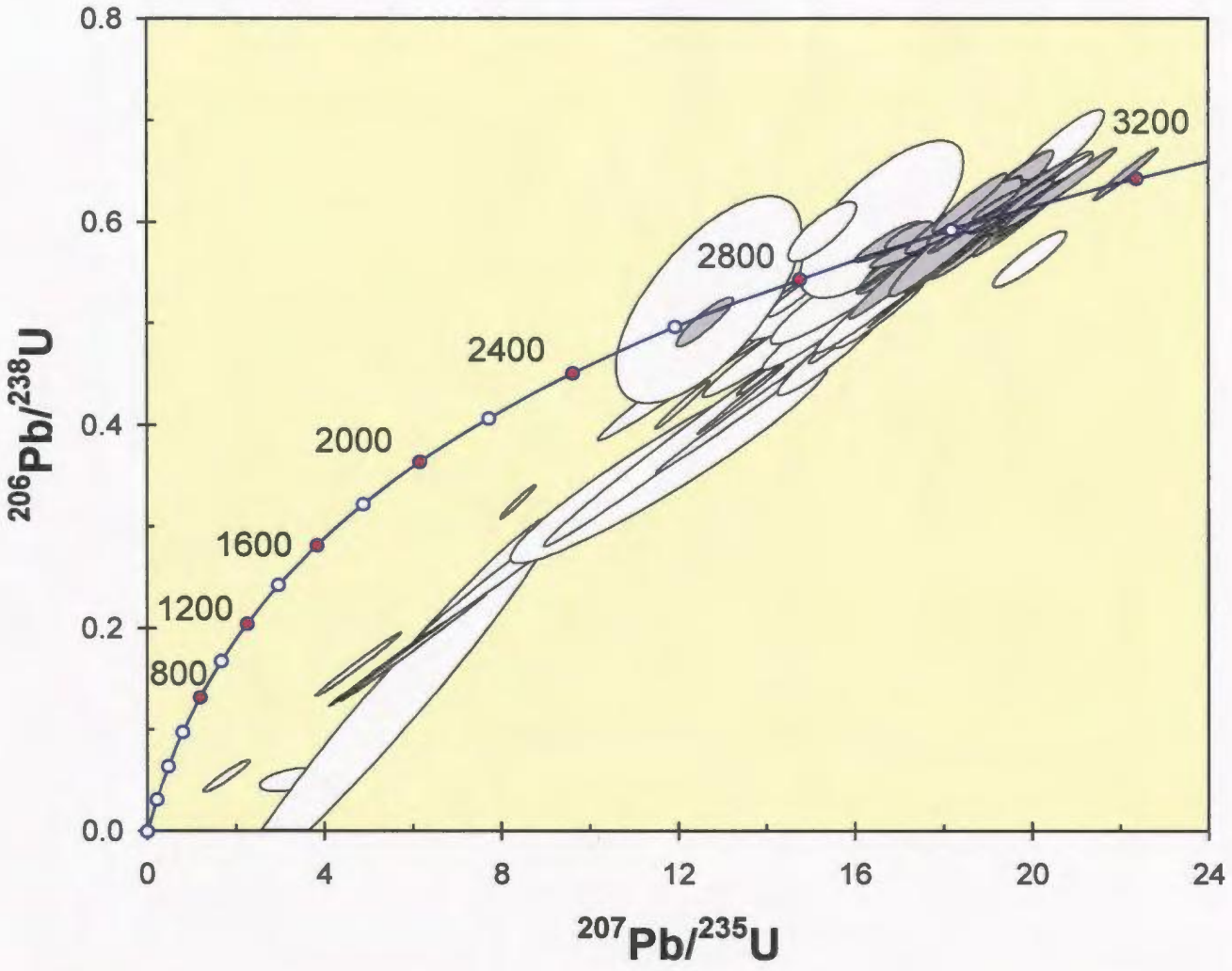

Figure A7. Concordia diagram for sample MM01-81 from thick, southern quartzofeldspathic layer. Error ellipses are 1σ. Grey ellipses indicate analyses use for age interpretations; they are between 94-104% concordant and have a % error <2.2. White ellipses indicate data which was not used for age interpretations (<94% or >104% concordant, and/or % error >2.2). Plot was constructed with Isoplot (Ludwig, 2000).

Table A1: U-Pb zircon ID-TIMS analyses which were not used for age determinations

Sample MM01-20

Single zircons	Weight (mg)	U (ppm)	Pb_{rad} (ppm)[a]	Pb_{com} (pg)[b]	$^{206}Pb^{d}/^{204}Pb$	Corrected atomic ratios[c,d]							Age		
						$^{208}Pb/^{206}Pb$	$^{208}Pb/^{238}U$	(±)	$^{207}Pb/^{235}U$	(±)	$^{207}Pb/^{206}Pb$	(±)	$^{206}Pb/^{238}U$	$^{207}Pb/^{235}U$	$^{207}Pb/^{206}Pb$
1	0.004	1504	585.1	89	1659	0.0163	0.38668	396	8.2027	848	0.15385	16	2107	2254	2389
2	0.004	1411	527.6	82	1623	0.0203	0.37275	148	7.5302	322	0.14652	14	2042	2177	2306
3	0.003	442	194.9	17	2067	0.0475	0.42476	152	9.3923	360	0.16037	18	2282	2377	2460
4	0.003	958	334.4	43	1460	0.0130	0.34867	134	7.2889	302	0.15161	16	1928	2147	2364
5	0.002	1243	540.6	33	2551	0.0127	0.43379	150	9.1981	348	0.15379	14	2323	2358	2388
6	0.002	1224	547.1	86	769	0.0574	0.42432	152	9.7674	390	0.16695	20	2280	2413	2527
7	0.003	3962	1683.7	37	8466	0.0251	0.42033	178	8.7425	390	0.15085	12	2262	2312	2356

[a] Total radiogenic Pb after correction for blank, common Pb, spike.

[b] Measured.

[c] Ratios corrected for fractionation, spike, 2-10 pg laboratory blank, initial common Pb at age fo the sample calculated from the model of Stacey and Kramers (1975) and 1 pg U blank.

[d] Two σ uncertainties are calculated with an error propagation program, refer to the last digits and are reported after the ratios.

Table A2: U-Pb zircon LAM-ICP-MS analyses which were not used for age determinations

Sample MM01-47

Analysis #	pit size (µm)	Atomic ratios $^{207}Pb/^{235}U$	(±)	$^{206}Pb/^{238}U$	(±)	$^{207}Pb/^{206}Pb$	(±)	Ages (Ma) $^{207}Pb/^{235}U$	1 ó	$^{206}Pb/^{238}U$	1 ó	$^{207}Pb/^{206}Pb$	2 ó	Conc. %	% error	U (ppm)
Recrystallized zone																
11	20x20	20.609	1.100	0.6368	0.0262	0.2299	0.0048	3120	52	3177	103	3051	33	104.1	1.10	892
Discordant (< 94% or >104%) data for MM01-47														discordant		
12	20x20	24.086	3.568	0.7108	0.1214	0.2361	0.0041	3272	144	3462	457	3094	28	111.9	0.90	1650
13	20x20	23.313	1.063	0.6923	0.0275	0.2443	0.0054	3240	44	3392	105	3148	35	107.7	1.11	798
14	30x30	21.050	1.459	0.5930	0.0371	0.2560	0.0072	3141	67	3002	150	3222	44	93.1	1.38	307
15	30x30	21.567	0.594	0.5990	0.0197	0.2574	0.0035	3164	27	3026	80	3231	21	93.6	0.66	495

Sample MM01-50

Analysis #	pit size (µm)	Atomic ratios $^{207}Pb/^{235}U$	(±)	$^{206}Pb/^{238}U$	(±)	$^{207}Pb/^{206}Pb$	(±)	Ages (Ma) $^{207}Pb/^{235}U$	1 ó	$^{206}Pb/^{238}U$	1 ó	$^{207}Pb/^{206}Pb$	2 ó	Conc. %	% error	U (ppm)
Discordant (< 94% or >104%) data for MM01-50																
12	24x24	24.072	0.658	0.6891	0.0224	0.2516	0.0037	3271	27	3379	86	3195	23	105.8	0.73	120
13	20x20	25.181	1.168	0.7094	0.0349	0.2577	0.0044	3315	45	3456	132	3232	27	106.9	0.83	129
14	20x20	23.990	0.960	0.6949	0.0272	0.2526	0.0056	3268	39	3401	104	3201	35	106.2	1.10	125
15	20x20	14.814	1.004	0.5154	0.0309	0.2049	0.0033	2803	64	2680	132	2865	26	93.5	0.90	329

Sample MM01-66

Analysis #	pit size (µm)	Atomic ratios $^{207}Pb/^{235}U$	(±)	$^{206}Pb/^{238}U$	(±)	$^{207}Pb/^{206}Pb$	(±)	Ages (Ma) $^{207}Pb/^{235}U$	1 ó	$^{206}Pb/^{238}U$	1 ó	$^{207}Pb/^{206}Pb$	2 ó	Conc. %	% error	U (ppm)
Discordant (< 94% or >104%) data for IV03-66																
10	30x30	12.095	4.189	0.4199	0.0841	0.1994	0.0262	2612	325	2260	382	2822	215	80.1	7.61	62
11	30x30	17.969	3.865	0.6367	0.0296	0.2109	0.0294	2988	207	3176	117	2913	226	109.0	7.74	297
12	30x30	15.294	0.848	0.5166	0.0262	0.2275	0.0071	2834	53	2685	111	3034	50	88.5	1.65	181
13	30x30	21.072	0.868	0.6542	0.0353	0.2326	0.0072	3142	40	3245	138	3070	49	105.7	1.60	84
14	30x30	14.553	2.414	0.4951	0.0683	0.3198	0.0898	2786	158	2593	294	3569	432	72.6	12.10	168
Concordant but % Error > 2.2																
15	30x30	15.331	1.445	0.5457	0.0214	0.2164	0.0102	2836	90	2807	89	2954	76	95.0	2.58	167

Table A2: U-Pb zircon LAM-ICP-MS analyses which were not used for age determinations (continued)

MM01-109

Analysis #	pit size (μm)	Atomic ratios $^{207}Pb/^{235}U$	(±)	$^{206}Pb/^{238}U$	(±)	$^{207}Pb/^{206}Pb$	(±)	Ages (Ma) $^{207}Pb/^{235}U$	1 ó	$^{206}Pb/^{238}U$	1 ó	$^{207}Pb/^{206}Pb$	2 ó	Conc. %	% error	U (ppm)
Young, metamorphic zircon? (higher U ppm)																
7	20x20	12.013	0.487	0.4973	0.0213	0.1720	0.0024	2605	38	2602	92	2578	23	101.0	0.91	457
Discordant (< 94% or >104%) data for MM01-109																
8	20x20	22.324	1.507	0.6663	0.0211	0.2397	0.0141	3198	66	3291	82	3118	93	105.6	2.99	100
9	20x20	15.704	6.844	0.1681	0.9906	0.2583	0.0708	2859	416	1002	5466	3237	432	31.0	13.35	301
10	20x20	40.403	6.535	0.7752	0.0613	0.2886	0.0442	3781	160	3700	223	3410	238	108.5	6.99	N/A*
Concordant but % Error > 2.2																
11	20x20	18.628	3.204	0.6061	0.1207	0.2154	0.0095	3023	166	3055	485	2947	71	103.7	2.42	237

*N/A = not available

MM01-78

Analysis #	pit size (μm)	Atomic ratios $^{207}Pb/^{235}U$	(±)	$^{206}Pb/^{238}U$	(±)	$^{207}Pb/^{206}Pb$	(±)	Ages (Ma) $^{207}Pb/^{235}U$	1 ó	$^{206}Pb/^{238}U$	1 ó	$^{207}Pb/^{206}Pb$	2 ó	Conc. %	% error	U (ppm)
Discordant (< 94% or >104%) data for MM01-78																
9	20x20	16.248	0.555	0.5820	0.0184	0.2005	0.0029	2892	33	2957	75	2830	24	104.5	0.85	337
10	20x20	15.861	0.467	0.5879	0.0134	0.2041	0.0041	2868	28	2981	54	2859	33	104.3	1.15	332

MM01-63

Analysis #	pit size (μm)	Atomic ratios $^{207}Pb/^{235}U$	(±)	$^{206}Pb/^{238}U$	(±)	$^{207}Pb/^{206}Pb$	(±)	Ages (Ma) $^{207}Pb/^{235}U$	1 ó	$^{206}Pb/^{238}U$	1 ó	$^{207}Pb/^{206}Pb$	2 ó	Conc. %	% error	U (ppm)
Metamorphic grain																
14	30x30	13.896	0.391	0.5514	0.0172	0.1955	0.0018	2743	27	2831	72	2789	15	101.5	0.53	1111
Discordant (< 94% or >104%) data for MM01-63																
15	20x20	14.001	0.728	0.5100	0.0267	0.2076	0.0063	2750	49	2657	114	2887	49	92.0	1.71	64

Table A.2: U-Pb zircon LAM-ICP-MS analyses which were not used for age determinations (continued)

MM01-81

		Atomic ratios						Ages (Ma)								
Analysis #	pit size (μm)	$^{207}Pb/^{235}U$	(±)	$^{208}Pb/^{238}U$	(±)	$^{207}Pb/^{206}Pb$	(±)	$^{207}Pb/^{235}U$	1 ó	$^{208}Pb/^{238}U$	1 ó	$^{207}Pb/^{206}Pb$	2 ó	Conc. %	% error	U (ppm)
Young age interpreted due to ancient lead loss																
44	20x20	12.635	0.532	0.5031	0.0199	0.1937	0.0035	2653	40	2627	85	2774	30	94.7	1.07	N/A
Discordant (< 94% or >104%) data for MM01-81																
45	40x40	3.236	0.555	0.0546	0.0091	0.4662	0.1441	1466	133	343	56	4138	458	8.3	11.08	N/A
46	20x20	1.793	0.427	0.0579	0.0126	0.2303	0.0077	1043	155	363	77	3054	53	11.9	1.75	441
47	20x20	5.646	2.946	0.1336	0.1469	0.2795	0.0663	1923	450	809	835	3360	371	24.1	11.03	N/A
48	20x20	4.778	0.788	0.1675	0.0258	0.2364	0.0040	1781	138	998	142	3096	27	32.2	0.88	N/A
49	30x30	5.544	1.171	0.1719	0.0371	0.2353	0.0043	1907	182	1022	204	3088	29	33.1	0.95	N/A
50	40x40	6.030	1.356	0.1842	0.0429	0.2357	0.0040	1980	196	1090	234	3091	27	35.3	0.87	558
51	20x20	11.148	4.050	0.3556	0.1317	0.2387	0.0051	2536	339	1961	626	3111	34	63.0	1.10	N/A
52	30x30	8.395	0.319	0.3265	0.0130	0.1997	0.0034	2275	34	1822	63	2823	28	64.5	0.99	N/A
53	30x30	11.830	2.936	0.3655	0.0811	0.2273	0.0116	2591	232	2008	383	3033	82	66.2	2.70	N/A
54	20x20	12.421	2.807	0.3948	0.0918	0.2417	0.0067	2637	212	2145	424	3131	44	68.5	1.40	N/A
55	20x20	13.438	1.552	0.4130	0.0481	0.2342	0.0054	2711	109	2229	219	3081	37	72.3	1.21	45
56	30x30	13.458	0.800	0.4267	0.0277	0.2352	0.0039	2712	56	2291	125	3088	27	74.2	0.86	N/A
57	30x30	12.129	0.503	0.4214	0.0196	0.2259	0.0047	2614	39	2267	89	3023	33	75.0	1.10	N/A
58	30x30	13.902	0.444	0.4488	0.0146	0.2365	0.0039	2743	30	2390	65	3096	26	77.2	0.85	N/A
59	30x30	15.483	0.984	0.4728	0.0348	0.2317	0.0045	2845	61	2496	152	3064	31	81.5	1.02	173
60	30x30	15.787	0.655	0.4907	0.0236	0.2381	0.0056	2864	40	2574	102	3108	37	82.8	1.19	N/A
61	30x30	16.033	0.719	0.5014	0.0171	0.2394	0.0116	2879	43	2620	73	3116	77	84.1	2.48	N/A
62	30x30	14.507	0.383	0.4861	0.0147	0.2245	0.0032	2783	25	2554	64	3013	23	84.8	0.75	N/A
63	30x30	19.997	0.673	0.5650	0.0224	0.2807	0.0111	3091	33	2887	92	3367	62	85.7	1.84	N/A
64	30x30	15.068	0.520	0.5028	0.0140	0.2306	0.0068	2820	33	2626	60	3056	47	85.9	1.54	N/A
65	30x30	16.598	0.846	0.5119	0.0285	0.2338	0.0038	2912	49	2665	122	3078	26	86.6	0.84	203
66	30x30	17.228	0.462	0.5352	0.0147	0.2471	0.0049	2948	26	2763	62	3167	31	87.3	0.99	N/A
67	30x30	17.084	0.403	0.5393	0.0140	0.2477	0.0042	2940	23	2781	59	3170	27	87.7	0.86	N/A
68	20x20	15.470	2.361	0.5152	0.0709	0.2294	0.0055	2845	146	2679	302	3048	39	87.9	1.26	N/A
69	30x30	16.426	0.534	0.5271	0.0157	0.2347	0.0036	2902	31	2729	66	3084	25	88.5	0.80	N/A
70	40x40	15.882	1.004	0.5249	0.0308	0.2313	0.0035	2870	60	2720	130	3061	24	88.8	0.79	N/A
71	30x30	16.615	0.465	0.5408	0.0142	0.2408	0.0041	2913	27	2787	60	3125	27	89.2	0.87	N/A
72	40x40	13.569	1.774	0.4914	0.0488	0.2076	0.0064	2720	124	2577	211	2887	50	89.2	1.72	N/A
73	30x30	16.464	1.030	0.5361	0.0351	0.2352	0.0040	2904	60	2767	147	3088	27	89.6	0.89	N/A
74	20x20	14.005	3.101	0.5056	0.0971	0.2123	0.0048	2750	210	2638	416	2923	36	90.2	1.24	N/A
75	30x30	16.691	0.533	0.5496	0.0188	0.2400	0.0083	2917	31	2824	78	3120	55	90.5	1.77	N/A
76	30x30	16.296	0.449	0.5408	0.0192	0.2329	0.0055	2894	26	2787	80	3072	38	90.7	1.22	N/A
77	40x40	15.278	1.506	0.5286	0.0359	0.2235	0.0073	2833	94	2736	151	3006	52	91.0	1.75	N/A
78	30x30	17.701	0.593	0.5545	0.0169	0.2406	0.0075	2974	32	2844	70	3124	49	91.0	1.58	N/A
79	20x20	16.568	2.153	0.5400	0.0695	0.2290	0.0060	2910	124	2784	291	3045	42	91.4	1.38	N/A
80	20x20	17.324	0.658	0.5507	0.0219	0.2359	0.0026	2953	36	2828	91	3093	18	91.4	0.57	N/A
81	30x30	16.832	0.398	0.5522	0.0138	0.2369	0.0041	2925	23	2834	57	3099	28	91.4	0.90	N/A
82	30x30	17.571	0.365	0.5635	0.0159	0.2441	0.0047	2967	20	2881	66	3147	30	91.6	0.96	N/A
83	20x20	17.492	1.929	0.5537	0.0669	0.2373	0.0050	2962	106	2840	277	3102	33	91.6	1.08	N/A
84	25x25	17.821	1.224	0.5527	0.0454	0.2338	0.0062	2980	66	2836	188	3078	42	92.1	1.37	179
85	30x30	17.845	0.686	0.5709	0.0166	0.2442	0.0083	2981	37	2911	68	3147	54	92.5	1.71	N/A
86	20x20	16.385	0.932	0.5467	0.0310	0.2257	0.0027	2900	54	2812	129	3022	19	93.0	0.64	N/A

*N/A = not available

Table A.2: U-Pb zircon LAM-ICP-MS analyses which were not used for age determinations (continued)

MM01-81 (continued)

		Atomic ratios						Ages (Ma)								
Analysis #	pit size (µm)	$^{207}Pb/^{235}U$	(±)	$^{206}Pb/^{238}U$	(±)	$^{207}Pb/^{206}Pb$	(±)	$^{207}Pb/^{235}U$	1 ó	$^{206}Pb/^{238}U$	1 ó	$^{207}Pb/^{206}Pb$	2 ó	Conc. %	% error	U (ppm)
Discordant (< 94% or >104%) data for MM01-81																
87	20x20	16.347	1.819	0.5463	0.0533	0.2252	0.0053	2897	106	2810	222	3018	38	93.1	1.25	39
88	30x30	18.202	0.592	0.5794	0.0177	0.2458	0.0045	3000	31	2946	72	3158	29	93.3	0.93	N/A
89	20x20	18.222	0.364	0.5707	0.0111	0.2391	0.0019	3002	19	2911	46	3114	13	93.5	0.41	N/A
90	30x30	17.515	0.476	0.5671	0.0158	0.2367	0.0060	2963	26	2896	65	3098	40	93.5	1.30	N/A
91	30x30	14.631	0.459	0.5275	0.0158	0.2114	0.0052	2792	30	2731	67	2916	40	93.6	1.37	N/A
92	25x25	20.743	0.555	0.6494	0.0165	0.2347	0.0052	3127	26	3226	65	3085	36	104.6	1.15	59
93	25x25	20.837	0.502	0.6479	0.0161	0.2336	0.0032	3131	23	3220	63	3077	22	104.6	0.72	138
94	20x20	16.649	1.515	0.6033	0.0629	0.2070	0.0206	2915	87	3043	253	2882	162	105.6	5.61	N/A
95	30x30	19.825	0.822	0.6371	0.0235	0.2232	0.0038	3083	40	3178	93	3004	27	105.8	0.90	N/A
96	20x20	15.300	0.620	0.5915	0.0239	0.1961	0.0054	2834	39	2996	97	2794	45	107.2	1.63	N/A
97	20x20	20.589	0.887	0.6679	0.0344	0.2329	0.0058	3119	42	3298	133	3072	40	107.3	1.29	N/A
Concordant but % Error >2.2																
98	20x20	12.723	1.708	0.5245	0.0831	0.1995	0.0357	2659	126	2718	351	2822	292	96.3	10.34	N/A

*N/A = not available

Appendix B

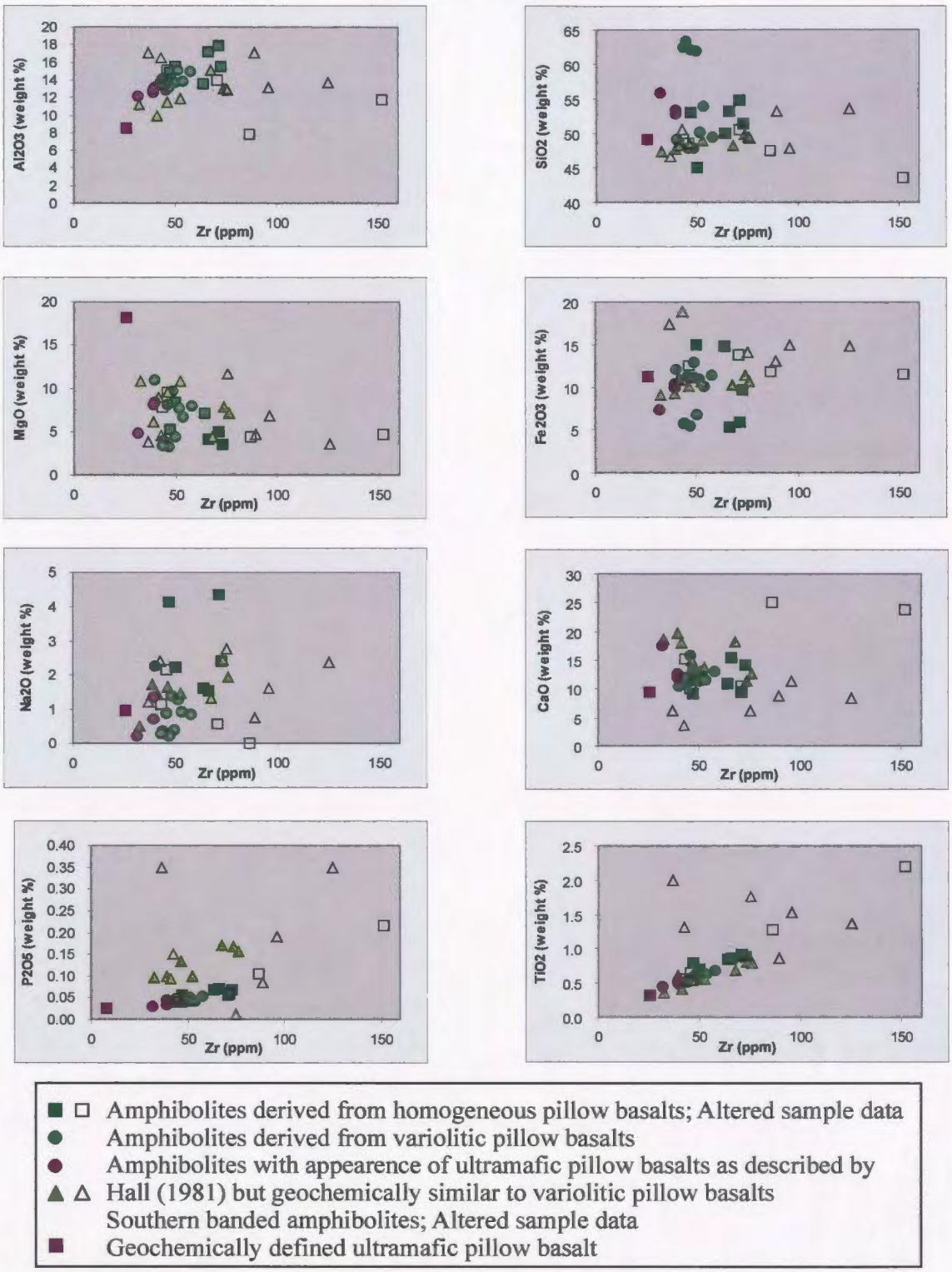

Figure B.1. Major element mobility, in samples of amphibolite derived from basaltic pillow lavas basalt, tested using bi-element plots. Elements are plotted against a typically immobile high field strength element (Zr) in variation diagrams. The least altered samples exhibit coherent and predictable trends for Zr.

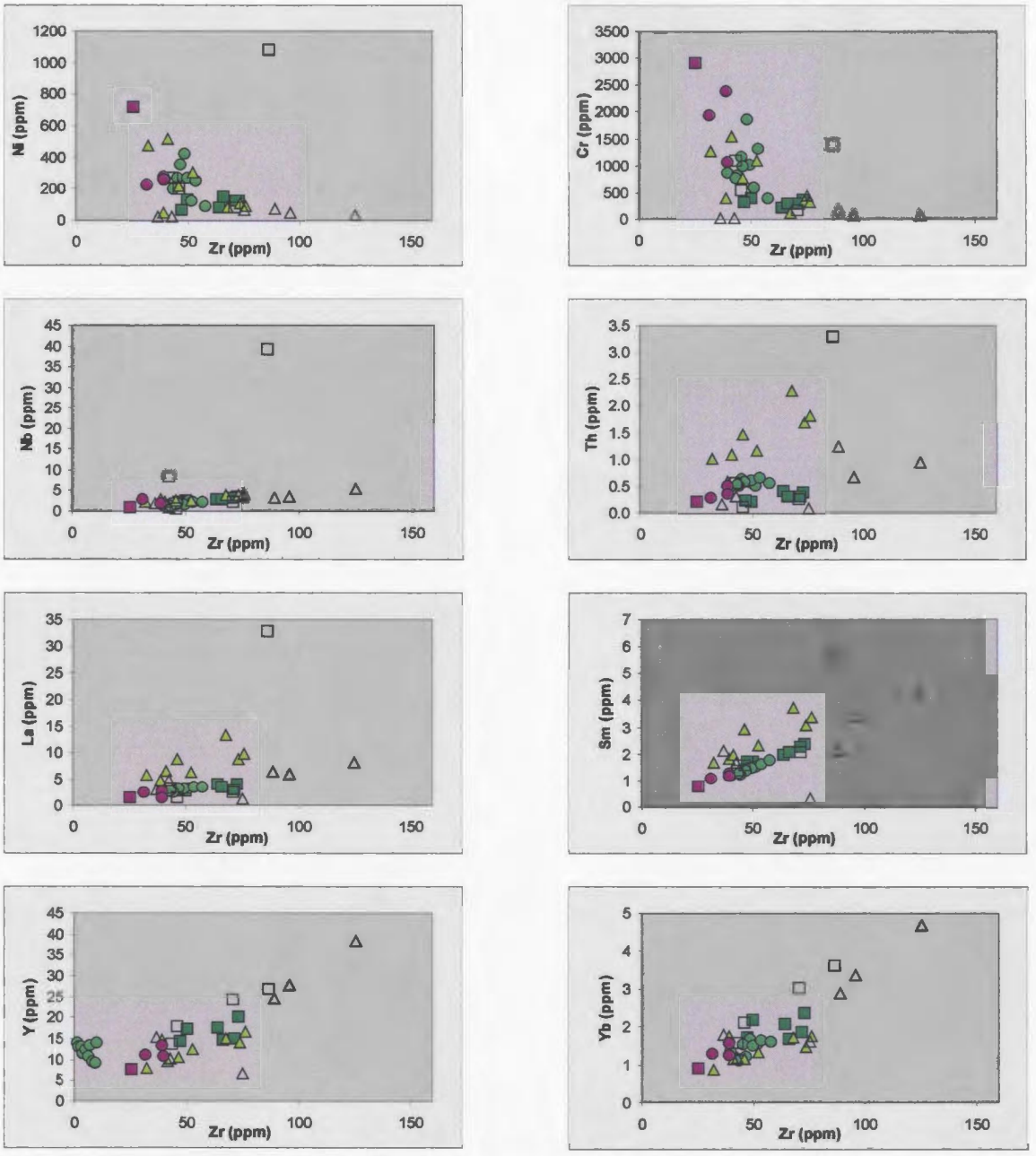

Figure B.2. Trace element mobility, in samples of amphibolite derived from basaltic pillow lavas, tested using bi-element plots. Elements are plotted against a typically immobile high field strength element (Zr) in variation diagrams. The least altered samples exhibit coherent and predictable trends for Zr.

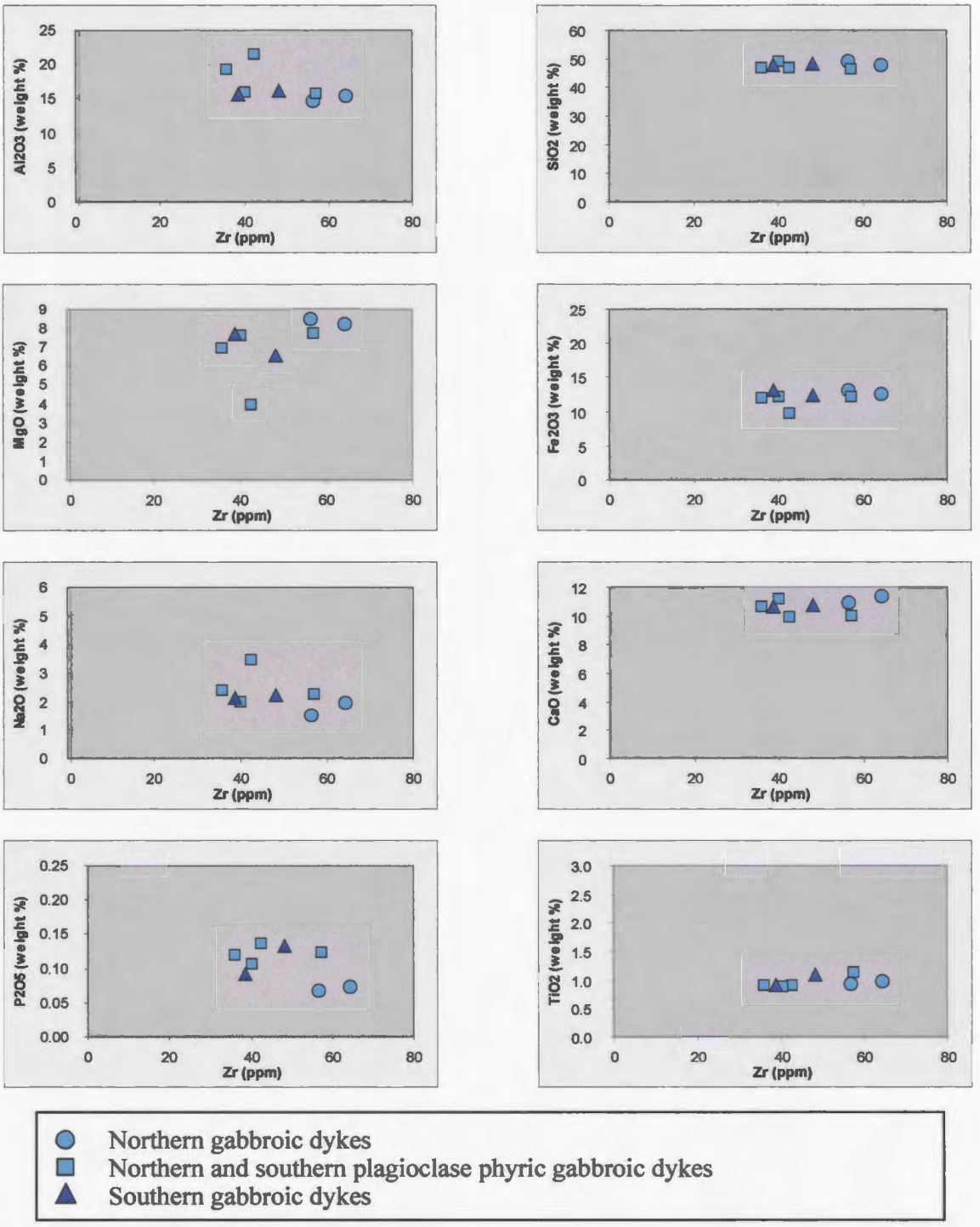

Figure B.3. Major element mobility in samples from mafic dykes, tested using bi-element plots. Elements are plotted against a typically immobile high field strength element (Zr) in variation diagrams. The least altered samples exhibit coherent and predictable trends for Zr.

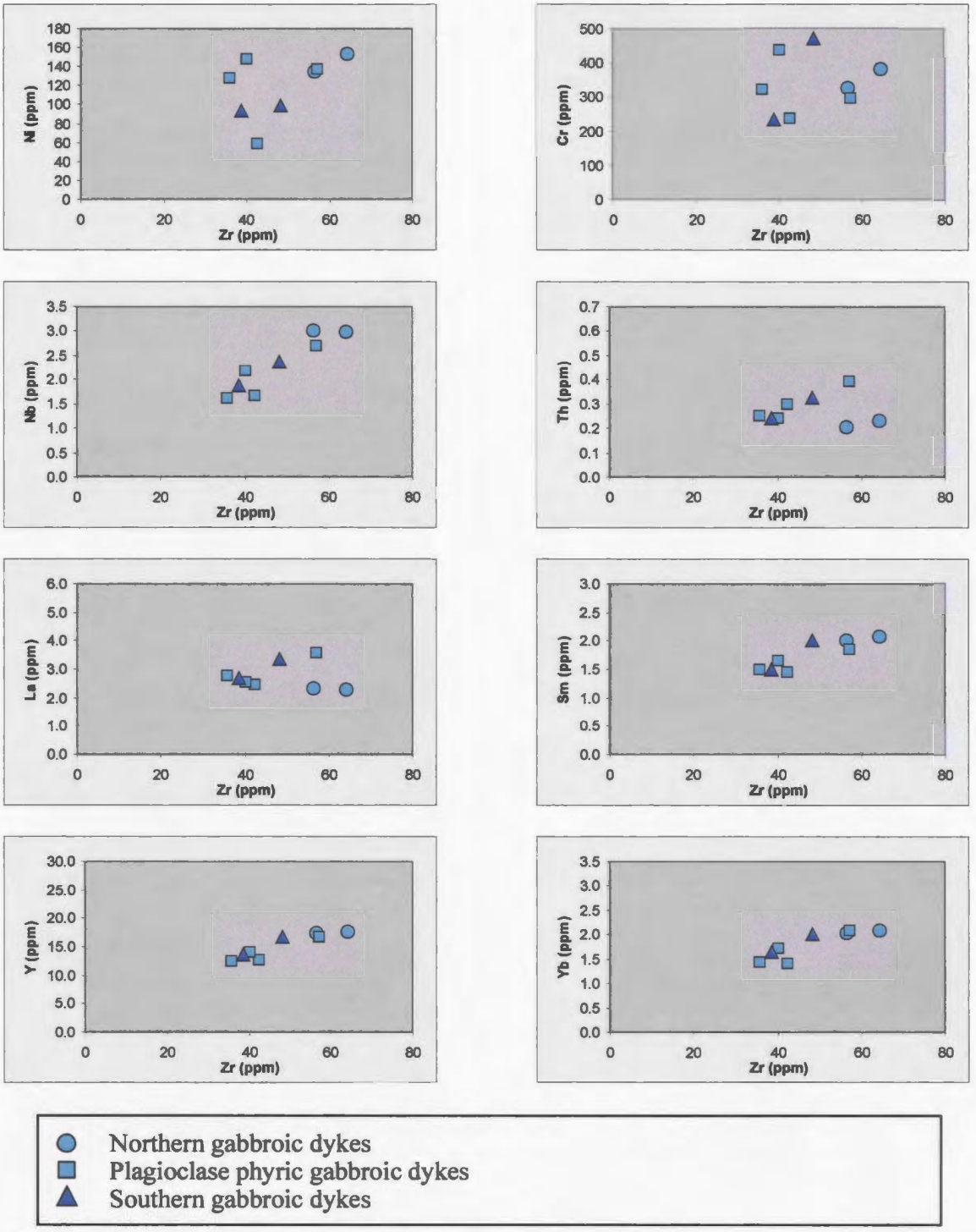

Figure B.4. Trace element mobility in samples of mafic dykes, tested using bi-element plots. Elements are plotted against a typically immobile high field strength element (Zr) in variation diagrams. The least altered samples exhibit coherent and predictable trends for Zr.

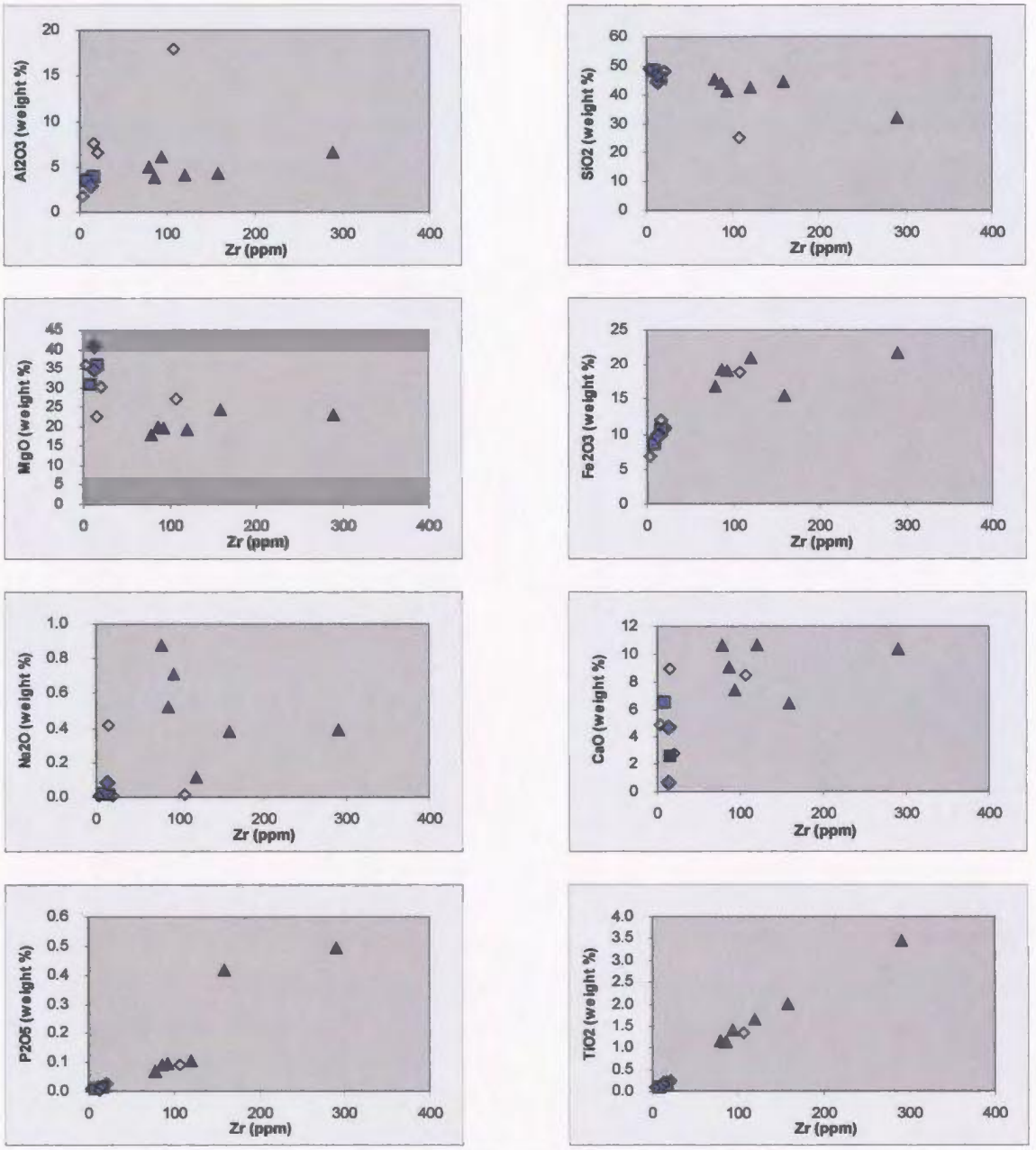

Figure B.5. Major element mobility in samples from ultramafic units tested using bi-element plots. Elements are plotted against a typically immobile high field strength element (Zr) in variation diagrams. The least altered samples exhibit coherent and predictable trends for Zr.

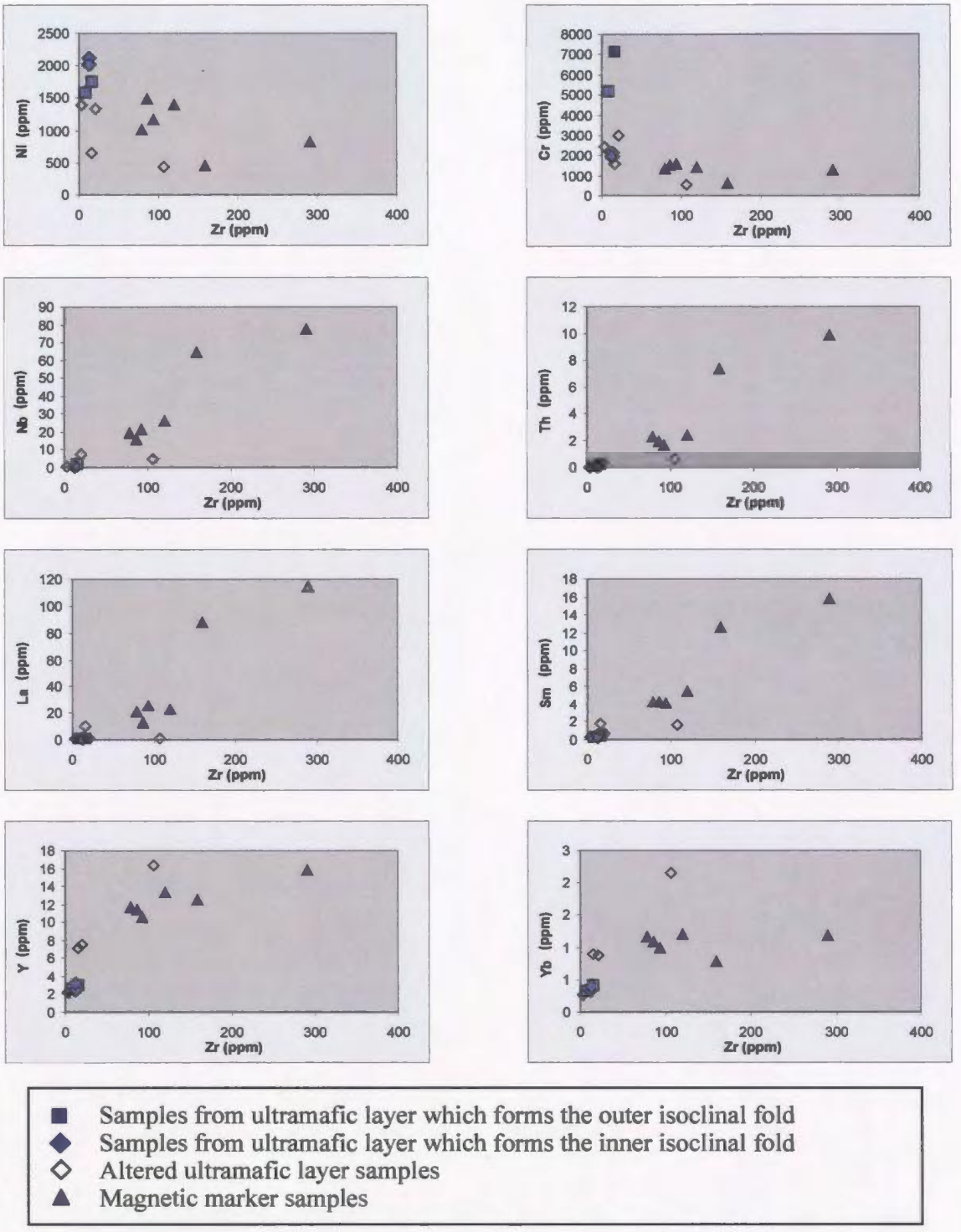

Figure B.6. Trace element mobility in samples from ultramafic units tested using bi-element plots. Elements are plotted against a typically immobile high field strength element (Zr) in variation diagrams. The least altered samples exhibit coherent and predictable trends for Zr.

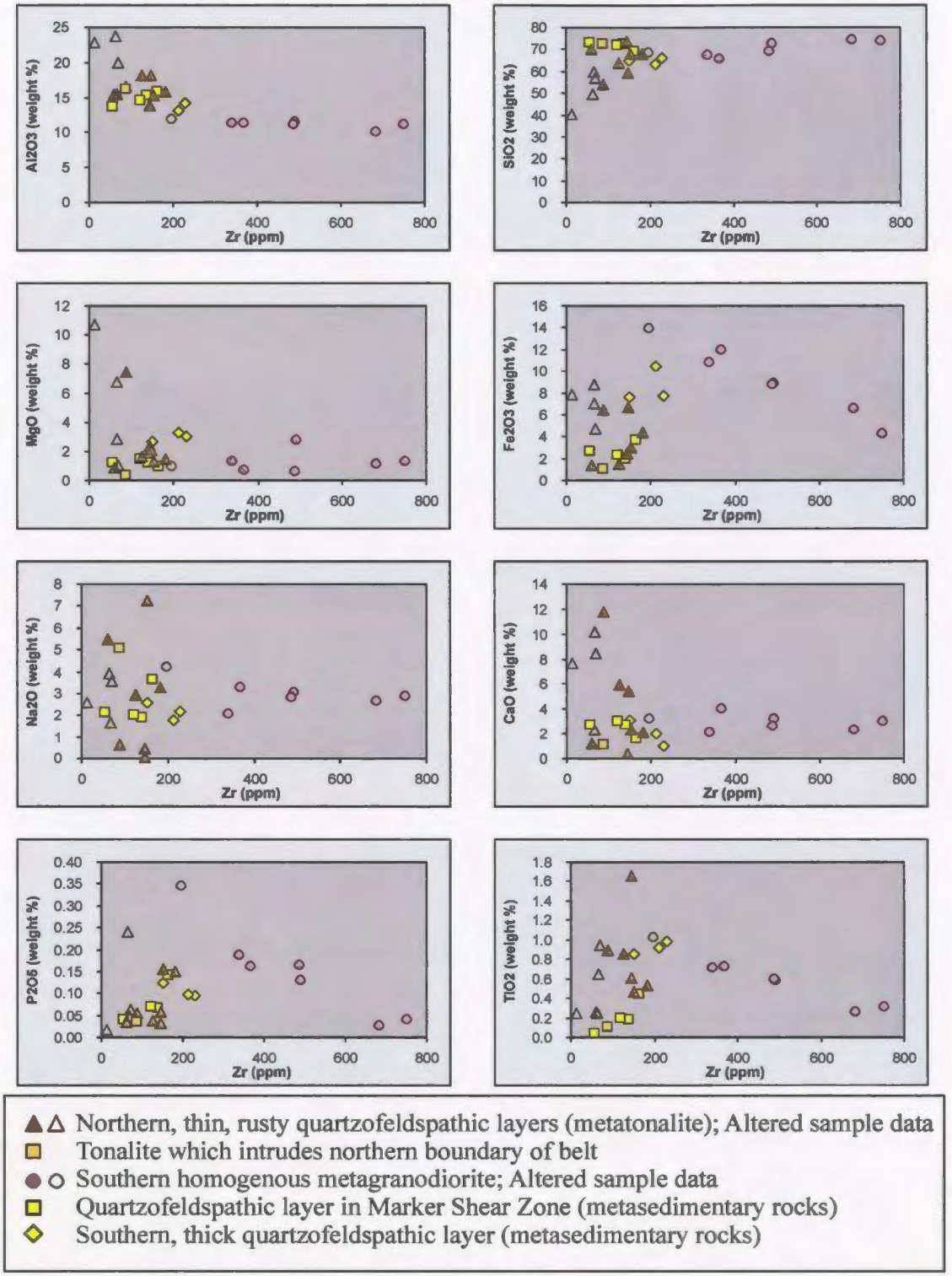

Figure B.7. Major element mobility in samples from felsic units tested using bi-element plots. Elements are plotted against a typically immobile high field strength element (Zr) in variation diagrams. The least altered samples exhibit coherent and predictable trends for Zr.

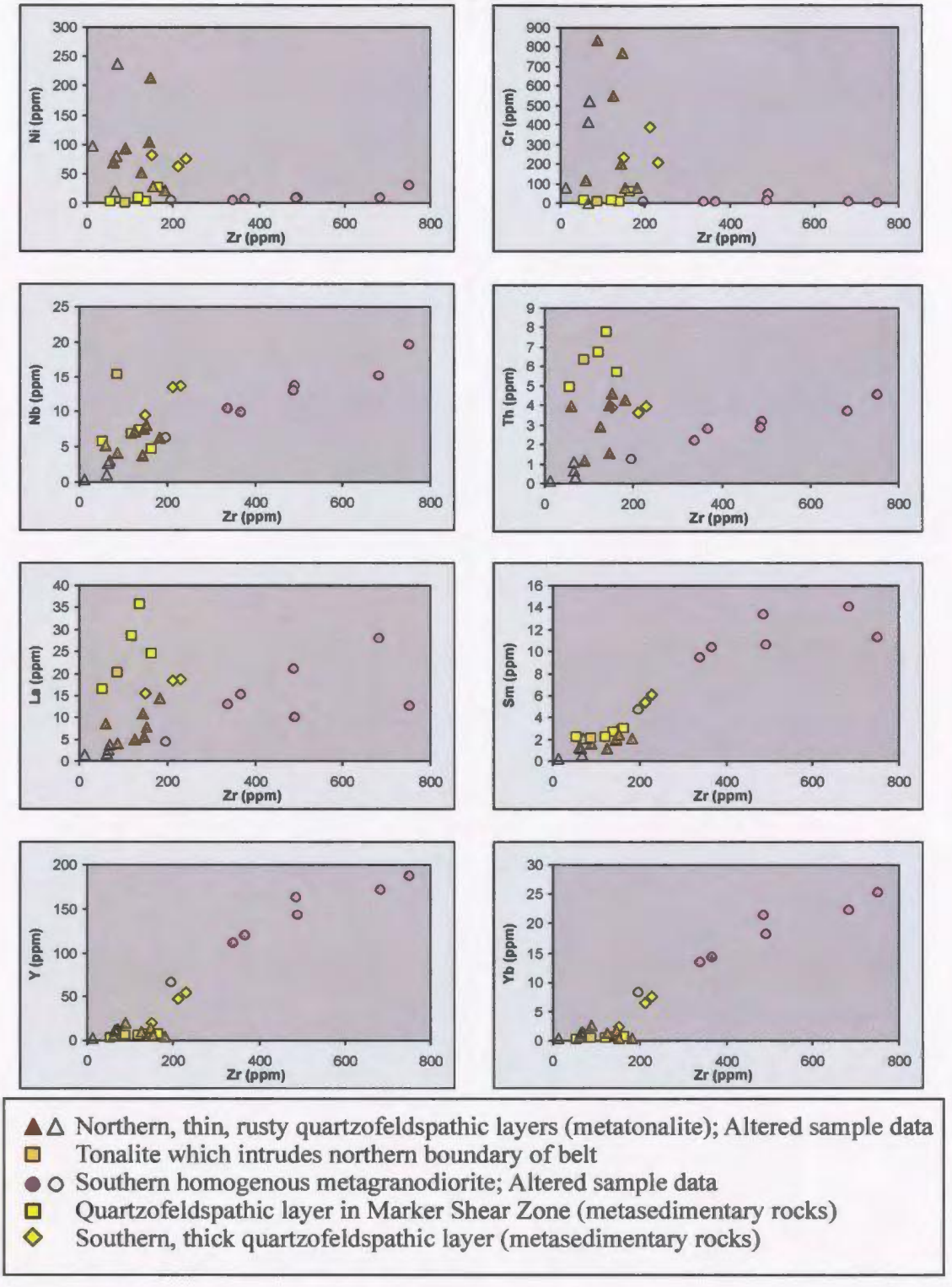

Figure B.8. Trace element mobility in samples from quartzofeldspathic units tested using bi-element plots. Elements are plotted against a typically immobile high field strength element (Zr) in variation diagrams. The least altered samples exhibit coherent and predictable trends for Zr.

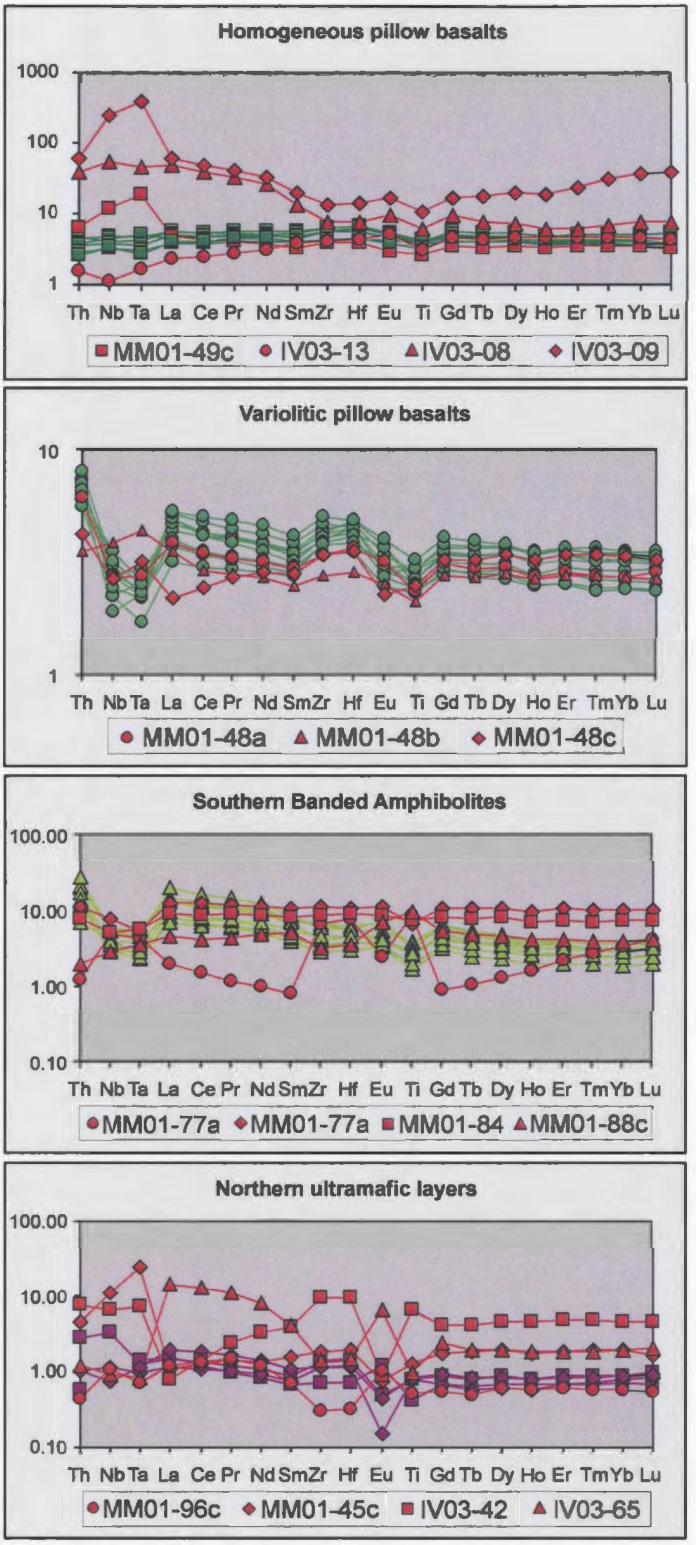

Figure B.9. Mafic and ultramafic samples which have the least alteration effects have consistent and coherent primitive mantle-normalized trace element patterns (green), whereas altered samples have inconsistent trends (red). The altered sample data were not used for analytical plots.

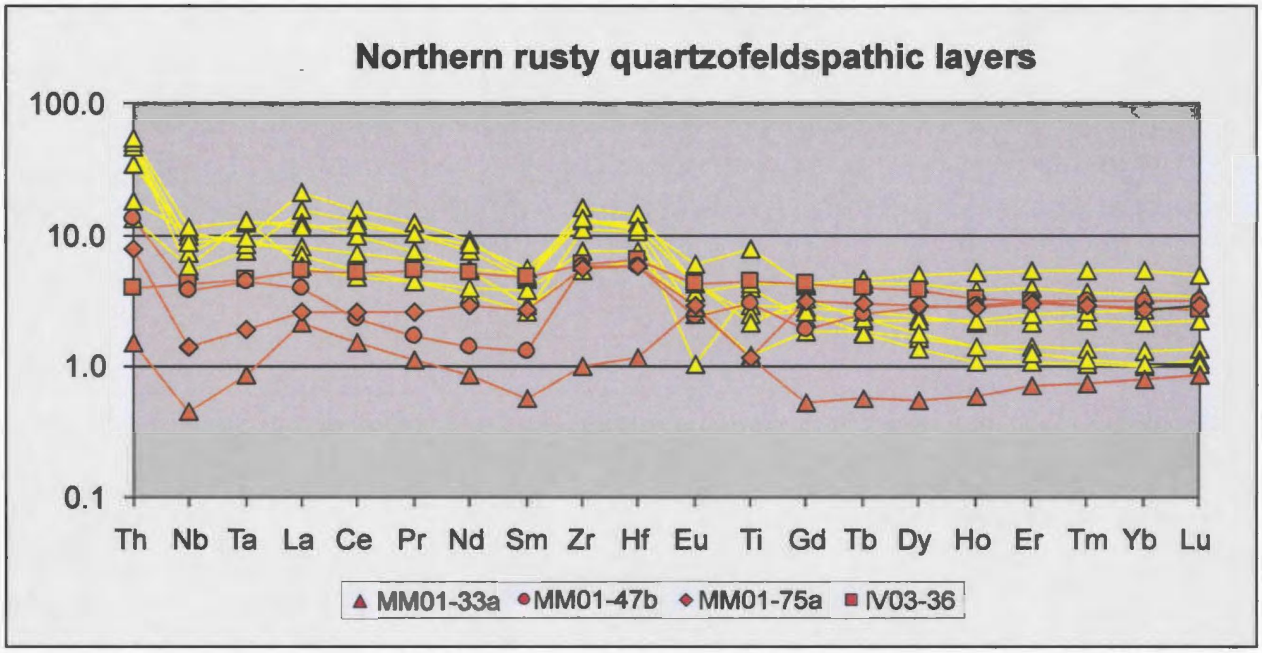

Figure B.10. Quartzofeldspathic samples which have the least alteration effects have consistent and coherent primitive mantle-normalized trace element patterns (yellow), whereas altered samples have inconsistent trends (red). The altered sample data were not used for analytical plots.

Table B.1. Major and trace element analyses of altered samples from the major lithological units of the Ivisârtoq greenstone belt, Greenland.

Northern Homogeneous Pillow Basalts Altered sample data (not used for analyses)					
(weight %)	**MM01-63b** BA in High Strain Zone	**MM01-49c** rim + core	**IV03-13** pillow core	**IV03-8** (strongly deformed)	**IV03-9**
SiO2	50.46	49.18	48.58	47.45	43.63
TiO2	0.90	0.56	0.65	1.27	2.19
Al2O3	13.98	13.40	15.10	7.90	11.72
Fe2O3(T)	13.87	10.75	12.58	11.79	11.46
MnO	0.25	0.26	0.19	0.33	0.28
MgO	6.43	7.80	9.47	4.37	4.70
CaO	10.43	15.24	9.98	25.16	23.88
K2O	0.26	0.16	0.52	0.00	0.01
Na2O	0.58	1.15	2.15	< LD	0.02
P2O5	0.06	0.04	0.05	0.10	0.21
Sum	97.21	98.52	99.25	98.37	98.12
LOI	0.90	0.53	0.93	0.19	0.69
Mg #	47.87	58.98	59.86	42.32	44.84
(ppm)					
S	35	17	38	22	22
Cl	629	1014	1041	399	914
Sc	60	45	44	40	42
V	355	228	263	242	246
Cr	178	1094	551	1380	1529
Ni	83.0	270	200	1078	667
Cu	55.6	53.9	12.7	11.8	12.4
Zn	71.0	76.6	46.5	105	98.9
Ga	18.0	15.1	12.8	25.9	47.5
Rb	3.90	7.63	46.0	0.283	0.625
Sr	59.53	58.43	60.23	65.84	282.90
Nb	2.17	8.21	0.79	39.33	174.96
Y	24.39	13.58	17.72	26.73	106.03
Zr	70.7	43.0	45.8	86.3	152
Ba	89.7	34.6	112	12.0	14.6
La	2.48	3.27	1.57	32.75	41.53
Ce	6.33	7.42	4.18	68.31	86.15
Pr	1.02	1.04	0.72	8.51	10.58
Nd	5.59	4.91	4.13	33.87	42.17
Sm	2.08	1.37	1.60	5.77	8.54
Eu	0.68	0.46	0.83	1.54	2.67
Gd	3.24	1.92	2.55	5.26	9.49
Tb	0.60	0.35	0.45	0.81	1.86
Dy	4.29	2.42	3.21	5.00	14.04
Ho	0.97	0.52	0.72	0.95	3.00
Er	2.93	1.58	2.12	2.85	10.58
Tm	0.45	0.24	0.32	0.47	2.12
Yb	3.01	1.58	2.13	3.61	17.64
Lu	0.44	0.23	0.30	0.53	2.64
Hf	1.87	1.15	1.28	2.26	4.15
Ta	0.11	0.78	0.07	1.87	16.29
Th	0.27	0.56	0.13	3.29	5.10

Analytical method:

Major elements (including S and Cl):X-ray fluorescence fused glass beads method

Trace elements analytic method: ICP-MS Sinter technique

ICP-MS Acid technique

LOI= loss on ignition; BA=banded amphibolite; LD= limit of detection

Table B.1. Major and trace element analyses of altered samples from the major lithological units of the Ivisârtoq greenstone belt, Greenland (continued).

Southern Banded Amphibolites
Altered sample data (not used for analyses)

(weight %)	MM01-77a	MM01-77d	MM01-84	MM01-88c	MM01-112 BA in thick S qtzfeld layer	MM01-2 h BA in Magnetic Marker
SiO2	49.51	53.54	47.91	46.57	50.46	53.29
TiO2	1.76	1.37	1.52	2.00	1.31	0.87
Al2O3	13.06	13.76	13.20	17.00	16.55	17.02
Fe2O3(T)	14.17	14.87	14.97	17.41	18.80	13.03
MnO	0.18	0.16	0.24	0.26	0.15	0.26
MgO	11.60	3.56	6.79	3.84	4.53	4.67
CaO	6.16	8.45	11.42	6.13	3.75	8.85
K2O	0.09	0.07	0.80	3.24	1.49	0.33
Na2O	2.77	2.37	1.63	1.24	2.43	0.74
P2O5	0.01	0.35	0.19	0.35	0.15	0.09
Sum	99.31	98.50	98.68	98.02	99.60	99.15
LOI	0.88	0.38	0.49	0.84	0.51	0.57
Mg #	61.86	32.18	47.34	30.40	32.30	41.55
(ppm)						
S	53	40	114	115	18	21
Cl	1478	2205	2124	2162	1137	810
Sc	71	34	48	44	33	36
V	143	180	366	233	255	269
Cr	441	75	82	13	28	164
Ni	66.4	33.7	54.5	21.9	28.3	73.4
Cu	6.18	223	16.7	14.1	11.6	106
Zn	21.9	43.9	88.1	101	120	63.5
Ga	13.3	23.4	20.3	24.6	26.8	23.2
Rb	2.93	0.568	19.1	162	89.8	16.5
Sr	34.61	107.96	229.32	166.76	118.20	100.15
Nb	3.51	5.59	3.68	2.07	1.11	3.26
Y	6.83	38.20	27.86	15.42	10.23	24.57
Zr	75.0	125	95.7	36.6	42.6	88.9
Ba	16.6	15.9	60.8	404	265	204
La	1.37	8.17	6.02	3.06	4.65	6.59
Ce	2.64	21.87	15.17	7.19	10.31	12.71
Pr	0.31	3.10	2.29	1.13	1.43	1.71
Nd	1.33	14.87	11.27	6.17	6.65	7.71
Sm	0.34	4.42	3.43	2.16	1.68	2.13
Eu	0.38	1.80	1.35	1.14	0.41	0.71
Gd	0.52	5.97	4.66	3.01	1.80	3.18
Tb	0.11	1.09	0.82	0.50	0.31	0.60
Dy	0.94	7.33	5.61	3.23	1.94	4.24
Ho	0.25	1.56	1.14	0.65	0.42	0.95
Er	0.99	4.76	3.42	1.90	1.26	2.91
Tm	0.19	0.69	0.50	0.27	0.18	0.44
Yb	1.61	4.70	3.36	1.81	1.19	2.89
Lu	0.28	0.72	0.51	0.29	0.17	0.42
Hf	2.29	3.13	2.67	1.04	1.03	2.09
Ta	0.18	0.22	0.24	0.15	0.10	0.14
Th	0.10	0.95	0.67	0.17	0.33	1.25

Analytical method:
Major elements (including S and Cl):X-ray fluorescence fused glass beads method
Trace elements analytic method: ICP-MS Sinter technique

LOI= loss on ignition; BA=banded amphibolite; qtzfeld=quartzofeldspathic

Table B.1. Major and trace element analyses of altered samples from the major lithological units of the Ivisârtoq greenstone belt, Greenland (continued).

	Northern Ultramafic Layers Altered sample data (not used for analyses)				**Northern thin rusty quartzofeldspathic (tonalitic) sheets** Altered sample data (not used for analyses)			
	MM01-45c	**IV03-42**	**IV03-65**	**MM01-96c**	IV03-36	MM01-47b	MM01-33a	MM01-75a
(weight %)	Outer Fold	Outer Fold	Outer Fold	Inner Fold				
SiO2	48.15	25.08	46.78	48.82	56.89	60.01	40.18	49.67
TiO2	0.26	1.34	0.21	0.11	0.94	0.65	0.25	0.25
Al2O3	6.51	18.03	7.64	1.81	19.96	15.41	22.81	23.67
Fe2O3(T)	10.92	18.93	12.10	6.82	4.69	8.73	7.83	7.06
MnO	0.21	0.22	0.20	0.18	0.06	0.17	0.03	0.06
MgO	30.31	27.20	22.84	36.05	1.00	6.76	10.72	2.83
CaO	2.81	8.43	8.90	4.88	8.51	2.28	7.64	10.14
K2O	0.02	0.01	0.04	0.00	3.09	3.32	0.83	1.22
Na2O	0.01	0.01	0.42	0.01	3.55	1.68	2.57	3.92
P2O5	0.03	0.09	0.02	0.01	0.06	0.05	0.02	0.24
Sum	99.22	99.35	99.13	98.69	98.74	99.05	92.87	99.07
LOI	6.38	14.66	4.38	9.36	1.22	1.93	N/A	N/A
Mg #	84.62	74.00	78.90	91.28	29.67	60.54	73.08	44.25
(ppm)								
S	274	57	69	123	20	24	24	19
Cl	3388	494	694	1339	1354	945	133	94
Sc	19	69	21	11	32	39	19	15
V	104	267	114	46	293	261	94	91
Cr	2996	564	1560	2453	523	412	77	3
Ni	1335	435	652	1391	238	80.8	97.2	19.7
Cu	50.3	138	117	4.41	96.6	49.6	222	111
Zn	62.7	97.0	34.2	35.6	45.4	231	14.2	7.72
Ga	8.62	13.1	5.94	2.06	17.8	15.6	18.4	21.7
Rb	6.72	1.57	0.11	0.238	108	323	84.4	69.6
Sr	7.63	236.49	99.43	12.35	173.54	31.77	177.38	134.49
Nb	7.82	4.66	0.64	0.77	3.06	2.70	0.32	1.00
Y	7.54	16.38	7.17	2.23	12.28	11.59	2.53	11.57
Zr	20.4	107	15.573	3.474	69.6	66.9	11.5	64.0
Ba	11.2	25.5	8.09	5.53	296	236	489	472
La	0.74	0.54	9.82	0.83	3.65	2.68	1.46	1.80
Ce	2.17	2.41	22.76	2.37	9.02	4.09	2.65	4.53
Pr	0.35	0.62	2.80	0.37	1.37	0.45	0.29	0.68
Nd	1.75	4.35	10.62	1.53	6.83	1.88	1.15	3.82
Sm	0.66	1.58	1.73	0.29	2.08	0.55	0.25	1.17
Eu	0.12	0.14	1.02	0.17	0.69	0.40	0.46	0.48
Gd	0.96	2.30	1.33	0.30	2.43	1.08	0.30	1.82
Tb	0.19	0.43	0.21	0.05	0.41	0.26	0.06	0.32
Dy	1.37	3.09	1.34	0.41	2.66	1.99	0.39	2.05
Ho	0.27	0.70	0.29	0.09	0.52	0.47	0.10	0.46
Er	0.85	2.16	0.86	0.27	1.48	1.46	0.33	1.42
Tm	0.13	0.32	0.13	0.04	0.21	0.22	0.05	0.21
Yb	0.88	2.15	0.90	0.27	1.34	1.47	0.38	1.30
Lu	0.12	0.32	0.14	0.04	0.19	0.22	0.06	0.20
Hf	0.59	2.83	0.44	0.10	1.94	1.77	0.36	1.74
Ta	0.98	0.29	0.03	0.03	0.19	0.18	0.04	0.08
Th	0.38	0.66	0.10	0.04	0.34	1.13	0.13	0.67

Analytical method:

Major elements (including S and Cl):X-ray fluorescence fused glass beads method
X-ray fluorescence pressed pellets method

Trace elements analytic method: ICP-MS Sinter technique
ICP-MS Acid technique

LOI= loss on ignition; N/A= not applicable; LD=limit of detection

Table B.2. Primitive mantle values based on C1 chondrite concentrations from Anders and Grevesse (1989).

Primitive Mantle

	(ppm)
Th	0.0853
Nb	0.713
Ta	0.0412
La	0.6806
Ce	1.749
Pr	0.258
Nd	1.312
Sm	0.4266
Zr	11.42
Hf	0.302
Eu	0.162
Ti	1264
Gd 160	0.5701
Tb	0.1053
Dy	0.7038
Ho	0.1612
Er	0.4608
Tm	0.0702
Yb	0.4713
Lu	0.0705

References

Anders, E., Grevesse, N., 1989. Abundances of the elements; meteoritic and solar. Geochimica et Cosmochimica Acta 53:197-214.

Aftalion, M., Bowes, D.R., Vrána, S., 1989. Early Carboniferous U-Pb zircon age for garnetiferous, perpotassic granulites, Blansky les massif. Czechoslovakia. Neues Jahrbuch fur Mineralogie, Monatshefte 4:145-152.

Allaart, J.H., 1982. Geologic map of Greenland, 1:500 000, Frederikshåb Isblink-Søndre Strømfjord. Grønlands Geologiske Undersøgelse, Copenhagen.

Allaart, J. H., Jensen, S.B., McGregor, V.R., Walton, B.J., 1977. Reconnaissance mapping for the 1:500 000 map sheet in the Godthåb-Isua region, southern West Greenland. Rapport Grønlands Geologiske Undersøgelse 85: 50-54.

Appel, P.W., 1988. Scheelite in Malene supracrustals of the Ivisârtoq area, southern West Greenland. Rapport Grønlands Geologiske Undersøgelse 140: 57-58.

Arndt, N.T., 1991. High Ni in Archean tholeiites. Tectonophysics 187: 411-420.

Arndt, N.T., Jenner, G.A., 1986. Crustally contaminated komatiites and basalts from Kambalda, Western Australia. Chemical Geology 56: 229-255.

Arndt, N., Lehnert, K., Vasil'ev, Y., 1995. Meimechites: highly magnesian lithosphere-contaminated alkaline magmas from deep subcontinental mantle. Lithos 34: 41-59.

Arndt, N., Chauvel, C., Czamanske, G., Fedorenko, V., 1998. Two mantle sources , two plumbing systems: tholeiitic and alkaline magmatism of the Maymecha River basin, Siberian flood volcanic province. Contributions to Mineralogy and Petrology 133: 297-313.

Baadsgaard, H., 1973. U-Th-Pb dates on zircons from the early Precambrian Amîtsoq gneisses, Godthåb district, West Greenland. Earth and Planetary Science Letters 19: 22-28.

Baadsgaard, H., 1976. Further U-Pb dates on zircons from the early Precambrian rocks of the Godthåbsfjord area, West Greenland. Earth and Planetary Science Letters 33:261-267.

Baragar, W.R.A., Mader, U., LeCheminant, G.M., 2001. Paleoproterozoic carbonatitic ultrabasic volcanic rocks (meimechites?) of Cape Smith Belt, Quebec. Canadian Journal of Earth Sciences 38: 1313-1334.

Bernstein, S., Leslie, A.G., Higgins, A.K., Brooks, C.K., 2000. Teritary alkaline volcanics in the Nunatak Region, Northeast Greenland: new observations and comparison with Siberian maymechites. Lithos 53: 1-20.

Bickle, M.J., 1982. The magnesium contents of komatiitic liquids. In: Arndt, N.T., Nisbet, E.G. (Eds.), Komatiites. George Allen and Unwin, London, pp. 479-494.

Black, L.P., Gale, N.H., Moorbath, S., Pankhurst, R.J., McGregor, V.R., 1971. Isotopic dating of very early Precambrian amphibolite facies gneisses from the Godthaab district, West Greenland. Earth and Planetary Sciences Letters 12: 245-259.

Blatt, H., Tracy, R., (Eds.) 1996. Petrology igneous, sedimentary, and metamorphic, second edition. W. H. Freeman and Company, New York.

Bolhar, R., Woodhead, J.D., Hergt, J.M., 2003. Continental setting inferred for emplacement of the 2.9-2.7 Ga Belingwe Greenstone Belt, Zimbabwe: Geology 31, 295-298.

Bolhar, R., Kamber, B.S., Moorbath, S., Whitehouse, M.J., Collerson, K.D., 2005. Chemical characterization of earth's most ancient clastic metasediments from the Isua Greenstone Belt, southern West Greenland. Geochimica et Cosmochimica Acta 69: 1555-1573.

Brewer, M.A., 1985. The petrology of the late Archaean gneisses and granites, Nunatarssuaq, Ivisârtoq region, southern West Greenland. PhD thesis, University of Exeter, Exeter, UK.

Brewer, M.A., Chadwick, B., Coe, K., Park, J.F.W., 1984. Further field observations in the Ivisârtoq region of southern West Greenland. Rapport Grønlands Geologiske Undersøgelse 120: 55-67.

Bridgwater , D., Keto, L., McGregor, B.R., Myers, J.S., 1976. Archaean gneiss complex of Greenland. In: Echer, A., Watt, W.S. (Eds.), Geology of Greenland. Grønlands Geologiske Undersøgelse, Copenhagen, pp. 18-75.

Brooks, C.K., Pedersen, A.K., Rex, D.C., 1979. The petrology and age of alkaline mafic lavas from the nunatak zone of central East Greenland. Bulletin Grønlands Geologiske Undersøgelse 133: 1-28.

Brown, M., Friend, C.R.L., 1980. The polyphase nature and internal structure of the Qôrqut granite complex east of Ũmánap suvdlua, Godthåbsfjord, southern West Greenland. Rapport Grønlands Geologiske Undersøgelse 100:76-79.

Brown, M., Friend, C.R.L., McGregor, V.R., Perkins, W.T., 1981. The late Archaean Qôrqut granite complex east of southern West Greenland. Journal of Geophysical Research 86: 10617-10632.

Brown, P.E., Evans, I.B., Becker, S.M., 1996. The Prince of Wales formation - Post-flood basalt alkali volcanism in the Tertiary of East Greenland. Contributions to Mineralogy and Petrology 123: 424-434.

Bucher, K., Frey, M., 1994. Petrogenesis of metamorphic rocks. Springer-Verlag, New York.

Cawthorn, R.G., McIver, J.R., McCarthy, T.S., Wyatt, B.A., 1979. Possible liquid immiscibility textures in high-magnesia basalts from the Ventersdorp Supergroup, South Africa. Journal of Geology 87: 105-113.

Chadwick, B. 1981. Field relations, petrography and geochemistry of Archaean amphibolite dykes and Malene supracrustal amphibolites, northwest Buksefjorden, southern West Greenland. Precambrian Research 14: 221-259.

Chadwick, B., 1985. Contrasting styles of tectonism and magmatism in the Late Archaean crustal evolution of the northeastern part of the Ivisârtoq region, inner Godthåbsfjord, southern West Greenland. Precambrian Research 27: 215-238.

Chadwick, B., 1986. Malene stratrigraphy and late Archaean structure: new data from Ivisârtoq, inner Godthåbsfjord, southern West Greenland. Rapport Grønlands Geologiske Undersøgelse 115: 74-85.

Chadwick, B., 1990. The stratigraphy of a sheet of supracrustal rocks within high-grade orthogneisses and its bearing on Late Archaean structure in southern West Greenland. Journal of the Geological Society, London 147: 639-652.

Chadwick, B., Coe, K. 1983. Geological map of Greenland, 1:100 000, Buksefjorden, 63 V.2 Nord, with descriptive text. Grønlands Geologiske Undersøgelse, Copenhagen.

Chadwick, B., Coe, K. 1988. Geological map of Greenland, 1:100 000, Ivisârtoq, 64 V.1 Nord, with descriptive text. Grønlands Geologiske Undersøgelse, Copenhagen.

Chadwick, B., Nutman, A.P., 1979. Archaean structural evolution in the northwest of the Buksefjorden region, southern West Greenland. Precambrian Research 9: 199-226.

Collins, W.J., Beams, S.D., White, A.J.R., Chappell, B.W., 1982. Nature and origin of A-type granites with particular reference to southeastern Australia. Contributions to Mineralogy and Petrology 80:189-200.

Condie, K.C., 1980. Origin and early development of the Earth's crust. Recambrian Research 11: 183-197.

Condie, K.C. 1993. Chemical composition and evolution of the upper continental crust: contrasting results from surface samples and shales. Chemical Geology 104: 1-37.

Condie, K.C., 1994. Greenstones through time. In: Condie, K.C. (Ed.), Archean crustal evolution. Elesevier Science B.V., New York, pp. 85-112.

Cox, R.A., 2002. Morphological, chemical, and geochronological techniques for characterizing detrital zircon. *In* Lentz, D.R., ed., Geochemistry of sediments and sedimentary rocks: Evolutionary considerations to mineral deposit-forming environments: Geological Association of Canada, Geotext 4: 47-62.

Crewe, M.A., 1984. A textural study of Archaean peridotites: Ujaragssuit nunât, Ivisârtoq regionk southern West Greenland. Rapport Grønlands Geologiske Undersøgelse 120: 70-74.

Crewe, M.A., 1986. The petrogenesis of Archaean basic and ultrabasic rocks from Ujaragssuit Nunât, Ivisârtoq region, southern West Greenland. PhD thesis, University of Exeter, Exeter, UK.

Crowley, J.L., Myers, J.S., Dunning, G.R., 2002. Timing and nature of multiple 3700-3600 Ma tectonic events in intrusive rocks north of the Isua greenstone belt, southern West Greenland. Geological Society of America Bulletin 114: 1311-1325.

Dalrymple, B.G., Czamanske, G.K., Fedorenko, V.A., Simonov, O.N., Lanphere, M.A., Likhachev, A.P., 1995. A reconnaissance 40Ar/39Ar geochronological study of ore-bearing and related rocks, Siberian Russia. Geochimica et Cosmochimica Acta 59: 2071-2093.

Dickin, A.P., 1995. Lead isotopes. *In* Radiogenic Isotope Geology. Cambridge, New York, 452 p.

Dimroth, E., 1970. Meimechites and carbonatites of the Castignon Lake complex, New Quebe. Neues Jahrbuch für Mineralogie Abhandlungen 112: 239-278.

Dubé, B., Dunning, G.R., Lauzière, K., and Roddick, J.C., 1996. New insights into the Appalachian orogen from geology and geochronology along the Cape Ray fault zone, southwest Newfoundland: Geological Society of America Bulletin 108: 101-116.

Duke, M.J.M., 1993. The geochronology, geochemistry and isotope geology of the type-Nuk gneisses of the Akia terrane, southern West Greenland. Ph.D. Thesis, University of Alberta, Edmonton, Canada.

Faure, G., 1986. Principles of isotope geology, second edition. John Wiley and Sons, New York.

Fedorenko, V., Czamanske, G., 1997. Results of new field and geochemical studies of the volcanic and intrusive rocks of the Maymecha-Kotuy area, Siberian flood-basalt Province, Russia. International Geology Review 39: 479-531.

Fedorenko, V.A., Czamanske, G.K., Zen'ko, T.E., Budahn, J.R., Siems, D.F., 2000. Field and geochemical studies of the melilite-bearing Arydzhangsky Suite, and an overall perspective on the Siberian alkaline-ultramafic flood-volcanic rocks. International Geology Review 42: 769-804.

Friend, C.R.L., Hall, R.P., 1977. Field work in the Ivisârtoq area, inner Godthåbsfjord, southern West Greenland. Rapport Grønlands Geologiske Undersøgelse 85: 54-60.

Friend, C.R.L., Hughes, D.J., 1978. Relict plutonic textures in Archaean ultramafic rocks from the Fiskenaesset region, southern West Greenland; implications for crustal thickness. In: Windley, B.F., Naqvi, S.M. (Eds.), Archaean geochemistry. Elsevier, Amsterdam, pp. 375-392.

Friend, C.R.L., Nutman, A.P., 2005. New pieces to the Archaean terrane jigsaw puzzle in the Nuuk region, southern West Greenland: steps in transforming a simple insight into a complex regional tectonothermal model. Journal of the Geological Society, London 162: 147-162.

Friend, C.R.L., Hall, R.P., Hughes, D.J., 1981. The geochemistry of the Malene (mid-Archaean) ultramafic-mafic amphibolite suite, southern West Greenland. In: Glover, J.E., Groves, D.E. (Eds.), Archaean geology. Special publication of the Geological Society of Australia 7, pp. 301-312.

Friend, C.R.L., Nutman, A.P., McGregor, V.R., 1987. Late-Archaean tectonics in the Færingehavn-Tre Brødre area, south of Buksefjorden, southern West Greenland. Journal of the Geological Society of London 144: 369-376.

Friend, C.R.L., Nutman, A.P., McGregor, V.R., 1988. Late Archaean terrane accretion in the Godthåb region, southern West Greenland. Nature 335: 535-538.

Friend, C.R.L., Brown M., Perkins, W.T., Burwell, A.D.M., 1985. The geology of the Qôrqut granite complex north of Qôrqut, Godthåbsfjord, southern West Greenland. Bulletin Grønlands Geologiske Undersøgelse 151.

Fowler, A.D., Jensen, L.S., Peloquin, S.A., 1986. Varioles in Archaean basalts: products of spherulitic crystallization. Canadian Journal of Mineralogy 25: 2775-289.

Fowler, A.D., Berger, B., Shore, M., Jones, M.I., Ropchan, J., 2002. Supercooled rocks: development and significance of varioles, spherulites, dendrites and spinifex in Archaean volcanic rocks, Abitibi Greenstone belt, Canada. Precambrian Research 115: 311-328.

Garde, A.A., 1987. Geological map of Greenland, 1:100 000, Isukasia, 65 V.2. Syd. Grønlands Geologiske Undersøgelse, Copenhagen.

Garde, A.A., 1989. Geological map of Greenland, 1:100 000, Fiskefjord, 64 V.1. Nord. Grønlands Geologiske Undersøgelse, Copenhagen.

Geyh, M.A., Schleicher, H., 1990. Absolute age determination: Physical and chemical dating methods and their application. Springer-Verlag. New York.

Goodwin, M. Alan., 1991. Precambrian Geology: The dynamic evolution of the continental crust. Academic Press. Toronto, Canada.

Green, M.G., Sylvester, P.J., Buick, R., 2000. Growth and recycling of early Archaean continental crust: geochemical evidence from the Coonterunah and Warrawoona Groups, Pilbara Craton, Australia. Tectonophysics 322: 69-88.

Griffin, W.L., McGregor, V.R., Nutman, A.P., Taylor, P.N., Bridgwater, D., 1980. Early Archaean graunulite-facies metamorphism south of Ameralik. Earth and Planetary Science Letters 50: 59-74.

Hall, R.P., 1980. The tholeiitic and komatiitic affinities of the Malene metavolcanic amphibolites from Ivisârtoq, southern West Greenland. Rapport Grønlands Geologiske Undersøgelse 97.

Hall, R.P., 1981. The Archaean geology of Ivisârtoq, inner Godthåbsfjord, southern West Greenland. Ph.D. Thesis, Portsmouth Polytechnic, UK.

Hall, R.P., Friend, C.R.L., 1979. Structural evolution of the Archaean rocks in Ivisârtoq and the neighbouring inner Godthåbsfjord region, southern West Greenland. Geology 7: 311-315.

Hall, R.P., Huges, D.J., Friend, C.R.L., 1987. Mid-Archaean basic magmatism of southern West Greenland. *In*: Park, R.G., Tarney, J. (Eds), Evolution of the Lewisian and comparable Precambrian high grade terrains. Geological Society, London, Special Publication 27: 261-275.

Hanchar, J.M., Miller, C.F., 1993. Zircon zonation patterns as revealed by cathodoluminescence and back-scattered electron images: implications for interpretation of complex crustal histories. Chemical Geology 110: 1-13.

Hanski, E., Huhma, H., Rastas, P., Kamenetsky, V.S., 2001. The Palaeoproterozoic komatiite-picrite association of Finnish Lapland. Journal of Petology 42: 855-876.

Horn, I., Rudnick, R.L., McDonough, W.F., 2000. Precise elemental and isotope ratio determination by simultaneous solution nebulization and laser ablation-ICP-MS: application to U-Pb geochronology. Chemical Geology 167: 405-425.

Jenner, G.A., Longerich, H.P., Jackson, S.E. and Fryer, B.J., 1990. ICP-MS - a powerful new tool for high precision trace element analysis in earth sciences: evidence from analysis of selected USGS standards. Chemical Geology 83: 133-148.

Jensen, L.S., 1976. A new cation plot for classifying subalkalic volcanic rocks. Ontario Division of Mines Miscellaneous Paper 66.

Kamber, B.S., Moorbath, S., Whitehouse, M.J., 2001. The oldest rocks on Earth: time constraints and geological controversies. *In*: Lewis, L.C., Knell, S.J. (Eds.), The Age of the Earth: From 4004 BC to AD 2002. Geological society of London, Special publication 190: 177-203.

Kamber, B.S., Ewart, A., Collerson, K.D., Bruce, M.C., McDonald, G.D., 2002. Fluid-mobile trace element constraints on the role of slab melting and implications for Archaean crustal growth models. Contributions to Mineralogy and Petrology 144: 38-56.

Kerrich, R., Wyman, D.A., 1997. Review of developments in trace-element fingerprinting of geodynamic settings and their implications for mineral exploration. Australian Journal of Earth Sciences 44: 465-487.

Kerrich, R., Wyman, D., Hollings, P., Polat A., 1999. Variability of Nb/U and Th/La in 3.0 to 2.7 Ga Superior Province ocean plateau basalts: implications for the timing of continental growth and lithosphere recycling. Earth and Planetary Science Letters 168: 101-115.

Kerrich, R., Wyman, D., Hollings, P., Polat A., 2000. Reply to the Comment by Kamber and Collerson on "Variability of Nb/U and Th/La in 3.0 to 2.7 Ga Superior Province ocean plateau basalts: implications for the timing of continental growth and lithosphere recycling". Earth and Planetary Science Letters 177: 341-345.

Ketchum, J.W.F., Jackson, S.E., Culshaw, N.G.,Barr, S.M., 2001. Depositional and tectonic setting of the Paleoproterozoic Lower Aillik Group, Makkovik Province, Canada: evolution of a passive margin-foredeep sequence based on petrochemistry and U-Pb (TIMS and LAM-ICP-MS) geochronology. Precambrian Research 105: 331-356.

King, P.L., White, J.R., Chappell, B.W., Allen, C.M., 1997. Characterization and origin of aluminous A-type granites from the Lachlan Fold Belt, southeastern Australia. Journal of Petology 38: 371-391.

Kinny, P.D., 1987. An ion mircoprobe study of uranium-lead and hafnium isotopes in natural zircon. Ph.D. thesis, Australian National University.

Kinzler R., Grove, T., Recca, S., 1990. An experimental study on the effect of temperature and melt composition on the partitioning of nickel between olivine and silicate melt. Geochimica et Cosmochimica Acta 54:1255-1265.

Komiya, T., Maruyama, S., Hirata, T., Yurimoto, H., Nohda, S., 2004. Geochemistry of the oldest MORB and OIB in the Isua supracrustal belt, southern West Greenland: implications for the composition and temperature of early Archean upper mantle. The Island Arc 13: 47-72.

Košler J. and Sylvester, P., 2003. Present trends and the future of zircon in geochronology: laser ablation ICPMS. *In*: Zircon: Experiments Isotopes, and Trace Element Investigations., Hanchar, J.M., Hoskin, W.O. (Eds), Reviews in Mineralogy and Geochemistry 53: 243-275.

Košler J., Fonneland, H., Sylvester, P., Tubrett, M., Pedersen, R., 2002. U-Pb dating of detrital zircons for sediment provenance studies - a comparison of laser ablation ICPMS and SIMS techniques. Chemical Geology 182: 605-618.

Krogh, T.E., 1982. Improved accuracy of U-Pb ages by the creation of more concordant systems using an air abrasion technique. Geochimicia et Cosmochimica Acta 46: 637-649.

Le Bas, M.J., 2000. IUGS Reclassification of the High-Mg and picritic and volcanic rocks. Journal of Petrology 41: 1467-1470.

Le Maitre, R.W., 2002. Igneous rocks: A classification and glossary of terms, 2nd ed. Cambridge University Press, New York.

Leal, L.G., 1980. Particle motions in a viscous fluid. Annual Review of Fluid Mechanics 12: 435-476.

Longerich, H.P., 1995. The analysis of pressed pellets of geological samples using wavelength dispersive x-ray fluorescence spectrometry. X-Ray Spectrometry 24: 123-136.

Lowe, D.R., Byerly, G.R., Heubeck, C., 1999. Structural divisions and development of the west-central part of the Barberton Greenstone Belt. In: Lowe, D.R., Byerly, G.R. (Eds) Geologic evolution of the Barberton Greenstone Belt, South Africa. Special Paper Geological Society of America 329: 37-82.

Ludwig, K.R., 1993. A computer program for processing Pg-U-Th isotope data, version 1.24, Denver. United States Geological Survey, Open File Report 88-542, 32 pp.

Ludwig, K.R., 1999. Using Isoplot/Ex, Version 2.01: a geochronological toolkit for Microsoft Excel. Berkeley Geochronology Center Special Publication No. 1a, pp 47.

Ludwig, K.R., 2000. Isoplot/Ex: a geochronological toolkit for Microsoft Excel. Berkeley Geochronology Center, California, USA.

Marsh, B.D., Philipp, J.R., 1996. Three-dimensional magmatic filling of Basement sill revealed by unusual crystal concentrations. Antarctic Journal of the United States 31: 39-41.

Martin, H., 1994. Archean grey gneisses and the genesis of continental crust. In: Condie, K.C. (Ed.), Archean crustal evolution. Elesevier Science B.V., New York, pp. 205-261.

McCuaig, T.C., Kerrich, R., Qianli, X., 1994. Phosphorus and high field strength element anomalies in Archean high-magnesian magmas as possible indicators of source mineralogy and depth. Earth and Planetary Science Letters 124: 221-239.

McDonough, W.F., 1990. Constraints on the composition of the continental lithospheric mantle: Earth and Planetary Scientific Letters 101: 1-18.

McDonough, W.F., Frey, F.A., 1989. Rare earth elements in upper mantle rocks. Review in Mineralogy 21: 100-145.

McGetchen, T.R., Pepin, R.O., Phillips, R.J.,1981. Characteristics of primary basaltic magmas. In: Basaltic volcanism study project. Pergamon Press, New York, pp. 409-429.

McGregor, V.R., 1968. Field evidence of very old Precambrian rocks in the Godthåb area, West Greenland. Rapport Grønlands Geologiske Undersøgelse 15: 31-35.
McGregor, V.R., 1969. Early Precambrian geology of the Godthåb area. Rapport Grønlands Geologiske Undersøgelse 19: 28-30.

McGregor, V.R., 1973. The early Precambrian gneisses of the Godthåb district, West Greenland. Philosophical Transactions of the Royal Society, London A273: 345-358.

McGregor, V.R., 1984. Geological map of Greenland, 1:100 000, Qôqut, 64 V.1. Syd, with descriptive text. Grønlands Geologiske Undersøgelse, Copenhagen.

McGregor, V.R., Mason, B., 1977. Petorgenesis and geochemistry of metabasaltic and metasedimentary enclaves in the Amîtsoq gneisses, West Greenland. American Mineralogist 62: 887-904.

McGregor, V.R., Friend, C.R.L., Nutman, A.P., 1991. The late Archaean mobile belt through Godthåbsfjord: A continent-continent collision zone? Bulletin of the Geological Society of Denmark 39: 179-197.

McLennan, S.M., Taylor, S.R., 1984. Archaean sedimentary rocks and their relation to the composition of the Archaean continental crust. In: A. Kroner, et al. (Editor), Archaean Geochemistry. Springer, New York, pp. 47-72.

Michard-Vitrac, A., Lancelot, J., Allègre, C.J., Moorbath, S., 1977. U-Pb ages on single zircons from the early Precambrian rocks of West Greenland and the Minnesota River Valley. Earth and Planetary Science Letters 35: 449-453.

Mojzsis, S.J., Arrhenius, G., McKeegan, K.D., Harrison, T.M., Nutman, A.P., Friend, C.R.L., 1996. Evidence for life on Earth before 3800 million years ago. Nature 384: 55-59.

Moorbath, S., Pankhurst, R.J., 1976. Further rubidium-strontium age and isotopic evidence for the nature of the late Archaean plutonic event in West Greenland. Nature 262: 124-126.

Moorbath, S., O'Nions, R.K., Pankhurst, R.J., 1975. The evolution of early Precambrian crustal rocks at Isua, West Greenland-geochemical and isotopic evidence. Earth and Planetary Science Letters 27: 229-239.

Moorbath, S., Taylor, P.N., Goodwin, R., 1981. Origin of granitic magma by crustal remobilisation: Rb-Sr and Pb/Pb geochronology and isotope geochemistry of the late Archaean Qôrqut granite complex of southern West Greenland. Geochemica et Cosmochimica Acta 45: 1051-1060.

Moorbath, S., O'Nions, R.K., Pankhurst, R.J., Gale, N.H., McGregor, V.R., 1972. Further rubidium-strontium age determinations on the very early Precambrian rocks of the Godthåb district: West Greenland. Nature 240: 78-82.

Murton, B.J., Peate, D.W., Arculus, R.J., Pearce, J.A., van der Laan, s., 1992. Trace element geochemistry of volcanic rocks from Site 786: the Izu-Bonin forearc. In: Fryer, P., Pearce, J.A., Stokking, L.B., et al. (Eds), Proceedings for the ocean drilling program. Scientific Results 125: 211-235.

Myers, J.S., 1985. Stratigraphy and structure of the Fiskenaesset Complex, southern West Greenland. Bulletin Grønlands Geologiske Undersøgelse 150.

Myers, J.S., 2001. Protoliths of the 3.7-3.8 Ga Isua greenstone belt, West Greenland. Precambrian Research 105: 129-141.

Myers, J.S., Crowley, J.L., 2000. Vestiges of life in the oldest Greenland rocks? A review of early Archean geology in the Godthåbsfjord region, and reappraisal of field evidence for > 3850 Ma life on Akilia. Precambrian Research 103: 101-124.

Nesbitt, H.W., Young, G.M., 1989. Formation and diagenesis of weathering profiles. Journal of Geology 97: 129-147.

Nisbet, E.G., 1987. The young Earth; An introduction to Archaean geology. Allen & Unwin, London, United Kingdom.

Nisbet, E.G., Cheadle, M.J., Arndt, N.T., Bickle, M.J., 1993. Constraining the potential temperature of the Archean mantle: A review of the evidence from komatiites. Lithos 30: 291-307.

Nutman, A.P., 1997. The Greenland sector of the North Atlantic Craton. In: de Wit, M., Ashwal, L. D. (Eds.), Greenstone Belts, Oxford monographs on geology and geophysics No.35. Oxford University Press, Oxford, pp. 665-674.

Nutman, A.P., Bridgwater, D., 1983. Deposition of Malene supracrustal rocks on an Amîtsoq basement in outer Ameralik, southern West Greenland. Rapport Grønlands Geologiske Undersøgelse 112: 43-52.

Nutman, A.P., Friend, C.R.L., Bennett, V.C., 2002. Evidence for 3650-3600 Ma assembly of the northern end of the Itsaq Gneiss Complex, Greenland: Implication for early Archean Tectonics. Tectonics 21: 1-28.

Nutman, A.P., Friend, C.R.L., Baadsgaard, H., McGregor, V.R., 1989. Evolution and assembly of Archaean gneiss terranes in the Godthåbsfjord region, southern West Greenland:Structural, metamorphic and isotopic evidence. Tectonics 8: 573-589.

Nutman, A.P., McGregor, V.R., Friend, C.R.L., Benett, V.C., Kinny, P.D., 1996. The Itsaq Gneiss Complex of southern West Greenland; the world's most extensive record of early crustal evolution (3900-3600 Ma). Precambrian Research 78: 1-39.

Palmer, A.R., 1983. The Decade of North American Geology 1983 geologic time scale. Geology (Boulder) 11: 503-504.

Pankhurst, R.J., Moorbath, S., McGregor, V.R., 1973. Late event in the geological evolution of the Godthaab district, West Greenland. Nature 243: 24-26.

Park, J. F. W., 1986. Fault systems in the Inner Godthåbsfjord region of the Archaean Block, southern West Greenland. PhD thesis, University of Exeter, Exeter, UK.

Parrish, R.R., 1987. An improved micro-capsule for zircon dissolution in U-Pb geochronology. Chemical Geology 66: 99-102.

Passchier, C.W., Trouw, R.A.J., 1996. Microtectonics. Springer, New York.

Pearce, J.A., Baker, P.E., Harvey, P.K., Luff, I.W., 1995. Geochemical evidence for subduction fluxes, mantle melting and fractional crystallization beneath the South Sandwich Island Arc. Journal of Petrology 36: 1073-1109.

Percival, J.A., Stern, R.A., Skulski, T., 2001. Crustal growth through successive arc magmatism, northeastern Superior Province, Canada. Precambrian Research 109: 203-238.

Philpotts, A.R., 1990. Principles of Igneous and Metamorphic Petrology. Prentice Hall, New Jersey.

Polat, A., Hofmann, A.W., 2003. Alteration and geochemical patterns in the 3.7-3.8 Ga Isua greenstone belt, West Greenland. Precambrian Research 126: 197-218.

Polat, A., Hofmann, A.W., Rosing, M.T., 2002. Boninite-like volcanic rocks in the 3.7-3.8 Ga Isua greenstone belt, West Greenland: geochemical evidence for intra-oceanic subduction zone processes in the early Earth. Chemical Geology 184: 231-254.

Polat, A., Kerrich, R., Wyman, D.A., 1999. Geochemical diversity in oceanic komatiites and basalts from the late Archean Wawa greenstone belts, Superior Province, Canada: trace element and Nd isotope evidence for a heterogeneous mantle. Precambrian Research 94: 139-173.

Potts, P.J., 1987. Handbook of Silicate Rock Analysis. Blackie, 602 p.

Poujol, M., Anhaeusser, C.R., Armstrong, R.A., 2002. Episodic granitoid emplacement in the Archaean Amalia-Kraaipan terrane, South Africa: confirmation from single zircon U-Pb geochronology. Journal of African Earth Sciences. 35: 147-161.

Révillon, S., Arndt, N.T., Chauvel, C., Hallot, E., 2000. Geochemical study of ultramafic volcanic and plutonic rocks from Gorgona Island, Colombia: the plumbing system of an oceanic plateau. Journal of petrology 41: 1127-1153.

Robertson, S., 1985. Late Archaean crustal evolution in the Ivisârtoq region, southern West Greenland. PhD thesis, University of Exeter, Exeter, UK.

Rollinson, H., 1993. Using geochemical data: evaluation, presentation, interpretation. Addison Wesley Longman Limited, Harlow, England.

Rosing, M.T.,1999. 13C-depleted carbon microparticles in >3700-Ma sea-floor sedimentary rocks from West Greenland. Science 283: 674-676.

Rosing, M.T., Rose, N.M., Bridgwater, D., Thomsen, H.S., 1996. Earliest part of Earth's stratigraphic record: A reappraisal of the >3.7 Ga Isua (Greenland) supracrustal sequence. Geology 24: 43-46.

Saverikko, M., 1985. The pyroclastic komatiite complex at Sattasvaara in northern Finland. Bulletin, Geological Survey of Finland 57: 55-87.

Schiøtte, L., Compston, W., Bridgwater, D., 1988. Late Archaean ages for the deposition of clastic sediments belonging to the Malene suparcrustals, southern West Greenland: Evidence from an ion probe U-Pb zircon study. Earth and Planetary Science Letters 87: 45-58.

Schiøtte, L., Compston, W., Bridgwater, D., 1989. U-Pb single-zircon age for the Tinissaq gneiss of southern West Greenland: A controversy resolved. Chemical Geology 79: 21-30.

Shervais, J.W., 1982. Ti-V plots and the petrogenesis of modern and opholitic lavas. Earth and planetary science letters 59: 101-118.

Smith, M.S., Dymek, R.F., Chadwick, B., 1992. Petrogenesis of Archaean Malene supracrustal rocks, NW Buksefjorden region, West Greeland: geochemical evidence for highly evolved Archaean crust. Precambrian Research 57: 49-90.

Sproule, R.A., Lesher, C.M., Ayer, J.A., Thurston, P.C., Herzberg, C.T., 2002. Spatial and temporal variations in the geochemistry of komatiites and komatiitic basalts in the Abitibi greenstone belt. Precambrian Research 115: 153-186.

Stacey, J.S., Kramers, J.D., 1975. Approximation of terrestrial lead isotope evolution by a two stage model. Earth Planetary Letters 26: 207-221.

Sun, S.S., McDonough, W.F., 1989. Chemical isotopic systematics of ocean basalts, implications for mantle compositions and processes. *In*: Saunders, A.D., Norry, M.J. (Eds.), Magmatism in ocean basins: Geological Society of London Special Publication 42: 313-345.

Taylor, P.N., Moorbath, S., Goodwin, R., Petrykowski, A.C., 1980. Crustal contamination as an indicator of the extent of early Archaean continental crust: Pb isotopic evidence from the late Archaean gneisses of West Greenland. Geochimica et Cosmochemica Acta 44:1437-1453.

Taylor, S.R., McLennan, S.M., 1985. The continental crust: its composition and evolution. Blackwell, Oxford, 321 pp.

Tilton, G.R., 1960. Volume diffusion as a mechanism for discordant lead ages. Journal of Geophysical Research 65: 2933-2945.

Tomlinson, K.Y., Hughes D.J., Thurston, P.C., Hall, R.P., 1999. Plume magmatism and crustal growth at 2.9 to 3.0 Ga in the Steep Rock and Lumpy Lake area, Western Superior Province. Lithos 46: 103-136.

Tomlinson, K.Y., Stevenson, R.K., Hughes, D.J., Hall, R.P., Thurston, P.C., Henry, P., 1998. The Red Lake greenstone belt, Superior Province: evidence of plume-related magmatism at 3 Ga and evidence of an older enriched source. Precambrian Research 89: 59-76.

Vavra, G., 1993. A guide to quantitative morphology of accessory zircon. Chemical Geology. 110: 90-99.

Walton, B.J., 1976. Mapping of Archaean rocks in the inner Godthåbsfjord region. Rapport Grønlands Geologiske Undersøgelse 80: 72-77.

Wetherill, G.W., 1956. Discordant uranium-lead ages. Transactions – American Geophysical Union 37: 320-327.

Whitehouse, M.J., Kamber, B.S., and Moorbath, S., 1999. Age significance of U-Th-Pb zircon data from early Archaean rocks of west Greenland - a reassessment based on combined ion-microprobe and imaging studies. Chemical Geology 160: 201-224.

Wiedenbeck, M., Alle, P., Corfu, F., Griffin, W.L., Meier, M., Oberli, F., von Quadt, A., Roddick, J.C., and Spiegel, W., 1995. Three natural zircon standards for U-Th-Pb, Lu-Hf, trace element and REE analysis. Geostandards Newsletter. 19, 1-23.

Wiedenbeck, M., Hancher, J.M., Peck, W.H., Sylvester, P., Valley, J., Whitehouse, M., Kronz, A., Morishita, Y., Nasdala, L., 2004. Further Characterisation of the 91500 zircon crystal. Geostandards and geoanalytical research 28: 9-39.

Wilson, M., 1989. Igneous petrogenesis. Unwin Hyman, London.

Winchester, J.A., Floyd, P.A., 1977. Geochemical discrimination of different magma series and their differentiation products using immobile elements. Chemical Geology 20: 325-343.

Wooden, J.L., Czamanske, G.K. Fedorenko, V.A., Arndt, N.T. Chauvel, C., Bouse, R.M., King, B.W., Knight, R.J., Siems, D.F., 1993. Isotopic and trace-element constraints on mantle and crustal contributions to Siberian continental flood basalts, Noril'sk area, Siberia. Geochimica et Cosmochimica Acta 57: 3677-3704.